8-2012

Shape Memory Assisted Self Healing (Smash) Polymeric and Composite Systems

Erika D. Rodriguez
Syracuse University

Recommended Citation

Rodriguez, Erika D., "Shape Memory Assisted Self Healing (Smash) Polymeric and Composite Systems" (2012). *Mechanical and Aerospace Engineering - Dissertations*. 73.
https://surface.syr.edu/mae_etd/73

SHAPE MEMORY ASSISTED SELF HEALING (SMASH) POLYMERIC AND COMPOSITE SYSTEMS

ABSTRACT

by

Erika D. Rodriguez

My research aims to develop a novel approach that uses the shape memory (SM) effect to aid self healing (SH) polymeric systems that are able to simultaneously close and re-bond cracks with a single thermal stimulus. This new concept is termed *shape memory assisted self healing* (SMASH). Additionally, a new type of shape memory termed reversible plasticity shape memory (RPSM) was also developed where both the elastic and plastic deformation found after deformation completely recover upon a thermal stimulation. I aim to utilize a broad range of polymeric and composite systems that include a single phase semi-crystalline system, a single phase amorphous blend, and a combination of these two polymers in a composite elastomer system to prove the versatility of the SMASH and RPSM effects.

Chapter 1 gives a polymer science background along with SM and SH material overview. **Chapter 2** discusses the fabrication and analysis of miscible blends that show the SMASH and RPSM effect using a semi-crystalline polymer, poly(ε-caprolactone) (PCL) to construct a SM PCL network (n-PCL) and PCL thermoplastic used as the SH agent (l-PCL). The PCL thermoplastic SH agent interpenetrated the n-PCL for form a single phase semi interpenetrating polymer network (SIPN). Films were made for testing to prove the SM and SH effects by varying the amount of SM network and SH agent to optimize both effects. Thermo-mechanical, tensile, and SH experiments were conducted to study the fixing, recovery and healing properties

of the polymeric system. **Chapter 3** focuses on a unique system for the fabrication of clear thin SMASH SIPN coatings that were developed for optical industrial applications. Here, an amorphous polymer composition, poly(tert-butyl acrylate) (poly(tBA)), was used in a blend of two forms, a network form for shape memory (n-tBA) and a linear form for self-healing (l-tBA), that, together, form a single phase SIPN. Thermal, thermo-mechanical, SM and SH scratch experiments were conducted to investigate both SM and SH mechanisms as influenced by the relative concentrations of n-tBA and l-tBA in the SIPN materials. **Chapter 4** introduces for the first time an innovative smart polymeric soft material where aligned nanofibers are used to construct anisotropy embedded in an elastomeric matrix. This system, termed "Anisotropic Shape Memory Elastomeric Composite" (A-SMEC) was investigated for RPSM and SMASH properties. In addition, the anisotropic mechanical and shape memory properties were investigated and interpreted in light of the underlying structure. **Chapter 5** builds upon the results of Chapter 4, presenting the fabrication and testing of laminated A-SMEC biomorphs that were designed to exploit anisotropic in RPSM behavior to yield predictably curled and twisted structures upon deformation. More specifically, the out-of-plane curvature and pitch were analyzed as a function of biomorph orientational lay-up. All polymeric systems described in this dissertation are examples of smart polymers that can be used to tailor mechanical performance while introducing new phenomena, such as self-healing, RPSM, and stretch-induced twisting. **Chapter 6** discusses the conclusions followed by future work that are sub-sectioned for each chapter of the dissertation.

SHAPE MEMORY ASSISTED SELF HEALING (SMASH) POLYMERIC AND COMPOSITE SYSTEMS

by

Erika D. Rodriguez

B.S., Smith College, 2006
M.S., Syracuse University, 2008

DISSERTATION
Submitted in partial fulfillment of the requirements for the
degree of Doctor of Philosophy in Mechanical and Aerospace Engineering.

Syracuse University
August 2012

To my parents and brother

Jesse Sr., Maria, and Jesse Jr. Rodriguez

for believing in me and being my #1 FANS!

ACKNOWLEDGMENTS

I first would like to thank my advisor, Dr. Mather, who believed in me and never gave up on me. Dr. Mather has given me the opportunity to travel the world to not only present my research work, but to also learn from the science community on an international level. He has given me the tools to reach my greatest potential both as a student and as a professional engineer. Dr. Mather has been a great role model and it is because of him that my standards are so ever high. I have learned to have a great work ethic and be passionate in my work. He has inspired me to work harder and set high expectations and standards for myself in order to do great work and go beyond the limits to succeed in all I did as a graduate student. These values will go beyond as a graduate student and will carry on through my professional career. Thank you for your support and guidance through my academic career as a graduate student. I loved the work I did as a graduate student. Thank you for such a rewarding experience.

I would also like to acknowledge and thank my mentor, Dr. Luo, for truly being one of the best mentors I have had during my academic career. Dr. Luo never gave up on me and was patient with me through every step. His wealth of knowledge, and to do great work was contagious. His passion for learning and teaching has given me a great example of a true scientist and engineer. His knowledge to critically think through problems was such a learning experience and a rewarding experience. I am honored to work under his mentorship.

I also would like to thank my dissertation committee, Dr. Glauser, Dr. Gilbert, Dr. Hasenwinkel, Dr. Henderson and Dr. Levy, for their support and guidance through my research progress. Your contributions has given me an indepth science foundation to my research.

I especially, would like to thank Dr. Levy for his support, guidance and patience for helping me study for my qualifying exams.

I would also like to recognize Lou Buda, Charles Brown, Phil Arnold, and Lester Schmutzler from the Physics Machine for their creative expertise and workmanship in constructing engineer tools for my research investigations.

I also would like to acknowledge Mike Brandt from the Electronic Shop for his expertise is all things electronic and for constructing instruments for my research experiments.

I also would not have been able to do my graduate work without the support from my graduate research colleagues, Bonifacio Alvarado, Richard M Baker, Dr. Taekwoong Chung, Kevin Davis, Bin Deng, Dr. Eric Benjamin Finkelstein, Xinzhu Gu, Qiongyu Guo, Morteza Haeri, Kayla Rhea Huffman, Christian Iversen, Dr. Kazuki Ishida, Hossein Birjandi Nejad, Eric S Ouellette, Kiran Kuriakose Simon, Abhendra Kumar Singh, Amir Torbati, Pushkar Varde, Jian Wu, Pine Yang, and Chengjun Zhu. Thank you for your collaboration, expertise and brainstorming sections.

I would also like to acknowledge all my undergraduate students, Sabrina M. Kowalski, Stephanie Dorta-Quiñones, Elizabeth A Matessino, and Derek Charles Weed, for their assistance in working with me on my experiments. I appreciate all your efforts and science contribution to my research. I would also like recognize Maria Mintskovsky, my high school student, who also assisted me in experiments. I appreciated her diligence and motivation to get the job done.

I would also like to thank Michelle E Lissner, Karen P. Low, Sabrina M. Kowalski, Kathleen J Datthyn-Madigan, Claudia Maria Aguilar Tabora, and Kimberly Drumm-Underwood for all their support and in assisting me through my graduate studies.

Most importantly, I would like to recognize the financial contributors who supported me through my research studies: Syracuse University in the form of a Science, Technology, Engineering and Mathematics (STEM) fellowship, AFRL SBIR, (Contract No. FA8651-07-C-0105), and Materials World Network, National Science Foundation (DMR-0758631).

Foremost, I have to thank my friends, my crazy Mexican familia (i.e. Mexican FBI), and my confidant for such a strong and supportive presence in my life and for being my #1 FANS! You have given me the encouragement and motivation to keep going and never give up.

TABLE OF CONTENTS

LIST OF TABLES xvii

LIST OF SCHEMES xxi

LIST OF FIGURES xxv

CHAPTER 1: INTRODUCTION 1

1.0 RESEARCH MOTIVATION 1

1.1 BACKGROUND 2

1.1.1 INTRODUCTION TO POLYMER SCIENCE 2

1.1.2 POLYMER STRUCTURE 3

1.1.3 POLYMER CLASSIFICATION 4

1.2 POLYMER MECHANICAL PROPERTIES 4

1.3 SHAPE MEMORY (SH) EFFECT IN POLYMERS 5

1.4 EXAMPLES OF SHAPE MEMORY POLYMERIC SYSTEMS 8

1.5 SELF HEALING IN POLYMERIC AND COMPOSITE SYSTEMS 11

1.5.1 INTRINSIC BASED SH MATERIALS 12

1.5.2 MICROENCAPSULATED SH MATERIALS 13

1.5.3 VASCULAR SH MATERIALS 14

1.6 FIBER REINFORCED POLYMER FABRICATION TECHNIQUES (ELECTROSPINNING) 15

1.7 MECHANICS OF FIBER REINFORCED POLYMERIC COMPOSITES 16

1.8 DISSERTATION OVERVIEW 18

1.9 REFERENCES 21

CHAPTER 2: LINEAR/NETWORK POLY(ε-CAPROLACTONE) BLENDS EXHIBITING SHAPE MEMORY ASSISTED SELF-HEALING (SMASH) 38

2.0 SYNOPSIS 38

2.1 INTRODUCTION 39

2.2 EXPERIMENTAL SECTION 44

2.2.1 MATERIALS 44

2.2.2 POLY(ε-CAPROLACTONE) DIACRYLATE SYNTHESIS 44

2.2.3 l-PCL:n-PCL MISCIBLE BLENDS 45

2.2.4 DEGREE OF SHAPE MEMORY NETWORK FORMATION 46
2.2.5 THERMAL CHARACTERIZATION 47
2.2.6 DYNAMIC MECHANICAL AND SHAPE MEMORY ANALYSES 47
2.2.7 SELF HEALING EXPERIMENTATION 49
2.3 RESULTS AND DISCUSSION 50
2.3.1 PREPARATION AND THERMAL ANALYSIS OF NETWORKS 50
2.3.2 DYNAMIC MECHANICAL ANALYSIS OF l-PCL:n-PCL NETWORKS 52
2.3.3 SHAPE MEMORY (SM) CHARACTERIZATION 53
2.3.4 SELF-HEALING (SH) CHARACTERIZATION 55
2.3.5 SELF HEALING EFFICIENCY ANALYSIS 57
2.4 DISCUSSION 58
2.4.1. FIVE STAGE OF HEALING 59
2.5 CONCLUSIONS 60
2.6 REFERENCES 62
CHAPTER 3: POLY(TERT–BUTYLACRYLATE) (poly(tBA)) COATINGS FOR SCRATCH REPAIR VIA SHAPE MEMORY ASSISTED SELF HEALING (SMASH) 94
3.0 SYNOPSIS 94
3.1 INTRODUCTION 94
3.2 EXPERIMENTAL METHODS 101
3.2.1 MATERIALS 101
3.2.2 tBA THERMOPLASTIC SYNTHESIS 102
3.3 FILM FABRICATION 103
3.3.1 l-tBA:n-tBA FILM FABRICATION 103
3.3.2 DEGREE OF SHAPE MEMORY NETWORK FORMATION 104
3.3.3 THERMOGRAVIMETRIC ANALYSIS (TGA) 105
3.3.4 DIFFERENTIAL SCANNING CALORIMETRY (DSC) STUDIES 105
3.3.5 DYNAMIC MECHANICAL ANALYSIS (DMA) 105
3.3.6 REVERSIBLE PLASTICITY SHAPE MEMORY (RPSM) CHARACTERIZATION 106
3.3.7 ONE WAY SHAPE MEMORY (1WSM) CHARACTERIZATION 107
3.4 COATING FABRICATION 108

3.4.1 CLEANING GLASS SLIDES VIA PIRANHA SOLUTION 108
3.4.2 SILANIZATION OF GLASS SLIDES 109
3.4.3 l-tBA:n-tBA COATING FABRICATION 110
3.4.4 OPTICAL MICROSCOPY (OM) AND SELF HEALING (SH) STUDIES...... 110
3.4.5 LIGHT TRANSMISSION STUDIES............ 112
3.5 RESULTS AND DISCUSSION 113
3.5.1 tBA THERMOPLASTIC SYNTHESIS 113
3.5.2 l-tBA:n-tBA FILM FABRICATION............ 113
3.5.3 DEGREE OF SHAPE MEMORY NETWORK FORMATION 114
3.5.4 THERMOGRAVIMETRIC ANALYSIS (TGA) 114
3.5.5 DIFFERENTIAL SCANNING CALORIMETRY (DSC) STUDIES 115
3.5.6 DYNAMIC MECHANICAL ANALYSIS (DMA) 116
3.5.7 REVERSIBLE PLASTICITY SHAPE MEMORY (RPSM) CHARACTERIZATION……………………………………………………………118
3.5.8 ONE WAY SHAPE MEMORY (1WSM) CHARACTERIZATION 119
3.6 l:n-tBA COATING FABRICATION 121
3.6.1 CLEANING GLASS SLIDES VIA PIRANHA SOLUTION 121
3.6.2 SILANIZATION OF GLASS SLIDES 121
3.6.3 l:n-tBA COATING FABRICATION 121
3.6.4 OPTICAL MICROSCOPY (OM) AND SELF HEALING (SH) STUDIES...... 122
3.6.5 LIGHT TRANSMISSION STUDIES............ 123
3.7 CONCLUSIONS............ 124
3.8 REFERENCES 126
CHAPTER 4: FABRICATION AND MECHANICAL TESTING OF SINGLE PLY ANISOTROPIC SHAPE MEMORY ELASTOMERIC COMPOSITES (A-SMEC) 169
4.0 SYNOPSIS............ 169
4.1 INTRODUCTION 170
4.2 EXPERIMENTAL SECTION 175
4.2.1 MATERIALS AND SAMPLE FABRICATION 175
4.2.2 MICROSTRUCTURAL CHARACTERIZATION………………………..... 176
4.2.3 DYNAMIC MECHANICAL ANALYSIS 177

4.2.4 MECHANICAL TESTING 177
4.2.5 SHAPE MEMORY ANALYSIS 179
4.3 RESULTS AND DISCUSSION 180
4.3.1 SAMPLE FABRICATION 180
4.3.2 DYNAMIC MECHANICAL ANALYSIS OF COMPOSITES 181
4.3.3 MECHANICAL TESTING CHARACTERIZATION 182
4.3.4 SHAPE MEMORY CHARACTERIZATION 186
4.4 CONCLUSION 189
4.5 REFERENCES 190
CHAPTER 5: LAMINATED ANISOTROPIC SHAPE MEMORY ELASTOMERIC COMPOSITES (A-SMEC): FABRICATION AND MECHANICALLY ACTIVATED SHAPE CHANGE (MASC) 220
5.0 SYNOPSIS 220
5.1 INTRODUCTION 220
5.1.1 MECHANICS OF LAMINATED COMPOSITES 220
5.1.2 ANISOTROPY IN LAMINATED COMPOSITES 222
5.1.3 ANISOTROPY IN BIOLOGICAL SYSTEMS 226
5.2 EXPERIMENTAL METHOD 229
5.2.1 MATERIALS 229
5.2.2 MATERIALS AND SINGLE PLY COMPOSITE FABRICATION 229
5.2.3 LAMINATED COMPOSITE FABRICATION 230
5.2.4 REVERSIBLE PLASTICITY SHAPE MEMORY (RPSM) 231
5.2.5 MECHANICAL TESTING 232
5.2.6 DEFORMATION AND SHAPE MEMORY RECOVERY ANALYSIS 233
5.2.7 CURVATURE AND PITCH ANALYSIS 234
5.3 RESULTS AND DISCUSSION 234
5.3.1 COMPOSITE SHEET FABRICATION 234
5.3.2 LAMINATED COMPOSITE FABRICATION 235
5.3.3 REVERSIBLE PLASTICITY SHAPE MEMORY (RPSM) 236
5.3.4 MECHANICAL TESTING AND MECHANICALLY ACTIVATED SHAPE CHANGE (MASC) 240
5.3.5 DEFORMATION AND SHAPE MEMORY RECOVERY ANALYSIS 243

5.3.6 CURVATURE AND PITCH ANALYSIS 243
5.4 CURVATURE MODELING 246
5.5 CONCLUSIONS 250
5.5 REFERENCES 251
CHAPTER 6: CONCLUSIONS AND FUTURE DIRECTIONS 289
6.0 OVERALL CONCLUSIONS 289
6.1 SINGLE PHASE SEMI-CRYSTALLINE POLYMERIC SMASH SYSTEMS 289
6.1.1 CONCLUSIONS 289
6.1.2 FUTURE DIRECTIONS 290
6.1.2.1 WATER IMMERSION STUDIES 290
6.1.2.2 HEALING KINETICS STUDIES 292
6.1.2.3 PUNCTURE TESTING 294
6.1.2.4 REVERSIBLE ADHESIVE STUDIES 295
6.1.2.5 SURFACE REVERSIBLE PLASTICITY STUDIES 297
6.1.2.6 SMALL ANGLE LIGHT SCATTERING (SALS) STUDIES 298
6.1.2.7 TACK STUDIES 299
6.1.2.8 T-PEEL TESTS 300
6.1.2.9 LAP SHEAR STUDIES 301
6.1.2.10 l-PCL:n-PCL SMASH COATINGS 302
6.1.2.11 HEALED CRACK REOPENING STUDIES 303
6.1.2.12 CRITICAL LIGAMENT WIDTH STUDIES 304
6.2 SINGLE PHASE AMORPHOUS POLYMERIC SMASH COATINGS 305
6.2.1 CONCLUSIONS 305
6.2.2 FUTURE DIRECTIONS 305
6.2.2.1 POLY(TERT-BUTYL ACRYLATE) (poly(tBA)):POLY(BUTYL ACRYLATE) (poly(BA)) COPOLYMER SMASH COATINGS........305
6.2.2.2 HEALING OF CRAZING 307
6.2.2.3 FILM SELF HEALING STUDIES 308
6.3 ANISOTROPIC SHAPE MEMORY COMPOSITES (A-SMEC) SYSTEMS 309
6.3.1 CONCLUSIONS 309
6.3.2 FUTURE DIRECTION 309

6.3.2.1 SELF HEALING STUDIES........ 309
6.3.2.2 FRACTURE MECHANICS STUDIES........ 311
6.3.2.3 TRIPLE SHAPE MEMORY STUDIES........ 312
6.3.2.4 AERODYNAMIC STUDIES........ 313
6.3.2.5 MECHANICAL MODELING........ 314
6.3.2.6 STRAIN INDUCED CRYSTALLIZATION STUDIES........ 315
6.4 ANISOTROPIC SHAPE MEMORY COMPOSITES (A-SMEC) LAMINATED COMPOSITES........ 315
6.4.1 CONCLUSIONS........ 315
6.4.2 FUTURE DIRECTION........ 316
6.4.2.1 LAMINATED COMPOSITES USING VARIOUS ANGLES........ 316
6.4.2.2 MULTI-LAYERED LAMINATED COMPOSITES........ 317
6.4.2.3 VARIABLE STRAIN INDUCED CURVATURE AND PITCH STUDIES........ 318
6.4.2.4 MECHANICAL MODELING........ 318
6.4.2.5 SPIRAL HANDEDNESS STUDIES........ 319
6.4.2.6 SPIRAL VS. SAMPLE WIDTH STUDIES........ 319
6.5 OTHER SYSTEMS........ 320
6.5.1 PCL/EPOXY SELF HEALING STUDIES........ 320
6.5.2 SMASH SYSTEM WITH TWO THERMAL TRANSITIONS STUDIES........ 322
6.5.3 SMASH HYDROGELS STUDIES........ 322
6.6 REFERENCES........ 324
APPENDIX 1: LINEAR/NETWORK POLY(ε-CAPROLACTONE) BLENDS WITH SHAPE MEMORY ASSISTED SELF-HEALING (SMASH)........ 326
A1.0 SUMMARY........ 326
A1.1 WATER IMMERSION STUDIES........ 327
A1.2 HEALING KINETICS STUDIES USING DIFFERENT PCL THERMOPLASTIC MOLECULAR WEIGHTS (M_w)........ 331
A1.3 PUNCTURE TESTING STUDIES........ 336
A1.4 REVERSIBLE ADHESIVE STUDIES........ 343
A1.5 SURFACE REVERSIBLE PLASTICITY STUDIES........ 344

A.1.6 SMALL ANGLE LIGHT SCATTERING (SALS) STUDIES 349

A1.7 TACK STUDIES 353

A1.8 T-PEEL STUDIES 356

A1.9 LAP SHEAR STUDIES 357

A1.10 TWO WAY SHAPE MEMORY (2WSM) 358

A1.11 POLY(ε-CAPROLACTONE) (PCL) THERMOPLASTIC SM STUDIES 359

APPENDIX 2: AMORPHOUS SMASH SYSTEM 360

A.2 SUMMARY 360

A2.1 POLY(TERT-BUTYL ACRYLATE) (poly(tBA)):POLY(BUTYL ACRYLATE) (poly(BA)) COPOLYMER SMASH COATING STUDIES 361

A2.2 CRAZING STUDIES USING l:n-tBa SMASH FILMS 365

A2.3 SELF HEALING (SH) STUDIES USING l:n-tBa SMASH FILMS 372

APPENDIX 3: ANISOTROPIC SHAPE MEMORY COMPOSITES (A-SMEC) SYSTEMS (PVAc/Sylgard 184) 375

A.3 SUMMARY 375

A3.1 ANISOTROPIC SHAPE MEMORY COMPOSITES (A-SMEC) SYSTEMS (PVAc/SYLGARD 184) 376

A3.2 AERODYNAMIC STUDIES 378

APPENDIX 4: ANISOTROPIC SHAPE MEMORY COMPOSITES (A-SMEC) LAMINATED COMPOSITES: POLY(VINYL ACETATE) (PVAc)/SYLGARD184 382

A.4 SUMMARY 382

A4.1 ANISOTROPIC SHAPE MEMORY COMPOSITES (A-SMEC) LAMINATED COMPOSITES: POLY(VINYL ACETATE) (PVAc)/SYLGARD184 383

APPENDIX 5: POLY (ε-CAPROLACTONE) (PCL)/EPOXY COMPOSITE SH STUDIES 391

A.5 SUMMARY 391

A5.1 POLY(ε-CAPROLACTONE) (PCL)/EPOXY COMPOSITE SELF HEALING (SH) STUDIES 392

APPENDIX 6: POLY(BUTYL METHACRYLATE) (PBMA):POLY(METHYL METHACRYLATE) (PMMA) SMASH T_g BASED COATING 399

A6.1 INTRODUCTION 399

A6.1.2 SAMPLE PREPARATION AND CHARACTERIZATION 400

A6.1.3 THERMAL CHARACTERIZATION 401

A6.1.4 THERMOMECHANICAL CHARACTERIZATION 402

A6.1.5 SCRATCH TESTING 402

A6.1.6 CONCLUSIONS 404

A6.1.7 REFERENCES 404

A6.1.8 FIGURES 405

APPENDIX 7: ANISOTROPIC SHAPE MEMORY ELASTOMERIC COMPOSITE (A-SMEC): POLY(ε-CAPROLACTONE) (PCL)/SYLGARD184 430

A7.0 SUMMARY 430

A7.1 ANISOTROPIC SHAPE MEMORY ELASTOMERIC COMPOSITE (A-SMEC) PCL(M_w~48k)/SYLGARD184 431

A7.2 ANISOTROPIC SHAPE MEMORY ELASTOMERIC COMPOSITE (A-SMEC) PCL(M_w~48k)/SYLGARD184 ASMEC vs SMEC DATA COMPARISON 453

A7.3 ANISOTROPIC SHAPE MEMORY ELASTOMERIC COMPOSITE (A-SMEC) PCL(M_w~65k)/SYLGARD184 ASMEC 461

APPENDIX 8: PCL:PEG WATER TRIGGERED SMASH SYSTEMS 475

A8.0 SUMMARY 475

A8.1 PCL:PEG WATER TRIGGERED SMASH SYSTEMS 476

APPENDIX 9: l-PEO:n-PEG SMASH SYSTEM 497

A.9.0 SUMMARY 497

A9.1 l-PEO(100k):n-PEG(2k) SMASH SYSTEM 498

APPENDIX 10: SYLGARD 184 CURING KINETICS 500

A10.0 SUMMARY 500

A10.1 SYLGARD 184 CURING KINETICS 501

APPENDIX 11: SHAPE MEMORY ELASTOMERIC COMPOSITE (SMEC) TO ANISOTROPIC SHAPE MEMORY ELASTOMERIC COMPOSITE (A-SMEC) 520

A11.0 SUMMARY 520

A11.1 SHAPE MEMORY ELASTOMERIC COMPOSITE (SMEC) TO ANISOTROPIC SHAPE MEMORY ELASTOMERIC COMPOSITE (A-SMEC) 521

APPENDIX 12: DERIVATION OF LAMINATED COMPOSITE STRIP CURVATURE 524

12.1 REFERENCES 535

VITA 536

LIST OF TABLES

Table 2-1. Gel fraction (G(%)) averages of three samples tested for each composition.

Table 2-2. Chart showing the onset degradation temperature of all compositions tested using a TA Q500 Thermogravimetric Analyzer (TGA) where each sample was heated to 600 °C at 10 °C/min. PCL Diacrylate(3k)$_{100}$ and PCL(65k)$_{100}$ are shown for comparison.

Table 2-3. Table showing averages of the melting (T_m) and crystalline (T_c) temperatures, the heat of melting (ΔH_m) and heat of crystallization (ΔH_c) for three samples tested for each composition.

Table 2-4. Fixing (R_f) and recovery (R_r) ratios for all compositions tested as a function of l-PCL wt-% content.

Table 3-1. Table showing the molecular weight (M_w), number average molecular weight (M_n), and polymer dispersity index (PDI) of the synthesized tBA thermoplastic.

Table 3-2. Gel Fraction (G(%)) averages of all l:n-tBA compositions with accompany standard deviation where three specimens were tested for each composition.

Table 3-3. Table showing the average onset degradation temperatures from three l:n-tBA specimens of each composition studied.

Table 3-4. Table showing the average T_g transitions and standard deviation among all the l:n-tBA compositions tested. Three specimens were tested for each composition.

Table 3-5. Table showing the average tensile storage modulus for all the l:n-tBA composition tested at 25 °C, 60 °C and 100 °C.

Table 3-6. The fixing (R_f) and recovery (R_r) ratios for RPSM experiments of all l:n-tBA compositions where three samples were tested for each composition.

Table 3-7. Summary table of 1WSM data for all l:n-tBA compositions tested.

Table 3-8. Table showing self healing efficiencies among all l:n-tBA compositions tested.

Table 3-9. Table of spectrometer data showing the average of the transmittance for four l:n-tBA scratches analyzed for each composition.

Table 4-1. Table showing tensile storage modulus (E') at 25 °C, 50 °C and 80 °C as a function of fiber orientation with Sylgard as a reference.

Table 4-2. Data chart showing values of tensile apparent modulus of PVAc fibrous web dogbone samples.

Table 4-3. Data chart showing values of tensile Young's modulus (E_y) for the A-SMEC and Sylgard samples.

Table 4-4. Data chart showing strain-to-failure values of PVAc fibrous web dogbone samples.

Table 4-5. Data chart showing values of strain-to-failure for the A-SMEC and Sylgard samples.

Table 4-6. Yield stress for all fibrous web samples tested as a function of fiber orientation angle.

Table 4-7. A-SMEC yield stress for all samples tested as a function of fiber orientation angle.

Table 4-8. Fixing (R_f) and recovery (R_r) ratios for all A-SMEC samples tested as a function of fiber orientation angle where the average of cycle two and three were reported.

Table 5-1. Table showing the average ε_m (maximum strain achieved by deformation), ε_u (fixed strain after unloading), ε_p (permanent strain after recovery), R_f (fixing ratio) and R_r (recovery ratio) with accompanying stand deviations for three samples tested among all the composites fabricated.

Table 5-2. Tables showing the average (a) Young's modulus and (b) average yield stress as a function of laminated composites tested.

Table 5-3. Table showing the average weights and thicknesses of each ply, laminated composite and Sylgard184 layer used to fabricate the laminated composites.

Table 5-4. Table showing the average widths and thicknesses for each laminated composite strip that was used for mechanical testing in the Linkam tensile stage. These values were used to calculate the stress values in the stress-strain graphs shown in Figure 5-7.

Table 5-5. Table showing the theoretical, experimental and difference in both values of the Young’s modulus as a function of laminated composite.

Table 5-6. Table showing the average D (%) and R (%) for all samples tested in relation to the composites fabricated.

Table 5-7. Table showing the curvature analysis conducted for four 0/22.5° laminated composite samples tested where a = primary and b = secondary curvature.

Table 5-8. Table showing the curvature analysis conducted for four 0/45° laminated composite samples tested where a = primary, b = secondary, and c= tertiary curvature.

Table 5-9. Table showing the curvature analysis conducted for four 0/67.5° laminated composite samples tested where a = primary, b = secondary, and c= tertiary curvature.

Table 5-10. Table showing the curvature analysis conducted for four 0/90° laminated composite samples tested where a = primary, b = secondary, and c= tertiary curvature.

Table 5-11. Table showing the pitch values for 0/22.5° laminated composites for four samples tested.

Table 5-12. Table showing the pitch values for 0/67.5° laminated composites for four samples tested.

Table 5-13. Table showing the pitch values for 0/90° laminated composites for four samples tested.

Table 5-14. Table showing the theoretical, experimental and difference of both values of the curvature as a function of laminated composites.

LIST OF SCHEMES

Scheme 1-1. Drawings showing (a) monomer, (b) polymer, (c) thermoplastic, (d) covalent crosslink, (e) elastomer, (f) thermoset, and (g) semi-interpenetrating polymer network (SIPN). Entanglement of polymer chains where (h) shows low molecular weight with no entanglements, (i) high molecular weight with chain entanglements.

Scheme 1-2. Scheme showing polymerization process where (a) initiation, (b) propagation, and (c) termination by recombination or disproportion. *I* stands for the initiator, 2 $A_o^{\bullet}$ are two radicals, M is the monomer unit and $A_1^{\bullet}$ is the active chain. $A_n^{\bullet}$ is the growing chain with n number of monomer units where A_{n+1} is after the addition of one monomer unit. $A_n^{\bullet}$ and $A_m^{\bullet}$ are two active chains, P_{n+m} is one polymer chain terminated by recombination, $P_n + P_m$ are two polymer chains terminated by disproportion.

Scheme 1-3. Polymer structure and morphology. (Adopted with permission of Sperling, L. H., *Introduction of Physical Polymer Science*. 4th Edition ed.; John Wiley and Sons Inc.: Hoboken, New Jersey, 2006; p 845).

Scheme 1-4. Diagram showing the polymer classifications. (Adopted with permission of Young, R. J.; Lovell, P. A., *Introduction to Polymers*. 2 ed.; Chapman and Hall: 1991.)

Scheme 1-5. Examples of polymeric shape memory (SM) systems showing (a) thermally (Langer, R., and Tirrell, D. A., Nature (2004) 428, 487), (b) infrared radiation (Koerner, H., et al., Nat. Mater. (2004) 3, 115), (c) water (Huang, W. M.; Yang, B.; An, L.; Li, C.; Chan, Y. S. Applied Physics Letters, 2005, 86, (11), 3.) and (d) magnetically (Mohr, R., et al., Proc. Natl. Acad. Sci. USA (2006) 103, 3540) triggered SM systems. (Adopted with permission of the authors above.)

Scheme 1-6. Triple shape memory system showing three distant shapes observed at three different triggering temperatures. (Adopted with permission of Luo, X. F.; Mather, P. T. *Advanced Functional Materials* 2010, 20, (16), 2649-2656.)

Scheme 1-7. Figure showing examples of polymeric and composite self healing (SH) systems showing (a) intrinsic, (b) microcapsule, and (c) vascular based systems (Adopted with permission of Blaiszik, B. J.; Kramer, S. L. B.; Olugebefola, S. C.; Moore, J. S.; Sottos, N. R.; White, S. R., Self-Healing Polymers and Composites. *Annual Review of Materials Research, Vol 40* 2010, 40, 179-211.)

Scheme 1-8. Schematic showing the electrospinning set up using a rotating mandrel.

Scheme 2-1. Schematic showing the shape memory assisted self healing (SMASH) effect. Schematic of sample in its (a) virgin state, (b) pre-damaged (notched) state, and (c) damaged and deformed state at a temperature below its T_m to observe reversible plasticity shape memory (RPSM). (d) Shows the healed state when the sample was heated above its T_m. The shape memory (SM) effect was thermally triggered for crack closure where healing was obtained by polymer chain diffusion across the damaged site then cooled below the T_m to complete the SH effect. The inserts show a schematic of the polymer chains in the blend at each step of the SMASH process.

Scheme 2-2. Preparation of the poly(ε-caprolactone) diol (3k) macromer by end capping of PCL diol with acryloyl chloride.

Scheme 2-3. ^{1}H NMR spectra for PCL diacrylate(3k). Equation (2) shows the formula used to obtain end-capping conversion. Chart shows the conversion values for all the batches of PCL diacrylate used to make samples. The acrylate-terminated macromers were characterized for

degree of functionalization using ^{1}H NMR. An example spectrum is shown here, along with a schematic of the macromer structure indicating the identification of proton resonances. To compute the degree of functionalization, we utilized the resonances from the “i” protons of the acrylate vinyl group and the “a” protons of the repeating unit of poly(ε-caprolactone).

Scheme 2-4. ^{1}H NMR spectra for PCL diol(3k). Equation (1) shows the formula used to obtain the repeat unit (n) values. Chart shows the repeat unit values for all the batches of PCL diol(3k) that were used to make samples.

Scheme 2-5. Preparation of blends containing n-PCL and l-PCL by UV-initiated thiol-ene polymerization in the presence of non-reactive l-PCL.

Scheme 2-6. Customized deeply double-edge notched (DDEN) punch.

Scheme 2-7. Scheme of l-PCL chain entanglement in n-PCL at the healed site.

Scheme 2-8. Schematic of the five stages of healing (adapted from references 11 and 38).

Scheme 3-1. Preparation of the tBA thermoplastic (SH agent) synthesis through the thermal initiated free radical polymerization process.

Scheme 3-2. Schematic showing preparation of tBA SMASH films by UV initiated polymerization process with a representative image of a film following de-molding to show the transparency property.

Scheme 3-3. Hydrolysis process on the glass substrate. The arrows indicate electron flow during the silanization process.

Scheme 3-4. Schematic showing preparation of tBA SMASH coating using a silanized glass slide. Representative image of a coating on a glass substrate to show the transparency.

Scheme 4-1. Three-step fabrication of shape memory elastomeric composites (A-SMEC). All samples tested were dogbone punched as a function of fiber orientation angle from the composite where 0° is the axial direction and 90° is the transverse direction.

Scheme 5-1. Three-step fabrication process of anisotropic shape memory elastomeric composites (A-SMEC).

Scheme 5-2. Top view of the A-SMEC sheet showing the cutting process as a function of fiber orientation using the paper-angle templates.

Scheme 5-3. Schematic showing the fabrication process of the laminated A-SMEC composites.

Scheme 5-4. Schematic showing the process of the mechanically activated shape change (MASC).

Scheme 5-5. Scheme showing each ply's behavior upon unloading where (a) shows the behavior in ply 1 where the fibers are aligned in either of the following angles: 22.5°, 45°, 67.5°, or 90°. (b) Shows the behavior of ply 2 where the fibers are aligned in the axial orientation. (c) Shows the behavior upon unloading of ply 1 and ply 2 when they are laminated to form a composite. The curvature response is associated with the displacement mismatch where ply 1 recovers more than ply 2 resulting in curvature towards ply 1.

Scheme 6-1. Schematic of specimen showing the location of the puncture and ligaments.

Scheme 6-2. Schematic showing dual notch damage and the location of the notches and ligament width.

LIST OF FIGURES

Figure 2-1. Dependence of the n-PCL:l-PCL gel fraction, G(%), by $CHCl_3$ extraction for of all compositions tested as a function of l-PCL wt-% content and taken for an average of three samples. The line represents linear regression of the data, revealing a small deviation of the expected extraction of all l-PCL.

Figure 2-2. Weight vs. temperature graph showing sample decomposition by weight change of all compositions tested using a TA Q500 Thermogravimetric Analyzer (TGA) where each sample was heated to 600 °C at 10 °C/min. PCL Diacrylate$(3k)_{100}$ and PCL$(65k)_{100}$ are shown for comparison.

Figure 2-3. Representative heating and cooling DSC traces showing the T_m and T_c of all compositions tested. The first and second heatings were conducted at 10.0 °C/min to 120 °C with a cooling rate of 3.0 °C/min to -90 °C.

Figure 2-4. Trends of transition temperatures and latent heats for the blends: (a) melting temperature (T_m) and heat of melting (ΔH_m), (b) crystalline temperature (T_c) and heat of crystallization (ΔH_c) as a function of l-PCL wt-% content showing average values from three samples tested for each composition.

Figure 2-5. Tensile storage modulus (E′) as a function of temperature for all compositions tested are shown. For all compositions, the first heating was at 3.00 °C/min to 90.00 °C, cooling at 3.00 °C/min to -90.00 °C and the second heating at 3.00 °C/min to 120.00 °C. The first heating for the l-PCL$_{100}$ sample was done at 3 °C/min to 50 °C, cooling at 3 °C/min to -90 °C and the second heating at 3 °C/ min to 70 °C. Second heating data are shown for all samples. The tan delta curves are also shown, indicating the ratio of the viscous to elastic contribution of the samples tested with a peak at T_g and a dramatic rise at T_m.

Figure 2-6. Tensile storage modulus obtained at (a) 25 °C and (b) 80 °C for all compositions as a function of l-PCL wt-% content for the average of two samples tested.

Figure 2-7. (a) Representative reversible plasticity shape memory cycle (RPSM) of l-PCL_0:n-PCL_{100} (black) and l-PCL_{50}:n-PCL_{50} (blue) compositions where each sample was stretched to a strain of 200% at RT and recovered at 80 °C. Strain vs. temperature curve (red) and stress vs. strain curve (green) are also shown for the l-PCL_{50}:n-PCL_{50} composition. (b) Reversible plasticity shape memory cycle (RPSM) for all nine compositions tested where each sample was stretched to a strain of 200% at RT. Shape recovery was tested at temperature, T ($T > T_m$) = 80 °C.

Figure 2-8. Fixing (R_f) and recovery (R_r) ratios bar graph for all nine compositions tested as a function of l-PCL wt-% content.

Figure 2-9. (a) Force vs. displacement curves for the virgin, damaged and healed state of a l-PCL_{50}:n-PCL_{50} sample. (b) Notched l-PCL_{50}:n-PCL_{50} sample with stereo micrographs of deformation and crack growth clamped in the Linkam tensile stage. (Scale bar: 500 µm) (c) Snapshots of crack closure and crack rebonding when the sample was unclamped from the Linkam tensile stage and heated to the temperatures shown (stereo micrographs scale bar: 500 µm).

Figure 2-10. Representative graphs of all compositions tested showing the initial deformation, damaged and healed force vs. displacement curves.

Figure 2-11. Dependence of self-healing efficiency (η) on l-PCL wt-% content. The average of three samples tested for SH efficiency following first, second and third thermal mending treatments are shown.

Figure 2-12. Average peak loads as a function of l-PCL wt-% content after each thermal mending treatment is shown. Three samples were tested for each composition.

Figure 2-13. Average tensile yield stress as a function of l-PCL wt-% content for each virgin and healed samples tested using the TST350 Linkam tensile stage are shown. Three samples were tested for each composition. In all cases, the undamaged cross-section was used in the determination of the tensile yield stress from tensile load data.

Figure 2-14. l-PCL$_{50}$:n-PCL$_{50}$ sample showing SEM micrographs of the (a) propagated crack surfaces, (b) elastic and plastic zones, (c) stereomicrograph of elastic and plastic zones (Scale bar: SEM - 100 μm, steromicrograph - 500μm). (d) Optical micrograph indicating the three crack regions. SEM micrographs of healed (e) initial crack region, (f) crack transition region, and (g) propagated crack region (Scale bar: optical micrograph- 100 μm, SEM – 50 μm).

Figure 3-1. Schematic showing the SMASH process for an amorphous coating.

Figure 3-2. Images of the custom made motorized scratch machine where the movable track was connected to a motor that allowed a forward or backward motion. The scratch was formed using a track speed of approximately 0.9 mm/sec.

Figure 3-3. Process of image analysis used for SH efficiency calculations. Image (a) of a damaged coating in ImageJ software to convert image to an 8-bit, (b) imported into Vision Assistant for image analysis, (c) performed a manual threshold (d) removed small objects, (e) filled in areas of the scratch in red.

Figure 3-4. Gel Permeation Chromatography (GPC) graph showing the light scattering and refractive index traces needed to calculate the molecular weight (M_w) and number average molecular weight (M_n) for the tert-butyl acrylate (tBA) thermoplastic.

Figure 3-5. Graph showing the dependence of the l:n-tBA blend's gel fractions (G(%)) by methanol extraction for all compositions tested as a function of tBA thermoplastic content. Data shows the average of three samples tested where the lines represent the linear regression of the actual and predicted data.

Figure 3-6. (a) Representative thermogravimetric analysis (TGA) curves showing degradation temperatures where all l:n-tBA compositions and neat tBA thermoplastic were heated at 10 °C/min to 600 °C. (b) Graph showing onset degradation temperature vs. tBA thermoplastic wt -% content for an average of three samples for each composition tested.

Figure 3-7. Graph showing representative (a) first heating traces of the exothermic peak indicating complete cure was not accomplished among the l:n-tBA systems where (b) second heating revealing the T_g transitions for all the compositions tested with no exothermic peak evident. (c) Graph showing the first heating and (b) second heating from samples that were post cured revealing complete cure and T_g transitions with no exothermic peak evident.

Figure 3-8. Graph showing the T_g obtained from the second heating of the post cured l:n-tBA samples. Three samples were tested for each composition as a function of tBA thermoplastic wt - % content.

Figure 3-9. (a) Representative traces showing tensile storage modulus (E') as a function of temperature among all l:n-tBA compositions tested. (b) Graph showing tensile storage modulus as a function of tBA thermoplastic content for three samples tested for each composition where standard error bars are shown. The tensile storage modulus was recorded at 25 °C, 60 °C, and 100 °C to observe the change in thermomechanical properties at these temperatures.

Figure 3-10. RPSM graphs showing for the following l:n-tBA compositions (a) (0:100) , (b) (10:90), (c) (25:75), and (d) (50:50).

Figure 3-11. (a) showing representative RPSM graphs and (b) showing the fixing (R_f) and recovery (R_r) ratios for all l:n-tBA compositions tested as a function tBA thermoplastic content.

Figure 3-12. 1WSM curves for (a) (0:100), (b) (10:90), (c) (25:75), and (d) (50:50) l:n-tBA compositions where 1mm thick rectangular specimen were thermally treated at 120 °C for 10 min and cooled at RT for 10 min prior to testing. Graphs also show strain vs. temperature in the back plane and stress vs. strain curves on the side plane.

Figure 3-13. The fixing (R_f) and recovery (R_r) ratios for all l:n-tBA compositions tested for 1WSM experiments.

Figure 3-14. Graph showing transmittance vs. wavelength to investigate the carbonyl group present on silanized glass slide using FTIR-ATR.

Figure 3-15. Representative optical micrographs (OM) showing the virgin, damaged and thermally treated states as a function of l:n-tBA compositions tested. The damaged samples also show the ends of the scratch to observe any material removal.

Figure 3-16. Optical micrographs (OM) for four (0:100) l:n-tBA coatings in their virgin, damaged and thermally treated states. The damaged samples also show the ends of the scratch to observe any material removal.

Figure 3-17. Optical micrographs (OM) for four (10:90) l:n-tBA compositions in their virgin, damaged and thermally treated states. The damaged samples also show the ends of the scratch to observe any material removal.

Figure 3-18. Optical micrographs (OM) for four (25:75) l:n-tBA compositions in their virgin, damaged and thermally treated states. The damaged samples also show the ends of the scratch to observe any material removal.

Figure 3-19. Optical micrographs (OM) for four (50:50) l:n-tBA compositions in their virgin, damaged and thermally treated states. The damaged samples also show the ends of the scratch to observe any material removal.

Figure 3-20. Graph showing self healing efficiency as a function of tBA thermoplastic content among all l:n-tBA compositions tested.

Figure 3-21. Scanning electron microscopy (SEM) images of the l:n-tBA coatings in their scratched and thermally treated states.

Figure 3-22. Graphs showing the transmittance vs. wavelength trend among the average of three samples tested for each l:n-tBA composition for coatings in their virgin, damaged and thermally treated states. The following compositions are shown: (a) (0:100), (b) (10:90), (c) (25:75), and (d) (50:50).

Figure 3-23. Graphs showing transmittance vs. wavelength for the l:n-tBA coatings in their virgin, damaged, and thermally treated states. Three (0:100) samples were tested where (a) shows Run 1, (b) Run 2, and (c) Run 3.

Figure 3-24. Graphs showing transmittance vs. wavelength for the l:n-tBA coatings in their virgin, damaged, and thermally treated states. Three (10:90) samples were tested where (a) shows Run 1, (b) Run 2, and (c) Run 3.

Figure 3-25. Graphs showing transmittance vs. wavelength for the l:n-tBA coatings in their virgin, damaged, and thermally treated states. Three (25:75) samples were tested where (a) shows Run 1, (b) Run 2, and (c) Run 3.

Figure 3-26. Graphs showing transmittance vs. wavelength for the l:n-tBA coatings in their virgin, damaged, and thermally treated states. Three (50:50) samples were tested where (a) shows Run 1, (b) Run 2, and (c) Run 3.

Figure 3-27. Figure showing the transmittance as a function of l-tBA SH thermoplastic content for the virgin, damaged and thermally treated states. This data reflects the average of four samples for each composition tested.

Figure 4-1. SEM images of (a) PVAc fibers (average diameter: 0.79 ± 0.20 μm), (b) topography of A-SMEC, (c) A-SMEC with axial fiber orientation, (d) composite with transverse fiber orientation.

Figure 4-2. (a) depicts an SEM of PVAc fibrous web used for testing (b) a 2D FFT of the SEM, (c) and (d) the resultant radial sum of intensities. (e) depicts an SEM of the PVAc fibers used to make the A-SMEC and used for testing, (f) a 2D FFT of the SEM image, (g) and (h) the resultant radial sum of intensities. SEMs, (a) and (e), were used to create the 2D FFTs, (b) and (f), by cropping the image to a square, then running the 2D Fast Fourier Transform (FFT) using Gywddion software's Hahn model. The resultant analytical images, (b) and (f), were then used to create radial intensity sum plots, (c) and (g). More specifically, utilizing an Image J plugin, "Oval_Profile" radial sums of the intensities at every angle were taken. As the 2D FFT rotates the images 90°, narrow peaks at 180° and 0°/360° are indicative of vertical alignment. As two peaks arise due the symmetry of this analysis, intensities from 0° to 90° correspond to intensities from 180° to 270°, similarly, intensities from 270° to 360° correspond to intensities from 90° to 180°. Intensity values from these sets were therefore averaged with their respective datum and plotted as angles from 90° to 270°, (d) and (h). Half max was established by obtaining the minimum datum for the given data and subtracting that value for all other data in the set. This value is reported as the dashed line on its' respective plot. The two points where the data and this half max line intersect yield a breadth of angles which is known as the full width at half max (FWHM). The resulting FWHM for the fiber web shown in (a) and (e) were 30° and 34° which confirms alignment for these two mats.

Figure 4-3. Glass transitions (T_g) of PVAc pellet, PVAc fibrous web and A-SMEC of the second heating are shown. By dividing the heat capacity of the A-SMEC by the heat capacity of the fibrous web mat, the fiber volume fraction of the was determined to be 19.8%.

Figure 4-4. Tensile storage modulus (E′) and tan delta versus temperature as a function of fiber orientation angle where Sylgard is plotted as a reference.

Figure 4-5. Scatter plot showing storage modulus at 25 °C, 50 °C and 80 °C as a function of fiber orientation angle, and showing Sylgard as reference lines at each temperature.

Figure 4-6. Representative stress-strain curves for (a) PVAc fibrous web and (b) A-SMEC dogbone samples as a function of fiber orientation angle with a Sylgard sample as a reference (-).

Figure 4-7. Stress-strain curves of PVAc fibrous web samples as a function of fiber orientation angle where (a) A-SMEC-0; (b) A-SMEC-22.5; (c) A-SMEC-45; (d) A-SMEC-67.5; and (e) A-SMEC-90.

Figure 4-8. Stress-strain curves of A-SMEC as a function of fiber orientation angle with a Sylgard sample as a reference where (a) Sylgard; (b) A-SMEC-0; (c) A-SMEC-22.5; (d) A-SMEC-45; (e) A-SMEC-67.5; and (f) A-SMEC-90.

Figure 4-9. Elastic modulus as a function of fiber orientation angle at RT for PVAc fibrous web and A-SMEC samples with Sylgard as a reference.

Figure 4-10. Representative stress-strain curves at 25 °C and 80 °C showing the extreme change in concavity of the geometry curve where (a) Sylgard; (b) A-SMEC-0; (c) A-SMEC-22.5; (d) A-SMEC-45; (e) A-SMEC-67.5; and (f) A-SMEC-90.

Figure 4-11. Plot showing Young's modulus as a function of fiber orientation angle is shown where (○) is for the A-SMEC and (--) is for the Sylgard at 25 ºC; (●) is for the A-SMEC and (-) is for the Sylgard at 80 ° C. Comparison of the elastic modulus of a biological system (i.e. bat wing membrane reported by Swartz et al.) and the A-SMEC as a function of fiber orientation angle. The A-SMEC regression line was found by plotting the logarithm of the modulus vs. the fiber orientation angle in and fitting a linear trendline. The bat wing regression had been previously reported by Swartz et al., and has been included to show how this A-SMEC modulus mimics that of the biological system.

Figure 4-12. Graph showing PVAc fibrous web and A-SMEC samples of average strain-to-failure as a function of fiber orientation angle with Sylgard as a reference (-) where the dashed lines (--) are the standard error of Sylgard.

Figure 4-13. Graph showing yield stress for samples in the fibrous web and A-SMEC state.

Figure 4-14. Shape memory cycles for an A-SMEC where the fibers are in the axial direction (A-SMEC-0). Backdrop is a strain-temperature curve and the side face is a stress-strain curve of cycle 1.

Figure 4-15. Shape memory cycles for all samples tested as a function of fiber orientation angle where (a) Sylgard; (b) A-SMEC-0; (c) A-SMEC-22.5; (d) A-SMEC-45; (e) A-SMEC-67.5; and (f) A-SMEC-90.

Figure 4-16. Graph of fixing (R_f) and recovery (R_r) ratios of A-SMEC samples as a function of fiber orientation angle with the inclusion of the Sylgard as reference line for R_f where the average among cycle two and three are shown.

Figure 5-1. Images showing (i) curvature and (ii) pitch analysis using Image J software. *a* and *b* in image (i) represent the primary and secondary curvature respectively. *c* in image (ii) is the distance used for the pitch value.

Figure 5-2. Image showing (a) PVAc aligned fibrous web (b) A-SMEC sheet (c) SEM of (i) aligned fibers (average fiber diameter: 0.81 ± 0.19 µm) (ii) topography of composite (iii) cross section in the axial (0°) direction (iv) cross section in the transverse (90°) direction.

Figure 5-3. Representative SEM images showing the cross section of the laminated composites where (a) 0/0°, (b) 0/22.5°, (c) 0/45°, (d) 0/67.5°, and (e) 0/90°. Samples were freeze fractured and broken in half to see the cross sections above.

Figure 5-4. Representative RPSM curves for single A-SMEC plies tested as function of fiber orientation. The following angles were tested: (a) 0°, (b) 22.5°, (c) 45°, (d) 67.5° and (e) 90°.

Figure 5-5. Graphs showing (a) representative RPSM curves as a function of fiber orientation, (b) strain vs. temperature, and (c) stress vs. strain for all composites tested.

Figure 5-6. Bar graph showing the fixing (R_f) and recovery (R_r) ratios as a function of fiber angle for three samples tested in each laminated composite.

Figure 5-7. Stress vs. strain curves for four samples tested as a function of laminated composites tested where the following graphs corresponds to (a) 0/0°, (b) 0/22.5°, (c) 0/45°, (d) 0/67.5°, and (e) 0/90°.

Figure 5-8. Graphs showing the average (a) Young's modulus and (b) the yield stress for four specimens tested as a function of laminated composites.

Figure 5-9. Bar graph showing the D (%) and R (%) as a function of laminated composites where four samples tested for each system.

Figure 5-10. Images of all four specimens recovered post-deformation after a thermal treatment of 80 °C for 5 min and cooled at RT for 5 min for all composites tested where (a) 0/0°, (b)

0/22.5°, (c) 0/45°, (d) 0/67.5°, and (e) 0/90°. The recovery was conducted four times to assess reproducibility.

Figure 5-11. Representative images of curvature for each laminated composite showing four samples tested where the following are shown (ply 2/ply 1): (a) 0/0°, (b) 0/22.5°, (c) 0/45°, (d) 0/67.5°, and (e) 0/90°. The circles are examples of how the curvature was analyzed using ImageJ software where a = primary, b = secondary, and c= tertiary curvature. The curvature response is towards ply 1 as this ply elastically recovers more than ply 2.

Figure 5-12. Graph showing curvature in relation to laminated composites tested. The accompanying image exemplifies the primary, secondary and tertiary curvature.

Figure 5-13. Representative images of pitch for each laminated composite showing four sample tested where the following are shown: (a) 0/0°, (b) 0/22.5°, (c) 0/45°, (d) 0/67.5°, and (e) 0/90°. The red lines are examples of how the pitch was analyzed using ImageJ software where a = primary and b = secondary pitch values.

Figure 5-14. Graph shows the pitch as a function of each laminated composite tested with an example image to show the primary (a) and secondary (b) pitch.

Figure 5-15. Graph showing the theoretical prediction of curvature corresponding to an applied deformation on the dual laminated composite strips. Lines are indicative of the theoretical model where the dots are the experimental values as a function of laminate system.

CHAPTER ONE

INTRODUCTION

1.0 RESEARCH MOTIVATION

Industrial polymer products such as those used in the aerospace, biomedical, architecture, and automotive industries sustain damage over time in use, resulting in permanent deformation and microcracks that hinder the mechanical performance. Cracks found on the surface and in the bulk of a material originate by either thermal, mechanical, chemical, and/or UV radiation stimulation and are hard to detect and thus repair.[1] One way to improve and regain the mechanical properties is to construct polymeric systems that are able to autonomously close the crack formed during damage and heal without the need of external intervention. My research aims to construct polymeric and composite systems that are able to achieve this function. To accomplish this, a combined effect of shape memory (SM) and self healing (SH) are incorporated into one polymeric autonomous system. In my research, a new and innovative concept termed *shape memory assisted self healing* (SMASH) is used in a variety of polymer systems to exhibit the SMASH effect while also paving the path of exploring a new shape memory type termed reversible plasticity shape memory (RPSM). RPSM is a phenomenon that we define as the recovery of both the temporal elastic and plastic regions of deformation.

This chapter will first provide a polymer science overview, followed by examples of shape memory and self healing polymeric systems that have been reported in literature. The chapter will then end with a brief description of the fabrication and mechanics of fiber reinforced composites. Collectively, these introductions will serve as helpful background and context for the original research presented in the rest of the dissertation.

1.1 BACKGROUND

1.1.1 INTRODUCTION TO POLYMER SCIENCE

A *polymer* is a large molecule made up of small structural units called *monomers*, which are covalently bonded together[2] (Scheme 1-1 (a) and (b)). This monomer linking is achieved by a process known as polymerization,[3] where the molecular weight of the polymer chains synthesized during the polymerization process is vital to obtain desired mechanical properties (Scheme 1-1 (h) and (i)). One way to synthesize polymers is through a free radical polymerization, a type of chain growth polymerization where a polymer chain is initiated by the addition of a monomer to a free-radical reactive site[4] (Scheme 1-2 (a)). After initiation, the active center is then transferred to the growing polymer chain end and another monomer unit is added, causing chain propagation (Scheme 1-2 (b)) where the polymerization process can then be terminated by recombination or disproportion (Scheme 1-2 (c)). Termination by recombination is where two active growing chains terminate with each other to form a single polymer molecule that is the size of both chains combined where termination by disproportion is the elimination of a hydrogen atom from an active growing chain by another active growing chain, forming two inactive polymer chains.[4] Scheme 1-2 (a) shows the initiation process where *I* stands for the initiator, 2 $A_o^\bullet$ are two radicals, M is the monomer unit and $A_1^\bullet$ is the active chain. Scheme 1-2 (b) is the propagation process where $A_n^\bullet$ is the growing chain with n number of monomer units where A_{n+1} is after the addition of one monomer unit. Scheme 1-2 (c) is the termination by recombination where $A_n^\bullet$ and $A_m^\bullet$ are two active chains, P_{n+m} is one polymer chain terminated by recombination, $P_n + P_m$ are two polymer chains terminated by disproportion. The free radical polymerization process can be initiated by a thermal (i.e. thermal initiator) or an ultraviolet (i.e.

photoinitiator) stimulus. The polymerization process explained above will be the primary method by which I synthesize the polymers I use in my research.

1.1.2 POLYMER STRUCTURE

There are two primary types of polymer physical structures that account for most industrial polymers in use today: *semi-crystalline* and *amorphous* (Scheme 1-3). Semi-crystalline polymers are defined by long range positional order of their constituent segments.[5] The term semi-crystalline is used as these polymers are not completely crystalline, but instead contain a small degree of amorphous regions where the majority of the polymer contains crystalline regions[3] (Scheme 1-3). Amorphous polymers are defined as having no long range order[5] (Scheme 1-3). Scheme 1-3 also shows a schematic of chain folding, a chain stem, and chain entanglements. A hallmark feature of polymeric materials is their thermal sensitivity, whereby the underlying structure and associated physical properties are easily altered by temperature variations. Semi-crystalline polymers are known to have three such thermal transitions: glass-rubber, crystallization (cooling), and melting (on heating) transitions. The glass-rubber transition (T_g) (often referred to as the glass transition) is the onset of softening where the amorphous regions in the semi-crystalline polymer become mobile. The crystalline transition (T_c) is the temperature at which crystal formation occurs upon cooling (or upon heating in the case of "cold crystallization" for polymers initially kinetically trapped in an amorphous state before heating). The melting transition (T_m) is the temperature at which the crystalline structures melt to an amorphous state upon heating. Amorphous polymers, however, only have a exhibit a T_g as these specific polymers do not contain crystalline structures.

1.1.3 POLYMER CLASSIFICATION

Architecturally, polymers can be further classified on the basis of the polymer chain topology or interconnectedness. Three polymer architectures are used in my line of research: *thermoplastic*, *elastomers*, and *thermosets* (Scheme 1-4). Thermoplastics can be amorphous or semi-crystalline and are primarily synthesized by chain polymerization (Scheme 1-1 (c)). Thermoplastics are linear or branched in architecture and can be molded and remolded to a specified geometry when heated above their T_g or T_m.[4] In contrast, *elastomers* are lightly crosslinked, highly extendible elastic network polymers (Scheme 1-1 (e)). Here, covalent crosslinks serve as permanent anchors that covalently bond neighboring polymer molecules together to prevent chain slippage from each other to form a network[4,6] (Scheme 1-1 (d)). These polymers have the ability to achieve a high degree of elongation and then recover immediately when the applied stress used to deform the elastomer is released.[4] As the polymer chains elongate, the low crosslink density serves two purposes: it hinders permanent flow and allows recovery driven by entropy.[4,7-9] *Thermosets* are architecturally identical to elastomers, but exist as more highly crosslinked network polymers where polymer chain movement is restricted to the crosslink density and generally have elastic stiffness and higher T_g than their lightly crosslinked elastomer counterparts (Scheme 1-1 (f)). Semi-interpenetrating polymer networks (SIPN) are systems where a non-crosslinked linear polymer is interpenetrated (or intertwined) within a crosslinked network where the network was crosslinked in the presence of the linear constituent[3,5] (Scheme 1-1 (g)).

1.2 POLYMER MECHANICAL PROPERTIES

A simple and direct way of testing the mechanical properties of polymers involves uniaxial tensile testing to obtain stress-strain curves as a variety of polymers respond differently from an applied load. Figure 1-1 shows a common stress-strain curve for fibers, rigid plastics, flexible plastics, and elastomers. The mechanical behavior of polymers depends strongly on the polymer molecular weight, degree of crystallinity, degree of crosslinking and the test temperature relative to T_g and T_m.[3] For example, for the polymer functionality, the toughness increases while elastic modulus decreases near or above the T_g for amorphous polymers and at T_m for semi-crystalline polymers.[3] Typically, polymers with high strength, but low extensibility (low strain) is achieved if there is a high degree of crystallinity, high crosslinking, or if T_g exceeds the test temperature significantly. Conversely, polymers achieving low strength but high extensibility either have low crystallinity, low crosslinking, or low T_g.

1.3 SHAPE MEMORY (SM) EFFECT IN POLYMERS

SM is a thermomechanical phenomenon in polymers where a polymeric system can be set in a temporarily fixed state, sustain this temporary deformation and subsequently recover its original memorized permanent geometry when electrically, irradiated or thermally stimulated.[7-15] More specifically, covalently crosslinked SM networks exhibit two phenomenas: (i) "shape fixing" occurs when a network initially deformed in the elastic state is cooled so as to vitrify or crystallize the constituent network chains. This chain immobilization renders the entropy elasticity of the network powerless in its desire to return the system to a stress-free state; (ii) recovery to the stress-free state "shape recovery" occurs when the network chains are remobilized by a trigger so that the network elasticity can return the system to its equilibrium shape. Here forward, attention will be focused on covalent crosslinking, as this is the only type used in my research. After a polymer has been covalently crosslinked through the polymerization process it becomes a thermoset or elastomer and cannot be remolded like thermoplastics.[8] The crosslinks therefore serve as permanent anchors in the network where the chains between crosslinks return to their high entropic state after the force needed to deform them is released. It is important to note that the crosslinks allow external loads to be translated down to the molecular level.

Covalent crosslinks are used in so-called “class I” shape memory polymers (SMP), which are covalently crosslinked glassy thermosets, while “class II” SM systems which are covalently crosslinked semi-crystalline thermosets. Figure 1-2 (a) and (b) shows a graph of tensile storage modulus (E’) versus temperature to show the distinct T_g and/or T_m transitions for both polymer classes. E’ is a common material property that is frequently used in polymer characterization to study thermal transitions of polymers through their dramatic effect on the elastic modulus. Class I polymer systems are known to be the simplest shape memory polymer type and exhibit a very sharp T_g that is correlate with a great shape memory effect (SME).[8] Temporary fixing is attained through network chain vitrification, which is the phenomenon of a polymer becoming glassy when cooled below its T_g.[5] Vitrification essentially freezes the polymer chains to prevent chain mobility. Shape recovery then occurs when the system is heated above either its T_g where entropy elasticity is used describe shape recovery. In a similar manner, class II polymers are able to be temporarily fixed by the formation of crystals that form organized lamellar structures of the polymer chains when cooled below the system’s T_m to prevent chain mobility. Its permanent shape may then be recovered when the sample is heated above the T_m. Some SM systems include SM polyurethanes (SMPUs) (class II), acrylate-SMPs (class I or II), single-phase interpenetrating network (IPN) SMP (class I or II), epoxy (class I), and elastic memory composites (EMCs) (class I).[7]

Both polymer classes can achieve a shape memory cycle (SMC) well known in the material science community termed one way shape memory (1WSM).[8,16,17] Here, a SMP is heated to a rubber elastic state that exists above T_g for an amorphous SMP (Class I) or above T_m for a semicrystalline SMP (Class II) and uni-axially deformed to a desired strain. The SMP is then cooled below its transition temperature to fix this temporal shape where the force is then released to observe the fixing properties of the system. The SMP is finally heated above its transition temperature again to restore the original geometry of the polymer system, to varying degree. Figure 1-3 shows an example of SMC using a poly(cyclooctene) (PCO) specimen.[18] The fixing and recovery are commonly quantified when 1WSM are conducted on systems in order to understand the SME. The general equations used are as follows:

$$R_f(N) = \frac{\varepsilon_u(N)}{\varepsilon_m(N)} \times 100\% \qquad (1\text{-}1)$$

and

$$R_r(N) = \frac{\varepsilon_u(N) - \varepsilon_p(N)}{\varepsilon_u(N) - \varepsilon_p(N-1)} \times 100\% \qquad (1\text{-}2)$$

where R_f is the fixing ratio, R_r is the recovery ratio, ε_m, ε_u, ε_p and N are the strain before unloading, the strain after unloading, permanent (unrecoverable) strain after shape recovery and the cycle number, respectively.[7,9]

It is important to explain the two primary phenomena of the SME – shape fixing and shape recovery – by applying well understood polymer physics concepts. For the shape recovery component of SME, entropy elasticity can be employed. Entropy elasticity is a theory that explains the mechanical behavior of crosslinked polymers where entropic springs are used as a model. When crosslinked polymers are undeformed, they are in an equilibrium state with high conformational entropy of the constituent network chains. As the network chains are deformed when a sample is mechanically loaded, this conformational entropy is lowered and a restoring force generated.[5] Polymer conformation is a term that describes the variety of segmental arrangements about the rotation of single bonds.[5] Upon the force release, the polymer crosslinked network can restore elastically leaving only some unrecoverable plastic deformation. However, entropy elasticity can only be employed for polymer networks when heated above the T_g for class I SMP or T_m for class II SMP when both are in their rubbery elastic state. Entropy elasticity (E_R) can be defined as[2,4]:

$$E_R = \frac{3\rho RT}{M_c} \quad (1\text{-}3)$$

where E_R defines the tensile elastic modulus, ρ is density, R is the gas constant, T is temperature, and M_c is the average polymer chain molecular weight between crosslinks.

1.4 EXAMPLES OF SHAPE MEMORY POLYMERIC SYSTEMS

SM systems rely on direct or indirect thermal stimuli to trigger the SME. There are several different methods for achieving the SME, including direct thermal, indirect thermal, water and magnetic field as stimuli. Some polymeric SM systems are summarized here. One SM system shows a direct thermal induced SME using natural and synthetic resources. A cationic polymerization process incorporating divinylbenzene, styrene, soybean oil and dicyclopentadiene or norbornadiene as the crosslinker was fabricated.[17,19] Varying the weight percentages of the soybean oil, styrene, divinylbenzene with the addition of fishoil and boron trifluoride diethyl etherate, a total of 97 % strain fixing and 100 % shape recovery from bending tests were observed.[19] Other direct thermal SM systems include the use of poly(ε-caprolactone)dimethacrylate polymer networks that can be manipulated into a flattened helix and recover into a small diameter hollow tube for biomedical applications.[17,20,21] Here, the flattened helix shape can be inserted in a small incision in the body and then expanded to its permanent hollow tube shape once positioned in the body[17,20,21] (Scheme 1-5 (a)).

The SME can also be proven by using indirect heating such as irradiation with infrared light. These systems include conductive fillers such as carbon nanotubes where heat can be transferred within the bulk of the system upon infrared light exposure.[10,17] Koerner et al. fabricated a thermoplastic elastomer containing uniform dispersed carbon nanotubes where the anisotropy of the nanotubes increased the rubbery modulus by a factor of 5.[10] When exposed to infrared photons, the nanotubes absorb this energy and increase the temperature of the system to result in the melting of the strain induced crystals found in the polymer chains.[10] This then triggers the relief of the stored strain energy of the system[10] (Scheme 1-5 (b)). The authors then took this concept further where heat was generated by current passing through the strain induced nanotube composite elastomer and is recovered upon exposure to an electrical current.[10]

Water triggered SM systems have also been considered to show the SME. Huang et al. explains water driven actuation using hydrophilic polyurethanes SMP.[13] First, the SMP was bent in a circular geometry at 40 °C and fixed at RT for one week in a humidity controlled environment.[13] After a 30 min RT water immersion, the deformed SMP gradually recovered. Here, the moisture progressively permeated into the polymer and plasticized it, thus resulting in the SME[13,17] Scheme 1-5 (c)). An additional experiment was conducted where the SMP specimen was sectioned into three and each section was immersed into RT water at different times (section 1: 0 min, section 2: 30 min, section 3: 5h).[13] This was done in order to reduce the T_g of each section and observe the recovery as a function of T_g.[13] Here, the T_g decreased with an increase of water immersion time where the T_g's reported were 36 °C, 28 °C, 10 °C[13]. The study showed the sample recovered between 10 °C and 40 °C[13] where the temperature corresponding to the T_g of that section recovered.[13]

Other SM systems include the incorporation of iron(II)oxide, magnetic nanoparticles, and a silica matrix processed into a thermoplastic SMP.[12,17] Here, a combination of polyetherurethane (TFX) with a multiblock copolymer, poly(*p*-dioxanone) (hard segment) and poly(ε-caprolactone) (soft segment), was used as a matrix.[12] The SM thermoplastic composite showed temporary fixing at RT where the SME could be observed upon an inductive heating process using an alternating magnetic field[12] (Scheme 1-5 (d)).

Additional intricate SM systems include a unique phenomenon that does not only include a dual shape SME but also a triple SME.[15,22-25] In our group,[26] Luo et al. invented a SM polymeric composite that conforms to three distinct shapes by tailoring the mechanical properties to specified temperatures.[15] A non-woven semi-crystalline poly(ε-caproplatone) (PCL) fiber mat was electrospun and embedded in a co-epoxy thermoset of an aromatic diepoxide (diglycidyl ether of bisphenol-A; DGEBA), an aliphatic diepoxide (neopentyl glycol diglycidyl ether; NGDE), and a curing agent (poly(propylene glycol)bis(2-aminopropyl); Jeffamine D230).[15] In terms of phase behavior, this system exhibited a distinctive epoxy T_g followed by the PCL T_m transition that yielded two rubbery plateaus. At low temperatures, both epoxy and fiber phase were in a rigid immobile chain state. Once the temperature increased to exceed the T_g of the co-epoxy network, the first rubbery plateau was evident followed by the second rubbery plateau once the temperature increased further to surpass the T_m of the PCL fiber phase. From these two rubbery plateaus three distinct shapes could be attained[15] (Scheme 1-6).

1.5 SELF HEALING IN POLYMERIC AND COMPOSITE SYSTEMS

Self healing (SH) is an effect in polymeric and composite materials where damage such as cracks formed on the surface or in the bulk of the system can heal autonomously and restore the mechanical properties of the material. Biological systems are known to have their own healing mechanisms when external or internal damage occurs where the healing process only incorporates the components the body provides.[27-30] Material scientists have been developing synthetic materials which can mimic this healing mechanism for industrial products that incur damage during long term use.[27] Many composite and polymeric materials have been developed and categorized into the following three areas: Intrinsic, vascular, and capsule based materials.[1,27,31] Some are explained here.

1.5.1 INTRINSIC SH MATERIALS

Intrinsic SH materials are of the simplest form of SH where the matrix material, itself, is capable of self-healing (Scheme 1-7 (a)). Here, mechanisms such as molecular diffusion, phase change, thermal reversible reactions, ionomer coupling, hydrogen bonding, and fusible thermoplastics can be employed in SH materials.[27] All these mechanisms can be grouped into three main areas: *reversible bonding*, *macromolecular chain inter-diffusion*, and *noncovalent healing*.[27,31] Most intrinsic SH materials can be damaged multiple times and are still capable of healing effectively to restore the mechanical properties.

One example of intrinsic SH is *reversible bonding* that involves the breaking (during damage) and reformation (during healing) of polymers post-damage where a unique chemical process termed the Diels-Alder (DA) cycloaddition reaction[32] is used. The reformation of covalent bonds to restructure damaged polymer chains is formed upon a thermal stimulus.[32]

The *macromolecular chain inter-diffusion* SH materials can be triggered by heating above the materials T_g or T_m. This is a common healing method for amorphous, semi-crystalline polymers and fiber reinforced composites.[1] The simplest form is the inclusion of a meltable thermoplastic that liquifies upon heating above a triggering temperature to allow for it to distribute itself and fill in the damaged area.[27,31] This effect is proven to be effective when the damaged polymers are of the same chemical structure. When the crack surfaces are brought in complete contact with each other, one of the polymers molecularly diffuses across the damaged site and chains entangle with eachother, this interlocking becoming the direct cause of the mechanical property restoration.[1,31]

Noncovalent healing involves reversible crosslinking in polymers through hydrogen bonding and ionic bonding segments in the system.[27,31] Specifically, ionomeric healing forms ionic sections that arrange in clusters to serve as reversible crosslinks where these clusters can be triggered to form by an external stimulus such as heat.[27,31]

1.5.2 MICROENCAPSULATED SH MATERIALS

Other SH systems incorporate microencapsulated healing agents where a propagated crack will rupture the capsule allowing the agent to fill in the damaged site by capillary action and bond the crack surfaces via in-situ polymerization[33-35] (Scheme 1-7 (b)). This SH system has been a widely accepted technique where this approach stimulated great overall interest in the SH polymer community. Some examples of the encapsulated SH materials are discussed here. First is the capsule-catalyst[27,31,33] system where the encapsulated liquid healing agent and polymerizer (i.e. catalyst) are randomly dispersed in a matrix. The encapsulation of the healing agent is necessary to prevent premature polymerization. The second involves the liquid healing agent and polymerization catalyst encapsulated in separate capsules which are known as multicapsule SH materials.[31,36,37] The third system, characterized by latent functionality, encompasses the encapsulated liquid healing agent and features a polymerizer that is already incorporated in the basic chemistry of the matrix.[27,31,38,39] The fourth and last capsule-based SH material incorporates the healing agent or polymerization catalyst to be phase separated within the matrix itself.[27,31,40,41] A disadvantage of microencapsulated SH materials is they have been shown to be effective only when damaged once, as the healing agents cannot be replenished for future damage.

1.5.3 VASCULAR SH MATERIALS

Other SH materials have vascular hollow tubes, channels or capillaries containing the SH agent that are embedded in a matrix (Scheme 1-7 (c)). These materials are quite elaborate where the channels may be in a single, interconnected, or three dimensional bio-inspired form.[27] Here, the cracks will propagate and damage a channel(s) allowing liquid healing agent to fill in the damaged area. The healing agent can then be refilled by externally replenishing or by neighboring channels. Replenishing of the healing agent can allow for the healing of multiple damage sites at multiple occurrences. However, although the SH agent can be continuously restored for multiple healing events, the interaction of the channels, matrix, and SH agent need to be designed to ensure the collection of these entities do not compromise the overall mechanical properties of the system. Parameters that are important factors to consider are those associated with vascular diameters, SH agent viscosity, bonding/adhesion between the matrix and vascular network and between the matrix and healing agent, and surface wettability.[31] Although the SH agent is combined in the fabrication process of the intrinsic and capsulated based SH materials, in the vascular SH systems, the formation of the channels are constructed and then the SH agent is incorporated usually through a vacuum-infiltration process.[27] An example of a channeled SH material involves two vascular networks that are inter-distributed where one stores the healing agent while the other holds the catalyst in one matrix. Some systems use hollow glass fibers[42-44] to house the healing agent and/or catalyst needed for polymerization. As explained for the capsule-based systems, it is essential to segregate the healing agent and the catalyst to prevent polymerization before damage. These multiple, interconnected channel networks have an added advantage compared to those with a single network because the healing process is more probable with a crack rupturing a channel regardless of the damage location.

Most SH systems known today rely on crack rebonding through a chemical reaction or thermal transformation where other systems achieve crack closure via SMA wires to assist in the healing process. [45,46] However, there has not been a fully polymeric system that can exhibit both the SM and SH mechanisms and initiate these effects in an autonomous manner. It is here, where the development of SMASH smart materials can improve the overall performance of SH systems by closing the crack first followed by crack rebonding. SMASH materials feature the added advantage of where minimizing that amount of healing agent required to assist in the restoration of the mechanical properties by virtually eliminating the volume of healing agent that would otherwise be needed to fill void space.

1.6 FIBER REINFORCED POLYMER FABRICATION TECHNIQUES (ELECTROSPINNING)

In my research, I also aim to prove that the SMASH and RPSM effect can be shown in a unique form of fiber-reinforced composites. Here, the fiber reinforcements are polymeric in nature and can be formed by a process termed electrospinning to produce non-woven nanofiber mats. Electrospinning is a process that involves the formation of an electrified jet of a polymeric solution that, with a “whipping” instability extensively draws out the solution axially to yield ultrafine fibers. The polymer solution pumped through a highly charged needle tip, leading to charge injection that resides at the liquid-vapor meniscus and ultimately breaks surface tension through the formation of a Taylor cone[47] and the creation of a liquid jet. If sufficiently viscous, the jet persists as a fiber that thins as solvent evaporates and is directed rapidly toward an oppositely charged collector in the form of a grounded or oppositely charged plate, screen, or rotating mandrel for nanofiber web collection.[48-50] Scheme 1-8 shows a schematic of the electrospinning setup employed in the research of this dissertation. Here, the electrospinning parameters such as those associated with the syringe tip and drum voltage, drum rotation and translation, flow rate, and tip-to-drum distance, can be altered to achieve a desired fiber diameter where the diameter and thickness of the fiber mat can contribute to the overall mechanical properties. If desired, the electrospinning process allows for the fabrication of highly orientated fibers by rotation of the mandrel at a high enough angular velocity so that the linear velocity of the drum surface exceeds the jet linear velocity, or approximately 10 m/s. Such orientation is expected to yield high and anisotropic mechanical properties when compared to an unoriented assembly of the same fibers.[48,50]

1.7 MECHANICS OF FIBER REINFORCED POLYMERIC COMPOSITES

Fiber-reinforced composites are a special class of materials that have high stiffness, toughness, and low density, all of which are advantageous traits for the aerospace industry.[51] A composite is a multiphase phase material consisting of two different constituent materials that are chemically dissimilar and have distinct mechanical properties to fabricate a new material.[51-55] The constituent materials alone are unable to attain the mechanical properties attained from its composite state.[53] Composites commonly include a reinforcement phase that is distributed within the matrix phase where the matrix not only protects the reinforcement phase, but also adds toughness to the overall system and enable stress transfer.[55] The goal of making such composites is to fabricate a new material by combining constituents with the best properties for the desired function.[55] Studies have shown that the best mechanical properties attained in fiber reinforced composites are those that are loaded parallel to the fiber direction.[55] This can be correlated to the composite modulus, where the fiber volume fraction and the matrix modulus are considered. Below are commonly used equations to calculate the modulus in the axial and transverse direction in relation to the fiber orientation:

$$E_l = E_m V_m + E_f V_f \tag{1-4}$$

$$\frac{1}{E_t} = \frac{V_m}{E_m} + \frac{V_f}{E_f} \tag{1-5}$$

where E_l is the modulus in the continuous longitudinal fiber direction, E_t is the modulus in the continuous transverse direction, E_m is the modulus of the matrix phase, E_f modulus of the fiber phase, V_m the volume fraction of the matrix, and the V_f is the volume fraction of the fibers.[51] The ratio of forces carried by each phase can also be calculated:

$$\frac{F_f}{F_m} = \frac{E_f V_f}{E_m V_m} \tag{1-6}$$

where F_f is the load carried by the fibers and F_m is the load carried by the matrix.[51] The longitudinal and transverse strength for fiber reinforced composites can also be calculated where the following relation applies:

$$\sigma_{cl} = \sigma'_m\left(1 - V_f\right) + \sigma^*_f V_f \tag{1-7}$$

$$\sigma_{ct} = E_c V_m \varepsilon_m + E_c V_f \varepsilon_f \tag{1-8}$$

where σ_{cl} is the strength of the composite in the longitudinal direction, σ_m' is the strength of the matrix, V_f is the volume fraction of the fibers, σ_f^* strength of the fibers, σ_{ct} is the strength in the transverse direction, E_c is the composite modulus, V_m and V_f is the volume fraction of the matrix and fibers, and ε_m and ε_f is the strain in the matrix and fiber phase.[51] My research will involve a polymer/polymer composite in which both the fiber reinforcement phase and the matrix phase are polymeric materials, the former being a stiff polymer and the latter being an elastomer. The mechanical response of these composites will depend on the properties of the individual phases themselves, the volume fractions, and the load transferred between them.

The sections above provided an overview of polymer science fundamentals followed by examples of SM and SH systems that have been proven to be effective in demonstrating these effects. Fabrication and mechanical properties of fiber reinforced composites were also briefly described in order to provide a background necessary for understanding the results shown in Chapter 4 and 5.

1.8 DISSERTATION OVERVIEW

My dissertation focuses on a new and unique effect that combines the SM and SH effects to yield a highly effective, fully polymeric self-healing system. The *shape memory assisted self healing* (SMASH) effect was developed to assist in crack closure followed by healing that restores the mechanical properties of damaged polymeric and composite systems used in industrial products. The following chapters explore the SMASH effect in a variety of different polymeric and composite systems to explore the underlying mechanisms and demonstrate performance. My dissertation also discusses a novel approach established in my group that focuses on a new type of shape memory termed *reversible plasticity shape memory* (RPSM), given that all the polymeric systems presented in this dissertation exhibit this phenomena. In the following, the organization of this dissertation is presented.

Chapter 1 provides a polymer science overview and explores the variety of SM and SH polymer and composite systems that have been successfully fabricated and reported in literature. Chapter 1 also provides a fabrication and mechanics background for fiber reinforced composites. **Chapter 2** focuses on the fabrication and analysis of a semi-crystalline miscible blend system to exhibit the SMASH and RPSM effect. Here, poly(ε-caprolactone) (PCL) in a network and linear architecture were used to construct a semi interpenetrating polymer network (SIPN) films of varying compositions. Various polymer characterization techniques were used to understand the thermal transitions, thermo-mechanical, mechanical properties and SH properties of the system. This work has been published and is titled, "Linear and Crosslinked Poly (ε-caprolactone) Polymers for Shape Memory Assisted Self-Healing (SMASH).[56]" **Chapter 3** concentrates on a distinctive approach of using the SMASH effect in amorphous coatings for optical industrial applications. Here, the use of poly(tert-butyl acrylate) (poly(tBA)) system in both a network and linear thermoplastic state were used to fabricate thin transparent and colorless SIPN coatings. Thermo-mechanical characterization, scratch damage, healing, and optical transmittance experiments were conducted to evaluate the SM and SH nature of the coatings. **Chapter 4** then explores a new and soft fiber-matrix composite that consists of oriented electrospun nanofibers embedded in an elastomeric matrix, resulting in anisotropic shape memory elastomeric composites (A-SMEC). Here, defined anisotropic mechanical behavior was observed as well as SM strain fixing that depended strongly on fiber orientation. **Chapter 5** then explores the A-SMEC concept further by introducing the concept of laminated composites constructed by lamination of A-SMEC plies. Owing to the anisotropy in strain-fixing of each A-SMEC ply in RPSM testing, deformation of laminated composites of the same leads to curvature and helicoidal spiral. Upon heating above the transition temperature of the fiber phase, such shapes returned to their equilibrium, stress-free shapes. The degree of curvature and pitch were analyzed as a function of fiber oriented plies embedded in the rubber elastomer matrix and the former compared with predictions from an analysis stemming from that used to explain the curvature of heated bimetallic strips. **Chapter 6** concludes my findings of each chapter and recommends future exploration of designed experiments for each system of the dissertation.

1.9 REFERENCES

(1) Wu, D. Y.; Meure, S.; Solomon, D.: Self-healing polymeric materials: A review of recent developments. *Progress in Polymer Science* **2008**, *33*, 479-522.

(2) Cowie, J. M. G.; Arrighi, V.: *Polymers: Chemistry and Physics of Modern Materials*; Taylor and Francis Group: Boca Raton, FL, 2008.

(3) Odian, G.: *Principles of Polymerization*; A JOHN WILEY & SONS, INC., PUBLICATION: Hoboken, New Jersey, 2004.

(4) Young, R. J.; Lovell, P. A.: *Introduction to Polymers*; 2 ed.; Chapman and Hall, 1991.

(5) Sperling, L. H.: *Introduction of Physical Polymer Science*; 4th Edition ed.; John Wiley ans Sons Inc.: Hoboken, New Jersey, 2006.

(6) University, C. W. R.: Polymer Structure. 2004.

(7) Mather, P. T.; Luo, X. F.; Rousseau, I. A.: Shape Memory Polymer Research. *Annual Review of Materials Research* **2009**, *39*, 445-471.

(8) Liu, C.; Qin, H.; Mather, P. T.: Review of progress in shape-memory polymers. *Journal of Materials Chemistry* **2007**, *17*, 1543-1558.

(9) Lendlein, A.; Kelch, S.: Shape-memory polymers. *Angewandte Chemie-International Edition* **2002**, *41*, 2034-2057.

(10) Koerner, H.; Price, G.; Pearce, N. A.; Alexander, M.; Vaia, R. A.: Remotely actuated polymer nanocomposites - stress-recovery of carbon-nanotube-filled thermoplastic elastomers. *Nature Materials* **2004**, *3*, 115-120.

(11) Leng, J. S.; Lan, X.; Liu, Y. J.; Du, S. Y.: Shape-memory polymers and their composites: Stimulus methods and applications. *Progress in Materials Science* **2011**, *56*, 1077-1135.

(12) Mohr, R.; Kratz, K.; Weigel, T.; Lucka-Gabor, M.; Moneke, M.; Lendlein, A.: Initiation of shape-memory effect by inductive heating of magnetic nanoparticles in thermoplastic polymers. *Proceedings of the National Academy of Sciences of the United States of America* **2006**, *103*, 3540-3545.

(13) Huang, W. M.; Yang, B.; An, L.; Li, C.; Chan, Y. S.: Water-driven programmable polyurethane shape memory polymer: Demonstration and mechanism. *Applied Physics Letters* **2005**, *86*, 3.

(14) Ratna, D.; Karger-Kocsis, J.: Recent advances in shape memory polymers and composites: a review. *Journal of Materials Science* **2008**, *43*, 254-269.

(15) Luo, X. F.; Mather, P. T.: Triple-Shape Polymeric Composites (TSPCs). *Advanced Functional Materials* **2010**, *20*, 2649-2656.

(16) Lendlein, A.: Shape-Memory Polymers. Kelch, S., Ed.: Angewandte Chemie, 2002; Vol. 41; pp 2034-2057.

(17) Behl, M.; Lendlein, A.: Shape-memory polymers. *Materials Today* **2007**, *10*, 20-28.

(18) Kunzelman, J.; Chung, T.; Mather, P. T.; Weder, C.: Shape memory polymers with built-in threshold temperature sensors. *Journal of Materials Chemistry* **2008**, *18*, 1082-1086.

(19) Li, F. K.; Larock, R. C.: *J. Appl. Polym. Sci.* **2002**, *84*, 1533.

(20) Langer, R.; Tirrell, D. A.: Designing materials for biology and medicine. *Nature* **2004**, *428*, 487-492.

(21) Lendlein, A.; Schmidt, A. M.; Schroeter, M.; Langer, R.: Shape-memory polymer networks from oligo(epsilon-caprolactone)dimethacrylates. *Journal of Polymer Science Part a-Polymer Chemistry* **2005**, *43*, 1369-1381.

(22) Bellin, I.; Kelch, S.; Langer, R.; Lendlein, A.: Polymeric triple-shape materials. *Proceedings of the National Academy of Sciences of the United States of America* **2006**, *103*, 18043-18047.

(23) Bellin, I.; Kelch, S.; Lendlein, A.: Dual-shape properties of triple-shape polymer networks with crystallizable network segments and grafted side chains. *Journal of Materials Chemistry* **2007**, *17*, 2885-2891.

(24) Qin, H. H.; Mather, P. T.: Combined One-Way and Two-Way Shape Memory in a Glass-Forming Nematic Network. *Macromolecules* **2009**, *42*, 273-280.

(25) Pretsch, T.: Triple-shape properties of a thermoresponsive poly(ester urethane). *Smart Materials & Structures* **2010**, *19*.

(26) Xie, T.; Xiao, X. C.; Cheng, Y. T.: Revealing Triple-Shape Memory Effect by Polymer Bilayers. *Macromolecular Rapid Communications* **2009**, *30*, 1823-1827.

(27) White, S. R.; Blaiszik, B. J.; Kramer, S. L. B.; Olugebefola, S. C.; Moore, J. S.; Sottos, N. R.: Self-healing Polymers and Composites. *American Scientist* **2011**, *99*, 392-399.

(28) Norris, C. J.; Meadway, G. J.; O'Sullivan, M. J.; Bond, I. P.; Trask, R. S.: Self-Healing Fibre Reinforced Composites via a Bioinspired Vasculature. *Advanced Functional Materials* **2011**, *21*, 3624-3633.

(29) Trask, R. S.; Rwilliams, H.; Bond, I. P.: Self-healing polymer composites: mimicking nature to enhance performance. *Bioinspiration & Biomimetics* **2007**, *2*, P1-P9.

(30) Norris, C. J.; Bond, I. P.; Trask, R. S.: The role of embedded bioinspired vasculature on damage formation in self-healing carbon fibre reinforced composites. *Composites Part a-Applied Science and Manufacturing* **2011**, *42*, 639-648.

(31) Blaiszik, B. J.; Kramer, S. L. B.; Olugebefola, S. C.; Moore, J. S.; Sottos, N. R.; White, S. R.: Self-Healing Polymers and Composites. *Annual Review of Materials Research, Vol 40* **2010**, *40*, 179-211.

(32) Murphy, E. B.; Bolanos, E.; Schaffner-Hamann, C.; Wudl, F.; Nutt, S. R.; Auad, M. L.: Synthesis and characterization of a single-component thermally remendable polymer network: Staudinger and Stille revisited. *Macromolecules* **2008**, *41*, 5203-5209.

(33) White, S. R.; Sottos, N. R.; Geubelle, P. H.; Moore, J. S.; Kessler, M. R.; Sriram, S. R.; Brown, E. N.; Viswanathan, S.: Autonomic healing of polymer composites. *Nature* **2001**, *409*, 794-797.

(34) Cosco, S.; Ambrogi, V.; Musto, P.; Carfagna, C.: Properties of poly(urea-formaldheyde) microcapsules containing an epoxy resin. *Journal of Applied Polymer Science* **2007**, *105*, 1400-1411.

(35) Yuan, L.; Liang, G. Z.; Xie, J. Q.; Li, L.; Guo, J.: Preparation and characterization of poly(urea-formaldehyde) microcapsules filled with epoxy resins. *Polymer* **2006**, *47*, 5338-5349.

(36) Keller, M. W.; White, S. R.; Sottos, N. R.: A self-healing poly(dimethyl siloxane) elastomer. *Advanced Functional Materials* **2007**, *17*, 2399-2404.

(37) Keller, M. W.; White, S. R.; Sottos, N. R.: Torsion fatigue response of self-healing poly(dimethylsiloxane) elastomers. *Polymer* **2008**, *49*, 3136-3145.

(38) Caruso, M. M.; Delafuente, D. A.; Ho, V.; Sottos, N. R.; Moore, J. S.; White, S. R.: Solvent-promoted self-healing epoxy materials. *Macromolecules* **2007**, *40*, 8830-8832.

(39) Caruso, M. M.; Blaiszik, B. J.; White, S. R.; Sottos, N. R.; Moore, J. S.: Full recovery of fracture toughness using a nontoxic solvent-based self-healing system. *Advanced Functional Materials* **2008**, *18*, 1898-1904.

(40) Cho, S. H.; Andersson, H. M.; White, S. R.; Sottos, N. R.; Braun, P. V.: Polydimethylsiloxane-based self-healing materials. *Advanced Materials* **2006**, *18*, 997-+.

(41) Cho, S. H.; White, S. R.; Braun, P. V.: Self-Healing Polymer Coatings. *Advanced Materials* **2009**, *21*, 645-+.

(42) Trask, R. S.; Bond, I. P.: Biomimetic self-healing of advanced composite structures using hollow glass fibres. *Smart Materials & Structures* **2006**, *15*, 704-710.

(43) Trask, R. S.; Williams, G. J.; Bond, I. P.: Bioinspired self-healing of advanced composite structures using hollow glass fibres. *Journal of the Royal Society Interface* **2007**, *4*, 363-371.

(44) Norris, C. J.; Bond, I. P.; Trask, R. S.: Interactions between propagating cracks and bioinspired self-healing vascules embedded in glass fibre reinforced composites. *Composites Science and Technology* **2011**, *71*, 847-853.

(45) Kirkby, E. L.; Rule, J. D.; Michaud, V. L.; Sottos, N. R.; White, S. R.; Manson, J. A. E.: Embedded shape-memory alloy wires for improved performance of self-healing polymers. *Advanced Functional Materials* **2008**, *18*, 2253-2260.

(46) Kirkby, E. L.; Michaud, V. J.; Manson, J. A. E.; Sottos, N. R.; White, S. R.: Performance of self-healing epoxy with microencapsulated healing agent and shape memory alloy wires. *Polymer* **2009**, *50*, 5533-5538.

(47) Reneker, D. H.; Yarin, A. L.: Electrospinning jets and polymer nanofibers. *Polymer* **2008**, *49*, 2387-2425.

(48) Andrady, A. L.: *Science and Technology of Polymer Nanofibers*; A John Wiley & Sons, INC. Publication, 2008.

(49) Luo, X. F.; Mather, P. T.: Preparation and Characterization of Shape Memory Elastomeric Composites. *Macromolecules* **2009**, *42*, 7251-7253.

(50) Seeram Ramakrishna: *An Introduction to Electrospinning And Nanofibers*; World Scientific Publishing Co. Pte. Ltd., 2005.

(51) William D. Callister, J.: *Fundamentals of Materials Science and Engineering, An Integrated Approach*; John Wiley & Sons, Inc., 2005; Vol. 2.

(52) Davidson, B. D.: *Mechanics of Continuous Fiber Reinforced Composites*.

(53) Chung, D. D. L.: *Composite Materials: Science and Applications*; Springer: Springer London Dordrecht Heidelberg New York, 2010; Vol. 2.

(54) Hahn, H. T.: RESIDUAL-STRESSES IN POLYMER MATRIX COMPOSITE LAMINATES. *Journal of Composite Materials* **1976**, *10*, 266-278.

(55) Smith, P. A.; Yeomans, J. A.: Benifits of Fiber and Particulate Reinforcment. *Materials Science and Engineering*, *2*.

(56) Rodriguez, E. D.; Luo, X. F.; Mather, P. T.: Linear/Network Poly(epsilon-caprolactone) Blends Exhibiting Shape Memory Assisted Self-Healing (SMASH). *ACS Applied Materials & Interfaces* **2011**, *3*, 152-161.

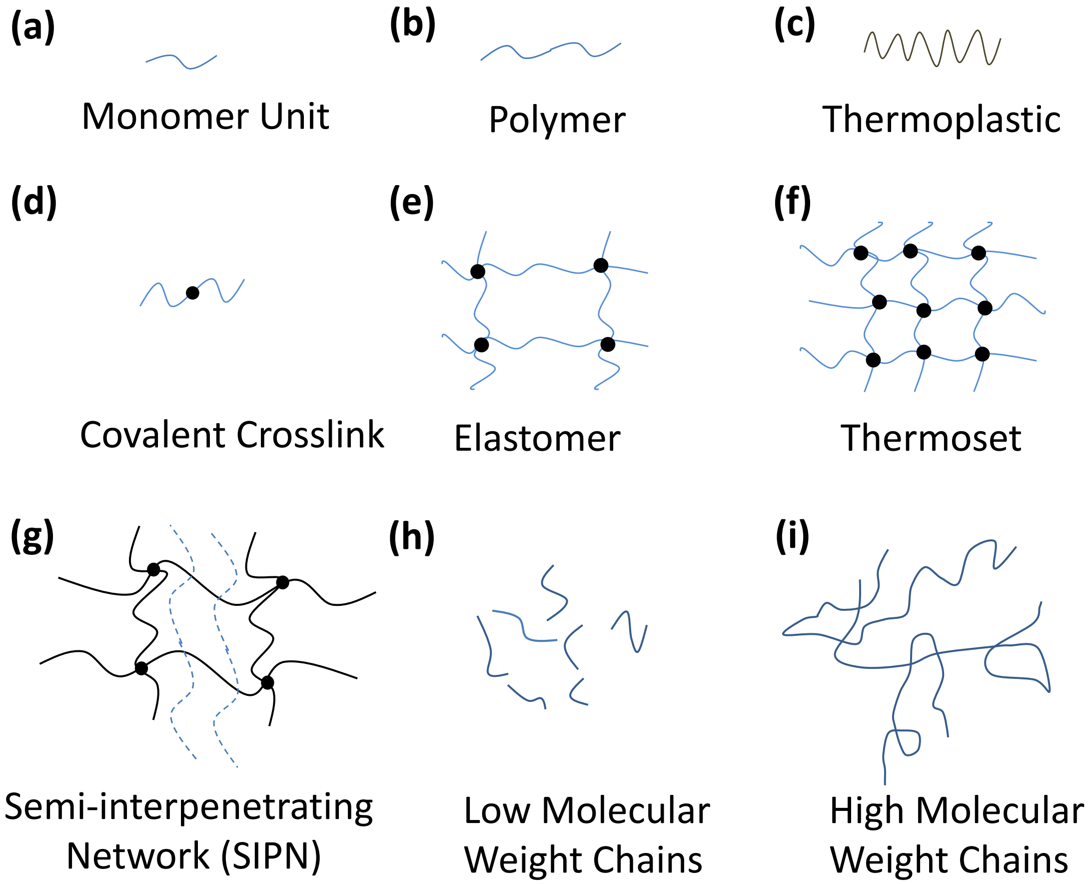

Scheme 1-1. Drawings showing (a) monomer, (b) polymer, (c) thermoplastic, (d) covalent crosslink, (e) elastomer, (f) thermoset, and (g) semi-interpenetrating polymer network (SIPN). Entanglement of polymer chains where (h) shows low molecular weight with no entanglements, (i) high molecular weight with chain entanglements.

(a)

$$I \rightarrow 2A_o^{\cdot}$$
$$A_o^{\cdot} + M \rightarrow A_1^{\cdot}$$

Initiation

(b)

$$A_n^{\cdot} + M \rightarrow A_{n+1}^{\cdot}$$

Propagation

(c)

Termination by

$$A_n^{\cdot} + A_m^{\cdot} \rightarrow P_{n+m}$$

Recombination

$$A_n^{\cdot} + A_m^{\cdot} \rightarrow P_n + P_m$$

Disproportion

Scheme 1-2. Scheme showing polymerization process where (a) initiation, (b) propagation, and (c) termination by recombination or disproportion. *I* stands for the initiator, 2 $A_o^{\bullet}$ are two radicals, M is the monomer unit and $A_1^{\bullet}$ is the active chain. $A_n^{\bullet}$ is the growing chain with n number of monomer units where A_{n+1} is after the addition of one monomer unit. $A_n^{\bullet}$ and $A_m^{\bullet}$ are two active chains, P_{n+m} is one polymer chain terminated by recombination, $P_n + P_m$ are two polymer chains terminated by disproportion.

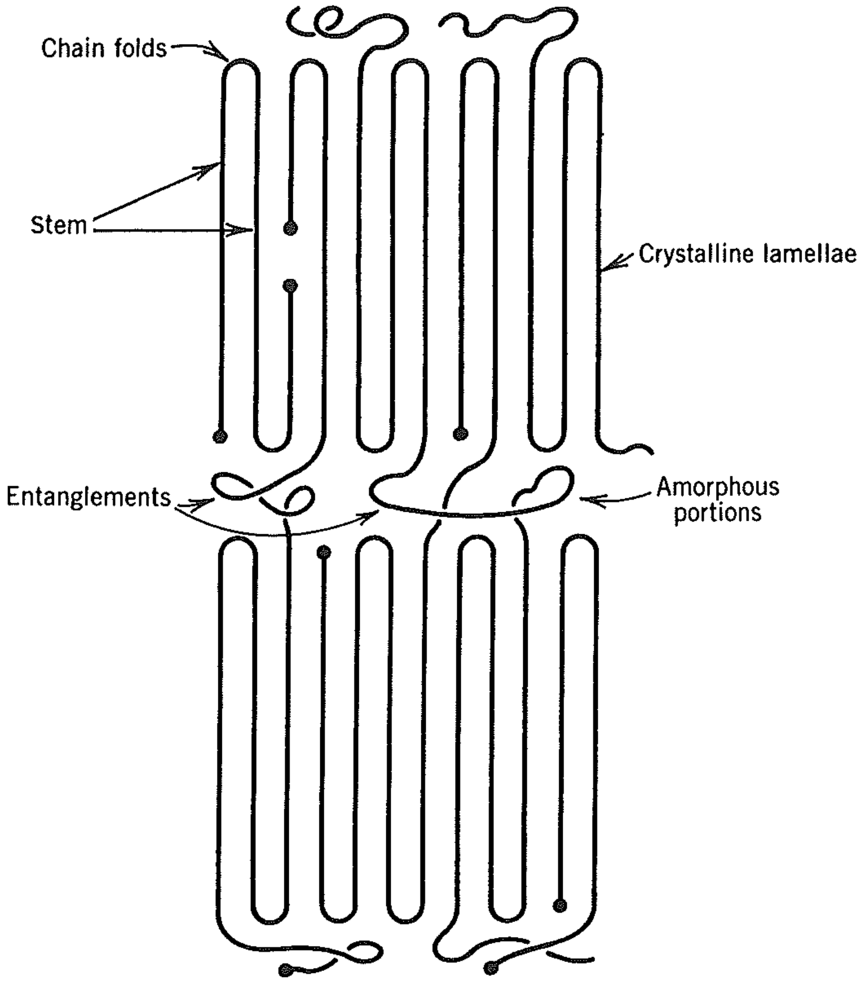

Scheme 1-3. Polymer structure and morphology. (Adopted with permission of Sperling, L. H., *Introduction of Physical Polymer Science*. 4th Edition ed.; John Wiley and Sons Inc.: Hoboken, New Jersey, 2006; p 845).

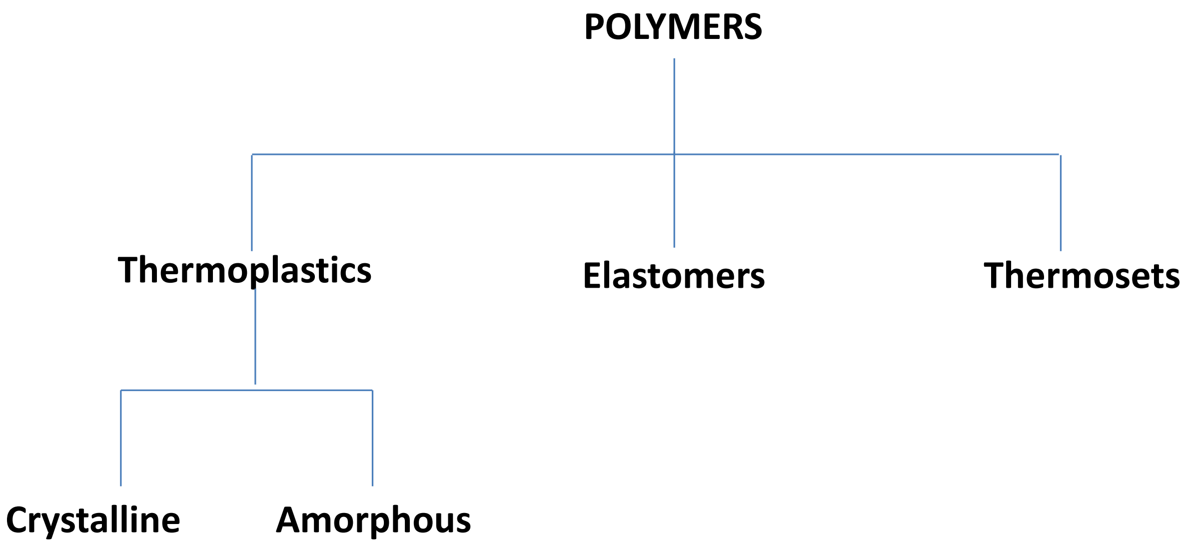

Scheme 1-4. Diagram showing the polymer classifications. (Adopted with permission of Young, R. J.; Lovell, P. A., *Introduction to Polymers*. 2 ed.; Chapman and Hall: 1991.)

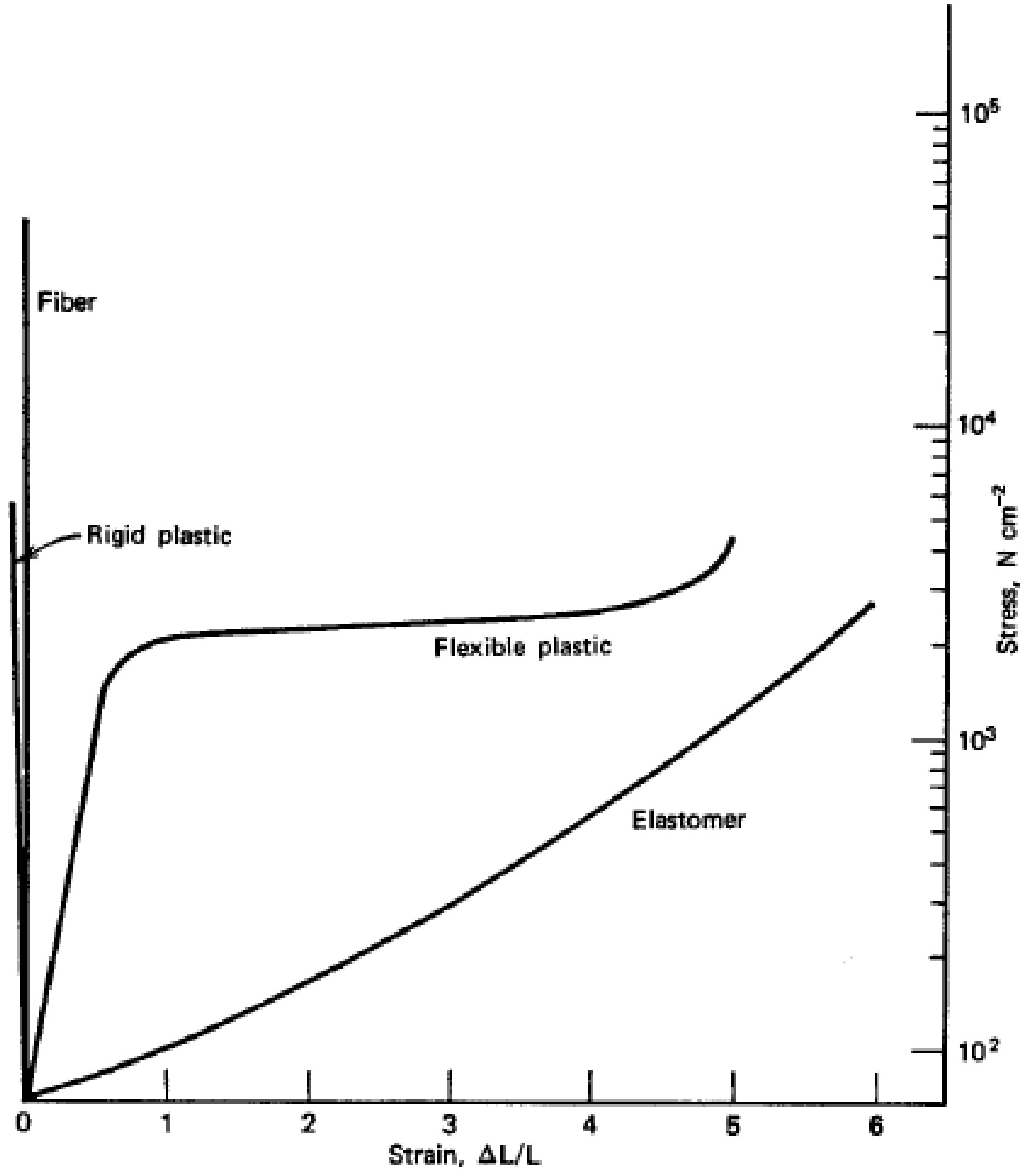

Figure 1-1. Common stress-strain trends of typical elastomers, flexible plastic, rigid plastic, and fiber specimens. (Adopted with permission of Odian, G., *Principles of Polymerization*. A JOHN WILEY & SONS, INC., PUBLICATION: Hoboken, New Jersey, 2004; p 812.)

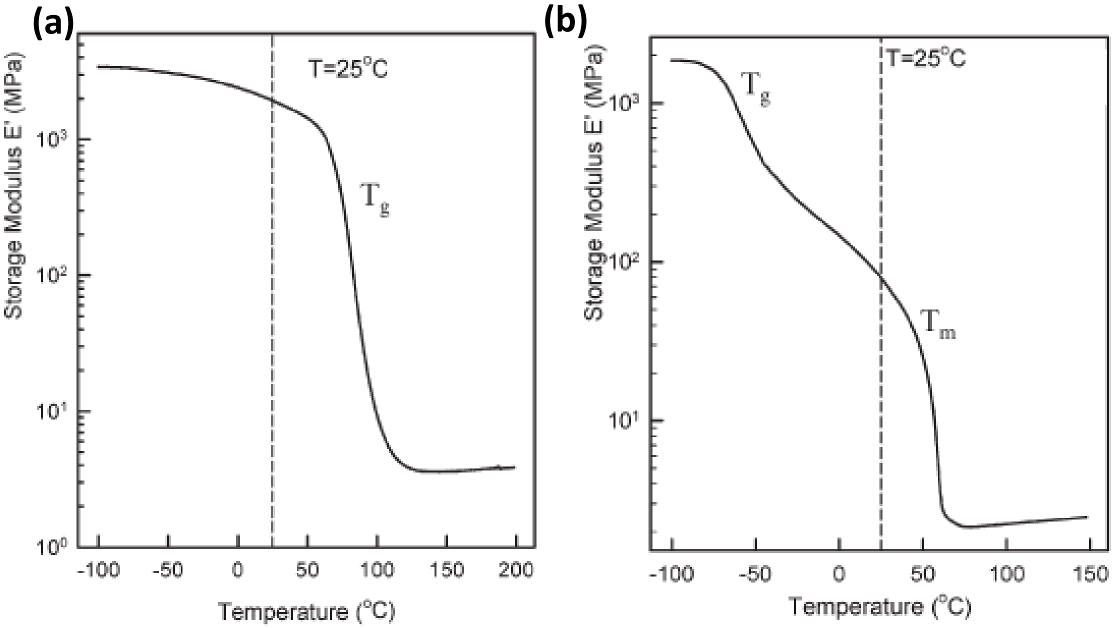

Figure 1-2. Graphs showing (a) covalently crosslinked glassy thermosets (class I) and (b) covalently crosslinked semi-crystalline thermosets (class II). (Adopted with permission of Liu, C.; Qin, H.; Mather, P. T. *Journal of Materials Chemistry* 2007, 17, (16), 1543-1558.)

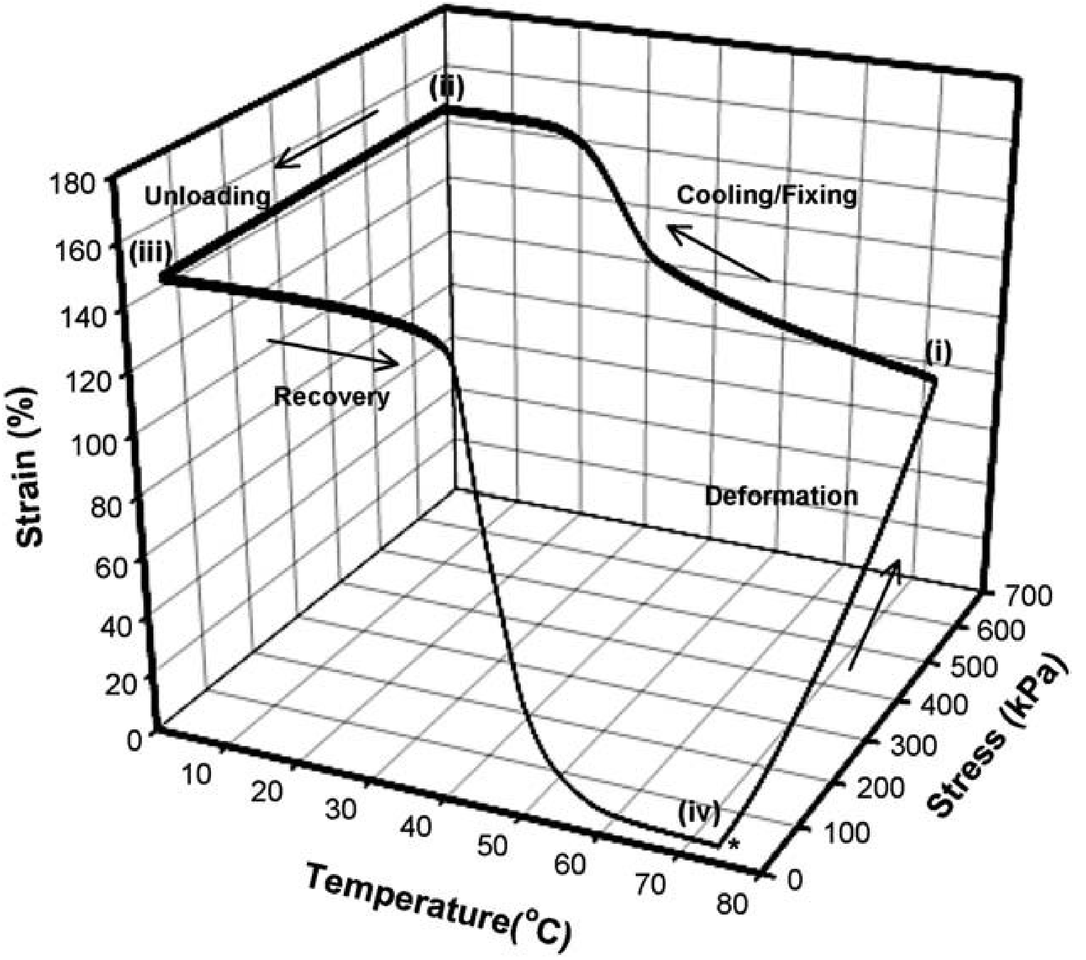

Figure 1-3. One way shape memory cycle (1WSMC) showing a 3-D representation of the 4 step process to explain the SM effect for a poly(cyclooctene) (PCO) polymer. The material elongates by increasing stress at 75 °C (i). Cooling (ii) and removing the stress (iii) results in a temporary ‘‘fixed’’ strain that is recovered to the original strained state upon heating (iv). (Adopted with permission of Kunzelman, J.; Chung, T.; Mather, P. T.; Weder, C. *Journal of Materials Chemistry* 2008, 18, (10), 1082-1086.)

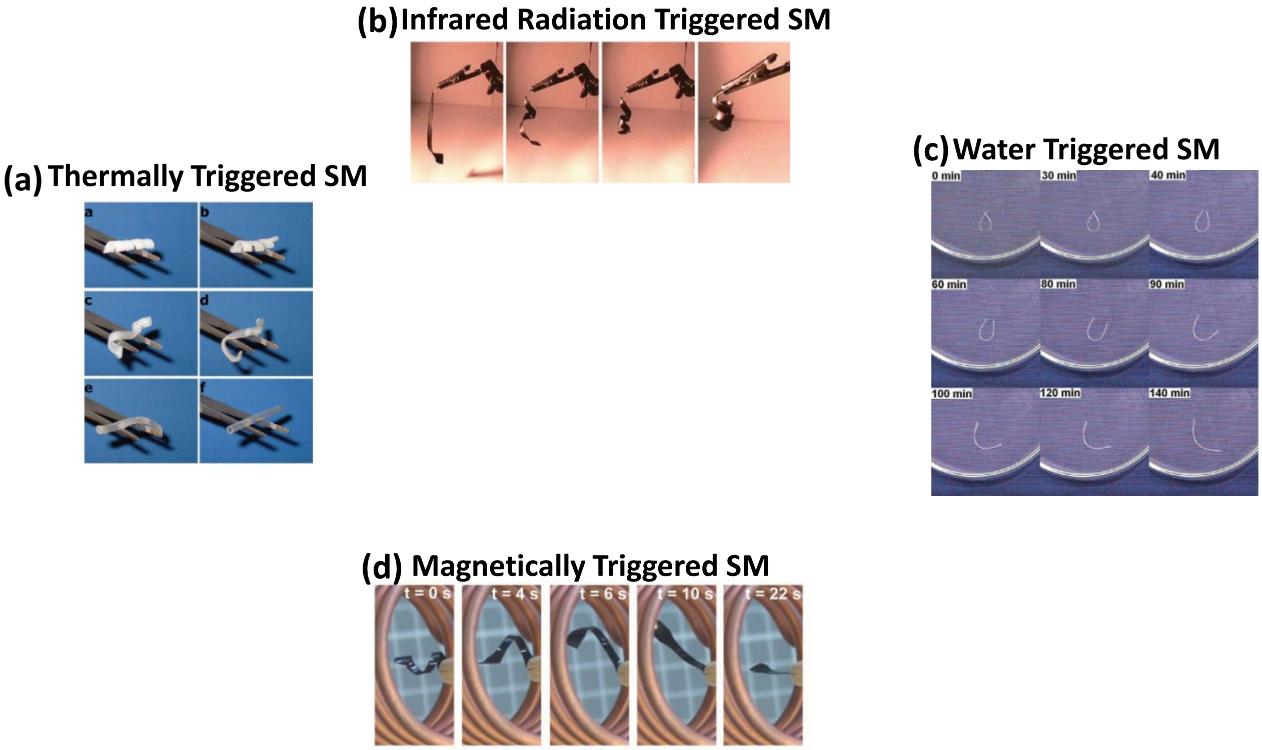

Scheme 1-5. Examples of polymeric shape memory (SM) systems showing (a) thermally (Langer, R., and Tirrell, D. A., Nature (2004) 428, 487), (b) infrared radiation (Koerner, H., et al., Nat. Mater. (2004) 3, 115), (c) water (Huang, W. M.; Yang, B.; An, L.; Li, C.; Chan, Y. S. Applied Physics Letters, 2005, 86, (11), 3.) and (d) magnetically (Mohr, R., et al., Proc. Natl. Acad. Sci. USA (2006) 103, 3540) triggered SM systems. (Adopted with permission of the authors above.)

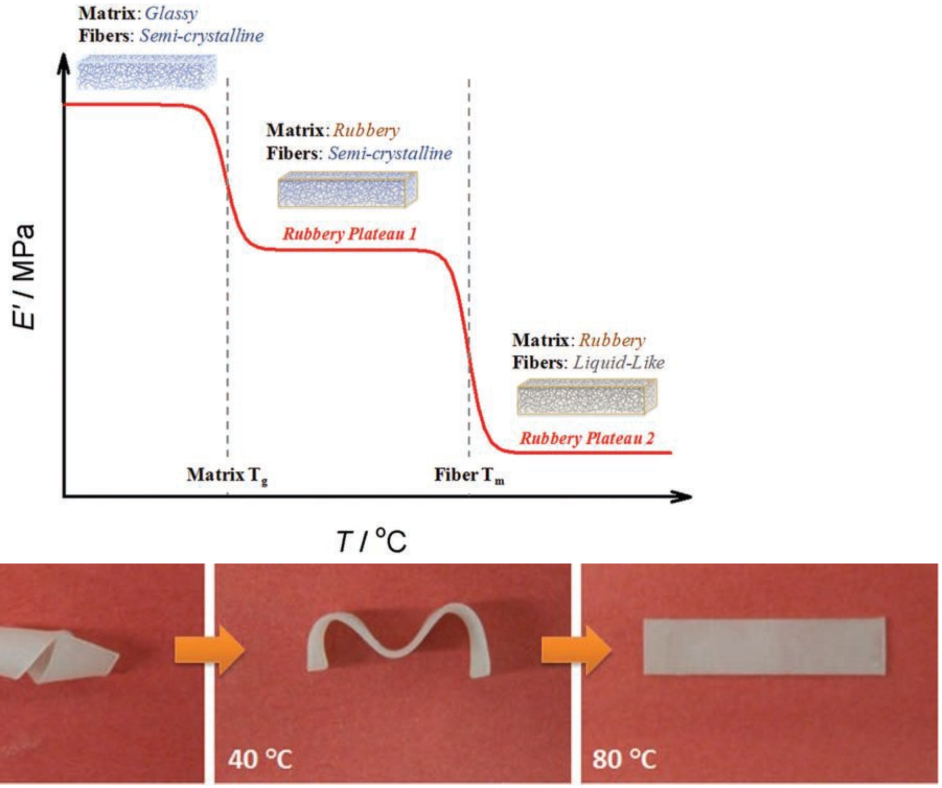

Scheme 1-6. Triple shape memory system showing three distant shapes observed at three different triggering temperatures. (Adopted with permission of Luo, X. F.; Mather, P. T. *Advanced Functional Materials* 2010, 20, (16), 2649-2656.)

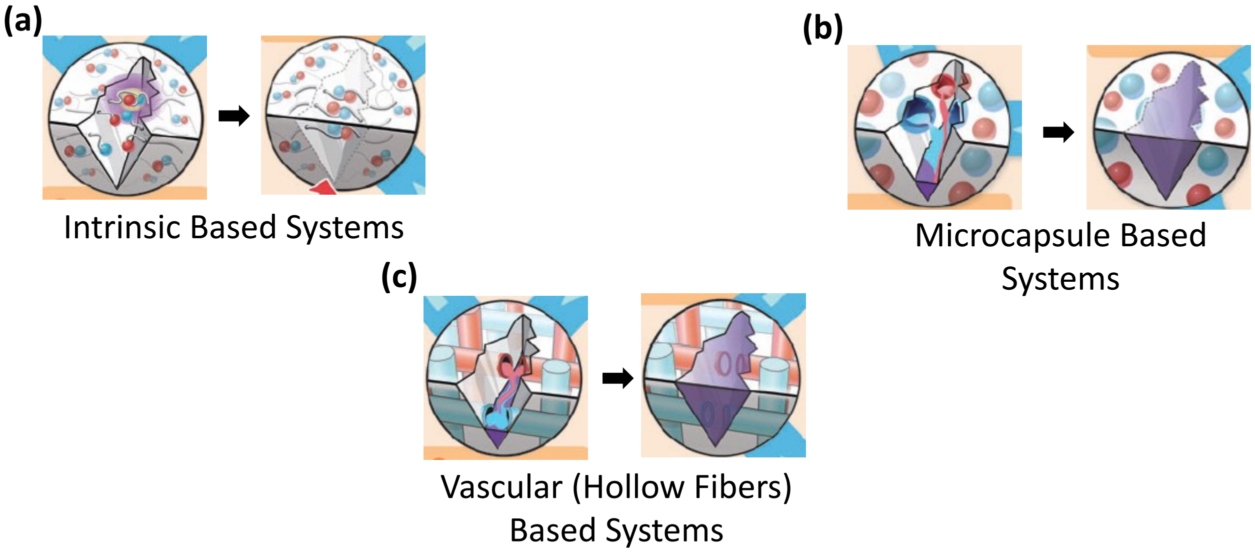

Scheme 1-7. Figure showing examples of polymeric and composite self healing (SH) systems showing (a) intrinsic, (b) microcapsule, and (c) vascular based systems (Adopted with permission of Blaiszik, B. J.; Kramer, S. L. B.; Olugebefola, S. C.; Moore, J. S.; Sottos, N. R.; White, S. R., Self-Healing Polymers and Composites. *Annual Review of Materials Research, Vol 40* 2010, 40, 179-211.)

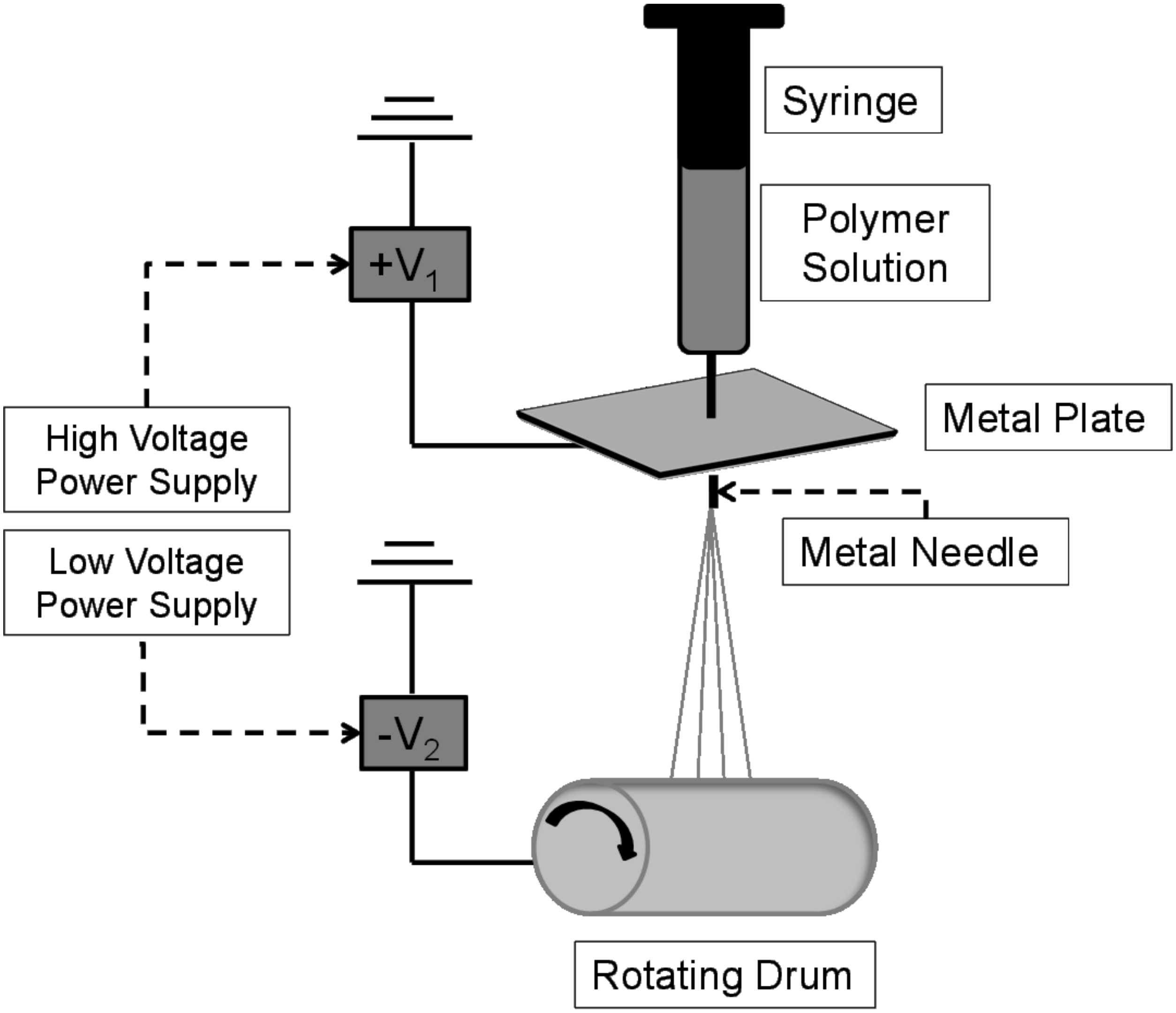

Scheme 1-8. Schematic showing the electrospinning set up using a rotating mandrel

CHAPTER TWO

LINEAR/NETWORK POLY(ε-CAPROLACTONE) BLENDS EXHIBITING SHAPE MEMORY ASSISTED SELF-HEALING (SMASH)*

2.0 SYNOPSIS

Self-healing (SH) polymers are responsive polymeric materials that can repair mechanical damage, such as cracks, in an autonomous fashion. In most SH polymer studies reported to date, crack closure was either unaddressed or achieved by manual intervention. Here, we report a new strategy that utilizes shape memory (SM) to prepare novel SH polymers that are capable of simultaneously closing and re-bonding cracks with a simple thermal trigger. This strategy, termed "shape memory assisted self-healing (SMASH)" (Scheme 2-1) is demonstrated in a blend system consisting of crosslinked poly(ε-caprolactone) network (n-PCL) with linear poly(ε-caprolactone) (l-PCL) interpenetrating the network to yield a semi-interpenetrating polymer network (SIPN). The SIPN exhibits a combination of SM response from the network component and SH capacity from the linear component. Thermomechanical analysis revealed that the thermoset, n-PCL, demonstrates reversible plasticity – a form of shape memory where large plastic deformation at room temperature is fully recoverable upon heating. This SM action assists to close any cracks formed during deformation and/or damage while l-PCL chains tackify the crack surfaces by diffusion to the free surface and ultimately across the area of damage during the same heating step as used for SM. In our study, we investigated the controlled damage and SMASH healing of blends with varying composition using tensile testing of essential work of

---

*This work appeared, in part, *ACS Applied Materials & Interfaces* **2011**, *3*, 152-161.

fracture film specimens. The healing component, l-PCL used had a high enough molecular weight (M_w) (M_w~65k g/mol) to enable re-entanglement after diffusion across the interface while the shape memory component, n-PCL was prepared from PCL telechelic diacrylates and a tetrathiol crosslinker, yielding exceptional shape memory. We found excellent self-healing of films by the SMASH mechanism, with nearly complete healing for l-PCL contents exceeding 25 wt-%. Applications are envisioned in the area of self-healing bladders, inflated structure membranes, and architectural building envelopes.

2.1 INTRODUCTION

The shape memory effect in polymers is a phenomenon wherein the polymeric article can be deformed to a temporary shape and stored in that form until later being triggered to return to its original state when stimulated by external heating or other means.[1-4] Such materials are considered enabling for a large number of applications in such diverse industries as automotive, architecture, aerospace, and medical devices. For semi-crystalline networks (type II SMPs as defined by Liu et al.,[5] also the current case as will be detailed later), a temporary deformation can be fixed by the crystallization of deformed polymer chains when cooling below melting temperature (T_m).[4,6] The permanent shape may be recovered next when the sample is heated above T_m due to the presence of permanent/covalent crosslinks, under the action of rubber elasticity. In particular, the crosslinks serve as permanent anchors for the network chains to return to their state of highest entropy.[3] In our case, the crosslinks were formed when the functional ends (acrylate) of network chain macromers reacted with thiol groups of a multifunctional crosslinker molecular using thiol-ene chemistry.[7-10] Previous studies have successfully used similar systems to create polymer materials with SM properties.[1,2,6,7]

Cracks that form in the bulk of a material caused by thermal, mechanical, chemical, and/or UV radiation stimulation are hard to detect and thus repair.[11] This damage has become a problem as the material's mechanical properties are severely compromised.[12] In fact, SH was a concept developed in the 1980's as a way to heal cracks that were not externally visible, in order to prolong the life of polymeric materials.[11] SH is a mechanism where microcracks rebond to heal the area of damage. One example of accomplishing SH is through macromolecular chain interdiffusion where the SH is triggered when the material is heated above its T_m, a common method of healing among thermoplastic semi-crystalline polymers.[11] Other SH systems incorporate microencapsulated healing agents where a propagated crack will rupture the capsule allowing the agent to fill in the damaged site by capillary action and bond the crack surfaces via in-situ polymerization.[12-14] For example, White et al. have demonstrated an autonomous healing polymeric composite system which integrates a ruthenium-based Grubbs' catalyst that initiates ring-opening metathesis polymerization of dicyclopentadiene (DCPD) in a thermoset matrix.[12] Due to damage, a crack will form in the bulk of the material, rupturing a monomer-filled microcapsule and lead to flow of the monomer into the crack site by capillary action. The Grubb's catalyst particles, which are randomly distributed throughout the matrix, will trigger polymerization upon contact with the monomer (here, the healing agent), even at room temperature, causing rebonding of the crack surfaces.[12]

As another capsule-based SH approach, the same group has reported on a self-healing poly(dimethyl siloxane) (PDMS) elastomer wherein two types of microcapsules are distributed within the matrix: (i) resin microcapsules that contains high-molecular weight, vinyl-functionalized PDMS and platinum catalyst, and (ii) microcapsules containing hydride-functionalized PDMS for reaction with the vinyl-functionalized resin of (i) in the presence of the platinum catalyst.[15] This material showed good SH response for films whose tears where realigned externally. Even solvents have been used as healing agents for thermosets. For example, solvent-containing microcapsules of phenylacetate (PA) and ethyl phenylacetate (EPA) have been dispersed in the EPON 828 epoxy system for SH purposes.[16] In this system, rupture of the capsules releases the solvent, locally swelling the epoxy matrix, yielding chain mobility, residual monomer diffusion and rebonding. Such action allows for additional, localized crosslinking and associated healing of the damaged areas.[16] Other work has included functional repair components that are contained in hollow glass fibers (HGF) and embedded in either carbon fiber reinforced epoxy or glass fiber reinforced epoxy in order to alleviate damage and sustain mechanical strength.[17-19] These systems are different from microencapsulated polymeric systems as the HGF serves to store functional agents for self repairing composites while also serving to reinforce the entire system.[18]

The SH systems described above all rely solely on a rebonding reaction, but do not provide often needed crack closure before healing. Addressing this need, Kirkby et al.[20,21] ingeniously integrated both SM and SH in a single material system. In their first report,[20] a small number of pre-tensioned shape memory alloy (SMA) wires were placed perpendicular to the crack surfaces of a tapered dual cantilever beam (TDCB) specimen made of a diethylenetriamine (DETA) cured epoxy resin, EPON 828, with Grubb's catalyst embedded in the resin matrix for later catalysis of healing. "Self-healing" was conducted by manually injecting DCPD monomers to the crack and activating the recovery (contraction) of SMA wires by passing through an electrical current, which led to significant crack closure (reduction of crack surface separation) and improved healing. The same strategy was later adopted in a microcapsule-based system[21] to achieve autonomous self-healing. Although proved to be effective in obtaining better healing under controlled laboratory conditions, this SMA based approach presents several drawbacks for practical applications. First, the SMA wires only provide a unidirectional recovery force; this means they have to be placed perpendicular to the crack in order to be effective. This is hard to realize since, unlike TDCB specimens, the directions of crack propagation in real applications are hardly predictable. Second, the incorporation of SMA wires leads to increased material cost and processing complexity. Therefore better strategies to achieve crack closure in SH polymers are still needed. This has been the main motivation of the current contribution. Other SH systems have been reported for which a combination of thermosetting resin and thermoplastic was used. Hayes et al.[22] studied epoxy resins (LY1556 and GY298), which served as the thermosetting host matrices, and linear poly(bisphenol-A-co-epichlorohydrin), which served as a thermoplastic healing agent. This system proved to be a solid-state healable system where the thermoplastic remained dissolved in the matrix upon curing. After the blend was fractured and then heated, the thermoplastic diffused to the damaged site, sealing the crack and healing the damage. In a similar manner, another group reported a blend of triethyltetramine (TETA) cured diglycidyl ether of bisphenol A (DGEBA) resin with polyethylene-co-methacrylic acid (EMAA) being incorporated as the healing agent.[23] It was found that EMAA formed a discrete phase in the resin (unlike the prior system) and reacted with the resin during healing. EMAA also showed an ability to achieve fracture strength recovery without the need of external forces to assist in healing. Our group has reported on a polymerization-induced phase separation (PIPS) system where a diglycidyl ether of bisphenol A (DGEBA) epoxy-resin-polycaprolactone (PCL) blend was used to enable a unique mechanism of self-healing.[24] The miscible blend underwent PIPS during epoxy cross-linking to produce a “brick and mortar” morphology that afforded thermal mending and reversible adhesion through “bleeding” of the PCL component under the action of differential thermal expansion of liquid PCL and solid epoxy. Finally, reversible chemistry has been exploited for self- healing by Bergman and Wudl.[25,26] In their work, covalent bonds broken during damage could be reformed by application of heat, allowing flow, and subsequent cooling that allowed rebonding.

Until now, fully polymeric systems exhibiting both SM and SH mechanisms have yet to be studied and that is the topic of the present contribution. In this chapter, we report on a unique system called *Shape Memory Assisted Self Healing* (SMASH) (Scheme 2-1), a concept we first introduced in 2009.[27] This system incorporates a covalently crosslinked network by end-linking end-functionalized poly(ε-caprolactone) (n-PCL) as a thermoset for SM properties and a linear poly(ε-caprolactone) (l-PCL) thermoplastic to provide a SH property. (Here, “l” in “l-PCL” stands for “linear”.) This SMASH material can achieve reversible plasticity shape memory (RPSM), a novel phenomenon which we define as the recovery of both the temporal elastic and plastic region of deformation. Consequently, gross damage in proximity to the crack(s) from damage can be reversed by heating.[1,5,6,28] The SMASH material incorporates a thermoplastic interpenetrating into the thermoset, pre- and post-photopolymerization. They also have near-identical T_m values, enabling use of a single heating phase to trigger both the SM and SH mechanisms without compromising the mechanical integrity of the entire system. We contend that such a system with fast and complete healing during a single heating event is quite original and capable of enabling easily maintained mechanical systems involving polymeric films under load, such as inflated structures or containment bladders. We prove that the SMASH concept works well without the addition of fiber or wire reinforcements and without external injection of healing agents.

2.2 EXPERIMENTAL SECTION

2.2.1 MATERIALS

Poly(ε-caprolactone) diol (M_n ~ 3,600 g/mol) (Scientific Polymer Products, Inc.) was first vacuum dried at room temperature (RT) over night to remove any adsorbed moisture prior to use. Poly(ε-caprolactone) (l-PCL) (M_w ~ 65,000 g/mol), pentaerythritol tetrakis(3-mercaptopropionate) (tetrathiol) 97%, anhydrous benzene (99.8%), triethylamine (99%), acryloyl chloride (98%), 2,2-dimethoxy-2-phenylacetophenone (DMPA) 99%, and deuterated chloroform, (99.8% deuteration), all purchased from Sigma Aldrich, and hexane (Fisher Scientific), were used as received.

2.2.2 POLY(ε-CAPROLACTONE) DIACRYLATE SYNTHESIS

10 g (3.3 mmol) of poly(ε-caprolactone) (PCL) diol was dissolved in 60 mL of anhydrous benzene under nitrogen purge at RT. 1.184 mL (8.5 mmol) of triethylamine and 0.694 mL (8.6 mmol) of acryloyl chloride was then added dropwise with constant magnetic stirring. The reaction was then carried out at 80 °C for 3 h. The solution was filtered to remove triethylamine hydrochloride and precipitated in 600 mL of hexane to yield a white powder, following which it was dried under vacuum (30 in.Hg) at 65 °C over night (Scheme 2-2). ^{1}H NMR analysis was then conducted to determine the degree of acrylate end-capping ($CDCl_3$, 4 mg/ml). The acrylate

end-capping conversion ratio was calculated from the NMR spectra and the conversion ratios ranged from 97-108% (Scheme 2-3) (quantitative conversion, within error) consistent with prior literature using this method.[7] ^{1}H NMR of PCL diacrylate(3k): (a) 4.07 (t, $-CH_2-\mathit{CH_2}-OCO-$), (b+d) 1.65 (m, $-\mathit{CH_2}-CH_2-O$, $-\mathit{CH_2}-CH_2-OCO-$), (c) 1.39 (m, $-CH_2-\mathit{CH_2}-CH_2-$), (e) 2.31 (t, $-OOC-\mathit{CH_2}-CH_2-$), (f) 4.24 (t, $-COO-\mathit{CH_2}-CH_2-O-$), (g) 3.70 (t, $-COO-CH_2-\mathit{CH_2}-O-$), (h) 6.12 (dd, $-OCO-\mathit{CH}=CH_2$), (i) 6.40 (dd, $-OCO-CH=\mathit{CH_2}$*cis*), (j) 5.83 (dd, $-OCO-CH=\mathit{CH_2}$*trans*) where the letters a–j correspond to the NMR spectrum shown in Scheme 2-3 and where the end-capping conversion values are shown. In preparing formulations for crosslinking, it was assumed that each PCL diacrylate featured a functionality of 2. As we will show, subsequent end-linking by thiol-ene reaction led to high gel fractions. Scheme 2-4 shows the NMR spectrum for PCL diol(3k) followed by the repeat unit (n) values needed to calculate the end-capping conversions.

2.2.3 l-PCL:n-PCL MISCIBLE BLENDS

Linear:network blends were prepared by the crosslinking of PCL diacrylate with tetrathiol in the presence of linear PCL (Scheme 2-5). Here, we show the reaction mechanism of thiol-ene addition that dominates over free-radical polymerization at large thiol:ene ratios,[29] though the acrylate end-groups themselves can undergo some competing chain-growth polymerization. The use of a thiol cross-linker for ene-based systems has become prevalent[10,29,30] due to advantages such as oxygen insensitivity and mobility of the thiyl radical.[10] Thus, l-PCL, PCL diacrylate and tetrathiol crosslinker (molar ratio of (PCL diacrylate)/tetrathiol = 2:1) of various l-PCL wt-% were mixed in 1.2 mL of chloroform (50 % w/v) by continuous magnetic stirring at RT until a clear, homogeneous solution was obtained. DMPA (2% relative to PCL diacrylate) was then added and quickly dissolved. The solution was injected to a custom-made glass mold that consisted of two glass slides (75 mm * 25 mm * 1 mm) with a 1 mm thick Teflon spacer placed in between the glass slides. The mixture was exposed to uniform UV irradiation at a power of 60 W, and λ_{max} of 352 nm for 1 h at RT in a custom made UV curing box consisting of two banks (top and bottom) of UV lamps.[31] The cured samples were removed from the mold and then placed under vacuum (30 in Hg) at 75 °C over night for complete chloroform removal. The samples are named as l-PCL_x:n-PCL_y where x and y stand for the weight percent of l-PCL and PCL diacrylate, respectively. Here, the mass of the crosslinker is excluded in the nomenclature weight percent for simplicity. The following compositions were prepared using the above method (l-$PCL_{wt\text{-}\%}$:n-$PCL_{wt\text{-}\%}$): l-PCL_0:n-PCL_{100}, l-PCL_{10}:n-PCL_{90}, l-PCL_{20}:n-PCL_{80}, l-PCL_{25}:n-PCL_{75}, l-PCL_{35}:n-PCL_{65}, l-PCL_{50}:n-PCL_{50}, l-PCL_{60}:n-PCL_{40}, l-PCL_{70}:n-PCL_{30}, and l-PCL_{80}:n-PCL_{20}.

2.2.4 DEGREE OF SHAPE MEMORY NETWORK FORMATION

To evaluate the extent of network formation, gel fraction measurements were conducted by first weighing and then immersing a small cured film in 20 mL of chloroform with constant agitation in a shaker (New Brunswick, C24) at 75 rpm and T= 37 °C for 24 h, extracting completely the chloroform-soluble l-PCL, as well as unreacted PCL diacrylate components. After drying under vacuum at 65 °C over night the sample mass was measured and the gel fraction was calculated according to:

$$G(\%) = \frac{m_d}{m_i} \cdot 100 \tag{2-1}$$

where m_i is the initial dry weight before extraction and m_d is the dry weight after extraction.[6,31] Gel fraction experiments were conducted for three replicates of each composition.

2.2.5 THERMAL CHARACTERIZATION

The thermal properties and phase behavior of the l-PCL:n-PCL blends were characterized using thermogravimetric analysis (TGA) and differential scanning calorimetry (DSC), anticipating pertinence to mechanical properties and healing behavior studied later. For the former, each sample with a mass ranging from 3.0 - 5.0 mg was loaded in a TA Q500 TGA instrument. The temperature was then ramped linearly to 600 °C at 10 °C/min under constant nitrogen purge to monitor the decomposition events evidenced by mass changes. DSC experiments were conducted using a TA Q200 DSC instrument equipped with a refrigerated cooling system (RCS). First, the samples were cooled to an equilibration temperature of -85 °C, heated to 120 °C at 10 °C/min, equilibrated at 120 °C for 1 minute, cooled to -90 °C at 3 °C/min, equilibrated at -90 °C for a 1 minute, and finally heated to 120 °C at 10 °C/min where the first cooling and second heating traces were recorded for detailed study. The melting temperature (T_m), crystallization temperature (T_c), heat of melting (ΔH_m) and heat of crystallization (ΔH_c) were recorded for all samples studied. Three separate experiments were conducted for each composition to assure reproducibility.

2.2.6 DYNAMIC MECHANICAL AND SHAPE MEMORY ANALYSES

Dynamic mechanical and shape memory properties of all compositions were studied using a TA Q800 dynamic mechanical analyzer (DMA). Each sample was cut from a crosslinked film as described above to yield tensile bar specimens with typical dimensions of 5.7 mm (length) x 2.5 mm (width) x 0.7 mm (thickness) and loaded under tension in the DMA apparatus. To measure linear viscoelastic properties and clearly reveal the thermal transitions, an oscillatory tensile deformation was applied with a small displacement amplitude of 15 μm (tensile strain < 0.4%), a frequency of 1 Hz, and a "force track" (the ratio of static to dynamic forces) of 110%. The temperature was first ramped to 90 °C at 3 °C/min to remove the thermal history, held isothermally at 90 °C for 20 minutes, then cooled down to -90 °C at 3 °C/min, held isothermally at -90 °C for 5 minutes, and finally heated to 120 °C at 3 °C/min. The tensile storage modulus values (E') and tanδ values from the second heating trace were reported. This DMA procedure was tested at least two times for every sample, and confirmed excellent reproducibility.

Shape memory of a particular type, Reversible Plasticity Shape Memory (RPSM), was examined for all compositions following a modified four-step thermomechanical cycling method,[31] now described. Each sample was punched into a dogbone geometry following the ASTM D638-03 Type V (scaled down by a factor of 2, TestResources, Inc., Shakopee, MN) with an average thickness of 0.5 ± 0.1 mm. Prior to testing, each sample was first placed in a pre-heated oven (Fisher Scientific Isotemp 825F) at 80 °C (> PCL T_m) for 10 min and left at RT for 10 min to eliminate the effects of thermal history (this will be referred to as thermal mending hereafter). During testing, the sample was first stretched at RT from a preloaded strain (ε_i) to a strain of 200% at a rate of 5%/min and held at 200% strain for 10 min to allow stress relaxation, yielding a strain of ε_m (step 1). To release the force/stress, the strain was programmed to decrease at 5%/min until the force reached a small value of 0.001 N, after which a large percentage of plastic strain/deformation remained (ε_u) for all the samples tested (step 2). Shape recovery was then triggered by heating to 80 °C at 3 °C/min and at this same low load (step 3) to a recovered strain, ε_r. Finally, the temperature was ramped back to 25 °C at 3 °C /min to complete the SM cycle (step 4). The fixing (R_f) and recovery (R_r) ratios were calculated for each composition. R_f was calculated using $R_f(\%)=(\varepsilon_u/\varepsilon_m)\cdot 100$ and R_r obtained by using $R_r\,(\%)= (\varepsilon_u - \varepsilon_r)/(\varepsilon_u - \varepsilon_i)\cdot 100$ where each of the strains are defined above.

2.2.7 SELF HEALING EXPERIMENTATION

Self Healing (SH) experiments were conducted using the deeply double-edge notched tensile (DDEN-T) geometry employed for fracture testing of polymeric films.[32-34] Cured l-PCL:n-PCL blend samples were first cut into a dogbone geometry (ASTM D638-03 Type 1, scaled down by a factor of 3), with an average thickness of 0.56 ± 0.08 mm and a width of 4.3 mm, using a custom made dogbone cutting die (TestResources, Inc., Shakopee, MN). For such specimens, the gauge length is 16.67 mm. The samples were thermally mended under the same conditions as the recovery step of SM experiments described above. Each sample was loaded in a TST350 *Linkam Tensile Stress Testing Stage* (Linkam Scientific Instruments, Ltd.) with a 200 N load cell and uniaxially stretched to a displacement of 10 mm (corresponding to a strain of 60% at a displacement rate of 0.1 mm/s (0.6 %/s) at RT. After being removed from the stage, the sample was heated to 80 °C for 10 min in a convection oven, leading to full recovery of its original shape. This loading-recovery process was repeated a second time to analyze whether the mechanical properties of the sample were compromised from the first stretch. Next, a custom made double edge notch punch (Scheme 2-6) was used to create two collinear, gauge-centered edge-cracks that were 0.5 mm long on each side of the dogbone neck. The notched sample was then stretched to a displacement of 5 mm (corresponding to a strain of 30%) to macroscopically and controllably damage the sample and propagate the cracks extensively, but leaving a central ligament. The whole process was followed by real time imaging using a Zeiss Discovery V8 stereo microscope with a QIMAGING (QICAM FAST1394) CCD camera. The damaged sample was then "self-healed" (or thermally mended) by heating to 80 °C and holding isothermally for 10 min, during which time the SM mechanism was triggered and assisted in crack closure by the n-PCL, while the SH mechanism allowed for crack rebonding. This healed specimen was then tested with the same tensile deformation *without* re-notching to measure SH efficiency, which was defined as:

$$\eta(\%) = \frac{P_{healed}^{\max}}{P_{virgin}^{\max}} \cdot 100 \qquad (2\text{-}2)$$

where the healed ($P_{healed}^{\max}$) and virgin ($P_{virgin}^{\max}$) peak loads were obtained from the force vs. displacement curves recorded for sample's virgin and healed state when stretched on the Linkam tensile stage. After this test, if the sample had not fractured in two it was thermally treated and tested yet one more time, labeled "After 2nd Thermal Mending", again without additional notching.

2.3 RESULTS AND DISCUSSION

2.3.1 PREPARATION AND THERMAL ANALYSIS OF l-PCL:n-PCL NETWORKS

Gel fraction (GF) experiments were conducted to evaluate the network content of the linear:network blends and the results are shown in Figure 2-1. To do this, nine compositions with varying l-PCL and n-PCL wt-% content were prepared by solvent blending followed by a UV-initiated thiol-ene reaction photopolymerization. Next, GF measurements were conducted by chloroform extraction, noting that l-PCL is soluble in this solvent. If all the PCL diacrylate molecules reacted with the thiol-ene groups during photopolymerization, the GF would show a linear, and downward trend, relationship with l-PCL wt-% (Figure 2-1). We anticipated extraction of the linear component and for the network component to remain. All samples were visually turbid prior to solvent swelling, but transformed into a transparent state after swelling was complete at 24 h. The samples all remained intact after swelling, but were significantly enlarged due to the solvent swelling the sample. A thin, white layer of unreacted PCL diacrylate and/or l-PCL was evident in the extraction jar where the GF experiment took place once the solvent evaporated. Gel fractions obtained (shown in Table 2-1) ranged from 90.7 ± 0.9% for l-PCL_0:n-PCL_{100} to 15.2 ± 1.5% for l-PCL_{80}:n-PCL_{20}. The GF values of the remaining compositions lay within the range stated above. Our GF show reasonable agreement with our expectation that only l-PCL would be extracted and that small (<10%) extraction of n-PCL components from the l-PCL_0:n-PCL_{100} samples occurred due to network imperfections.

TGA analysis was conducted on all compositions made and on the PCL diacrylate and PCL thermoplastic. Figure 2-2 shows a graph of weight loss (%) vs. temperature. Table 2-2 reveals an onset degradation temperature that was approximately 390 °C among all the compositions tested as well as for the PCL diacrylate and PCL thermoplastic. DSC experiments were conducted to help gain an understanding of the thermal transitions of each composition as they relate to the thermomechanical properties, which will be presented below. First cooling and second heating DSC traces are shown in Figure 2-3 for all linear:network compositions, as well as the PCL $diacrylate_{100}$ and l-PCL_{100} samples for comparison. While all compositions tested show similar melting and crystallization temperatures, a clear trend in T_m is evident: as the percentage of l-PCL increases, the melting point increases in a manner approaching pure linear PCL. Further, it is visually evident that intermediate compositions feature broader melting transitions than the limiting cases. These trends are discussed quantitatively in what follows. The average of three traces of T_m, T_c, ΔH_m, and ΔH_c are shown in Table 2-3. The trends of T_m, T_c, ΔH_m, and ΔH_c as a function of l-PCL wt-% are shown in Figure 2-4. T_m, T_c, ΔH_m, and ΔH_c values showed an overall increasing trend with the increase of l-PCL wt-% content among the compositions. This phenomenon is attributed not only to a higher l-PCL M_w compared to the PCL diacrylate M_w, but may also be due to the increase of l-PCL lamellar thickness, which requires more energy to melt. This latter postulation is beyond the scope of the present paper, but bears future investigation.

2.3.2 DYNAMIC MECHANICAL ANALYSIS OF l-PCL:n-PCL NETWORKS

Thermomechanical testing was conducted to understand how the linear viscoelastic properties of the compositions depended on temperature. This set of testing is important to provide context for subsequent characterization of SM cycles. Tensile storage modulus (E') and tan(δ) as a function of temperature are reported for all compositions (Figure 2-5). All samples showed two distinct thermal transitions: the glass transitions (T_g) were evident at ~ -50 °C where the initiation of polymer chain mobility occurred, while the melting transitions (T_m) appeared at near 55 °C. The tensile storage modulus was at or above 1 GPa (1000 MPa) below T_g, beyond which it decreased gradually to ~100 MPa and then sharply to ca. 1 MPa beyond T_m for crosslinking samples or below a measurable level for l-PCL$_{100}$. This drop in modulus above T_m was to a modulus plateau indicative of the crosslink density of the entropic rubbery state. As self-healing will be shown to depend on shape memory for crack closure, this rubber elastic state is critical to the successful healing of cracks. While the tensile storage modulus at 25 °C was largely insensitive to the l-PCL content in the blends, the modulus at 80 °C did decrease markedly with l-PCL wt-%

content, owing to the dilution of the crosslinked network. These trends in composition are shown in Figure 2-6.

2.3.3 SHAPE MEMORY (SM) CHARACTERIZATION

All of the blends containing some portion of n-PCL exhibited shape memory, owing to the fixing of strain by PCL crystallization and recovery of strain by rubber elasticity. Similar reports of shape memory in PCL networks have appeared in the literature.[3,7] Here, we exploit a shape memory cycle (SMC) for semi-crystalline polymers that we term as Reversible Plasticity Shape Memory (RPSM).[27,35] RPSM is a SMC where the material can be deformed to a temporary state below a critical temperature (here, T_m), thereby achieving high levels of strain through both elastic (pre-yield) and plastic (post-yield) deformation regions. Remarkably, heating above T_m leads to recovery of both pre- and post-yield strain under the action of unimpeded rubber elasticity, thus the term "reversible plasticity." Representative RPSM cycles are shown in Figure 2-7 (a) for two compositions (discussed further below). In contrast, conventional SMCs involve deformation above T_g or T_m in order to reach a desired temporal strain where only the elastic deformation region is evident and recovered.[1,5-7,28] RPSM assists in the SH process, as it promotes contact between the cracked surfaces formed during damage. Figure 2-7 (b) shows the RPSM cycles for all compositions tested.

As shown in Figure 2-7 (a), each sample was stretched at RT to ~200% strain to achieve temporary deformation (Figure 2-7 (a), step 1-2). During this deformation step, the PCL crystalline lamellae and constituent polymer chains are envisioned to deform with alignment parallel to the loading axis, experiencing cold draw beyond the yield point. This is evident in the dashed green curve representing a projection of the data on the stress-strain plane for the l-PCL$_{50}$:n-PCL$_{50}$ composition. The sample was then fixed at this strain to allow for any stress relaxation of the material. The strain was released to observe the initial elastic shape recovery (Figure 2-7 (a), step 2-3), and the sample then heated to 80 °C to trigger quite complete shape recovery (Figure 2-7 (a), step 3-4). Finally, the sample was cooled to RT to complete the cycle (Figure 2-7 (a), step 4-5). All blend compositions were tested in such a manner and showed behavior similar to that shown in Figure 2-7 (a) where these results are shown in Figure 2-7 (b). This demonstrates that RPSM can be achieved for the semi-crystalline thermoset/thermoplastic SMASH systems. We anticipated that this behavior would assist in the self-healing process by aiding in the crack closure step.

The shape memory fixing and recovery figures-of-merit, R_f and R_r, calculated from the RPSM cycles for all samples tested are reported in Table 2-4. All compositions achieved a temporary deformation of 200% strain before unloading (ε_m) with a strain ranging from 148.3 to 161.8% after unloading (ε_u) and a residual strain ranging from 11.6% to 50% (ε_r) after shape recovery. The residual strain is quite small compared to the high temporal deformation that each sample achieved prior to shape recovery. Quantitatively, R_f increased from 74.1 to 80.9 % as l-PCL content increased. This is associated with the fact that l-PCL in general has great fixing properties at RT regardless of the n-PCL content. R_r decreased from 92.7% to 69.1% as l-PCL content increased. This is associated to the fact that l-PCL alone does not exhibit high SM capacity. Figure 2-8 shows the R_f and R_r bar graph indicating this trend. The high recovery ratios observed in the SM cycles will increase the probability of SH as this recovery will assist in closing cracks found in the bulk of the material.

2.3.4 SELF-HEALING (SH) CHARACTERIZATION

Having demonstrated shape memory behavior conducive to requisite crack-closure, SH experiments (described in Experimental Section) were conducted in order to test for the degree of mechanical healing as a function of l-PCL content (wt-%). In particular, SH efficiency was determined by comparing the peak loads achieved during tensile testing of the virgin and healed states of samples damaged to the DDEN-T geometry (Scheme 2-6). Each sample in their virgin, damaged, and healed states was stretched above its yield point then thermally treated to recover and heal by l-PCL diffusion. SH experiments revealed that samples containing 25 wt-% or more of l-PCL completely healed after the first thermal treatment with no evidence of crack reopening (See Figure 2-10 for representative stress-strain curves for all eight compositions tested). Most importantly, these samples show that the initial cracks made prior to stretching and the propagated crack created while stretching have completely healed when heated above their T_m. A representative example is shown in Figure 2-9 (a) for a l-PCL_{50}:n-PCL_{50} composition. Data reported in Figures 2-9 (a) and Figure 2-11 are for individual specimens that are tested first without damage (Virgin 1st stretch, Virgin 2nd stretch) and then following damage (notched) and repeated mending cycles (After 1st, 2nd and 3rd thermal mending). Such testing was repeated in triplicate for all compositions. The peak loads corresponding to the initial deformation, damaged, and healed states of this composition were 26.6 N, 24.3 N, and 27.5 N, respectively (Figure 2-9 (a)). The data recorded from the force vs. displacement curves were compiled to obtain the average peak loads as a function of l-PCL wt-% obtained after the first, second, and third thermal mending steps for all compositions tested (Figure 2-12). It is noted that loads and displacements are plotted (Figure 2-9 and Figure 2-10) instead of stresses and strains, owing to the geometric complexity of the samples post-damage (notched) state making the latter difficult to estimate accurately. Furthermore, there are variable length "toe-regions" (compliant regions near the origin) in the force vs. displacement curves indicative of variable sample slack incurred during sample loading – these regions should be ignored. It is hypothesized that the variable sample slack may be associated to uneven clamping. Nevertheless, the average tensile yield stress as a function of l-PCL wt-% for the sample's virgin and healed state were calculated and shown in Figure 2-13. In all cases, the undamaged cross-section was used in the determination of the tensile yield stress from tensile load data. The average tensile yield stress was the same for samples in the virgin state where the samples in the healed state increased and plateaued for the higher PCL content samples. This trend was also evident in the SH efficiency data. Importantly, loads were compared for SH efficiency only for individual samples so that internal consistency was assured. We observed that the peak loads associated with the initial deformations were consistently higher than the peak loads of samples in the damaged state. However, heating the samples resulted in remarkable healing. In their healed state, the samples exhibited mechanical properties comparable to the virgin state when comparing the peak loads before damage and after healing. During the second and third thermal mending steps, there was no indication of crack reopening, but rather a necking effect that is apparent in ductile thermoplastic materials.[36]

Figure 2-9 (b) shows the force vs. displacement curve for a notched l-PCL_{50}:n-PCL_{50} sample that was stretched in its damaged state, showing stereo micrographs of the sample in its pre-stretched, initial crack opening, crack transition, and propagated crack state. We observed in Figure 2-9 (b) the sample after damage and before uni-axial stretching followed by the sample's yield point of initial crack opening (transition from the elastic to plastic deformation state). This state was then followed by initial crack growth (crack transition) and finally the propagated cracked state where an hour-glass geometry was evident. This characteristic curve showing crack propagation gives way to the same form as the undamaged sample (yield, followed by cold-drawing), as seen by comparing the solid blue curved (damaged) with the solid red curve (healed) of Figure 2-9 (a). This shows indirectly that the collinear cracks have been closed and rebonded successfully by the SMASH mending process. More directly, Figure 2-9 (c) shows the thermally-stimulated closure of the two collinear cracks upon heating the l-PCL$_{50}$:n-PCL$_{50}$ sample above T$_m$. As the melting point is exceeded, the sample contracts axially, closing the cracks. At the same time, the samples become optically transparent, indicating that melting of both n-PCL and l-PCL is associated with healing, as expected.

2.3.5 SELF HEALING EFFICIENCY ANALYSIS

Figure 2-11 shows the SH efficiency trend for all compositions tested where complete healing was evident with compositions containing 25 wt-% of l-PCL and greater. SH efficiency was calculated as a function of l-PCL wt-% for the first, second and third thermal mending treatments (Figure 2-11). In a thorough review paper on self-healing,[11] it was suggested that the ratio of fractured stress or the elongation-at-break for the healed and virgin states of the sample can serve as a measure of the SH efficiency. However, such properties could not be directly applied to the present (SMASH) system, as a complete fracture into two pieces would prohibit the SM mechanism. Instead, crack propagation of the collinear cracks proceeded to the point of partial fracture, yielding a finite ligament[37] located between the two partially propagated cracks. The strain energy stored in the ligament was ostensibly sufficient to drive the shape recovery component of self-healing (Figure 2-9 (c)).

Figure 2-11 also shows that compositions containing 20 wt-% of l-PCL and below have only modest SH efficiency for the first thermal mending treatment, with values ranging from ~ 50 to 80%. Compositions containing 25 wt-% of PCL and higher featured 90% or higher SH efficiency after the first thermal mending treatment and sustained this efficiency for the second and third thermal mending treatments for which the initial and propagated crack regions did not reopen. Thus, excellent shape-memory assisted self-healing is achieved when the l-PCL content in the SMASH system is above 25 wt-%. As proven above (Figure 2-11), the material is capable not only of recovering its elastic and plastic region, as shown in the SEM micrographs in Figure 2-14 of damage by its SM mechanism, but the material also has the capacity to heal both the initial and propagated region of damage and still sustain its mechanical properties, quite a distinguishable phenomenon. All samples that contained 20 wt-% of l-PCL or lower showed no evidence of complete healing after the first thermal mending treatment.

2.4 DISCUSSION

The crack profile created during crack propagation is an important area to study as this helps explain the fracture mechanics of ductile polymer materials. During the damage step of our self-healing experiments, the hour-glass crack profile that formed (Figure 2-9 (b)) was one that is characteristic for semi-crystalline materials. We have also classified the crack profile into three regions on the basis of SEM observations of the healed specimens seen in Figure 2-14: *(i) initial crack region* created by the DDEN-T cutting die, the *(ii) crack transition region* where the sample reached its yield point and the initiation of crack propagation begins, and *(iii) the propagated crack region* where new crack surfaces were made. Additional SEM images of this crack profile (edge views) are given in Figure 2-14. This is discussed further below. Scheme 2-7 includes a schematic of our envisioned l-PCL chain diffusion across the crack surfaces and re-entanglement for SH.

The crack profile observed in our experiments has also been observed by Fayolle et al. where they report that the essential work of fracture (EWF) can be used to study ductile fracture under plane stress conditions.[37] (We have not employed this method for toughness measurements, as complete fracture is required.) The load-displacement curves and underlying phenomena of EWF-type analyses can be categorized into two components, the essential work of fracture (EWF) and non-essential work of fracture (non-EWF).[33,34,37] EWF is defined as the work needed to form new crack surfaces in the process zone, which is also referred to as the ligament region located between the two notches formed, while non-EWF is the work consumed in the outer plastic region. Consequently, the area under the force vs. displacement curve (characteristic shape shown in our Figure 2-9 (b), blue curve) recorded for each fracture test yields the total fracture energy.

2.4.1. FIVE STAGE OF HEALING

The process of SH within the SMASH material can be explained from the material's SM mechanism and understanding the diffusion and l-PCL chain entanglement across the site of prior fracture. Considering the l-PCL chains to be capable of diffusion through the n-PCL network, the envisioned five stages of healing are as follows: (1) *polymer rearrangement*, (2) *surface approach*, (3) *surface wetting*, (4) *chain diffusion*, and (5) *equilibrium*, *randomization, and recrystallization* (Scheme 2-8).[11,38] After the SMASH material has been damaged at RT, two phenomena occur when the material is heated above T_m: (1) the l-PCL chains start to *rearrange* as the polymer chains become mobile and the surface tackifies through a population of linear chain ends. (2) The n-PCL transitions from a fixed, strained state to a deformed rubber state, the rubber elasticity gradually overwhelming the stiffness of the diminishing crystalline phases. Thus, the n-PCL-based SM drives crack closure, bringing the crack surfaces into proximity (*surface approach*). Following this *surface approach*, l-PCL *surface wetting* will take place as the two damaged crack surfaces make contact and the initial stage of l-PCL *chain diffusion* across the crack surfaces occurs. Finally, the system will approach a state of *equilibrium* as complete l-PCL chain diffusion occurs and chain *randomization* leads to strengthening re-entanglement. Finally, as the SMASH material is cooled to RT, both the n-PCL and l-PCL components re-crystallize, yielding a surface “scar” as evidence of the crack rebonding (Figure 2-14).

2.5 CONCLUSIONS

We have presented a new self-healing polymeric system that combines shape memory and thermoplastic diffusion for crack-closure and rebonding, respectively. Dynamic mechanical analysis revealed that all samples featuring some n-PCL (network) component exist in a rubbery state above T_m, whereas the healing agent, l-PCL$_{100}$, becomes a viscous liquid above the T_m. A particular type of shape memory, RPSM, was demonstrated, wherein a large deformation of 200% strain at RT was followed by nearly complete recovery upon heating above T_m. Self-healing tests showed that damage imparted in the controlled manner of DDEN-T specimens was well-healed when the samples were heated above T_m. Those samples that contained 25 wt-% of l-PCL and higher showed complete healing where only necking occurred in subsequent testing, indicating that the two crack surfaces fully rebonded together due to re-entanglement of the l-PCL adhesive component in the material. Thus, both the initial and propagated cracks were healed during thermal mending. SH efficiency analysis revealed that the mechanical properties for the compositions containing 25 wt-% of l-PCL and higher showed an efficiency of 95% or higher. We anticipate further studies with this and other SMASH systems exploring application as self-healing tank-lining bladders, inflated structure membranes, and architectural building envelopes, among others. Heating for such applications could be supplied externally by a maintenance procedure of convection or radiative heating, externally by ambient conditions such as sunlight or aerodynamic heating, or internally by Joule heating.[39] Given the low rubber modulus above T_m, the SMASH article may need to be mechanically supported. Certainly, the heating scheme will be tailored to the demands of particular applications.

2.6 REFERENCES

(1) Mather, P. T.; Luo, X. F.; Rousseau, I. A.: Shape Memory Polymer Research. *Annu. Rev. Mater. Res.* **2009**, *39*, 445-471.

(2) Rousseau, I. A.: Challenges of Shape Memory Polymers: A Review of the Progress Toward Overcoming SMP's Limitations. *Polym. Eng. Sci.* **2008**, *48*, 2075-2089.

(3) Lendlein, A.; Kelch, S.: Shape-memory polymers. *Angew. Chem., Int. Ed.* **2002**, *41*, 2034-2057.

(4) Lendlein, A.; Schmidt, A. M.; Schroeter, M.; Langer, R.: Shape-memory polymer networks from oligo(epsilon-caprolactone)dimethacrylates. *J. Polym. Sci. Part a-Polym. Chem.* **2005**, *43*, 1369-1381.

(5) Liu, C.; Qin, H.; Mather, P. T.: Review of progress in shape-memory polymers. *Journal of Materials Chemistry* **2007**, *17*, 1543-1558.

(6) Chung, T.; Romo-Uribe, A.; Mather, P. T.: Two-way reversible shape memory in a semicrystalline network. *Macromolecules* **2008**, *41*, 184-192.

(7) Lee, K. M.; Knight, P. T.; Chung, T.; Mather, P. T.: Polycaprolactone-POSS chemical/physical double networks. *Macromolecules* **2008**, *41*, 4730-4738.

(8) Knight, P. T.; Lee, K. M.; Chung, T.; Mather, P. T.: PLGA-POSS End-Linked Networks with Tailored Degradation and Shape Memory Behavior. *Macromolecules* **2009**, *42*, 6596-6605.

(9) Lowe, A. B.: Thiol-ene "click" reactions and recent applications in polymer and materials synthesis. *Polym. Chem.* **2010**, *1*, 17-36.

(10) Hoyle, C. E.; Bowman, C. N.: Thiol-Ene Click Chemistry. *Angew. Chem., Int. Ed.* **2010**, *49*, 1540-1573.

(11) Wu, D. Y.; Meure, S.; Solomon, D.: Self-healing polymeric materials: A review of recent developments. *Progress in Polymer Science* **2008**, *33*, 479-522.

(12) White, S. R.; Sottos, N. R.; Geubelle, P. H.; Moore, J. S.; Kessler, M. R.; Sriram, S. R.; Brown, E. N.; Viswanathan, S.: Autonomic healing of polymer composites. *Nature* **2001**, *409*, 794-797.

(13) Cosco, S.; Ambrogi, V.; Musto, P.; Carfagna, C.: Properties of poly(urea-formaldheyde) microcapsules containing an epoxy resin. *J. Appl. Polym. Sci.* **2007**, *105*, 1400-1411.

(14) Yuan, L.; Liang, G. Z.; Xie, J. Q.; Li, L.; Guo, J.: Preparation and characterization of poly(urea-formaldehyde) microcapsules filled with epoxy resins. *Polymer* **2006**, *47*, 5338-5349.

(15) Keller, M. W.; White, S. R.; Sottos, N. R.: A self-healing poly(dimethyl siloxane) elastomer. *Advanced Functional Materials* **2007**, *17*, 2399-2404.

(16) Caruso, M. M.; Blaiszik, B. J.; White, S. R.; Sottos, N. R.; Moore, J. S.: Full recovery of fracture toughness using a nontoxic solvent-based self-healing system. *Advanced Functional Materials* **2008**, *18*, 1898-1904.

(17) Williams, G.; Trask, R.; Bond, I.: A self-healing carbon fibre reinforced polymer for aerospace applications. *Compos. Part a-Appl. Sci. Manuf.* **2007**, *38*, 1525-1532.

(18) Trask, R. S.; Bond, I. P.: Biomimetic self-healing of advanced composite structures using hollow glass fibres. *Smart Materials & Structures* **2006**, *15*, 704-710.

(19) Trask, R. S.; Williams, G. J.; Bond, I. P.: Bioinspired self-healing of advanced composite structures using hollow glass fibres. *J. Royal Soc. Interface* **2007**, *4*, 363-371.

(20) Kirkby, E. L.; Rule, J. D.; Michaud, V. L.; Sottos, N. R.; White, S. R.; Manson, J. A. E.: Embedded shape-memory alloy wires for improved performance of self-healing polymers. *Advanced Functional Materials* **2008**, *18*, 2253-2260.

(21) Kirkby, E. L.; Michaud, V. J.; Manson, J. A. E.; Sottos, N. R.; White, S. R.: Performance of self-healing epoxy with microencapsulated healing agent and shape memory alloy wires. *Polymer* **2009**, *50*, 5533-5538.

(22) Hayes, S. A.; Jones, F. R.; Marshiya, K.; Zhang, W.: A self-healing thermosetting composite material. *Compos. Part a-Appl. Sci. Manuf.* **2007**, *38*, 1116-1120.

(23) Meure, S.; Wu, D. Y.; Furman, S.: Polyethylene-co-methacrylic acid healing agents for mendable epoxy resins. *Acta Mater.* **2009**, *57*, 4312-4320.

(24) Luo, X. F.; Ou, R. Q.; Eberly, D. E.; Singhal, A.; Viratyaporn, W.; Mather, P. T.: A Thermoplastic/Thermoset Blend Exhibiting Thermal Mending and Reversible Adhesion. *ACS Appl. Mater. Interfaces* **2009**, *1*, 612-620.

(25) Chen, X. X.; Dam, M. A.; Ono, K.; Mal, A.; Shen, H. B.; Nutt, S. R.; Sheran, K.; Wudl, F.: A thermally re-mendable cross-linked polymeric material. *Science* **2002**, *295*, 1698-1702.

(26) Chen, X. X.; Wudl, F.; Mal, A. K.; Shen, H. B.; Nutt, S. R.: New thermally remendable highly cross-linked polymeric materials. *Macromolecules* **2003**, *36*, 1802-1807.

(27) Rodriguez, E. D.; Luo, X.; Mather, P. T.: Shape memory miscible blends for thermal mending. In *International Society for Optical Engineering (SPIE)*; Ounaies, Z., Li, J., Eds.; SPIE: San Diego, CA, USA, 2009; Vol. 7289.

(28) Luo, X. F.; Mather, P. T.: Preparation and Characterization of Shape Memory Elastomeric Composites. *Macromolecules* **2009**, *42*, 7251-7253.

(29) Cramer, N. B.; Bowman, C. N.: *J. Polym. Sci., Part A: Polym. Chem.* **2001**, *39*, 3311–3319.

(30) Decker, C.: *Macromol. Rapid Commun.* **2002**, *23*, 1067–1093.

(31) Chung; Taekwoong: NEW SHAPE MEMORY EFFECTS IN SEMICRYSTALLINE POLYMERIC NETWORKS. Case Western Reserve University, 2009.

(32) Fayolle, B.; Tcharkhtchi, A.; Verdu, J.: Temperature and molecular weight dependence of fracture behaviour of polypropylene films. *Polymer Testing* **2004**, *23*, 939-947.

(33) Karger-Kocsis, J.; Barany, T.; Moskala, E. J.: Plane stress fracture toughness of physically aged plasticized PETG as assessed by the essential work of fracture (EWF) method. *Polymer* **2003**, *44*, 5691-5699.

(34) Karger-Kocsis, J.; Ferrer-Balas, D.: On the plane-strain essential work of fracture of polymer sheets. *Polymer Bulletin* **2001**, *46*, 507-512.

(35) Rodriguez, E. D.; Luo, X. F.; Mather, P. T.: Linear/Network Poly(epsilon-caprolactone) Blends Exhibiting Shape Memory Assisted Self-Healing (SMASH). *ACS Applied Materials & Interfaces* **2011**, *3*, 152-161.

(36) Maspoch, M. L.; Santana, O. O.; Grando, J.; Ferrer, D.; Martinez, A. B.: The essential work of fracture of a thermoplastic elastomer. *Polymer Bulletin* **1997**, *39*, 249-255.

(37) Fayolle, B.; Tcharkhtchi, A.; Verdu, J.: Temperature and molecular weight dependence of fracture behaviour of polypropylene films. *Polym. Test.* **2004**, *23*, 939-947.

(38) Wool, R. P.; O'Conner, K. M.: A theory of crack healing in polymers. *J. Appl. Phys.* **1981**, *52*, 5953-5964.

(39) Luo, X. F.; Mather, P. T.: Conductive shape memory nanocomposites for high speed electrical actuation (vol 6, pg 2146, 2010). *Soft Matter* **2010**, *6*, 6210-6210.

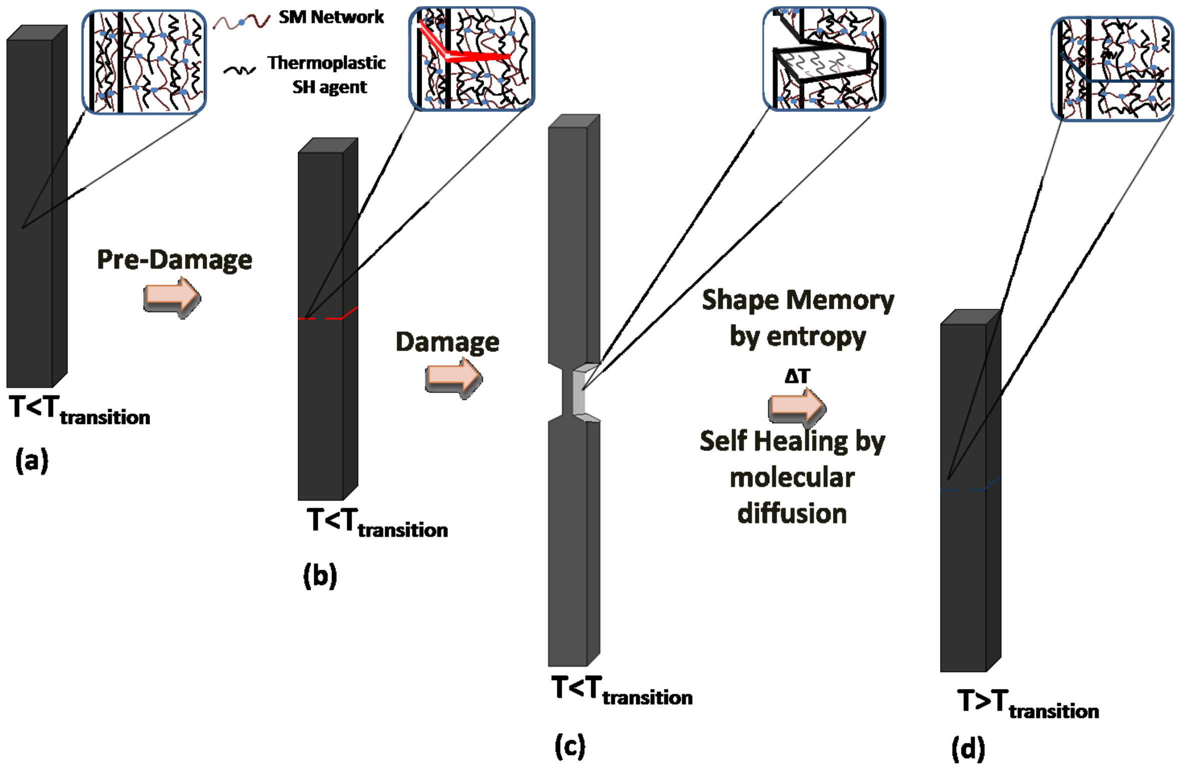

Scheme 2-1. Schematic showing the shape memory assisted self healing (SMASH) effect. Schematic of sample in its (a) virgin state, (b) pre-damaged (notched) state, and (c) damaged and deformed state at a temperature below its T_m to observe reversible plasticity shape memory (RPSM). (d) Shows the healed state when the sample was heated above its T_m. The shape memory (SM) effect was thermally triggered for crack closure where healing was obtained by polymer chain diffusion across the damaged site then cooled below the T_m to complete the SH effect. The inserts show a schematic of the polymer chains in the blend at each step of the SMASH process.

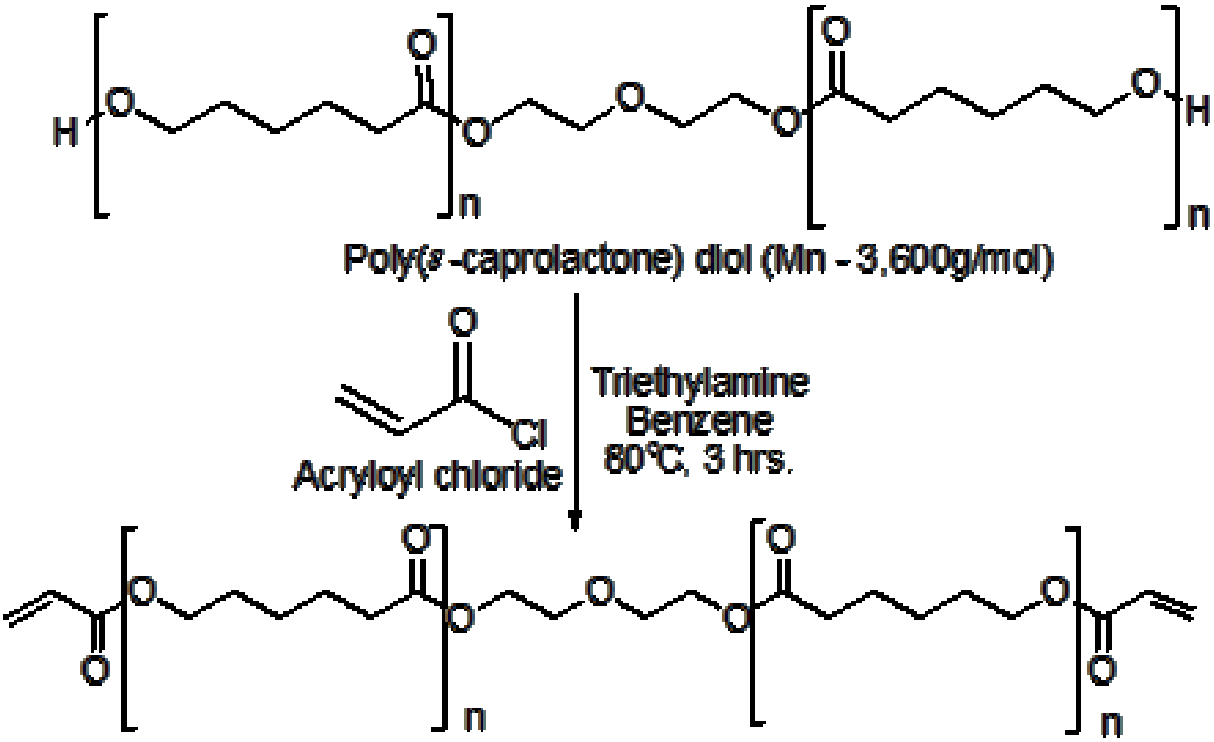

Scheme 2-2. Preparation of the poly(ε-caprolactone) diol (3k) macromer by end capping of PCL diol with acryloyl chloride.

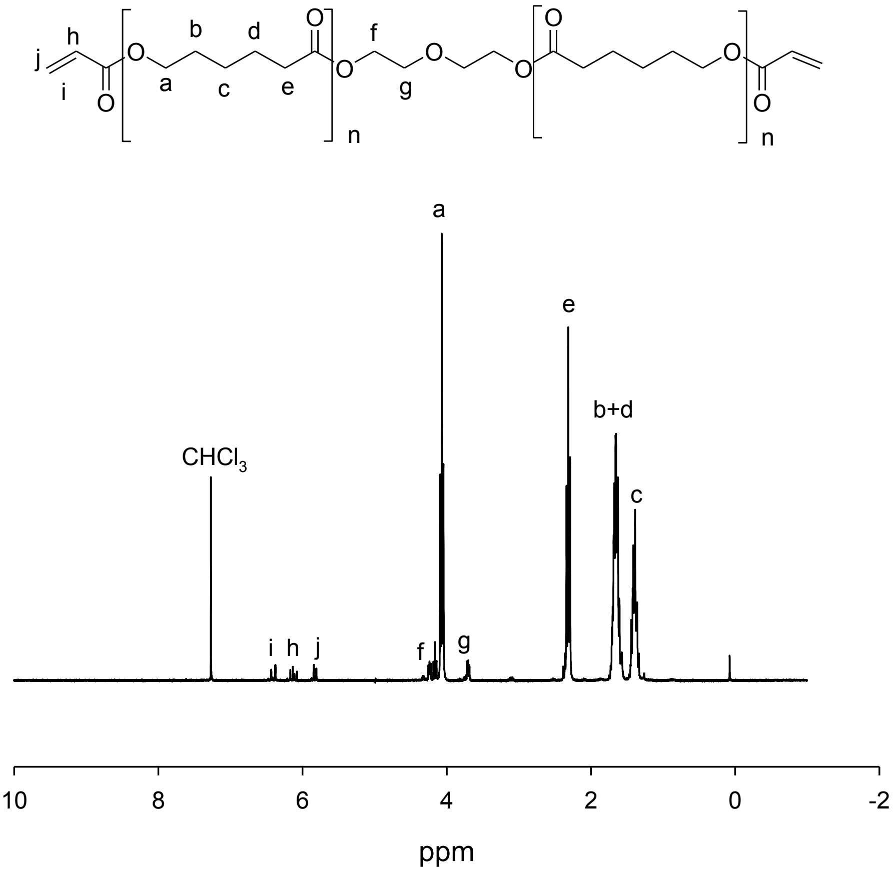

$$Conversion(\%) = \frac{I_{vinyl-i}}{\left(\frac{I_{methylene-a}}{2n}\right)} \cdot 100 \qquad (2)$$

PCL diacrylate(3k) Batch	$I_{vinyl-i}$	$I_{methylene-a}$	Conversion (%)
1	0.90	26.10	105
2	0.14	4.42	97
3	1.00	28.11	108

Scheme 2-3. ^{1}H NMR spectra for PCL diacrylate(3k). Equation (2) shows the formula used to obtain end-capping conversion. Chart shows the conversion values for all the batches of PCL diacrylate used to make samples. The acrylate-terminated macromers were characterized for degree of functionalization using ^{1}H NMR. An example spectrum is shown here, along with a

schematic of the macromer structure indicating the identification of proton resonances. To compute the degree of functionalization, we utilized the resonances from the “i” protons of the acrylate vinyl group and the “a” protons of the repeating unit of poly(ε-caprolactone).

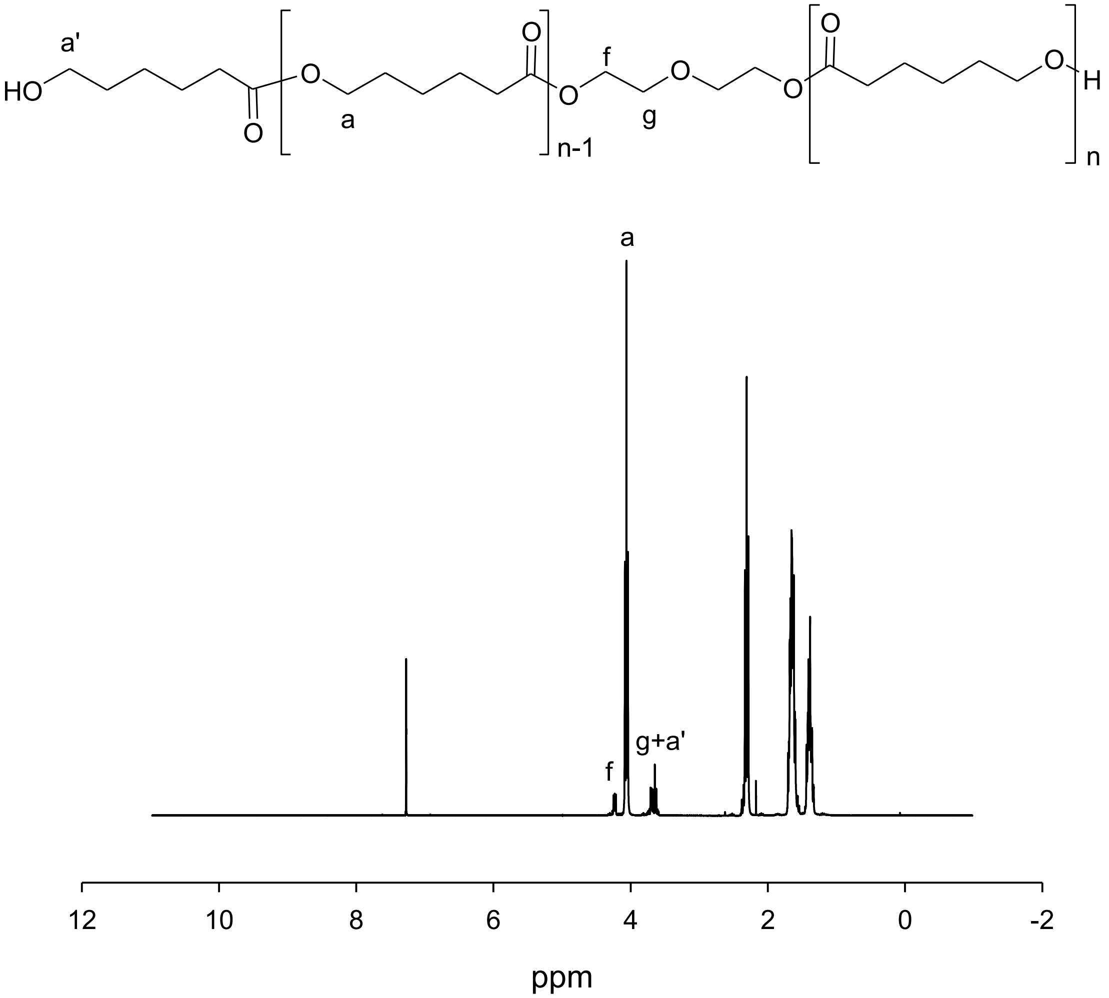

$$n-1=\frac{I_{methylene-a}}{I_{methylene-f}} \qquad (1)$$

PCL diol(3k) Batch	$I_{methylene-a}$	$I_{methylene-f}$	n
1	14.40	1.00	15.40
2	14.24	1.00	15.24

Scheme 2-4. ^{1}H NMR spectra for PCL diol(3k). Equation (1) shows the formula used to obtain the repeat unit (n) values. Chart shows the repeat unit values for all the batches of PCL diol(3k) that were used to make samples.

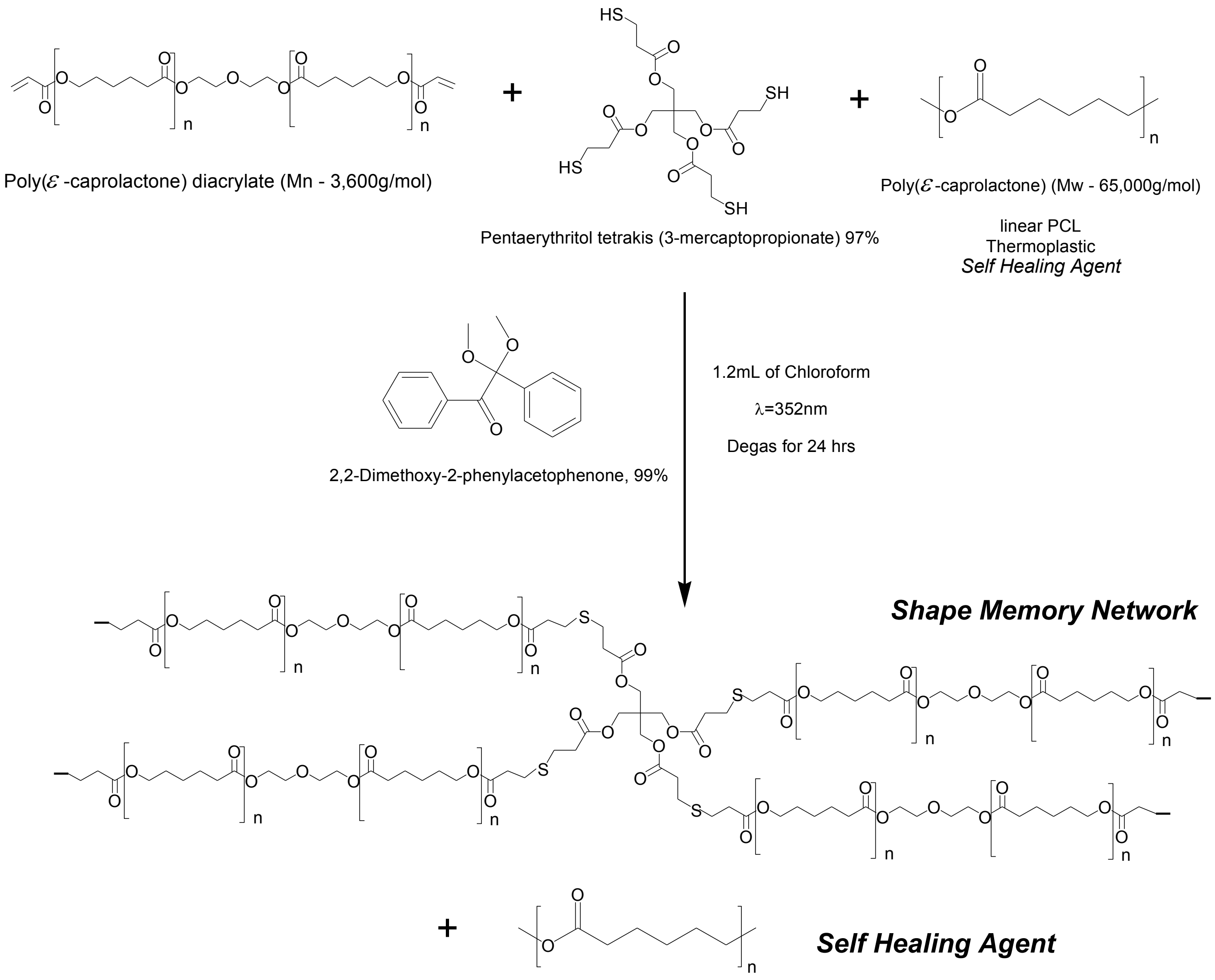

Scheme 2-5. Preparation of blends containing n-PCL and l-PCL by UV-initiated thiol-ene polymerization in the presence of non-reactive l-PCL.

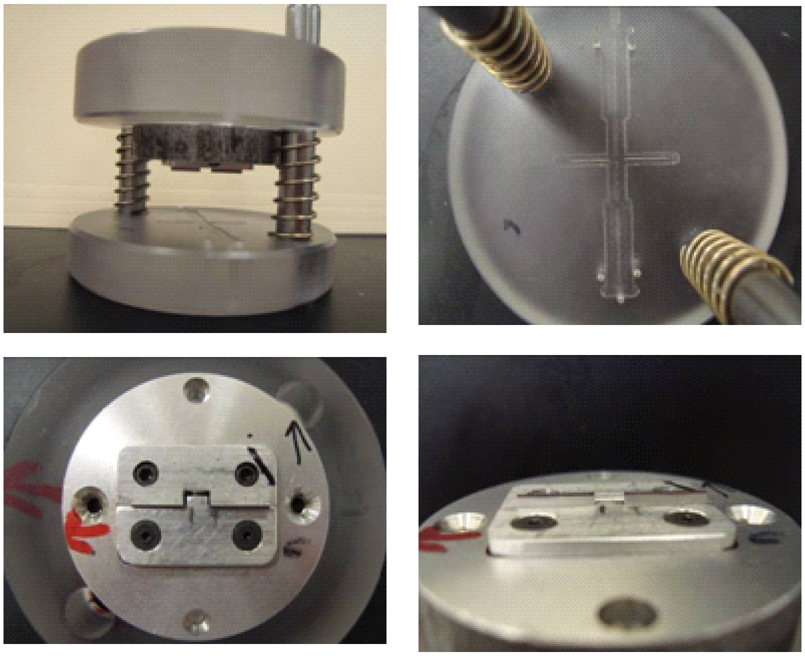

Scheme 2-6. Customized deeply double-edge notched (DDEN) punch.

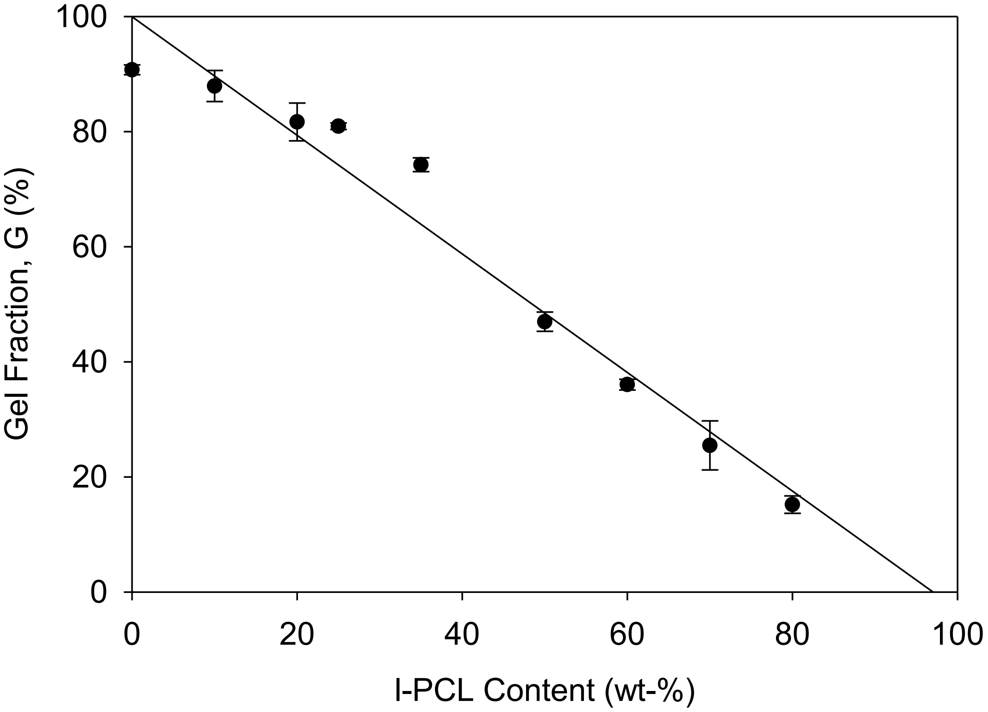

Figure 2-1. Dependence of the n-PCL:l-PCL gel fraction, G(%), by $CHCl_3$ extraction for of all compositions tested as a function of l-PCL wt-% content and taken for an average of three samples. The line represents linear regression of the data, revealing a small deviation of the expected extraction of all l-PCL.

Table 2-1. Gel fraction (G(%)) averages of three samples tested for each composition.

l-PCL$_{wt-\%}$:n-PCL$_{wt-\%}$	**G (%)**	**STDEV**
(0:100)	90.7	0.9
(10:90)	87.9	2.7
(20:80)	81.7	3.3
(25:75)	80.9	0.6
(35:65)	74.2	1.2
(50:50)	47.0	1.7
(60:40)	36.0	0.9
(70:30)	25.5	4.3
(80:20)	15.2	1.5

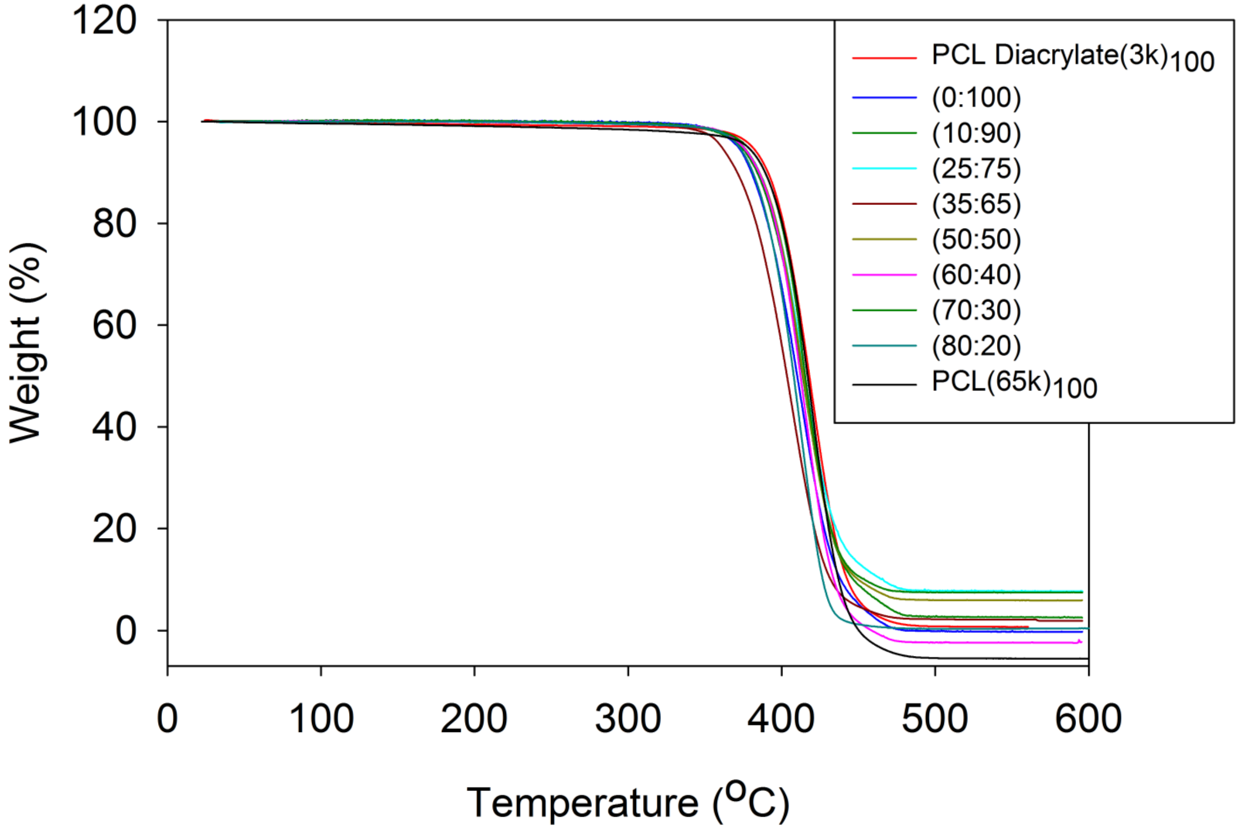

Figure 2-2. Weight vs. temperature graph showing sample decomposition by weight change of all compositions tested using a TA Q500 Thermogravimetric Analyzer (TGA) where each sample was heated to 600 °C at 10 °C/min. PCL Diacrylate(3k)$_{100}$ and PCL(65k)$_{100}$ are shown for comparison.

Table 2-2. Chart showing the onset degradation temperature of all compositions tested using a TA Q500 Thermogravimetric Analyzer (TGA) where each sample was heated to 600 °C at 10 °C/min. PCL Diacrylate(3k)$_{100}$ and PCL(65k)$_{100}$ are shown for comparison.

Composition	Onset Degradation Temperature (°C)
PCL Diacrylate$_{100}$	394
(0:100)	381
(10:90)	386
(20:80)	385
(25:75)	389
(35:65)	376
(50:50)	390
(60:40)	389
(70:30)	395
(80:20)	386
l-PCL$_{100}$	395

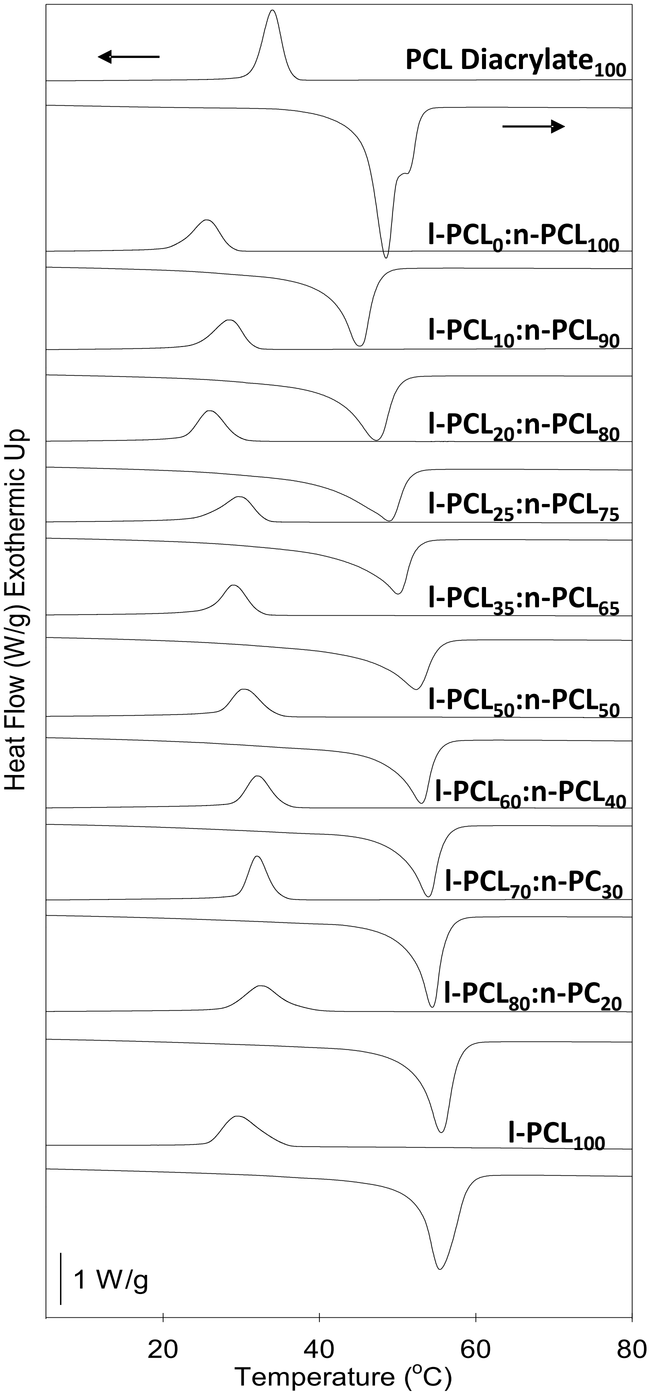

Figure 2-3. Representative heating and cooling DSC traces showing the T_m and T_c of all compositions tested. The first and second heatings were conducted at 10.0 °C/min to 120 °C with a cooling rate of 3.0 °C/min to -90 °C.

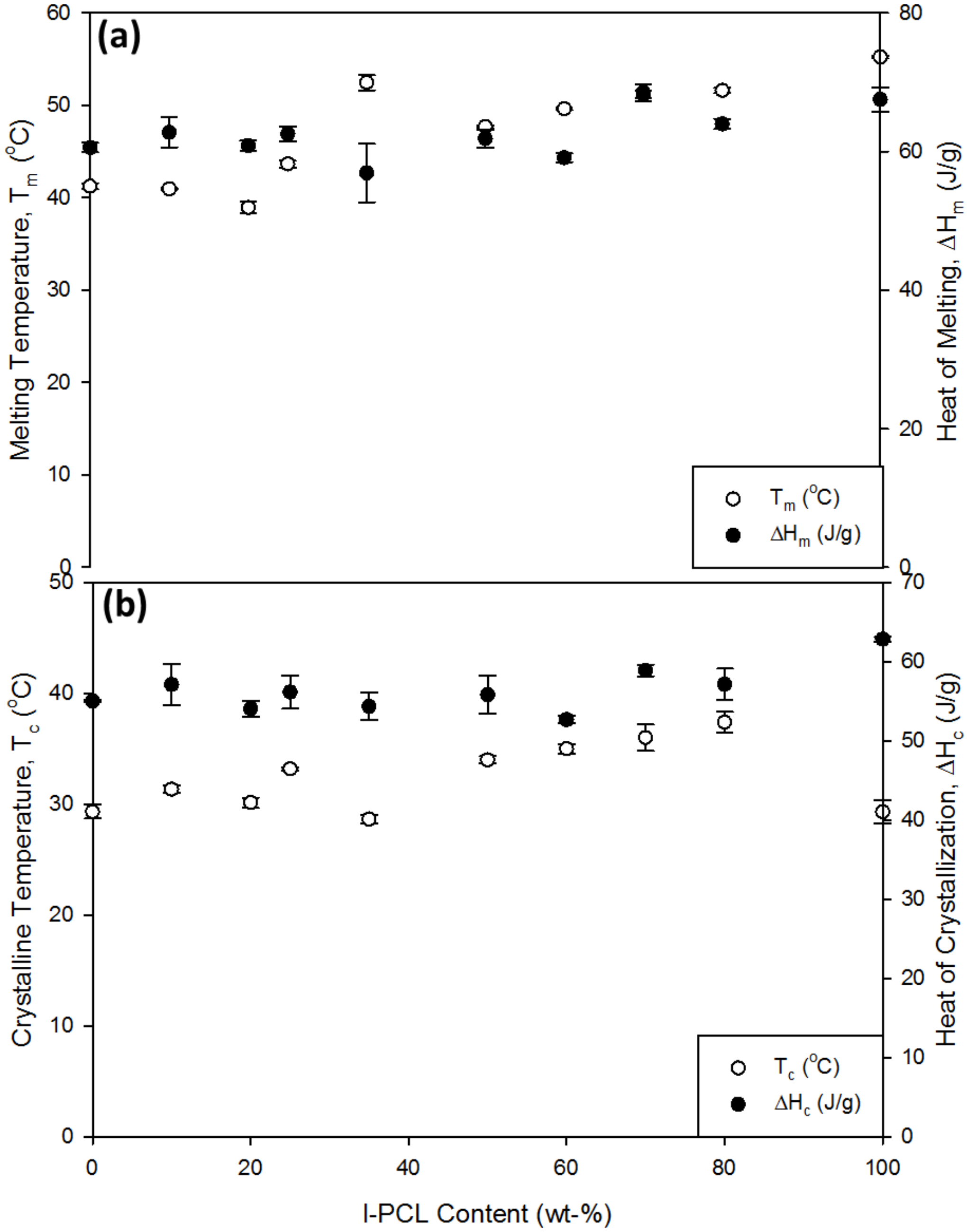

Figure 2-4. Trends of transition temperatures and latent heats for the blends: (a) melting temperature (T_m) and heat of melting (ΔH_m), (b) crystalline temperature (T_c) and heat of crystallization (ΔH_c) as a function of l-PCL wt-% content showing average values from three samples tested for each composition.

Table 2-3. Table showing averages of the melting (T_m) and crystalline (T_c) temperatures, the heat of melting (ΔH_m) and heat of crystallization (ΔH_c) for three samples tested for each composition.

l-PCL$_{wt\text{-}\%}$:n-PCL$_{wt\text{-}\%}$	**T_m (°C)**	**ΔH_m (J/g)**	**T_C (°C)**	**ΔH_C (J/g)**
100% PCL Diacrylate	45.5	88.7	36.4	85.0
(0:100)	41.2	60.6	29.3	55.0
(10:90)	40.9	62.8	31.3	57.1
(20:80)	38.9	60.8	30.1	54.0
(25:75)	43.6	62.6	33.2	56.2
(35:65)	52.5	56.9	28.6	54.3
(50:50)	47.7	61.9	34.0	55.8
(60:40)	49.6	59.1	35.0	52.7
(70:30)	51.2	68.5	36.0	58.9
(80:20)	51.6	64.0	37.4	57.1
100% l-PCL	55.2	67.5	29.3	62.8

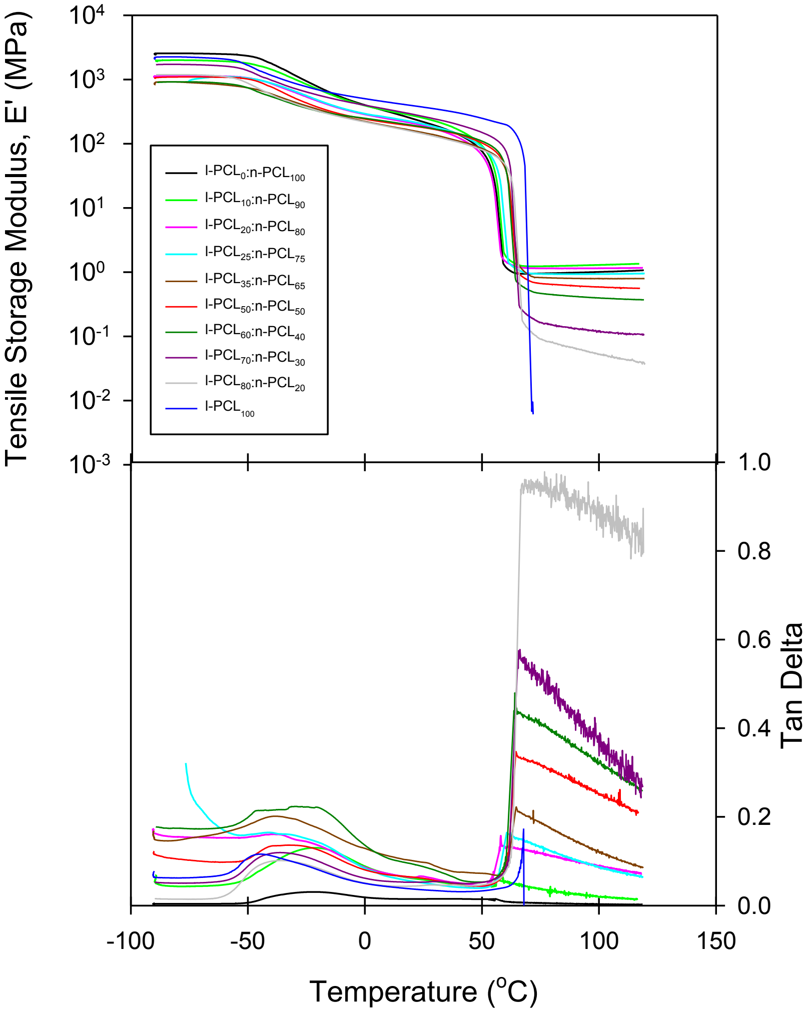

Figure 2-5. Tensile storage modulus (E′) as a function of temperature for all compositions tested are shown. For all compositions, the first heating was at 3.00 °C/min to 90.00 °C, cooling at 3.00 °C/min to -90.00 °C and the second heating at 3.00 °C/min to 120.00 °C. The first heating for the l-PCL$_{100}$ sample was done at 3 °C/min to 50 °C, cooling at 3 °C/min to -90 °C and the second heating at 3 °C/ min to 70 °C. Second heating data are shown for all samples. The tan delta curves are also shown, indicating the ratio of the viscous to elastic contribution of the samples tested with a peak at T_g and a dramatic rise at T_m.

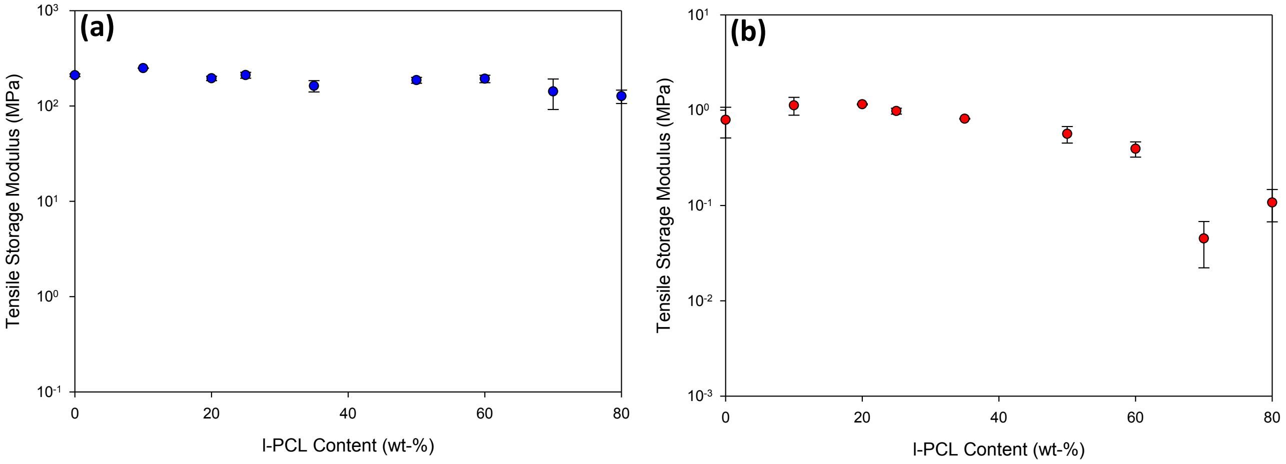

Figure 2-6. Tensile storage modulus obtained at (a) 25 °C and (b) 80 °C for all compositions as a function of l-PCL wt-% content for the average of two samples tested.

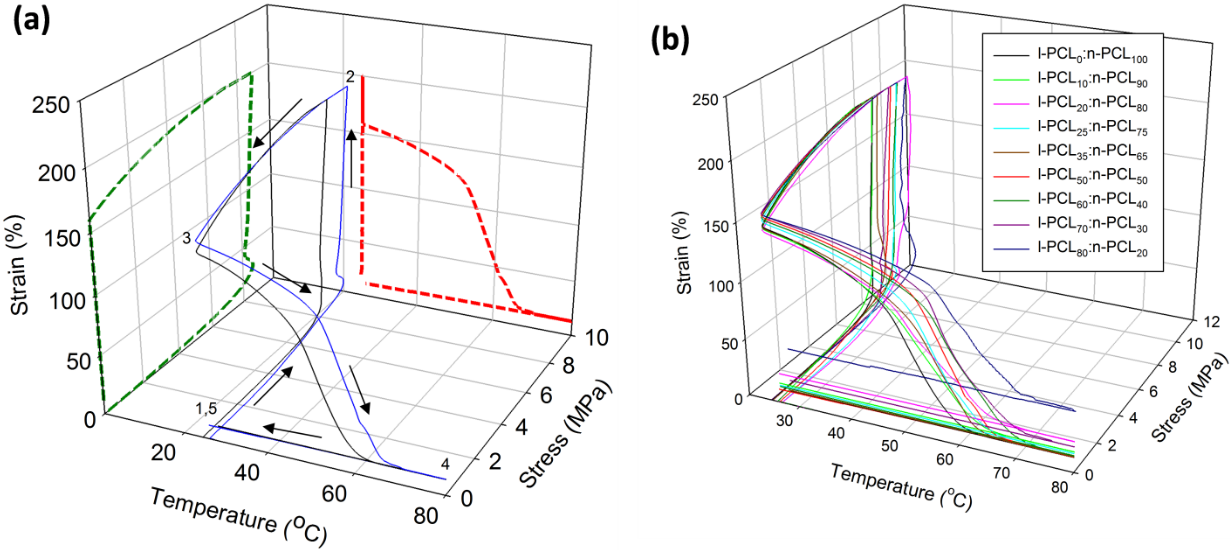

Figure 2-7. (a) Representative reversible plasticity shape memory cycle (RPSM) of l-PCL$_0$:n-PCL$_{100}$ (black) and l-PCL$_{50}$:n-PCL$_{50}$ (blue) compositions where each sample was stretched to a strain of 200% at RT and recovered at 80 °C. Strain vs. temperature curve (red) and stress vs. strain curve (green) are also shown for the l-PCL$_{50}$:n-PCL$_{50}$ composition. (b) Reversible plasticity shape memory cycle (RPSM) for all nine compositions tested where each sample was stretched to a strain of 200% at RT. Shape recovery was tested at temperature, T (T > T_m) = 80 °C.

Table 2-4. Fixing (R_f) and recovery (R_r) ratios for all compositions tested as a function of l-PCL wt-% content.

l-PCL$_{wt\text{-}\%}$:n-PCL$_{wt\text{-}\%}$	ε_m (%)	ε_u (%)	ε_p (%)	$\boldsymbol{R_f}$ (%)	$\boldsymbol{R_r}$ (%)
(0:100)	200	151.9	12.7	75.9	91.6
(10:90)	200	150.3	17.3	75.1	88.5
(20:80)	200	148.3	25.9	74.1	82.6
(25:75)	200	156.0	15.4	78.0	90.1
(35:65)	200	150.7	13.0	75.4	91.4
(50:50)	200	160.1	11.6	80.1	92.7
(60:40)	200	158.2	14.4	79.1	90.9
(70:30)	200	161.8	22.0	80.9	86.5
(80:20)	200	161.7	50.0	80.8	69.1

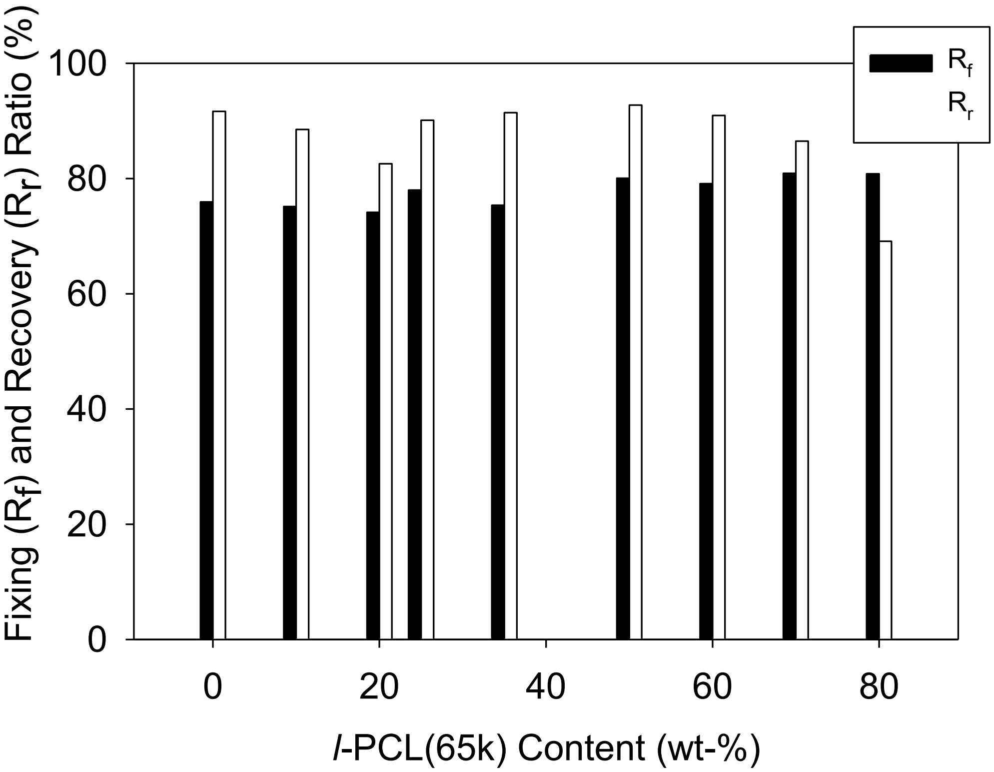

Figure 2-8. Fixing (*R_f*) and recovery (*R_r)* ratios bar graph for all nine compositions tested as a function of l-PCL wt-% content.

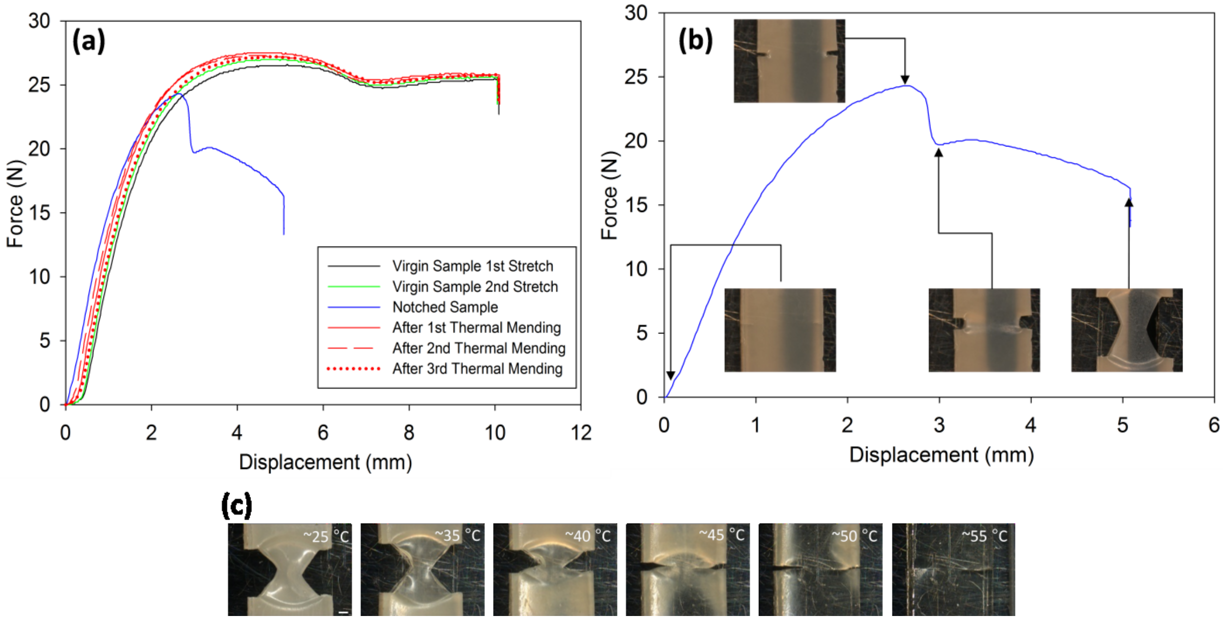

Figure 2-9. (a) Force vs. displacement curves for the virgin, damaged and healed state of a l-PCL$_{50}$:n-PCL$_{50}$ sample. (b) Notched l-PCL$_{50}$:n-PCL$_{50}$ sample with stereo micrographs of deformation and crack growth clamped in the Linkam tensile stage. (Scale bar: 500 μm) (c) Snapshots of crack closure and crack rebonding when the sample was unclamped from the Linkam tensile stage and heated to the temperatures shown (stereo micrographs scale bar: 500 μm).

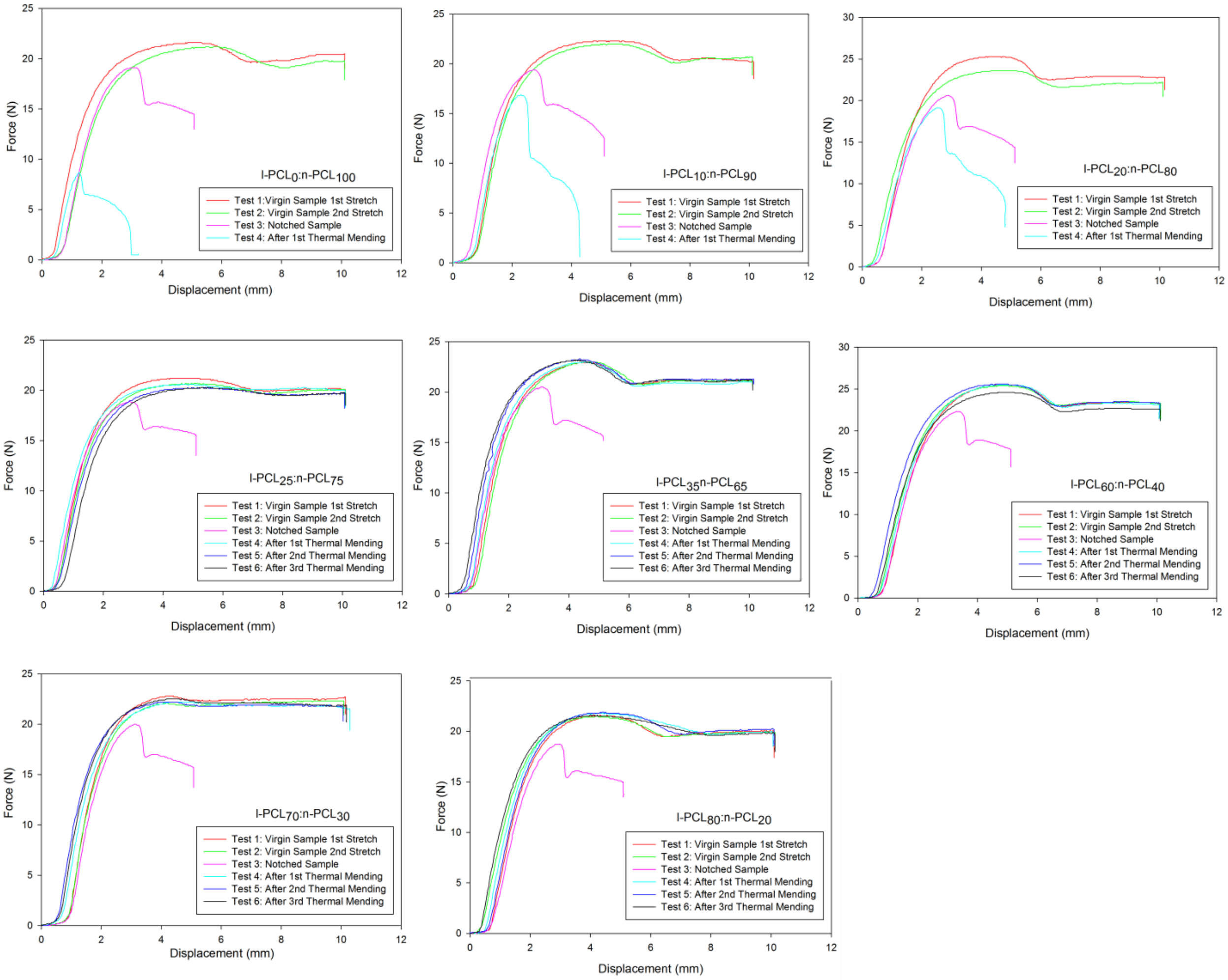

Figure 2-10. Representative graphs of all compositions tested showing the initial deformation, damaged and healed force vs. displacement curves.

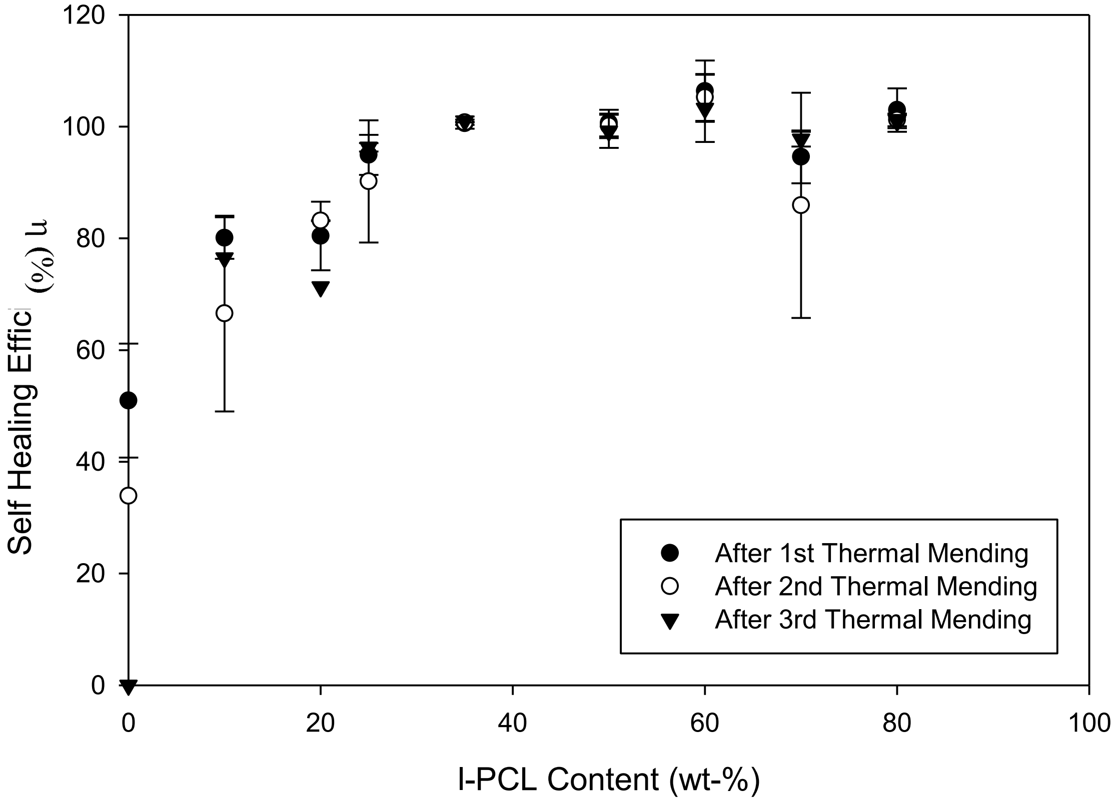

Figure 2-11. Dependence of self-healing efficiency (η) on l-PCL wt-% content. The average of three samples tested for SH efficiency following first, second and third thermal mending treatments are shown.

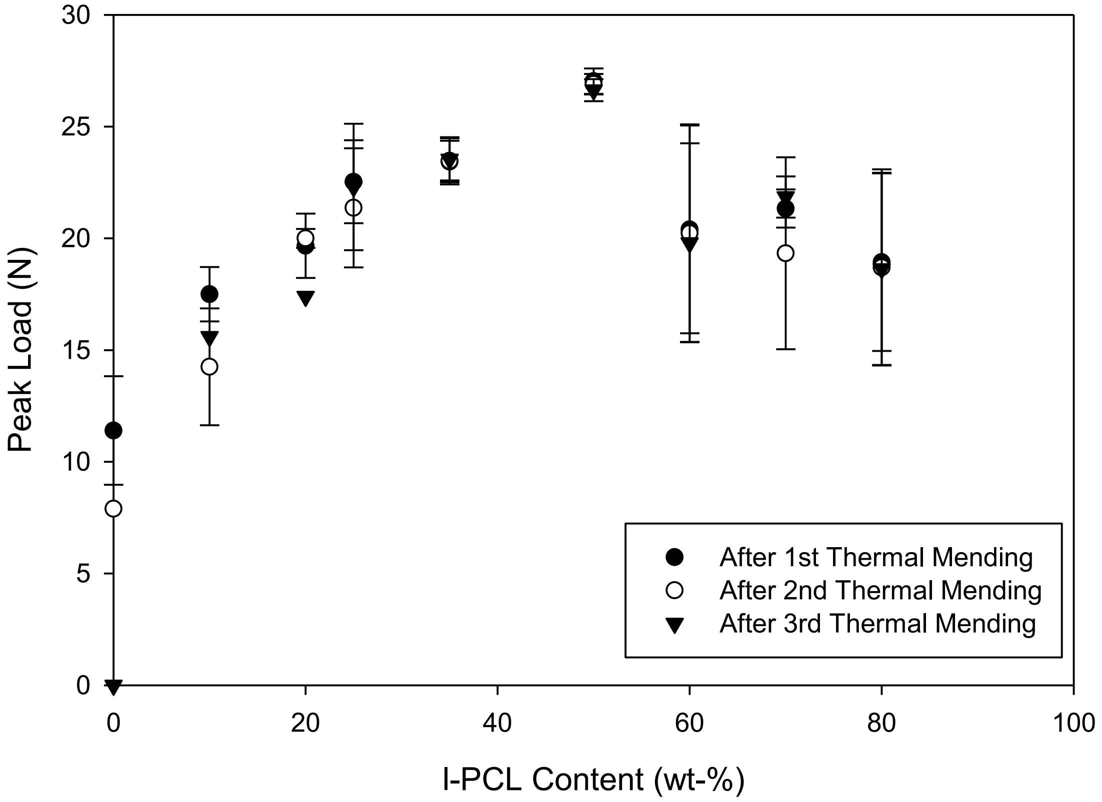

Figure 2-12. Average peak loads as a function of l-PCL wt-% content after each thermal mending treatment is shown. Three samples were tested for each composition.

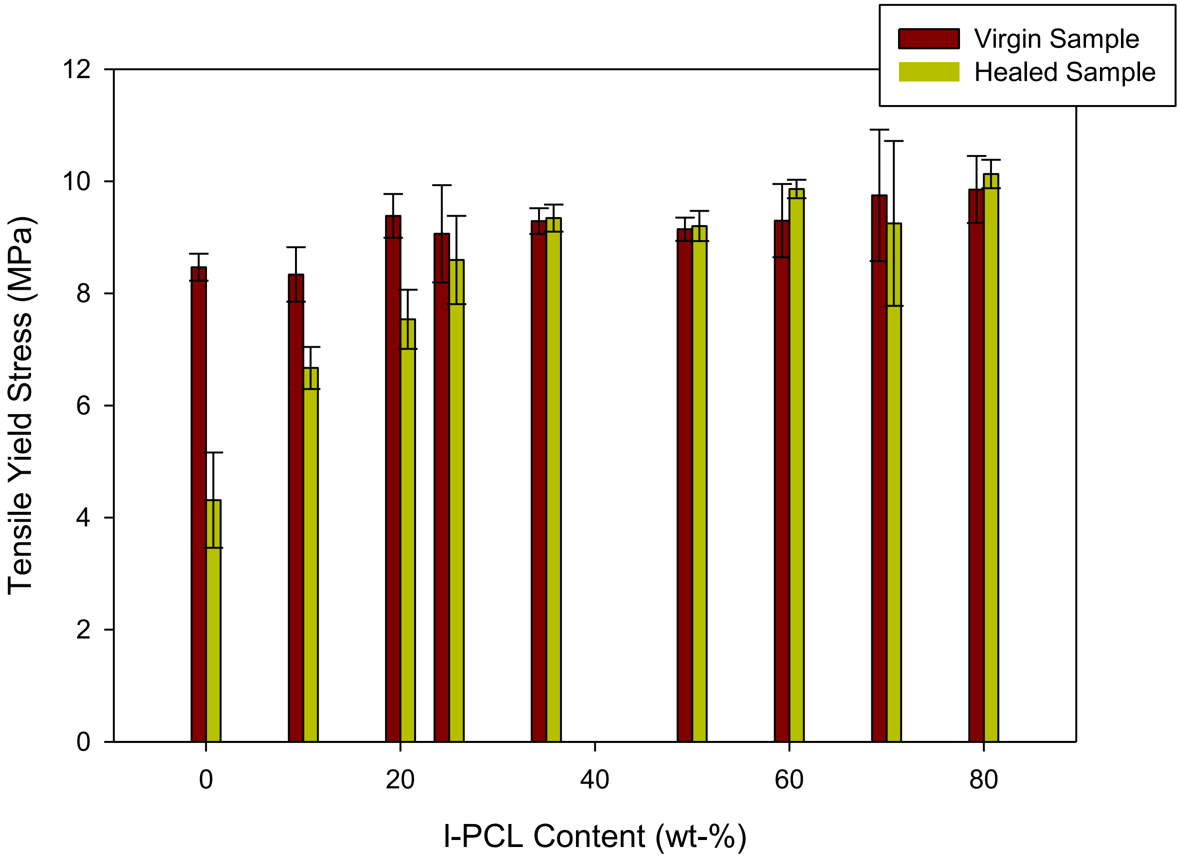

Figure 2-13. Average tensile yield stress as a function of l-PCL wt-% content for each virgin and healed samples tested using the TST350 Linkam tensile stage are shown. Three samples were tested for each composition. In all cases, the undamaged cross-section was used in the determination of the tensile yield stress from tensile load data.

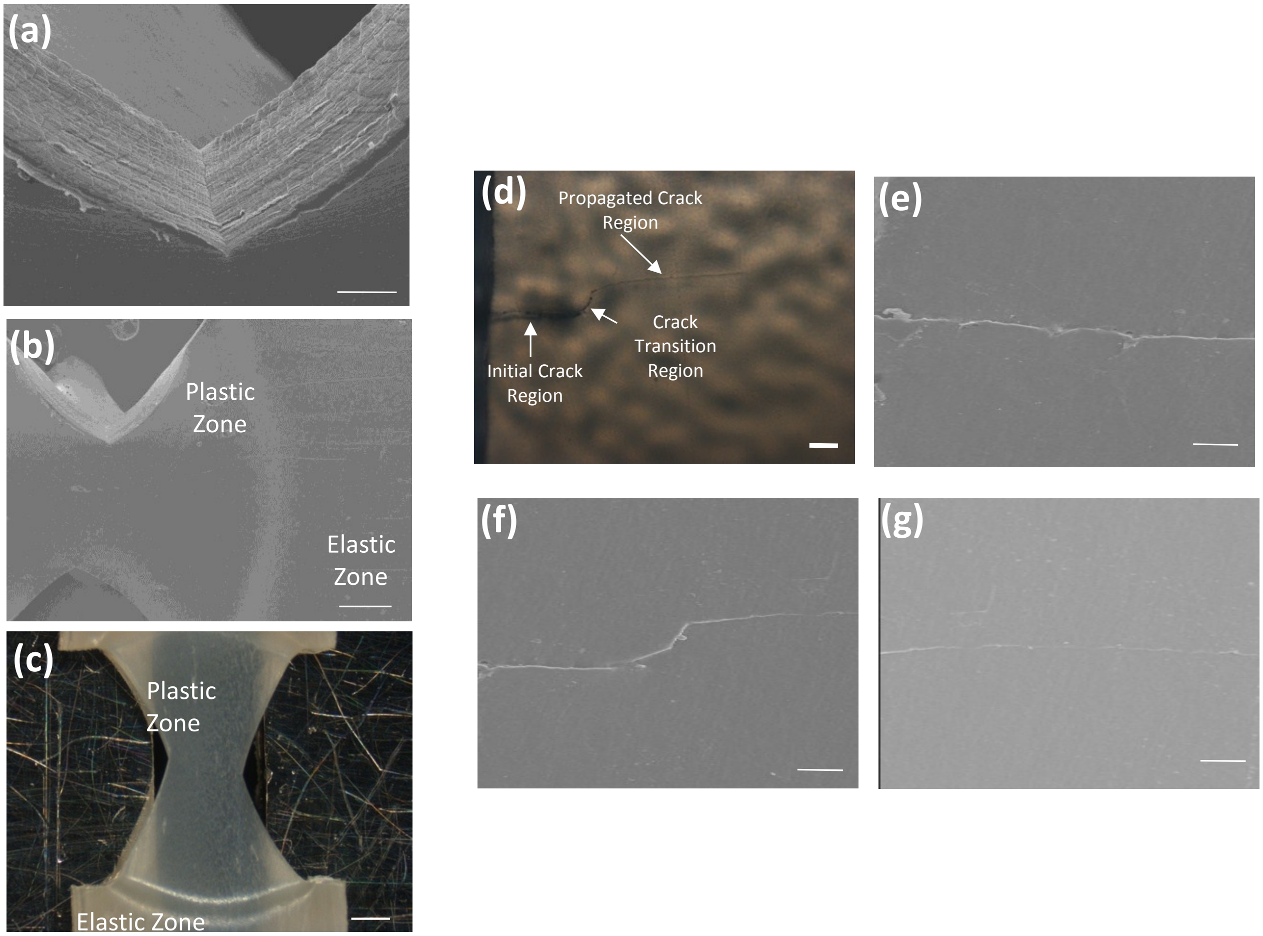

Figure 2-14. l-PCL$_{50}$:n-PCL$_{50}$ sample showing SEM micrographs of the (a) propagated crack surfaces, (b) elastic and plastic zones, (c) stereomicrograph of elastic and plastic zones (Scale bar: SEM - 100 µm, steromicrograph - 500µm). (d) Optical micrograph indicating the three crack regions. SEM micrographs of healed (e) initial crack region, (f) crack transition region, and (g) propagated crack region (Scale bar: optical micrograph- 100 µm, SEM – 50 µm).

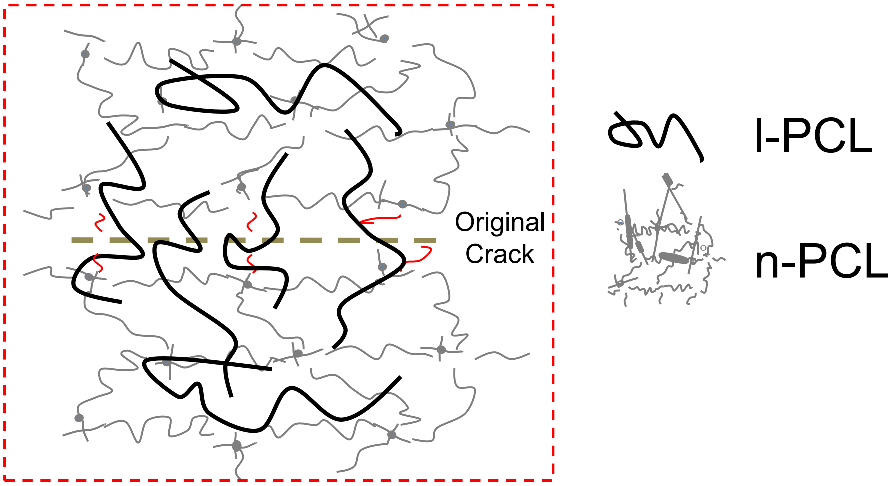

Scheme 2-7. Scheme of l-PCL chain entanglement in n-PCL at the healed site.

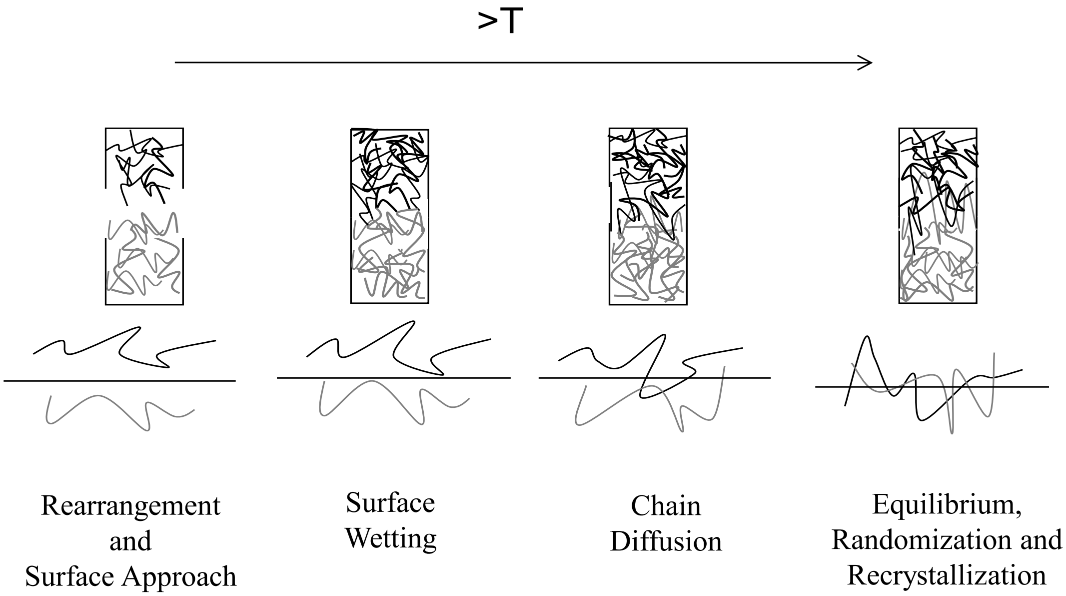

Scheme 2-8. Schematic of the five stages of healing (adapted from references 11 and 38).

CHAPTER THREE

POLY(TERT–BUTYL ACRYLATE) (POLY(tBA)) COATINGS FOR SCRATCH REPAIR VIA SHAPE MEMORY ASSISTED SELF HEALING (SMASH)

3.0 SYNOPSIS

This chapter focuses on the design, fabrication, and in-depth characterization of semi-interpenetrating polymer networks (SIPN) of a single phase amorphous poly(tert-butyl acrylate) (poly(tBA)) SMASH polymeric system for use as films and coatings for optical industrial applications. The shape memory (SM) network and self healing (SH) thermoplastic agent were varied to study the optimum SM and SH needed for scratch repair in coatings.

3.1 INTRODUCTION

A coating's primary function is to protect sensitive surfaces from their environment. Self-healing (SH) coatings for the automotive and aerospace industries have been in demand to help reduce the degree of metallic corrosion and damage in hopes to increase the lifetime of the materials and associated components. SH coatings, particularly clear coatings, have also been in high demand to protect eyeglass lenses and other optical industrial and military products in order to reduce the degree of microcracking and scratches that may impair visibility.

The US army has a continuous need to prevent eye injuries on the battlefield that may result from fragmenting munitions and/or laser weapon exposure. To help protect against such eye injuries, polycarbonate protective military eyewear is worn.[1] This eyewear, however, is susceptible to scratches and microcracks from constant use.[1] Therefore, a SH coating that has high mechanical and scratch resistant properties is needed to help reduce the degree of damage and to optimize the visibility through the eyewear. This coating can also be used for corrective eyewear as well as windshields/windows in automobiles and motorcycles.

To date, there are amorphous SH materials that have been reported in literature and are summarized in the following sections. The automotive industry has been especially interested in incorporating SH coatings into the next generation of cars in order to address the irrevocable damage seen in car frames.[2,3] Some SH coatings currently on the market are those developed by Bayer Material Science which created healable coatings for the automotive industry.[3] Polyurethane coatings have covalent bonds that assist in the resistance and hardness of the coating. These coatings also have mechanical resilience and high strength, which are essential for extreme environments. The unique system gains its high elastic properties from the reversible hydrogen bonds of the urethane and urea chemical structure. This reversibility of hydrogen bonds is what allows the crosslinked polyurethanes to have their shape memory effect (SME). The SME is what assists in the healing process upon a damage event. When a scratch is induced in the coating, material is physically displaced. Upon a thermal stimulus, the hydrogen bonds that were displaced during damage are repositioned, returning to their original state in order to heal the scratch. These polyurethanes are especially attractive as they exhibit a high glossy finish and have good optical properties. These qualities are aesthetically pleasing for automotive frames.

Other systems include the use of a metallo-supramolecular polymer to fabricate an optically healable material.[4] Burnworth et al. fabricated a material that contained a telechelic macromolecular rubbery polymer, poly(ethylene-co-butylene), with ligand end groups, 2,6-

bis(1'methylbenzimidazolyl)pyridine (Mebip), that are reversibly linked with metal-ion binding agents. When the material is damaged by a razor blade, UV is used to thermally mend the damaged area. This is done when the metal-ligands in the material absorb the UV light energy, which it is then converted into heat to heal the damage. The sample was able to heal with a 8 kPa stress applied while exposing it to a UV light. Mechanical testing was conducted on the virgin, damaged and healed state where the virgin and healed samples exhibited the same mechanical properties by inspection of the reported stress-strain curves. This means that although the damage induced was 50-70% deep into the sample's thickness, the specimens tested were able to restore their mechanical properties completely.

Other amorphous SH materials include more intricate systems that incorporate solvent filled capsules. Jackson et al. developed a transparent SH polymer where the solvent filled capsules, dispersed in a thermoplastic matrix, plasticize the area of damage to assist in healing via solvent welding.[5] A well-known concept established in the SH community explains the need of the initiation of a crack where it propagates and ruptures the capsules allowing the SH agent to fill in the damaged area for healing.[6,7] This concept was also adopted in this system where urea-formaldehyde capsules were filled with dibutylphthalate (DBP), a plasticizer, and embedded in a polymethylmethacrylate (PMMA) matrix. This capsule-polymer pair was chosen as they have a close matching of refractive index, decreasing the degree of light scatter and/or reflections from the solvent-matrix interface.[5] Previous studies have shown that the capsule sizes are important as large cracks induced are unable to be healad when the healing agent is stored in relatively small capsules. This is due to an insufficient amount of SH agent to heal the large degree of damage. In this study, small (1.5 μm) and large (75 μm) capsules were incorporated in the matrix where the degree of healing was studied based on the degree of damaged. The DBP locally plasticizes the thermoplastic polymer matrix when it fills in the crack plane. Over a period of time, the solvent swells the crack faces of the matrix allowing for crack closure. When this occurs healing takes place via solvent welding. The solvent welding mechanism allows for the PMMA chains to become mobile and diffuse in the area of damage to heal the area. Disadvantages for this system, however, include the unnecessary excess of capsule material when DBP is dispersed in the matrix. Although the system is quite innovative and promising in proving the SH concept, only a single healing event can occur upon capsule rupture as there is no replenishing techniques to restore the plasticizer once the crack has been healed. If there were replenishing techniques, the ruptured capsules would be unable to store the plasticizer while keeping it from interacting with the matrix. The empty capsules would also leave unwanted voids in the bulk of the material which can lead to weakening of the material properties.

Other transparent systems have been developed for optical devices used in industrial applications. Carotenuto et al. fabricated a nanocomposite polymer system that can be spin-coated on glass plates to yield a non-defective high quality colorful film with transparent properties.[8] These systems can be used for color filters in optical products or liquid crystal industrial displays. The system explained here was constructed by incorporating red nano-sized pigments, which serve as soluble dyes, into core inorganic particles. These core particles were then randomly dispersed in hydrophobic polymers to yield a pigmented core polymer composite.

SH coatings have also been used to minimize the degree of corrosion on metal surfaces. Coatings in general need to be inert and stable in extreme environments where oxygen and water exposure are the main factors in creating corrosion on metals. Cho et al. developed two types of siloxane based SH coatings using microencapsulated techniques.[9] The first coating involved encapsulating the catalyst needed for polymerization where the siloxane (SH agent) were in the form of small droplets dispersed in a coating matrix. The second approach involved encapsulating both the catalyst and the SH agent and distributing them in the matrix. It was observed from past studies that the encapsulation of both the catalyst and SH agent has proven to be more effective because they are both separated from each other and the matrix. Any interaction between these would result in a low SH efficiency.[9] The degree of SH was assessed by accelerated corrosion studies where encapsulated coated steel substrates were tested in their damaged and healed states. The samples were damaged using a razor blade then thermally treated at 50 °C for 24 h to allow them to heal. The damaged and healed samples where then submerged in a sodium chloride (NaCl) solution for a monitored amount of time. All the damaged samples showed evidence of corrosion after a 24 h submersion. However, the healed samples showed no evidence of corrosion after 120 h of submersion. Although this system is unique in nature, it still bears the same disadvantages as the system developed by Jackson and coworkers such as the inability to heal multiple times, an excess of material after capsule rupture, and no replenishing SH agent techniques.

Other anti-corrosion SH coatings include a layer-by-layer (LbL) deposition procedure developed by Andreeva et al.[10] Poly(ethyleneimine) (PEI), poly(styrene sulfonate) (PSS) and 8-hydroxyquinoline (8HQ) were deposited on a pretreated aluminum alloy AA2024 substrate where each nanolayer had a 5-10 nm thickness. First, the positively charged PEI layer was applied and binded well to the negatively charged Al_2O_3 layer of the aluminum alloy. In general, the aluminum alloys are coated with an oxide film which does not protect against corrosion and adhere well to polymers. For this reason the aluminum alloy AA2024 was pretreated prior to the polymer coating deposition. After the first layer was sprayed, the PSS and 8HQ were then deposited on the metallic surface. The three-layer SH coating was constructed where three mechanisms were employed. The first mechanism consisted of polyelectrolytes that allowed for the stabilization of pH levels at the metallic surface when exposed to corrosive environments. The second mechanism involved an inhibitor (8HQ) in the multilayer coating that could undergo triggered release in the presence of corrosion in order to prevent corrosion spreading on the metallic surface. The third mechanism then allowed for the mobility of the polyelectrolytes to seal areas of damage. This system is quite intricate and well developed, however, this coating is activated upon the presence of corrosion already on the substrate and essentially is not used as an anticorrosive protection, but instead a suppressor of additional corrosion.

All the systems mentioned prior are great examples of SH systems that are or can be used for SH coatings for protective purposes. The example developed by Bayer, proved to be a great transparent SH coating to address surface damage found in the automotive industry with the facilitation of the SM effect. However, greater commercial availability would be desired to target the need to repair other types of damage seen in industrial products. None of the other systems mentioned above utilize the shape memory (SM) effect to assist in crack closure in order to minimize the area between the cracked surfaces to heal the area of damage. The SM effect for crack closure is critical as a minimum amount of healing material is needed for rebonding the damage. One SM amorphous system which has been studied includes crosslinking unsaturated polyesters with methacrylates formed by radical reactions to develop an elastic bi-component polyester SM network.[11] The thermoset has transparent and rubber-like properties with transition temperatures tailored from -26 to 29 °C to meet specific applications for the SM effect. Although, this system proves to have great SM capacity, the system does not have SH ability should the system incur damage during its lifetime.

Borroero-Lopez et al. have studied the mechanical properties of amorphous thin brittle coatings by conducting scratch testing.[12] They constructed an amorphous diamond-like carbon (DLC) with *silicon carbide* and titanium dioxide to make thin coatings on soda-lime glass. Unique techniques such as the use of radio frequency plasma-enhanced chemical vapor deposition and filtered-arc deposition were used to fabricate the coating on the glass substrate. Scratch testing was conducted by using a Revetest Scratch Tester with a 200 μm Rockwell-C tip where the stylus was dragged across the coating surface while the normal load was increased to observe the point of coating fracture. This was done in order to measure the fracture strength of brittle coatings on glass substrates. The fracture strength is known to be the stress where a crack is first formed. The studies revealed that fracture initiated at surface defects of the coatings.

Until now, there has not been a SM and SH amorphous coating of a fully polymeric material that can recover elastic and plastic deformation while rebonding cracks. Specifications required to achieve such demands include a system that is transparent, has a low thermoplastic viscosity, does not crystallize, is curable, has surface SM, and has a healing agent incorporated in the system. We aimed to achieve a coating containing both SM and SH capability by combining a crosslinked polymer network with linear polymer chains interpenetrating the SM network to form a SIPN. The crosslinked network contributes to the SM and the linear chains provide the

SH ability. Some potential monomers for the base polymer include styrene, butyl acrylate, and methyl acrylate. We chose a single phase SIPN system where the SM network and healing thermoplastic agent were fabricated from the same monomer and have the same glass transition (T_g). The same T_g was selected for both the SM network and SH thermoplastic so that the SM and SH mechanisms can be triggered upon a single heating event.

Here, a new amorphous coating was created where polymerized tert-butyl acrylate (tBA) was selected to form a crosslinked tBA SM network and a tBA SH thermoplastic. A thin coating of this system was cured on glass substrates for scratch repair for optical surfaces such as telescope, microscope and binocular lenses. Upon damage at room temperature (RT), the scratched coatings were heated above their T_g, which is well above RT, to initiate the surface SM effect and allow for crack closure. The SM effect allows for crack surface contact where the SH agent molecularly diffuses across the damaged site where it is then cooled to RT to complete the healing process through vitrification of the polymer chains (Figure 3-1). *The* SM network and SH agent weight percentages were varied to optimize both effects. Films were used to conduct thermal and thermo-mechanical testing where the coatings were fabricated to conduct scratch testing and transmittance studies.

3.2 EXPERIMENTAL METHODS

3.2.1 MATERIALS

Tert-butyl acrylate, (tBA) monomer (98% pure) (molecular weight of 128.17 g/mol), tetrathyleneglycol dimethacrylate (TEGDMA) crosslinker (molecular weight of 330.37 g/mol), and azobisisobutyronitrile (AIBN) (98 % pure) photoinitiator (molecular weight 164.21 g/mol) were purchased from Sigma Aldrich. The tBA monomer contained 10-20 ppm monomethyl ether hydroquinone inhibitor in order to impede premature polymerization, oxidation and darkening during storage.[13] A SDHR-4 distillation (Scientific Polymer Products, INC) column was used to remove the inhibitor to purify the tBA monomer. TEGDMA, AIBN, methanol, (3-acryloxyproply) trimethoxysilane (coupling agent) and tetrahydrofuran (THF) were used as purchased.

3.2.2 tBA THERMOPLASTIC SYNTHESIS

A thermally initiated free radical polymerization process was conducted to synthesize tBA thermoplastic, which served as the SH agent for the SMASH system. 10 mL (8.33 g) of tBA monomer and 0.083 g (1 wt-%) AIBN (photoinitiator) were dissolved in 20 mL distilled toluene. Toluene was used because it was miscible with the tBA monomer, has a high boiling point of 110 °C and also obviated the degree of the Trommsdorff effect when compared to neat polymerization. Here, the Trommsdorff effect is an autoacceleration in the polymerization rate where it increases local viscosity leading to an unstable free radical polymerization process.[14] The reaction was conducted at 70 °C under nitrogen purge and constant magnetic stirring for 6 h. The solution was precipitated using a BUCHI R - 210 rotary evaporator at 55 °C and rotated at a rate of 20 RPM. This step was conducted in order to extract a portion of toluene from the solution, increasing the concentration for further processing. The resulting viscous solution was dissolved in 30 mL anhydrous tetrahydrofuran (THF) followed by re-precipitation in a 150 mL methanol/150 mL water solution to yield the desired tBA thermoplastic. The thermoplastic was left under the fume hood for 24 h to dry and was further dried for 24 h under vacuum at 45 °C. Scheme 3-1 shows the mechanism of tBA thermoplastic synthesis for the thermally initiated free radical polymerization process employed. TGA analysis was then conducted to confirm complete solvent removal and dryness of the thermoplastic. Gel Permeation Chromatography (GPC) analysis was conducted to determine number-average molecular weight (M_n), weight-average molecular weight (M_w) and polydispersity index (PDI).

3.3 FILM FABRICATION

3.3.1 l-tBA:n-tBA FILM FABRICATION

l-tBa:n-tBA films were made by forming the SM network through free radical polymerization in the presence of the synthesized tBA thermoplastic. This was done by crosslinking the tBA monomer, containing both TEGDMA (5 wt-% of tBA monomer) and poly(tBA), where AIBN (1 wt-% of tBA monomer) formed free radicals to initiate the polymerization process. The tBA thermoplastic was not covalently crosslinked with the shape memory network, but simply randomly inter-coiled within the network to form a semi-interpenetrating polymer network (SIPN).[14,15] Accordingly, a solution of tBA monomer, tBA thermoplastic, TEGDMA crosslinker, and AIBN photo initiator was prepared in a 20 mL vial and stirred at RT with magnetic stirring until the thermoplastic completely dissolved to make a homogeneous solution. No solvent was added to the solution and the thermoplastic powder dissolved completely in the tBA monomer. The solution was then syringed in a glass mold made of two 75 (l) x 25 (w) x 1 (th) mm glass slides with a 1 mm thick Teflon spacer positioned in between the two glass slides and the assembly binder-clipped together. Prior to mold fabrication and solution injection, the glass slides were pre-treated with RainX to ensure that the cured films did not adhere to the glass slides. Ultraviolet (UV) irradiation was then used for 1 h at RT to cure tBA SMASH films. This was done by placing the samples in an enclosed box that contained upper and lower 60 W UV

($2.0\ mW/cm^2$) lamps, each featuring a wavelength of 352 nm in order to allow for uniform curing. Each sample was then removed from the glass molds and placed in individual bags. Scheme 3-2 shows the preparation of the tBA SMASH systems via the UV initiated polymerization process. A post cure step was then conducted to complete the curing process. The weight percentages (wt - %) of the tBA monomer and thermoplastic were varied to yield the following compositions (l-$tBA_{wt-\%}$:n-$tBA_{wt-\%}$): l-tBA_0:n-tBA_{100}, l-tBA_{10}:n-tBA_{90}, l-tBA_{25}:n-tBA_{75}, and l-tBA_{50}:n-tBA_{50}. The wt- % were varied in order to adjust and possibly optimize both the SM and SH effects.

3.3.2 DEGREE OF SHAPE MEMORY NETWORK FORMATION

The degree of SM network formation was evaluated by gel fraction measurements. A small cured sample from each composition weighing (pre-extraction) 21.8 ± 3.0 mg was submerged in 20 mL of methanol, a good swelling solvent for this polymer. Each sample was agitated in a shaker at 60 RPM at 25 °C for 24 h. This process allowed for the extraction of the linear tBA thermoplastic and unreacted tBA monomer from the SM network. After 24 h, the sample was then washed using fresh methanol to remove any polymer from the surface and dried at 40 °C for 24 h in a vacuum oven. The samples were than weighed again to compare the weights pre- and post extraction. This procedure was done three times on three different samples for each composition to assess statistical reproducibility. Gel Fraction (G(%)) was calculated using the following equation:

$$G(\%) = \frac{m_e}{m_i}\ x\ 100\% \tag{3-1}$$

where $G(\%)$ is the gel fraction percentage, m_i is the initial dry weight before extraction and m_e is the dry weight after extraction.[16] This equation calculated the amount of SM network formed.[17]

3.3.3 THERMOGRAVIMETRIC ANALYSIS (TGA)

Thermogravimetric Analysis (TGA) was conducted to obtain the onset degradation temperature for all compositions made. All samples weighing 4.0 ± 0.6 mg were heated to 600 °C at 10 °C/min using a TA Q500 TGA instrument. The experiments were conducted under constant nitrogen purge and the sample decomposition by weight loss as a function of temperature was recorded. The onset temperature of degradation was determined. Three different samples were tested from each composition to assess statistical reproducibility.

3.3.4 DIFFERENTIAL SCANNING CALORIMETRY (DSC) STUDIES

Differential Scanning Calorimetry (DSC) experiments using a TA Q200 DSC were conducted to observe the T_g values for each composition tested. Each sample weighing 4.0 ± 0.7 mg was first equilibrated to -85 °C, isothermally held for 1 min, then heated to 150 °C at 10 °C/min, held isothermally for 1 min, cooled from 150 °C to -50 °C at 10 °C/min, isothermally held for 1 min, and heated again to 150 °C at 10 °C/min. An exothermic peak was evident above T_g on the first heating which indicated the films were not completely cured. Therefore, the samples were post cured at 120 °C for 10 min in a convection oven and cooled at RT for 10 min to completely cure. This was confirmed by running DSC before and after the post cure treatment. Each sample was then tested three times to assess reproducibility.

3.3.5 DYNAMIC MECHANICAL ANALYSIS (DMA)

Thermo-mechanical characterization was conducted using a TA Q800 Dynamic Mechanical Analyzer (DMA). Each sample was cut from a cured film in a rectangular geometry where the sample had average dimensions of 7.0 ± 1.1 (l) x 2.0 ± 0.3 (w) x 0.9 ± 0.1 (th) mm. Each sample was loaded under tension using tensile film clamps in the DMA apparatus. Tensile storage modulus vs. temperature was recorded and the thermal transitions were observed in order to study the viscoelastic properties of the compositions. This was done by applying an oscillatory tensile deformation with a displacement amplitude of 15 µm (tensile strain < 0.4%), a frequency of 1 Hz and, a force track (ratio of static to dynamic forces) of 108 %. Each sample was first heated to an equilibration temperature of 120 °C to remove the thermal history, then ramped to -50 °C at 3 °C/min, held isothermally for 5 min, and finally heated to 120 °C at 3 °C/min. The tensile storage modulus (E′) of the second heating was reported. Each sample of each composition was tested three times to assess statistical reproducibility. The tensile storage modulus at 25 °C, 60 °C, and 100 °C are also reported to study the tensile storage modulus change as a function of temperature. These three temperatures were chosen to identify characteristic thermomechanical properties in the following three states: glass at 25 °C, transition at 60 °C, and rubber at 100 °C.

3.3.6 REVERSIBLE PLASTICITY SHAPE MEMORY (RPSM) CHARACTERIZATION

A new and unique shape memory characterization has been developed in our group referred to as reversible plasticity shape memory (RPSM). RPSM was developed to characterize the reversal of plastic deformation in shape memory polymers (SMP) which most materials are incapable of exhibiting. RPSM is a five-step thermo-mechanical method conducted on the DMA. RPSM was conducted on all compositions using a dogbone geometry following the ASTM Standard D638-

03 Type IV (scaled down by a factor of 4, TestResources, Inc., Shakopee, MN) with an average thickness of 0.35 ± 0.01 mm. All samples were first dogbone-punched from cured films and heated at 120 °C for 10 min and cooled at RT to remove the thermal history. Each sample was then clamped using the tensile film fixtures where the temperature was equilibrated at RT and held isothermally for 1 min. The strain was then ramped to 30% at 5%/min to plastically deform the sample and this strain was held for 10 min (step 1 - 2). The strain was then ramped down at 5%/min until the static force reached 0.001 N in order to unload the sample and observe shape fixing (step 2 - 3). The sample was then heated from 25 °C to 80 °C at 3 °C/min to allow shape recovery (more or less, depending on shape memory capacity) where this temperature was held isothermally for 5 min (step 3 – 4) then ramped back to 25 °C at 3 °C /min to complete the RPSM cycle (step 4 - 5). This was conducted three times to assess data reproducibility. The fixing (R_f) and recovery (R_r) ratios were then calculated by using the following equations:

$$R_f(N) = \frac{\varepsilon_u(N)}{\varepsilon_m(N)} \times 100\% \tag{3-2}$$

$$R_r(N) = \frac{\varepsilon_u(N) - \varepsilon_p(N)}{\varepsilon_u(N) - \varepsilon_p(N-1)} \times 100\% \tag{3-3}$$

where ε_m, ε_u, ε_p and N are the strain before unloading, the strain after unloading, permanent (unrecoverable) strain after shape recovery and the cycle number, respectively.[18-20]

3.3.7 ONE WAY SHAPE MEMORY (1WSM) CHARACTERIZATION

One Way Shape Memory (1WSM), also referred to as conventional SM, was also conducted on the tBA systems testing a rectangular specimen where the average dimensions were 5.7 ± 0.5 (l) x 1.7 ± 0.2 (w) x 0.9 ± 0.1 (th) mm. Distinct from RPSM described above, here 1WSM involves shape fixing with deformation above T_g, followed by cooling under load to a temperature below T_g. Accordingly, the samples were heated at 120 °C for 10 min and cooled at RT for 10 min prior to testing to remove the thermal history. The sample was clamped in the DMA using tensile fixtures and heated to 80 °C, held isothermally for 1 min, and the strain was set to 0%. The force was then ramped to 0.5 N/min until 40% strain was achieved in order to elastically deform the sample and then held isothermally for 2 min. The temperature was then ramped from 80 °C to 0 °C at 3 °C/min, and held isothermally for 5 min in order to temporally fix this deformation. The force was then ramped down to 0.001 N at 0.05 N/min and held for 2 min to observe the fixing properties of the sample. The sample was finally heated back to 80 °C to complete the 1WSM cycle. Three cycles were conducted for each l-tBA:n-tBA system. The fixing and recovery ratios were calculated using equation 2 and 3 defined in the previous section.

3.4 COATING FABRICATION

3.4.1 CLEANING GLASS SLIDES VIA PIRANHA SOLUTION

Hydroxylation and silanization of glass substrates were carried out to promote covalent bonding, and thus better adhesion, between the glass substrate and the tBA SMASH polymeric system. This was done by using a (3-acryloxyproply) trimethoxysilane, 95 % (Gelest, Inc.) coupling agent. First, 1 mm thick un-treated soda-lime glass microscope slides were cleaned by rinsing with acetone followed by gently scrubbing with detergent soap and rinsing with deionized water. Hydroxylation of the glass slides was carried out through the use of a piranha solution of (2:1) sulfuric acid and hydrogen peroxide (*Caution*: piranha solution is explosive, reactive, and corrosive.[21,22] Use extreme caution as temperatures may exceed 100 °C during preparation.[21,22])

This was done by preparing a solution of 26 mL sulfuric acid and adding 13 mL hydrogen peroxide drop-wise while stirring with a glass rod. The piranha solution was used to remove surface impurities, leaving the natural hydroxyl groups on the glass available for bonding to the silane coupling agent. This solution was brought to 60 °C using a hot plate and the glass slides were submerged for 1 h ensuring that all slides were not touching each other to result in successful hydroxylization of the glass surfaces. The slides were then removed from the bath where they were thoroughly rinsed with deionized water, and dried under vacuum at RT until visibly dry. The remaining solution was allowed to react overnight in a glass jar covered with aluminum foil where the foil was punctured with holes several times to allow gas to escape under a fume hood. After the solution was cooled it was left in the fume hood for two weeks, followed by neutralization with sodium bicarbonate. This was done by adding small amounts of sodium bicarbonate powder to the piranha solution at RT while stirring with a glass rod. The pH was checked after each addition, and when the solution reached pH 7, the resulting viscous, opaque white solution was washed down the sink with copious amounts of tap water.

3.4.2 SILANIZATION OF GLASS SLIDES

The silanization process was adopted from the Gelest user guide[23] where after the hydroxylation process a (95:5) solution of ethanol and deionized water (38 mL ethanol and 2 mL deionized water) was prepared. The solution was acidified to pH 4 - 5 using acetic acid, which was added drop-wise and tested using pH paper. It is believed that acetic acid was used to prevent polymerization of the coupling agent. 1-% by volume (0.4 mL) (3-acryloxyproply) trimethoxysilane, 95-% was added drop-wise to the solution while stirring with a glass rod at RT for 5 min. The glass slides were submerged and the bath was agitated for 5 min. Here, hydrolysis occurred, during which the methoxy groups on the end of the silane reacted with the newly formed hydroxyl groups on the substrate to form a covalently bonded layer of silane at the surface of the glass (Scheme 3-3). This process produced methanol as a byproduct (Scheme 3-3). The glass slides were then removed and rinsed thoroughly with fresh ethanol to remove excess, unbonded silane from the surface. The slides were cured at 110 °C for 10 min in a convection isothermal oven in order to cure the silane layer formed on the glass substrate surface. FTIR-ATR was conducted on non-silanized and silanized glass slides to evaluate the presence of the carbonyl group within the (3-acryloxyproply) trimethoxysilane coupling agent. FTIR-ATR was conducted in order to observe the presence of the carbonyl group.

3.4.3 l-tBA:n-tBA COATING FABRICATION

10 μm thick coatings were prepared to simulate coatings on optical surfaces. This was done by UV curing a l-tBA:n-tBA network on the chemically modified silanized glass substrate. The sample preparation and compositions detailed in section 3.3.1 were used to make coatings. Here, the solution was syringed onto a silanized glass slide with a 10 μm thick spacer, which was pre-cut from a ShimStock sheet to the height and width of the slide. A second, non-silanized slide was then placed on top, sandwiching the liquid. The second slide was treated with RainX to prevent coating-glass adhesion. The slides were secured together with binder clips. The coatings were then UV cured for 1 h (Scheme 3-4). The non-silanized glass slide was then removed to expose the 10 μm coating cured on the silanized glass substrate.

3.4.4 OPTICAL MICROSCOPY (OM) AND SELF HEALING (SH) STUDIES

To test the amount of SH that occurred and optical transparency of the coatings, scratch tests analyzed with optical microscopy (OM) and spectrometer studies were carried out. Our characterization principle was that scratch-damaged samples would exhibit diminished light transmission compared to the pristine coatings. OM imaging was conducted using an Olympus BX-51 polarizing microscope and Q Capture Pro software. Prior to scratching, the coating was heated to 120 °C for 20 min and cooled at RT for 20 min to remove the thermal history. The OM was calibrated for proper light alignment and image focusing. An OM micrograph of the coating in its virgin state at 10x magnification was captured. The sample was then scratched using a razor blade in a custom built motorized scratching machine at RT (Figure 3-2). Here, the coating was firmly fastened into the sample holder and placed on the movable track. The track was connected to a motor that was attached to the back of the scratch machine. The motor is connected to a controller, from which the user can toggle the direction of stage (and sample) translation relative to the razor blade. Here, each coating was scratched in a forward motion in order to form a uniaxial scratch where a track speed of 0.9 mm/sec was used. A second OM micrograph was then taken of the scratched coating. The damaged coating was then thermally treated by heating it in an isothermal oven at 120 °C for 20 min resulting in crack closure and healing through the SMASH effect. The coating was then cooled at RT for 20 min where a final OM micrograph was taken. This process was repeated four times for each composition to study reproducibility. OM images were used in evaluating the SH efficiency. This was done by importing all the OM micrographs in .TIFF format into the ImageJ software where in some cases the use of the paint tool to fill in the area of the scratch in black was performed for ease of analysis. The .TIFF images were then converted to an 8-bit format and saved as a .bmp (Figure 3-3 (a)). The images were then imported into Vision Assistant software, version 7.1, (Figure 3-3 (b)) where the images were analyzed to obtain the area in pixels of the scratched and thermally treated coatings. This was done by constructing a program containing a series of steps in the Vision Assistant software. First, a manual threshold on the images was conducted to isolate the area of the scratch (highlighted red) from the rest of the coating surface (Figure 3-3 (c)). The next step was to remove small objects from the image (Figure 3-3 (d)). The following step filled in the remaining areas in the scratched area in red (Figure 3-3 (e)). Finally, a histogram was created and an excel spreadsheet was produced that listed the overall area of the image, non-scratched, and scratched regions in pixels. The SH efficiency was defined as:

$$SH_{Efficiency}(\%) = \frac{A_{ss} - A_{TTS}}{A_{ss}} x100\% \qquad (3\text{-}4)$$

where A_{SS} is the area in pixels of scratched surface and A_{TTS} is the area in pixels of the thermally treated surface. For example, if $A_{TTS} = A_{SS,}$ the SH efficiency would be 0 %. If $A_{TTS} = 0$, the SH efficiency would be 100 %. A graph of SH efficiency vs. tBA thermoplastic wt - % content was recorded for each composition tested.

3.4.5 LIGHT TRANSMISSION STUDIES

Light transmission were also carried out to quantify the transmittance of light through the virgin, damaged and thermally treated states of the coatings relative to a pristine glass surface using a spectrometer in conjunction with a light microscope. Following OM imaging of each l-tBa:n-tBA SMASH coatings, a S2000 Ocean Optics, Inc fiber optic spectrometer was attached to the OM microscope. OOIBase32 software was then used to analyze the percent transmittance of light through the coated glass at each of the states. To switch from absorbance to percent transmittance, a dark reference consisting of a razor blade covering the light source, and a reference consisting of a pristine glass slide was stored, giving the software a baseline to compare the coated samples. A graph of transmittance vs. wavelength was recorded for each composition. This process was conducted three times on each coating to obtain reproducibility.

3.5 RESULTS AND DISCUSSION

3.5.1 tBA THERMOPLASTIC SYNTHESIS

tBA thermoplastic was made via a thermally initiated free radical polymerization process to be used as the SH agent in the SMASH system. The resultant thermoplastic after precipitation and drying step was a brittle, white, and porous material. GPC analysis revealed an average M_n= 86,200 g/mol, M_w= 177,000 g/mol and a PDI of 2.06 based on three 5 mg of thermoplastic/ 1 mL of THF samples. Figure 3-4 shows the GPC data analysis for the light scattering and refractive index traces where Table 3-1 shows the numerical values obtained to calculate the M_n, M_w, and PDI averages. The M_n's of two out of the three samples had similar values where the third sample had a higher M_n. The M_w values followed the same behavior. This behavior is expected as the molecular weights are hard to control and reproduce when conducting a free radical polymerization process. The PDI had approximately the same values among all three samples tested where these PDI values were reasonable for free radial polymerization techniques.

3.5.2 l-tBA:n-tBA FILM FABRICATION

SMASH films were fabricated using a UV polymerization method where four compositions explained in section 3.3.1 were made. All films were removed from the glass mold with ease where all the samples were robust, rigid and transparent post cure with a smooth topography. It was observed, however, that the l-tBA$_{50}$:n-tBA$_{50}$ sample contained bubbles in the bulk of the film in all three film fabrication reproductions. It is hypothesized that the local viscosity formed from the high thermoplastic content is the source of the bubbles.

3.5.3 DEGREE OF SHAPE MEMORY NETWORK FORMATION

Degree of shape memory network formation was measured by gel fraction experiments. This was done by submerging small cured specimens of each composition in methanol and agitating for 24 h at 25 °C where each sample was weighed pre- and post-methanol extraction. Gel fractions were calculated using Eqn. 3-1. In Section 3.3.2., all samples remained amorphous pre- and post-extraction and the samples expanded in volume in methanol during the 24 h period. The sample volume expansion is due to solvent swelling of the tBA network. All samples remained intact during the swelling and subsequent drying process. Figure 3-5 shows a linear relationship of gel fraction % as a function of tBA thermoplastic content where Table 3-2 shows the gel fractions (G%) for the average of three samples tested among the four compositions made. The G values show a decreasing trend with a decrease in network formation. This means that with the increase in tBA thermoplastic content, the degree of network formation decreased which was as expected. It is confirmed that all thermoplastic content was successfully extracted leaving the network formed as the G values are similar in magnitude to that of network wt-%.

3.5.4 THERMOGRAVIMETRIC ANALYSIS (TGA)

TGA analysis was conducted in order to examine the onset degradation temperatures of all compositions tested. The onset degradation temperatures are important to analyze as the samples start to decompose and lose their structural and mechanical properties at the onset point. Figure

3-6 (a) shows representative TGA curves of each compositions and neat tBA thermoplastic. tBA monomer could not be analyzed using the TGA as it is a volatile liquid and cannot be accurately tested. It is hypothesized that the tBA monomer will evaporate completely prior to degradation. There is a common trend among all the compositions and thermoplastic where the first weight drop indicates the onset degradation temperature ranging from 259 °C ± 1.3 to 260 °C ± 0.3 (Table 3-3) for three samples tested. The onset degradation temperature is hypothesized to be the tBA side chains degrading by cleavage from the backbone. Beyond, this initial degradation event, the increase in weight loss with the increase in temperature is hypothesized to be the backbone of the tBA polymer degrading. Figure 3-6 (b) shows the onset degradation temperature vs. tBA thermoplastic wt-% content for an average of three samples tested. All onset temperatures were similar in magnitude which was as expected since the polymers used did not change among the compositions studied.

3.5.5 DIFFERENTIAL SCANNING CALORIMETRY (DSC) STUDIES

DSC analysis was conducted in order to evaluate the T_g of all the compositions and neat tBA thermoplastic. T_g is an important polymer characteristic as it reveals the onset of chain molecular motion in polymeric systems. This is where polymers transition from a hard glassy state to a rubbery state.[24] Figure 3-7 (a) shows representative curves of the first heating traces where an exothermic peak is evident. This peak suggests that all compositions cured for 1 h under UV exposure were not completely cured. Figure 3-7 (b) shows the second heating of these same samples where the exothermic peak was no longer evident, but instead the T_g's were revealed ranging from 47 °C to 49 °C (Table 3-4). This means, therefore, that all the samples completely cured upon the second heating. All samples were then post cured at 120 °C for 10 min (as the process adopted henceforth) and cooled at RT for 10 min where DSC analysis was repeated. Figure 3-7 (c) shows the first heating of the post cured samples showing the T_g transitions only with no evidence of exothermic peaks. This means all samples that were post cured showed complete curing. Figure 3-7 (d) shows the second heating of the post cured samples where these T_g values were reported and are shown to have the same values as the as cured samples in the 2nd heating trace. Figure 3-8 shows the average T_g values of three samples tested as a function of tBA thermoplastic wt- %. Table 3-4 shows the numerical values of the average T_g's with accompanying standard deviations. The T_g values were approximately the same in magnitude regardless of composition. It was initially hypothesized that more crosslinking formed due to a higher monomer wt-% would increase the T_g as more energy is required for polymer chain motion between crosslinks. This would mean that a higher thermoplastic content would lead to a lower T_g. However, this was not an evident trend among these films studied and indicates that T_g is dominated by the repeating unit composition in such materials. Similar results were found in a similar system where semi-crystalline polymers were used instead. These results are shown and explained in Chapter 2 and has been published.[17]

3.5.6 DYNAMIC MECHANICAL ANALYSIS (DMA)

DMA experiments were conducted to obtain the tensile storage modulus (E′) transitions as a function of temperature. Figure 3-9 (a) shows representative traces of the E′ transitions as a function of temperature for each composition tested. Here, the onset T_g and rubbery plateau is observed. Figure 3-9 (b) shows the average E′ as a function of tBA thermoplastic wt - % content for three specimens tested at 25 °C, 60 °C and 100 °C. Table 3-5 shows the average numerical values of E′ with standard deviations. At 25 °C the samples are rigid and chain mobility is highly restricted where E′ was 411.6 ± 27.6 MPa for tBA_{50}:n-tBA_{50} sample and 607.8 ± 100.5 MPa for the tBA_0:n-tBA_{100} composition. As the temperature increases to 60 °C, the T_g is observed where chain movement initiates. Here, the E′ was 20.3 ± 1.0 MPa for the tBA_{50}:n-tBA_{50} sample and 178.0 ± 184.3 MPa for the tBA_0:n-tBA_{100} composition. Increasing the temperature further to 100 °C the rubber plateau is observed where the polymer chains are in a rubber elastic state. The E′ was 0.3 ± 0.02 MPa for tBA_{50}:n-tBA_{50} and 1.0 ± 0.13 MPa for tBA_0:n-tBA_{100} sample. Although above the T_g, the tBA SMASH system is able to sustain its geometry due to the crosslinks present in the tBA thermoset network. The elimination of the crosslinks would result in the sample to flow. There is a definite trend of decreasing E′ with the increase of thermoplastic content and this trend is observed among all three temperatures. This is expected as the increase of thermoplastic content decreases the effective crosslink density by dilution. Since the thermoplastic has a linear architecture and is not covalently crosslinked to the SM network it does not bear a significant amount of load to have a high mechanical response to forces. It can also be observed that the samples that have a higher network formation yield a higher rubbery modulus at 100 °C. This is evident for the tBA_0:n-tBA_{100}, l-tBA_{10}:n-tBA_{90}, and l-tBA_{25}:n-tBA_{75} samples which showed the same tensile storage modulus at 100 °C. However, for the tBA_{50}:n-tBA_{50} sample, the rubber modulus was significantly lower when compared to the other composites. It is known in polymer physics fundamentals[25] that the modulus (E) is directly proportional to the crosslink density (n) (mol/m^3) as shown in the following equation: $E = 3nRT$ where the R = gas constant and T = temperature. Therefore, with increasing thermoplastic content there is a decrease in tensile storage modulus because of the decrease in crosslink density, again by dilution.

3.5.7 REVERSIBLE PLASTICITY SHAPE MEMORY (RPSM) CHARACTERIZATION

RPSM was characterized to reveal a new SM effect, reversible plasticity SM. Here, each specimen was deformed below its T_g, unloaded to observe fixing and then recovered above T_g to regain its original shape. Figure 3-10 shows a representative 3D RPSM graph of l-tBA:n-tBA compositions where the sample, already in its vitrified state, is elastically and plastically deformed to achieve 30% strain (step 1 - 2) at RT (Figure 3-10 (a)). Here, the polymer chains are presumed to align in the direction of loading during deformation. The sample is then unloaded to observe the fixing properties (step 2 - 3) (Figure 3-10 (a)). Rubber elasticity can be used to explain the polymer chain response. When the crosslinked polymer chains are at equilibrium, in its undeformed state, the tBA polymer chains are in a highly coiled entropic conformation. As the network is uni-axially stretched at RT to achieve 30% strain, the entropy is significantly reduced since the number of polymer conformations decreases. Upon force release, the polymer chains, which can be modeled as entropic springs, elastically recover. The sample is able to elastically recover due to the stored energy the sample gained during deformation. The specimen is then heated to 80 °C to observe the recovery of plastic deformation for near complete shape recovery (step 3 - 4) (Figure 3-10 (a)) of each specimen. Here, the polymer chains go from a vitrified state to a rubbery state, allowing for the network chains to regain their highly coiled configuration. The sample is then cooled to RT to complete the RPSM cycle (step 4 -5) (Figure 3-10 (a)). This process was done three times on three different samples from each composition. The back plane shows a graph of strain vs. temperature to further convey the elastic and plastic deformation followed by shape recovery (black dashed line). The side plane shows a stress vs. strain to show the complete cycle in 2D (black solid line). Figure 3-10 shows RPSM curves for

(a) (0:100), (b) (10:90), (c) (25:75), and (d) (50:50). All graphs showed evidence of an elastic region, yield point, plastic deformation and cold drawing region which are unique phenomena among viscoelastic polymers. Figure 3-11 (a) shows representative RPSM curves for all compositions tested on one graph to compare each composition among each other. It can be observed that all samples, regardless of tBA SH thermoplastic content can achieve 30% strain without failure, demonstrate near complete fixing upon unloading, and reveal near complete shape recovery. Figure 3-11 (b) shows a bar graph of the fixing (R_f) and recovery (R_r) ratios among all compositions tested as a function of thermoplastic wt-% content. Table 3-6 shows the average R_f which ranged from 95.9 % to 97.8 % and R_r of 83.6 % to 97.3 % among all compositions. This suggests that all compositions regardless of thermoplastic content were able to maintain the temporal geometry after unloading. Similarly, the samples were also able to recover with evidence of small residual strains after shape recovery. RPSM plays a critical role for surface damage on coatings because most damage incurred initiates below the coating's T_g and therefore results in a significant amount of plastic deformation. The RPSM effect shows that elastic and plastic deformation can occur and yet are reversible upon a thermal stimulus. This is critical as this recovery is necessary for scratch repair on coatings.

3.5.8 ONE WAY SHAPE MEMORY (1WSM) CHARACTERIZATION

One Way Shape Memory (1WSM) was conducted on all compositions to observe a unique and different form of shape memory when compared to RPSM. Whereas the samples were stretched below their T_g in RPSM, here the samples were first heated above their T_g and cooled to achieve temporal deformation and heated again for shape recovery. Figure 3-12 (a) through (d) shows the 1WSM for (0:100), (10:90), (25:75), and (50:50) respectively. Each sample was heated to 80 °C where it was in its beginning point of the rubbery state and then elastically deformed to achieve 40% strain. Microscopically, the polymer chains aligned in the direction of the uni-axial force then vitrified to this temporal shape when cooled to 0 °C. Here, the polymer chains are in their low configuration state (low entropic state) where temporal fixing is maintained when cooled below T_g. The load is released to observe the fixing properties of the system and then heated to 80 °C for sample restoration of its original highly entropic state. All samples showed great fixing properties upon unloading where high recovery was also evident among all three cycles tested for each composition. Although the amount of fixing and recovery was unaffected in the l-tBA_{50}:n-tBA_{50} sample, this sample showed a significant amount in strain decrease when comparing cycle 1 to cycle 2 and 3. It is postulated that this is due to the sample overshooting in strain owing to the high SH thermoplastic content. Figure 3-13 shows a bar graph of the average R_f and R_r where Table 3-7 shows the average R_f ranging from 98.3% to 98.9 % and R_r ranging from 91.7 % to 95.7 %. These values were calculated using Eqns. (2) and (3) explained in section 3.3.6. The 1WSM data shows that all compositions are able to achieve the desired strain regardless of thermoplastic content. This means that the SM effect is not impaired or limited from the low or high thermoplastic content. The data also shows great cycle lifetimes where the specimens tested for three consecutive 1WSM cycles did not deteriorate or have compromised mechanical properties. This is also true when studying the R_r trends where the thermoplastic does not interfere with the recovery of the samples. However, it is important to observe that the R_r are not 100% as cycle 1 in relation to cycle 2 and 3 does not have the same starting point. It is hypothesized that this discrepancy is related to the thermal expansion of the DMA clamp fixtures and also due to the sample thermal expansion which is referred to as thermal strain. This means that the polymer chains are occupying a larger volume in the sample and thus results in the sample expanding at a given temperature. Although, RPSM is more relevant for scratch repair in coatings, 1WSM serves to show that conventional SM is achieved in fully amorphous systems.

3.6 l:n-tBA COATING FABRICATION

3.6.1 CLEANING GLASS SLIDES VIA PIRANHA SOLUTION

Chemical modification of glass slides was accomplished using a piranha solution to remove organic impurities from the surface of the as-purchased glass slides to expose the natural hydroxyl groups. Visually the glass slides looked the same when compared to the as-purchased slides.

3.6.2 SILANIZATION OF GLASS SLIDES

Silanization of glass slides was carried out to promote good adhesion of the l:n-tBA coatings to the glass substrate as well as to prevent delamination from the glass by using a (3-acryloxyproply) trimethoxysilane coupling agent. The glass slides visually looked transparent where FTIR-ATR analysis was conducted and revealed the presence of carboxyl groups, which showed a peak at 1729.26 cm^{-1} (Figure 3-14). This indicated, at least qualitatively, a successful salinization process.

3.6.3 l:n-tBA COATING FABRICATION

The silanized glass slides prepared in the previous section were then used to make the 10 µm tBA coatings of various compositions. All coatings cured were approximately 10 µm in thickness and were uniform along the length and width of the coating substrate. All coatings did not delaminate upon the removal of the top unsilanized slides. Visually, all coatings looked transparent post cure where Scheme 3-4 shows a representative image of a coating on a glass substrate.

3.6.4 OPTICAL MICROSCOPY (OM) AND SELF HEALING (SH) STUDIES

Optical microscopy (OM) was carried out to assess the SH efficiency of each l:n-tBA coating by taking OM micrographs at three different coating stages: virgin, damaged, and thermally treated. Figure 3-15 bears representative optical micrographs at each as a function of coating composition. Here, the OM micrographs show no evidence of coating-glass substrate delamination where a uniform degree of damage is observed. Figures 3-16 – 3-19 show all micrographs for each composition where 4 tests were conducted on each coating. The SH efficiency was then calculated by comparing the area in pixels of the scratch and thermally treated coating. The average SH efficiencies of each composition are documented in Figure 3-20 and Table 3-8 where the SH efficiency increased with increasing thermoplastic wt-% content. For the l:n-tBA (0:100) coating there was a SH % of 45 $\pm$ 28 % where the l:n-tBA (50:50) coating was 81 $\pm$ 13 %. This therefore, means a direct relationship between the SH efficiency and the increase in amount of linear tBA thermoplastic was observed. Thus, means that the l-tBA_{50}:n-tBA_{50} shows the best healing for repairing of scratches on coatings among the compositions examined. Figure 3-21 show representative SEM micrographs of all the compositions studied for this system. It can be observed that the scratches visually have a variable degree of damage, although noting the damage was done uniformly with the same normal force used for all compositions tested. It is important to note that the damage was performed at RT which is significantly lower than the T_g of the coating (T_g ~46 °C) ($T_{scratch} < T_{g, coating}$). This means the coating was probably damaged in a brittle manner at RT. It is hypothesized that this causes uncontrolled brittle damage where small cracks are formed perpendicular to the primary scratch that is formed. These small uncontrolled cracks dissipate energy where the energy created to make the cracks should ideally be stored in the coating so that this energy can be reused for crack closure assisted by SM and thus enabling the damage to heal. In reexamining the representative SEM's there is evidence of significant brittle damage which are indicative of the flakes that are seen around the scratch formed (Figure 3-21). When the coatings are then thermally treated to allow for SM and SH to initiate, there is evidence of crack closure when compared to the damaged state. The SEM micrographs also show a smooth topography once thermally treated as it is hypothesized that plastic deformation was evident on the ridges of the scratch perimeter (Figure 3-21 scratched coatings on the top row). However, in some instances there is also evidence of some material removal where small holes at the damaged site are observed, post crack-closure. The inset SEM's show the ends of the scratch to observe if material removal, or "plowing", was apparent. The SEM show no signs of material removal, but instead along the length of the scratch. This presents a challenge for SH, as material removal will render the coating to be permanently damaged as the SM effect cannot close the scratch completely due to the insufficient material needed for crack closure.

3.6.5 LIGHT TRANSMISSION STUDIES

Light transmission studies were performed to analyze the transmittance percentage of l:n-tBA coatings at the virgin, damaged, and thermally treated states. Figure 3-22 shows average transmittance (%) vs. wavelength (nm) graphs of three samples in each composition. Figures 3-23 to 3-26 show all the raw transmittance (%) vs. wavelength (nm) graphs for each of the four compositions where three tests were performed on each coating. Figure 3-27 and Table 3-9 shows the average of the transmittance within the visible spectrum among four scratches analyzed. Analyzing the spectrometer data, it can be observed that samples in their virgin state allow approximately an average of 98% of the light to pass though the coating where in the damaged state an average of 88% of light was able to pass through relative to the glass slide (Table 3-9). After heating the coating, the light allowed through the thermally treated crack fluctuated slightly between compositions and is consistently greater than that of the damaged state where the transmittance was approximately an average of 95% (Table 3-9). It is also important to observe a small visible scar that is evident after thermal treatment, which may impair the visibility for users vision. The goal is to have the coating appear in its virgin state. Therefore, further studies are explained in Chapter 6 to solve the scarring problem found on the coating's surface.

3.7 CONCLUSIONS

This chapter detailed the fabrication and characterization of crosslinked poly(tert–butyl acrylate**)** (poly(tBA)) SIPN single phase blends for optical applications. Films were fabricated where thermal and thermo-mechanical analyses were conducted in order to observe the thermal transitions and viscoelastic properties as a function of temperature necessary for crack closure and healing. Scratch testing, optical microscopy, and light transmission analyses were conducted on thin, clear 10 μm coatings on glass to observe the SM and SH effect needed for scratch repair on coating surfaces. Transmittance studies were conducted pre- and post-damage and after thermal treatment where the l-tBA$_{50}$:n-tBA$_{50}$ composition proved to be the best system for SM and healing for scratch repair. Such SMASH coatings can be used for eye glassware, microscope, telescope and binocular lenses, and for industrial products as well as other applications where transparent SMASH coatings are needed for scratch repair.

3.8 REFERENCES

(1) Markey, M.; Moody, H.: Combination Antifog/Antiscratch Coating Applied to Special Protective Eyewear, Cylindrical System (SPECS): Experimental Trials. *ARMY SOLDIER AND BIOLOGICAL CHEMICAL COMMAND NATICK MA SOLDIER SYSTEMS CENTER* **1999**.

(2) Rad, A. S.; Binaeian, E.; Mirabi, A.: Automotive Clear Coat Polyurethane (Desmodur Z4470+Different Desmophen) with Respect to Some Physical and Self-healing Properties. *Asian Journal of Chemistry* **2012**, *24*, 1313-1315.

(3) Science, B. M.: Se**lf-healing coatings based on polyurethane raw materials**.

(4) Burnworth, M.; Tang, L. M.; Kumpfer, J. R.; Duncan, A. J.; Beyer, F. L.; Fiore, G. L.; Rowan, S. J.; Weder, C.: Optically healable supramolecular polymers. *Nature* **2011**, *472*, 334-U230.

(5) Jackson, A. C.; Bartelt, J. A.; Braun, P. V.: Transparent Self-Healing Polymers Based on Encapsulated Plasticizers in a Thermoplastic Matrix. *Advanced Functional Materials* **2011**, *21*, 4705-4711.

(6) Blaiszik, B. J.; Kramer, S. L. B.; Olugebefola, S. C.; Moore, J. S.; Sottos, N. R.; White, S. R.: Self-Healing Polymers and Composites. *Annual Review of Materials Research, Vol 40* **2010**, *40*, 179-211.

(7) White, S. R.; Sottos, N. R.; Geubelle, P. H.; Moore, J. S.; Kessler, M. R.; Sriram, S. R.; Brown, E. N.; Viswanathan, S.: Autonomic healing of polymer composites. *Nature* **2001**, *409*, 794-797.

(8) Carotenuto, G.; Her, Y. S.; Matijevic, E.: Preparation and characterization of nanocomposite thin films for optical devices. *Industrial & Engineering Chemistry Research* **1996**, *35*, 2929-2932.

(9) Cho, S. H.; White, S. R.; Braun, P. V.: Self-Healing Polymer Coatings. *Advanced Materials* **2009**, *21*, 645-+.

(10) Andreeva, D. V.; Fix, D.; Mohwald, H.; Shchukin, D. G.: Self-healing anticorrosion coatings based on pH-sensitive polyelectrolyte/inhibitor sandwichlike nanostructures. *Advanced Materials* **2008**, *20*, 2789-+.

(11) Zhou, J. W.; Schmidt, A. M.; Ritter, H.: Bicomponent Transparent Polyester Networks with Shape Memory Effect. *Macromolecules* **2010**, *43*, 939-942.

(12) Borrero-Lopez, O.; Hoffman, M.; Bendavid, A.; Martin, P. J.: The use of the scratch test to measure the fracture strength of brittle thin films. *Thin Solid Films* **2010**, *518*, 4911-4917.

(13) Scientific Polymer Products, I.: TECHNICAL BULLETIN TB-101: INHIBITOR REMOVERS AND PREPACKED COLUMNS.

(14) Odian, G.: *Principles of Polymerization*; A JOHN WILEY & SONS, INC., PUBLICATION: Hoboken, New Jersey, 2004.

(15) Sperling, L. H.: *Introduction of Physical Polymer Science*; 4th Edition ed.; John Wiley ans Sons Inc.: Hoboken, New Jersey, 2006.

(16) Chung, T.; Romo-Uribe, A.; Mather, P. T.: Two-way reversible shape memory in a semicrystalline network. *Macromolecules* **2008**, *41*, 184-192.

(17) Rodriguez, E. D.; Luo, X. F.; Mather, P. T.: Linear/Network Poly(epsilon-caprolactone) Blends Exhibiting Shape Memory Assisted Self-Healing (SMASH). *ACS Applied Materials & Interfaces* **2011**, *3*, 152-161.

(18) Mather, P. T.; Luo, X. F.; Rousseau, I. A.: Shape Memory Polymer Research. *Annual Review of Materials Research* **2009**, *39*, 445-471.

(19) Luo, X. F.; Mather, P. T.: Preparation and Characterization of Shape Memory Elastomeric Composites. *Macromolecules* **2009**, *42*, 7251-7253.

(20) Ge, Q.; Luo, X. F.; Rodriguez, E. D.; Zhang, X.; Mather, P. T.; Dunn, M. L.; Qi, H. J.: Thermomechanical behavior of shape memory elastomeric composites. *Journal of the Mechanics and Physics of Solids* **2012**, *60*, 67-83.

(21) Huang, Z. Y.; Wang, P. C.; MacDiarmid, A. G.; Xia, Y. N.; Whitesides, G.: Selective deposition of conducting polymers on hydroxyl-terminated surfaces with printed monolayers of alkylsiloxanes as templates. *Langmuir* **1997**, *13*, 6480-6484.

(22) Mohan, T.; Kargl, R.; Kostler, S.; Doliska, A.; Findenig, G.; Ribitsch, V.; Stana-Leinschek, K.: Functional Polysaccharide Conjugates for the Preparation of Microarrays. *Acs Applied Materials & Interfaces* **2012**, *4*, 2743-2751.

(23) Gelest, I.: Gelest Coupling Agents. 2 ed., 2006.

(24) Young, R. J.; Lovell, P. A.: *Introduction to Polymers*; 2 ed.; Chapman and Hall, 1991.

(25) Sperling, L. H.: *Introduction of Physical Polymer Science*; 4th Edition ed.; John Wiley and Sons Inc.: Hoboken, New Jersey, 2006.

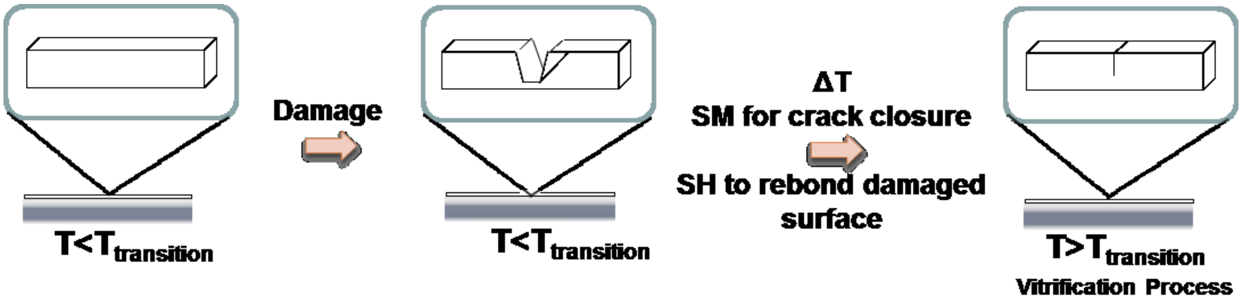

Figure 3-1. Schematic showing the SMASH process for an amorphous coating.

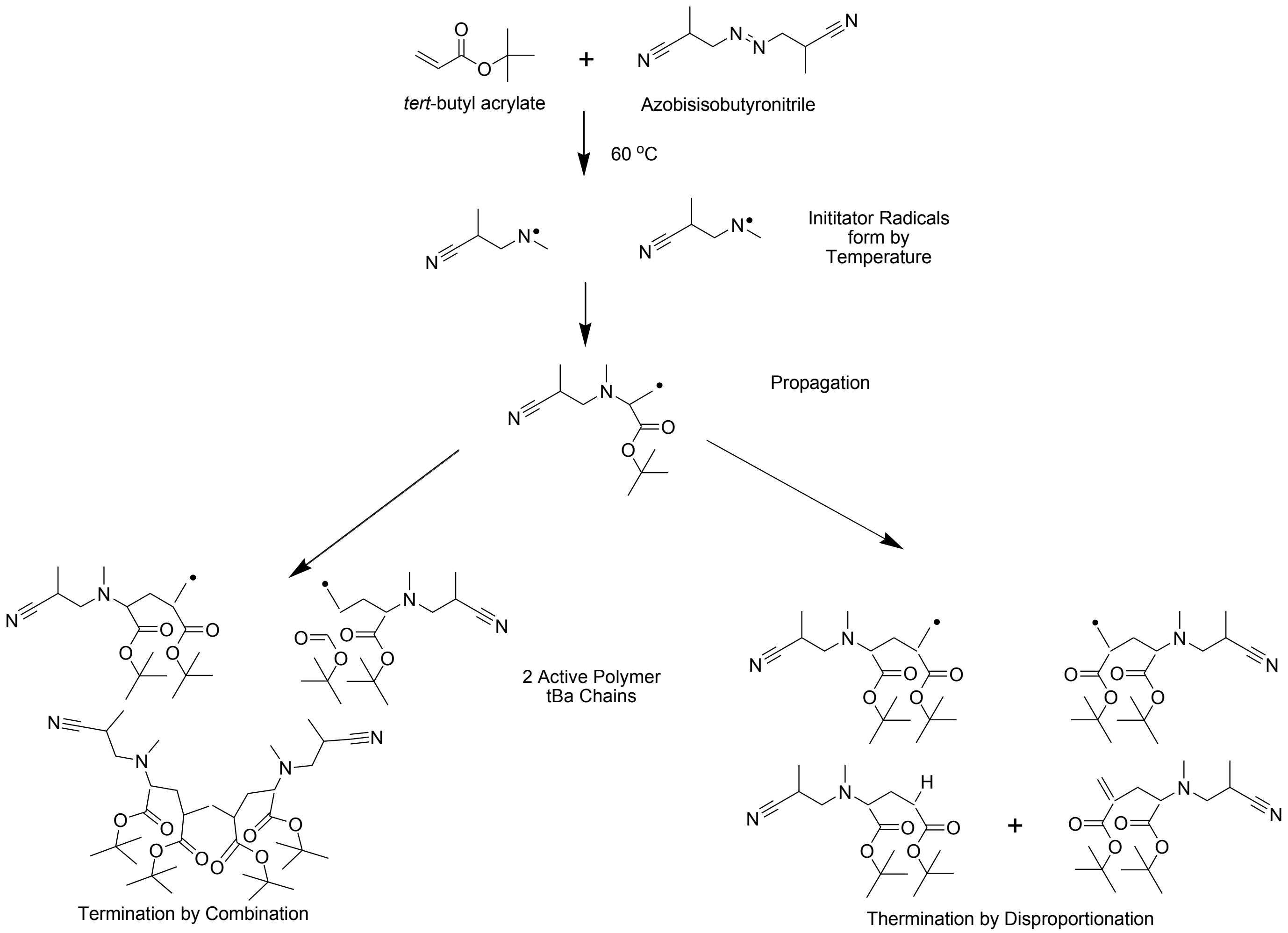

Scheme 3-1. Preparation of the tBA thermoplastic (SH agent) synthesis through the thermal initiated free radical polymerization process.

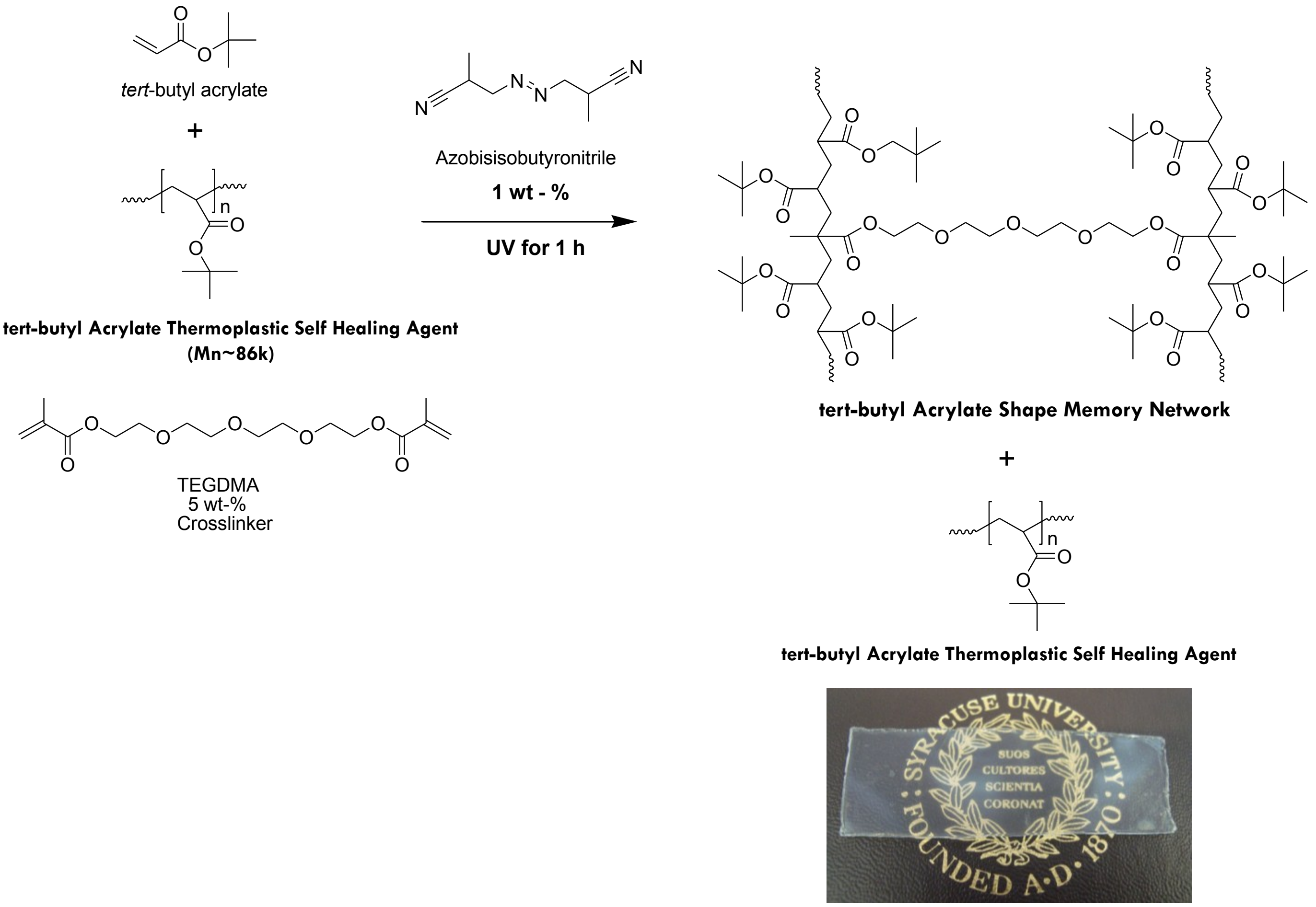

Scheme 3-2. Schematic showing preparation of tBA SMASH films by UV initiated polymerization process with a representative image of a film following de-molding to show the transparency property.

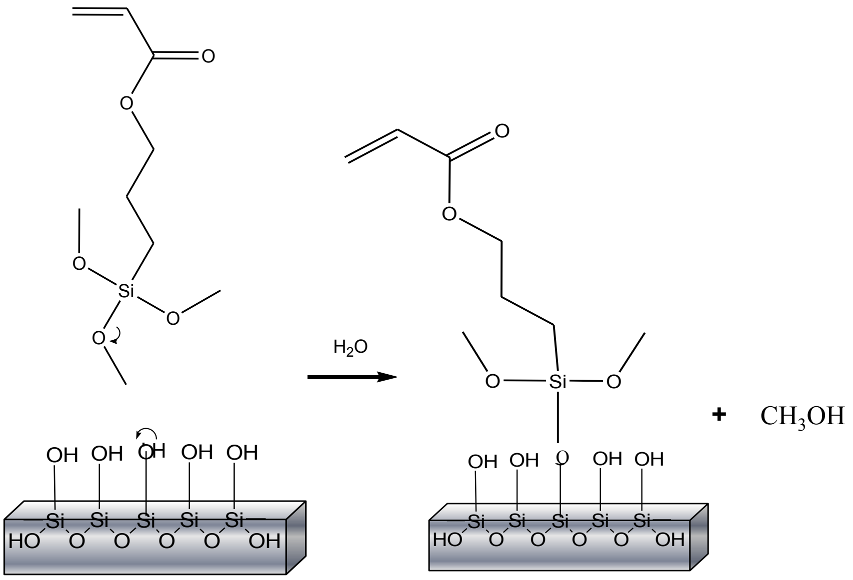

Scheme 3-3. Hydrolysis process on the glass substrate. The arrows indicate electron flow during the silanization process.

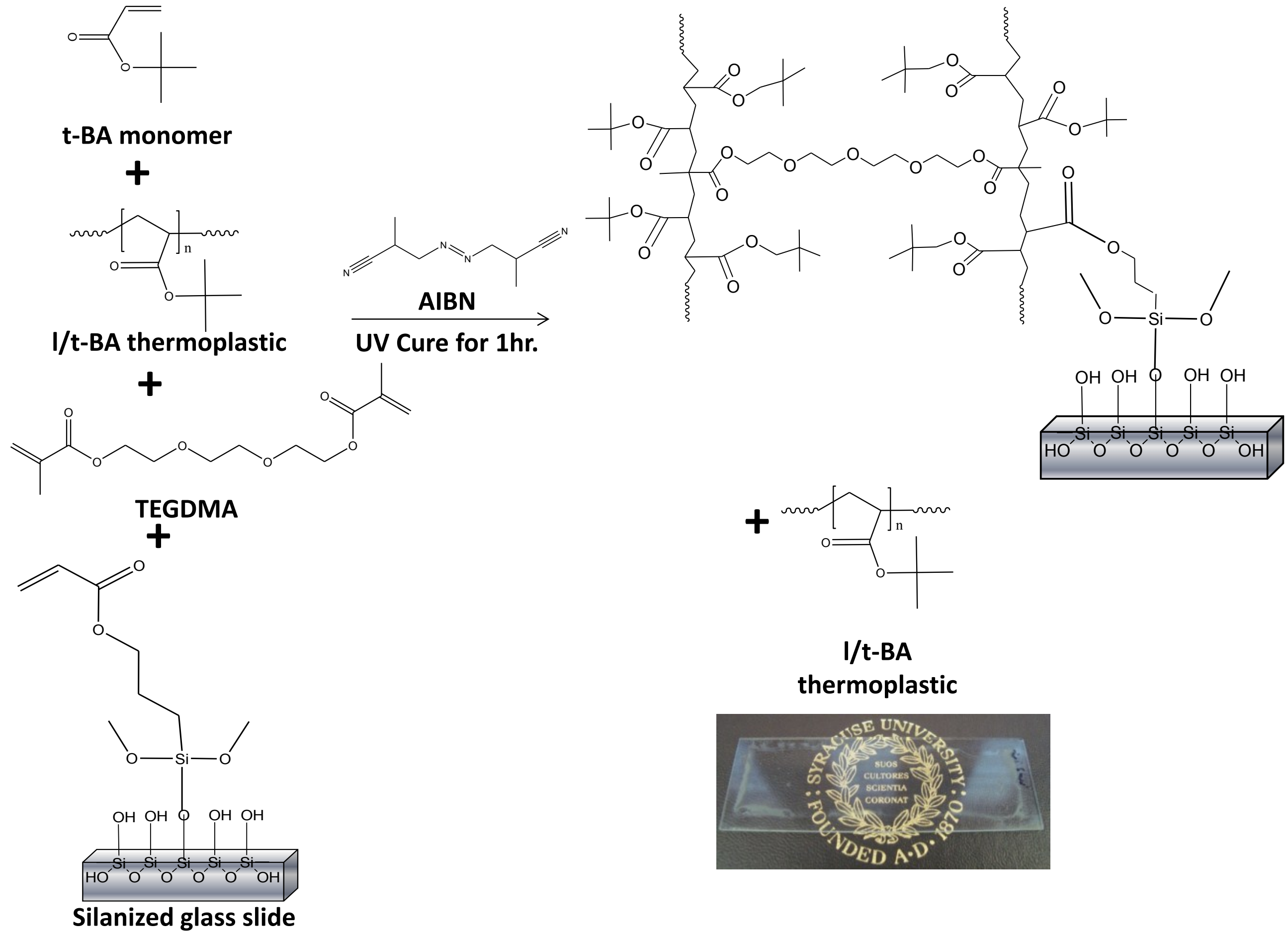

Scheme 3-4. Schematic showing preparation of tBA SMASH coating using a silanized glass slide. Representative image of a coating on a glass substrate to show the transparency.

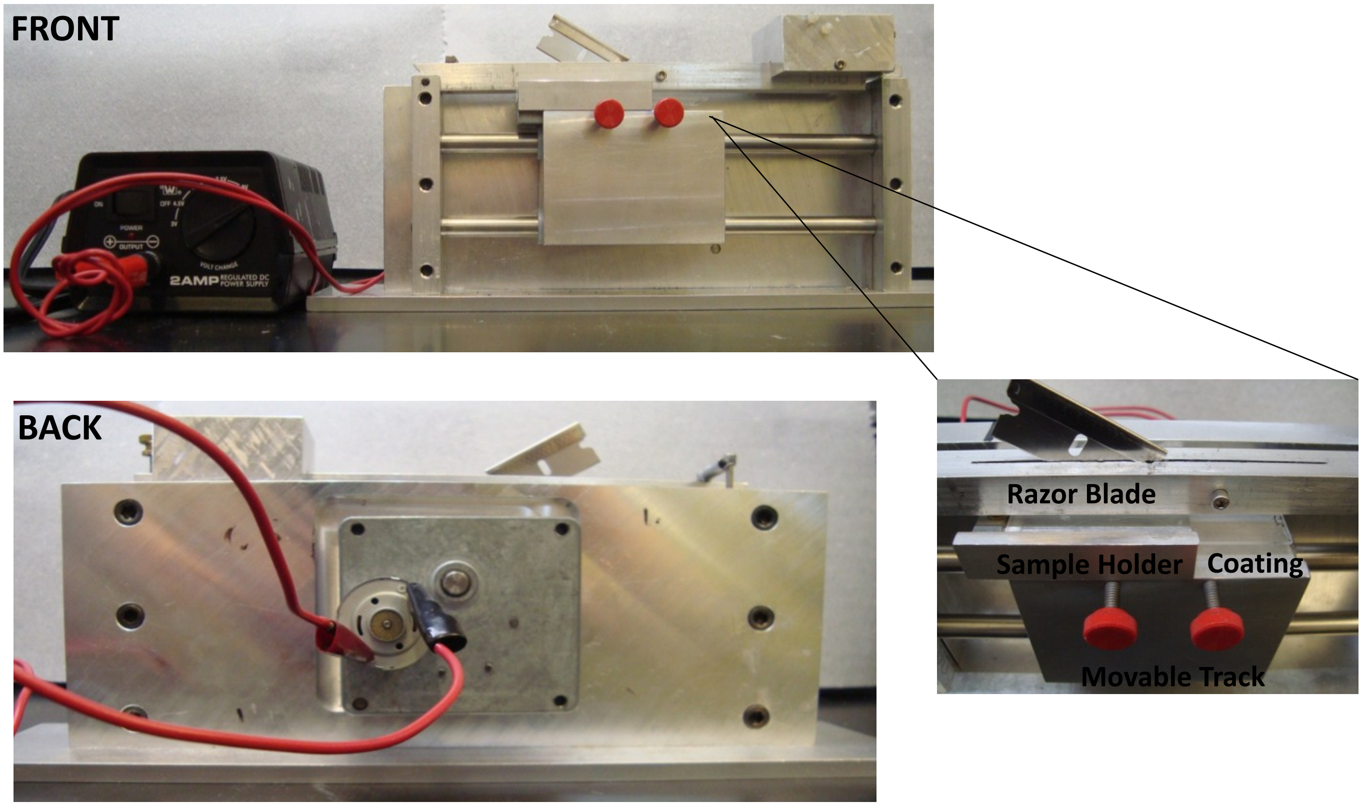

Figure 3-2. Images of the custom made motorized scratch machine where the movable track was connected to a motor that allowed a forward or backward motion. The scratch was formed using a track speed of approximately 0.9 mm/sec.

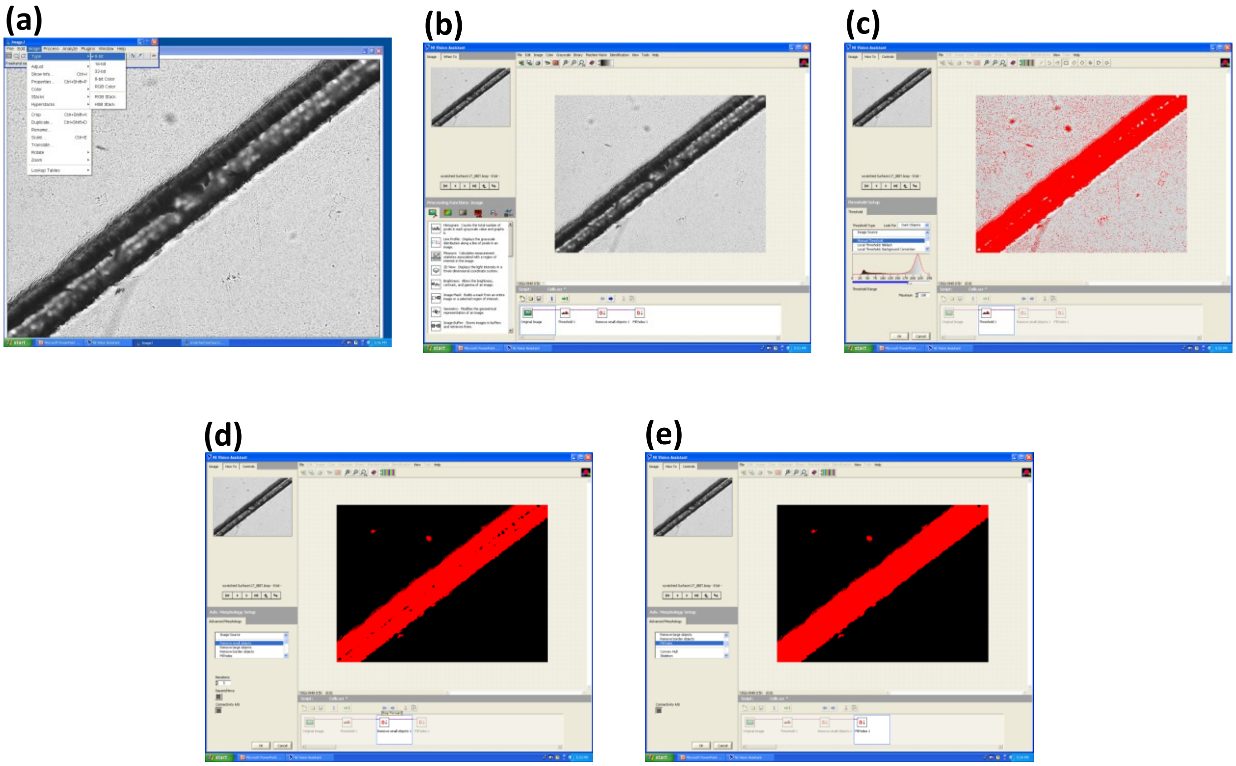

Figure 3-3. Process of image analysis used for SH efficiency calculations. Image (a) of a damaged coating in ImageJ software to convert image to an 8-bit, (b) imported into Vision Assistant for image analysis, (c) performed a manual threshold (d) removed small objects, (e) filled in areas of the scratch in red.

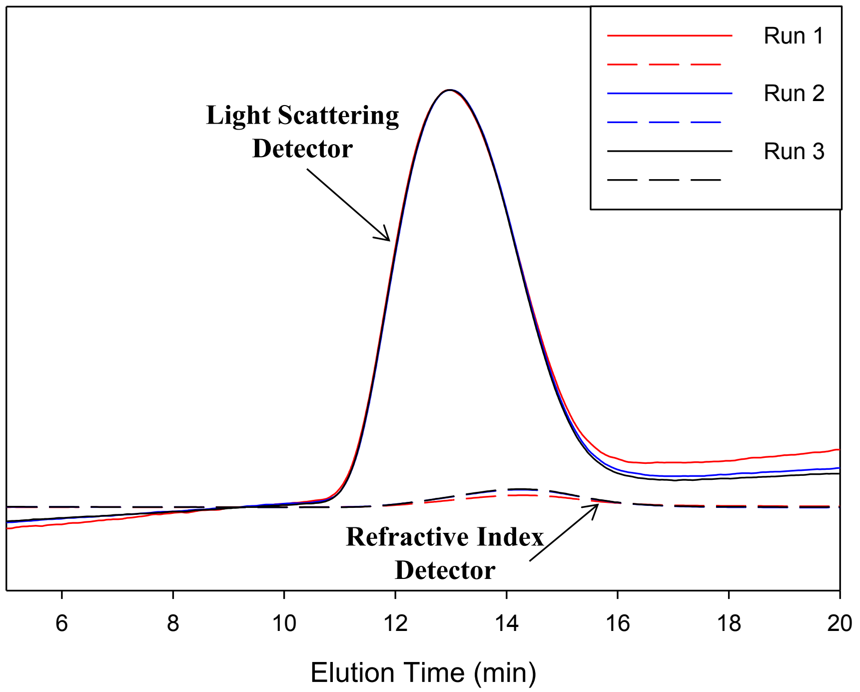

Figure 3-4. Gel Permeation Chromatography (GPC) graph showing the light scattering and refractive index traces needed to calculate the molecular weight (M_w) and number average molecular weight (M_n) for the tert-butyl acrylate (tBA) thermoplastic.

Table 3-1. Table showing the molecular weight (M_w), number average molecular weight (M_n), and polymer dispersity index (PDI) of the synthesized tBA thermoplastic.

Sample	M_n (g/mol)	M_w (g/mol)	PDI
1	7.02E+04	1.44E+05	2.046
2	6.95E+04	1.45E+05	2.085
3	1.19E+05	2.43E+05	2.049
Average	**8.61E+04**	**1.77E+05**	**2.06**

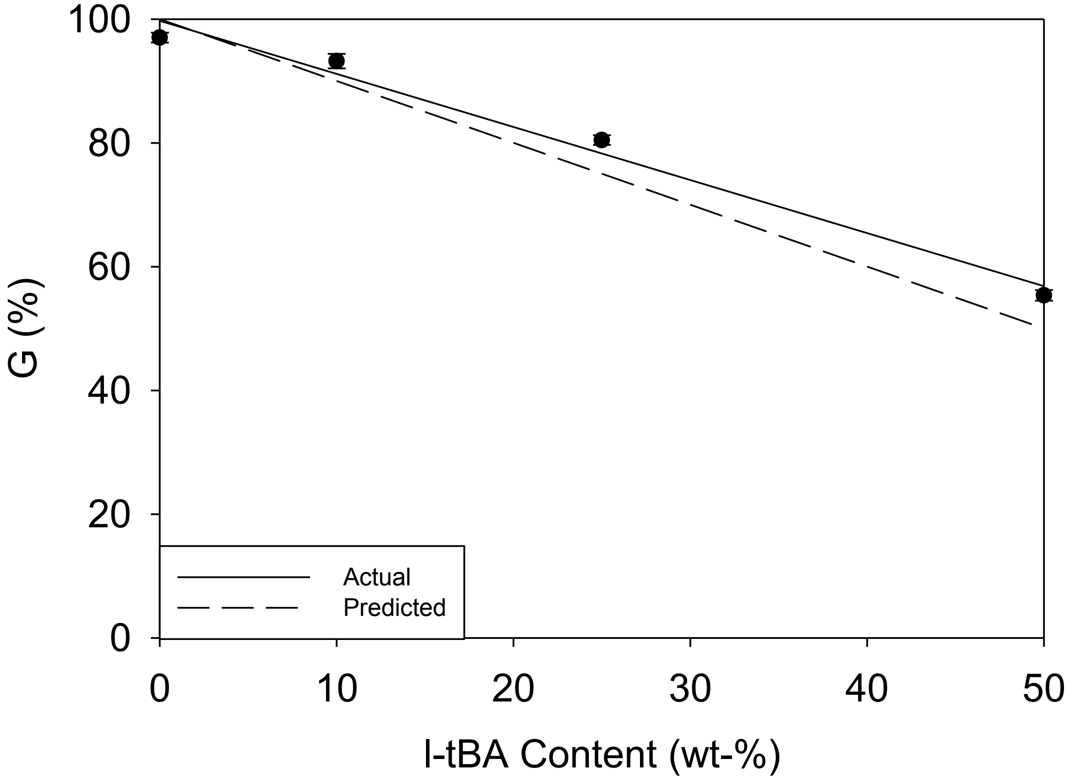

Figure 3-5. Graph showing the dependence of the l:n-tBA blend's gel fractions (G(%)) by methanol extraction for all compositions tested as a function of tBA thermoplastic content. Data shows the average of three samples tested where the lines represent the linear regression of the actual and predicted data.

Table 3-2. Gel Fraction (G(%)) averages of all l:n-tBA compositions with accompany standard deviation where three specimens were tested for each composition.

Composition	AVE G(%)	STDEV
(0:100)	97.0	0.8
(10:90)	93.2	1.2
(25:75)	80.5	0.8
(50:50)	55.4	0.9

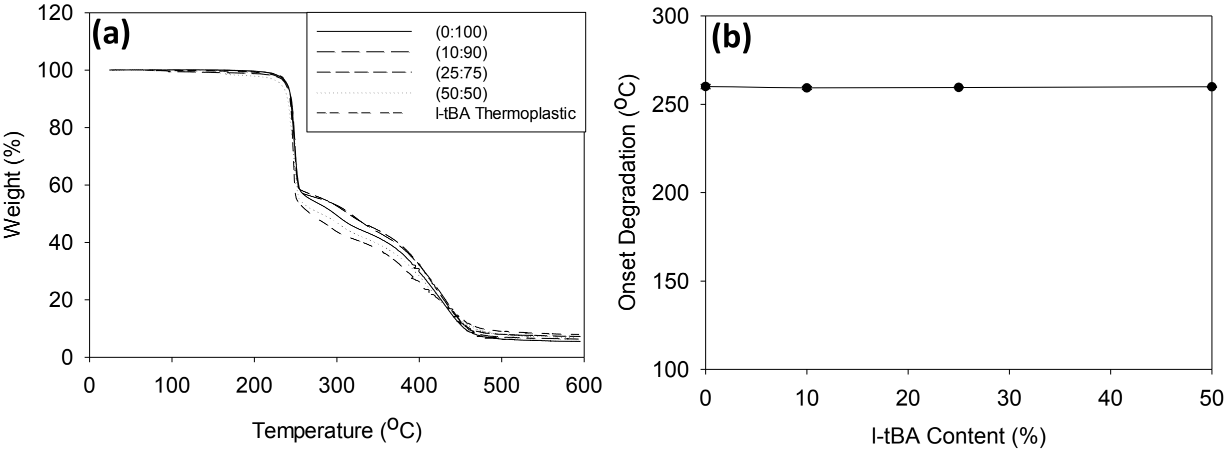

Figure 3-6. (a) Representative thermogravimetric analysis (TGA) curves showing degradation temperatures where all l:n-tBA compositions and neat tBA thermoplastic were heated at 10 °C/min to 600 °C. (b) Graph showing onset degradation temperature vs. tBA thermoplastic wt -% content for an average of three samples for each composition tested.

Table 3-3. Table showing the average onset degradation temperatures from three l:n-tBA specimens of each composition studied.

Composition	AVE Onset Degradation (°)	STDEV
(0:100)	260.0	1.3
(10:90)	259.2	0.9
(25:75)	259.5	0.3
(50:50)	259.9	0.3

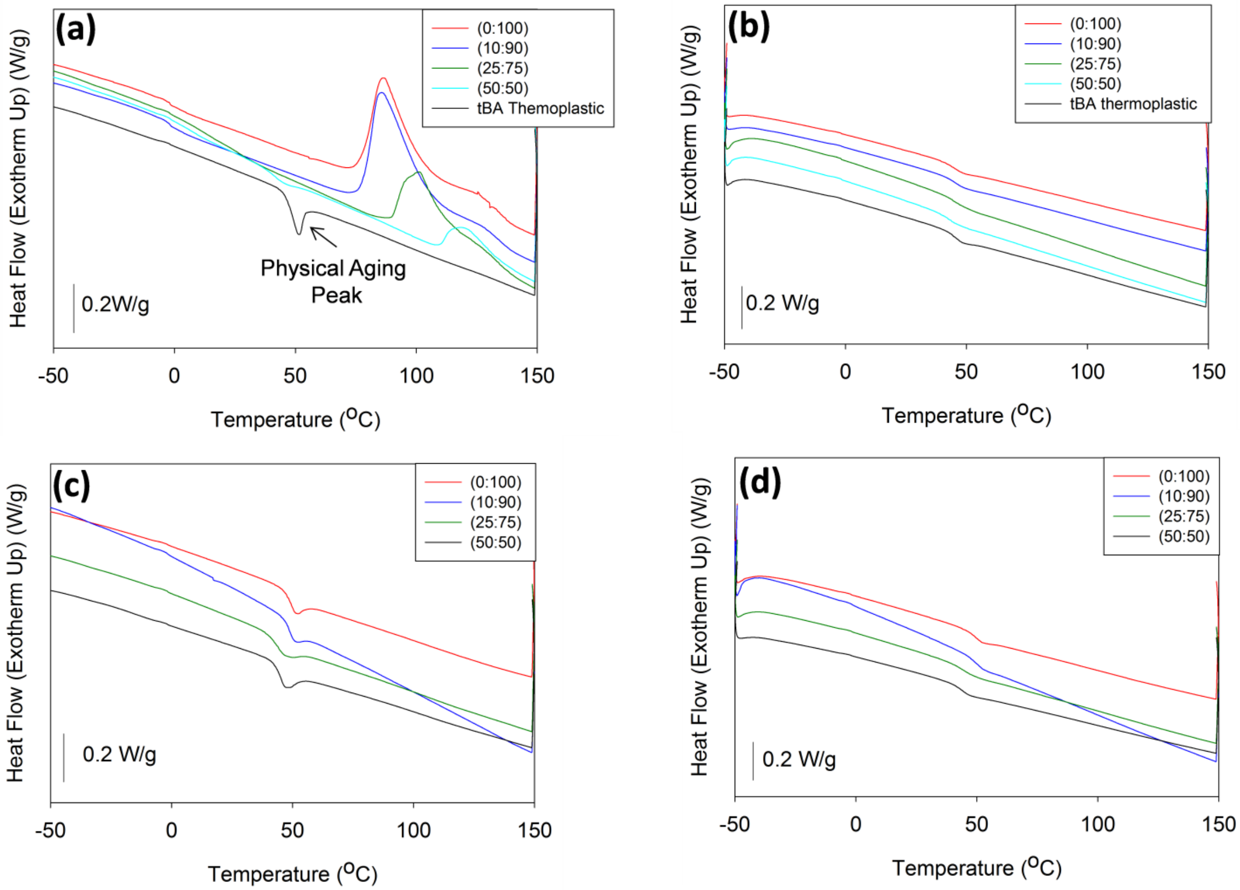

Figure 3-7. Graph showing representative (a) first heating traces of the exothermic peak indicating complete cure was not accomplished among the l:n-tBA systems where (b) second heating revealing the T_g transitions for all the compositions tested with no exothermic peak evident. (c) Graph showing the first heating and (b) second heating from samples that were post cured revealing complete cure and T_g transitions with no exothermic peak evident.

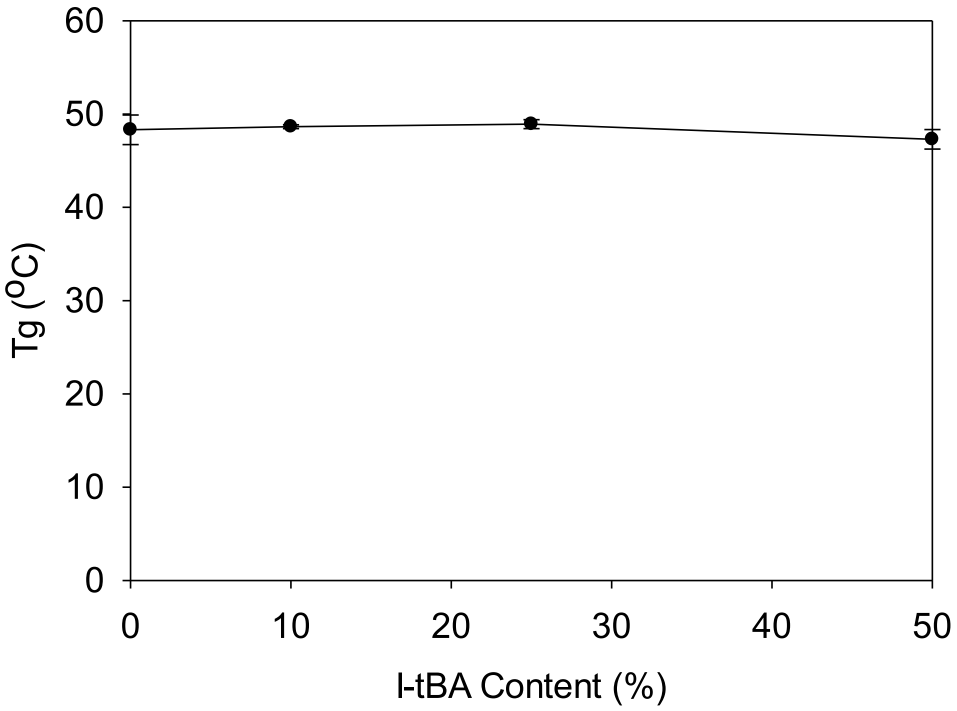

Figure 3-8. Graph showing the T_g obtained from the second heating of the post cured l:n-tBA samples. Three samples were tested for each composition as a function of tBA thermoplastic wt -% content.

Table 3-4. Table showing the average T_g transitions and standard deviation among all the l:n-tBA compositions tested. Three specimens were tested for each composition.

Composition	AVE T_g (^oC)	STDEV
(0:100)	48.3	1.6
(10:90)	48.6	0.2
(25:75)	48.9	0.5
(50:50)	47.3	1.0

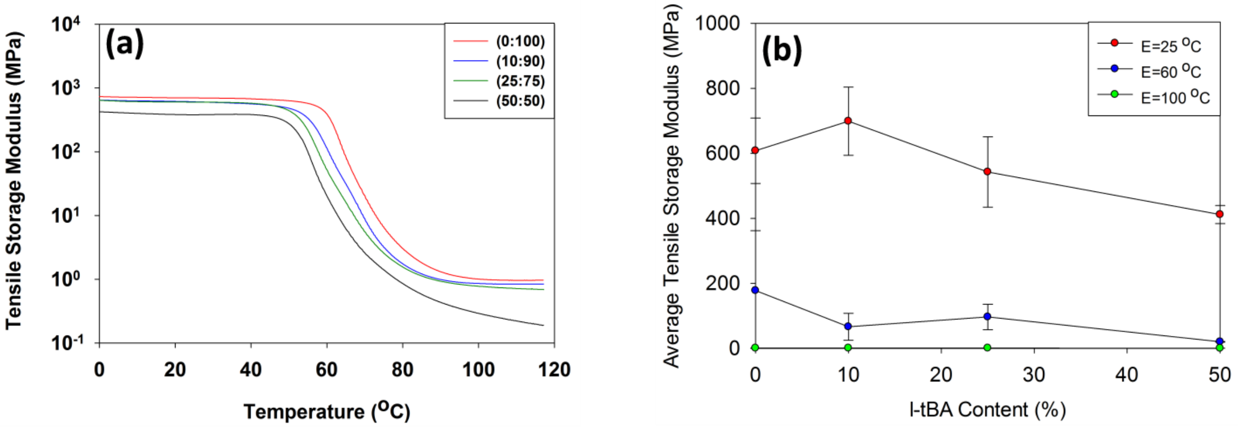

Figure 3-9. (a) Representative traces showing tensile storage modulus (E′) as a function of temperature among all l:n-tBA compositions tested. (b) Graph showing tensile storage modulus as a function of tBA thermoplastic content for three samples tested for each composition where standard error bars are shown. The tensile storage modulus was recorded at 25 °C, 60 °C, and 100 °C to observe the change in thermomechanical properties at these temperatures.

Table 3-5. Table showing the average tensile storage modulus for all the l:n-tBA composition tested at 25 °C, 60 °C and 100 °C.

Composition	AVE $E'_{25°C}$ (MPa)	STDEV	AVE $E'_{60°C}$ (MPa)	STDEV	AVE $E'_{100°C}$ (MPa)	STDEV
(0:100)	607.8	100.5	178.0	184.3	1.0	0.13
(10:90)	698.6	104.6	66.4	41.6	0.9	0.08
(25:75)	542.3	108.0	96.6	38.9	0.9	0.11
(50:50)	411.6	27.6	20.3	1.0	0.3	0.02

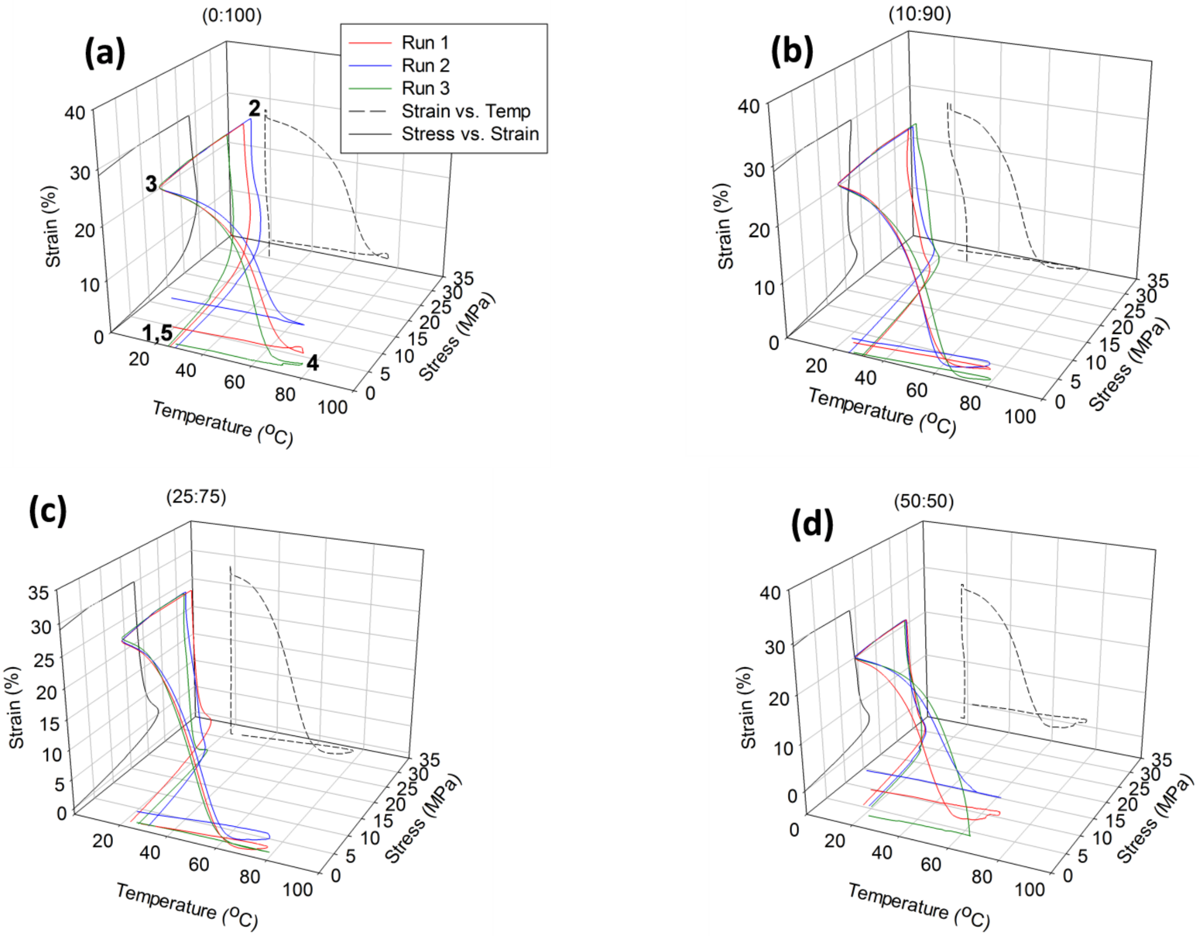

Figure 3-10. RPSM graphs showing for the following l:n-tBA compositions (a) (0:100) , (b) (10:90), (c) (25:75), and (d) (50:50).

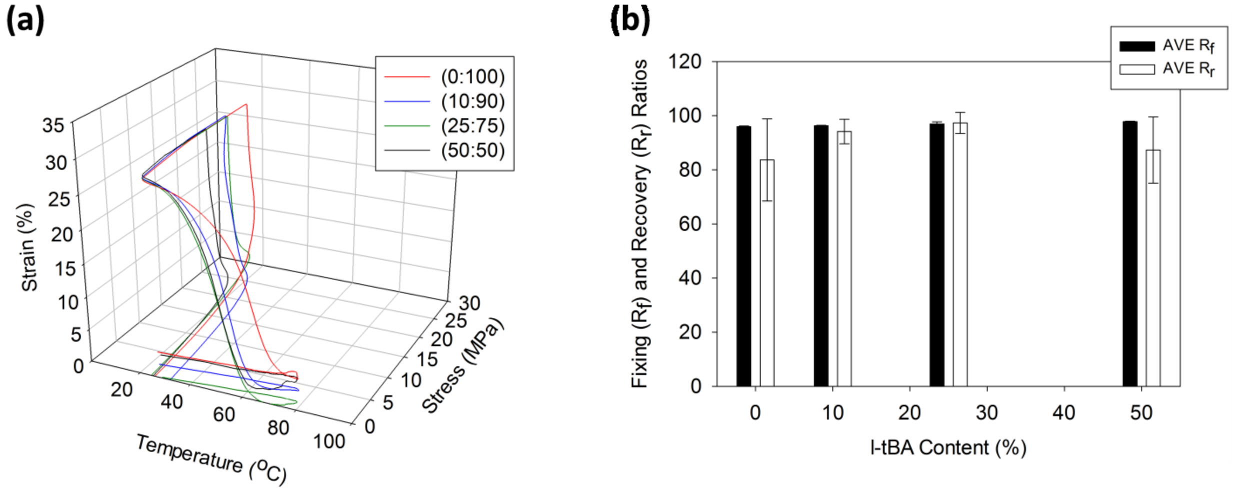

Figure 3-11. (a) showing representative RPSM graphs and (b) showing the fixing (R_f) and recovery (R_r) ratios for all l:n-tBA compositions tested as a function tBA thermoplastic content.

Table 3-6. The fixing (R_f) and recovery (R_r) ratios for RPSM experiments of all l:n-tBA compositions where three samples were tested for each composition.

Composition	AVE R_f	STDEV	AVE R_r	STDEV
(0:100)	95.9	0.3	83.6	15.2
(10:90)	96.3	0.1	94.1	4.5
(25:75)	97.0	0.8	97.3	3.9
(50:50)	97.8	0.2	87.3	12.2

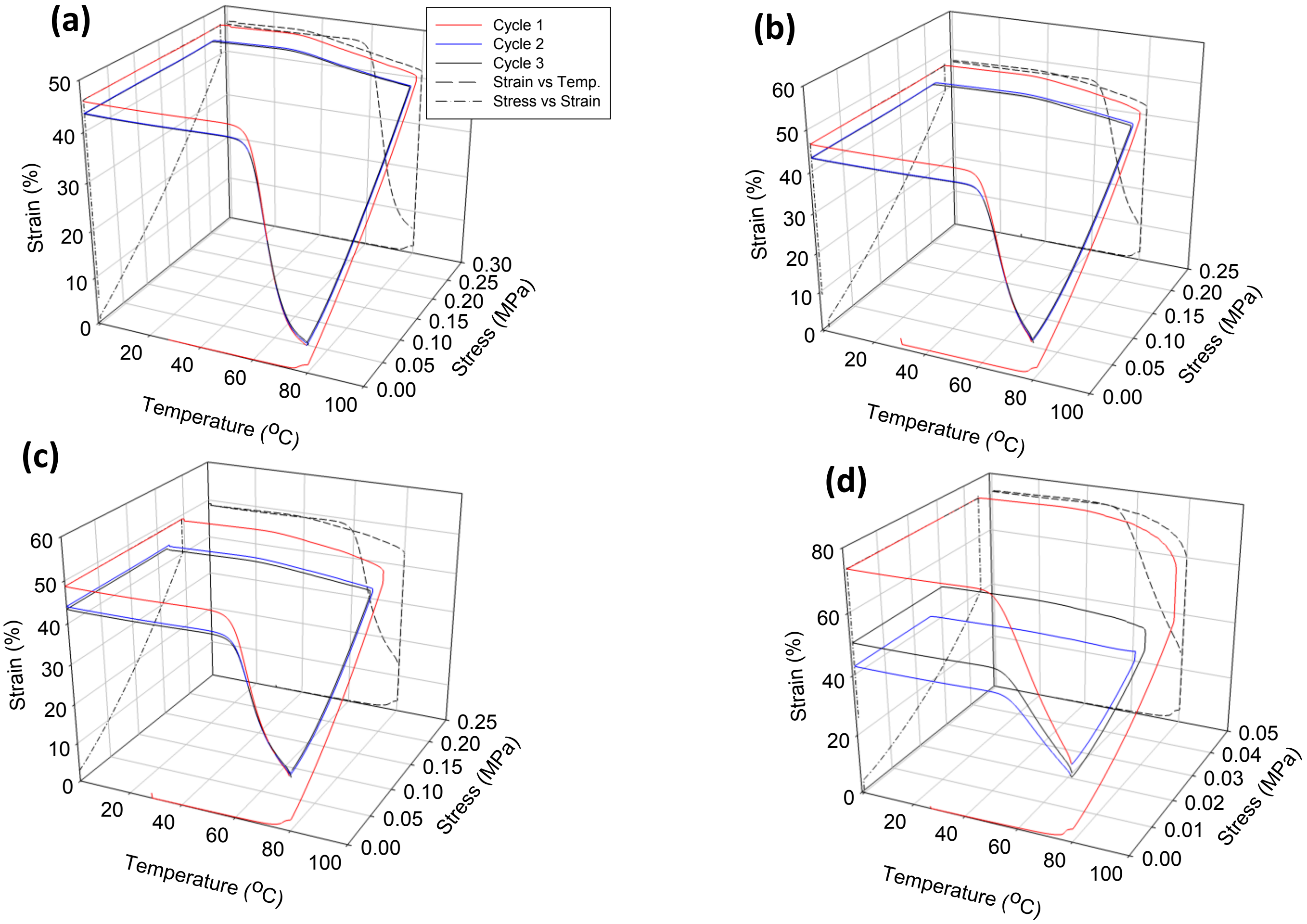

Figure 3-12. 1WSM curves for (a) (0:100), (b) (10:90), (c) (25:75), and (d) (50:50) l:n-tBA compositions where 1mm thick rectangular specimen were thermally treated at 120 °C for 10 min and cooled at RT for 10 min prior to testing. Graphs also show strain vs. temperature in the back plane and stress vs. strain curves on the side plane.

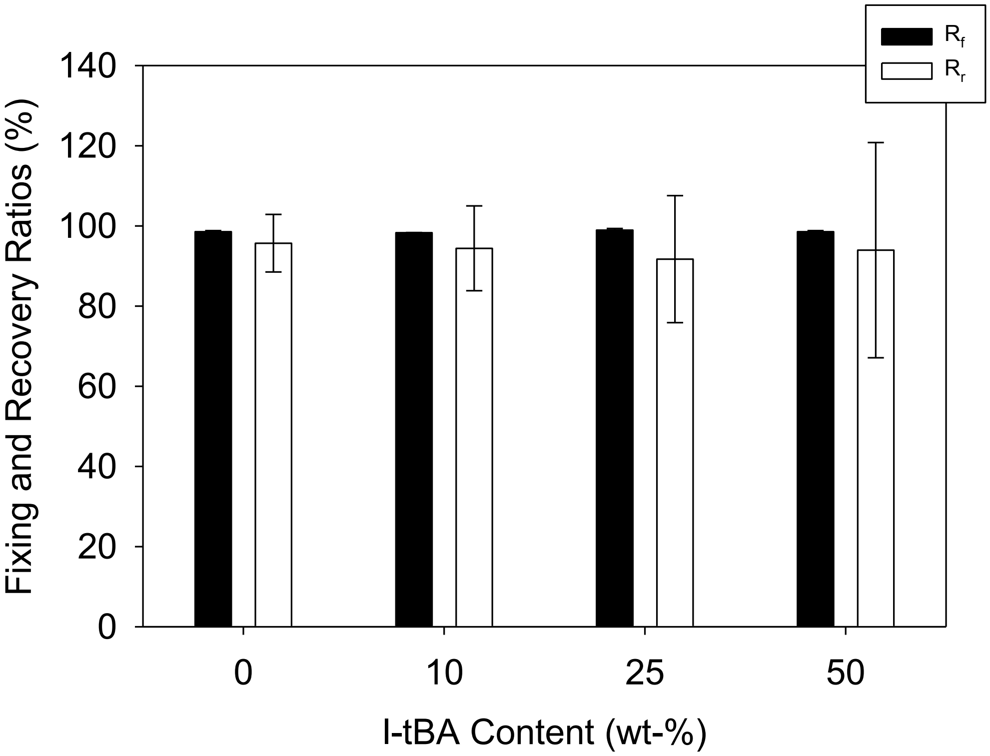

Figure 3-13. The fixing (R_f) and recovery (R_r) ratios for all l:n-tBA compositions tested for 1WSM experiments.

Table 3-7. Summary table of 1WSM data for all l:n-tBA compositions tested.

Composition	**AVE R_f**	**STDEV**	**AVE R_r**	**STDEV**
(0:100)	98.6	0.3	95.7	7.2
(10:90)	98.3	0.1	94.4	10.6
(25:75)	98.9	0.4	91.7	15.8
(50:50)	98.5	0.3	93.9	26.8

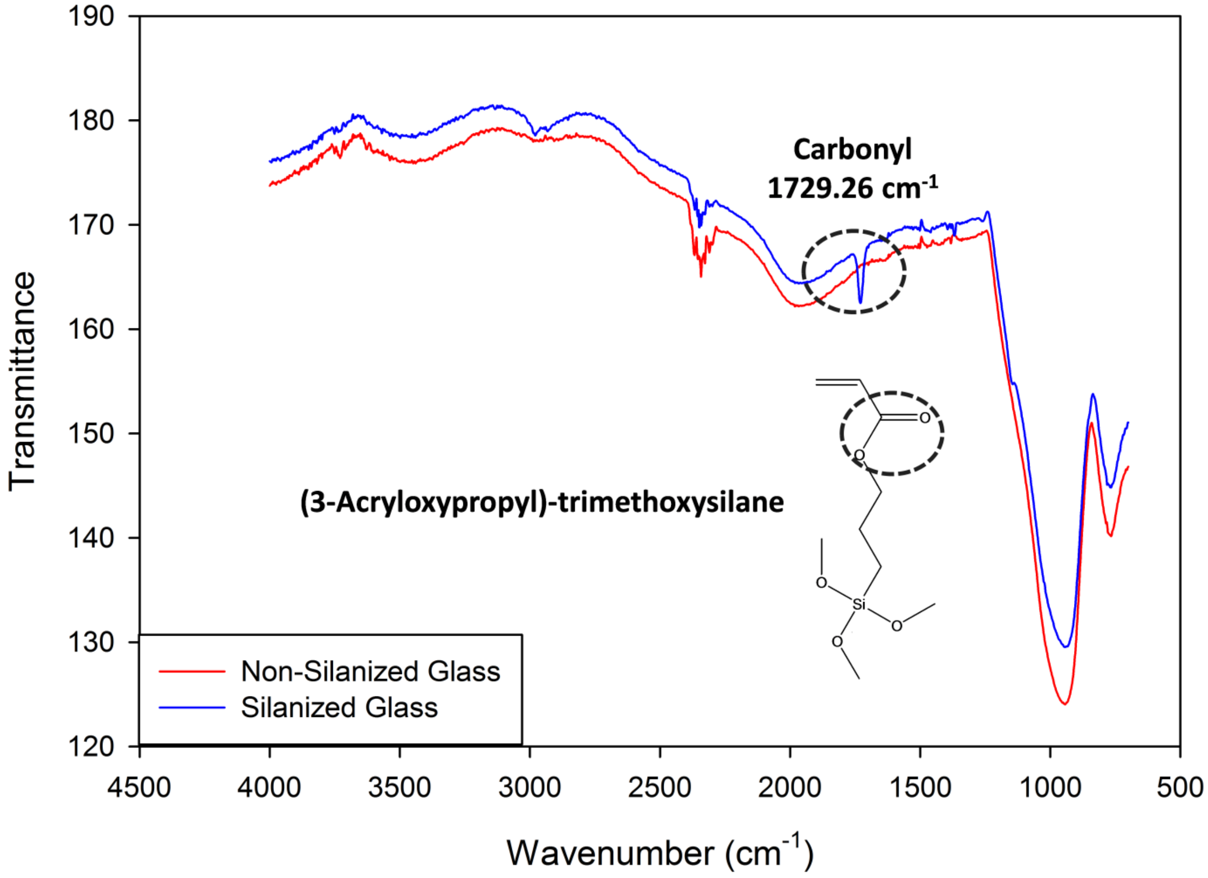

Figure 3-14. Graph showing transmittance vs. wavelength to investigate the carbonyl group present on silanized glass slide using FTIR-ATR.

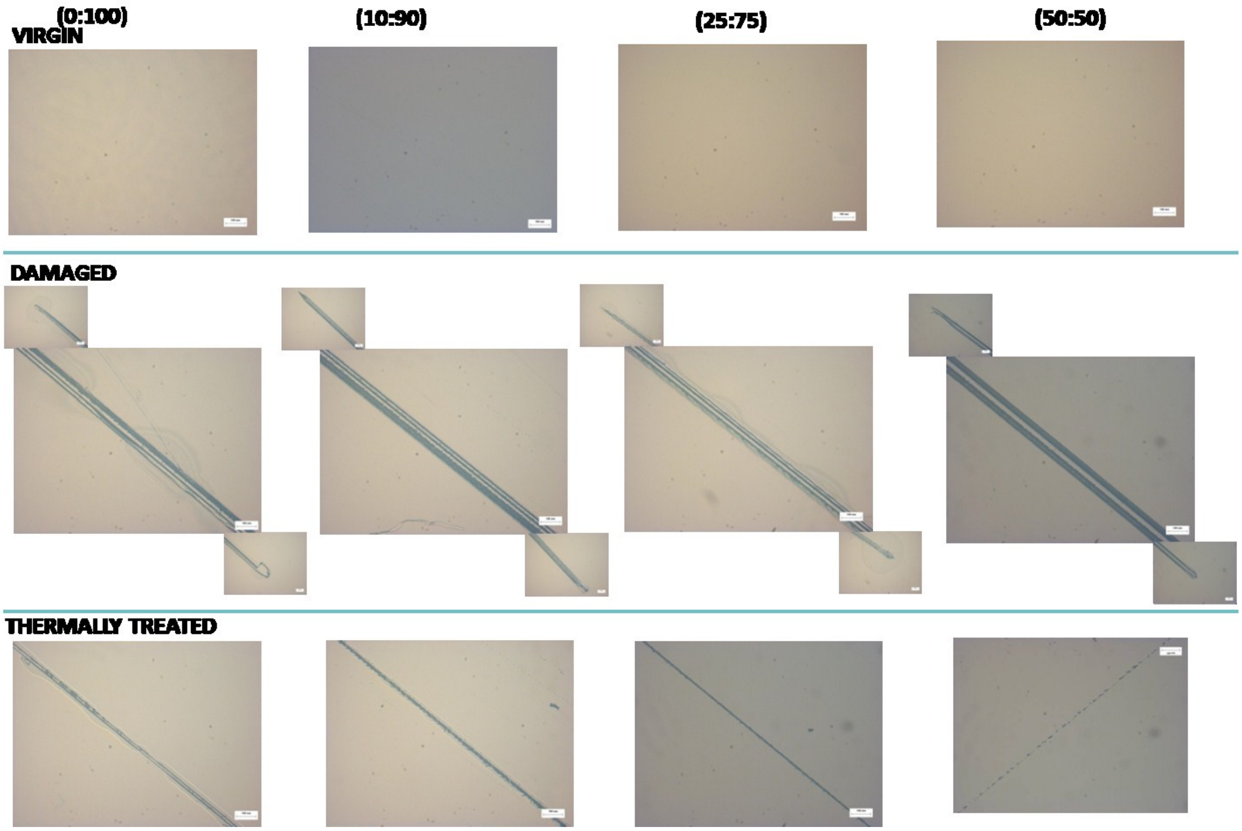

Figure 3-15. Representative optical micrographs (OM) showing the virgin, damaged and thermally treated states as a function of l:n-tBA compositions tested. The damaged samples also show the ends of the scratch to observe any material removal.

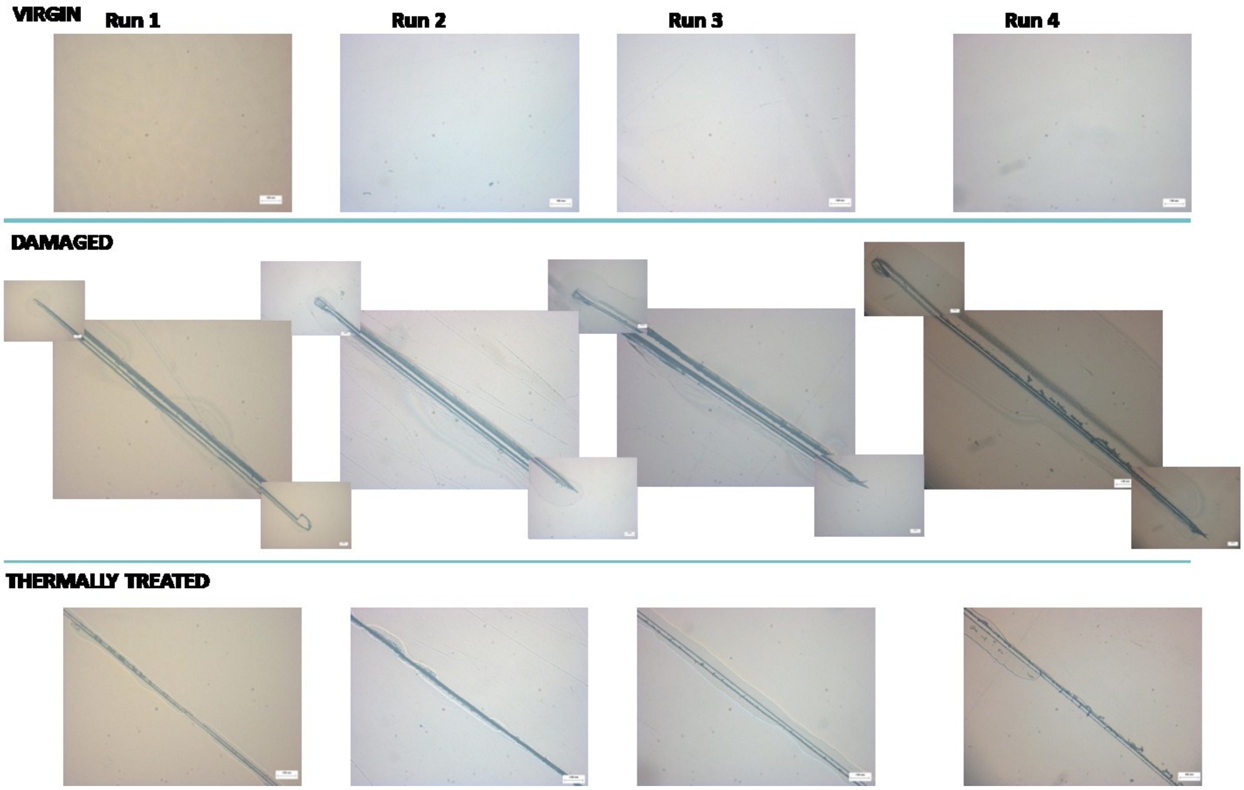

Figure 3-16. Optical micrographs (OM) for four (0:100) l:n-tBA coatings in their virgin, damaged and thermally treated states. The damaged samples also show the ends of the scratch to observe any material removal.

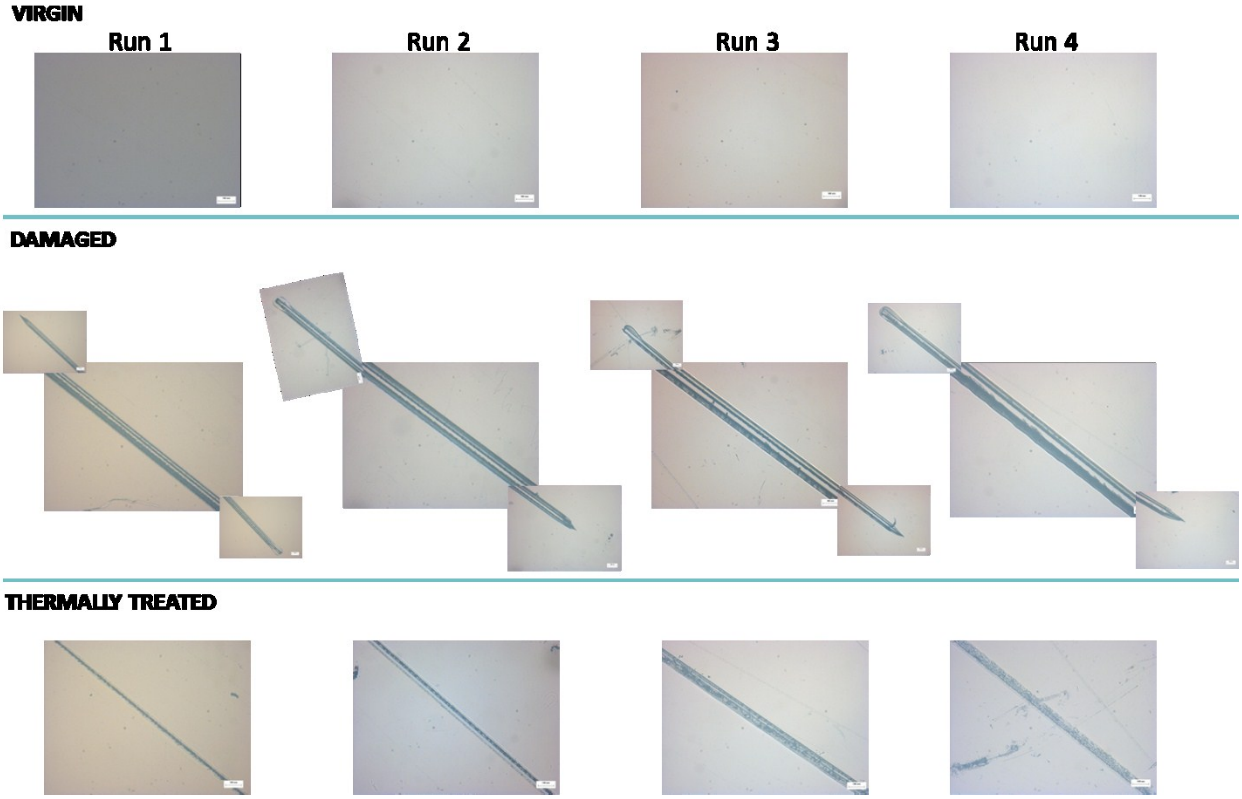

Figure 3-17. Optical micrographs (OM) for four (10:90) l:n-tBA compositions in their virgin, damaged and thermally treated states. The damaged samples also show the ends of the scratch to observe any material removal.

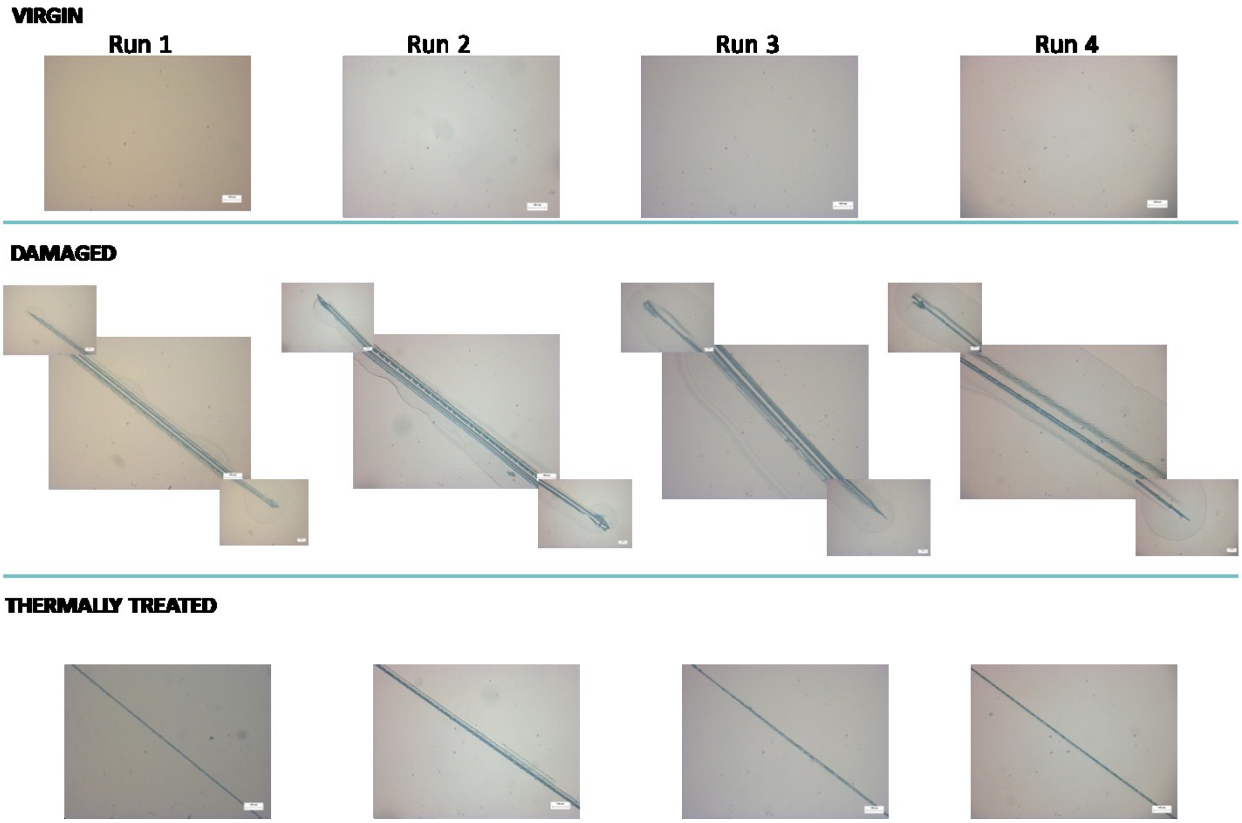

Figure 3-18. Optical micrographs (OM) for four (25:75) l:n-tBA compositions in their virgin, damaged and thermally treated states. The damaged samples also show the ends of the scratch to observe any material removal.

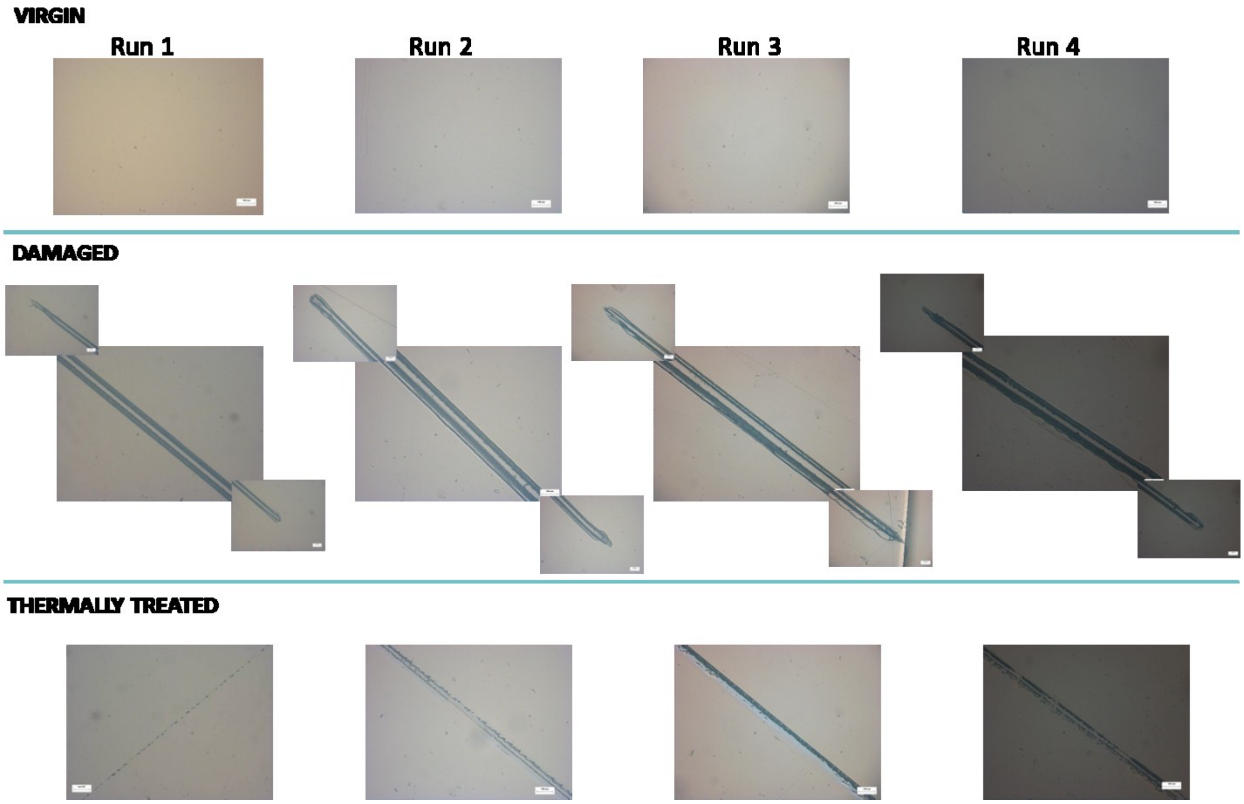

Figure 3-19. Optical micrographs (OM) for four (50:50) l:n-tBA compositions in their virgin, damaged and thermally treated states. The damaged samples also show the ends of the scratch to observe any material removal.

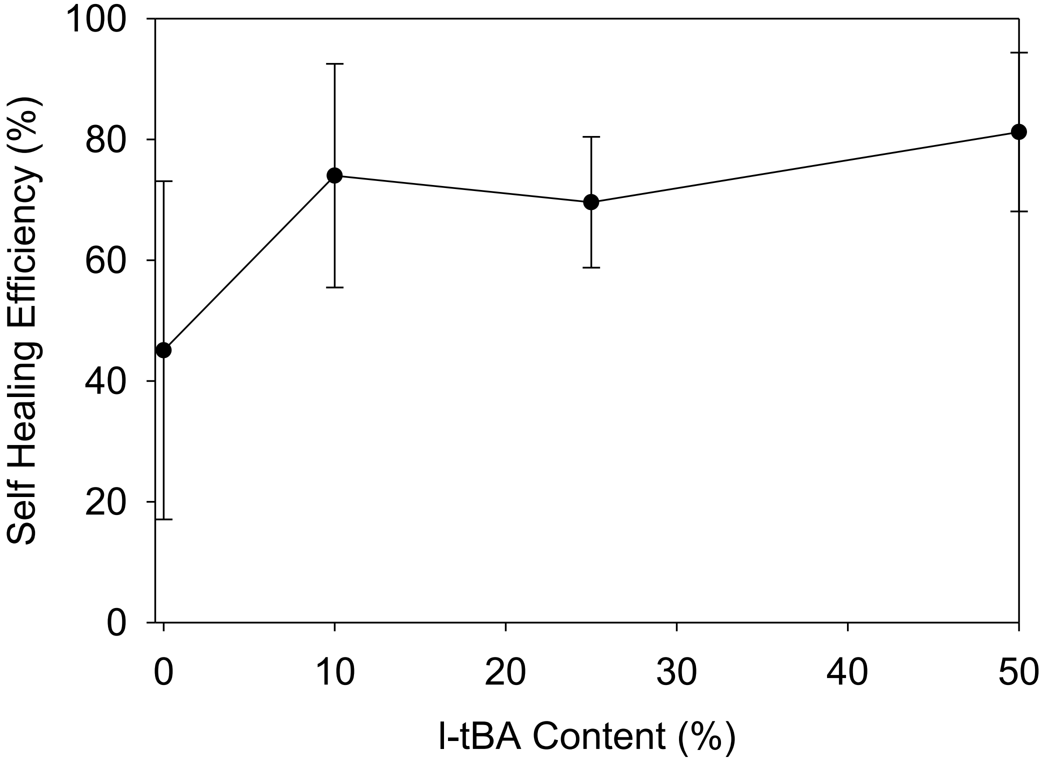

Figure 3-20. Graph showing self healing efficiency as a function of tBA thermoplastic content among all l:n-tBA compositions tested.

Table 3-8. Table showing self healing efficiencies among all l:n-tBA compositions tested.

Sample	AVE A_{SS}	STDEV	AVE A_{TTS}	STDEV	AVE SH (%)	STDEV
(0:100)	8.6E+04	3.3E+04	4.1E+04	8.4E+03	4.5E+01	2.8E+01
(10:90)	1.8E+05	4.0E+04	5.2E+04	4.8E+04	7.4E+01	1.9E+01
(25:75)	8.5E+04	2.7E+04	2.4E+04	5.0E+03	7.0E+01	1.1E+01
(50:50)	1.9E+05	2.9E+04	3.6E+04	2.5E+04	8.1E+01	1.3E+01

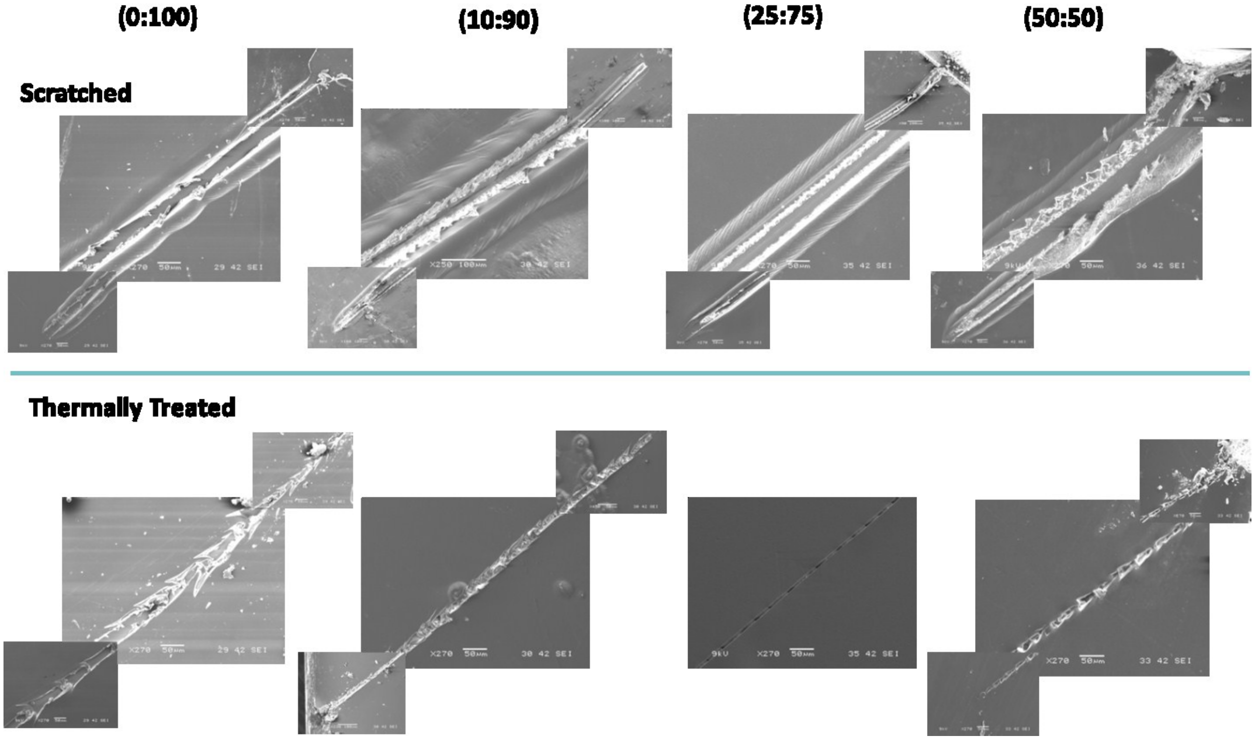

Figure 3-21. Scanning electron microscopy (SEM) images of the l:n-tBA coatings in their scratched and thermally treated states.

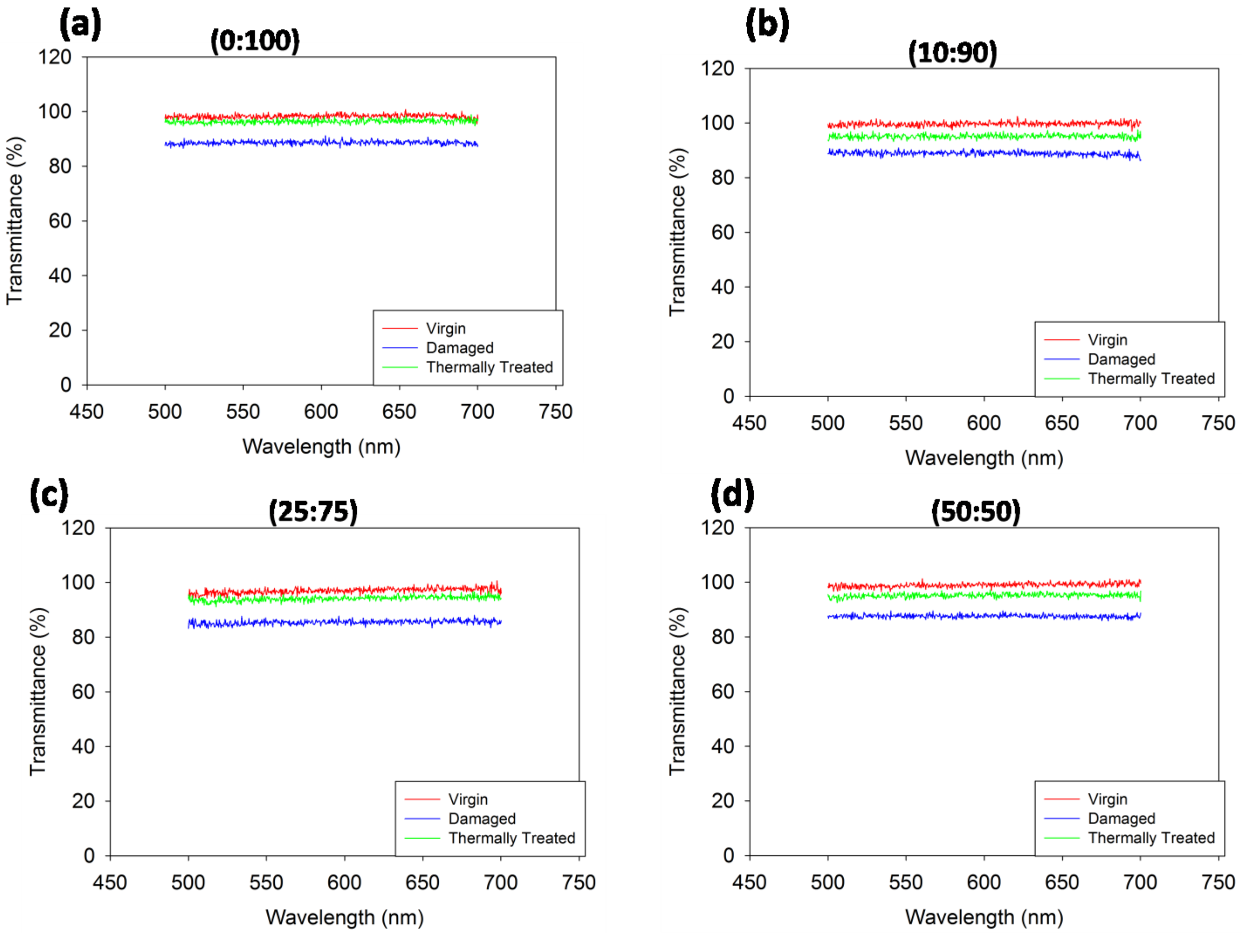

Figure 3-22. Graphs showing the transmittance vs. wavelength trend among the average of three samples tested for each l:n-tBA composition for coatings in their virgin, damaged and thermally treated states. The following compositions are shown: (a) (0:100), (b) (10:90), (c) (25:75), and (d) (50:50).

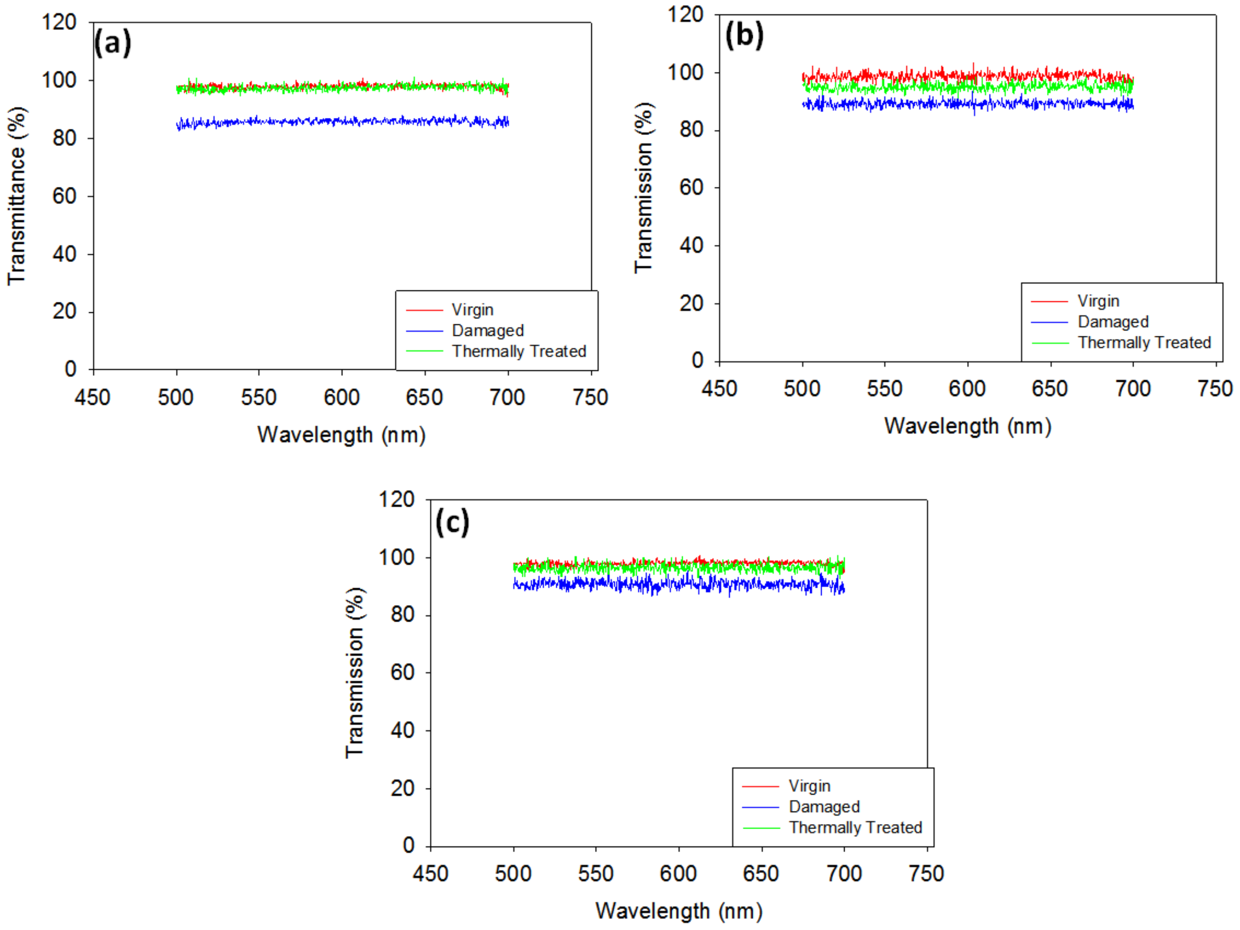

Figure 3-23. Graphs showing transmittance vs. wavelength for the l:n-tBA coatings in their virgin, damaged, and thermally treated states. Three (0:100) samples were tested where (a) shows Run 1, (b) Run 2, and (c) Run 3.

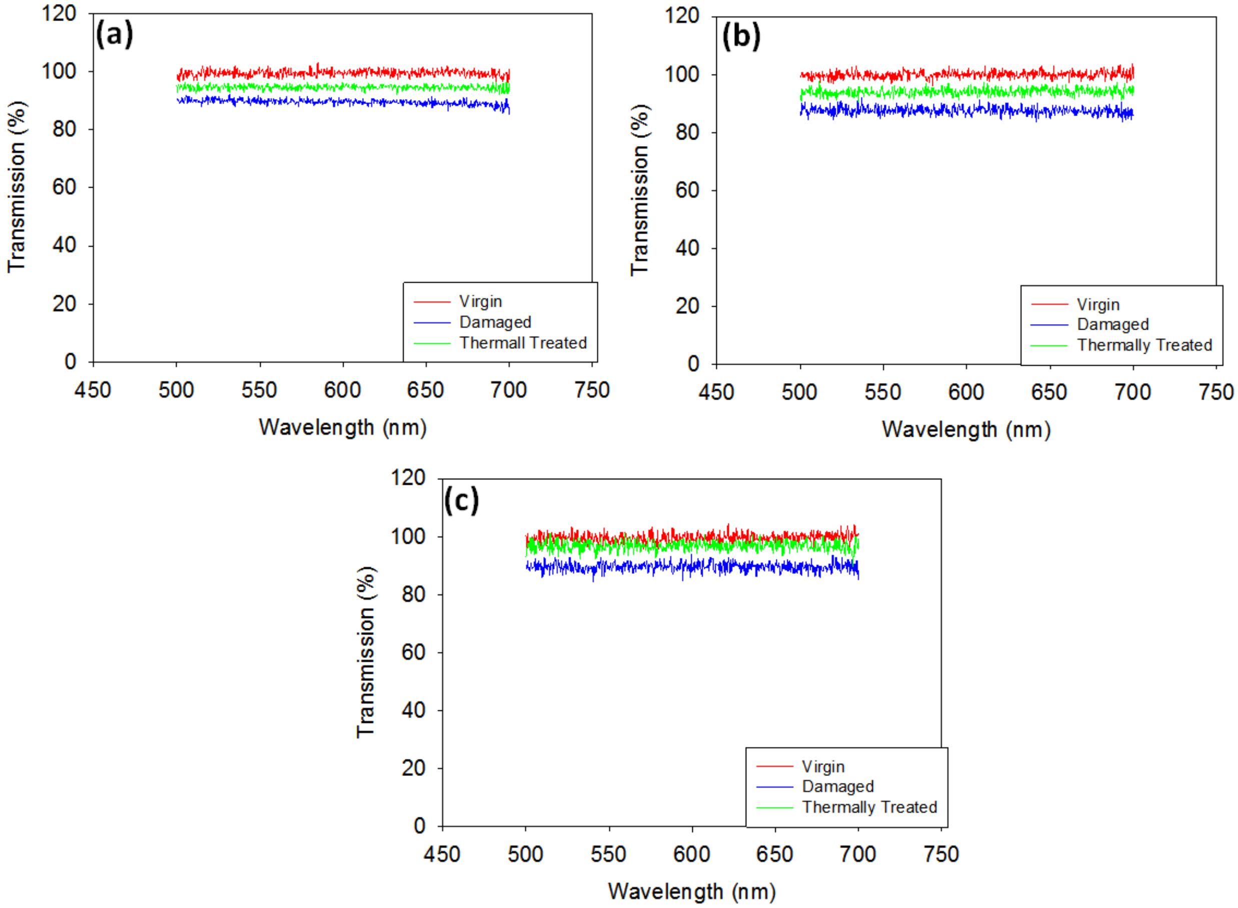

Figure 3-24. Graphs showing transmittance vs. wavelength for the l:n-tBA coatings in their virgin, damaged, and thermally treated states. Three (10:90) samples were tested where (a) shows Run 1, (b) Run 2, and (c) Run 3.

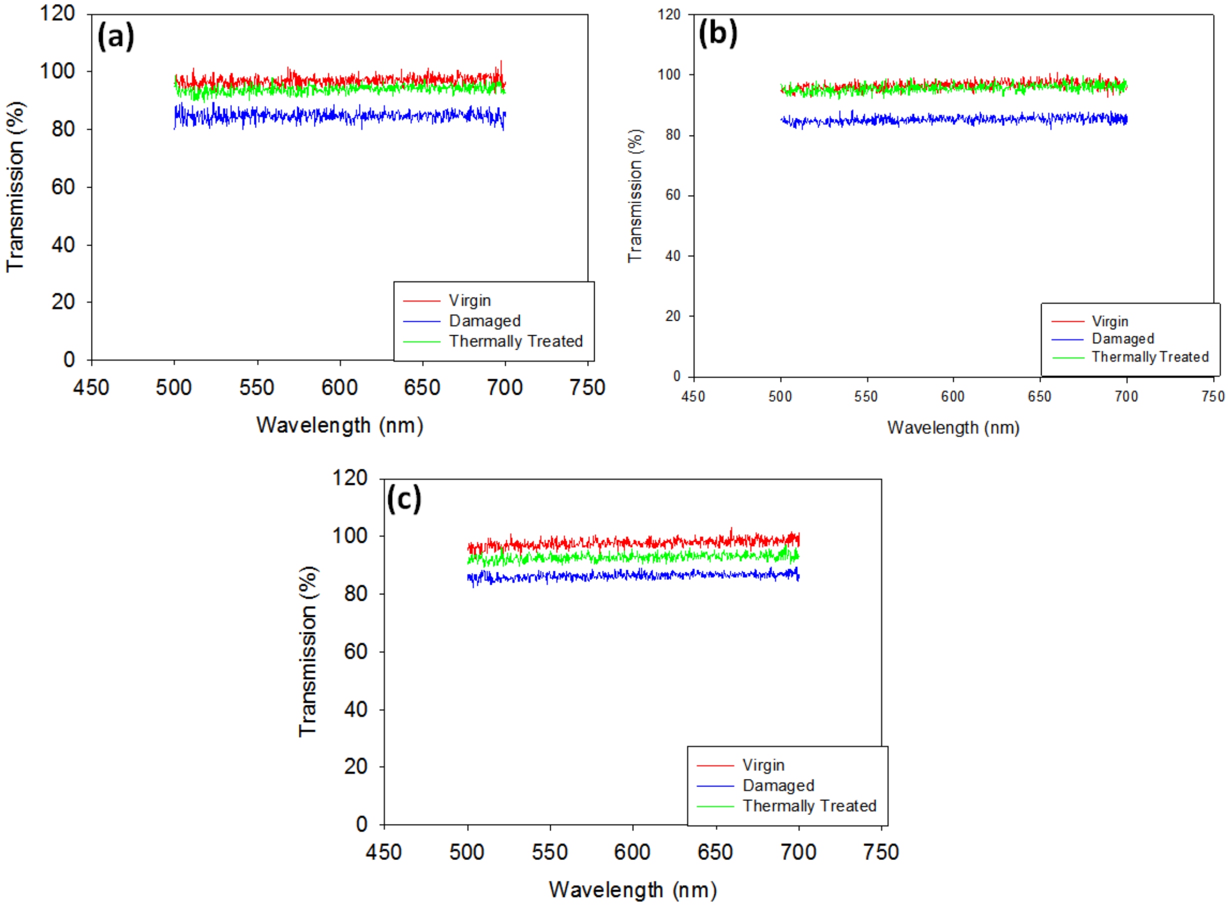

Figure 3-25. Graphs showing transmittance vs. wavelength for the l:n-tBA coatings in their virgin, damaged, and thermally treated states. Three (25:75) samples were tested where (a) shows Run 1, (b) Run 2, and (c) Run 3.

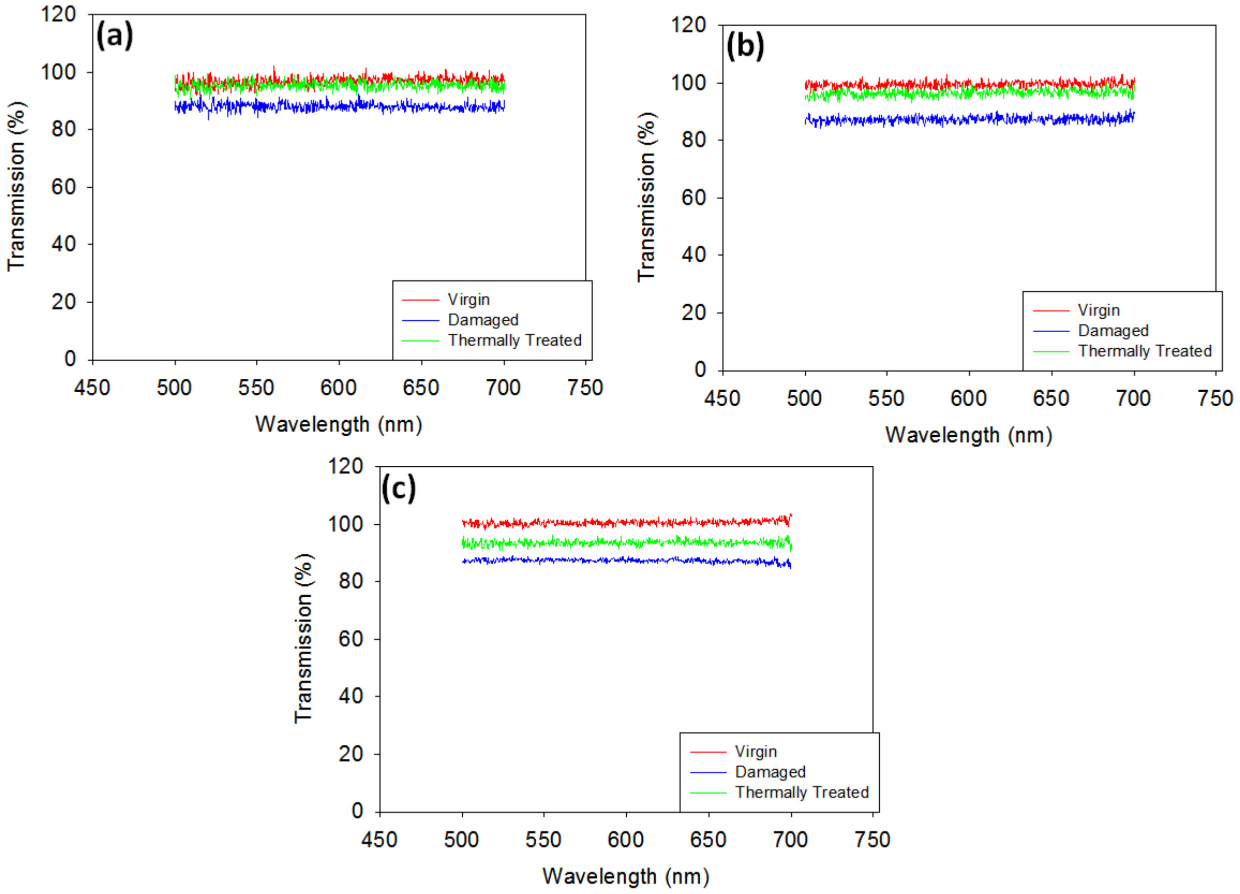

Figure 3-26. Graphs showing transmittance vs. wavelength for the l:n-tBA coatings in their virgin, damaged, and thermally treated states. Three (50:50) samples were tested where (a) shows Run 1, (b) Run 2, and (c) Run 3.

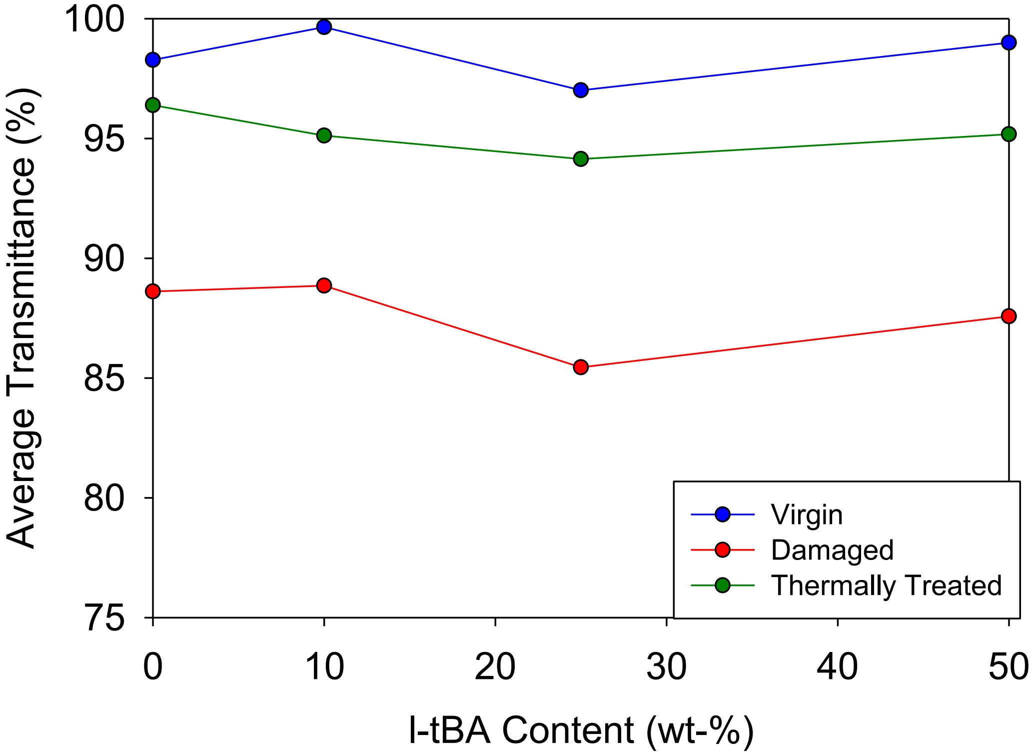

Figure 3-27. Figure showing the transmittance as a function of l-tBA SH thermoplastic content for the virgin, damaged and thermally treated states. This data reflects the average of four samples for each composition tested.

Table 3-9. Table of spectrometer data showing the average of the transmittance for four l:n-tBA scratches analyzed for each composition.

	Average Transmittance (%)			
Sample	**(0:100)**	**(10:90)**	**(25:75)**	**(50:50)**
Virgin	98.3	99.6	97.0	99.0
Damaged	88.6	88.9	85.4	87.6
Thermally Treated	96.4	95.1	94.1	95.2

CHAPTER FOUR

FABRICATION AND MECHANICAL TESTING OF ANISOTROPIC SHAPE MEMORY ELASTOMERIC SINGLE PLY COMPOSITES (A-SMEC)

4.0 SYNOPSIS

Anisotropic shape memory elastomeric composites (A-SMEC) were fabricated using a three step process by electrospinning an aligned poly(vinyl acetate) (PVAc) fibrous web, infiltrating with Sylgard-184, a silicone rubber matrix, and curing. Mechanical testing of the A-SMEC's was conducted using a Linkam tensile stage to investigate anisotropy in Young's modulus (E_Y), strain-to-failure (ε_f), and yield stress (σ_y) as a function of fiber orientation angle, χ, where the following values of χ were studied: 0° (axial), 22.5°, 45°, 67.5°, and 90° (transverse). At room temperature (RT), strong anisotropy in E_Y was observed, with a $E_Y = 48.4 \pm 9.7$ MPa for axial fiber orientation and $E_Y = 4.0 \pm 0.4$ MPa for transverse fiber orientation, while the σ_y was similarly anisotropic with $\sigma_Y = 4.6 \pm 0.1$ MPa for axial fiber orientation and $\sigma_Y = 0.9 \pm 0.1$ MPa for transverse fiber orientation. Strong anisotropy in ε_f was also observed, with $\varepsilon_f = 197.9 \pm 62.0$ % for axial fiber orientation and a much higher $\varepsilon_f = 350.9 \pm 52.2$ % in the transverse fiber orientation direction. Shape memory (SM) characterization revealed surprisingly small anisotropy in the shape fixing ratio (R_f) with $R_f = 95.6$ % for axial fiber orientation and $R_f = 86.2$ % for transverse fiber direction and a minimum is R_f (72.1%) measured for a sample with $\chi = 67.5°$. Near complete shape recovery (R_r) for all A-SMECs tested, regardless of fiber orientation angle, was observed. Such soft, anisotropic materials may be used in the fabrication of laminated composite elastomers.

4.1 INTRODUCTION

Shape memory polymers (SMP) have a unique ability to be temporarily fixed in a non-equilibrium shape with internal stresses stored by immobilizing constituent network chains of the SMP through either vitrification or crystallization upon cooling below the glass transition temperature (T_g) or melting temperature (T_m), respectively. Subsequent external stimulation that reverses this immobilization, whether electrically, photo-thermally, thermally stimulated to restore its original geometry.[1-3] While extensive studies have examined such SM phenomena, comparatively little attention has been given to the construction of SMP[4] systems that are soft in nature[4,5] and exhibit anisotropic mechanical behavior. Although extensive research and development has been conducted for rigid anisotropic materials, forming the basis for modern laminated composites[6] used in the automotive and aerospace industries, we are motivated to develop *soft* anisotropic composite materials and SMPs that mimic some characteristics of biological materials. If successful, such anisotropic elastomers could form a basis for soft laminated structures analogous to their rigid counterparts but with benefits of softness required for some applications.[7]

As one example of a biological material we are motivated to mimic, the skin membrane of a bat's wing has distinctive properties of an anisotropic fibrous network wherein the bat's wing is stiff in the airfoil (chord) direction, yet compliant and collapsible in the span direction for animal perching.[8] To accommodate these requirements, the skin membrane is both elastic and anisotropic, with mechanical properties that are dictated by a composite structure bearing internal, closely spaced fibers.[8] In particular, the mechanical anisotropy is due to the nature of the bat's skin membrane itself, involving a complex arrangement of both collagen and elastin fiber bundles, that are mechanically distinct materials and their respective orientations enabling in the specific functions of the skin.[8] In particular, the collagen fibers are used for the membrane's structural stability for aerodynamic flight while the elastin serves as the elastic component for wing retractability. It has been deduced that these constituent fibers also play a critical role in the transmittance of aerodynamic forces from the surface of the wing to the upper limb skeleton.[9] A synthetic elastomer with similar mechanical anisotropy would be useful for micro air vehicle (MAV) systems featuring flapping wings, an area of recent interest to aerodynamics researchers funded by the U.S. Air Force.[10] Such biomimicry would improve the adaptability, agility and speed in unmanned aerodynamic vehicles.[10]

As mentioned above, several studies of soft shape memory polymers have been reported. Osada et al. constructed a SM hydrogel where water-swollen gels were prepared by co-polymerizing *n*-stearyl acrylate, acrylic acid, and a crosslinker.[11,12] Below 25 °C, the water-swollen hydrogel is rigid, due to substantial crystallization of pendant *n*-stearyl acrylate. Furthermore, such crystallization was found to enable shape fixing of the hydrogels, where the SM was coming from crosslinking. Above 50 °C, the hydrogel behaves like a soft, compliant gel capable of relatively large (>100%), reversible deformations. Thus, stretching the compliant hydrogel at elevated temperature, followed by cooling to crystallize the side chains allowed for good shape fixing, while subsequent heating to melt the side changes cause shape recovery to the equilibrium shape. Relative to the mentioned goal, softness was possible through hydration and no mechanical anisotropy was reported.

Soft SMP are also possible without hydration by crosslinking initially elastomeric polymers and incorporating some mechanism of strain fixing other than vitrification. In one case, covalent cross-linking of, semi-crystalline *trans*-polyisoprene (TIP) yielded a SM network capable of achieving 100 MPa in stiffness at RT for shape fixing and superelastic mechanical properties with sufficient shape recovery above its T_m of 67 °C.[13] In other cases from our own group, main-chain liquid crystalline (smectic) elastomers were found to feature good shape memory[4,14], while POSS-functionalized and crosslinked poly(hydroxyl alkanoate) prepared by bacterial synthesis offered yet another soft SM approach.[5] In both of these cases, the softness of the SMPs was exploited for the purpose of reversible embossing of imprinted, temporary topographical features, while macroscopic anisotropy was not observed.

Some progress has been made in the preparation of anisotropic elastomers, though without SM. For example, Li et al. constructed a highly anisotropic thermoplastic elastomer composite by melt-blending poly(styrene-b-butadiene-co-butylene-b-styrene) (SBBS) and a liquid crystal polymer (LCP) and injection molding the blend.[15] The LCP uniquely orients in fiber form along the injection direction in the SBBS matrix where the micro-phase-separated polystyrene (PS) phase in the matrix conforms along the injection direction yielding high anisotropy. This composite showed high stiffness in the melt injection direction, yet high compliance in the transverse direction. Indeed, the modulus in the injection direction was 47–fold greater than in the transverse direction owing to the anisotropic arrangement. Elongation-at-break, ε_Y, was reported to be 56–fold smaller in the injection direction when compared to the transverse direction.

Cohen et. al. demonstrated another unique anisotropic elastomer utilizing orientation of a triblock copolymer. Here, the lamellar phase of a triblock polystryene-polybutadiene-polystrene (PS/PB/PS) copolymer was oriented in film form via roll-casting.[16] (Numerous other reports of roll-casting triblock copolymers have appeared and the interested readers are referred to those papers without further discussion.[17-22]) The roll casting process yielded highly oriented lamellar block copolymer films featuring strongly anisotropic mechanical properties. Samples with different lamellar orientations were uniaxially strained to understand the deformation mechanism and show the difference in mechanical properties. When uniaxially loaded in directions parallel, perpendicular, diagonal to the lamellar structure, the measured Young's moduli were 180 ± 10, 65 ± 3, and 43 ± 4 MPa respectively.[16] The higher moduli were evident in samples that had lamellae in the parallel orientation and, interestingly, lower in the diagonal orientation than the perpendicular direction. Loading parallel to the lamellar structure led to a plastic-to-rubber transition, while perpendicular loading led to layer folding similar to that of chevron morphology where kink boundaries were generated at higher strains.[16]

Still another soft and aniotropic material, liquid single crystal elastomers (LSCE) offer a unique approach to anisotropy. Finkelmann's group has published extensively on nematic and smectic LSCE's.[23-25] In one study[25] the mechanical anisotropy for the LSCE smectic A elastomer was examined for its temperature-dependence and associated with network chain entropy elasticity, specifically perpendicular to the normal of the smectic layers.[25] In the transverse direction, the mechanical response was concluded to be controlled by an enthalpic elastic response wherein the smectic layers contributed a modulus of two orders of magnitude greater than that of the the soft spacers.[25] The modulus has also shown to decrease with increasing temperature in the transverse direction.

Our group has adopted a composite approach involving electrospinning of thermoplastic fibers to enable the creation of soft SMPs. In this approach, an isotropic shape memory elastomeric composite (SMEC) was constructed through a three step fabrication process using an electrospun nonwoven poly(ε-caprolactone) (PCL) semi-crystalline fibrous web with Sylgard-184 (hereafter "Sylgard") silicone infiltrating the mat, serving as the elastomeric matrix.[26] In such a composite, the separate roles of strain fixing and strain recovery were distributed between the two interpenetrating phases of the composite: strain fixing with the thermoplastic fiber phase (PCL) and recovery by the elastomeric silicone phase. In this case, the SMEC was macroscopically isotropic and we reasoned that orientation of the fiber phase could lead to the desired anisotropy in a straightforward manner.

Thus, for the present report we aimed to construct an anisotropic shape memory elastomeric composite (A-SMEC) by electrospinning aligned fibers of poly(vinyl acetate) (PVAc), serving as the composite reinforcement and SM fixing contribution to the system, and infiltrating with Sylgard, to serve as the elastomeric matrix while also assisting in the composites shape recovery capability. We selected PVAc over previously studied PCL for the fiber phase due to the much higher stiffness of PVAc that was expected to yield high mechanical anisotropic in fiber-aligned composites. We will show that anisotropy in Young's modulus (E_Y), strain-to-failure (ε_f) and yield stress (σ_y), is achieved. We further show the SM effect is tailored as a function of fiber orientation angle, where shape fixing depends on the orientation angle of the electrospun microfibers incorporated in the matrix.

4.2 EXPERIMENTAL SECTION

4.2.1 MATERIALS AND SAMPLE FABRICATION

The anisotropic shape memory elastomeric composite (A-SMEC) was composed of two commercially available polymers - poly(dimethylsiloxane) (Sylgard-184 from Dow Corning) and poly(vinyl acetate) (PVAc) (PVAc; M_w = 249k g/mol from Aldrich) - and fabricated via a three step process shown in Scheme 4-1.[26] PVAc was electrospun from a relatively concentrated mixed solvent solution in MeOH/DMF (volumetric ratio= 7:3). In particular, 2.00 g PVAc was dissolved in and 10.0 mL of the solvent mixture and stirred continuously until a transparent, clear, and homogenous solution was achieved. Using a custom electrospinning apparatus, fibers from a charged needle (+13.5 kV) were electrospun onto a rotating drum at slightly negative potential (-5 kV) using a large angular velocity of 3000 RPM. The drum diameter was 5.08 cm, the tip-collector distance was 7 cm, and the flow rate was 0.7 mL/h, which ran for 10.75 h to yield fibrous webs which were easily removed from the rotating drum. To enhance orientation of the fibers, a square steel plate (15.0 (l) x 12.5 (w) cm) was mounted to the syringe hub with the plate normal oriented parallel to the flow direction (Scheme 4-1), the idea being to yield parallel electrical field lines between the drum and the plate. Qualitatively, we observed dramatically higher fiber orientation which such a plate was added to the set-up, all other conditions remaining the same. The average fiber diameter was measured by analyzing an SEM micrograph in ImageJ (Version 1.45s) software where a total of 90 measurements were used to obtain the average. The fibrous web was then infiltrated by a two-part mixture of Sylgard-184 (base: curing agent ratio = 10:1), assisted by vacuum application (ca. 760 mm Hg) for 20 min to ensure complete infiltration of Sylgard into the PVAc fibrous web. After carefully removing the excess Sylgard from the fibrous web with a spatula, the Sylgard was cured at 30 °C for 48 h (Scheme 4-1). Dogbones were then punched from the A-SMEC sheet so as to yield a range of fiber orientation angles, χ, relative to the loading direction: $\chi = 0°$ (axial), 22.5°, 45°, 67.5°, and 90° (transverse), as shown in Scheme 4-1. For clarity we will refer to A-SMEC samples with varying orientation angles, χ, listed above using the nomenclature, A-SMEC-χ. For example, the specimen with fiber orientation angle inclined 45° from the loading direction will be referred to as A-SMEC-45.

4.2.2 MICROSTRUCTURAL CHARACTERIZATION

The as-processed fibrous webs were analyzed using scanning electron microscopy (SEM) and image analysis ImageJ to obtain the average fiber diameter. 2D Fast Fourier Transform (FFT) analysis was applied to SEM images of the same fibrous webs to obtain the degree of fiber orientation, expressed as the angular breadth from an azimuthal sweep of the 2D-FFT streak using the Gywddion software's Hahn model. Utilizing an ImageJ plugin, "Oval_Profile" radial sums of the magnitude/intensity were taken and the data was analyzed to study degree of fiber alignment. Degree of alignments were then determined using the full width at half max (FWHM) approach. The weight fraction and volume fraction estimates of the fibers in the matrix were then measured in two ways: (i) gravimetrically using weights before and after Sylgard infiltration, and (ii) calorimetrically using the heat capacity step at T_g for the PVAc, where $X_f = \Delta Cp_{ASMEC} / \Delta Cp_{PVAc}$.

4.2.3 DYNAMIC MECHANICAL ANALYSIS

Dynamic mechanical properties for all samples were studied using a TA Q800 dynamic mechanical analyzer (DMA). Each sample was cut at the specified angles mentioned in section 2.1 from an A-SMEC sheet to obtain a rectangular sample with average dimensions of 7.46 ± 1.04 mm (length) x 2.47 ± 0.33 mm (width) x 0.38 ± 0.04 mm (thickness). Each sample was clamped into the DMA tensile fixture to measure the linear viscoelastic properties to obtain thermo-mechanical transitions. This was done using oscillatory tensile deformation with small displacement amplitudes of 15 μm (tensile strain < 0.4%) with a 1 Hz frequency, a preload of 0.001 N, and force track (ratio of static to dynamic forces) of 110%. First, the temperature was equilibrated at 0 °C and held for 5 min. The temperature was then ramped to 100 °C at 3 °C/min where the tensile storage modulus values (E´) and tan delta values as a function of temperature were recorded. This procedure was done for all the A-SMEC samples to reveal dependence on fiber orientation angle (χ). Neat Sylgard was also tested using the same displacement, frequency and force track parameters stated above. However, the sample was first heated to 100 °C at 3 °C/min, held at this temperature for 1 min, cooled to 0 °C at 3 °C/min, held isothermally for 1 min, then cooled further to -150 °C to immobilize the polymer chains, held for 5 min, and then heated to 120 °C at 3 °C/min. This procedure was conducted specifically on Sylgard to observe the T_g at the lower temperature. Thermal transitions as a function of temperature sweep of the second heating were reported.

4.2.4 MECHANICAL TESTING

Mechanical properties of both the PVAc fibrous web and A-SMEC state were studied using a Linkam TST 350 tensile stress testing system. Each sample was punched into a dogbone geometry using an ASTM Standard D638-03 Type IV (scaled down by a factor of 4, TestResources, Inc., Shakopee, MN). The dogbones were cut at angles (χ) of 0° (axial), 22.5°, 45°, 67.5°, and 90° (transverse) and isothermally elongated at constant velocity according to ASTM standard. Here the deformation temperature was at RT, at a constant velocity of 20.8 μm/s, and using a sensitive load cell with 20 N capacity. Plots of engineering stress vs engineering strain were then calculated from the raw data. The apparent tensile modulus of the fibrous web specimens were calculated by finding the slope of the elastic region of the stress-strain curve. The porosity of the fibrous web samples resulted in the loss of the true cross sectional area and therefore the Young's modulus could not be determined. The strain-to-failure data for the PVAc fibrous web specimens elicited broad shoulders that were evident before complete failure occurred. This proved to be an unanticipated result as PVAc is a glassy polymer. This can likely be attributed to the unaligned fibers being oriented in the load direction by means of fiber bending to plastically conform and orient in the applied loading direction. Therefore, in order to obtain the strain-to-failure values for the PVAc fibrous web specimens we fit a linear trendline at the inflection point of the ductile region of the stress-strain curve and extrapolated to the strain intercept of the linear trendline. The A-SMEC Young's moduli values were obtained by fitting a linear trendline in the elastic region of the stress-strain curve, and the strain-to-failure was reported as the strain at the point of fracture, where the tensile stress dropped to zero. The yield stress for both the fibrous web and the A-SMEC samples was calculated using a 2% offset method whereby the elastic region of the stress-strain curve was fitted by a linear trendline, offset in strain by 2% and the stress intercept with this new trendline was then reported as the yield stress.

4.2.5 SHAPE MEMORY ANALYSIS

The SM characteristics were quantified for all A-SMEC samples with the five fiber orientation angles mentioned prior. A well studied 4-step SM cycle referred to as the one way shape memory (1WSM)[1,2,27] method was performed on all A-SMECs. Samples were tested using a TA Q800 dynamic mechanical analyzer (DMA) with a preload force of 0.001 N. The samples were heated to 80 °C and held isothermally for 5 min. With the strain set to 0 % prior to stretching the sample, the force was ramped at 0.5 N/min until 100 % strain was achieved, and this force was held for 2 min. (step 1). The temperature was then decreased from 80 °C to 0 °C at 3 °C/min and held at 0 °C for 5 min for fixing of temporal geometry (step 2). The force was then released to 0.001 N at 0.5 N/min and held for 2 min to observe elastic recovery and sample fixing (step 3). Finally, the temperature was increased from 0 °C to 80 °C at 3 °C/min and then held isothermally for 5 min to allow complete shape recovery (step 4). This 4-step process was repeated two more times on the same sample in order to observe SM reproducibility. The fixing ratio (R_f) and recovery ratio (R_r) were calculated using the following equations:

$$R_f(N) = \frac{\varepsilon_u(N)}{\varepsilon_m(N)} \times 100\% \tag{4-1}$$

and

$$R_r(N) = \frac{\varepsilon_u(N) - \varepsilon_p(N)}{\varepsilon_u(N) - \varepsilon_p(N-1)} \times 100\% \tag{4-2}$$

where ε_m, ε_u, ε_p and N are the strain before unloading, the strain after unloading, permanent (unrecoverable) strain after shape recovery and the cycle number, respectively. The averages of R_f and R_r from the second and third cycle are reported, as the values from the first cycle are not included. Data from the 80 °C tensile testing was then compared to the RT tensile testing to understand the difference in mechanical properties.

4.3. RESULTS AND DISCUSSION

4.3.1 SAMPLE FABRICATION

The three step process for fabricating the A-SMEC system was conducted where an anisotropic PVAc fibrous web was e-spun using the parameters specified in the experimental section. The fibrous web was then infiltrated with Sylgard and cured to construct an anisotropic shape memory elastomeric composite (A-SMEC). Figure 4-1 shows representative scanning electron microscopy (SEM) micrographs of aligned fibers (a), topography of the A-SMEC (b), cross section of the A-SMEC when the fibers are aligned in the axial (c), and transverse direction (d). The average PVAc fiber diameters were 0.79 $\pm$ 0.20 μm and 0.77 $\pm$ 0.18 μm that were obtained for the two fibrous webs using 90 measurements on each web. SEM images of the fibrous webs were then subjected to a 2D FFT which was used to evaluate the degree of anisotropy. The two fibrous webs proved to have a high degree of orientation which amounted to be 30° and 34°. Further calculation can be seen in Figure 4-2 showing fibrous web SEM micrographs, 2D FFT images, and the resultant orientation plots.

This A-SMEC system showed a smooth layer of Sylgard on the surface, contrary to the report of Luo et al.[26] isotropic SMEC, where the material's topography appeared to be porous. This could potentially be due to the arrangement of compacted anisotropic fibers where only small voids were present between fibers. SEM images of the cross sections clearly showed complete Sylgard infiltration along the width and length of the A-SMEC while also showing the fibers in the A-

SMEC were preserved in the Sylgard matrix (Figure 4-1). Using the mass of the fibrous web, mass of the A-SMEC, and the densities of the PVAc (ρ = 0.934 g/ml) and Sylgard (ρ = 0.965 g/mol), the overall volume and mass fractions of the A-SMEC was estimated to be 17.6% and 17.1% respectively. Alternatively, the fiber volume fraction determined via DSC heating capacities was calculated to be 19.8% where the $\Delta C_{pPVAc\ fibers}$= 0.5020J/g °C and $\Delta C_{pA\text{-}SMEC}$= 0.09920J/g °C. The higher value of the DSC method can be attributed to localized testing compared to testing the entire fibrous webs as the method based on mass does. The DSC traces of the PVAc pellets, PVAc fibrous web, and A-SMEC are shown in Figure 4-3.

4.3.2 DYNAMIC MECHANICAL ANALYSIS OF COMPOSITES

All A-SMEC samples were cut into a rectangular geometry as a function of fiber direction (Figure 4-1) to obtain the thermo-mechanical properties using the DMA. Such testing yielded the linear viscoelastic properties of the A-SMEC as functions of temperature to obtain the tensile storage modulus and tan delta (Figure 4-4). The highest tensile storage modulus (~100 MPa) was obtained from the fibers orientated axially in the A-SMEC whereas the lowest (below 10 MPa) value was obtained from the fibers in the transverse direction. The tensile storage modulus then decreased significantly when the temperature increases above the fiber's T_g, regardless of fiber orientation. This is indicative starting at 60 °C (Figure 4-4). The T_g given by the DMA data for all A-SMEC tested ranged from 50 to 55 °C which was attributed to the PVAc chain mobility. This range in temperature is slightly higher, ~10 °C higher, when comparing the T_g values from DSC analysis which was anticipated. Note that the Sylgard matrix remained in its rubbery state through the entire temperature sweep (Figure 4-4, dashed blue line) as expected, given that the T_g of Sylgard is -115.2 °C.[26]

From the data of Figure 4-4, the orientation-dependence of tensile storage modulus could be extracted as seen in Figure 4-5. The tensile storage modulus was then analyzed at 25 °C, 50 °C and 80 °C as a function of fiber orientation angle (Table 4-1). It is evident that the tensile storage modulus is higher below the T_g of PVAc and gradually decreases as the temperature increases above this transition. However, regardless of temperature the Sylgard remains in its rubbery state and is shown as reference lines in Figure 4-5.

4.3.3 MECHANICAL TESTING CHARACTERIZATION

The fibrous web and A-SMEC dogbone samples were mechanically strained to failure to obtain apparent modulus (fibrous web samples), Young's modulus, and strain-to-failure versus fiber orientation using the Linkam TST350 tensile stress testing system. The average thickness of the fibrous web sample was 0.13 $\pm$ 0.03 mm, and the average thickness of A-SMEC samples was 0.31 $\pm$ 0.03 mm. These thicknesses were used to construct the stress-strain curves from the raw load-displacement data. Both the fibrous web and A-SMEC samples tested showed anisotropy with respect to apparent modulus (E_A), tensile storage modulus (E'), Young's modulus (E_Y), strain-to-failure (ε_f), and yield stress (σ_y), where representative stress-strain curves are shown in Figure 4-6 with Sylgard as a reference line in both plots. Figure 4-7 and Figure 4-8 show all stress-strain curves for the fiber and composite dogbone samples respectively.

The E', E_A, and E_Y were analyzed from the stress-strain curves at RT for both the fibrous webs and A-SMEC specimens. The fibrous web samples have a higher modulus than the A-SMEC samples at any given orientation (Figure 4-9). It is important to mention that the fibrous web encompassed voids containing air where the modulus of air is 0 MPa, however upon infiltration of Sylgard, noting that the Sylgard's modulus is 0.4 MPa in the A-SMEC state, fibrous web specimens' porosity gives a likely explanation for the difference in moduli. Fibrous web is filled solely with air of a given volume fraction, however upon Sylgard infiltration, the total sample volume increases. As the fiber volume remains the same and the total sample volume increases, the fiber volume fraction decreases upon the infiltration/curing step. When considering the fibrous web E_A, both air and Sylgard are negligible. Since PVAc's modulus is orders of magnitude higher than either the modulus of air or Sylgard, the fiber volume fraction in the fibrous web state is hypothesized to be the sole contributor to the material modulus of a given fiber angle. It is also important to observe that the PVAc fibrous samples, themselves, exhibit a higher modulus and can bear more load then the Sylgard specimens. The Sylgard's E_Y and E' moduli are also shown as reference lines in Figure 4-9. In analyzing the composite's E_Y, the fibers in the axial direction showed the highest tensile E_Y of 48.4 $\pm$ 9.7 MPa. As χ increased away from axial (0°), the E_Y decreased where the A-SMEC-90 had E_Y of 4.0 $\pm$ 0.4 MPa (E_A and E_Y data for the fibrous web and A-SMEC samples are shown in Table 4-2 and 4-3 respectively). Importantly, the A-SMEC E' showed the same qualitative trend as E_Y, decreasing with increasing χ. In fact, the E_A, E_Y, and E' all showed decreasing slopes as χ increases for the fibrous web, and A-SMEC, samples.

The dependence of E_Y on fiber orientation angle was evaluated at 25 °C and 80 °C. Figure 4-10 shows that the PVAc fibers are the largest contributor in the A-SMEC E_Y at 25 °C owing to the temperature below the PVAc's T_g. However, it is evident that the A-SMEC anisotropy is completely lost when the samples are heated above the fiber's T_g where the A-SMEC exhibits a

E_Y similar to that of neat Sylgard. More specifically, as the temperature increased to 80 °C, the fibers transition from a glassy to rubbery state where the Sylgard becomes a dominant contributor to the E_Y. It is important to mention that the trend seen in Figure 4-10 follows fiber reinforced composite theory by showing a dependence of E_Y on χ.[28]

Given our motivation to achieve anisotropic elastomers in a biomimetic fashion, it is interesting to compare the E_Y of a biological bat wing with our A-SMEC system. Swartz et al. reported that the mean E_Y of a bat wing skin was 23.92 MPa with a range of 1.02 - 250.26 MPa. Coincidentally, our reported values in Figure 4-11 fall within the range of this previously published data. Specifically, the E_Y data obtained for our A-SMEC system is nearly identical to a biological bat wing skin as reported by Swartz et al. Furthermore, the anisotropy trend of the biological skin membrane to our A-SMEC system is clearly evident when comparing E_Y as a function of χ. Our experimental data also follows the empirical model of modulus dependence on χ used for fiber reinforced composites.[29] The A-SMEC regression line seen in Figure 4-11 was found by plotting the logarithm of the modulus vs. χ and fitting a linear trendline. The bat wing regression had been previously reported by Swartz et al., and has been included to show how this A-SMEC modulus mimics that of the biological system.

The ε_f values were then compared for the fibrous web and A-SMEC systems. As shown, in Figure 4-12, the ε_f for the fibrous web samples (Table 4-4) were much lower than that of the A-SMEC samples at any given χ due to the elasticity of Sylgard in the A-SMEC state. The A-SMEC average ε_f was calculated to be 350.9 $\pm$ 52.2 %, when the fibers are transversely oriented and 197.9 $\pm$ 62.0 % when the fibers are axially oriented (Table 4-5). A ε_f was also recorded for neat Sylgard, 445.2 ± 48.9 %, and is shown as a reference line in Figure 4-12. In the A-SMEC system, the Sylgard serves as the elastomeric matrix to assist in increasing the ε_f while also contributing in the shape recovery. The oriented fibers alone are incapable of exhibiting such behavior. Overall, the A-SMEC samples demonstrated to have, on average, higher ε_f than that of the fibrous web sample at any given orientation, which we attribute to the inclusion of Sylgard. In comparing our system to a bat wing's skin membrane, Swartz et al. reports a failure strain of 0.68 with a range of 0.13 – 2.32. We report a strain of 3.51 ± 0.52 (transverse) and 1.98 ± 6.2 (axial). In considering that our reported values are notably higher than what has been reported in literature, our A-SMEC system shows advantageous strain accommodation.

As was the case for E_Y, the measured yield stress (2% offset method) decreased monotonically with χ. Figure 4-13 shows higher yield stresses represented in the fibrous web samples when compared to the A-SMEC samples. This indicates a higher stress required for yielding in the fibrous web state when compared to the A-SMEC state. This is evident when the fibers are in the axial direction; however, this is contrary to the fibers in the transverse direction where the yield stress values are smaller in magnitude. Table 4-6 and Table 4-7 show the yield stress for the fibrous webs and composites respectively.

The stress-strain curves obtained from the conventional DMA data at 80 °C and mechanical tensile data at 25 °C were then compared. The concavity in the data collected at 25 °C is indicative of the higher modulus attained from the aligned PVAc fibers. It is important to note that the deformation temperature (i.e. RT) were performed below the T_g of PVAc fibers thus yielding a high modulus. However, the concavity in the data collected at 80 °C was indicative of the A-SMEC exhibiting elastomeric behavior due the deformation temperature being above both constituents' T_gs. Although, the strain rates used to obtain the data shown in Figure 4-10 are different, it is still important to convey the differences in concavity at the specified temperatures as a function of angle to highlight the modulus difference at these respective temperatures. From a molecular level, the PVAc fiber chains at RT are orienting in the loading direction where the elastomer is transferring the load onto the fibers to bear the loading, noting that this load is carried by the Sylgard when the fibers are transverse to the loading. However, at 80 °C we hypothesize that both the PVAc fibers and Sylgard network, already in their rubbery state, are deforming elastically exhibiting no alignment during loading.

4.3.4 SHAPE MEMORY CHARACTERIZATION

All A-SMEC with varying χ were tested for the SM effect, and it was found that the fixing (R_f) decreased systematically with angle. Figure 4-14 shows a well known 4-step shape memory thermo-mechanical cycle method to demonstrate fixing for an A-SMEC with fibers axially oriented. At 80 °C, PVAc, exists in a viscous liquid state ($T-T_g$ = 25 °C), while the Sylgard, exists in a rubbery-elastic state, easily deformed at this temperature (Step 1). Strain fixing was then attained by cooling the A-SMEC from 80 °C to 0 °C (Step 2) which is well below the fiber's T_g and was expected to rigidify the internal fibrous web enough to resist the Sylgard elasticity and fix the strain. The stress was then released to reveal the degree of strain fixing (Step 3). Despite the elastomeric matrix's natural contraction, the Sylgard was forced to comply to deformation although the temperature was above its T_g of ~ -115.2 °C[26]. Since fibers were elongated and then fixed below their T_g, the Sylgard was apparently unable to contract as it does when it is in its neat state. Finally, the temperature was increased to 80 °C, and near complete shape recovery of the fibers (R_r~ 98%), was observed upon completing the shape memory cycle (SMC) (Step 4). The backdrop in Figure 4-14 and 4-15 is a strain-temperature curve where the side face is a stress-strain curve of cycle 1.

We note that PVAc fibers within the A-SMEC not only serve as reinforcements, but also contribute the SM effect by enabling temporary shape fixing while the Sylgard matrix provides the elasticity for shape recovery. In analyzing the fixing and recovery of neat Sylgard, the elastomer is able to achieve an average of 115% of elastic strain at 80 °C. However, the Sylgard is unable to fix such a deformation on cooling to 0 °C, as evidenced by sample contraction when completely unloaded, as the elastomer remains in a rubber-elastic state at this temperature. Figure 4-15 shows conventional shape memory curves for all A-SMEC tested with varying χ. In Figure 4-15, all A-SMECs exhibit elastic deformation at 80 °C where the fixing is attained when the specimens are cooled to 0 °C. It is important to observe the difference in fixing at 0 °C among all A-SMECs tested. The fixing is directly correlated with the fiber χ in the A-SMECs where near perfect fixing is attained upon unloading the A-SMEC-0 and gradually decreases as the χ increases to A-SMEC-90. All A-SMECs are then heated from 0 °C to 80 °C where near complete recovery is observed among all A-SMECs at 80 °C.

To quantify the SM effect, the fixing ratio (R_f) and recovery ratio (R_r) were calculated using Eqns. (1) and (2) given in the experimental section and the results are shown in Figure 4-16. Analyzing A-SMEC-0, good fixing was obtained, (R_f) = 95.6 %, and excellent recovery as well, with a R_r=99.3 %. Surprisingly, A-SMEC-90, with fibers transversely oriented, featured good fixing as well, with R_f =86.2 %, and expectedly good recovery, R_r = 99.0 %. The A-SMEC's with fiber orientation angles, χ = 22.5 and 45 showed R_f and R_r between the A-SMEC-0 and A-SMEC-90 systems as shown in Figure 4-15. The average R_f and R_r values are shown in Table 4-8. However, χ = 67.5 showed to have the lowest fixing of R_f = 72.1 % which was not as expected. This discrepancy could be owed to the small deviations of fiber alignment throughout the fibrous PVAc web used to fabricate the A-SMEC.

The decrease in fixing with increasing χ is attributed to anisotropy in the PVAc fiber orientation within the elastomeric matrix. As shown in Figure 4-15, near-complete fixing is achievable for χ = 0° and 22.5° samples, indicating that, in these cases, the PVAc fibers are able to resist Sylgard's contracting nature above its T_g; the rigidity of the glassy fibers dominates the rubber elasticity of the matrix. A-SMEC samples with larger χ featured lower fixing values- the lowest A-SMEC-67.5 with R_f = 72.1 %. There, the elasticity of the Sylgard matrix overcomes the rigidity of the PVAc fibers, which is lower in the loading direction due to the off axis fiber orientation. At present, we are unable to explain the large R_f values achieved even by A-SMEC's with large χ. We speculate, however, that the fiber orientation changes during sample deformation (~100%) prior to cooling, toward the deformation direction, allowing fixing. Apparently, this is reversible (Figure 4-15 (e) and (f) multiple cycles). Microscopic investigations are needed to test this idea.

4.4 CONCLUSIONS

We have successfully fabricated anisotropic shape memory elastomeric composites (A-SMEC) by using aligned PVAc fibers to reinforce a Sylgard elastic matrix for anisotropic mechanical properties. Temperature-dependent mechanical properties for A-SMEC's with varying orientation angle, χ, relative to the loading were measured, revealing the offset of the transitions of the A-SMEC and neat Sylgard. Anisotropy of the A-SMEC was quantified through mechanical tensile testing, specifically yielding the apparent modulus, Young's modulus, strain-to-failure and yield stress. Anisotropy was further quantified through shape memory testing to show the fixing and recovery behavior as a function of fiber orientation angle. More specifically, the A-SMEC's featured decreasing fixing capacity, R_f with increasing χ, while shape recovery, R_r, was invariably high. We anticipate application development of A-SMEC materials that exploits the unique combination of elastomeric behavior, anisotropy, and shape memory.

4.5 REFERENCE

(1) Mather, P. T.; Luo, X. F.; Rousseau, I. A.: Shape Memory Polymer Research. *Annual Review of Materials Research* **2009**, *39*, 445-471.

(2) Liu, C.; Qin, H.; Mather, P. T.: Review of progress in shape-memory polymers. *Journal of Materials Chemistry* **2007**, *17*, 1543-1558.

(3) Lendlein, A.: Shape-Memory Polymers. Kelch, S., Ed.: Angewandte Chemie, 2002; Vol. 41; pp 2034-2057.

(4) Burke, K. A.; Mather, P. T.: Soft shape memory in main-chain liquid crystalline elastomers. *Journal of Materials Chemistry* **2010**, *20*, 3449-3457.

(5) Ishida, K.; Hortensius, R.; Luo, X. F.; Mather, P. T.: Soft bacterial polyester-based shape memory nanocomposites featuring reconfigurable nanostructure. *Journal of Polymer Science Part B-Polymer Physics* **2012**, *50*, 387-393.

(6) Reddy, J. N.: *Mechanics of Laminated Composite Plates and Shells: Theory and Analysis*; 2 ed.; CRC Press: New York, NY, 2003.

(7) Mather, P. T.: Soft answers for hard problems. *Nature Materials* **2007**, *6*, 93-94.

(8) Swartz, S. M.; Groves, M. S.; Kim, H. D.; Walsh, W. R.: Mechanical properties of bat wing membrane skin. *Journal of Zoology* **1996**, *239*, 357-378.

(9) Padian, K.; Rayner, J. M. V.: THE WINGS OF PTEROSAURS. *American Journal of Science* **1993**, *293A*, 91-166.

(10) Lachance, M.: By studying bats, researchers look to enhance micro air vehicles. Air Force Material Command, 2009.

(11) Tanaka, Y.; Kagami, Y.; Matsuda, A.; Osada, Y.: THERMOREVERSIBLE TRANSITION OF THE TENSILE MODULUS OF A HYDROGEL WITH ORDERED AGGREGATES. *Macromolecules* **1995**, *28*, 2574-2576.

(12) Osada, Y.; Matsuda, A.: SHAPE-MEMORY IN HYDROGELS. *Nature* **1995**, *376*, 219-219.

(13) M. Irie, K. O., and C.M. Wayman: *Shape Memory polymers*; Cambridge University Press, 1998.

(14) Rousseau, I. A.; Mather, P. T.: Shape memory effect exhibited by smectic-c liquid crystalline elastomers. *Journal of the American Chemical Society* **2003**, *125*, 15300-15301.

(15) Li, Y. J.; Iwakura, Y.; Nakayama, K.; Shimizu, H.: Highly anisotropic properties of thermoplastic elastomer composites with aligned hierarchical structures. *Composites Science and Technology* **2007**, *67*, 2886-2891.

(16) Cohen, Y.; Albalak, R. J.; Dair, B. J.; Capel, M. S.; Thomas, E. L.: Deformation of oriented lamellar block copolymer films. *Macromolecules* **2000**, *33*, 6502-6516.

(17) Honeker, C. C.; Thomas, E. L.: Impact of morphological orientation in determining mechanical properties in triblock copolymer systems. *Chemistry of Materials* **1996**, *8*, 1702-1714.

(18) Prasman, E.; Thomas, E. L.: High-strain tensile deformation of a sphere-forming triblock copolymer mineral oil blend. *Journal of Polymer Science Part B-Polymer Physics* **1998**, *36*, 1625-1636.

(19) Ha, Y. H.; Thomas, E. L.: Deformation behavior of a roll-cast layered-silicate/lamellar triblock copolymer nanocomposite. *Macromolecules* **2002**, *35*, 4419-4428.

(20) Dair, B. J.; Avgeropoulos, A.; Hadjichristidis, N.; Capel, M.; Thomas, E. L.: Oriented double gyroid films via roll casting. *Polymer* **2000**, *41*, 6231-6236.

(21) Honeker, C. C.; Thomas, E. L.; Albalak, R. J.; Hajduk, D. A.; Gruner, S. M.; Capel, M. C.: Perpendicular deformation of a near-single-crystal triblock copolymer with a cylindrical morphology. 1. Synchrotron SAXS. *Macromolecules* **2000**, *33*, 9395-9406.

(22) Honeker, C. C.; Thomas, E. L.: Perpendicular deformation of a near-single-crystal triblock copolymer with a cylindrical morphology. 2. TEM. *Macromolecules* **2000**, *33*, 9407-9417.

(23) Komp, A.; Finkelmann, H.: A new type of macroscopically oriented smectic-A liquid crystal elastomer. *Macromolecular Rapid Communications* **2007**, *28*, 55-62.

(24) Komp, A.; Ruhe, J.; Finkelmann, H.: A versatile preparation route for thin free-standing liquid single crystal elastomers. *Macromolecular Rapid Communications* **2005**, *26*, 813-818.

(25) ABfalg, N.; Finkelmann, H.: A smectic A liquid single crystal elastomer (LSCE): Phase behavior and mechanical anisotropy. *Macromolecular Chemistry and Physics* **2001**, *202*, 794-800.

(26) Luo, X. F.; Mather, P. T.: Preparation and Characterization of Shape Memory Elastomeric Composites. *Macromolecules* **2009**, *42*, 7251-7253.

(27) Chung, T.; Romo-Uribe, A.; Mather, P. T.: Two-way reversible shape memory in a semicrystalline network. *Macromolecules* **2008**, *41*, 184-192.

(28) Young, W. C.; Budynas, R. G.: *Roark's Formulas for Stress and Strain*; McGraw-Hill, 2002.

(29) Young, W. C., & Budynas, R. G.: *Roark's Formulas for Stress and Strain*; McGraw-Hill, 2002.

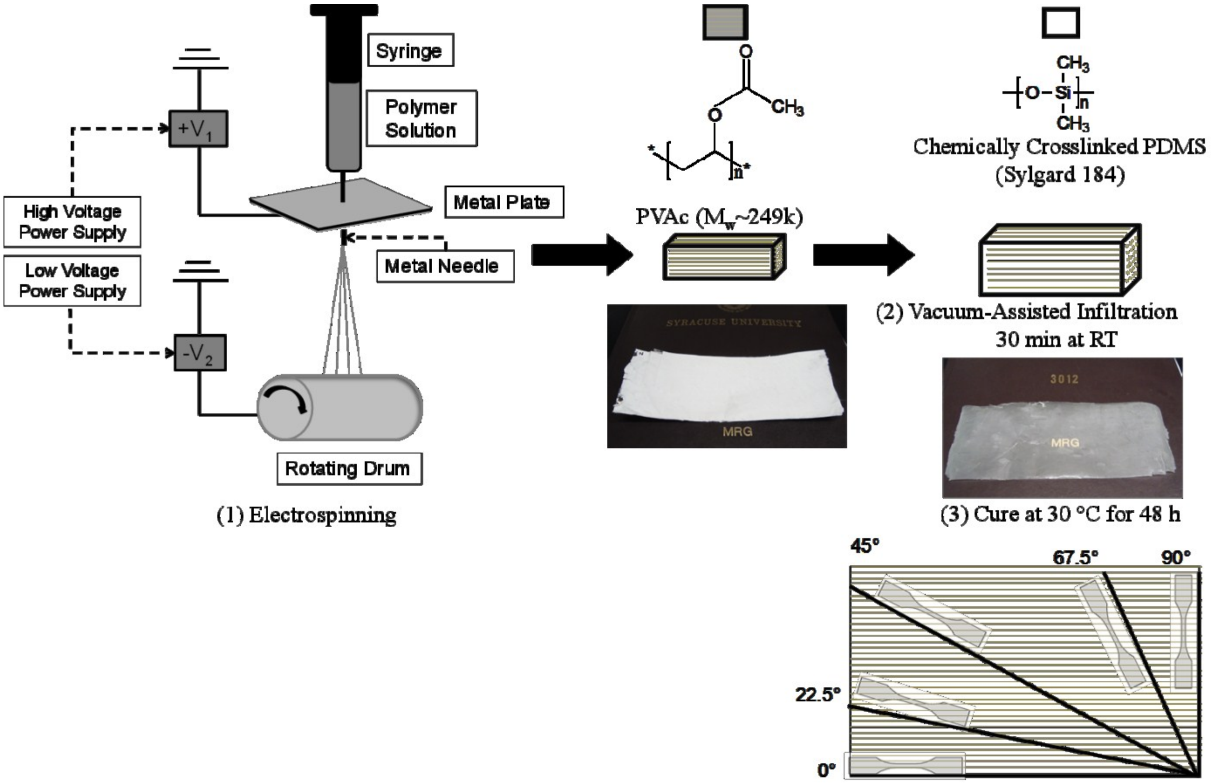

Scheme 4-1. Three-step fabrication of shape memory elastomeric composites (A-SMEC). All samples tested were dogbone punched as a function of fiber orientation angle from the composite where 0° is the axial direction and 90° is the transverse direction.

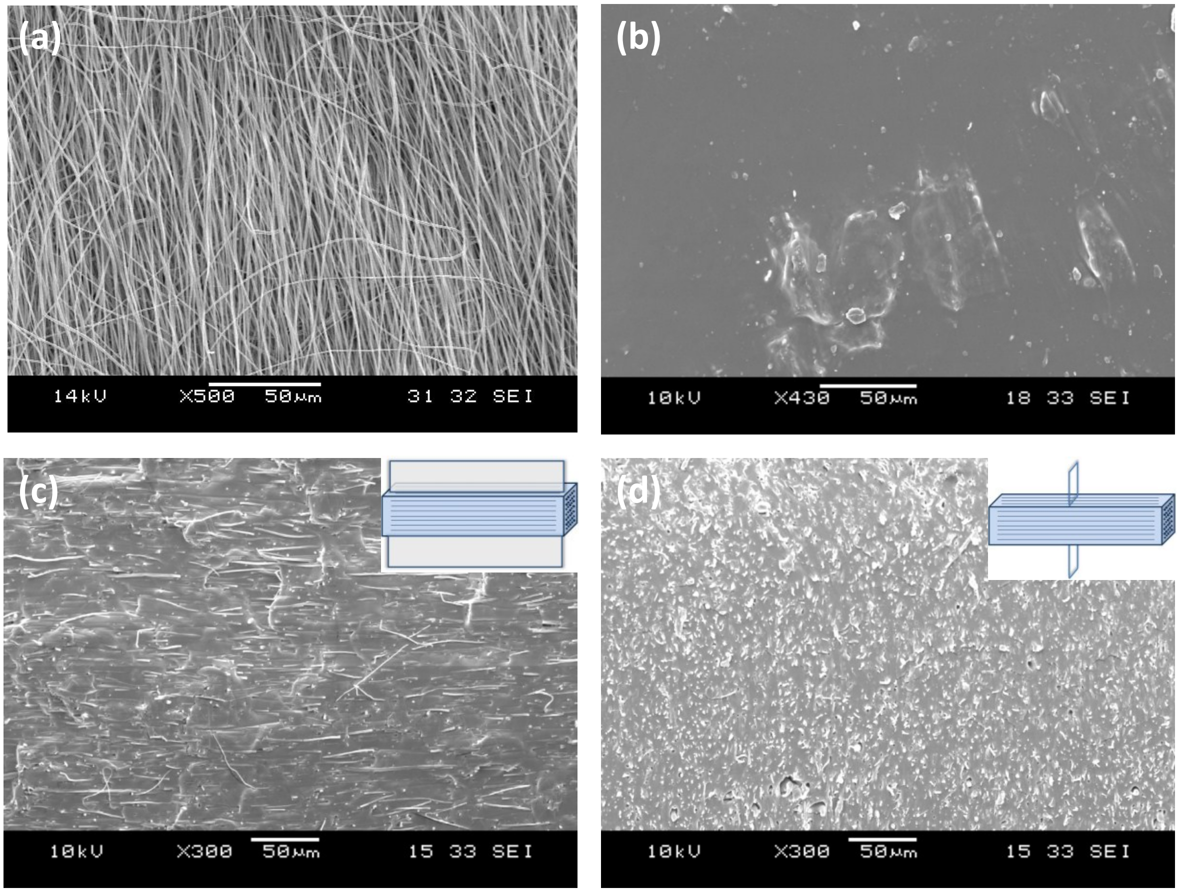

Figure 4-1. SEM images of (a) PVAc fibers (average diameter: 0.79 ± 0.20 μm), (b) topography of A-SMEC, (c) A-SMEC with axial fiber orientation, (d) composite with transverse fiber orientation.

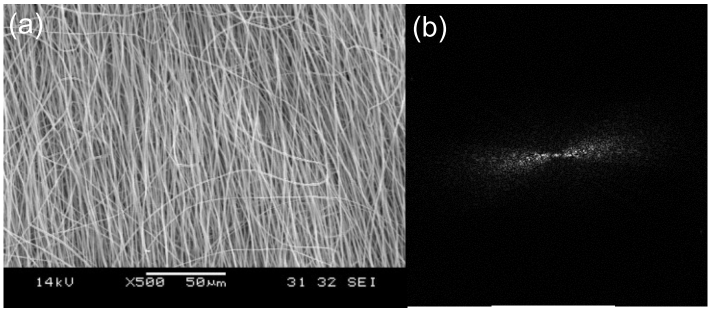

Average Fiber Diameter: 0.79 ± 0.20µm

2D FFT

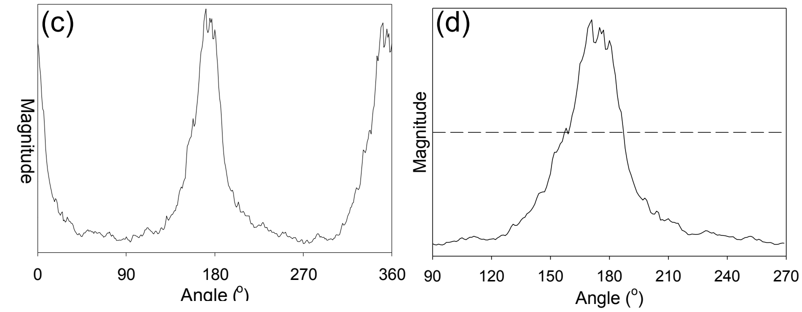

Radial Sum of Intensity

Resultant Fiber Alignment

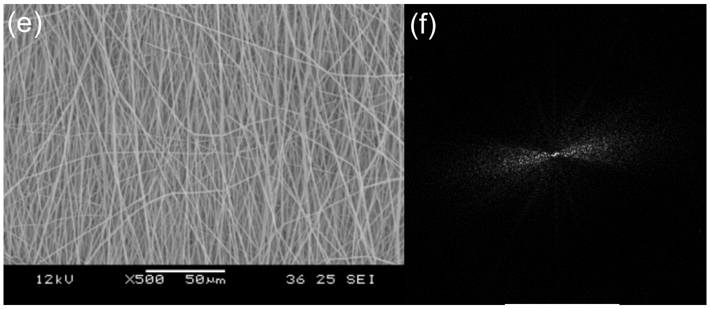

Average Fiber Diameter: 0.77 ± 0.18µm

2D FFT

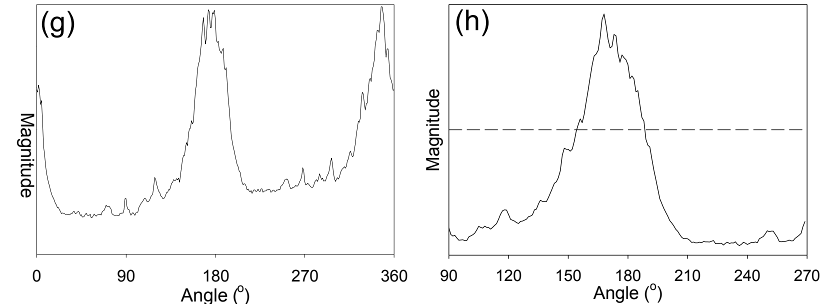

Radial Sum of Intensity

Resultant Composite Alignment

Figure 4-2. (a) depicts an SEM of PVAc fibrous web used for testing (b) a 2D FFT of the SEM, (c) and (d) the resultant radial sum of intensities. (e) depicts an SEM of the PVAc fibers used to make the A-SMEC and used for testing, (f) a 2D FFT of the SEM image, (g) and (h) the resultant radial sum of intensities. SEMs, (a) and (e), were used to create the 2D FFTs, (b) and (f), by cropping the image to a square, then running the 2D Fast Fourier Transform (FFT) using Gywddion software's Hahn model. The resultant analytical images, (b) and (f), were then used to create radial intensity sum plots, (c) and (g). More specifically, utilizing an Image J plugin, "Oval_Profile" radial sums of the intensities at every angle were taken. As the 2D FFT rotates the images 90°, narrow peaks at 180° and 0°/360° are indicative of vertical alignment. As two peaks arise due the symmetry of this analysis, intensities from 0° to 90° correspond to intensities from 180° to 270°, similarly, intensities from 270° to 360° correspond to intensities from 90° to 180°. Intensity values from these sets were therefore averaged with their respective datum and plotted as angles from 90° to 270°, (d) and (h). Half max was established by obtaining the minimum datum for the given data and subtracting that value for all other data in the set. This value is reported as the dashed line on its' respective plot. The two points where the data and this half max line intersect yield a breadth of angles which is known as the full width at half max (FWHM). The resulting FWHM for the fiber web shown in (a) and (e) were 30° and 34° which confirms alignment for these two mats.

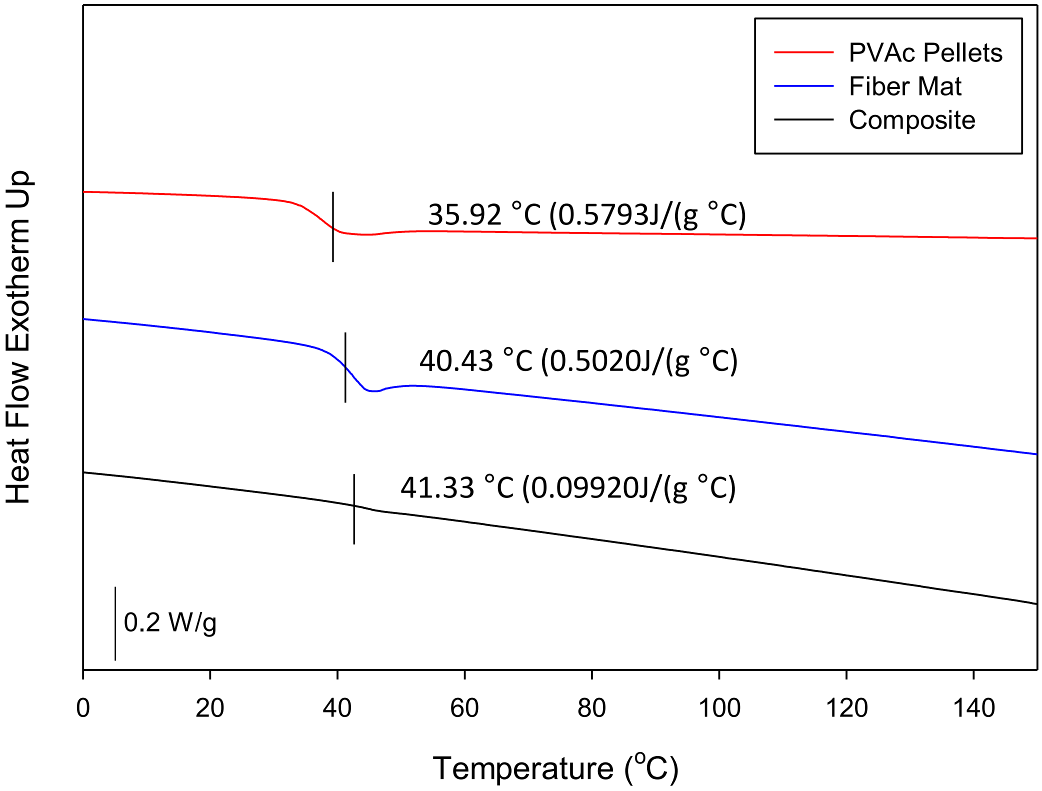

Figure 4-3. Glass transitions (T_g) of PVAc pellet, PVAc fibrous web and A-SMEC of the second heating are shown. By dividing the heat capacity of the A-SMEC by the heat capacity of the fibrous web mat, the fiber volume fraction of the was determined to be 19.8%.

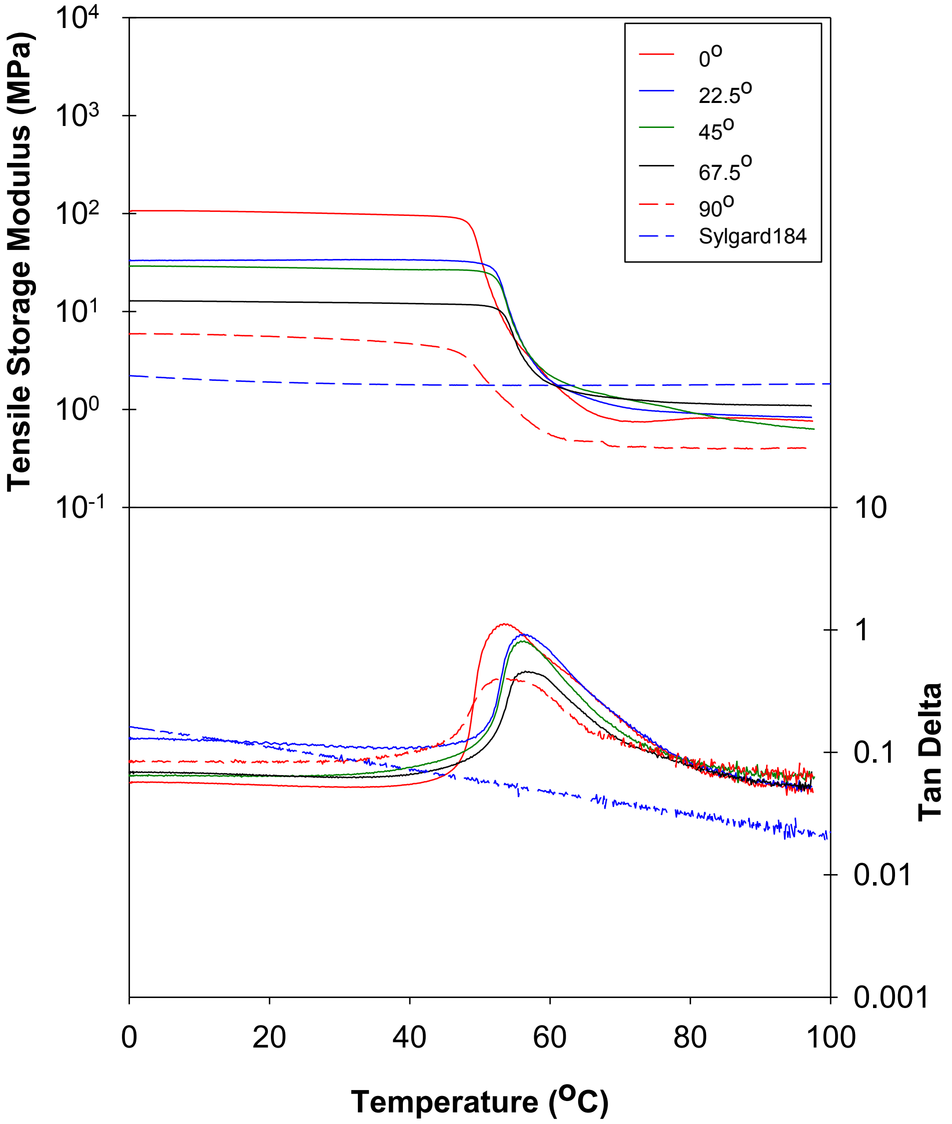

Figure 4-4. Tensile storage modulus (E′) and tan delta versus temperature as a function of fiber orientation angle where Sylgard is plotted as a reference.

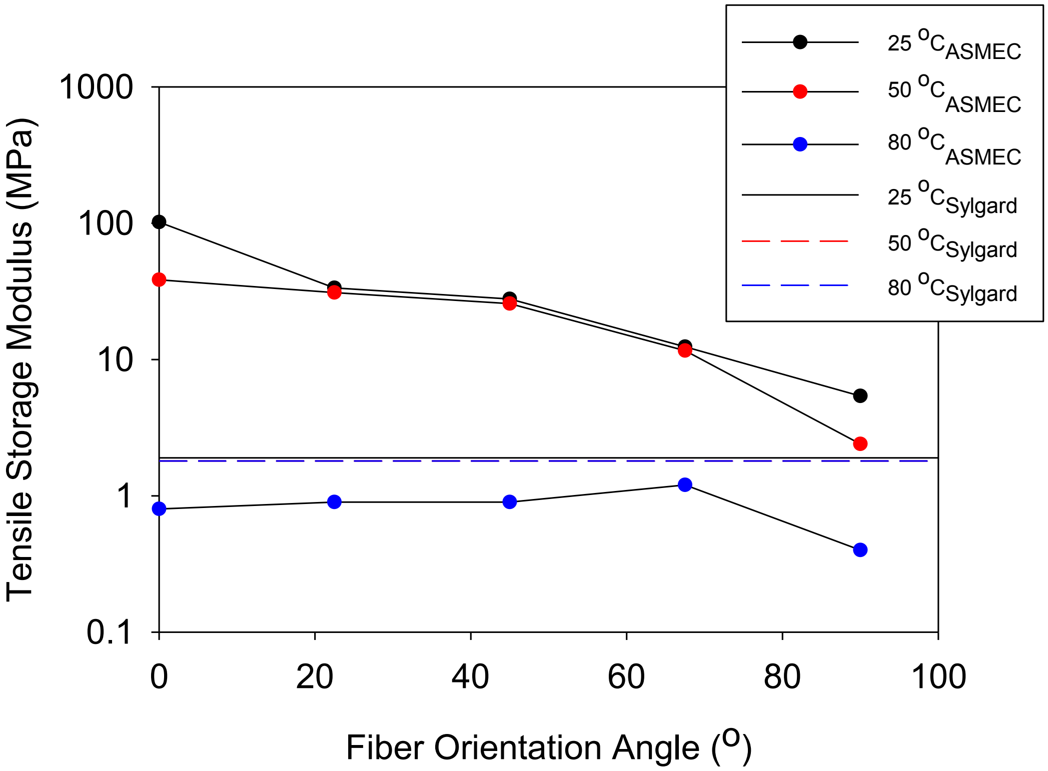

Figure 4-5. Scatter plot showing storage modulus at 25 °C, 50 °C and 80 °C as a function of fiber orientation angle, and showing Sylgard as reference lines at each temperature.

Table 4-1. Table showing tensile storage modulus (E') at 25 °C, 50 °C and 80 °C as a function of fiber orientation with Sylgard as a reference.

Angle (°)	$E'_{25°C}$ (MPa)	$E'_{50°C}$ (MPa)	$E'_{80°C}$ (MPa)
Sylgard184	1.9	1.8	1.8
0	101.6	38.4	0.8
22.5	33.5	31.0	0.9
45	27.8	25.7	0.9
67.5	12.4	11.6	1.2
90	5.4	2.4	0.4

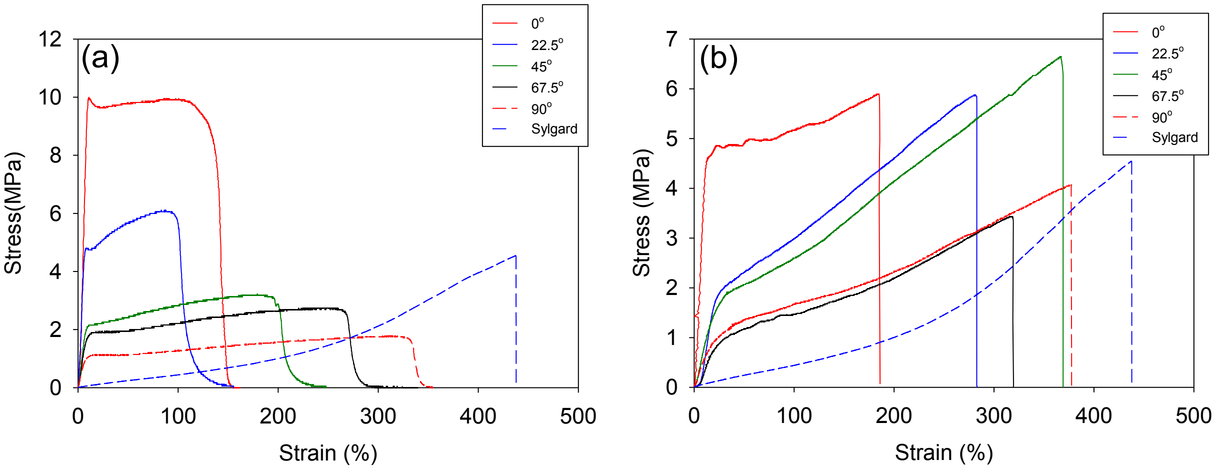

Figure 4-6. Representative stress-strain curves for (a) PVAc fibrous web and (b) A-SMEC dogbone samples as a function of fiber orientation angle with a Sylgard sample as a reference (-).

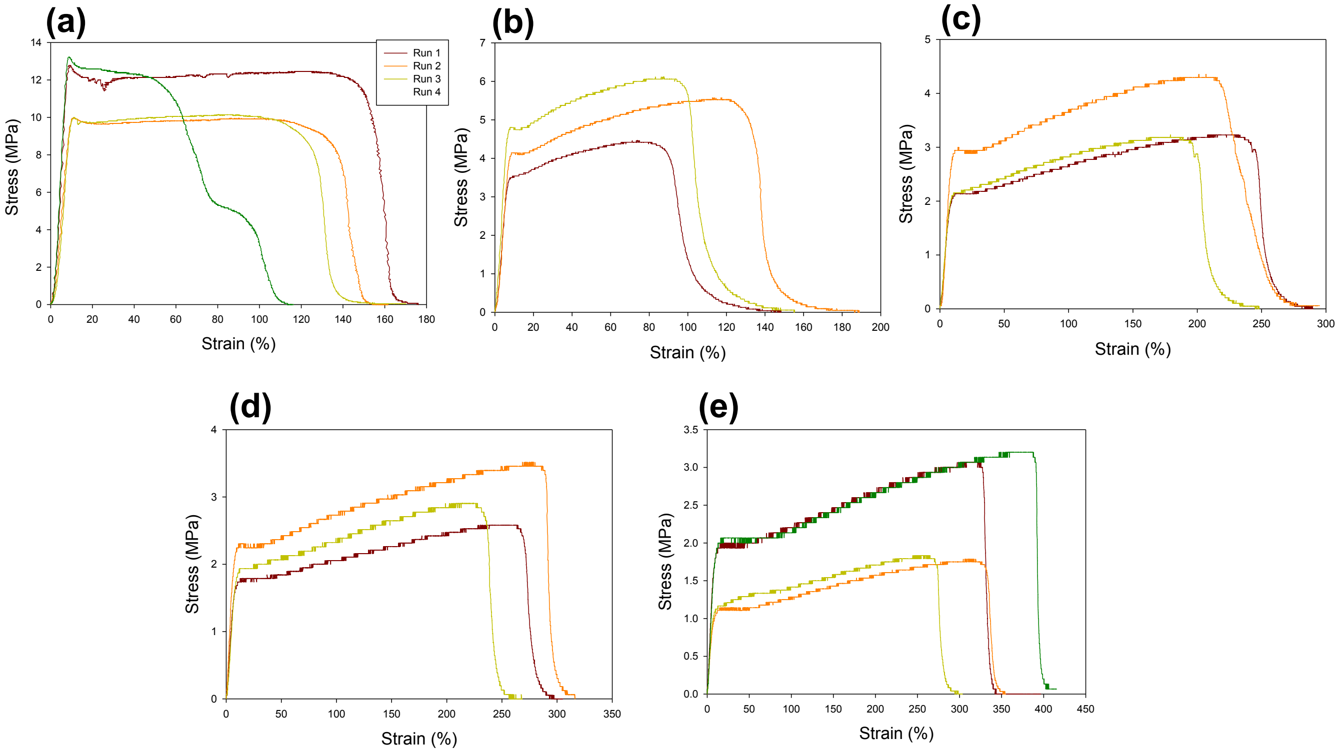

Figure 4-7. Stress-strain curves of PVAc fibrous web samples as a function of fiber orientation angle where (a) A-SMEC-0; (b) A-SMEC-22.5; (c) A-SMEC-45; (d) A-SMEC-67.5; and (e) A-SMEC-90.

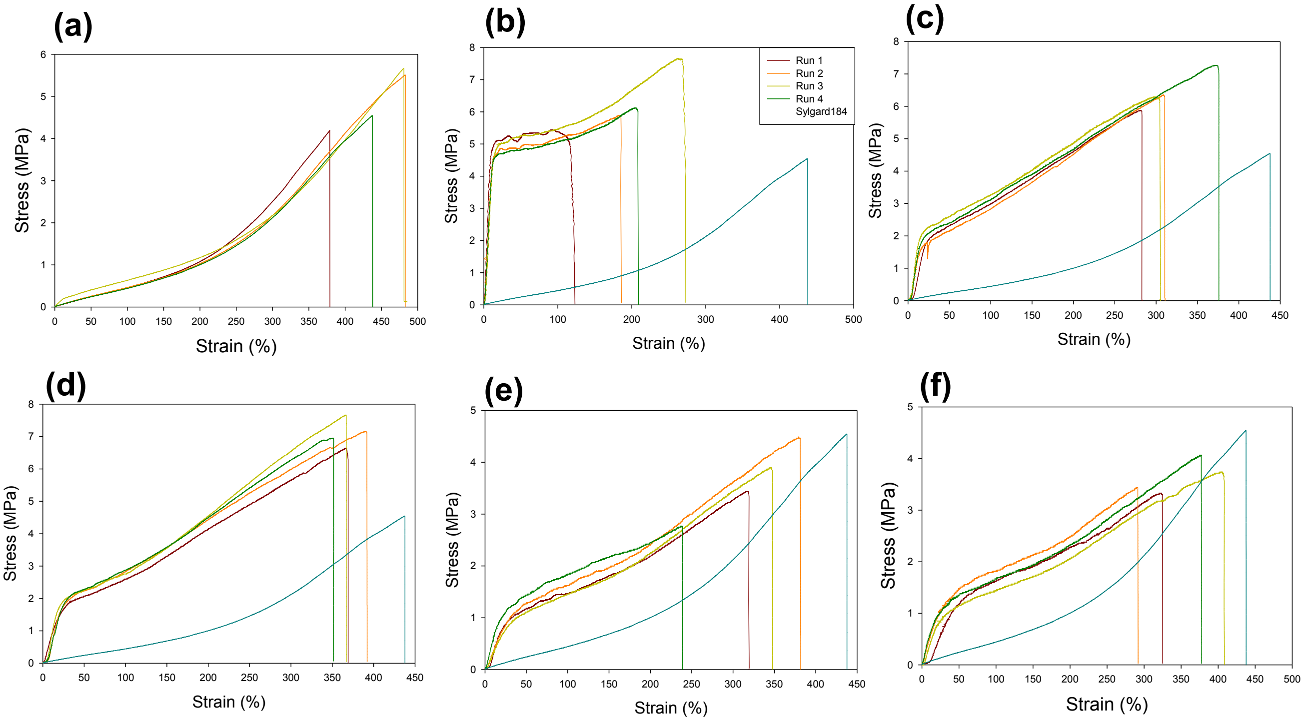

Figure 4-8. Stress-strain curves of A-SMEC as a function of fiber orientation angle with a Sylgard sample as a reference where (a) Sylgard; (b) A-SMEC-0; (c) A-SMEC-22.5; (d) A-SMEC-45; (e) A-SMEC-67.5; and (f) A-SMEC-90.

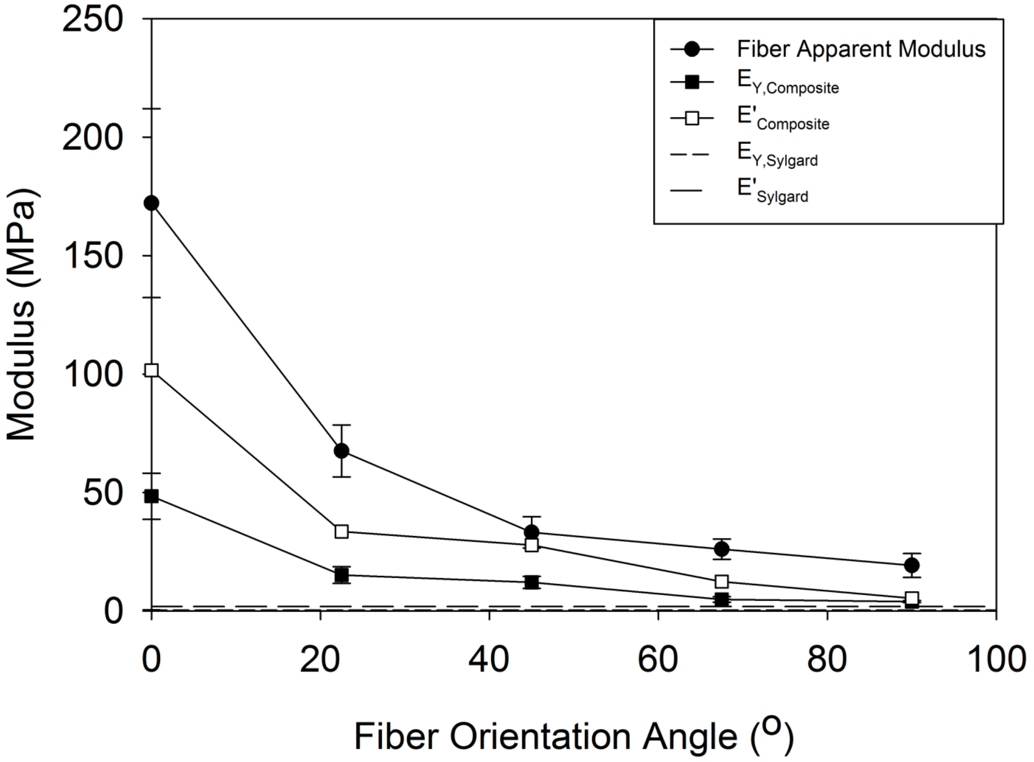

Figure 4-9. Elastic modulus as a function of fiber orientation angle at RT for PVAc fibrous web and A-SMEC samples with Sylgard as a reference.

Table 4-2. Data chart showing values of tensile apparent modulus of PVAc fibrous web dogbone samples.

Tensile Apparent Modulus (MPa)

Run	**0°**	**22.5°**	**45°**	**67.5°**	**90°**
1	202.2	63.4	27.5	25.0	23.7
2	131.7	66.4	40.0	32.3	14.6
3	144.3	83.0	27.5	24.5	15.1
4	210.3	57.5	37.7	22.6	23.5
AVG	172.1	67.6	33.2	26.1	19.2
STDEV	39.9	11.0	6.6	4.3	5.1

Table 4-3. Data chart showing values of tensile Young's modulus (E_y) for the A-SMEC and Sylgard samples.

Tensile Young's Modulus (MPa)

Run	0°	22.5°	45°	67.5°	90°	Sylgard
1	62.3	11.3	9.1	5.6	3.5	0.5
2	40.0	13.5	12.8	4.2	4.5	0.4
3	45.8	19.5	15.1	3.7	3.9	0.5
4	45.7	16.4	11.4	6.1	3.9	0.4
AVG	48.4	15.2	12.1	4.9	4.0	0.4
STDEV	9.7	3.5	2.5	1.1	0.4	0.03

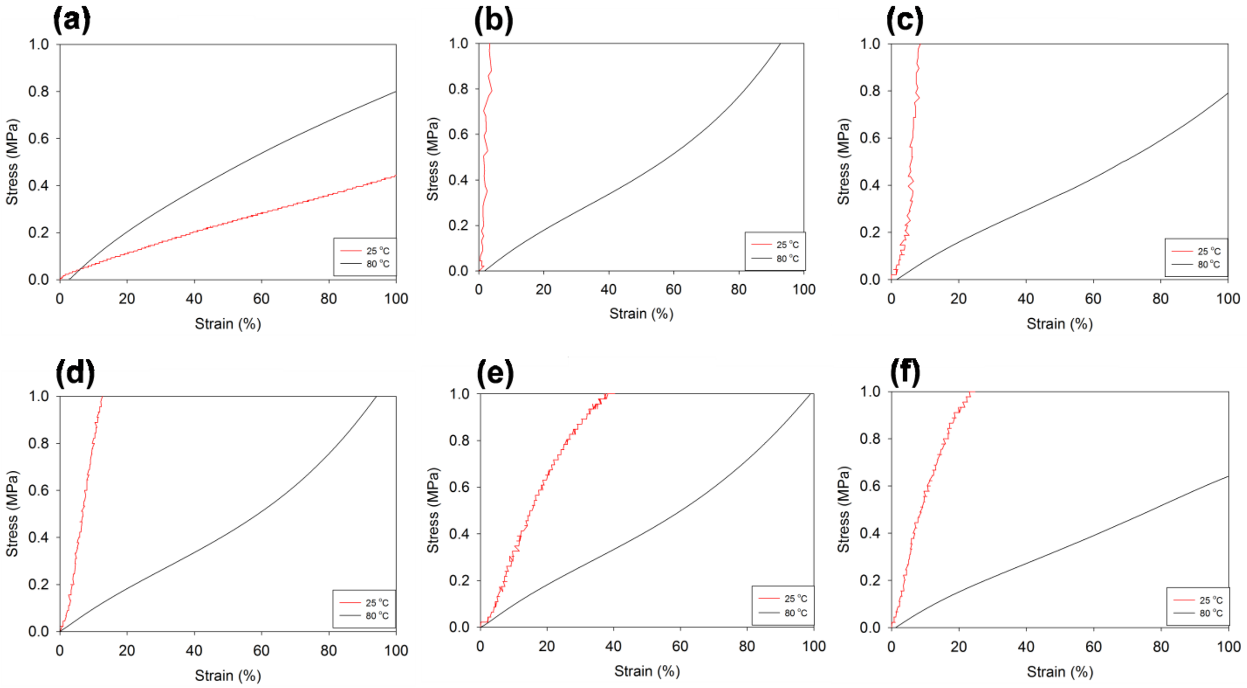

Figure 4-10. Representative stress-strain curves at 25 °C and 80 °C showing the extreme change in concavity of the geometry curve where (a) Sylgard; (b) A-SMEC-0; (c) A-SMEC-22.5; (d) A-SMEC-45; (e) A-SMEC-67.5; and (f) A-SMEC-90.

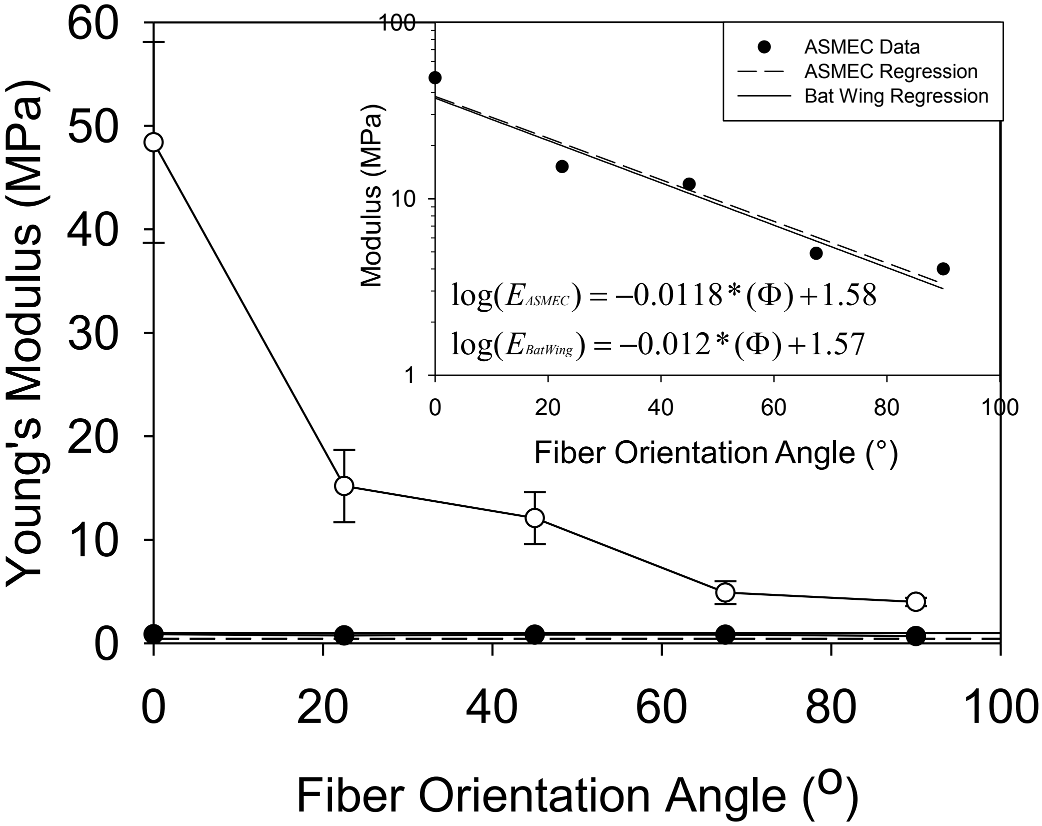

Figure 4-11. Plot showing Young's modulus as a function of fiber orientation angle is shown where (○) is for the A-SMEC and (--) is for the Sylgard at 25 ºC; (●) is for the A-SMEC and (-) is for the Sylgard at 80 ° C. Comparison of the elastic modulus of a biological system (i.e. bat wing membrane reported by Swartz et al.) and the A-SMEC as a function of fiber orientation angle. The A-SMEC regression line was found by plotting the logarithm of the modulus vs. the fiber orientation angle in and fitting a linear trendline. The bat wing regression had been previously reported by Swartz et al., and has been included to show how this A-SMEC modulus mimics that of the biological system.

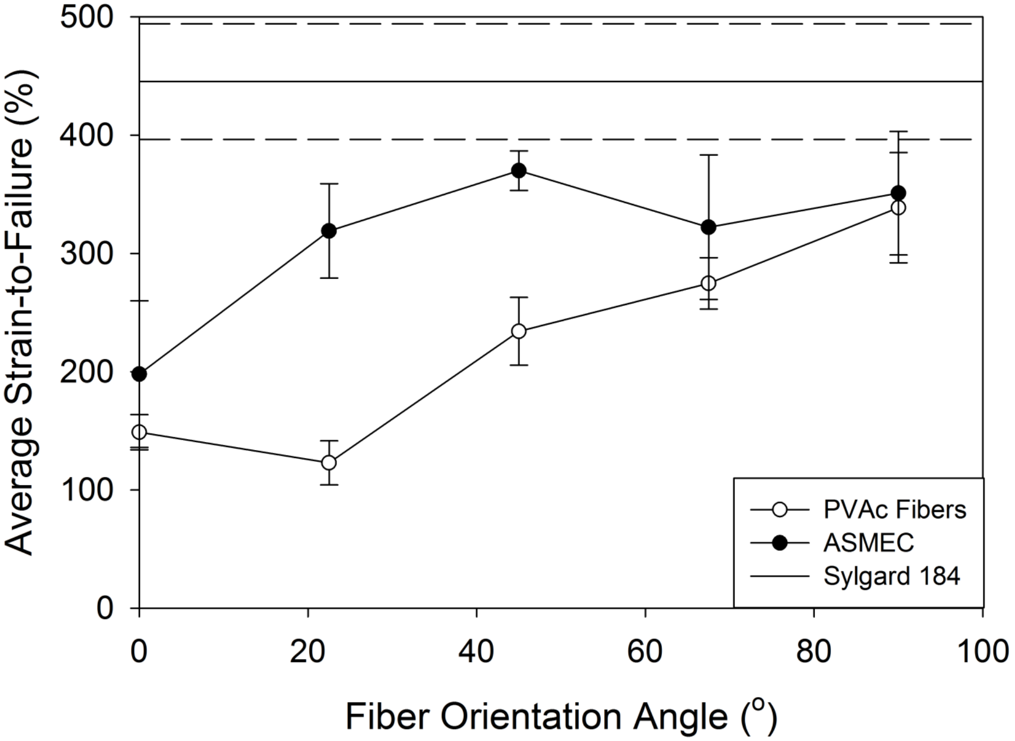

Figure 4-12. Graph showing PVAc fibrous web and A-SMEC samples of average strain-to-failure as a function of fiber orientation angle with Sylgard as a reference (-) where the dashed lines (--) are the standard error of Sylgard.

Table 4-4. Data chart showing strain-to-failure values of PVAc fibrous web dogbone samples.

Strain-to-Failure (%)

Run	**0°**	**22.5°**	**45°**	**67.5°**	**90°**
1	164.4	103.3	255.5	280.1	335.9
2	147.3	142.1	262.2	295.8	341.6
3	134.8	111.0	210.0	244.3	281.7
4	-	135.1	208.8	278.4	395.6
AVG	148.8	122.9	234.1	274.6	338.7
STDEV	14.9	18.7	28.7	21.7	46.6

Table 4-5. Data chart showing values of strain-to-failure for the A-SMEC and Sylgard samples.

Strain-to-Failure (%)						
Run	**0°**	**22.5°**	**45°**	**67.5°**	**90°**	**Sylgard**
1	123.2	283.2	369.1	319.5	325.3	378.9
2	186.1	310.9	392.2	381.9	292.0	483.0
3	273.3	305.9	366.9	348.2	408.6	481.0
4	209.1	376.0	351.7	238.9	377.8	437.8
AVG	197.9	319.0	370.0	322.1	350.9	445.2
STDEV	62.0	39.9	16.7	61.1	52.2	48.9

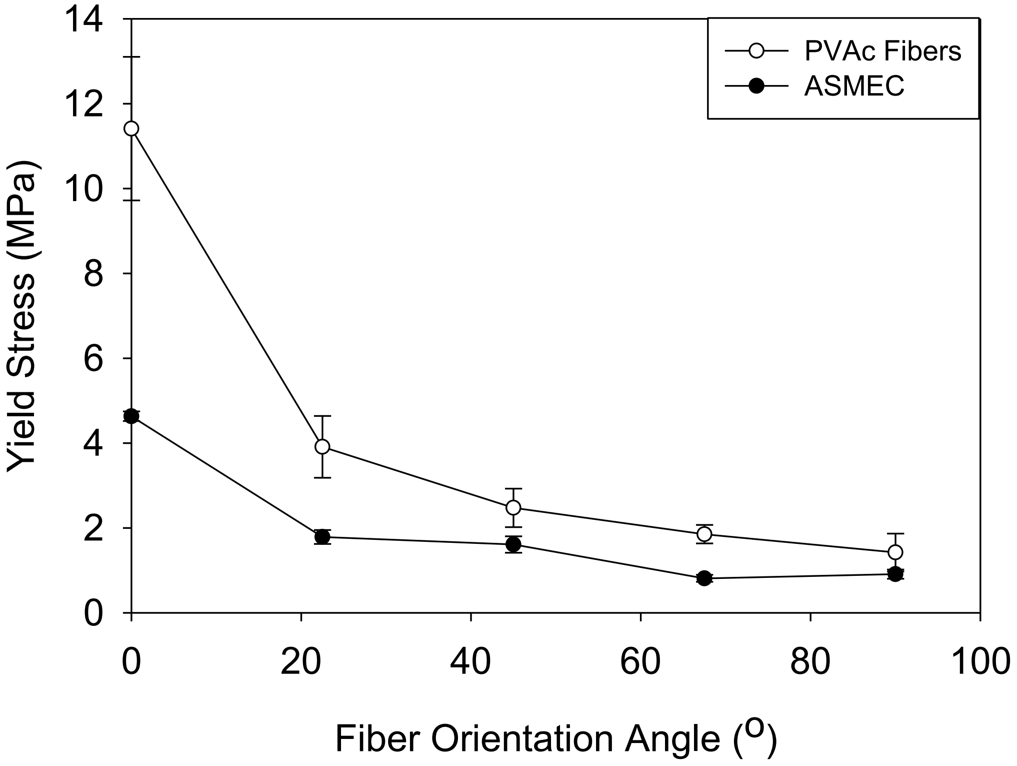

Figure 4-13. Graph showing yield stress for samples in the fibrous web and A-SMEC state.

Table 4-6. Yield stress for all fibrous web samples tested as a function of fiber orientation angle.

			Fiber Yield Stress (MPa)		
Run	**0°**	**22.5°**	**45°**	**67.5°**	**90°**
1	12.7	3.5	2.1	1.7	1.8
2	9.9	4.2	2.9	2.2	1.0
3	10.0	4.8	2.1	1.8	1.1
4	13.1	3.2	2.9	1.8	1.8
AVE	11.4	3.9	2.5	1.9	1.4
STDEV	1.7	0.7	0.5	0.2	0.4

Table 4-7. A-SMEC yield stress for all samples tested as a function of fiber orientation angle.

Composite Yield Stress (MPa)					
Run	0°	22.5°	45°	67.5°	90°
1	4.8	1.8	1.4	0.8	1.0
2	4.6	1.6	1.6	0.8	0.9
3	4.7	2.0	1.6	0.7	0.8
4	4.5	1.8	1.8	0.9	0.9
AVE	4.6	1.8	1.6	0.8	0.9
STDEV	0.1	0.2	0.2	0.1	0.1

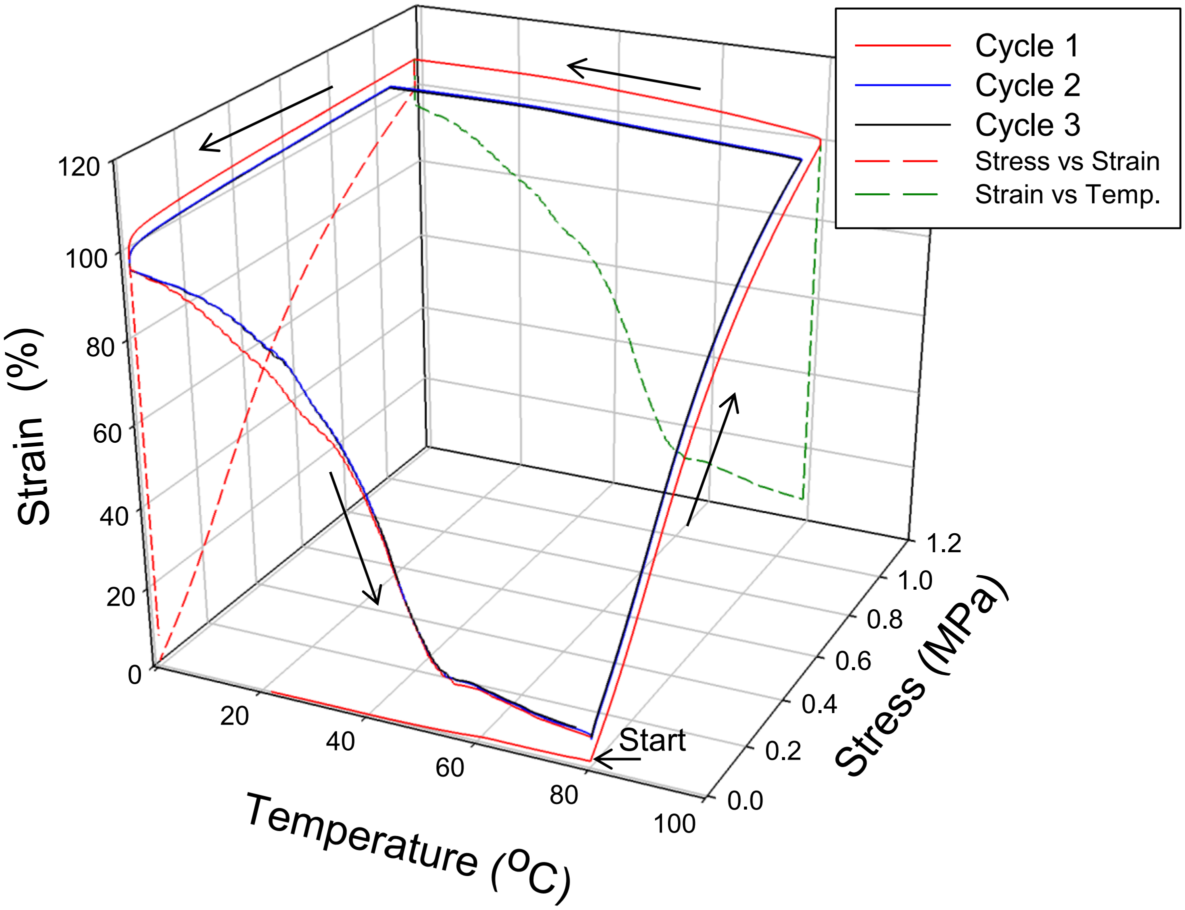

Figure 4-14. Shape memory cycles for an A-SMEC where the fibers are in the axial direction (A-SMEC-0). Backdrop is a strain-temperature curve and the side face is a stress-strain curve of cycle 1.

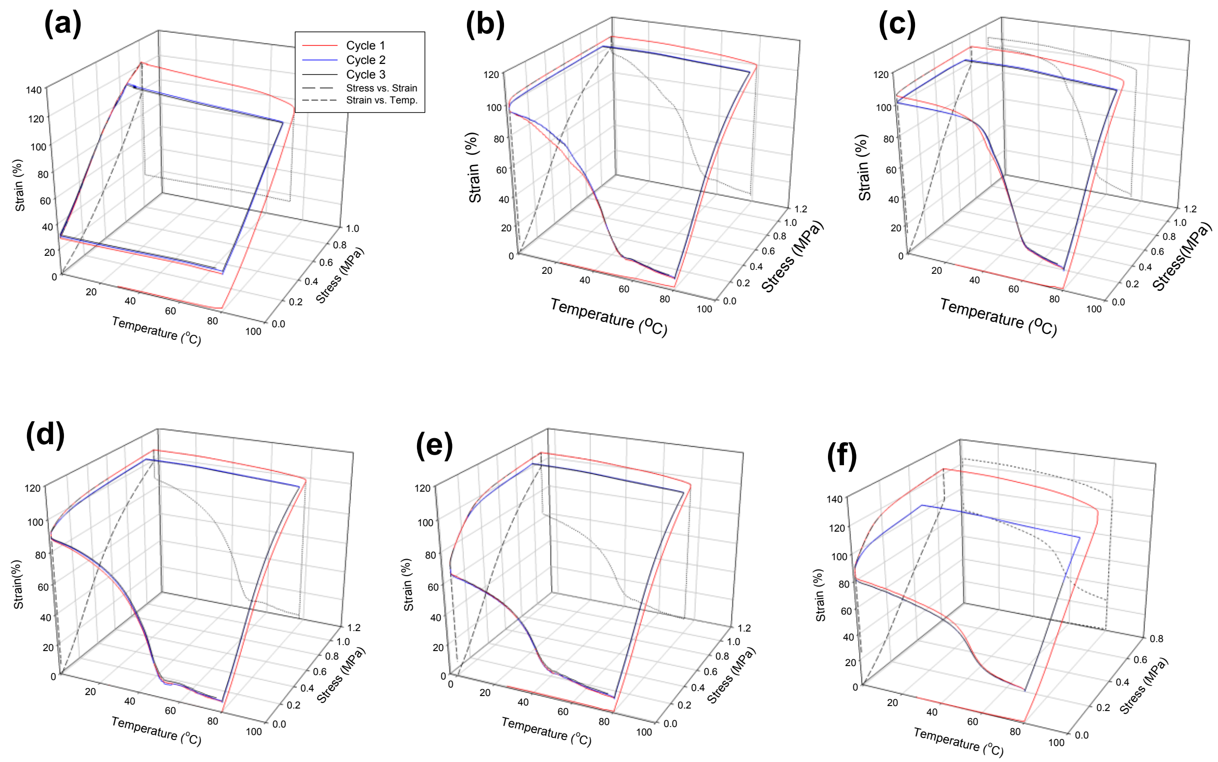

Figure 4-15. Shape memory cycles for all samples tested as a function of fiber orientation angle where (a) Sylgard; (b) A-SMEC-0; (c) A-SMEC-22.5; (d) A-SMEC-45; (e) A-SMEC-67.5; and (f) A-SMEC-90.

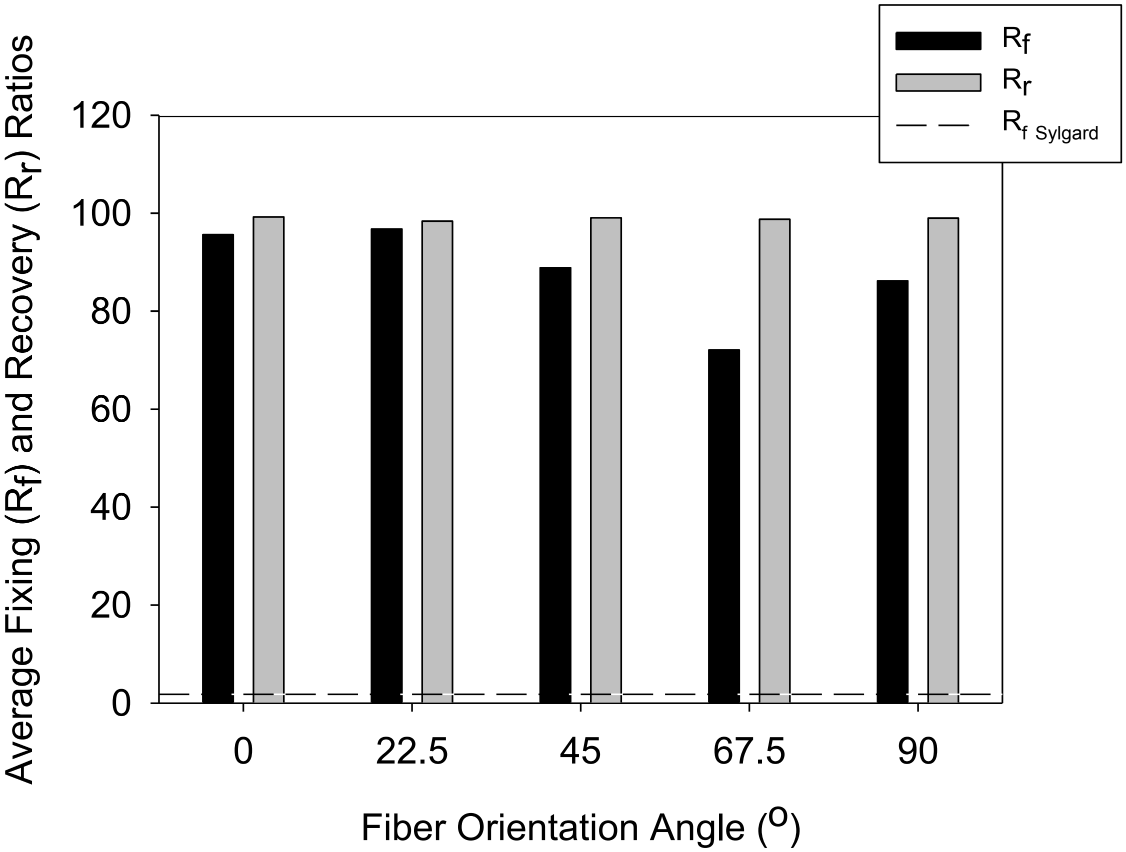

Figure 4-16. Graph of fixing *(R_f)* and recovery (*R_r*) ratios of A-SMEC samples as a function of fiber orientation angle with the inclusion of the Sylgard as reference line for R_f where the average among cycle two and three are shown.

Table 4-8. Fixing (R_f) and recovery (R_r) ratios for all A-SMEC samples tested as a function of fiber orientation angle where the average of cycle two and three were reported.

Angle (°)	AVE R_f	AVE R_r
Sylgard184	29.2	27.4
0	95.6	99.3
22.5	96.8	98.4
45	88.9	99.1
67.5	72.1	98.8
90	86.2	99.0

CHAPTER FIVE

LAMINATED ANISOTROPIC SHAPE MEMORY ELASTOMERIC COMPOSITES (A-SMEC): FABRICATION AND MECHANICALLY ACTIVATED SHAPE CHANGE (MASC)

5.0 SYNOPSIS

This chapter expands on the anisotropic shape memory elastomeric composites (A-SMEC) explained in Chapter 4 where laminated fiber reinforced A-SMECs were fabricated to study the curvature and pitch changes as a function of fiber orientation angle. The bimetal strip curvature model was modified and used to explain the curvature seen in the A-SMEC strips where theoretical and experimental curvature was compared.

5.1 INTRODUCTION

The following sections will provide a brief explanation of theoretical equations used to explain the mechanics of composites. In addition, examples of warpage, curvature and spiral geometry that were observed in industrial and biological systems where theoretical models were employed to explain such behavioral responses will also be reported.

5.1.1 MECHANICS OF LAMINATED COMPOSITES

As previously mentioned and described in Chapter 1 Section 1.7, the theoretical equations of Young's modulus, ratio of forces, and strength in the longitudinal and transverse for fiber reinforced composites will be used to help describe the trends seen in the data in this chapter.

The modulus in the longitudinal and transverse direction in relation to the fiber orientation are given by:

$$E_l = E_m V_m + E_f V_f \tag{5-1}$$

$$\frac{1}{E_t} = \frac{V_m}{E_m} + \frac{V_f}{E_f} \tag{5-2}$$

where E_l is the modulus in the longitudinal fiber direction, E_t is the modulus in the transverse direction, E_m is the matrix phase modulus, E_f is the fiber phase modulus, V_m is the matrix volume fraction, and the V_f is the fiber volume fraction.[1] It is important to consider that if the modulus of the matrix is significantly higher than that of the fiber modulus, Eqn. (5-2) may not be valid. However, this is not the case for the A-SMEC systems explained in this chapter as the matrix exhibits elastomeric properties and has a lower modulus than the embedded fibers in the system. The longitudinal and transverse stresses can also be used to calculate the tensile stress in the composite when loaded axially:

$$\sigma_l = \sigma_m'\left(1 - V_f\right) + \sigma_f^* V_f \tag{5-3}$$

$$\sigma_t = E_c V_m \varepsilon_m + E_c V_f \varepsilon_f \tag{5-4}$$

where σ_l is the composite strength in the longitudinal direction, σ_m' is the matrix strength, V_f is the fiber volume fraction, and σ_f^* is the fiber strength.[1] σ_t is the strength in the transverse direction, E_c is the modulus of the composite, V_m is the matrix volume fraction, and ε_f and ε_m is the strain in the fibers and matrix respectively. Additionally, the dual laminated composite modulus ($E_{\text{laminated composite}}$) for the composites fabricated and characterized in this chapter can be calculated by the following equation:

$$E_{laminated\ composite} = \frac{A_{p1}E_{p1}+A_{p2}E_{p2}+A_sE_s}{A_{p1}+A_{p2}+A_s} \tag{5-5}$$

where A_{p1}, A_{p2} and A_s is the area of ply 1, ply 2 and Sylgard respectively. E_{p1}, E_{p2}, and E_s are the Young's moduli for ply 1, ply 2 and Sylgard respectively. Eqn. (5-5) can be used to calculate $E_{\text{laminated composite}}$ for any given laminated composite.

5.1.2 ANISOTROPY IN LAMINATED COMPOSITES

Residual stresses in unsymmetric laminate composites have found to create warpage effects during the curing process and fabrication. Residual stresses are stresses that are unrecovered when the external force or thermal processing has been removed from the system.[1,2] Laminated composites are found to have residual stresses due to the unsymmetric expansion properties of the individual materials used to make the composite.[3] This occurs when there is a difference in coefficients of thermal expansion (CTE) between the varying fiber-aligned plies and matrix.[3-7] It's these residual stresses that are a resultant of the warping (curvature) that are found in the laminates composite plates.[3] The Classical Laminated Plate Theory (CLPT) has been shown to model such curvature. Before CLPT is explained it is first important to define some terms. A *lamina* refers to one layer or singular ply where *laminae* denotes more than one *lamina* and *laminate* refers to a series of *laminae* that are bonded to each other.[8]

Classical Laminated Plate Theory (CLPT) can be used to study the curvature of anisotropic laminate composites. This theory defines stresses, strains and deformations in thin plates that undergo small deformations.[8] CLPT is valid for large dimensions, in-plane, relative to its maximum thickness where only plane stress is observed and where minor deflections are involved, again relative to the maximum thickness.[8] However, many researchers have studied warping (curvature) in thin unsymmetric laminates composites for which CLPT does not completely support the theoretical curvature geometry with the experimental results.[3,9-11] The CLPT assumes a linear behavior where the strain varies linearly through the thin thickness of the composite and there is a two-dimensional plane stress analysis.[12] The CLPT predicts a saddle shape for room temperature (RT) anisotropic fiber reinforced composites.[3,9-11] However, the CLPT can not predict the curvature found in thin unsymmetrical laminate composites.[3,9,10] Therefore, a nonlinear extension of the CLPT was developed in order to account for the non-planar geometries as the laminates were cylindrical in nature and also found to have multiple shape conformations.[9,10] Some of the additional shapes found were referred to as a snap-through phenomenon where two shapes were obtained at RT.[9] The nonlinear extension of the CLPT was done by including the geometric nonlinearity in the strain-displacement relationship.[9] Hyer, a scholar in this theory, discovered that the resultant shape depends on the permanent geometry of the laminate when using the modified CLPT.[10] When the laminate sidelength is smaller than a critical length, a saddle geometry results; however, when side length is larger than the critical length, then a saddle or two cylindrical shapes can form where the thickness of the laminate was also correlated to the curvature shape.[10]

Additionally, it has been reported that the higher processing temperature required for highly temperature resistant resins (bismaleimides, epoxies, etc.) and thermoplastics leads to reduced levels of moisture and essentially leads to residual stresses.[13] Composites that have a non-symmetric cross-ply (lamina) configuration have shown to have warpage from residual stresses. White et al. studied the residual stress developed during cure in a Graphite/BMI (modified polyimide resin) composite system using a $[0_4/90_4]_T$ lamina configuration. Using a specified curing cycle, the warpage due to the residual stress, the longitudinal and transverse modulus and strength was observed and studied during cure.[13] The tested specimens of 51 x 216 mm were chosen and a cylindrical curvature was detected. At the initial stages of the cure minimal curvature was observed and then increased promptly towards the end of the curing process where a dimensionless curvature value of 31.8×10^4 was reported.[13] Evidence of transverse cracking was also observed in the laminate during the curing process which resulted in the reduction of residual stress and essentially a drop in curvature.[13] This decrease was due to the dissipation of energy at the cracks sites that formed in the specimens. The authors argued that when the transverse modulus was developed first, followed by the transverse strength, transverse cracking was evident.[13] Additionally, the authors also argued that when the transverse strength was lower than that of the transverse modulus, residual stresses were produced. When there was evidence of transverse cracking, the elastic analysis dominated the curvature effect since the cracking reduced the residual stress in the laminate system. This study also used the laminated plate theory (LPT) to model the dimensionless curvature during the cure process.

Barnes et al. studied the macro and micro stresses found in laminated composites. Here, the authors state that there are ‘microstresses’ found between fibers within each ply and are referred to as the primary level of stresses.[7] There is also a second level of stresses referred to as 'macrostresses' that are formed at a ply-to-ply level for multiaxial laminates.[7] These stresses are formed because of the variable individual ply coefficient of thermal expansion in the different directions.[7] Lastly, there are also tertiary stresses created from the differential thermal histories from the cooling process where these stresses arise through the thickness of the laminates.[7]

We now turn our attention to soft anisotropic materials. Other systems, such as flat twist nematic elastomer (TNE) films, have been found to exhibit helicoids and spiral geometries of relevance to this Chapter. Sawa et al. showed both experimentally and theoretically how TNE changes geometry upon a thermal stimulus.[14] Nematic elastomers (NE) are a distinct class of materials where they are crosslinked with liquid crystal elastomers. Here, the chiral arrangement from the liquid crystal mesogens engender a nematic orientation property where the material maintains softness and elasticity.[14] With this combination of properties, the TNE exhibits distinctive shapes that are sensitive to external stimuli. After studying the films response to temperature it was observed that the nematic orientation order changes by 90° from top to the bottom surface.[14] The shape of the TNE is primarily directed by the width-to-thickness ratio where narrow TNE films exhibit a helicoid configuration upon a temperature change. However, as the width-to-thickness ratio increases to a critical value, the films form into spiral ribbons when exposed to a specified temperature. This paper also explains the handedness of the spiral change as well as the pitch analysis with respect to the width-to-thickness ratio and the temperature. Furthermore, the paper also proposes theoretical predictions on how the curvature can be modeled by considering an elastic energy and a curvature tensor.[14]

5.1.3 ANISOTROPY IN BIOLOGICAL SYSTEMS

Biological systems found in the human body have shown to have anisotropic fiber configuration. Specifically, native extracellular matrix (ECM) is known to be made of a fibrous protein matrix.[15] For example, the dermis ECM is divided into two compartments: a superficial papillary and deep reticular layer. The superficial layer is comprised of Type III collagen and elastin small diameter fibers that are nominally arranged in an anisotropic fashion. Whereas the deep reticular layer is made of Type I collagen and elastin large diameter fibers that are arranged in random bundles.[15] Additionally, the ECM is also used as a communication medium for phenotypic signals of the skin where these signals control cell function and healing remodeling.[15] Researchers are studying such biological systems to synthetically fabricate tissue engineering scaffolds for biomedical applications.

Heart muscle tissue known as myocardium has been shown to be highly anisotropic where the fibers are organized in an anti-symmetric architecture.[16] Myocardium has multiple layers of ECM where highly compacted oriented cells are evident and where ECM is the main driving force for cell alignment.[17] Researchers have studied myocardial fibers in order to synthetically tissue engineer grafts for heart tissue repair.[18,19] Engelmayr et al. has asserted that the scaffolds made in the past have not replicated cardiac anisotropy and therefore developed an elastic poly(glycerol sebacate) (PGS) accordion-like honeycomb (ALH) that was a 3D porous stiff anisotropic scaffold.[18,19] Here, the author states that the use of a ALH scaffolds can assist in the development of cell alignment with similar mechanical properties found in native myocardium.[18,19]

Researchers are now looking for methods for analyzing tissue engineering scaffolds when an electrospinning process is used for fabrication. Ayres et al. fabricated tissue engineering scaffolds via electrospinning and used the fast Fourier transform (FFT) to measure the degree of fiber alignment.[15] The authors hypothesized that electrospinning can replicate the fiber diameter size and pore dimensions that are found in native ECM. Here, gelatin was used in an electrospinning solution where the concentrations, solvents, and mandrel rotation were varied. The FFT function was used to study the fiber anisotropy as this function converts the data from real to frequency space. The result yielded a grayscale pixelated image to reveal the degree of fiber orientation.[15] A fiber specimen that has symmetric fiber alignment yielded a pixel image that was a circularly symmetric shape because the pixel frequency was identical in any direction. Conversely, a fiber specimen that is highly anisotropic, showed a pixilated image where the pixels were directed in an elliptical shape thus proving fiber alignment.[15] A graph of intensity vs degree of fiber alignment was then generated from the FFT pixelated image by taking a circular projection and performing a pixel intensity radial summation from 0° to 360°. The results showed that using specified electrospinning parameters, the fiber diameter and pore dimensions can be altered to achieve desirable mechanical propertied while using FFT to assist in evaluating the the fiber anisotropy.

Synthetic hydrogels have also been great candidates for cardiac tissue engineering due to their viscoelastic and soft attributes necessary for imitating native tissue.[17] Polymers such as poly(ethylene glycol) (PEG), polyurethane (PU), polylactide (PLA), polyacrylamide (PAAm) and polyactide-glycolic acid (PLGA) are common polymers that are used for cardiac tissue engineering as the water affinity, degradation rate, modulus, physical and chemical properties can be tailored to meet the desired requirements.[17] Human tendons and ligaments have also been shown to be are highly anisotropic composite materials that contain collagen fibrous bundles that are encompassed in a mucoso-polysaccharide and elastin hydrogel-like structure.[20]

Other biological systems that exhibit spiral effects are plants referred to as Passiflora edulis, which are climbing plants that have long, flexible and curly tendrils.[21] In it's natural state, the tendrils form spirals or helices where both handednesses are observed. Godinho and coworkers synthetically model this behavior by using liquid crystalline cellulosic fibers.[21] This was done by first electrospinning aligned fibers where a specially designed fiber collector to obtain the alignment was constructed. The fiber collector consisted of two aluminum strips parallel to each other that were fixed together by conductive aluminum wires. The paper explained the study of the physical mechanism of self-winding due to the intrinsic curvature displayed in the tendrils.

Despite this breadth of relevant past work, little work, has been done to understand the curvature of soft elastic anisotropic fiber reinforced composite strips that deform under in-plane stress conditions upon unloading at RT. In the following chapter, laminae with varying fiber orientations were used to make dual laminated composites where upon the removal of a tensile load, the residual stresses in the composite produced unique out-of-plane curvature. In this sense, we reveal an approach to mechanically activated shape change (MASC) in a soft material.

5.2 EXPERIMENTAL METHOD

5.2.1 MATERIALS

Poly(vinyl acetate) (PVAc) (M_w = 260k g/mol), methanol (MeOH), and dimethylformamide (DMF) were purchased from Sigma Aldrich. Gel Permeation Chromatography (GPC) confirmed the M_w of PVAc was 249k g/mol. The PVAc pellets were dried at room temperature (RT) overnight prior to use. Poly(dimethylsiloxane) (Sylgard 184) was purchased from Dow Corning and stored in a refrigerator prior to use.

5.2.2 MATERIALS AND SINGLE PLY COMPOSITE FABRICATION

The anisotropic shape memory elastomeric composite (A-SMEC) was composed of two commercially available polymers, poly(dimethylsiloxane) and poly(vinyl acetate) (PVAc), and fabricated using a three step process shown in Scheme 5-1. First, PVAc fibers were electrospun to achieve aligned fibers. Electrospinning is a term used to describe a set of equipment that draws out fibers from a polymer solution and the fibers collect on a rotating mandrel where a specified voltage is used for fiber drawing.[22-24] A solution with a volumetric ratio of 7:3 of MeOH:DMF and 2.00 g of PVAc was made and stirred at 500 RPM at 30 °C overnight. The electrospinning parameters used to achieve fiber orientation were as follows: RPM = 3000, drum diameter = 2 in., syringe voltage = +13.5 kV, drum voltage = -0.5 kV, flow rate = 0.7 mL/h, drum-to-tip distance = 7 cm and runtime = 7 h. A steel plate was attached to the syringe to allow for parallel electrical field lines between the drum and the plate. The parallel electrical field lines enhanced the anisotropy of the fibrous web further than the high angular velocity of the drum alone. The resulting fibrous web was then infiltrated by a two-part mixture of Sylgard184 (base:

curing agent ratio = 10:1) with vacuum (30 in.Hg) applied for 20 min to ensure complete infiltration of Sylgard into the PVAc fibrous web. After carefully removing the excess Sylgard from the fibrous web with a spatula, the Sylgard was cured at 30 °C for 48 h (Scheme 5-1). Scanning Electron Microscopy (SEM) was used to image the topography of the fibrous webs and composite sheets. The fiber SEM micrograph was used to calculate the average fiber diameter by using ImageJ software for the analysis process.

5.2.3 LAMINATED COMPOSITE FABRICATION

Once the A-SMEC single sheet was fabricated, 25.30 (l) x 25.30 (w) mm plies were cut at the following angles: 0° (axial), 22.5°, 45°, 67.5°, and 90° (transverse) (Scheme 5-2). A protractor was used to make paper-angle templates to achieve the desired fiber orientation during the cutting process. An arrow was drawn on the top-most-left corner of each ply in order to line up the arrows during the lay up process (Scheme 5-3). These plies were then used to make the following dual laminated composites (bottom ply/top ply): 0/0°, 0/22.5°, 0/45°, 0/67.5°, and 0/90°. The laminated composites were fabricated by first applying a thin layer of Sylgard184 (base: curing agent ratio = 10:1) in between the plies so that the two plies were laminated by the Sylgard layer. This layered sample was then placed in-between two metal plates where a 1000 g weight was applied on the top plate (Scheme 5-3). Weigh paper was used between the metal plates and layered composite to prevent excess Sylgard from touching the metal plates. The layer of Sylgard and 1000 g weight were used to allow for good adhesion between the top and bottom ply. The composites were then cured at 30 °C for 24 h. SEMs were taken of the cross section of each laminated composite to check for adhesion between the ply-Sylgard interface, observe the fiber orientation in the composite lay-up and study the cross section morphology.

5.2.4 REVERSIBLE PLASTICITY SHAPE MEMORY (RPSM)

A new effect well established in our group is a phenomenon described as reversible plasticity shape memory (RPSM) where it measures and tests for the reversal of the elastic and plastic deformation upon a thermal stimulus. RPSM effect was quantified using a dynamic mechanical analyzer (DMA) using a 5 step process. This was done in order to understand the fixing and recovery ratios of each system as a function of fiber orientation at RT. Single A-SMEC sheets were tested using the following fiber orientations: 0° (axial), 22.5°, 45°, 67.5°, and 90° (transverse). The A-SMEC sheet used for RPSM testing was the same as explained and characterized in Chapter 4. Please see chapter 4 for A-SMEC sheet characterization. The RPSM experiment was conducted by first removing the thermal history by heating each sample in an isothermal oven at 80 °C for 10 min and cooling at RT for 10 min. Rectangular strips with dimensions of 5.14 $\pm$ 0.37 (l) x 1.90 $\pm$ 0.31 (w) x 0.35 $\pm$ 0.03 (th) mm were cut from the A-SMEC sheet where the sample was then clamped in the DMA using the tensile fixtures and equilibrating the temperature to RT where the preload was set to 0.001 N (step 1). This temperature was held isothermally for 1 min. The sample was then uni-axially strained at 5 %/min to 100 % (step 2). Once the sample achieved the desired strain, this strain was held for 10 min. The strain was then decreased to 0 % at 5 %/min until the force reached the preload of 0.001 N (step 3) to observe temporal fixing of the sample. The sample was then heated to 80 °C at 3 °C/min to allow for shape recovery (step 4) and then cooled to RT to complete the RPSM cycle (step 5). A 3D plot showing stress vs. strain and temperature were plotted as a function of layup configuration for the laminated composites. Three different samples were tested for each composite system for reproducibility. The fixing (R_f) and recovery (R_r) ratios were then calculated using the following equations:

$$R_f(N) = \frac{\varepsilon_u(N)}{\varepsilon_m(N)} \times 100\% \tag{5-6}$$

$$R_r(N) = \frac{\varepsilon_u(N) - \varepsilon_p(N)}{\varepsilon_u(N) - \varepsilon_p(N-1)} \times 100\% \tag{5-7}$$

where ε_m is the maximum strain achieved by deformation, ε_u is the fixed strain after unloading, ε_p is the permanent strain after recovery, and N is the cycle number.[24,25]

5.2.5 MECHANICAL TESTING

To observe and measure the curvature and pitch resulting from tensile deformation of each laminated system (MASC), uniaxial tensile testing was performed. Small rectangular strips with cross section dimensions of 1.55 ± 0.23 (w) x 0.6 ± 0.05 (th) mm were cut from each of the laminates. The rectangular strip was cut parallel to the axial fiber orientation (i.e. bottom ply). Each strip was measured for thickness and width prior to deformation. Uniaxial tensile testing was performed using a Linkam TST 350 tensile testing system where a 20 N load cell, $\text{velocity}_{\text{deformation}}$ = 100 μm/sec and $T_{\text{deformation}}$ = 25 °C were used. Small pieces of sand paper covered the sample tabs to prevent sample slippage from the tensile clamps. Each specimen was marked using a black sharpie to designate the 15 mm gauge length, and the tensile clamps were positioned at these black marks. This position indicated the zero position. The force and displacement values were 'zeroed' prior to deformation using the Linksys32 software. Samples were then deformed to 100 % strain. Scheme 5-4 shows pictorial representation of the mechanical testing and MASC processes. Prior to unclamping the samples, the distance between the two black marks post-deformation was measured and used for percent deformation (*D* (%)) and percent recovery (*R* (%)) calculations (these calculations will be explained in section 5.2.6). The samples were then quickly unclamped where the curvature and pitch were observed by imaging. Four samples were tested for each laminated system for reproducibility. Force and displacement data were recorded where stress vs strain curves were calculated using the gauge length, width and thickness of the each sample. The Young's modulus and yield stress were also calculated from the stress vs. strain curves.

5.2.6 DEFORMATION AND SHAPE MEMORY RECOVERY ANALYSIS

Percent deformation (*D* (%)) and percent recovery (*R* (%)) analysis were conducted for each composite to study and compare the deformation and recovery among all the systems tested. Post uniaxial testing, each specimen was then recovered by heating in an isothermal oven at 80 °C for 5 min and cooled at RT for 5 min where images were taken after shape recovery. Representative videos were taken of each system on a hot plate for shape recovery observation. The following equations were used to calculate *D* (%) and *R* (%):

$$D(\%) = \frac{L_{deform} - L_{orig}}{L_{orig}} x\ 100\ \% \qquad (5\text{-}8)$$

$$R(\%) = \frac{(L_{deform} - L_{recov})}{L_{deform-}L_{orig}} x\ 100\ \% \qquad (5\text{-}9)$$

where *D*(%) is the deformation achieved in percentage after the sample was stretched, *R*(%) is the recovery attained in percentage when the sample was heated to recover, L_{orig} is the original length before deformation, L_{deform} is the length post-deformation, and L_{recov} is the length after recovery. A bar graph of $D(\%)$ and $R(\%)$ was produced.

5.2.7 CURVATURE AND PITCH ANALYSIS

ImageJ analysis was conducted in order to calculate the curvature and pitch for each sample subjected to mechanically activated shape change (MASC). Each image was imported into ImageJ where circles were drawn by tracing over curvature sections formed on the sample. ImageJ reported a diameter value of the circle drawn in pixels where this value was then converted to millimeters by using a calibrated reference (Figure 5-1). Pitch was also calculated by measuring the distance between peaks from the curvature that was formed (Figure 5-1). The following equations were used to calculate curvature and pitch:

$$k[mm^{-1}] = \frac{1}{R\ [mm]} \qquad (5\text{-}10)$$

$$Pitch = Peak - to - Peak\ Distance\ [mm] \qquad (5\text{-}11)$$

Graphs of curvature and pitch as a function of laminated composite systems were produced.

5.3 RESULTS AND DISCUSSION

5.3.1 COMPOSITE SHEET FABRICATION

An A-SMEC composite sheet was constructed in order to cut small plies for laminated composite fabrication. First, an aligned fibrous web was e-spun using the parameters mentioned in Section 5.2.2 where Sylgard184 was infiltrated in the fibrous web and allowed to cure to form an A-SMEC sheet. The fibrous web had dimensions of 158.0 (l) mm x 126.1 (w) mm with an average thickness of 0.16 ± 0.03 mm and weighed 1.05 g. The A-SMEC sheet had dimensions of 157.5 (l) mm x 127.5 (w) mm with an average thickness of 0.33 ± 0.05 mm and weighed 6.05 g. In comparing the weights of the fibrous web to the A-SMEC sheet, the calculated fiber density was 17.35 wt-%. Figure 5-2 (a) shows an image of the aligned fibrous web where Figure 5-2 (b) shows the A-SMEC sheet depicting the axial and transverse orientations. Figure 5-2 (c) (i) shows an SEM micrograph of PVAc aligned fibers where the average fiber diameter was 0.81 ± 0.19 µm. Figure 5-2 (c) (ii) to (iv) shows the surface morphology (topography) of the composite and the cross section of the composite in the axial and transverse direction respectively. The SEM micrographs show complete infiltration of Sylgard184 along the thickness of the fibrous web while also showing evidence that the fiber alignment was preserved in the Sylgard elastic matrix. Additionally, the SEMs confirmed a two-phase morphology in the composite system.

5.3.2 LAMINATED COMPOSITE FABRICATION

Laminated composites were fabricated by cutting plies from the A-SMEC sheet at different angles in relation to the axial direction and cured by laminating the plies using a thin Sylgard layer. The average weight of the single plies prior to the layering process was 183.2 ± 19.4 mg with an average thickness of 0.27 ± 0.03 mm. The dual laminated composites had an average weight of 391.4 ± 18.8 mg with an average thickness of 0.56 ± 0.03 mm. The thin layer of Sylgard used for laminate the two plies had an average weight of 25.1 ± 5.1 mg with an average thickness of 0.02 ± 0.01 mm. SEM micrographs of the laminated composites were taken where Figure 5-3 shows represented SEMs of each laminated composite’s cross section. The SEMs show that the plies were laminated well where good adhesion is evident between the ply-Sylgard interface while keeping fiber alignment in their respective piles. Figure 5-3 (a) shows the 0/0°

composite where the top and bottom plies have fibers that are oriented in the axial direction (coming out of the page). Figure 5-3 (b) shows the 0/22.5° composite where the top ply has fibers oriented in the axial direction and the bottom ply has fibers oriented at an angle of 22.5°. Figure 5-3 (c) shows the 0/45° composite where the top ply has fibers oriented in the axial direction and the bottom oriented in the 45° direction. Figure 5-3 (d) shows the 0/67.5° composite having the top ply with fibers oriented in the axial direction and the bottom oriented in the 67.5° direction. Lastly, Figure 5-3 (e) shows the 0/90° composite where the top ply is indicative of the fibers oriented in the axial direction and the bottom oriented in the 90° direction. In observing the cross section of the bottom ply, the fiber surface goes from having a dotted to a striated morphology indicating the change in fiber orientation. The smooth region in between the plies is the Sylgard bonding layer.

5.3.3 REVERSIBLE PLASTICITY SHAPE MEMORY (RPSM)

To characterize the shape memory (SM) effect of the composites, a unique SM referred to as reversible plasticity shape memory (RPSM), was achieved and shown in the 3D plots in Figure 5-4. Here, single A-SMEC plies were first stretched at RT, which is below the T_g of the PVAc fibers but above the T_g of the elastomeric matrix, to achieve 100 % strain (Figure 5-4 (a), step 1 - 2). Although macroscopically the PVAc fibers are oriented, it is hypothesized that the PVAc fibers are further molecularly aligned along the axis of each fiber. This means that the electrospinning process transforms the PVAc chains from a high entropy coiled conformation to a low entropy, oriented state. It is important to observe that the PVAc glassy fibers are first elastically and then plastically deformed at RT due to the deformation temperature being below the T_g of the fibers ($T_{def} < T_{g,PVAc}$ where the $T_{g,\ PVAc} = 40.43$ °C; previously reported in Chapter

4). Conversely, the elastomeric matrix, already in its rubbery plateau, is only elastically deforming and conforming to the deformation due to the temperature being higher than the T_g of the matrix ($T_{def} > T_{g,Sylgard}$ where the $T_{g,\ Sylgard} = -115.2$ °C[24]). Due to this, the elastomeric crosslinked thermoset matrix, Sylgard184, aligns in the direction of deformation where the polymer chains and crosslinks orient in the same direction as those of the PVAc fibers. The force was then released to a preload of 0.001 N after 100 % strain was accomplished (Figure 5-4 (a), step 2 - 3). This step was conducted to observe and study the fixing properties that are attained for each of the composite in relation to the fiber alignment. Once the force reached the preload, the temperature was increased from RT to 80 °C at 3 °C/min to observe shape recovery (Figure 5-4 (a), step 3 - 4) and finally cooled to RT to complete the RPSM cycle (Figure 5-4 (a), step 4 - 5). It can be seen in all the curves in Figure 5-4 that the fixing properties vary with changing fiber angle. Specifically, the fixing properties decrease with increasing fiber angle. It is evident in Figure 5-4 (a) that the composite with fibers oriented in the axial direction showed the highest fixing achieved when compared to the other composites. This is essentially due to the highly oriented PVAc fibers that are serving as reinforcements. PVAc is a highly glassy rigid polymer as opposed to its elastomeric counterpart which is a rubber. Here, the fibers prevent the elastomer from contracting and returning to a highly entropic state, forcing the elastomer to conform to the temporal deformation. However, the composites with the lowest fixing were those that had fibers embedded in the matrix in the transverse direction (Figure 5-4 (e)). The lower fixing is attributed to the inability of the fibers to prevent the elastomer from contracting and returning to its higher entropic state. For these composites, the contraction force occurs perpendicular to the direction of fiber orientation, resulting in the inability of the fibers to resist the contractile force. The intermediate angles between 0° and 90° have fixing effects between the fixing of these two extreme orientations. The 3D plots in Figure 5-4 (a) - (e) also shows the strain vs. temperature in the back face and the stress vs strain in the side face for each composite tested. For comparison, representative RPSM curves were overlaid to observe the difference in fixing among the specimens tested and is shown in Figure 5-5 (a). Representative curves of strain vs. temperature are shown in Figure 5-5 (b) where the difference in fixing is more apparent among the composites with varying fiber angles. Here, all specimens achieved 100% strain, however the fixing was directly guided by the fiber orientation upon unloading at RT. As the fiber angle increased the fixing decreased. Once the fixity was recorded, the sample was then heated from RT for 80 °C to initiate shape recovery and then brought back to RT to complete the cycle. All samples recovered with minimal residual stresses. Representative curves of stress vs. strain were also shown as a function of composite tested to observe the mechanical response of the loading and unloading (Figure 5-5 (c)). Here, all samples exhibited a linear elastic response until each reached their yield point. It is apparent that the yield point was directed by the fiber angle. Once the specimens reached the yield point, plastic deformation was apparent followed by the cold drawing region. It is hypothesized that the matrix and fibers were molecularly aligned in the loading direction before unloading occurred at 100% strain. The sample recovery then followed where all the specimens exhibited a different recovery path owing to the difference in fixing. Note that the recovery was promoted by heating each sample. From Figure 5-5 (c), the Young’s modulus showed to be higher among the specimens that have fibers oriented in the 0° direction where the lowest was evident in the samples with fibers oriented in the 90° orientation. The specimens with fibers oriented at the intermediate angles fell within these two extreme angles. The Young’s modulus trend is confirmed for consistency when looking at strain-to-failure data shown and explained in Chapter 4 as both data sets show the same phenomenon.

These values can be explained quantitatively by considering the modulus equation shown in Section 5.1.1 for fiber reinforced composites that have fibers in an axial orientation (E_l) (Eqn. (5-1)). E_l predicts the modulus of the fibers and matrix are linearly proportional to the overall composite modulus. The modulus of the PVAc fibers is higher than that of the Sylgard matrix and therefore contributes to a higher overall composite modulus. It is also important to state that the PVAc fibers alone have higher mechanical properties than the matrix because PVAc is a glassy rigid amorphous material where the matrix is a low crosslinked rubber with high elasticity. Conversely, the modulus equation shown in Section 5.1.1 for fiber reinforced composites with fibers in the transverse direction (E_t) (Eqn. (5-2)), predicts that the overall modulus is proportional to the ratio of the volume fraction and modulus of the fibers and matrix. Therefore, if the modulus of the fiber phase is higher the overall composite modulus will be high as these two are linearly proportional to each other. Additionally, the strength of the composite, as seen in Figure 5-5 (c) from the stress vs. strain curves, can be explained through the composite strength equation (Eqn. (5-3)) shown section 5.1.1 where the strength of the matrix, fibers and the fiber volume fraction are linearly proportional to the strength of the composite when the fibers are in the longitudinal direction (σ_l). The strength of the composite in the transverse direction can be explained by equation 4 (σ_t) in section 5.1.1. The composite modulus (E_c), volume fraction of the matrix and fiber (V_m, V_f) phase and the strain of the matrix and fibers (ε_m and ε_f) are linearly proportional to the transverse strength.

The fixing (R_f) and recovery (R_r) ratios were calculated using Eqn. (5-6) and (5-7) detailed in Section 5.2.4. Figure 5-6 shows a bar graph of the fixing (R_f) and recovery (R_r) ratios for three samples tested as a function of fiber alignment. The R_f decreased with increasing fiber orientation where the R_f ranged from 84.5 ± 6.9 % (0°) to 21.1 ± 0.5 % (90°) (Table 5-1). It is evident from the values shown in Table 5-1 that the fixing effect decreases with increasing fiber angle. This was expected, as the fibers are gradually rotated from an angle enabling reinforcement to an angle unable to resist the overall elasticity and entropic contraction of the elastomer matrix. R_r for all composites was found to be in the range of 60 - 80%. It is hypothesized that the composites did not completely recover to 100% due to residual stresses that may have been unrecovered.

5.3.4 MECHANICAL TESTING AND MECHANICALLY ACTIVATED SHAPE CHANGE (MASC)

To observe the curvature and pitch of the laminated composites, each sample was uni-axially strained to 100%. It was observed that the all the specimens bowed upward slightly when clamped firmly in between the tensile clamps pre-deformation. It is hypothesized that sample bowing was due to uneven clamping. All samples turned white while strained which is theorized to be evidence of plastic deformation. Once strained, the samples were unclamped rapidly to allow the fibers and elastomeric matrix to elastically relax where the change in geometry was observed and studied. Figure 5-7 shows all the stress vs. strain curves where four specimens were tested for each system. All stress vs. strain curves showed evidence of an elastic region, yield point and cold drawing region regardless of fiber composite configuration. This behavior is quite common among viscoelastic polymeric materials. From the stress vs. strain curves, the Young's modulus and yield stress were calculated and shown in Figure 5-8 (a) and (b). Table 5-2 (a) shows the average Young's modulus as a function of dual laminated composite. For simplicity, henceforth ply 1 will be referred to as the ply with the changing fiber angle (22.5°, 45°, 67.5°, or 90°) where ply 2 will be referred to as the ply whose fibers remain oriented in the axial direction (0°). The Young's modulus showed a decreasing trend when ply 1 had an increasing fiber angle relative to ply 2. As summarized in Table 5-2 (a), the highest Young's modulus achieved was shown among the 0/0° specimens (49.3 $\pm$ 6.8 MPa), where the lowest was evident in the 0/90° specimens (37.2 $\pm$ 5.1 MPa). The modulus of the composite can be explained by the theoretical equation for calculating $E_{composite}$ for laminated systems. As explained in Section 5.1.1 Eqn. (5-5), the area (A) and modulus (E) of ply 1, ply 2 and the Sylgard layer found in between the plies divided by the area of each will yield the overall modulus of the composite. Since the area of both plies (A_{p1} and A_{p2}), Sylgard layer (A_s) and the modulus of ply 2 (E_{p2}) are constant, the only variable changing is the modulus of ply 1 (E_{p1}).Therefore, as E_{p1} increases, the $E_{composite}$ increases and if E_{p1} decreases the $E_{composite}$ decreases because they are linearly proportional to each other. To test this theory, Eqn. (5-5) was used to calculate the theoretical $E_{laminated\ composite}$ values, which were then compared to the experimental $E_{laminated\ composite}$ values. When calculating the theoretical $E_{laminated\ composite}$ values, the thicknesses of the single plies shown in Table 5-3 and the width values from Table 5-4 were used to determine the area (A_{p1}, A_{p2} and A_s) for ply 1 ,ply 2 and the Sylgard layer. The modulus of ply 1, ply 2 and the Sylgard184 (E_{p1}, E_{p2}, and E_s) were taken from Table 4-3 which was calculated from the strain-to-failure data. Table 5-5 shows the theoretical and experimental values of the Young's modulus where the 0/0° laminated composite only had a 3.7% difference between experimental and theoretical. This was calculated by using the following equation: $(E_{experimental} - E_{theoretical})/(E_{theoretical}) * 100$. This means that the experimental data is following the expected theoretical theory of (Eqn. (5-5)). However, the remaining composites (0/22.5°, 0/45°, 0/67.5°, and 0/90°) showed to have a 23% or greater difference (Table 5-5). This discrepancy in difference may be due to the different strain rates used to obtain the single ply's Young's modulus and the laminated composite's Young's modulus. The strain rate is an important variable as the Young's modulus is strain rate dependent among glassy (amorphous) polymers below their T_g. This is due to the fact that the conformations of polymer chains are a function of strain rate. For example, if a high strain rate is applied, this leads to higher modulus values. The faster the polymer chains are deformed, the less time they have to conform to the applied loading and will resist the deformation thus leading to a higher Young's modulus. However, if a slow strain rate is applied, the polymer chains will have a longer amount of time to change their conformations to the loading direction thus yielding in a lower Young's modulus. Therefore, the conformations of polymer chains effect the Young's modulus of materials. It is also important to mention that the fibrous web used to fabricate single A-SMEC plies was not the same fibrous web used to make the laminated composite strips. This may have resulted in a different fiber volume fraction, different degree of fiber alignment as well as not cutting the ply exactly at the desired angles. All these could be factors that may have contributed in the dissimilarities of the $E'_{\text{experimental}}$ and $E'_{\text{theoretical}}$ values. However, both data sets show a trend of decreasing Young's modulus as ply 1 increases in fiber angle.

The average yield stress was then calculated where the highest was observed for the 0/0° system (3.2 + 0.1 MPa) Table 5-2 (b) and the lowest among the 0/90° system (1.9 $\underline{+}$ 0.1 MPa) Table 5-2 (b). The yield stress is higher in the 0/0° system as there is more stress required to elastically and plastically deform the PVAc fibers in the axial direction since both plies are acting as reinforcements along the loading direction. Conversely, less stress is needed to elastically and plastically deform the 0/90° specimens as ply 1 has fibers in the transverse direction and the contraction of the elastomeric matrix is dominating the reinforced fibers in ply 2. Although these systems are dual laminated composites, they still exhibit the same trend of mechanical behavior as those observed for the single ply composite systems explained in Section 5.3.3.

5.3.5 DEFORMATION AND SHAPE MEMORY RECOVERY ANALYSIS

Percent deformation (*D (%)*) and recovery (*R (%)*) were then calculated for each specimen tested using Eqn. (5-8) and (5-9) explained in Section 5.2.6. This was done after the samples were strained using the Linkam tensile stage and after analyzing the pitch and curvature of the dual laminated composites. The samples were heated to 80 °C for 5 min and cooled at RT for 5 min for shape recovery post-deformation. Figure 5-9 shows a bar graph of *D (%)* and *R (%)* where all samples regardless of fiber orientation achieved a range of 101.1 to 101.9 % *D (%)* where the *R (%)* was approximately 97 % for all composites (Table 5-6). These sets of experiments are another way to conduct RPSM experiments on laminated composites ($\text{RPSM}_{\text{dual}}$), similar to what was done for the single ply composites ($\text{RPSM}_{\text{single}}$). For these $\text{RPSM}_{\text{dual}}$ experiments, slightly higher recovery ratios were evident when compared to the $\text{RPSM}_{\text{single}}$ data explained in Section 5.3.3. It can be hypothesized that larger recovery ratios are owed to the initial recovery when the samples were unclamped and relaxed to form a temporal geometry change. It can also be observed from the $\text{RPSM}_{\text{dual}}$ experiments that both the elastic and plastic deformation are completely reversible upon a thermal stimulus where all samples are shown in Figure 5-10.

5.3.6 CURVATURE AND PITCH ANALYSIS

Each specimen was uniaxially strained in order to observe the curvature and pitch after each sample was unclamped from the Linkam tensile stage, allowing the sample to elastically recover.

Figure 5-11 shows images of the curvature configurations that were formed from the various laminated composites tested. It can be observed that as the fiber angle in ply 1 increases in relation to ply 2, more curvature is evident leading to a tighter curl observed. For this reason, different circles formed and are identified as follows: a = primary, b = secondary, and c= tertiary curvature as seen in Figure 5-11. Curvature (*k*) analysis was conducted by using Eqn. (5-10) explained in Section 5.2.7 to calculate the curvature. Figure 5-12 shows a graph of curvature vs. laminate composite system where the primary, secondary, and tertiary curvatures are labeled corresponding to each system. Figure 5-12 shows an obvious trend of increasing curvature when ply 1 has a fiber angle larger than ply 2. For example, the 0/22.5° composite showed primary and secondary curvature where the primary curvature was a tight curl that had a k range between 0.12 to 0.56 mm^{-1} and a secondary curvature describing the loose curls ranging from 0.08 to 0.38 mm^{-1} k values (Table 5-7). In the extreme case, the 0/90° system exhibited primary, secondary and tertiary curvature ranging from 0.77 to 0.91 mm^{-1} for primary, 0.56 to 0.58 mm^{-1} for secondary, and 0.47 to 0.51 mm^{-1} for tertiary curvature (Table 5-10). All other composites that had intermediate angles between the two extreme angles had k values that fell into their range (Table 5-8 – 5-9).

The ply with a higher fiber angle naturally contracts more than the ply whose fibers are in the axial direction upon relaxation. Ply 2 elastically recovers while ply 1 is elastically recovering in its plane. The elastic recovery from two planes in the laminated composite is acting as a coupling moment yielding a curvature response. This curvature phenomenon can also be explained through the fixing observed from the RPSM data among all laminated composites. In general, low fixing will yield more elastic recovery. For example, for 0/0° specimen, there is no curvature evident as the elastic recovery in both plies is equal. However, in a 0/22.5° laminated composite, the elastic recoveries from ply 1 (22.5°) and ply 2 (0°) are different and therefore yields a curvature response due to the difference in fiber orientation angle. Therefore, as the fiber angle in ply 1 increases, the fixing ratio decreases and yields a high elastic recovery response. It can be postulated that ply 1 wants to recover more than ply 2 and therefore the curve response is formed in the composite. If this is considered, then as the fiber angle in ply 1 increases, the amount of elastic recovery increases and the more curvature response is apparent towards ply 1 in the laminated composite system. This results in a trend of increasing curvature with increasing fiber angle in ply 1. Scheme 5-5 shows each ply's behavior upon unloading in its un-laminated and laminated state to assist in describing the curvature response. Scheme 5-5 (a) shows the behavior in ply 1 where the fibers are aligned in either of the following angles: 22.5°, 45°, 67.5°, or 90°. Scheme 5-5 (b) shows the behavior of ply 2 where the fibers are aligned in the axial orientation. Scheme 5-5 (c) shows the behavior upon unloading of ply 1 and ply 2 when they are laminated to form a composite. The curvature response is associated with the displacement mismatch where ply 1 recovers more than ply 2 resulting in the curvature towards ply 1.

The pitch observed in the laminated composites showed a dependence in fiber angle in ply 1. Pitch images corresponding to the laminated composites tested in this study are presented in Figure 5-13. The pitch is more visually evident among the 0/22.5° specimens as there is a prominent distinction between the peak-to-peak distance (Figure 5-13 (b)) as opposed to the 0/90° specimens (Figure 5-13 (e)). Figure 5-14 shows a graph of pitch vs. laminated composites where some systems exhibited primary and secondary pitch values and labeled (a) and (b) in Figure 5-13. Here, there is an evident trend of a decrease in pitch with increasing fiber angle in ply 1. For instance, when looking at the 0/22.5° system, the pitch values ranged from 1.3 to 4.6 mm (Table 5-11) where the 0/90° system showed a range from 1.2 to 2.0 mm (Table 5-13). Pitch values for the 0/67.5° system were between the 0/0° and 0/90° systems (Table 5-12). It can also be observed that as fiber angle increases in ply 1, the specimen exhibits a chiral effect where the sample strip curled within itself. This is apparent for the 0/45°, 0/67.5°, and 0/90° systems. This yielded a slight difficulty in deciphering between the peak-to-peak distances especially for the 0/45° system where no pitches could be identified. It is hypothesized that the pitch can be explained by the directionality of fixing in the ply with variable fiber angle. However, further studies need to be conducted to model the pitch response among the A-SMEC strips.

5.4 CURVATURE MODELING

To model the curvature in relation to fixed strain, the theory developed for bimetallic strips can be applied. The goal is to theoretically model the curvature seen among the laminated composites strips and relate it to the applied strained that yields the out-of-plane curvature. Bimetallic strips can model a change of temperature to a mechanical displacement where they are systems composed of two different types of metals[26,27] each having a different coefficient of thermal expansion (CTE). The difference in the two CTEs results in a bending moment in the bimetallic system as one of the strips undergoes a larger thermal expansion than the other. The greater the difference in the thermal expansion, the greater the bending moment. This bending moment results in a curvature of the system, with a larger bending moment resulting in more curvature. Also, the flexural rigidity of the system acts to resist the curvature, and therefore a stiffer bimetallic system results in a smaller curvature given the same bending moment. This is shown in Eqn. (5-12), which relates the curvature of the system, *k*, to bending moment (*M*) and flexural rigidity (*EI*).[28,29]

$$k = \frac{1}{R} = \frac{M}{EI} = \frac{6E_1E_2t_1t_2(t_1+t_2)(\varepsilon_{T1}-\varepsilon_{T2})}{(E_1{t_1}^2)^2+(E_2{t_2}^2)^2+2E_1E_2t_1t_2(2{t_1}^2+3t_1t_2+2{t_2}^2)} \tag{5-12}$$

where R = radius, E_1 and E_2, t_1 and t_2 and ε_{T1} and ε_{T2} are the Young's modulus, thicknesses and thermal strains of material 1 and 2 respectively. ε_{T1} is traditionally attributed to the thermal expansion of each material at a specified temperature where ε_T is equal to the product of CTE (α) and change in temperature (ΔT) ($\varepsilon_T = \alpha\Delta T$). However, Eqn. (5-12) will be modified to compute the curvature seen in the A-SMEC laminated composite strips. ε_T will be replaced by the fixed strain (ε_f) attained after unloading the laminated composites, which is the maximum strain each ply can sustain after unloading and before shape recovery is observed by a thermal stimulus. ε_f is directly related to the amount of curvature observed in the laminated system. Therefore the amount of uniaxial deformation induced to the laminate composite strip at RT will result in a change in curvature observed. Therefore, in modifying Eqn. (5-12), the following equation can be used to calculate the theoretical curvature[28,29]:

$$k = \frac{1}{R} = \frac{M}{EI} = \frac{6E_1E_2t_1t_2(t_1+t_2)(\varepsilon_{f1}-\varepsilon_{f2})}{(E_1{t_1}^2)^2+(E_2{t_2}^2)^2+2E_1E_2t_1t_2(2{t_1}^2+3t_1t_2+2{t_2}^2)} \tag{5-13}$$

Let

$$\varepsilon_{f1} = R_{{fixing}_1} * \varepsilon_{deformation} \tag{5-14}$$

$$\varepsilon_{f2} = R_{{fixing}_2} * \varepsilon_{deformation} \tag{5-15}$$

where

$R_{fixing_1} = fixing\ ratio\ from\ RPSM = \frac{\varepsilon_u}{\varepsilon_m}$ (see Section 5.2.4 and Table 5-1)

$\varepsilon_{deformation} = total\ deformation\ induced\ on\ system$

Equations for ε_{f1} and ε_{f2} (Eqn. (5-14) and (5-15)) could therefore be used to calculate fixed strain at any given deformation induced on the laminated composite in order to calculate the corresponding curvature, which will be discussed later. This can be calculated, assuming that the R_{fixing} is independent of $\varepsilon_{deformation}$. In order to use Eqn. (5-13) to model the curvature in the A-SMEC laminate strips the following assumptions must be obeyed:

(i) The net strain is zero at the neutral axis. This is due to the fact that along this neutral axis the length of the laminated composite is not changing. Therefore, there is no net strain at this neutral axis.

(ii) The net stress on any given face is zero in order for static equilibrium to apply

(iii) The strain in the y axis (through the thickness) is linear for ply 1 and ply 2 in the laminated composite system

(iv) The stress changes only along the thickness (y axis) of the laminate as the Young's modulus is different for ply 1 and ply 2

Eqn. (5-13) was derived and is shown in Appendix 12 where *M* and *EI* were integrated along the width and thickness of the laminate composite model. Here, Eqn. (5-13) was used to calculate the theoretical values and these values were compared to the experimental findings. To calculate a theoretical curvature of a dual laminated composite, the Young's modulus (E_1 and E_2) of the single A-SMEC plies tested on the Linkam tensile stage to obtain strain-to-failure data (Table 4-

3) were used and the thicknesses (t_1 and t_2) of the actual single plies for mechanical testing were used and shown in Table 5-3. The strain (ε_{f1} and ε_{f2}) values were taken from the fixed strain after unloading values from the RPSM data of the single A-SMEC plies (Table 5-1). The experimental curvature values were obtained by taking the average of the (a) location (i.e tighter curl) of each specimen among the four samples tested for each laminated composite system (Tables 5-7 to 5-10). Table 5-14 shows the comparison of the theoretical to experimental curvature values. For the 0/0°, 0/45° and 0/90° laminated composite strips tested there was a difference of 5.6% or lower between the theoretical and experimental curvature. However, for the 0/22.5° and 0/67.5° composite strips, the difference in theoretical to experimental curvature was 21.1% or higher. The difference was calculated by using the following equation: Abs($k_{experimental}$ - $k_{theoretical}$)/($k_{theoretical}$)*100. This inconstancy of values may be associated with human error or variability of fiber density in the A-SMEC plies used for testing. Regardless of this inconstancy, both the experimental and theoretical data shows a trend of increasing curvature with an increase in fiber angle in ply 1. Overall, the experimental data is consistent with what is expected from the theoretical model.

As mentioned previously, Eqn. (5-13) can be used to predict a curvature given an applied deformation. Using the model, deformations ranging from 0 to 500% were input in increments of 5 into Eqn. (5-14) and (5-15) to calculate the $\varepsilon_{f1}$and ε_{f2}. $\varepsilon_{f1}$and ε_{f2} were input into Eqn. (5-13) to calculate the curvature (k) corresponding to the deformation applied. Figure 5-15 shows the theoretical model where the experimental data is overlaid for comparison. From the theoretical model, 0/0° composite showed no curvature as expected, however, the 0/67.5° laminate showed the highest curvature, not the 0/90° system which was expected. This inconsistency could be attributed to variable fiber alignment throughout the A-SMEC sheet used to fabricate the laminated composite which could lead to an inaccurate Young's modulus. This difference could also be associated with not cutting each ply exactly at the desired angle. Overall, however, the experimental values agree with the theoretical model. A more detailed theoretical model is needed for further analysis.

5.5 CONCLUSIONS

This chapter focused on a unique and innovative composite system that is soft in nature, exhibits anisotropic behavior and has RPSM characteristics that engender a new mechanically activated shape change (MASC) phenomenon. The fabrication and characterization of dual laminated fiber reinforced anisotropic shape memory elastomeric composites (A-SMEC) were explained. The data collected showed a dependence of mechanical properties on fiber orientation and exhibited a curvature and pitch response post-deformation at RT. The curvature response increased with increasing fiber angle in ply 1. The pitch behavior however, decreased with increasing fiber angle in ply 1. These smart, soft materials and the MASC phenomenon can be used for tissue engineering scaffolds and biomedical implants where anisotropic and elastomer behavior is required.

5.5 REFERENCES

(1) William D. Callister, J.: *Fundamentals of Materials Science and Engineering, An Integrated Approach*; John Wiley & Sons, Inc., 2005; Vol. 2.

(2) Budynas, R. G.: *Advanced Strength and Applied Stress Analysis*; WCB McGraw-Hill, 1999; Vol. 2.

(3) Schlecht, M.; Schulte, K.; Hyer, M. W.: ADVANCED CALCULATION OF THE ROOM-TEMPERATURE SHAPES OF THIN UNSYMMETRIC COMPOSITE LAMINATES. *Composite Structures* 1995, *32*, 627-633.

(4) Dano, M. L.; Hyer, M. W.: Snap-through of unsymmetric fiber-reinforced composite laminates. *International Journal of Solids and Structures* 2002, *39*, 175-198.

(5) Hahn, H. T.: RESIDUAL-STRESSES IN POLYMER MATRIX COMPOSITE LAMINATES. *Journal of Composite Materials* 1976, *10*, 266-278.

(6) Jeronimidis, G.; Parkyn, A. T.: RESIDUAL-STRESSES IN CARBON FIBER-THERMOPLASTIC MATRIX LAMINATES. *Journal of Composite Materials* 1988, *22*, 401-415.

(7) Barnes, J. A.; Byerly, G. E.: THE FORMATION OF RESIDUAL-STRESSES IN LAMINATED THERMOPLASTIC COMPOSITES. *Composites Science and Technology* 1994, *51*, 479-494.

(8) Davidson, B. D.: *Mechanics of Continuous Fiber Reinforced Composites*.

(9) Schlecht, M.; Schulte, K.: Advanced calculation of the room-temperature shapes of unsymmetric laminates. *Journal of Composite Materials* 1999, *33*, 1472-1490.

(10) Hyer, M. W.: THE ROOM-TEMPERATURE SHAPES OF 4-LAYER UNSYMMETRIC CROSS-PLY LAMINATES. *Journal of Composite Materials* 1982, *16*, 318-340.

(11) Hyer, M. W.: SOME OBSERVATIONS ON THE CURED SHAPE OF THIN UNSYMMETRIC LAMINATES. *Journal of Composite Materials* 1981, *15*, 175-194.

(12) Baker, A. A.; Dutton, S.: *Composite Materials for Aircraft Structures*; American Institute of Aeronautics and Astronautics: Reston, Virginia, 2004; Vol. 2.

(13) White, S. R.; Hahn, H. T.: MECHANICAL PROPERTY AND RESIDUAL-STRESS DEVELOPMENT DURING CURE OF A GRAPHITE BMI COMPOSITE. *Polymer Engineering and Science* 1990, *30*, 1465-1473.

(14) Sawa, Y.; Ye, F. F.; Urayama, K.; Takigawa, T.; Gimenez-Pinto, V.; Selinger, R. L. B.; Selinger, J. V.: Shape selection of twist-nematic-elastomer ribbons. *Proceedings of the National Academy of Sciences of the United States of America* 2011, *108*, 6364-6368.

(15) Ayres, C.; Bowlin, G. L.; Henderson, S. C.; Taylor, L.; Shultz, J.; Alexander, J.; Telemeco, T. A.; Simpson, D. G.: Modulation of anisotropy in electrospun tissue-engineering scaffolds: Analysis of fiber alignment by the fast Fourier transform. *Biomaterials* 2006, *27*, 5524-5534.

(16) Valderrabano, M.: Influence of anisotropic conduction properties in the propagation of the cardiac action potential. *Progress in Biophysics & Molecular Biology* 2007, *94*, 144-168.

(17) Li, Z.; Guan, J.: Hydrogels for Cardiac Tissue Engineering. *Polymers* 2011, *3*, 740-761.

(18) Engelmayr, G. C.; Cheng, M. Y.; Bettinger, C. J.; Borenstein, J. T.; Langer, R.; Freed, L. E.: Accordion-like honeycombs for tissue engineering of cardiac anisotropy. *Nature Materials* 2008, *7*, 1003-1010.

(19) Jean, A.; Engelmayr, G. C.: Finite element analysis of an accordion-like honeycomb scaffold for cardiac tissue engineering. *Journal of Biomechanics* 2010, *43*, 3035-3043.

(20) Ramakrishna, S.; Mayer, J.; Wintermantel, E.; Leong, K. W.: Biomedical applications of polymer-composite materials: a review. *Composites Science and Technology* 2001, *61*, 1189-1224.

(21) Godinho, M. H.; Canejo, J. P.; Feio, G.; Terentjev, E. M.: Self-winding of helices in plant tendrils and cellulose liquid crystal fibers. *Soft Matter* 2010, *6*, 5965-5970.

(22) Andrady, A. L.: *Science and Technology of Polymer Nanofibers*; A John Wiley & Sons, INC. Publication, 2008.

(23) Ramakrishna, S.: *An introduction to electrospinning and nanofibers*; World Scientific Publishing Co Pte Ltd., 2005.

(24) Luo, X. F.; Mather, P. T.: Preparation and Characterization of Shape Memory Elastomeric Composites. *Macromolecules* 2009, *42*, 7251-7253.

(25) Mather, P. T.; Luo, X. F.; Rousseau, I. A.: Shape Memory Polymer Research. *Annual Review of Materials Research* 2009, *39*, 445-471.

(26) Devries, W. R.; Lauderbaugh, L. K.: A MODEL FOR BENDING BIMETALLIC STRIP. *Journal of Engineering for Industry-Transactions of the Asme* 1984, *106*, 62-69.

(27) Reddy, P. S.; Prasad, R.; Sengupta, D.; Kishore, P.; Shankar, M. S.; Narayana, K. S.; Tiwari, U. K.: Method for Enhancing and Controlling Temperature Sensitivity of Fiber Bragg Grating Sensor Based on Two Bimetallic Strips. *Ieee Photonics Journal* 2012, *4*, 1035-1041.

(28) Darling, R. B.: Introduction to Microelectromechanical Systems: Thermal Sensors and Actuators. 2011.

(29) Clyne, T. W.: Residual stresses in surface coatings and their effects on interfacial debonding. *Interfacial Effects in Particulate, Fibrous and Layered Composite Materials* 1996, *116-*, 307-330.

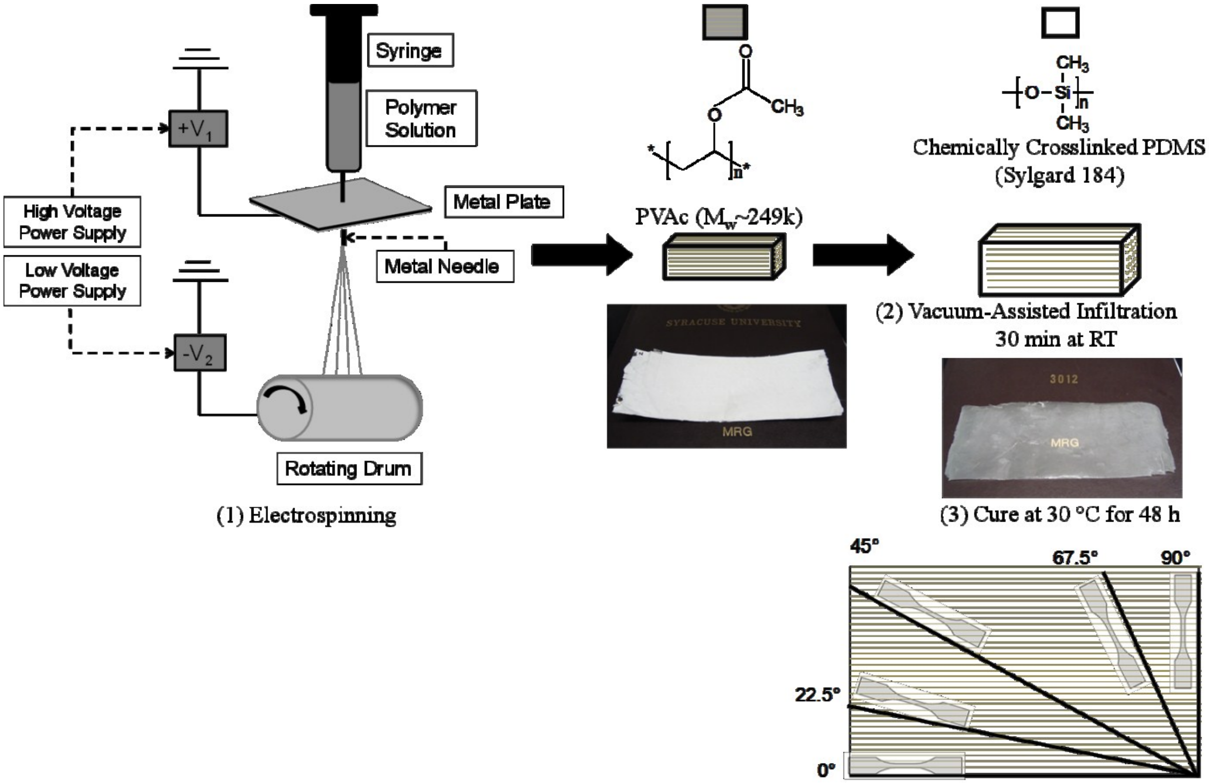

Scheme 5-1. Three-step fabrication process of anisotropic shape memory elastomeric composites (A-SMEC).

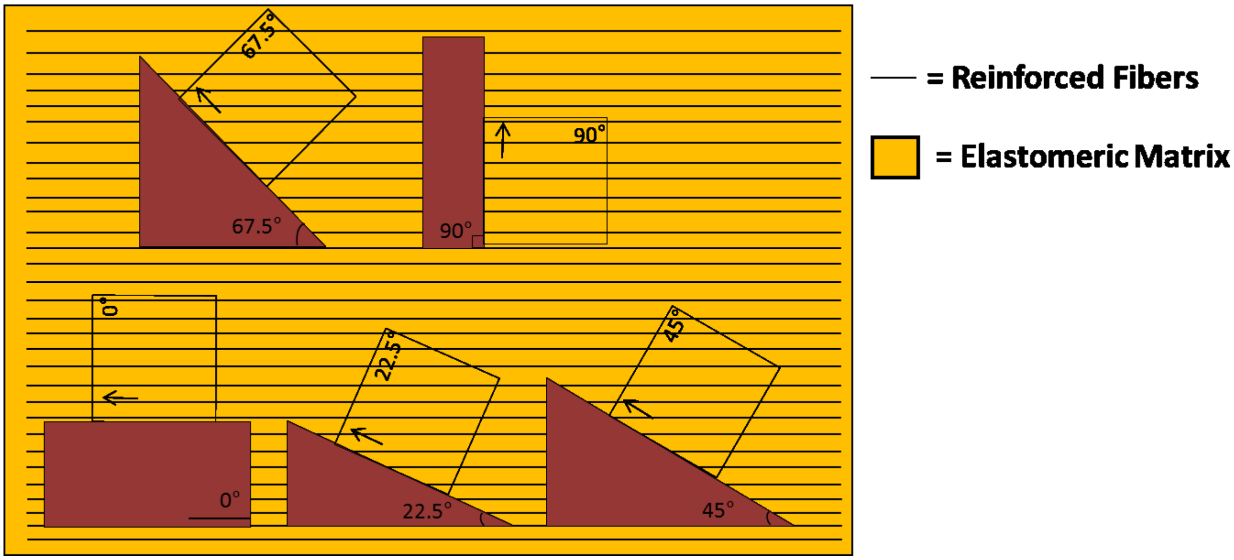

Scheme 5-2. Top view of the A-SMEC sheet showing the cutting process as a function of fiber orientation using the paper-angle templates.

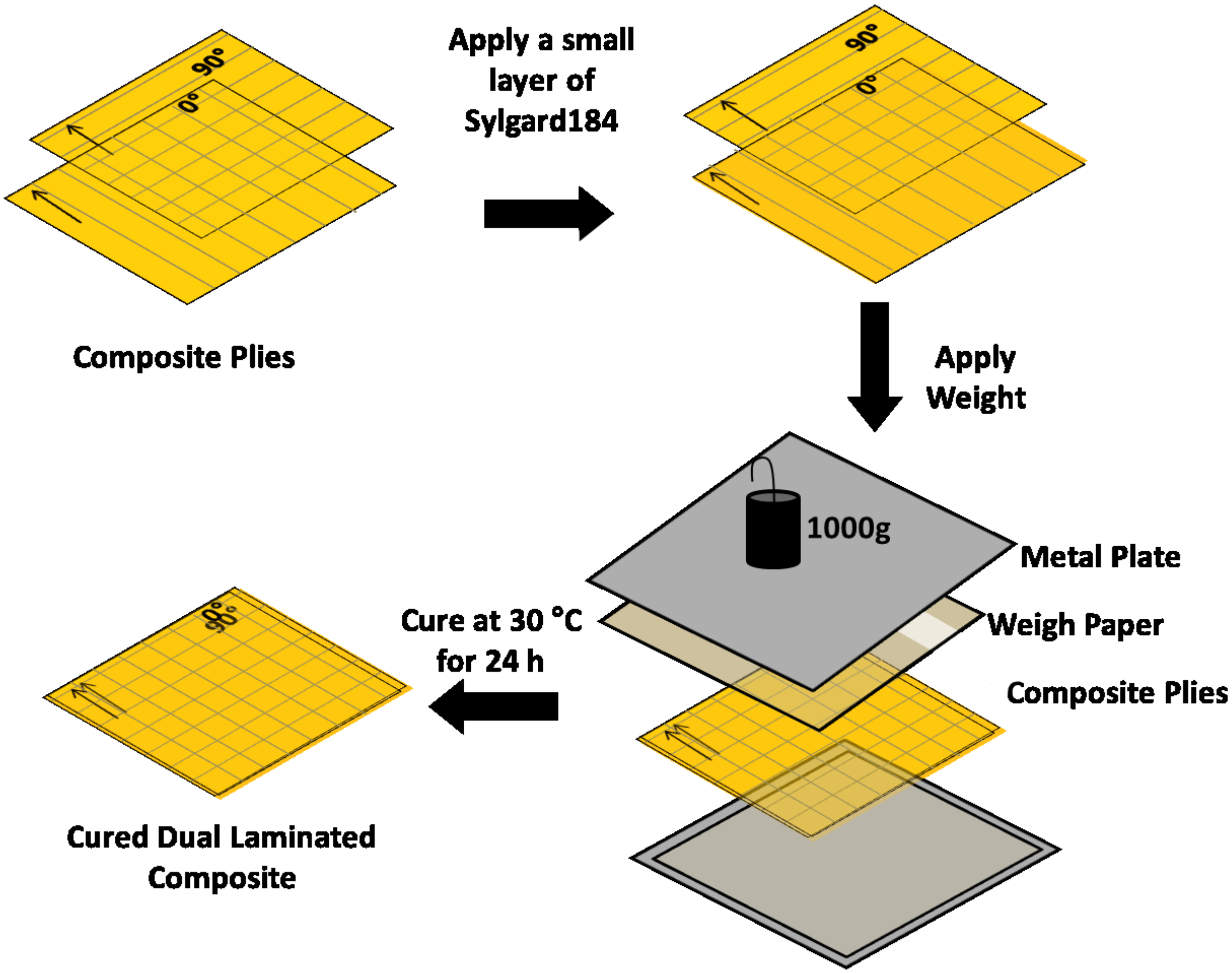

Scheme 5-3. Schematic showing the fabrication process of the laminated A-SMEC composites.

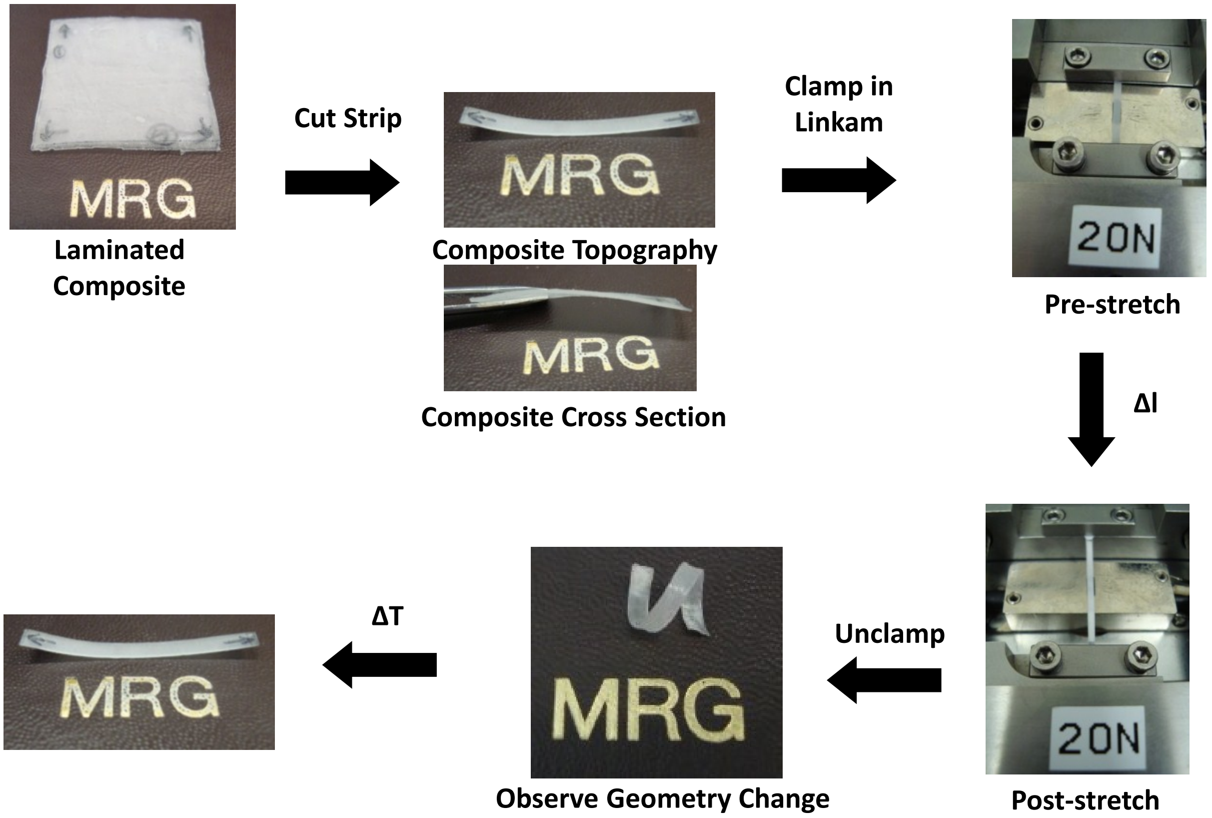

Scheme 5-4. Schematic showing the process of the mechanically activated shape change (MASC).

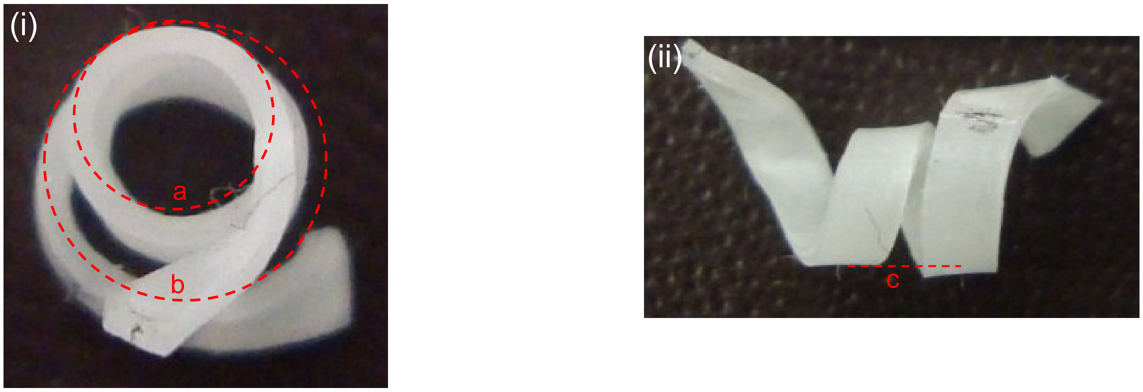

Figure 5-1. Images showing (i) curvature and (ii) pitch analysis using Image J software. *a* and *b* in image (i) represent the primary and secondary curvature respectively. *c* in image (ii) is the distance used for the pitch value.

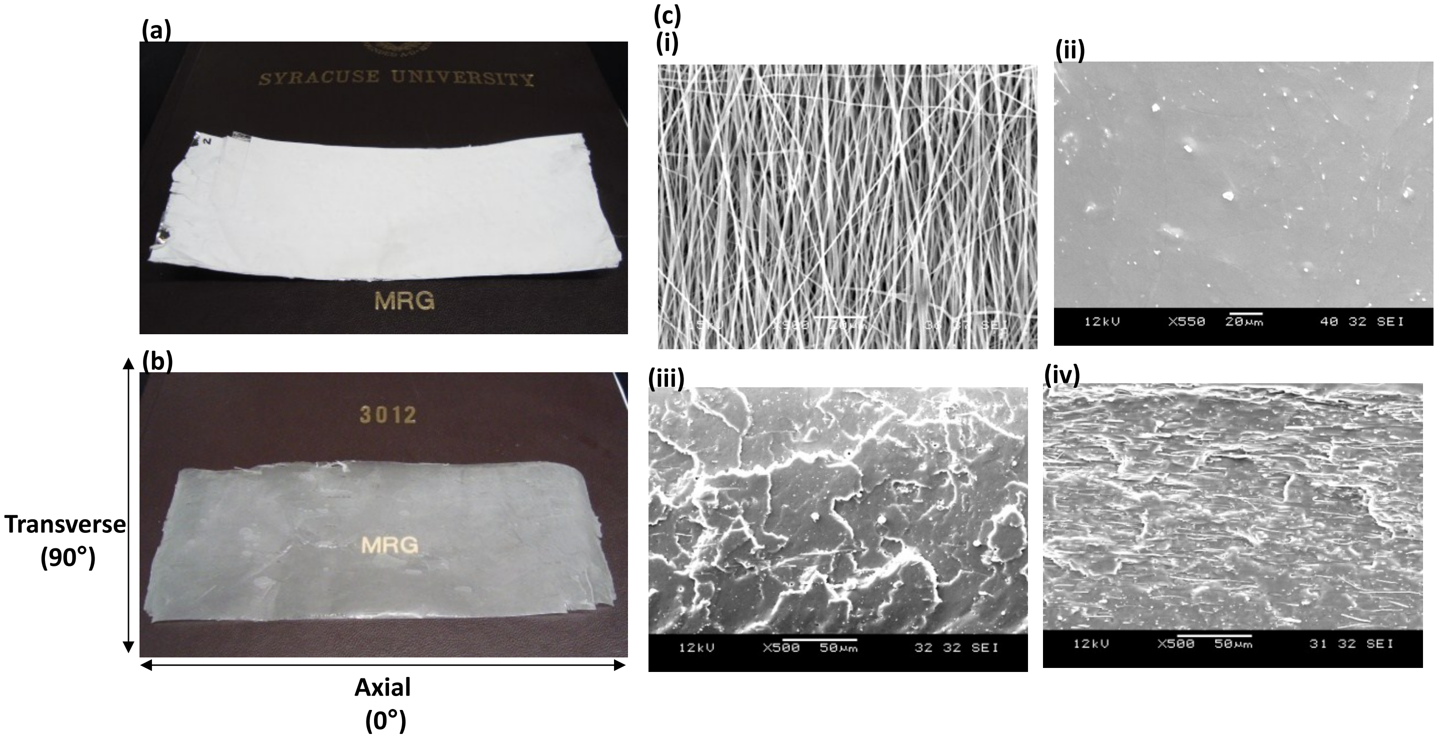

Figure 5-2. Image showing (a) PVAc aligned fibrous web (b) A-SMEC sheet (c) SEM of (i) aligned fibers (average fiber diameter: 0.81 ± 0.19 μm) (ii) topography of composite (iii) cross section in the axial (0°) direction (iv) cross section in the transverse (90°) direction.

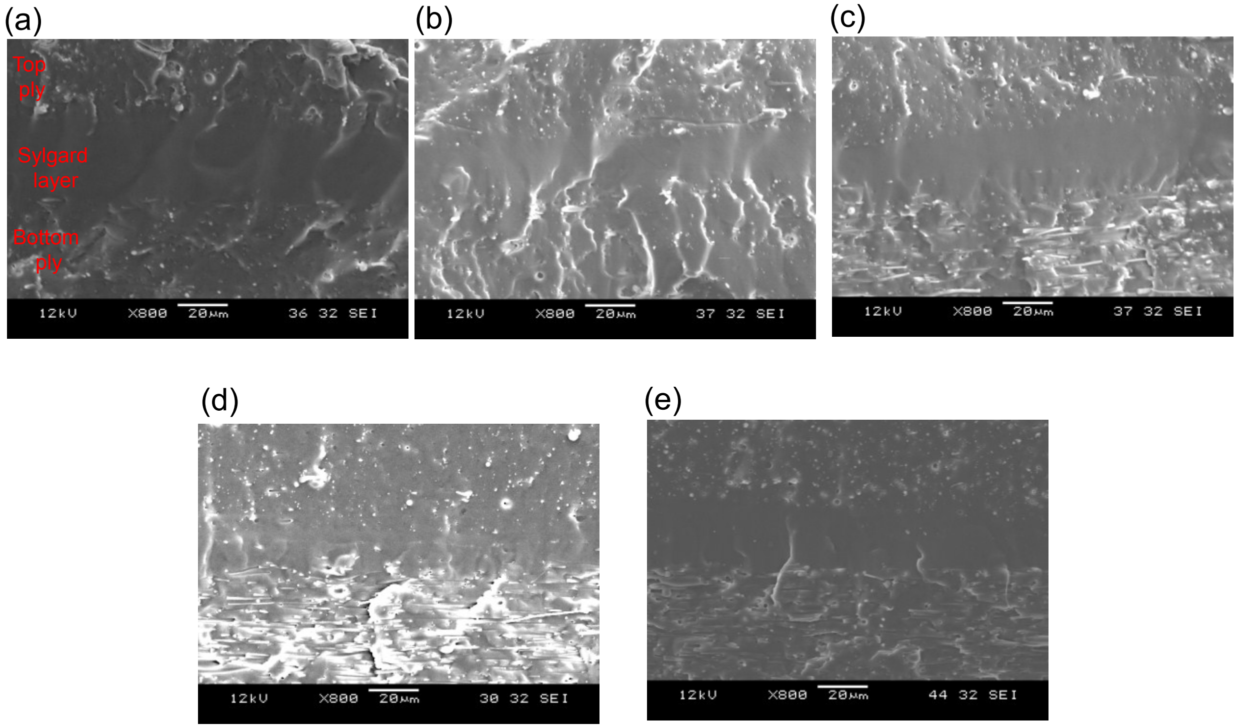

Figure 5-3. Representative SEM images showing the cross section of the laminated composites where (a) 0/0°, (b) 0/22.5°, (c) 0/45°, (d) 0/67.5°, and (e) 0/90°. Samples were freeze fractured and broken in half to see the cross sections above.

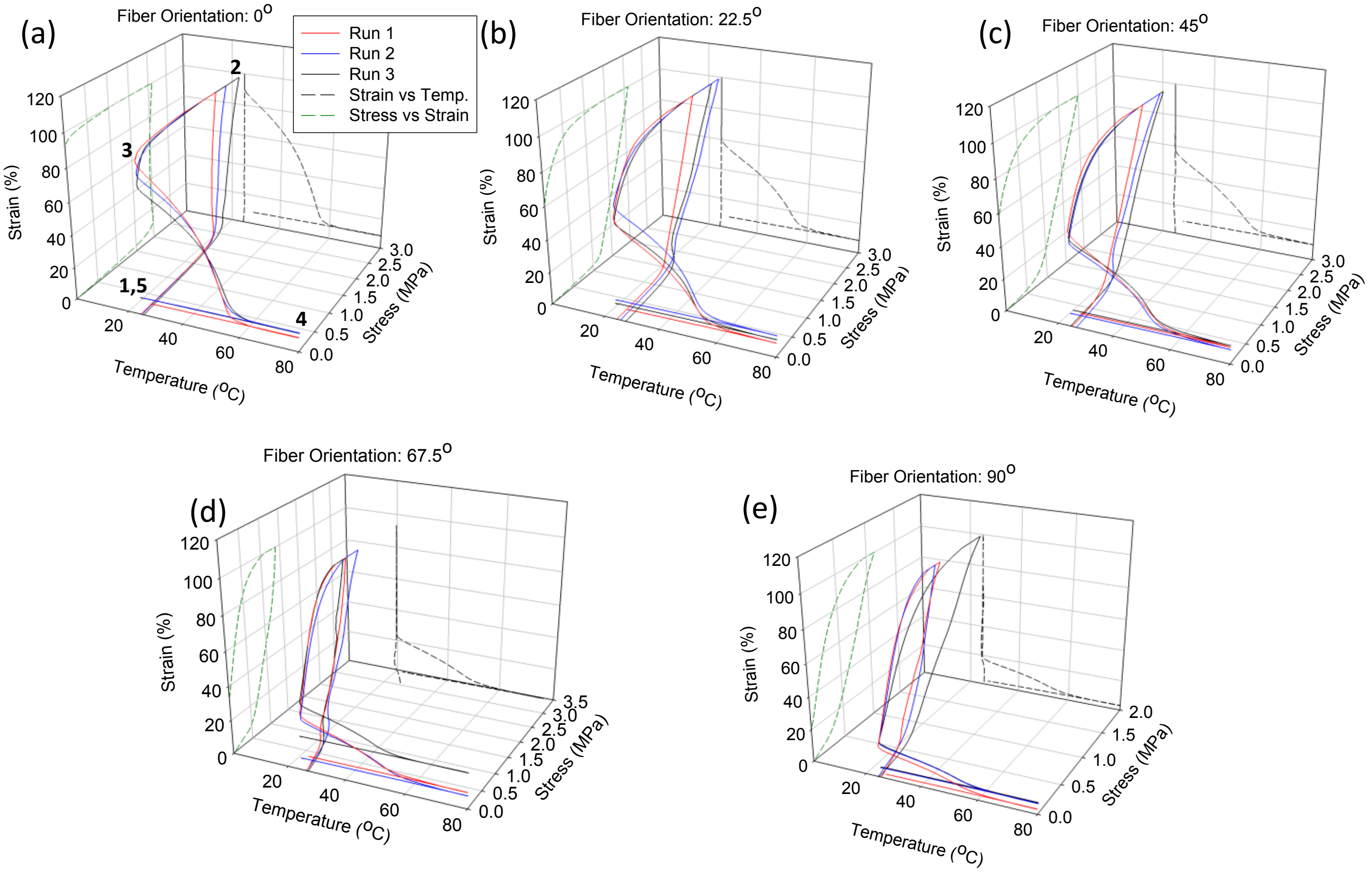

Figure 5-4. Representative RPSM curves for single A-SMEC plies tested as function of fiber orientation. The following angles were tested: (a) 0°, (b) 22.5°, (c) 45°, (d) 67.5° and (e) 90°.

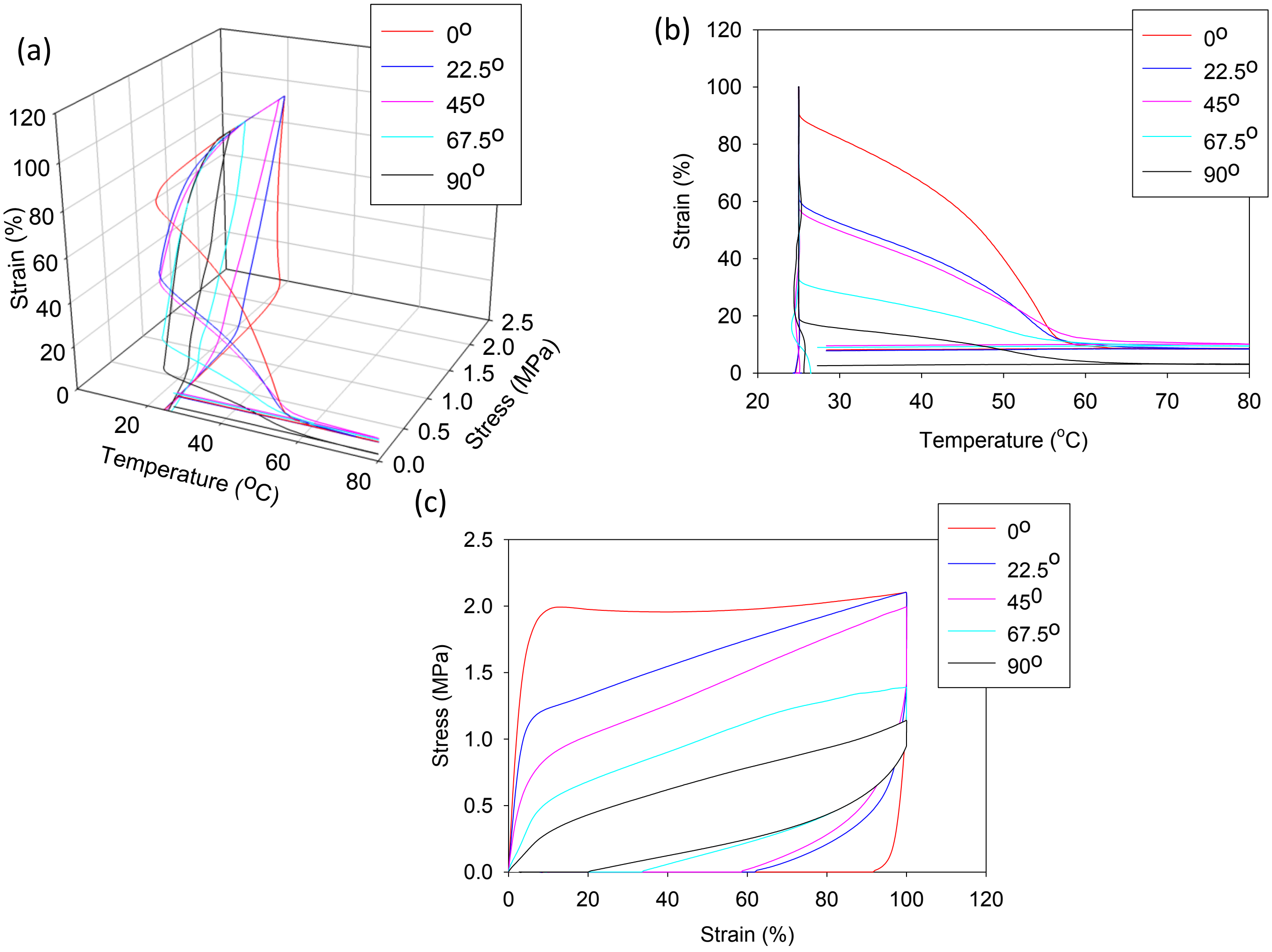

Figure 5-5. Graphs showing (a) representative RPSM curves as a function of fiber orientation, (b) strain vs. temperature, and (c) stress vs. strain for all composites tested.

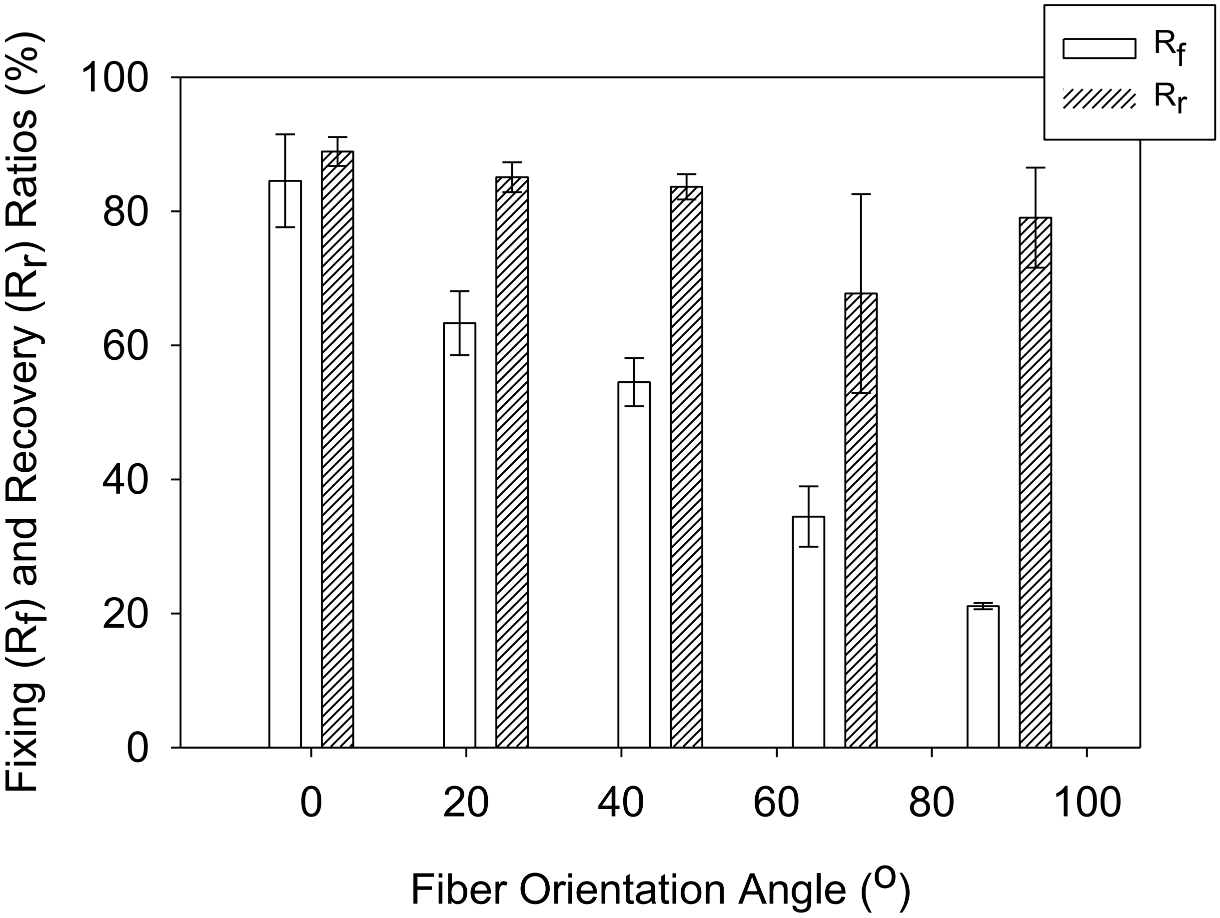

Figure 5-6. Bar graph showing the fixing (R_f) and recovery (R_r) ratios as a function of fiber angle for three samples tested in each laminated composite.

Table 5-1. Table showing the average ε_m (maximum strain achieved by deformation), ε_u (fixed strain after unloading), ε_p (permanent strain after recovery), R_f (fixing ratio) and R_r (recovery ratio) with accompanying stand deviations for three samples tested among all the composites fabricated.

COMPOSITE	**Average ε_m (%)**	**STDEV**	**Average ε_u (%)**	**STDEV**	**Average ε_p (%)**	**STDEV**	**Average ε_p(N-1)(%)**	**STDEV**	**Average R_f (%)**	**STDEV**	**Average R_r (%)**	**STDEV**
0°	100	0.02	84.6	6.9	9.4	1.1	0.08	0.10	84.5	6.9	88.9	2.2
22.5°	100	0.06	63.4	4.8	9.5	1.9	0.04	0.06	63.3	4.8	85.1	2.2
45°	100	0.06	54.6	3.6	8.9	1.3	0.01	0.01	54.5	3.6	83.6	1.9
67.5°	100	0.03	34.5	4.5	11.6	6.9	0.02	0.03	34.4	4.5	67.7	14.8
90°	100	0.04	21.1	0.5	4.4	1.6	0.01	0.01	21.1	0.5	79.0	7.5

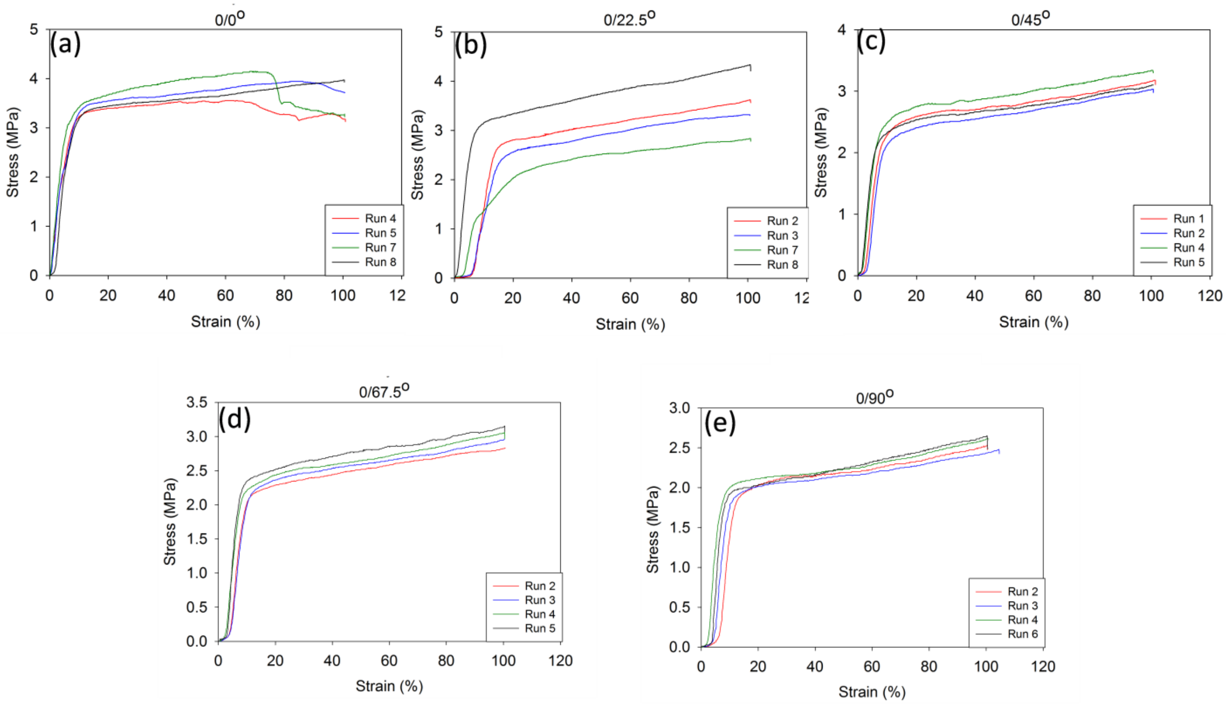

Figure 5-7. Stress vs. strain curves for four samples tested as a function of laminated composites tested where the following graphs corresponds to (a) 0/0°, (b) 0/22.5°, (c) 0/45°, (d) 0/67.5°, and (e) 0/90°.

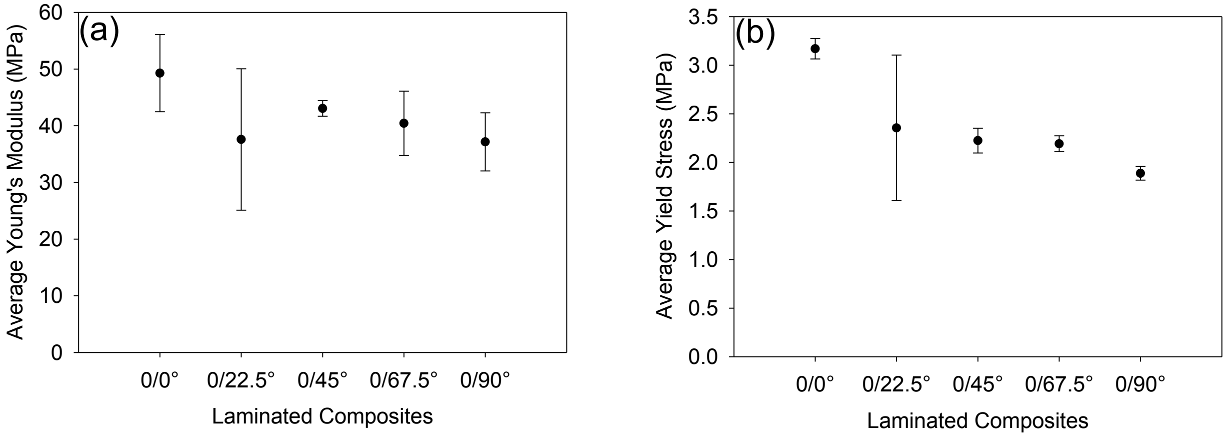

Figure 5-8. Graphs showing the average (a) Young's modulus and (b) the yield stress for four specimens tested as a function of laminated composites.

Table 5-2. Tables showing the average (a) Young's modulus and (b) average yield stress as a function of laminated composites tested.

(a)

COMPOSITE	AVE YOUNG'S MODULUS (MPa)	STDEV
0/0°	49.3	6.8
0/22.5°	37.6	12.5
0/45°	43.1	1.4
0/67.5°	40.4	5.7
0/90°	37.2	5.1

(b)

COMPOSITE	AVE YIELD STRESS (MPa)	STDEV
0/0°	3.2	0.1
0/22.5°	2.4	0.7
0/45°	2.2	0.1
0/67.5°	2.2	0.1
0/90°	1.9	0.1

Table 5-3. Table showing the average weights and thicknesses of each ply, laminated composite and Sylgard184 layer used to fabricate the laminated composites.

Individual Plies				Laminated Composite		Syglard 184 Layer	
Laminated Composite	**Square Angle (°)**	**Weight (mg)**	**Average Thickness (mm)**	**Weight (mg)**	**Average Thickness (mm)**	**Sylgard 184 weight (mg)**	**Sylgard 184 thickness (mm)**
$0/0_A$	0_{1A}	176.3	0.28	377.4	0.5	32.5	-0.01
	0_{1B}	168.5	0.25				
$0/0_B$	0_{2A}	171.09	0.26	404.1	0.6	26.8	0.01
	0_{2B}	206.23	0.33				
$0/22.5_1$	0	172.2	0.25	393.2	0.6	32.7	0.04
	22.5	188.2	0.28				
$0/22.5_2$	0	209.13	0.32	404.2	0.6	20.8	0.02
	22.5	174.21	0.26				
$0/45_1$	0	228.8	0.31	415.8	0.6	21.5	0.03
	45	165.4	0.24				
$0/45_2$	0	176.5	0.26	352.8	0.5	19.1	0.01
	45	157.3	0.24				
$0/67.5_1$	0	177.0	0.27	393.6	0.6	30.1	0.02
	67.5	186.4	0.29				
$0/67.5_2$	0	210.5	0.32	400.9	0.6	22.7	0.01
	67.5	167.7	0.25				
$0/90_1$	0	210.9	0.31	400.8	0.6	22.1	0.02
	90	167.78	0.25				
$0/90_2$	0	176.72	0.25	371.3	0.5	22.3	0.02
	90	172.25	0.26				

Table 5-4. Table showing the average widths and thicknesses for each laminated composite strip that was used for mechanical testing in the Linkam tensile stage. These values were used to calculate the stress values in the stress-strain graphs shown in Figure 5-7.

Composite	Sample Number	AVE Thickness (mm)	AVE Width (mm)
0/0°	4	0.6	1.6
	5	0.6	1.7
	7	0.6	0.9
	8	0.7	1.4
0/22.5°	2	0.7	1.9
	3	0.7	1.8
	7	0.6	1.6
	8	0.6	1.3
0/45°	1	0.6	1.7
	2	0.6	1.6
	4	0.5	1.6
	5	0.5	1.6
0/67.5°	2	0.6	1.7
	3	0.6	1.5
	4	0.6	1.6
	5	0.6	1.4
0/90°	2	0.6	1.4
	3	0.6	1.8
	4	0.6	1.5
	6	0.6	1.2

Table 5-5. Table showing the theoretical, experimental and difference in both values of the Young's modulus as a function of laminated composite.

Laminated Composite	$E_{Theoretical}$ **(MPa)**	$E_{Experimental}$ **(MPa)**	$E_{Difference}$ **(MPa)**	$E_{Difference}$ **(%)**
0/0°	47.6	49.3	1.7	3.7
0/22.5°	30.6	37.6	7.0	22.8
0/45°	30.7	43.1	12.4	40.6
0/67.5°	26.9	40.4	13.5	50.1
0/90°	26.3	37.2	10.9	41.6

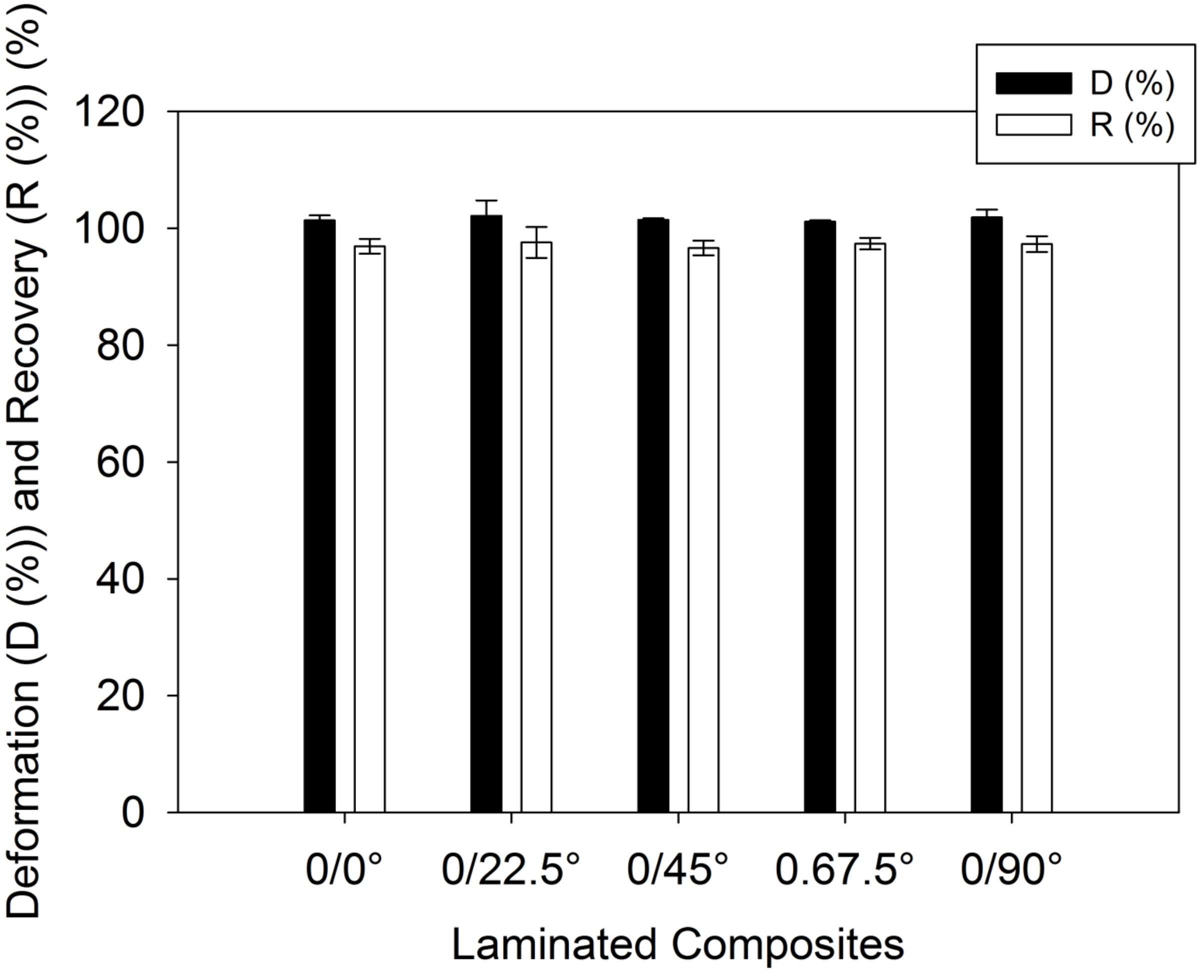

Figure 5-9. Bar graph showing the D (%) and R (%) as a function of laminated composites where four samples tested for each system.

Table 5-6. Table showing the average D (%) and R (%) for all samples tested in relation to the composites fabricated.

COMPOSITION	AVE D (%)	STDEV	AVE R (%)	STDEV
0/0°	101.3	0.8	96.9	1.3
0/22.5°	102.1	2.7	97.6	2.7
0/45°	101.4	0.2	96.6	1.2
0.67.5°	101.1	0.2	97.4	1.0
0/90°	101.9	1.3	97.3	1.3

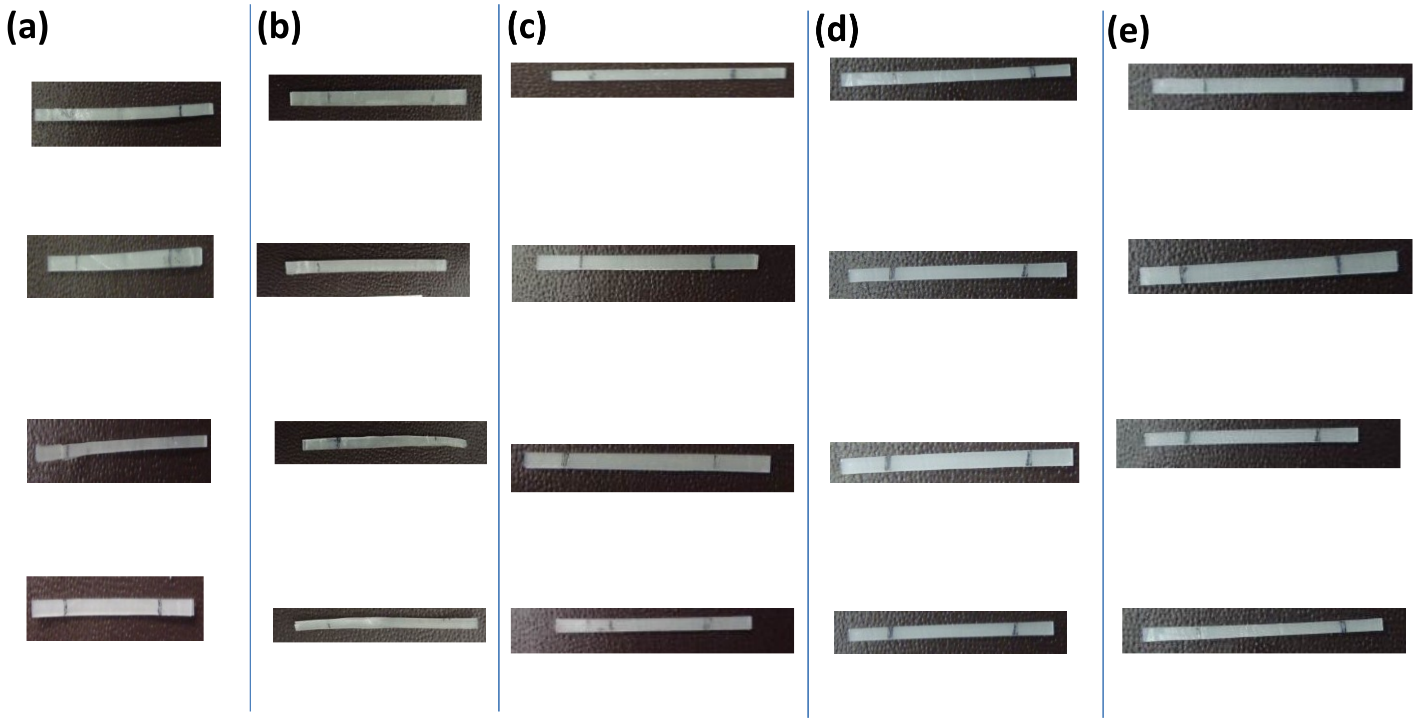

Figure 5-10. Images of all four specimens recovered post-deformation after a thermal treatment of 80 °C for 5 min and cooled at RT for 5 min for all composites tested where (a) 0/0°, (b) 0/22.5°, (c) 0/45°, (d) 0/67.5°, and (e) 0/90°. The recovery was conducted four times to assess reproducibility.

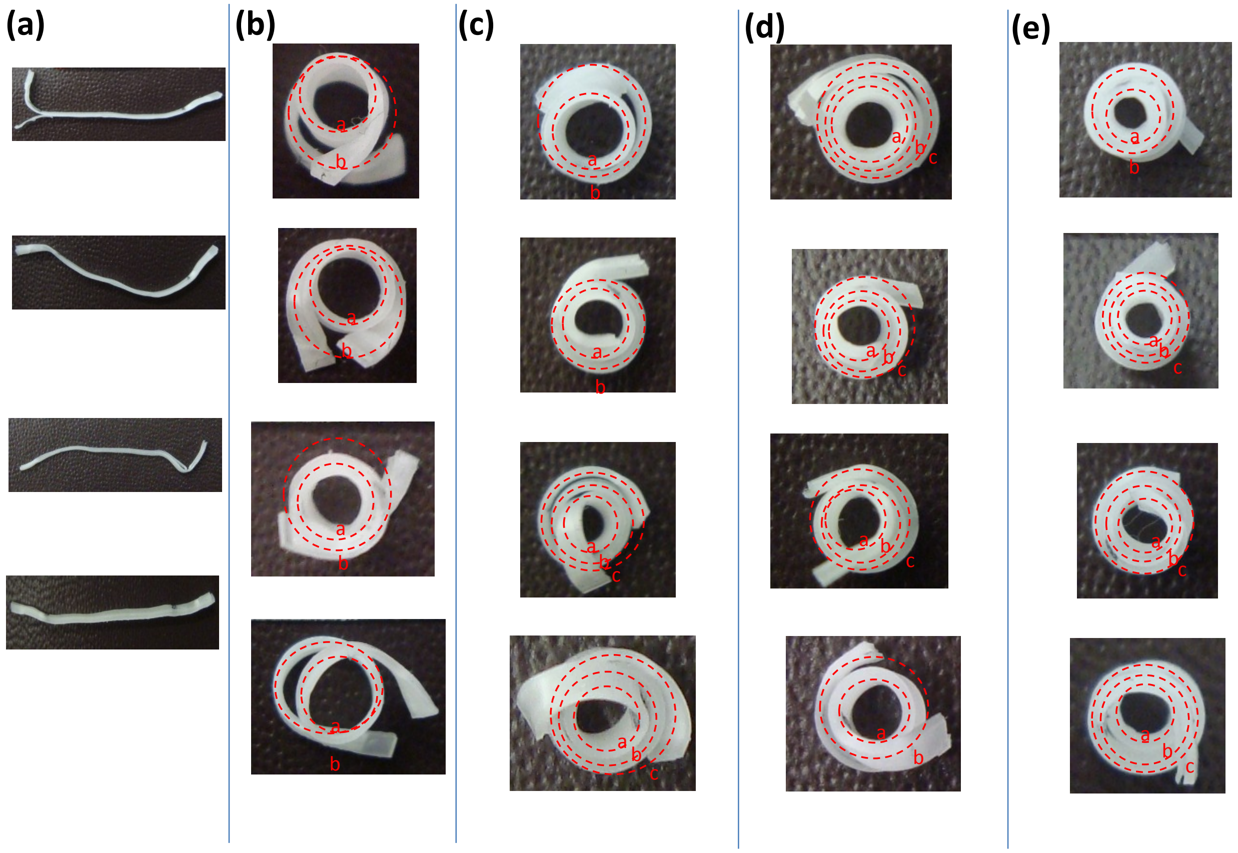

Figure 5-11. Representative images of curvature for each laminated composite showing four samples tested where the following are shown (ply 2/ply 1): (a) 0/0°, (b) 0/22.5°, (c) 0/45°, (d) 0/67.5°, and (e) 0/90°. The circles are examples of how the curvature was analyzed using ImageJ software where a = primary, b = secondary, and c= tertiary curvature. The curvature response is towards ply 1 as this ply elastically recovers more than ply 2.

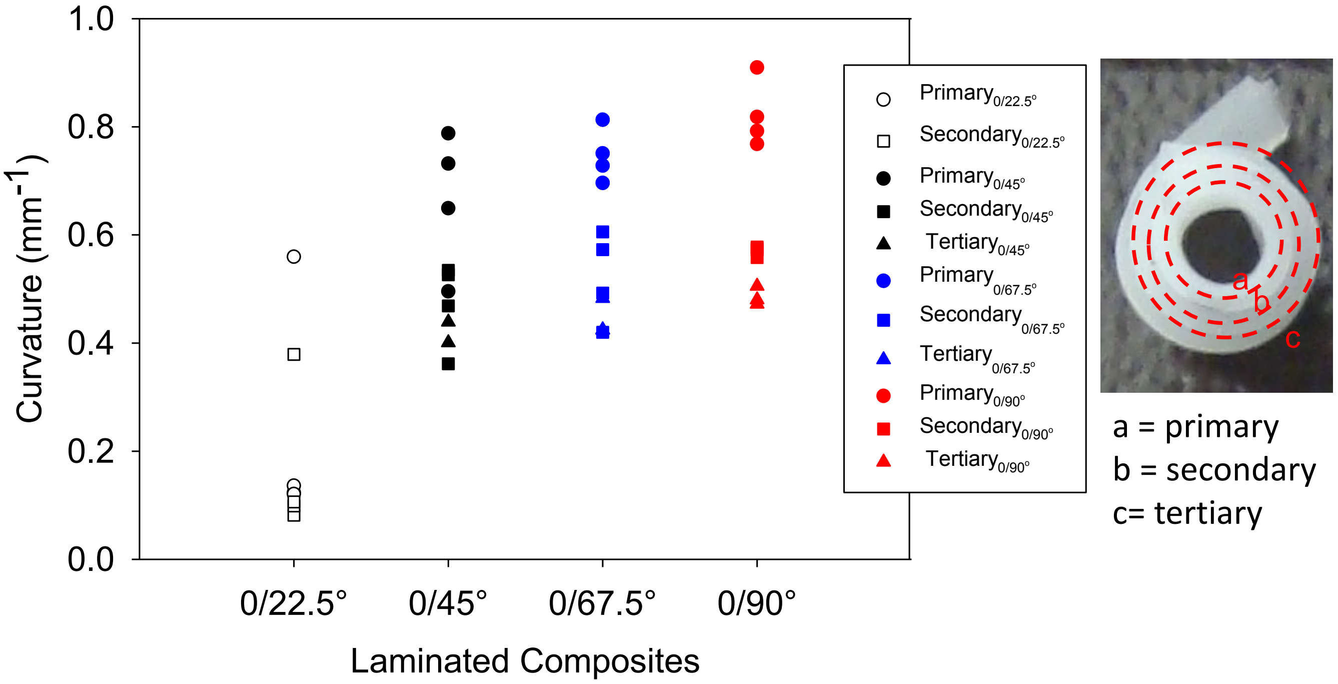

Figure 5-12. Graph showing curvature in relation to laminated composites tested. The accompanying image exemplifies the primary, secondary and tertiary curvature.

Table 5-7. Table showing the curvature analysis conducted for four 0/22.5° laminated composite samples tested where a = primary and b = secondary curvature.

Composite	Sample Number	Location	Diameter (mm)	Radius (mm)	k (mm^{-1})
0/22.5°	2	a	16.3	8.1	0.12
		b	24.5	12.3	0.08
	3	a	14.7	7.3	0.14
		b	20.2	10.1	0.10
	7	a	3.6	1.8	0.56
		b	5.3	2.6	0.38
	8	a	16.6	8.3	0.12
		b	18.8	9.4	0.11

Table 5-8. Table showing the curvature analysis conducted for four 0/45° laminated composite samples tested where a = primary, b = secondary, and c= tertiary curvature.

System	Sample Number	Location	Diameter (mm)	Radius (mm)	k (mm^{-1})
0/45°	1	a	4.0	2.0	0.50
		b	5.5	2.8	0.36
	2	a	3.1	1.5	0.65
		b	4.3	2.1	0.47
	4	a	2.5	1.3	0.79
		b	3.7	1.9	0.53
		c	5.0	2.5	0.40
	5	a	2.7	1.4	0.73
		b	3.8	1.9	0.53
		c	4.6	2.3	0.44

Table 5-9. Table showing the curvature analysis conducted for four 0/67.5° laminated composite samples tested where a = primary, b = secondary, and c= tertiary curvature.

System	Sample Number	Location	Diameter (mm)	Radius (mm)	k (mm^{-1})
0/67.5°	2	a	2.5	1.2	0.81
		b	3.3	1.7	0.61
		c	4.1	2.1	0.48
	3	a	2.7	1.3	0.75
		b	4.1	2.0	0.49
		c	4.7	2.4	0.42
	4	a	2.7	1.4	0.73
		b	3.5	1.7	0.57
		c	4.7	2.4	0.42
	5	a	2.9	1.4	0.70
		b	4.8	2.4	0.42

Table 5-10. Table showing the curvature analysis conducted for four 0/90° laminated composite samples tested where a = primary, b = secondary, and c= tertiary curvature.

System	Sample Number	Location	Diameter (mm)	Radius (mm)	k (mm^{-1})
0/90°	2	a	2.2	1.1	0.91
		b	3.5	1.7	0.58
	3	a	2.4	1.2	0.82
		b	3.5	1.7	0.58
		c	4.2	2.1	0.47
	4	a	2.6	1.3	0.77
		b	3.5	1.7	0.57
		c	4.2	2.1	0.48
	6	a	2.5	1.3	0.79
		b	3.6	1.8	0.56
		c	4.0	2.0	0.51

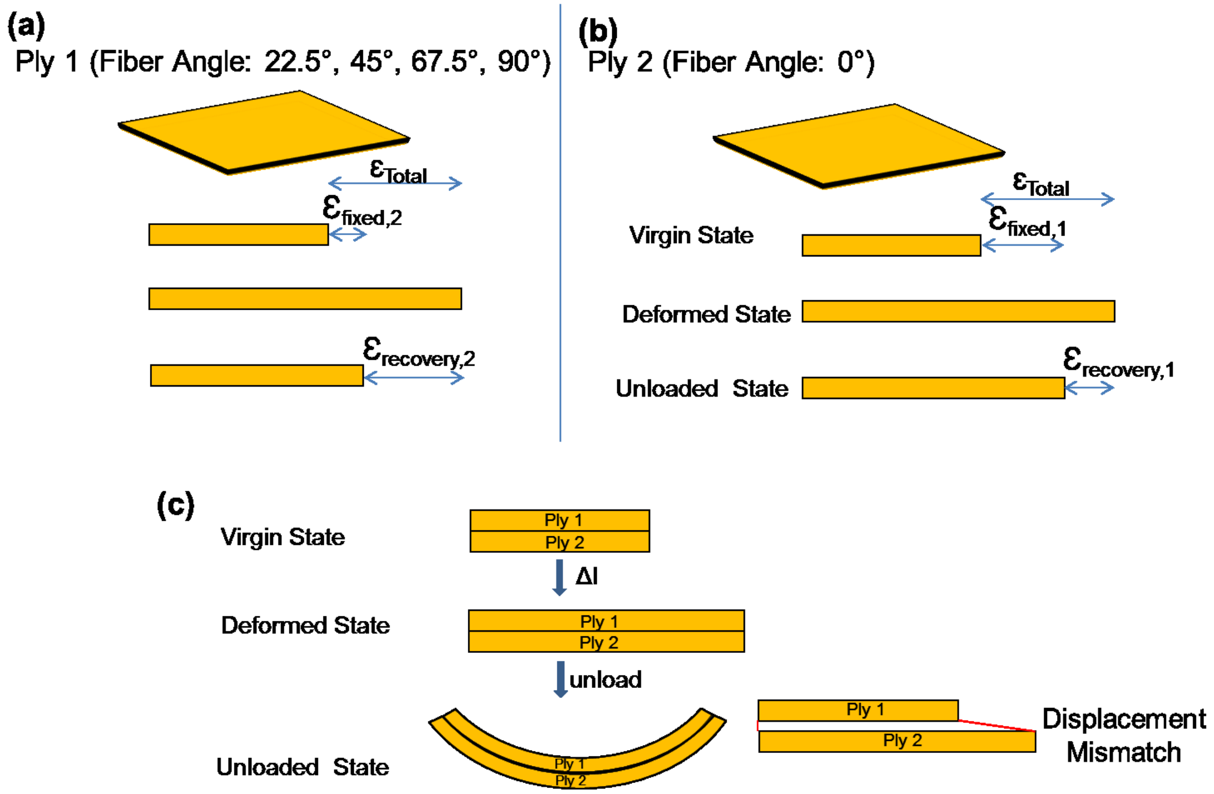

Scheme 5-5. Scheme showing each ply's behavior upon unloading where (a) shows the behavior in ply 1 where the fibers are aligned in either of the following angles: 22.5°, 45°, 67.5°, or 90°. (b) Shows the behavior of ply 2 where the fibers are aligned in the axial orientation. (c) Shows the behavior upon unloading of ply 1 and ply 2 when they are laminated to form a composite. The curvature response is associated with the displacement mismatch where ply 1 recovers more than ply 2 resulting in curvature towards ply 1.

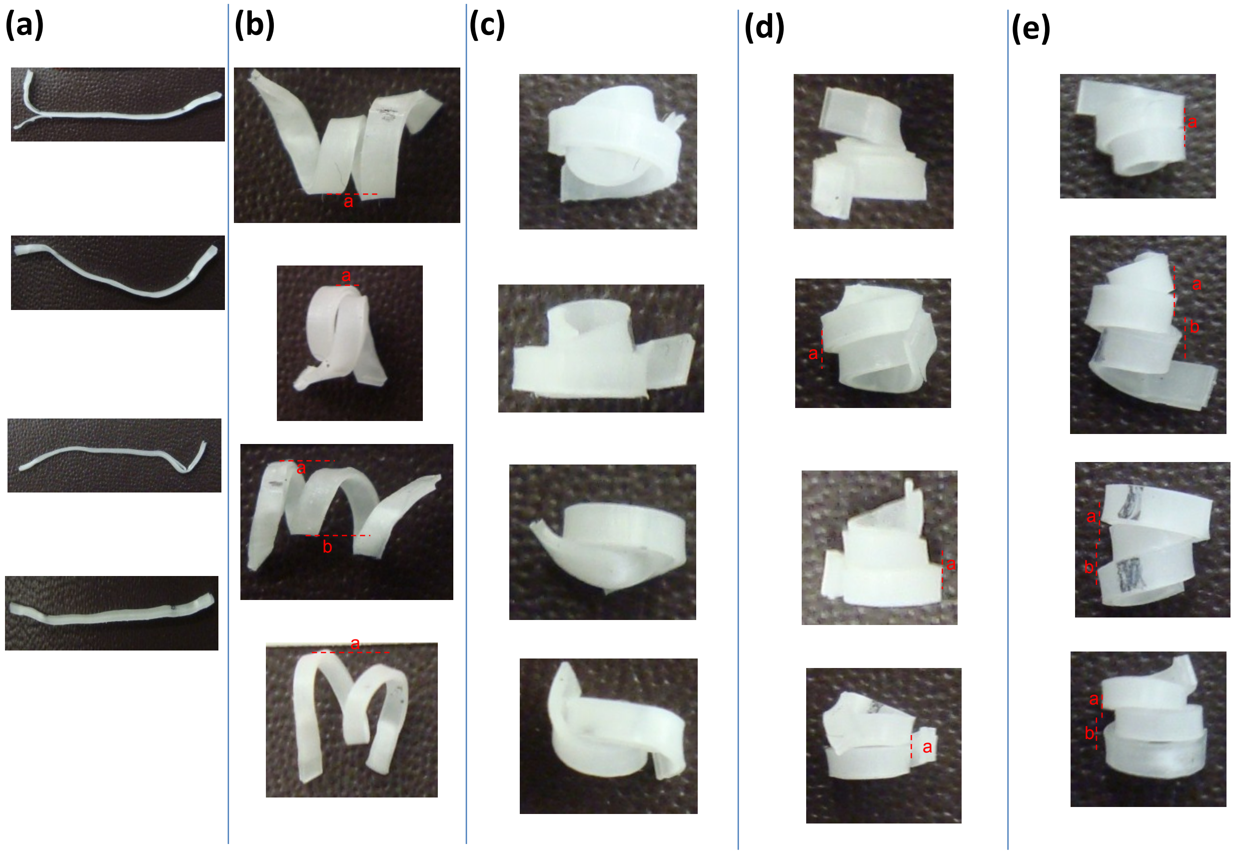

Figure 5-13. Representative images of pitch for each laminated composite showing four sample tested where the following are shown: (a) 0/0°, (b) 0/22.5°, (c) 0/45°, (d) 0/67.5°, and (e) 0/90°. The red lines are examples of how the pitch was analyzed using ImageJ software where a = primary and b = secondary pitch values.

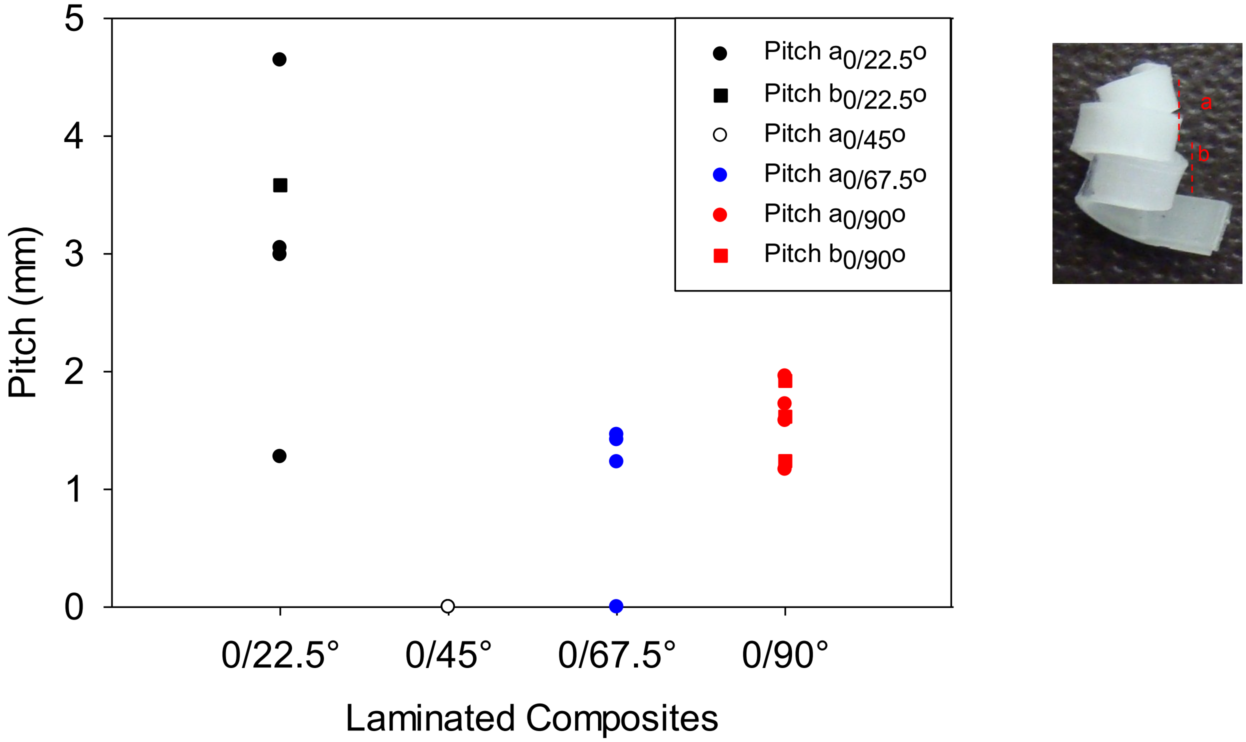

Figure 5-14. Graph shows the pitch as a function of each laminated composite tested with an example image to show the primary (a) and secondary (b) pitch.

Table 5-11. Table showing the pitch values for 0/22.5° laminated composites for four samples tested.

System	Sample Number	Location	Pitch (mm)
0/22.5°	2	a	3.0
	3	a	1.3
	7	a	3.0
		b	3.6
	8	a	4.6

Table 5-12. Table showing the pitch values for 0/67.5° laminated composites for four samples tested.

System	Sample Number	Location	Pitch (mm)
0/67.5°	2	a	0.0
	3	a	1.4
	4	a	1.5
	5	a	1.2

Table 5-13. Table showing the pitch values for 0/90° laminated composites for four samples tested.

System	Sample Number	Location	Pitch (mm)
0/90°	2	a	1.6
	3	a	2.0
		b	1.9
	4	a	1.7
		b	1.6
	6	a	1.2
		b	1.2

Table 5-14. Table showing the theoretical, experimental and difference of both values of the curvature as a function of laminated composites.

Laminated Composite	**$k_{Theoretical}$ (mm^{-1})**	**$k_{Experimental}$ (mm^{-1})**	**$k_{Difference}$ (mm^{-1})**	**$k_{Difference}$ (%)**
0/0°	0.00	0.00	0.00	0.0
0/22.5°	0.57	0.24	0.33	58.6
0/45°	0.63	0.67	0.04	5.6
0/67.5°	0.95	0.75	0.20	21.1
0/90°	0.84	0.82	0.02	1.8

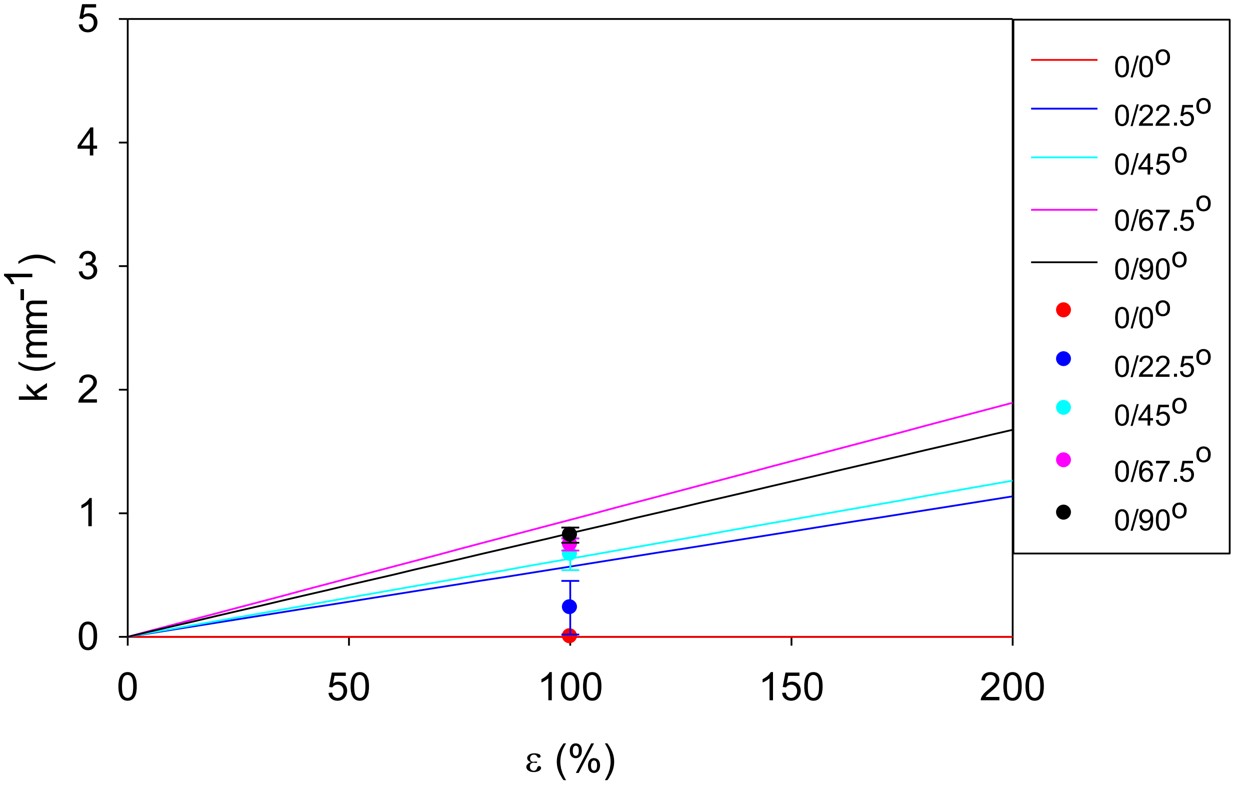

Figure 5-15. Graph showing the theoretical prediction of curvature corresponding to an applied deformation on the dual laminated composite strips. Lines are indicative of the theoretical model where the dots are the experimental values as a function of laminate system.

CHAPTER SIX

CONCLUSIONS AND FUTURE DIRECTIONS

6.0 OVERALL CONCLUSIONS

In my research, I developed and fabricated polymeric and composite thermal responsive smart systems that exhibit the shape memory assisted self healing (SMASH) and reversible plasticity shape memory (RPSM) effects. The fabrication of a single phase semi-crystalline system and amorphous based system was explored and characterized. Anisotropic shape memory elastomeric composite (A-SMEC) systems and dual laminated A-SMECs were also characterized and studied where both exhibited the SMASH and RPSM effects. The following are the conclusions and recommended studies for future directions of each system.

6.1 SINGLE PHASE SEMI-CRYSTALLINE POLYMERIC SMASH SYSTEMS

6.1.1 CONCLUSIONS

Chapter 2 explained the development of semi-crystalline miscible blends exhibiting the SMASH and RPSM effects. Here, PCL thermoplastic was used as the self healing (SH) agent and interpenetrated into a PCL diacrylate shape memory (SM) network using pentaerythritol tetrakis-(3-mercaptopropionate) (tetrathiol) as the crosslinker and 2,2-dimethoxy-2-phenylacetophenone (DMPA) as the photoinitator. The weight percentages (wt - %) of the SM network and the SH agent were varied to optimize the SM and SH effects. Thermal, thermo-mechanical, SM and SH characterizations were conducted. The SM fixing ratios (R_f) were approximately in the 70 – 80%

range where the SM recovery ratios (R_r) were in the 80 – 90% range. Damage in the form of cracks was introduced in dogbone specimens to evaluate the degree of healing. The data revealed that a minimum of 25 wt - % SH agent is required for complete healing, where anything lower than 25 wt - % had partial to no healing. It was also observed from optical and scanning electron microscopy (SEM) micrographs that both the crack induced region and propagated crack region completely healed with samples that have 25 wt - % or greater of SH agent.

6.1.2 FUTURE DIRECTIONS

6.1.2.1 WATER IMMERSION STUDIES

Motivation: Water immersion studies should be conducted to investigate the effectiveness of the SM and SMASH effect in an aqueous environment. In particular, the ability of films, once fully submerged, to recover and heal cracks should be studied. These systems can be used as films or as protective coatings on surfaces where aqueous environments are unavoidable. Applications for these smart polymers include architectural envelopes and inflated structural membranes.

Methods: The following are methods to conduct SM and SMASH experiments

Experiment 1: SM Studies

To test the ability of the SM effect to work in an aqueous environment, SM studies should also be conducted where the deformed (not damaged) samples are immersed in a 25 °C and 80 °C water bath to study shape recovery.

Experiment 2: SMASH Studies

To test the ability of the SMASH effect to work in an aqueous environment, experiments similar to those conducted in Chapter 2 section 2.2.5 should be performed, with the use of an 80 °C water bath for thermal repair rather than a convection oven.

Anticipated Results:

Experiment 1: SM Studies

Results from these experiments would potentially reveal that the deformed sample can recover at 80° C and not 25 °C. 25 °C is well below the T_m of the system where chain mobility not possible for shape recovery.

Experiment 2: *SMASH Studies*

Results from these experiments would potentially reveal the need for a composition with a higher content of the SM component to store enough energy to push water out of the crack area to allow crack closure. However, a higher content of the SM component leads to a lower percentage of SH agent, which may inhibit crack rebonding.

Preliminary Results:

Experiment 1: SM Studies

Preliminary studies showed that when a l-$PCL_{50wt\text{-}\%}$:n-$PCL_{50wt\text{-}\%}$ sample was deformed to achieved 90.1 $\%_{deformation}$ the $\%_{recovery}$ was only 1.6% at RT (Figure A1.1.1). This means that there was minimal shape recovery evident. Further studies would be to conduct the experiments in triplicate to study how reproducible the data is. In addition, further studies include conducting the same experiment using an 80 °C water bath.

Experiment 2: *SMASH Studies*

Preliminary studies showed that after stretching a notched l-$PCL_{50wt\text{-}\%}$:n-$PCL_{50wt\text{-}\%}$ sample and submerging in an 80 °C water bath for 1 h, cooling to RT and re-stretching, there was evidence of crack closure, but only partial healing (Appendix A1.1.2). Therefore the same experiment was conducted using a l-$PCL_{80wt\text{-}\%}$:n-$PCL_{20wt\text{-}\%}$ sample, but instead the sample was left in an 80 °C water bath for 30 min (Appendix A1.1.4). Results showed complete healing at the damaged site when the sample was re-stretched. These preliminary studies show that the SMASH effect can be effective in an aqueous environment when the SH agent content is high, with minimal SM content required. This means that only a minimal amount of the SM network is required for crack closure, but a significant amount of SH agent is required for crack rebonding. The following steps would be to reproduce the experiments in triplicate to confirm results and obtain statistical significance.

6.1.2.2 HEALING KINETICS STUDIES

Motivation: Healing kinetics of the SMASH effect should be conducted to identify a system with optimal healing characteristics. A system that can completely heal in the least amount of time at a realistic operational temperature is optimal.

Methods: To identify the optimal system, the molecular weight (M_w) of the l-PCL healing agent should be varied and its impact on the healing kinetics observed. Several M_w's should be considered, such as: 10k, 50k, and 100k. For each molecular weight, the healing as a function of time should be studied, with the SH efficiency investigated at 10 min, 30 min, and 1 h.

Anticipated Results: Results from these experiments may reveal that a longer time is needed to achieve healing across the damaged site for a higher M_w l-PCL healing agent. It can be postulated that polymer diffusion and chain rearrangement for longer chains would require a longer time to reach the area of damage. Polymer physics concepts can be employed where chain diffusion can be correlated to the molecular weight of the polymer:

$$D \, \alpha \, M^{-2} \tag{6-1}$$

where D is the chain diffusion coefficient and M is the molecular weight of the polymer.[1] This equation predicts that the diffusion coefficient is proportional to the inverse of the molecular weight squared[1] which means that as the molecular weight increases, the diffusion coefficient decreases. Reptation time (T_R) is the chain motion time and is also dependent on molecular weight (M) where the following relationship is predicted:

$$T_R \,\alpha\, M^3 \tag{6-2}$$

This equation state the reptation time is proportional to the molecular weight cubed which explains that as the M_w increases, the reptation time also increases.[1] Experimentally, the exponent of Eqn. (2) is found to be closer to 3.4. Thus as the molecular weight of the l-PCL chains increases, it would take longer for the chains to diffuse across the damage site and completely rebond the crack surfaces. It is also important to consider that there is a minimum M_w required for the restoration of mechanical properties as polymer chain entanglements at the damaged site are needed to recover such properties. A lower M_w, would yield a lower degree of entanglement at the damaged site and therefore a specified M_w would need to be identified for complete healing.

Preliminary Results: Appendix 1.2 shows gel fraction, DSC and thermo-mechanical data for the following samples tested: l-PCL(14k)$_{10wt\text{-}\%}$:n-PCL(3k)$_{90wt\text{-}\%}$, l-PCL(14k)$_{25wt\text{-}\%}$:n-PCL(3k)$_{75wt\text{-}\%}$, l-PCL(14k)$_{50wt\text{-}\%}$:n-PCL(3k)$_{50wt\text{-}\%}$, l-PCL(14k)$_{60wt\text{-}\%}$:n-PCL(3k)$_{40wt\text{-}\%}$, l-PCL(14k)$_{70wt\text{-}\%}$:n-PCL(3k)$_{30wt\text{-}\%}$, and l-PCL(70k)$_{10wt\text{-}\%}$:n-PCL(3k)$_{90wt\text{-}\%}$, l-PCL(70k)$_{25wt\text{-}\%}$:n-PCL(3k)$_{75wt\text{-}\%}$, l-PCL(70k)$_{50wt\text{-}\%}$:n-PCL(3k)$_{50wt\text{-}\%}$, l-PCL(70k)$_{60wt\text{-}\%}$:n-PCL(3k)$_{40wt\text{-}\%}$, l-PCL(70k)$_{70wt\text{-}\%}$:n-PCL(3k)$_{30wt\text{-}\%}$. From the thermo-mechanical data, it can be hypothesized that all compositions would need to be heated above 60 °C for SM and SH as the rubber plateau is evident at this temperature.

6.1.2.3 PUNCTURE HEALING

Motivation: Puncture testing should be conducted to determine if the SMASH effect is effective for healing puncture damage and not just cracks or surface scratches. This study is pertinent to NASA satellite deployment devices that may incur damage in the form of puncture from micrometeoroid and/or orbital debris while in orbit.[2]

Methods: To investigate whether or not SMASH can be used to heal puncture damage, samples should be punctured with needles of various diameters. The samples should then be uni-axially strained to propagate the damage, then thermally treated and strained again to investigate the SH efficiency.

Anticipated Results: These experiments are expected to reveal a maximum diameter of puncture damage, above which healing is no longer achieved. The inability for crack closure and healing would be directly correlated to the ligament widths in the perimeter of the puncture because the area around the puncture would not have the necessary stored energy to close the crack needed for healing (See Scheme 6-1).

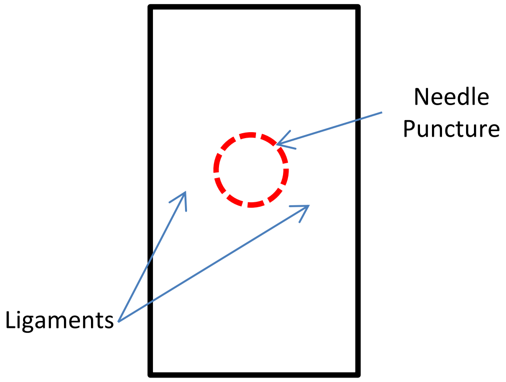

Scheme 6-1. Schematic of specimen showing the location of the puncture and ligaments.

Preliminary Results: Preliminary results shown in Appendix 1.3 reveal that the use of a 1.23 mm diameter needle to puncture a l-PCL$_{70wt\text{-}\%}$:n-PCL$_{30wt\text{-}\%}$ specimen can allow for crack closure upon thermal treatment, however healing was only partially evident. This was observed when the damaged area reopened when the sample was re-deformed. A possible reason for low healing efficiency could be an insufficient amount of healing time, or a higher M_w thermoplastic may be needed for chain re-entanglement at the damaged site.

6.1.2.4 REVERSIBLE ADHESIVE STUDIES

Motivation: Reversible adhesive studies should be conducted to study the adhesive reversibility effects in the l-PCL:n-PCL films on a variety of substrates. A reversible adhesive material is one that can form a rigid bond between itself and another substrate at a low temperature and then debond upon increasing the temperature.[3,4] Applications would include pressure sensitive reversible post-it notes used at RT where other applications include using this system as a glue agent.

Methods: To investigate the reversible adhesive effect, two studies can be conducted.

Experiment 1:

A substrate (glass and/or metal substrates) should be superglued on a metal rheometer disposal top plate and another substrate superglued to a bottom plate. The substrates should then be heated to 80 °C and a l-PCL$_{50wt\text{-}\%}$:n-PCL$_{50wt\text{-}\%}$ film placed between the two substrates and a compressive force of 0.5 N applied. At 80 °C the PCL film is in its amorphous rubber state and yields a tacky surface. The system can then be cooled down to RT to allow the PCL to recrystallize to construct a rigid bond between film-substrate interface. Tensile testing at RT should then be conducted by moving the top rheometer plate upward, and the debonding force recorded at RT.

Experiment 2:

A l-PCL$_{50\text{wt-}\%}$:n-PCL$_{50\text{wt-}\%}$ film should be placed in between two glass slides in a lap shear configuration. Next, a 1000 g weight would be placed on the system to allow the compressive force to assist in the bonding process at 80 °C. The system can then be cooled at RT to allow the crystallization of the PCL chains. A 50 g weight can then be hung from one of the glass substrates to observe if the overall system can support the weight.

Anticipated Results:

Experiment 1: The first experiment is expected to reveal that a minimum stress is required to debond the top plate from the bottom plate when the PCL film is used as an adhesive.

Experiment 2: The second experiment is expected to reveal the maximum weight the system can support before debonding is observed.

Preliminary Results:

Experiment 2: Appendix 1.4 shows preliminary results where a 50 g weight was successfully hung from the glass-film system at RT where there is no evidence of debonding. Further studies include using different weights to hang on the system to find the critical weight before debonding at different times.

6.1.2.5 SURFACE REVERSIBLE PLASTICITY STUDIES

Motivation: Surface reversible plasticity studies should be conducted to study whether damage in the form of plastic deformation induced on the surface of the l-PCL:n-PCL system is recoverable. If this system is used for protective coatings for industrial applications, surface damage would need to be conducted in order to study surface mechanical properties of the coating.

Methods: A spatula, conical scribe or micro indenter can be used to perform damage on the surface of all the PCL compositions. The samples should be heated at 80 °C in a convection oven for 10 min to allow shape recovery and cooled at RT for 10 min to allow the films to recrystallize. The recovery of the damage can then be examined by taking stereomicrographs of the virgin, damaged and thermally treated states for proper comparison.

Anticipated Results: It is expected that the plastic deformation is reversible by heating above the thermal transition (T_m ~60 °C) of the specimen. This is postulated as reversibly plasticity was observed in the bulk as shown in Chapter 2.

Preliminary Results: Initial studies showed that the plastic deformation is recoverable above a thermal stimulus (See Appendix 1.5). Further studies include reproducing the experiments to observe reducibility of the results as well as damaging the same area to study if surface recovery is evident.

6.1.2.6 SMALL ANGLE LIGHT SCATTERING (SALS) STUDIES

Motivation: To study and measure the polymer structure on a micron-scale, Small Angle Light Scattering (SALS) tests should be performed on deformed l-PCL:n-PCL samples. SALS uses transmission from a laser beam that penetrates through the polymer sample of interest to obtain a scattering pattern of visible light. The pattern is what allows one to understand of the orientation of polymer chains. In an academic exchange program with Universidad Nacional Autonoma de Mexico (UNAM) and under the instruction of Dr. Angel Romo-Uribe, SALS studies were conducted. The SALS equipment had a light source with a vertical polarized He-Ne laser with a wavelength of l = 632.8 nm and 0.8 mW power.[5] The model of the laser was 1500 manufactured by JDS Uniphase Corp., Santa Rosa California, USA.[5] The goal of the study would be to observe when and how the polymer chains orient as function of uniaxial deformation. This experiment is important as it yields information on how polymer chains respond to a uniaxial load as well as understanding the micro structure of polymers.

Methods: To study the polymer structure on a micron-scale and chain orientation, a l-PCL(65k)$_{70wt\text{-}\%}$:n-PCL(3k)$_{30wt\text{-}\%}$ sample should be used to conduct SALS experiments in its virgin and deformed state. First, a virgin SALS image should be conducted to use as a baseline. The same sample should then be manually stretched in a tensile mechanical device to a specified length where a SALS image should be taken. This process should be conducted until orientation is seen in the SALS images.

Anticipated Results: It is expected that polymer chain orientation would be achieved as a function of deformation induced on the sample.

Preliminary Results: The initial results showed that the polymer chain orientation was evident when the sample was stretched to L_{10} =15.2 mm. Appendix 1.6 shows preliminary data of SALS images as a function of deformation. At L_{10}, the SALS image showed an elliptical halo at the equator where the sample started to become clear at the center. It is postulated that the elliptical halo at the equator suggests that there is polymer orientation in the meridian axis. Further studies include reproducing the data in triplets to confirm results and to obtain statistical significance as well as testing at high deformation lengths. Other studies also include testing other PCL compositions.

6.1.2.7 TACK STUDIES

Motivation: To measure the amount of tack a l-PCL(65k)$_{50wt-\%}$:n-PCL(3k)$_{50wt-\%}$ film can exhibit on a glass substrate, tack measurements can be performed on a TA AR-G2 rheometer. Some applications for the PCL SMASH system include gluing agents on substrates as well as adhesives on paper products.

Methods: To test the amount of tack, a l-PCL(65k)$_{50wt-\%}$:n-PCL(3k)$_{50wt-\%}$ film was super-glued to the top plate and the glass substrate was attached to the bottom plate. A compression force was applied to allow complete film-substrate contact. The tensile force was then conducted to separate the substrate from the film where the compressive and tensile forces were recorded.

Anticipated Results: Expected results may reveal that a l-PCL(65k)$_{50wt-\%}$:n-PCL(3k)$_{50wt-\%}$ film can be successfully bonded to a glass substrate when the film is heated to above its T_m of ~60 °C and compressed to initiate the bonding process. The bonding process can then be completed by cooling down to RT to allow the PCL chains to recrystallize. Contact time and compressive force to bond the film-substrate can be varied to observe and study their effect on how well the film can bond and debond to the glass substrate.

Preliminary Results: Initial results showed that the film-substrate adhesion could be quantified by a tensile tack force needed to debond the substrate from the PCL SMASH film. See Appendix 1.7 for preliminary results. Preliminary data showed that as the compressive force increased to bond the film to the substrate, the peak tensile force required to debond increased. Additionally, as the contact time increased, the peak tensile load decreased. Further studies include reproducing the data in triplets to confirm results and to obtain statistical significance as well as testing higher contact times and compressive force to observe the amount of tensile force (tack force) required to debond the film from the substrate.

6.1.2.8 T-PEEL TESTS

Motivation: To test the bonding/adhesive properties of a l-PCL$_{50wt\text{-}\%}$:n-PCL$_{50wt\text{-}\%}$ film with itself, a T-Peel experiment should be conducted. Applications for such experiments include the fabrication of industrial structures made from PCL SMASH sheets where the joints of the structure can be simply joined with each other by a thermal stimulus. The PCL SMASH sheets would become tacky at the joints by local heating when the temperature is above its T_m thus allowing for the bonding of neighboring surfaces then cooled down to recrystallize to complete the bonding process.

Methods: To conduct the T-Peel test, two PCL SMASH strips should be heated to 90 °C for 10 min and compressed to each other using a 200 g weight then cooled for 10 min at RT. The system should then be clamped in the DMA to conduct a tensile test on the system. The following procedure can be conducted: equilibrate at RT, isothermal for 1.0 min, and ramp force at 0.10 N/min to 18 N until the strips are debonded.

Anticipated Results: Results may reveal that the two PCL SMASH strips can be firmly bonded with each other at an elevated temperature that is above the strips T_m and cooled to RT to complete the bonding process. It can then be debonded with itself when a tensile test is performed.

Preliminary Results: Initial results revealed that the two PCL strips were able to successfully bond to each other at a temperature higher than its T_m and stayed bonded to each other when the system was cooled at RT (Appendix 1.8). A T-Peel test revealed that an approximately 0.8 N was required to debond the two strips. Further studies include reproducing the data in triplicate to confirm results and to obtain statistical significance as well as conducing T-Peels tests with other PCL SMASH compositions with varying thermoplastic SH agent.

6.1.2.9 LAP SHEAR STUDIES

Motivation: To study and measure the shear force created to debond a PCL film from a metal substrate, lap shear experiments should be conducted. Lap shear experiments consist of bonding two ends of two flat objects together in an overlapping configuration and measuring their resistance to shear forces. Applications for this test include making structures that incorporate

PCL SMASH and other substrate materials where shear forces may be unavoidable in industrial use.

Methods: To measure the adhesiveness of the PCL film from a metal substrate, a l-PCL$_{60\text{wt-}\%}$:n-PCL$_{40\text{wt-}\%}$ film should be compressed between two metallic strips using a 200 g weight and then placed in oven at 80 °C for 10 min then cooled at RT for 10 min. The system should then be clamped in the Linkam tensile stage using a deformation velocity of 100 µm/sec with a 200 N load cell to conduct the lap shear experiment.

Anticipated Results: Results could reveal that a specified shear force is required to debond the PCL film from the metal substrate.

Preliminary Results: Initial studies revealed that approximately 1.2 N of shear force was required to debond the top metallic substrate from the PCL film (Appendix 1.9). However, the data is quite noisy. Therefore, further studies include reproducing the data in triplets to confirm results and to obtain statistical significance as well as obtaining smoother and reliable data.

6.1.2.10 l-PCL:n-PCL SMASH COATINGS

Motivation: The ability of the l-PCL:n-PCL system to be used as a SMASH coating should be investigated to determine its applicability for industrial applications where damage in the form of scratches can be conducted to study the surface SM and SH effects.

Methods: Similar methods that were conducted for the tBA system in Chapter 3 section 3.4.3 should be conducted on the l-PCL:n-PCL system.

Anticipated Results: It can be hypothesized that similar results to those observed in Chapter 2 would be seen in the PCL coatings, where shape memory can assist in the surface crack closure and surface healing.

6.1.2.11 HEALED CRACK REOPENING STUDIES

Motivation: Healed crack reopening studies should be conducted to understand the number of times a healed crack can be reopened and exhibit the same amount of healing while also sustaining its mechanical properties. This study is important in order to observe whether the same area that was damaged prior can be re-healed if damaged again. Systems that have been reported in literature, specifically those that use SH microcapsules, can only heal once. Therefore, it is hypothesized that this system can heal an indefinite amount of times if no material is removed from the overall system.

Methods: To investigate the number of times a crack can be healed, the method reported in Chapter 2 section 2.2.5 should be employed to reopen the healed crack. The sample should then be thermally treated and cooled to complete the healing cycle. Mechanical testing would then reveal if the crack reopens and how the mechanical properties are affected. Each sample should be retested three times to observe healing as a function of repeated damage.

Anticipated Results: It is hypothesized that if there is no material removed, the polymeric systems would completely heal after every crack reopening. PCL thermoplastic serving as the SH agent always exhibits a tacky nature above its thermal transition and therefore the assumption is that the damage can heal indefinitely since there will always be thermoplastic to diffuse across the damage site. Additionally, as seen in chapter 2, the SM effect is reproducible among samples that were deformed three times and showed near complete recovery each time.

6.1.2.12 CRITICAL LIGAMENT WIDTH STUDIES

Motivation: Critical ligament width studies should be performed to study the critical ligament width where no crack closure is possible. The ligament width is the area between a dual notched damage (see Scheme 6-2). The ligament width is critical in polymer fracture mechanics as this sample area stores the required energy needed for crack closure. To change the ligament width, different notch lengths can be considered. This will decrease the ligament width until the cracks can no longer close due to an insufficient amount of stored energy in the ligament.

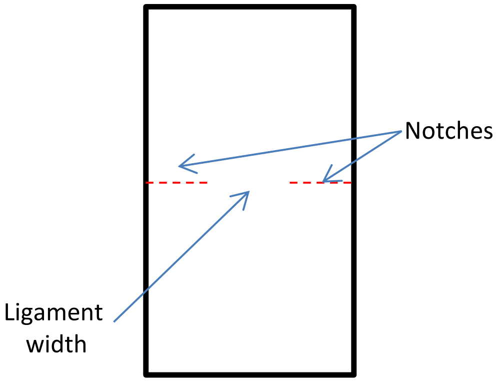

Scheme 6-2. Schematic showing dual notch damage and the location of the notches and ligament width.

Methods: To determine the critical ligament width, similar SH experiments to those performed in chapter 2 section 2.2.5 should be conducted. Notch lengths should be varied and the SH efficiency should be calculated for each resulting ligament width. Notch lengths to consider are the following: 0.1, 0.3, 0.5, 0.7, 0.9 mm.

Anticipated Results: It is hypothesized that there is a maximum notch length at which crack closure cannot be achieved. Pre-inducing large notches in the sample results in a smaller ligament and therefore may result in a limited amount of stored energy available for crack closure. Therefore, optimizing the notch length would be important to maximize the SM efficiency which is vital for SH.

6.2 SINGLE PHASE AMORPHOUS POLYMERIC SMASH COATINGS

6.2.1 CONCLUSIONS

Chapter 3 discussed the development of a single phase amorphous coating for scratch repair for optical applications. Here, a poly(tBA) thermoplastic, used as a SH agent, was synthesized using a free radical polymerization method. A semi-interpenetrated network (SIPN) was cured using tBA monomer crosslinked with TEGDMA and AIBN as a photointiator in the presence of the tBA thermoplastic. Films were made for thermal and thermo-mechanical characterization where 10 µm coatings were made for scratch testing and transmittance experiments. The coatings were analyzed for SH efficiency by comparing the area of the scratch and thermally treated state of the coatings. Results revealed that the coating that had 50 wt-% in the SIPN exhibited the most healing.

6.2.2 FUTURE DIRECTIONS

6.2.2.1 TERT-BUTYL ACRYLATE(tBA):BUTYL ACRYLATE (BA) COPOLYMER SMASH COATINGS

Motivation: In chapter 2, it was found that the T_g of the tBA coating was quite high (~T_g 48 °C) and irreversible damage was introduced at RT. The scratch morphology at RT was brittle where evidence of material removal was shown on the SEM micrographs (Chapter 3, Figure 3-21). Although the SH efficiency was reasonably high at ca. 81% when the SH thermoplastic content was 50 wt - % compared to the network content, a visible scar was still evident and essentially impaired the visibility through the clear coating. Therefore, further work includes the fabrication of a co-polymer network using two amorphous monomers of tert-butyl acrylate (tBA) and butyl acrylate (BA). Here, the T_g of tBA is 45 °C where the T_g of BA is -43 °C. When using 82 wt-% of tBA and 12 wt-% BA to make a co-polymer network coating, the T_g will be approximately 25 °C which is an ideal T_g for industrial use as most damage occurs at RT. Since the coating's T_g would be at RT, the coating would essentially be damaged and yet healing at the same temperature. These percentages were calculated using the Flory-Fox Equation (Appendix 6).

Methods: The protocol used in Chapter 3 section 3.4.3 should be employed to determine the SH efficiency of a new tBA:BA copolymer system.

Anticipated Results: The results may reveal a higher SH efficiency among all composition coatings tested due to the reduction of the coating's T_g. It can be hypothesized that since the scratch is being performed at the coating's T_g, there will be no material removal and a more controlled crack will form. Since a more controlled crack is formed the stored energy will not be dissipated, but instead remain in the coating to allow this stored energy to close the crack.

Preliminary Results: Initial studies reveal that after damaging a $tBA_{82wt\text{-}\%}$:$BA_{18wt\text{-}\%}$ (50:50) coating and thermally treated at 120 °C for 1 h, it exhibited the most healing where no visible scar was observed (Appendix 2.1). This was done in triplicate to obtain reproducible results (Figure A2.1.3). Figure A2.2.1 and Figure A2.1.2 shows thermogravimetric analysis (TGA) and differential scanning calorimetry (DSC) graphs respectively where the onset degradations temperatures and T_g are shown in the respective charts. Figure A2.1.4 shows a self healing (SH) efficiency (%) vs run number graph for the $tBA_{82wt\text{-}\%}$:$BA_{18wt\text{-}\%}$ (50:50) coating tested where it shows an average 98% SH efficiency. Further studies include obtaining SEM images to check for evidence of surface scaring. UV spectroscopy analysis can then be conducted to evaluate the degree of visible light penetrating the coating in its virgin, damaged and healed state. These experiments would show if there is any visible light impaired through the coating. Additionally, future studies can also include testing other coating compositions.

6.2.2.2 HEALING OF CRAZING

Motivation: Crazing is a form of localized plastic deformation and is considered a type of damage among amorphous polymers.[6] Crazing is a direct result of uniaxial tensile deformation where these microvoids form perpendicular to the loading direction.[6,7] Therefore, the motivation is to study the crazing effect that is evident during tensile testing as a function the wt-% of the SH thermoplastic agent within the SIPN networks. In addition, the degree of crazing observed as a function of deformation is also important to study in order to identify a crazing threshold before the systems are not recoverable.

Methods: Crazing experiments should be carried out by first performing a thermal removal step on all compositions fabricated at 120 °C for 10 min, followed by cooling at RT for 10 min. Sample should then be deformed at different strains using the 200 N load cell in the Linkam stage at RT. Small angle x-ray scattering (SAXS) can then be performed by exposing all deformed compositions to 1 h of x-ray radiation. The microstructure and morphology of the mircofibril crazes in the bulk of the system can then be studied.

Anticipated Results: It can be hypothesized that less crazing is evident with an increase in thermoplastic content. The thermoplastic SH agent adds to the overall ductility of the system yielding more elastic properties. In addition, it can also be hypothesized that more crazing will result with an increase in deformation and a decrease in SH agent.

<u>*Preliminary Results*</u>*:* During deformation, l:n-tBA films showed evidence of crazing where the films went from a clear (amorphous) to a white appearance. Appendix 2.0 shows preliminary results where crazing is evident in the l:n-tBA (0:100), (10:90) and (25:75) films during deformation. Crazing was observed regardless of thermoplastic content where the crazed formed perpendicular to the loading direction. Initial studies also revealed the crazing is reversible upon a thermal treatment as the sample returns to a transparent state. Although, not yet confirmed, this may mean the crazes healed upon a thermal stimulus where reversible crazing is possible. Further studies include reproducing the data in triplicate to confirm results and to obtain statistical significance as well as deforming at higher strains to obtain the degree of crazing.

6.2.2.3 FILM SELF HEALING STUDIES

<u>*Motivation*</u>*:* To study the degree of healing when damage is in the form of notches, SH studies should be conducted on l:n-tBA films when notches are induced in the system. This experiment would study how well the system can heal from more drastic type of damages. Applications include the fabrication of industrial structures where SM, SH and transparency are required.

<u>*Methods*</u>*:* To conduct the SH studies to study the degree of healing, procedures explained in Chapter 2 section 2.2.5 should be performed. The thermal treatment however would be as follows: 120 °C for 10 min, cool for 10 min at RT where a thermal removal step would be conducted using the same thermal treatment prior to testing the films.

<u>*Preliminary Results*</u>***:*** Results may reveal that SM and SH can be evident in films when compared to coatings.

Anticipated Results: Initial results show that when l:n-tBA films of (0:100), (10:90) and (25:75) are notched and uniaxially deformed, all specimens show great shape recovery effects when thermally treated (Appendix 2.3). However, there is no evidence of healing as the notches reopen upon deformation after thermal treatment. Future studies include varying the healing time, temperature or M_w of thermoplastic to achieve complete healing of the damage area.

6.3 ANISOTROPIC SHAPE MEMORY COMPOSITES (A-SMEC) SYSTEMS

6.3.1 CONCLUSIONS

Chapter 4 discussed the fabrication of a novel soft anisotropic fiber-reinforced-phase-separated elastomer termed Anisotropic Shape Memory Elastomer Composite (A-SMEC). Post-tensile testing revealed the orientation of the fiber reinforcements tailored the mechanical properties and SM effect. High mechanical properties were detected in specimens that had axially orientated fibers where the lowest was observed in specimens with transverse fiber orientation. SM fixing (R_f) was approximately 95.6% for composites that had fibers in the axial direction and low fixing of R_f = 86.2% with fibers in the transverse direction.

6.3.2 FUTURE DIRECTION

6.3.2.1 SELF HEALING STUDIES

Motivation: To expand the SMASH effect to fiber-reinforced composites, the degree of healing in A-SMEC systems should be conducted. These studies are vital for the composite community as this system would be the first of their kind to not only exhibit SM but also SH effects in one composite system.

Methods: To determine if the SMASH effect can be employed in fiber-reinforced composites, experiments similar to those used in Chapter 2 section 2.2.5 should be conducted with electrospinning times varied to obtain fiber mats with varying thicknesses and fiber densities. SH experiments as a function of fiber mat density can then be conducted to observe the dependence of SH efficiency on fiber density.

Anticipated Results: It is expected that as the fiber density increases in the composite, more healing will be achieved. If the fiber density is low then no-to-partial healing could be evident. Therefore, the degree of healing may change depending on the fiber density. This is hypothesized as the covalent bonds in the elastomeric network have been broken and essentially irrecoverable and the need for more SH agent is required to assist in restoring the mechanical properties of the elastomeric SM composite. Additionally, studies also need to be conducted on whether there is good adhesion at the fiber-elastomer interface. If there is no bonding, healing will be difficult as the fiber healing agent will not be able to bond and heal at the damaged elastomer crack plane.

Preliminary Results: Appendix 3.1 shows some preliminary data where shape recovery is evident; however healing has not been maximized for complete crack rebonding (Figure A3.1.1). This is evident as the cracks reopened after being thermally treated. The sample was deformed in its virgin, damaged and thermal treated states where shorter and longer thermal treatments were performed on the same sample. After the shorter thermal treatments the cracks reopened upon deformation. After the longer thermal treatment, the mechanical properties showed to be higher when compared to the samples virgin state. Factors to consider are fiber density in the composite, healing time and healing temperature to observe complete healing at the crack site.

Further studies include reproducing the data in triplets to confirm results and to obtain statistical significance.

6.3.2.2 FRACTURE MECHANICS STUDIES

Motivation: Fracture mechanics studies should be conducted to investigate the fracture toughness of the A-SMECs. These investigations would be vital to study as engineers can develop fracture resistant composites for both industrial and government aerospace products that endure multi directional loading.

Methods: To evaluate the fracture toughness of A-SMECs, experiments similar to those conducted in Chapter 2 section 2.2.5 should be performed.

Anticipated Results: The fracture mechanics of fiber reinforced composites have two different phenomena when the fibers are axially and transversely oriented in the composite. For the mode I "opening mode" condition, theoretical predictions state that the displacement of the crack faces are perpendicular to the crack plane.[6,8] However, when a dual notch damage (Scheme 6-2) is induced in anisotropic fiber reinforced composites, it can be postulated that the fibers in the axial direction will prohibit crack growth in a linear path (i.e. along the width of the specimen), but instead propagate in elastomer "rich" regions of the composite. This means that the cracks may propagate parallel to the loading direction as compared to theoretical predictions of cracks propagating perpendicular to the load.

Preliminary Results: Preliminary investigations (Appendix 3.1) show that the cracks do not propagate in a linear fashion along the width of the sample, but instead propagate parallel to the fiber orientation. The fibers that are parallel to the loading direction serve as reinforcements to prevent crack opening and propagation. It can be hypothesized that the reason for the crack growing parallel to the load is due to the elastomer matrix's low modulus between the fiber bundles where the cracks are guided by taking the least resistant path. Future studies include testing A-SMEC specimens where the fibers are embedded in the matrix in the transverse direction. Further studies include reproducing the data in triplicate to confirm results and to obtain statistical significance.

6.3.2.3 TRIPLE SHAPE MEMORY STUDIES

Motivation: Triple shape memory is a phenomenon that has not been observed in A-SMEC systems previously. To study if an A-SMEC system can exhibit three distinct shapes, triple shape memory studies should be conducted. Sylgard184 and PVAc have two distinct T_g's where Sylgard 184 has a T_g = -115.2 °C[9] and PVAc has a T_g = ~36 °C. Due to these two T_g's, the A-SMEC system is a candidate for a triple shape memory response.

Methods: To investigate the capability of using A-SMECs as triple shape memory polymers, a rectangular specimen should be heated above the T_g of the PVAc fibers (above T_g ~36 °C), where the sample would be deformed to shape 1 ("Z" shape) at 50 °C and fixed at 0 °C. The sample should then be heated back to 50 °C to recover to the original shape. Shape 2 (helix shape) can then be formed at 50 °C and cooled below the Sylgard's T_g (below T_g of -115 °C) to -120 °C. From 120 °C the helixed sample can be heated gradually to 50 °C, where the sample would recover to a "Z" shape (shape 1) followed by its original memorized shape.

Anticipated Results: It can be postulated that a rubbery plateau is evident between -115.5 °C and 36 °C with a second rubbery plateau evident after 36 °C thus leading to three temporal shapes at these thermal transitions.

6.3.2.4 AERODYNAMIC STUDIES

Motivation: The main motivation of developing A-SMEC systems was to biologically emulate bat wing morphology and aerodynamic properties for engineered systems in order to construct unmanned air vehicles for military uses. An initial collaboration between Brown University's bat flight research program with Dr. Kenny Breuer and Dr. Sharon M. Swartz[10,11] was started to aerodynamically model a bat wing prototyped and made in collaboration with my advisor and myself. The Brown University's bat flight research program was developed in order to study the roles of bats' bones, wing motion and skin morphology.[12] In Dr. Breuer and Dr. Swartz's lab, live bats have been flown in a wind tunnel to aerodynamically model their flight mechanics during flight.

Methods: In order to model the aerodynamic properties of a synthetically made bat wing, a bat wing structure should be constructed. The prototype should be constructed by doing the following: two 0.125 in. diameter carbon rods should be cured onto the leading and trailing edge of two 6.3 (l) x 3.9 (w) in. A-SMEC sheets using Sylgard 184. The carbon rods will allow for structural stability for wind tunnel mounting. Approximately 1 in. will separate the two skins for mounting purposes. The prototype should be mounted in a wind tunnel under similar flight conditions as those seen in bats natural environments in order to understand the flight mechanics.

Anticipated Results: It can be postulated that the initial prototype will provide evidence of how well the structure truly models an actual bat wing skin.

Preliminary Results: Preliminary investigations shown in Appendix 3.2 reveal the A-SMEC skins that incorporated poly(ε-caprolactone) (PCL M_w~65k) as fiber reinforcements are too thick to see any aerodynamic phenomena and therefore need skin membranes that are more compliant need to be constructed by decreasing the thickness. In comparing Brown's prototype (Figure A3.2.1) the use of neat silicone rubber with no reinforcements served to be more compliant with high performance where the prototype seemed to have flap-like motion when the forced air in the wind tunnel passed by the structure. Syracuse University's prototype showed minimal flapping motion in the wind tunnel under the same conditions. Further investigations can be conducted to perfect the bat wing prototype by considering the geometry of the bat wing skin and weight of the overall system to properly biomimic a bat wing's morphology and aerodynamic properties.

6.3.2.5 MECHANICAL MODELING

Motivation: In order to predict the mechanical properties of A-SMEC systems, mechanical modeling should be performed.

Methods: To model the system, a 3D finite-deformation constitutive modeling framework should be adopted where an effective phase model (EPM) can be used to model a shape memory elastomer composite (SMEC). In a recent paper published in our group, a shape memory elastomer composite (SMEC) was fabricated and characterized by Luo et al. and modeled in collaboration with Dr. Jerry Qi at the University of Colorado Boulder.[13] Here, the SMEC contained fibers that were isotropic and randomly aligned where it was modeled for its thermo-mechanical behavior using a 3D finite-deformation constitute model framework.[13]

Anticipated Results: The model chosen would predict the mechanical behavior as a function of fiber anisotropy and the mechanical behavior at various temperatures.

6.3.2.6 STRAIN INDUCED CRYSTALLIZATION STUDIES

Motivation: To study if strain induced crystallization is occurring while deforming the fibers in the A-SMEC systems, wide and small angle x-ray scattering (WAXS and SAXS) experiments should be conducted. The WAXS/SAXS x-ray experiments are used to analyze the microstructure and orientation of the polymer chains as well as the lamellar crystalline structures. This study can further add in the understanding of the A-SMEC mechanical responses post deformation.

Methods: To study strain induced crystallization in the A-SMEC systems at RT, place the Linkam tensile stage in the WAXS/SAXS x-ray machine and deform A-SMEC strips in situ at different fiber angles and at various deformations values.

Anticipated Results: Anticipated results may reveal a higher degree of polymer molecular chain orientation induced at higher deformation values. In addition, a higher degree of induced crystals (i.e. lamellar structures) may be evident at higher deformation values.

6.4 ANISOTROPIC SHAPE MEMORY COMPOSITES (A-SMEC) LAMINATED COMPOSITES

6.4.1 CONCLUSIONS

Chapter 5 was a continuation of Chapter 4 where the fabrication and characterization of dual laminated composites to study the pitch and curvature response of the A-SMEC's was described. Preliminary studies showed that more curvature and pitch is observed with an increase in fiber angle of the second ply. RPSM was also characterized where the SM fixing was directly tailored to the fiber anisotropy. Fibers in the axial direction showed to have the highest fixing with the lowest showing in specimens where the fibers were oriented in the transverse direction.

6.4.2 FUTURE DIRECTION

6.4.2.1 LAMINATED COMPOSITES USING VARIOUS ANGLES

Motivation: Chapter 5 explained the fabrication and characterization of dual laminated composites where the following composites were studied: 0/0°, 0/22.5°, 0/45°, 0/67.5°, and 0/90°. The next step is to use other fiber orientations to understand the mechanical behavior and geometrical changes for any fiber orientation combination.

Method: A similar method used in chapter 5 should be conducted in order to make the laminated composites with the following plies: 45/22.5°, 45/67.5°, 45/90°, 67.5/90°, 67.5/22.5°, 90/22.5°, and 0/22.5/45/67.5/90°.

Anticipated Results: Some results may yield a different form of curvature and pitch that were not observed and shown in the samples tested in Chapter 5. This postulation can be due to the residual stresses that are formed post deformation.

Preliminary Results: Appendix 4.1 shows initial results of strips that were tested and cut from the side of the composite system where only arc type geometry was evident (Figures A4.1.1 - A4.1.4). When the strips were cut from the bottom on the composite system (Figure A4.1.5 - A4.1.7) curvature was evident where some showed arc geometry. $\%_{deformation}$ and $\%_{recovery}$ values revealed that all sample tested were deformed in the range of 40 - 85% where all recovery ratios were approximately 90 %.

6.4.2.2 MULTI-LAYERED LAMINATED COMPOSITES

Motivation: In chapter 5, the investigation of bilayer laminated composites where fabricated to study the curvature and pitch responses. Further studies can include the addition of more than two plies for composite fabrication to study the mechanical behavior and geometrical changes.

Method: Sample fabrication and experiments explained in chapter 5 should be performed where a three or four lamina pile-up can be used to construct the laminated composites with more than two plies. The possibility of constructing a twisted, chiral lay-up that would naturally yield chiral mechanical and shape memory properties may also be fabricated using the following lay-up sequence: 0/15/30/45/60.

Anticipated Results: Some results may yield a different form of curvature and pitch that were not observed and shown in the samples tested in Chapter 5 as there is a different degree of residual stress incurred in the composite due to fiber anisotropy.

Preliminary Results: Appendix 4.1 shows one sample of the following multilayered system: 0/22.5/45/67.5/90°. This system showed an arc-type geometry. Further studies include reproducing the data in triplets to confirm results and to obtain statistical significance as well as fabricating other systems using various lay-up configurations.

6.4.2.3 VARIABLE STRAIN INDUCED CURVATURE AND PITCH STUDIES

Motivation: Deformation studies should be conducted to study the curvature and pitch responses as a function of uniaxial strain induced and fiber anisotropy. These studies would be important as the strain-curvature correlation would allow for the fabrication of industrial and/or biomedical devices/materials based on desired curvature requirements.

Methods: The same experimental methods described in Chapter 5 should be performed.

Anticipated Results: It can be hypothesized, and predicted from our simple model adaptation, that an increase in curvature response will result from an increase in deformation as well as an increase in fiber angle. This can be related to the increase in residual stress induced in the sample with an increase of deformation.

6.4.2.4 MECHANICAL MODELING

Motivation: A theoretical mechanical model should be developed to predict the curvature and pitch responses in laminated composites as a function of fiber orientation, mechanical strain, deformation temperature and the number of laminae that make up the composite itself.

Methods: A model should be constructed to study the mechanical response to loading and temperature.

Anticipated Results: The model can predict the curvature and pitch responses as a function of fiber orientation, deformation, deformation temperature and the number of lamina in the composite at specified temperatures and strains induced.

6.4.2.5 SPIRAL HANDEDNESS STUDIES

Motivation: Preliminary results show that when laminated A-SMECs strips are deformed, out-of-plane spiral geometries are observed when the strips are elastically recovered post deformation. Therefore, studies should be conducted on the handedness (i.e. left handed or right handed) of the spiral as a function of laminated A-SMEC systems. These studies not only can assist in the further understanding of the mechanical responses of the systems, but also assist in projecting the spiral response in relation to fiber orientation. This may prove important for biomedical devices or biomedical materials where a mechanical response of a specified geometry is desired.

Methods: To study the spiral handedness of the A-SMEC strips, experiments explained in Chapter 5, section 5.2.5 should be performed.

Anticipated Results: Initial results may reveal a dependence of left handed or right handed spirals on a ply orientation whether they are positively or negatively orientated. For example, if 0/22.5° was considered the handedness may differ between a 0/-22.5° or 0/22.5° configuration.

6.4.2.6 SPIRAL VS. SAMPLE WIDTH STUDIES

Motivation: To study the degree of spiral dependence on sample width, deformation studies should be conducted. As stated in the introductory section of Chapter 5, the width of the material strip can have an effect on the curvature response. For example, if a sample strip has a wider width, less curvature is observed. However, if the sample strip has a thinner width more curvature is observed.

Methods: To study the spiral as a function sample width, experiments explained in Chapter 5, section 5.2.5 should be performed where the width of the samples should be varied in the range of 0.1 to 1.0 mm.

Anticipated Results: Initial results could reveal that a tighter curvature is observed in those samples with a smaller sample width and loose curvature when the sample width is wider.

6.5 OTHER SYSTEMS

6.5.1 PCL/EPOXY SELF HEALING STUDIES

Motivation: In a recent paper published in our group by Luo et al. the fabrication and characterization of a triple shape memory system was employed.[14] Here, diglycidyl ether of bisphenol-A (DGEBA) (monomer 1), neopentyl glycol diglycidyl ether (NGDE) (monomer 2), and poly(propylene glycol)bis(2-aminopropyl (Jeffamine D230) crosslinker was used to make a co-polymer SM thermoset matrix. An isotropic poly(ε-caproplactone) (PCL) fiber mat was embedded in the matrix to serve at the SH agent. The next phase in this line of research is to observe and quantify the SH capability of the composite system.

Methods: SH experimental methods laid out in Chapter 2 section 2.2.5 should be performed where the electrospinning times can be varied to obtain different fiber mat thicknesses and densities. SH experiments as a function of fiber mat densities should be conducted to observe the degree of SH.

Anticipated Results: Results may reveal the need for a thick fiber mat where complete healing can be achieved with a high fiber density in the composite.

<u>*Preliminary Results*</u>: As seen in Appendix 5.1, preliminary results showed that partial healing was evident among the samples tested when uniaxially tested. The tensile testing was used to measure the degree of healing from evidence of crack rebonding. In the first experiment, a PCL (M_w~70 - 90k)/Epoxy composite was fabricated with a fiber mat that had an average thickness of 0.17 mm (Figure A5.1.1 - A5.1.3). The force vs. displacement curves in Figure A5.1.3 showed a red curve indicative of the deformation of the sample in its virgin state. The blue curve showed the deformation in the samples notched state and black curve in the sample's thermally treated state. The elastic region, yield point and cold drawing regions were evident on the red and blue curves. The yield points are the same when the sample is in its virgin and damaged state. However, when the cracks started to propagate a decrease in force and displacement on the sample's notched state (blue curve) was observed. The sample then completely fractured after the thermal treatment and restretching processes. The second experiment was done using the same procedures explained above but the sample fabricated was a PCL (M_w65k)/Epoxy composite where a different M_w for the PCL was used. Similar results were evident when compared to the PCL (M_w~70 - 90k)/Epoxy composite (Figures A5.1.4 – A5.1.6). An important observation to point out, however, is the higher yield point of the sample in its damaged state when compared to its virgin state (Figures A5.1.5 – A5.1.6). This is attributed to a longer cooling time which allowed the PCL chains to crystallize for a longer period of time thus having higher mechanical properties. Although the sample was allowed to recrystallize for a longer period of time, there was no evidence of healing at the damaged site. Since there was no crack healing, this could lead to catastrophic damage during the the lifecycle of the system. Further studies include the fabrication of thicker PCL fiber mats where there is a higher density of fibers in the composite, as well as testing different healing temperatures and healing times.

6.5.2 SMASH SYSTEM WITH TWO THERMAL TRANSITIONS STUDIES

Motivation: A SMASH system where the SM network has a lower thermal transition needed for crack closure and the SH agent has a higher thermal transition needed for healing should be constructed. Here, the SMASH effect can happen in succession where the crack closure would act first due to its lower thermal transition and the healing process would follow owing to the higher thermal transition.

Methods: The same experimental methods explained in Chapter 2 section 2.2.5 should be performed where the thermal treatment starts 20 °C lower than the SM network's thermal transition and ends 20 °C above the SH agent's thermal transition to ensure a thermal transition is not missed.

Anticipated Results: It can be hypothesized that the SMASH effect can be optimized and more efficient if crack closure happened first for complete crack-surface contact where the healing agent can then be liquified above its thermal transition to maximize the healing process. This can assist in the use of minimal healing agent needed for healing by maximizing the SM effect first for crack closure. This method can also assist in preventing the healing agent from overfilling the cracked area and prevent crack closure from being maximized.

6.5.3 SMASH HYDROGELS STUDIES

To broaden the SMASH effect to other systems, SMASH hydrogels should be fabricated for biomedical and industrial applications. Hydrogels are 3D crosslinked polymers that have a strong affinity for water but are prevented from dissolving in water by the covalent crosslinks. Today many hydrogels are used for age related degenerative spine conditions[15], contact lenses[1], pharmaceuticals[16], tissue engineering[16] and drug delivery systems.[1,16] Some polymers used to make hydrogels are poly(vinyl alcohol), acrylic, polyHEMA, glycopolymers, acrylamide, poly(ethylene oxide), N-vinyl-2-pyrrolidinone, and poly(2-hydroxylethyle methacrylate).[1] There have been studies conducted where the concept of shape memory has been proven in hydrogels[17] and different hydrogel systems exhibit the self healing[18] effect, however to date these two effects have yet to be shown in one hydrogel system. Many hydrogels undergo wear and tear during use and the need for both shape memory and self healing in one hydrogel would assist in sustaining the mechanical properties.

6.6 REFERENCES

(1) Sperling, L. H.: *Introduction of Physical Polymer Science*; 4th Edition ed.; John Wiley ans Sons Inc.: Hoboken, New Jersey, 2006.

(2) Tarazaga, P. A.; Peairsa, D. M.; Wilkieb, W. K.; Inmana, D. J.: Structural Health Monitoring of an Inflatable Boom Subjected to Simulated Micrometeoroid/Orbital Debris Damage. In *SPIE*, 2006; Vol. Vol. 6176.

(3) Luo, X. F.; Ou, R. Q.; Eberly, D. E.; Singhal, A.; Viratyaporn, W.; Mather, P. T.: A Thermoplastic/Thermoset Blend Exhibiting Thermal Mending and Reversible Adhesion. *Acs Applied Materials & Interfaces* **2009**, *1*, 612-620.

(4) Luo, X. F.; Lauber, K. E.; Mather, P. T.: A thermally responsive, rigid, and reversible adhesive. *Polymer* **2010**, *51*, 1169-1175.

(5) Romo-Uribe, A.; Alvarado-Tenorio, B.; Romero-Guzmán, M. E.: A SMALL-ANGLE LIGHT SCATTERING INSTRUMENT TO STUDY SOFT CONDENSED MATTER. 2010; Vol. 30; pp 190-200.

(6) Young, R. J.; Lovell, P. A.: *Introduction to Polymers*; 2 ed.; Chapman and Hall, 1991.

(7) Kausch, H. H.; Gensler, R.; Grein, C.; Plummer, C. J. G.; Scaramuzzino, P.: Crazing in semicrystalline thermoplastics. *Journal of Macromolecular Science-Physics* **1999**, *B38*, 803-815.

(8) Broek, D.: *Elementary Engineering Fracture Mechanics*; 4 ed.; Kluwer Academic Publishers, 1986.

(9) Luo, X. F.; Mather, P. T.: Preparation and Characterization of Shape Memory Elastomeric Composites. *Macromolecules* **2009**, *42*, 7251-7253.

(10) Downs, M.: Bats in Flight Reveal Unexpected Aerodynamics. 2006.

(11) Tian, X. D.; Iriarte-Diaz, J.; Middleton, K.; Galvao, R.; Israeli, E.; Roemer, A.; Sullivan, A.; Song, A.; Swartz, S.; Breuer, K.: Direct measurements of the kinematics and dynamics of bat flight. *Bioinspiration & Biomimetics* **2006**, *1*, S10-S18.

(12) Brown University's Bat Flight Research Program. 2012.

(13) Ge, Q.; Luo, X. F.; Rodriguez, E. D.; Zhang, X.; Mather, P. T.; Dunn, M. L.; Qi, H. J.: Thermomechanical behavior of shape memory elastomeric composites. *Journal of the Mechanics and Physics of Solids* **2012**, *60*, 67-83.

(14) Luo, X. F.; Mather, P. T.: Triple-Shape Polymeric Composites (TSPCs). *Advanced Functional Materials* **2010**, *20*, 2649-2656.

(15) Yue, J. J.; Morgenstern, R.; Morgenstern, C.; Lauryssen, C.: Shape Memory Hydrogels – A Novel Material for Treating Age-related Degenerative Conditions of the Spine. *E U R O P E A N M U S C U L O S K E L E T A L R E V I E W* **2011**, 184- 188.

(16) Jagur-Grodzinski, J.: Polymeric gels and hydrogels for biomedical and pharmaceutical applications. *Polymers for Advanced Technologies* **2010**, *21*, 27-47.

(17) Osada, Y.; Matsuda, A.: SHAPE-MEMORY IN HYDROGELS. *Nature* **1995**, *376*, 219-219.

(18) Phadke, A.; Zhang, C.; Arman, B.; Hsu, C. C.; Mashelkar, R. A.; Lele, A. K.; Tauber, M. J.; Arya, G.; Varghese, S.: Rapid self-healing hydrogels. *Proceedings of the National Academy of Sciences of the United States of America* **2012**, *109*, 4383-4388.

APPENDIX 1.0

LINEAR/NETWORK POLY(ε-CAPROLACTONE) BLENDS WITH SHAPE MEMORY ASSISTED SELF-HEALING (SMASH)

A1.0 SUMMARY

Please refer to Chapter 6 for an explanation of experiments presented in this appendix.

APPENDIX 1.1

WATER IMMERSION STUDIES

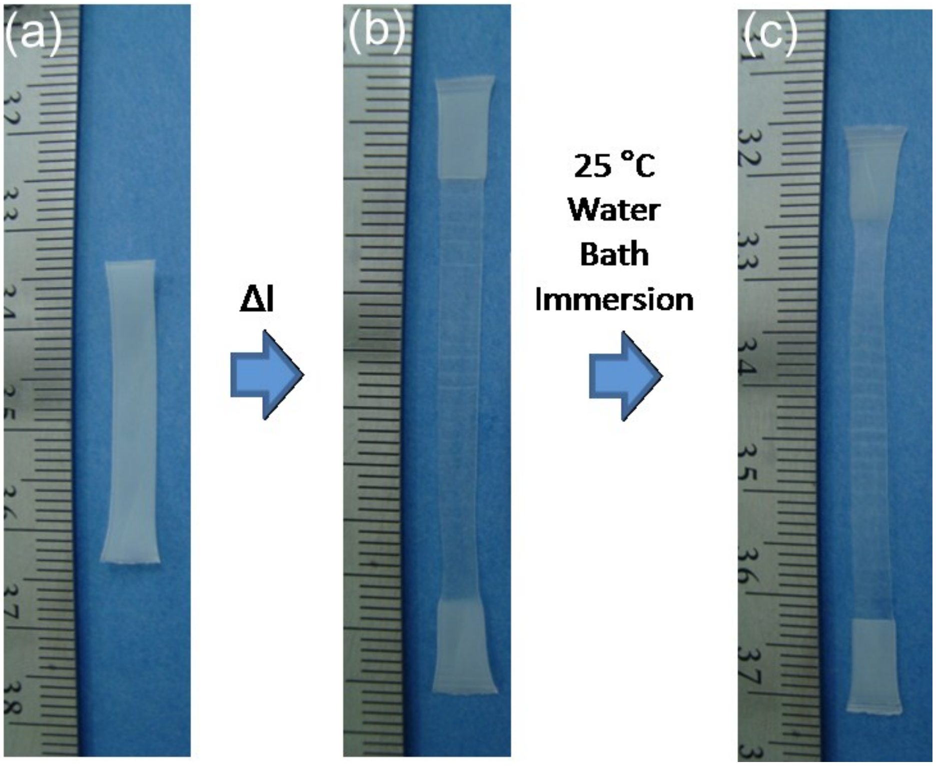

Figure A1.1.1. Images showing water triggered SMASH experiment using a l-PCL$_{50\text{wt-}\%}$:n-PCL$_{50\text{wt-}\%}$ sample where (a) initial length (b) stretched length, and (c) recovered length in water where sample was submerged in 25 °C water bath for 30 min. $\%_{\text{deformation}}$ was 90.1% with a $\%_{\text{recovery}}$ of 1.6 %.

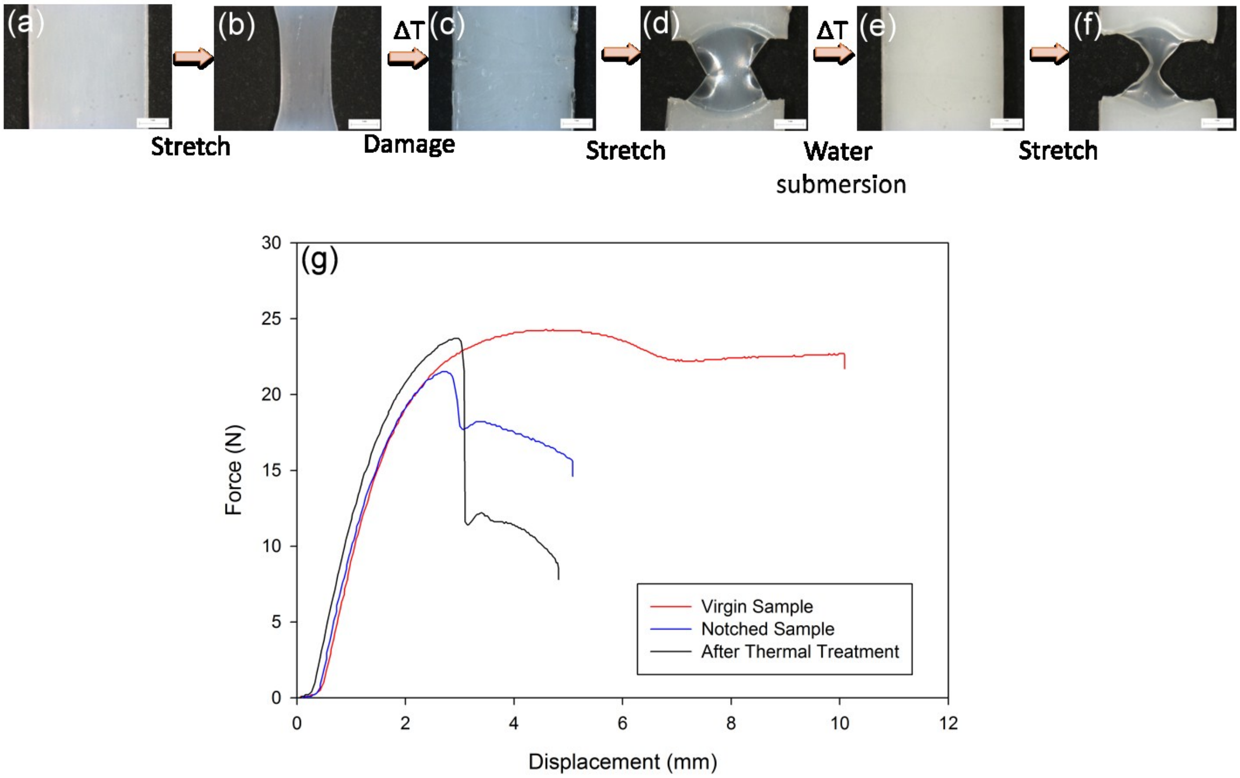

Figure A1.1.2. l-PCL$_{50wt-\%}$:n-PCL$_{50wt-\%}$ sample stretched using Linkam tensile stage with a 200 N load cell, a 100 µm/sec stretch rate and a stretch temperature at RT. (a) virgin, (b) deformed, (c) recovered at 80 °C for 10 min. and cooled at RT for 10 min then notched, (d) damaged and deformed, (e) sample recovered by submersing it in water at 80 °C for 2 h. Cooled at RT for 10 min, and (f) deformed sample where there is evidence of crack reopening. (g) Force vs displacement graph for virgin, notched and thermally treated states. (Scale bar: 1 mm).

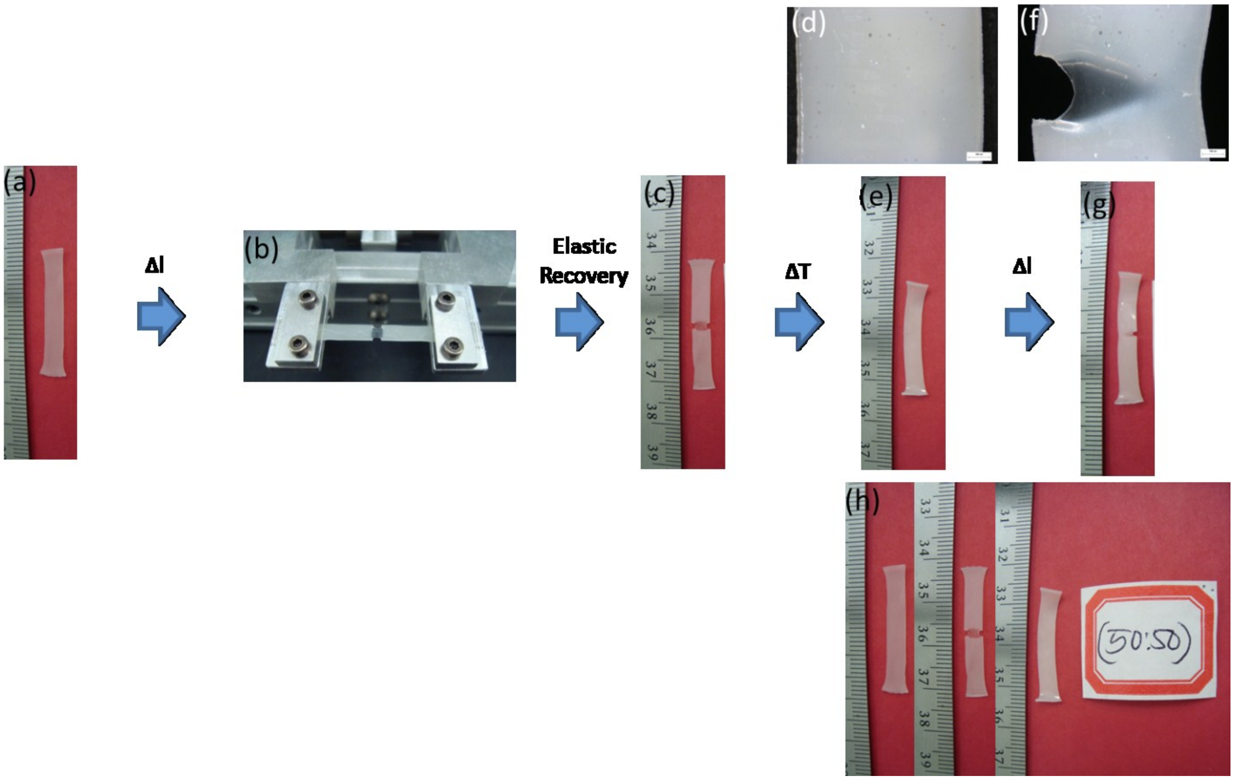

Figure A1.1.3. Schematic showing thermally triggered water experiment using a l-PCL$_{50wt-\%}$:n-PCL$_{50wt-\%}$ sample. Images showing (a) virgin sample, (b) 0.5 mm notches induced in sample then clamped in mechanical tensile device to stretch sample and observe crack propagation, (c) sample unclamped where elastic recovery was evident, (d) sample submerged in a 80 °C water bath for 30 min. Stereomicrograph shows sample after thermal treatment with evidence of crack closure, (e) full sample profile after thermal treatment, (f) stereomicrograph of sample after deformation, evidence of one crack reopening, (g) full sample profile after deformation, (h) the sample in the virgin, damage and healed state adjunct to each other for comparison. %$_{deformation}$ was 8.2% with a %$_{recovery}$ of 104 %.

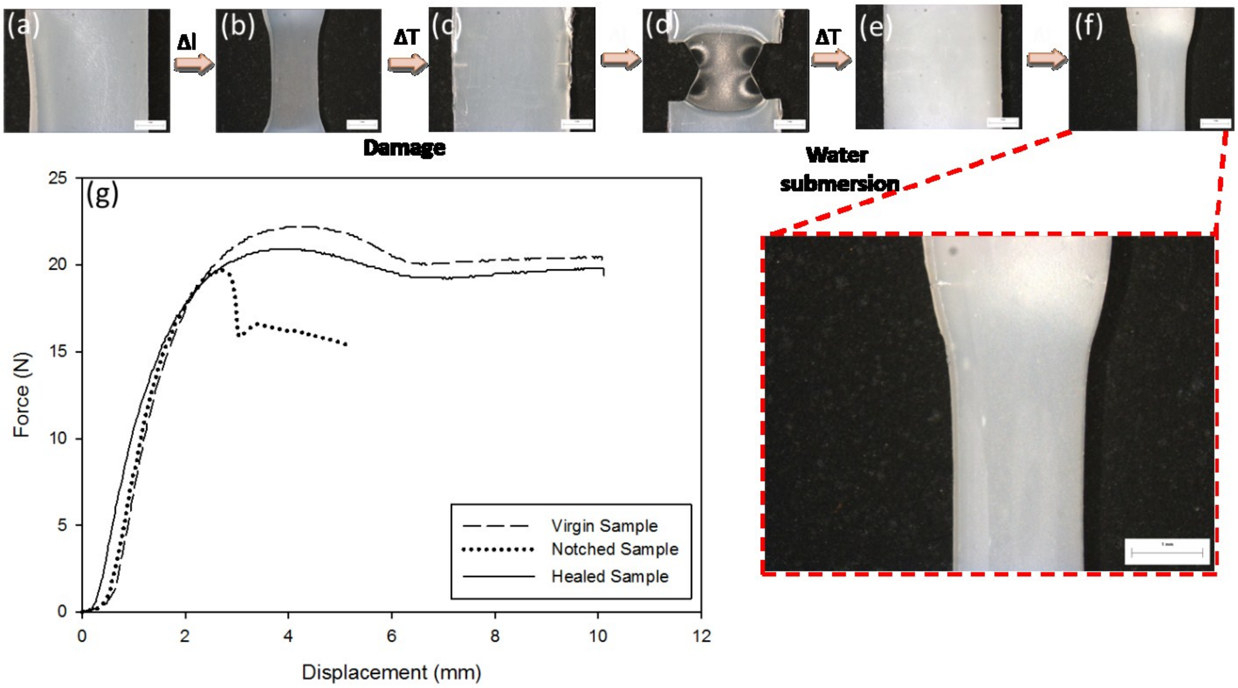

Figure A1.1.4. l-PCL$_{80wt\text{-}\%}$:n-PCL$_{20wt\text{-}\%}$ sample stretched using Linkam tensile stage with a 200 N load cell, 100 µm/sec, stretch rate at RT, (a) virgin, (b) deformed, (c) sample recovered at 80 °C for 10 min and cooled at RT for 10 min then notched, (d) damaged and deformed, (e) sample recovered by submersing a deformed sample in water at 80 °C for 30 min and cooled to RT for 10 min, (f) deformed sample after thermal treatment, and (g) force vs displacement graph for virgin, notched and thermally treated states. (Scale bar: 1 mm).

APPENDIX 1.2

HEALING KINETICS STUDIES USING DIFFERENT PCL THERMOPLASTIC MOLECULAR WEIGHTS (M_W)

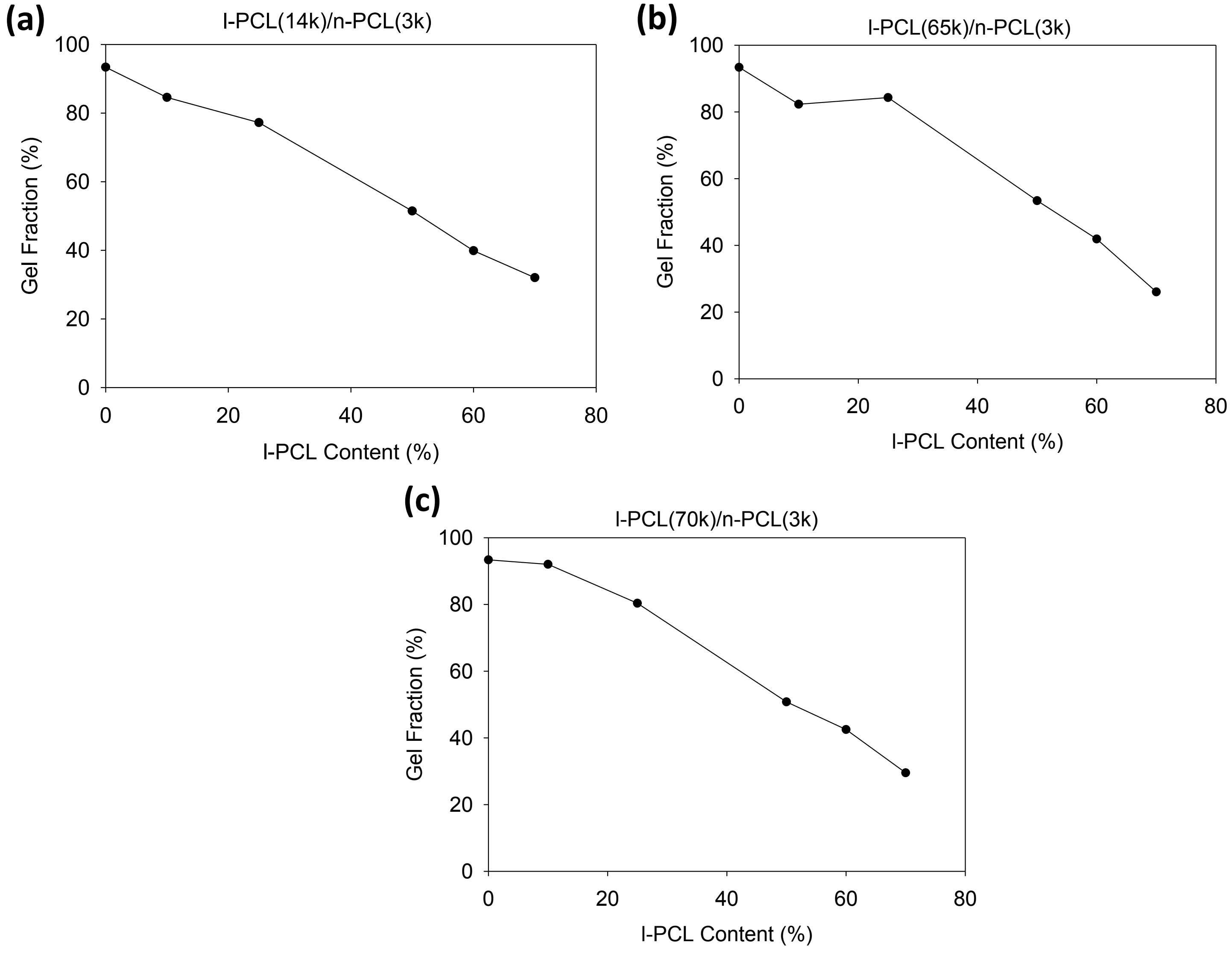

Figure A1.2.1. Graphs showing gel fractions as a function of l-PCL wt - % content of (a) compositions using 14k M_w PCL thermoplastic, (b) compositions using 65k M_w PCL thermoplastic, and (c) compositions using 70k M_w PCL thermoplastic.

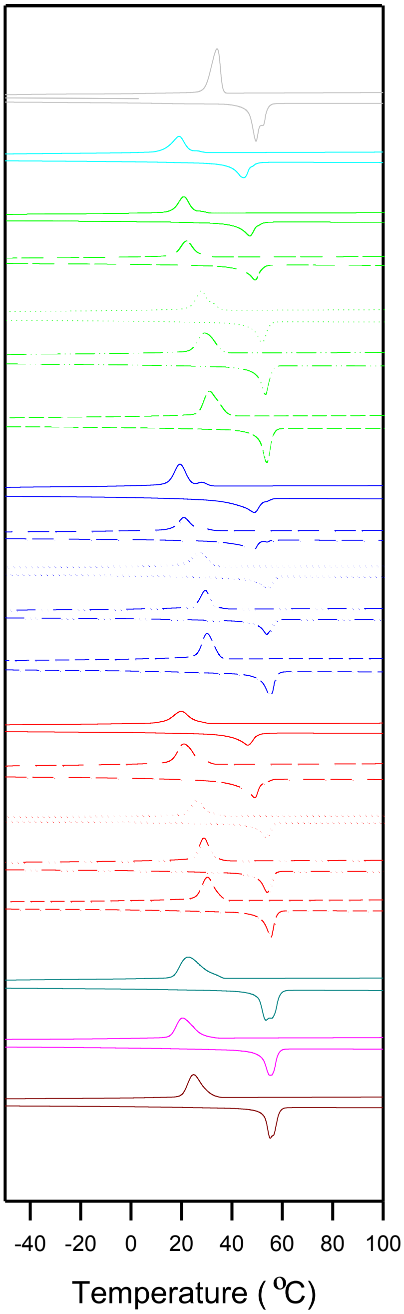

Figure A1.2.2. Differential Scanning Calorimetry (DSC) traces showing the T_c and T_m among all compositions tested. Equilibrate at -80.00 °C, ramp 10.00 °C/min to 120.00 °C, ramp 10.00 °C/min to -90.00 °C, isothermal for 1.00 min, and ramp 10.00 °C/min to 120.00 °C, isothermal for 1.00 min where the second heating traces is shown.

Table A1.2.1. Table showing the T_m, heat of melting, T_c and heat of crystallization as a function of PCL thermoplastic M_w with corresponding compositions.

	T_m (°C)	ΔH (J/g) Heat of Melting	T_c (°C)	(J/g) Heat of Crystallization
PCL Diacrylate$_{100\%}$	46.5	85.9	36.3	79.6
l-PCL/n-PCL(3k) (0:100)	39.0	56.5	23.4	57.2
l-PCL(14k)/n-PCL(3k)				
(10:90)	40.6	63.1	24.7	57.2
(25:75)	43.1	63.5	26.6	61.8
(50:50)	47.1	72.5	32.0	66.2
(60/40)	48.9	78.3	35.8	71.3
(70/30)	49.8	80.9	38.1	73.4
l-PCL(65k)/n-PCL(3k)				
(10:90)	39.7	66.6	24.2	60.7
(25:75)	42.6	62.6	24.6	62.5
(50:50)	47.0	65.2	32.5	62.4
(60:40)	49.3	72.1	32.7	64.1
(70:30)	50.6	73.6	35.4	65.2
l-PCL(70k)/n-PCL(3k)				
(10:90)	39.3	64.5	26.1	62.1
(25:75)	42.1	65.0	26.7	61.5
(50:50)	48.2	69.5	31.1	65.5
(60:40)	49.8	72.3	33.2	66.1
(70:30)	51.5	71.8	35.6	66.7
l-PCL(14k)$_{100\%}$	50.2	82.1	33.2	78.8
l-PCL(65k)$_{100\%}$	51.3	75.1	28.9	66.1
l-PCL(70k)$_{100\%}$	52.7	76.3	31.3	70.9

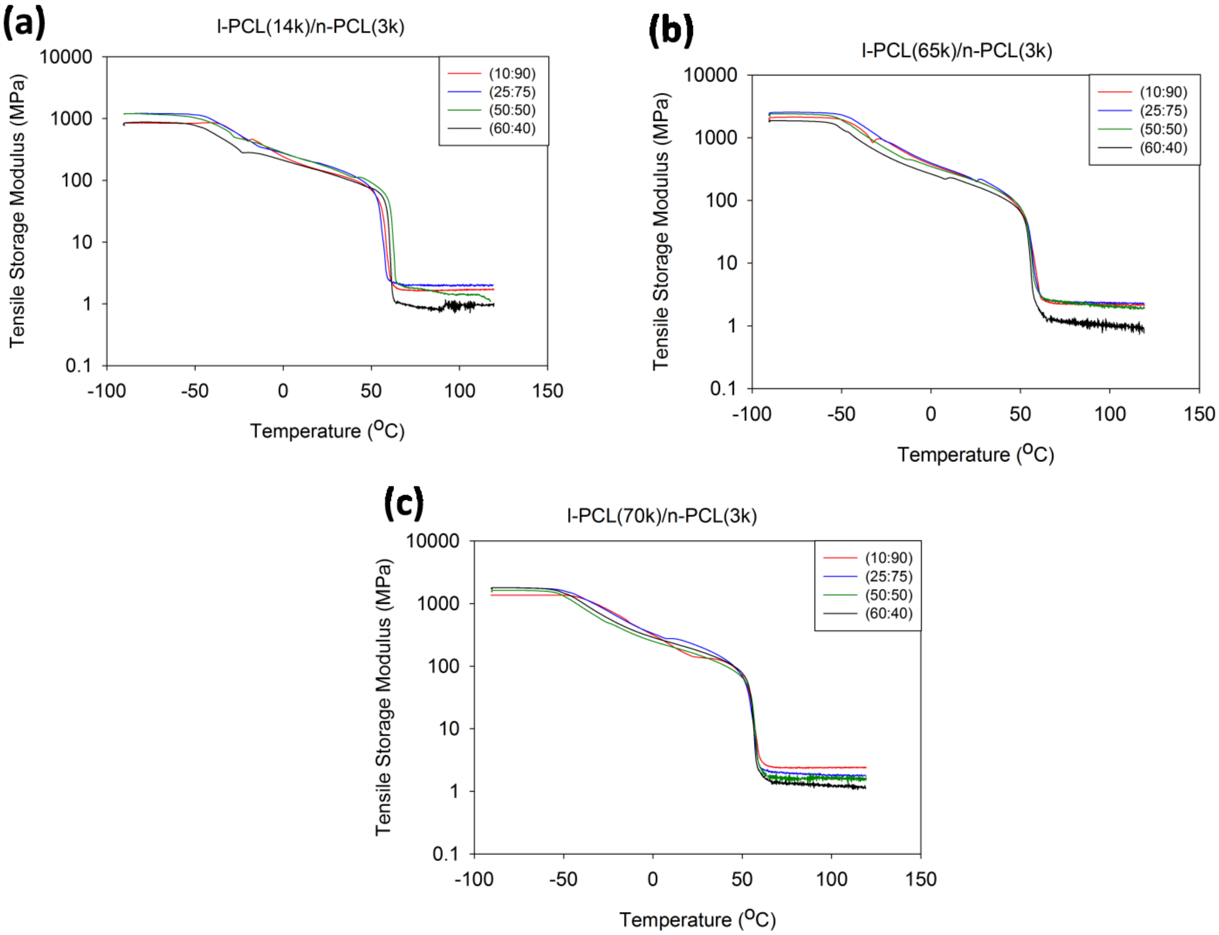

Figure A1.2.3. Graphs showing tensile storage modulus as a function of temperature for (a) l-PCL(14k):n-PCL(3k) (b) l-PCL(65k):n-PCL(3k) and (c) l-PCL(70k):n-PCL(3k) blends for the following compositions: (10:90), (25:75), (50:50) and (60:40).

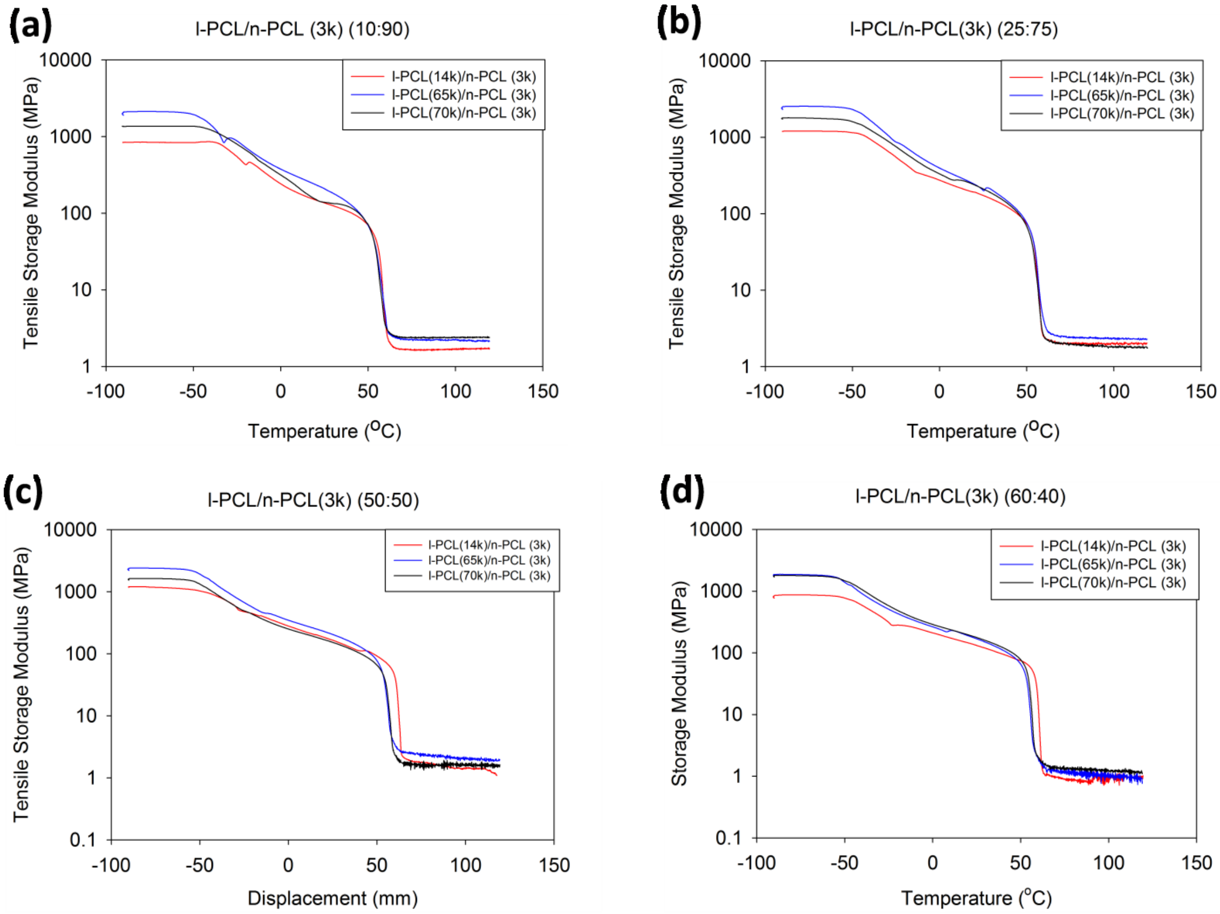

Figure A1.2.4. Tensile storage modulus as a function of temperature for (a) l-PCL(65k)$_{10wt-\%}$:n-PCL(3k)$_{90wt-\%}$, (b) l-PCL(65k)$_{25wt-\%}$:n-PCL(3k)$_{75wt-\%}$, and, (c) l-PCL(65k)$_{50wt-\%}$:n-PCL(3k)$_{50wt-\%}$ and (d) l-PCL(65k)$_{60wt-\%}$:n-PCL(3k)$_{40wt-\%}$ compositions with varying thermoplastic M$_w$.

APPENDIX 1.3

PUNCTURE TESTING STUDIES

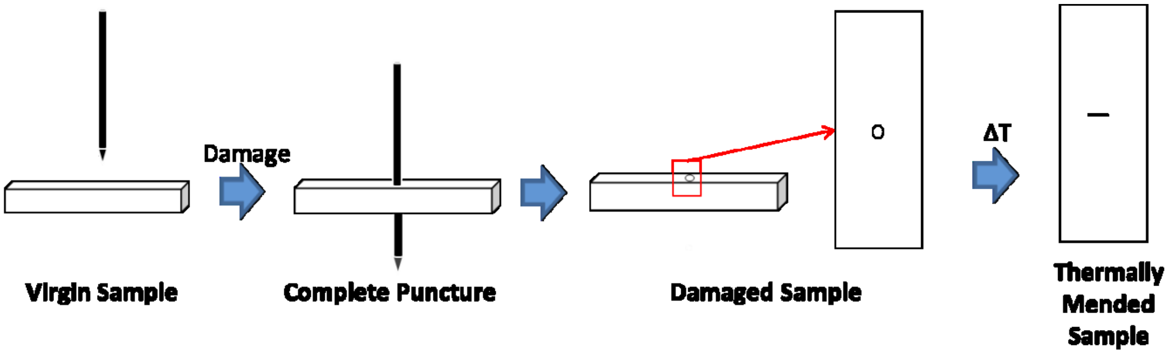

Scheme A1.3.1. Schematic showing process of puncture testing.

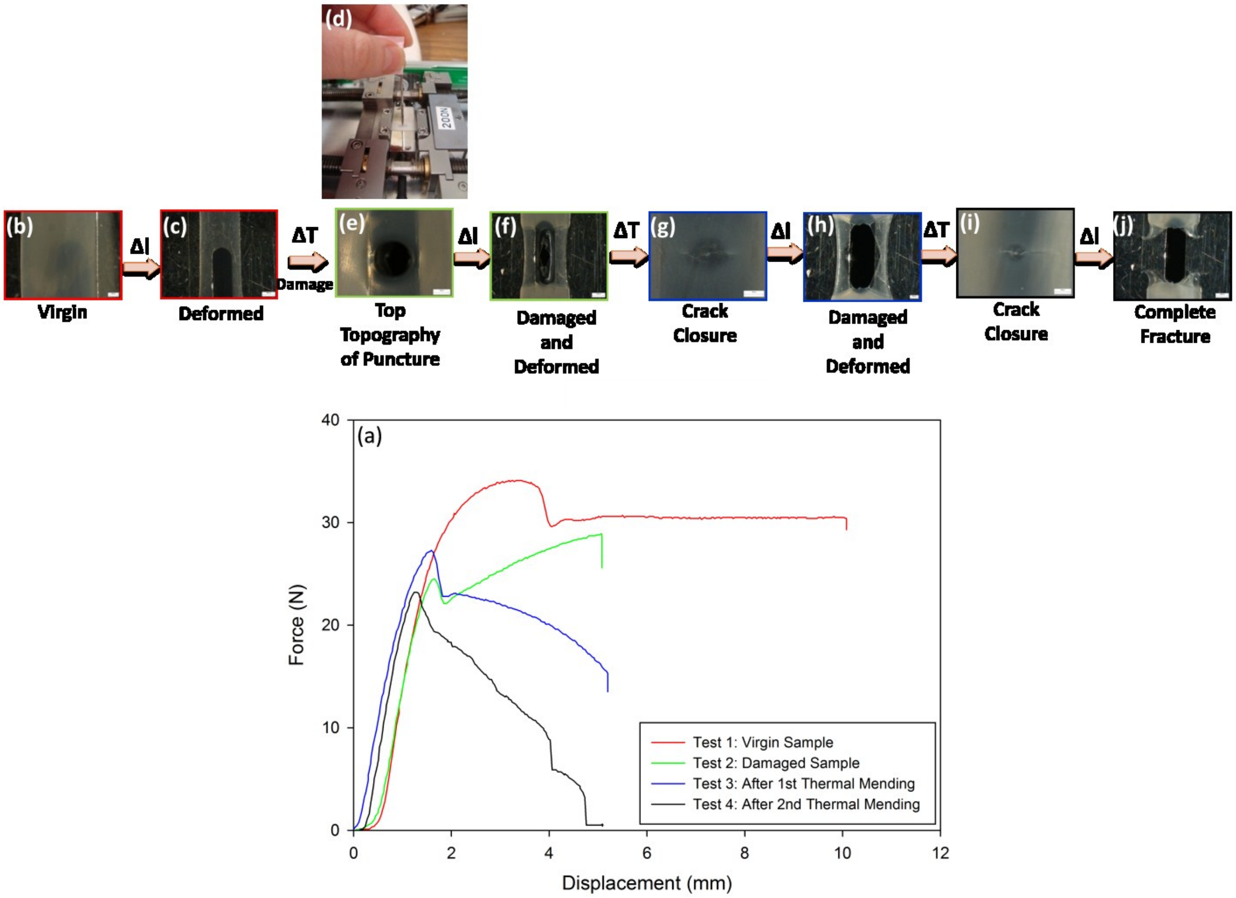

Figure A1.3.1. Puncture testing was conducted to quantify the SMASH effect. (a) Force vs displacement graph of a l-PCL(65k)$_{50wt\text{-}\%}$:n-PCL(3k)$_{50wt\text{-}\%}$ sample where stereomicrographs show (b) virgin sample, (c) deformed sample using a 200 N load cell and stretch rate of 100 µm/sec. Sample was thermally treated for 10 min at 80 °C and cooled to RT for 10 min for shape recovery post stretch, (d) puncture process, (e) punctured sample using a 1.23 mm diameter needle, (f) damaged and deformed, (g) sample after thermal treatment for 10 min at 80 °C and cooled to RT for 10 min. for crack closure and crack bonding, (h) deformed, (i) thermal treatment for 10 min. at 80 °C and cooled to RT for 10 min, and (j) complete fracture. (Scale bar: 300, 500 and 1000 µm).

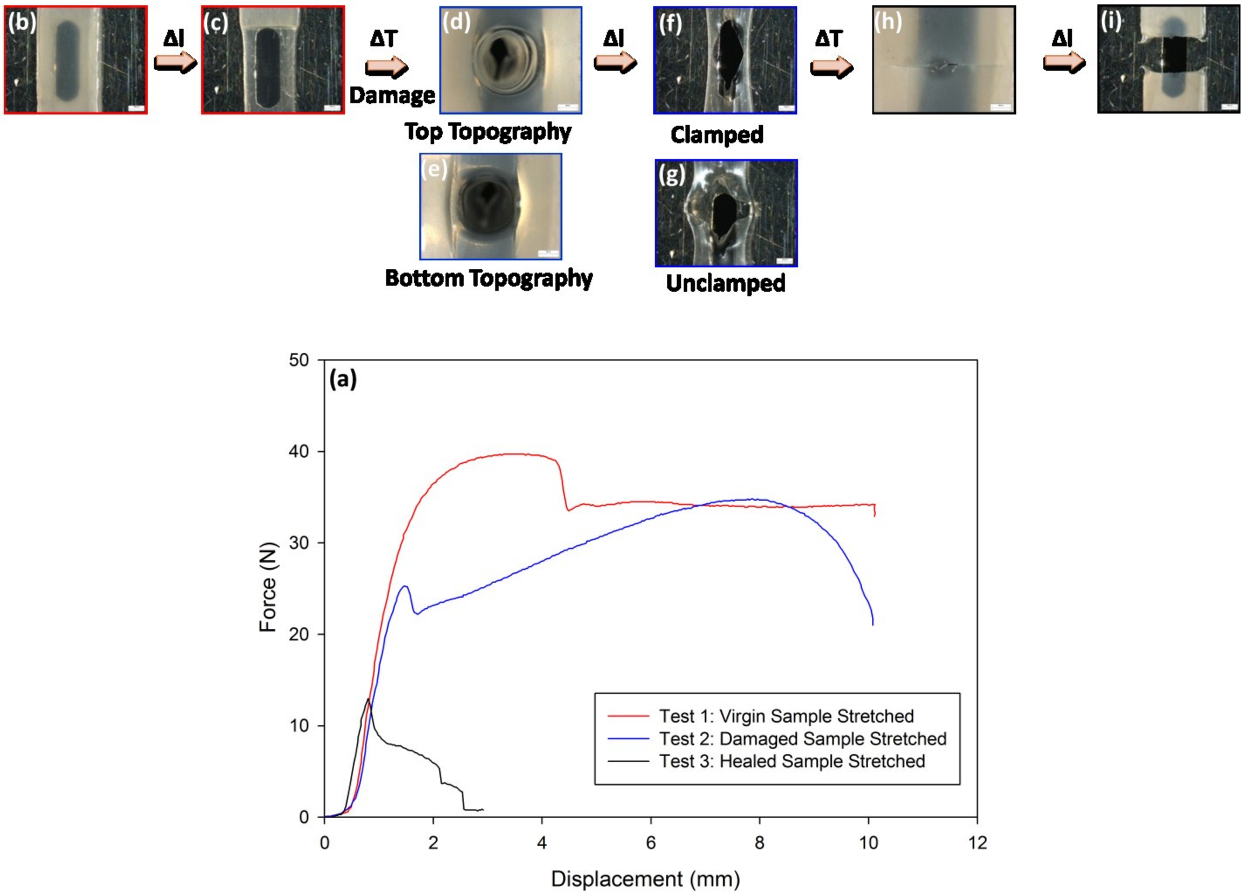

Figure A1.3.2. SMASH effect was quantified by performing puncture testing. (a) Force vs displacement graph of a l-PCL(65k)$_{50wt\text{-}\%}$:n-PCL(3k)$_{50wt\text{-}\%}$ sample showing stereomicrographs of (b) virgin, (c) deformed using a 200 N load cell with a stretch rate of 100 µm/sec. Sample was then recovered at 80 °C for 30 min and cooled at RT for 10 min. Sample was then punctured showing (d) top view of puncture a 1.23 mm diameter needle, (e) bottom view of puncture, (f) punctured and deformed sample clamped, (g) punctured and deformed sample unclamped showing elastic recovery, (h) sample was thermally treatment for 30 min. at 80 °C and cooled to RT for 120 min, and (i) complete fracture (Scale bar: 500 and 1000 µm).

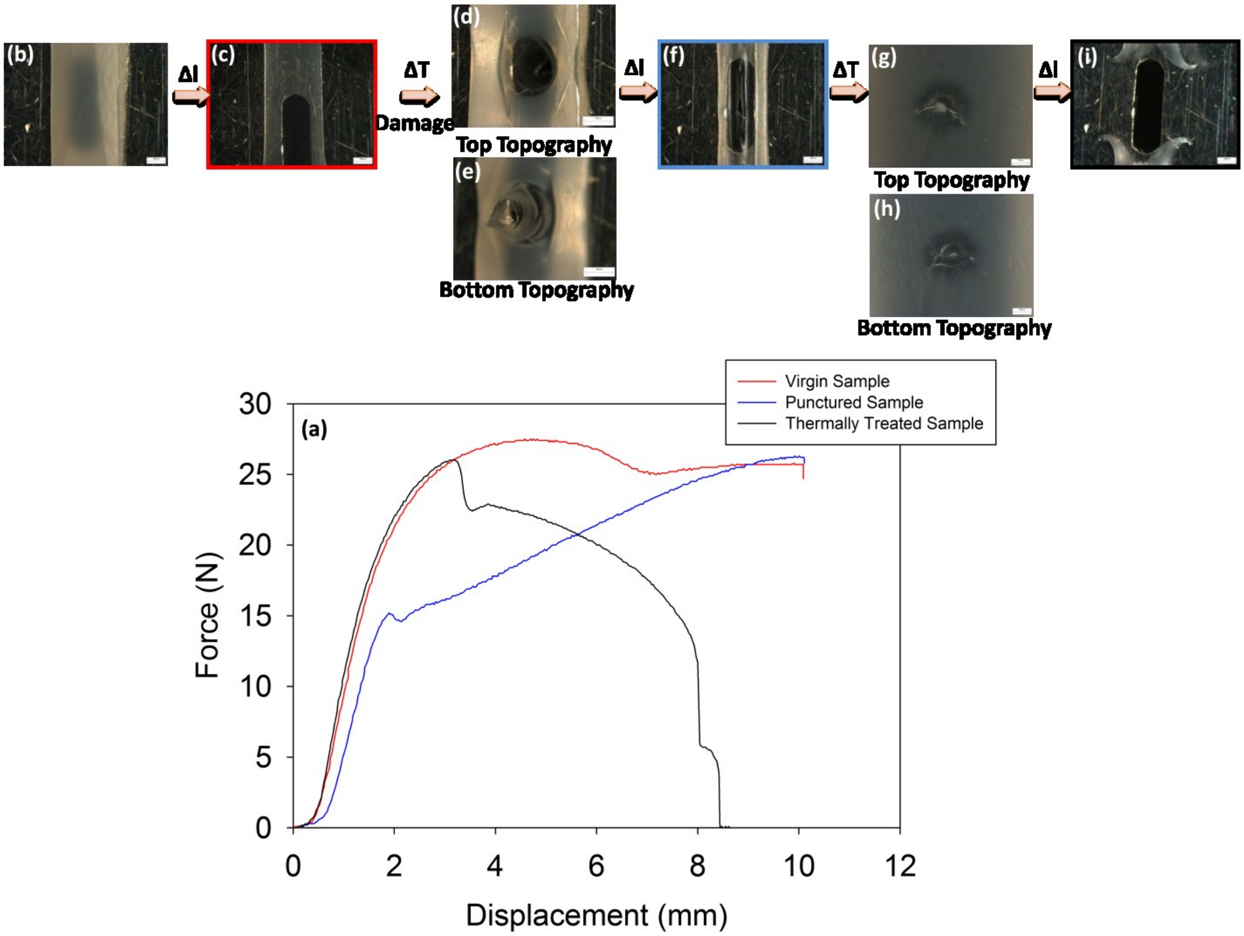

Figure A1.3.3. Puncture damage was performed to quantify the SMASH effect. (a) Force vs displacement graph of a l-PCL(65k)$_{70wt-\%}$:n-PCL(3k)$_{30wt-\%}$ sample showing stereomicrographs of (b) virgin state with an average sample thickness of 0.27 mm, (c) deformed sample using a 200 N load cell with a stretch rate of 100 µm/sec, (d) top view of puncture using a 1.23 mm diameter needle, (e) bottom view of puncture, (f) punctured and deformed, (g) top view of sample after thermally treated for 10 min at 80 °C and cooled to RT for 10 min, (h) bottom view of sample after thermal treatment, and (i) complete fracture. (Scale bar: 200 and 1000 µm).

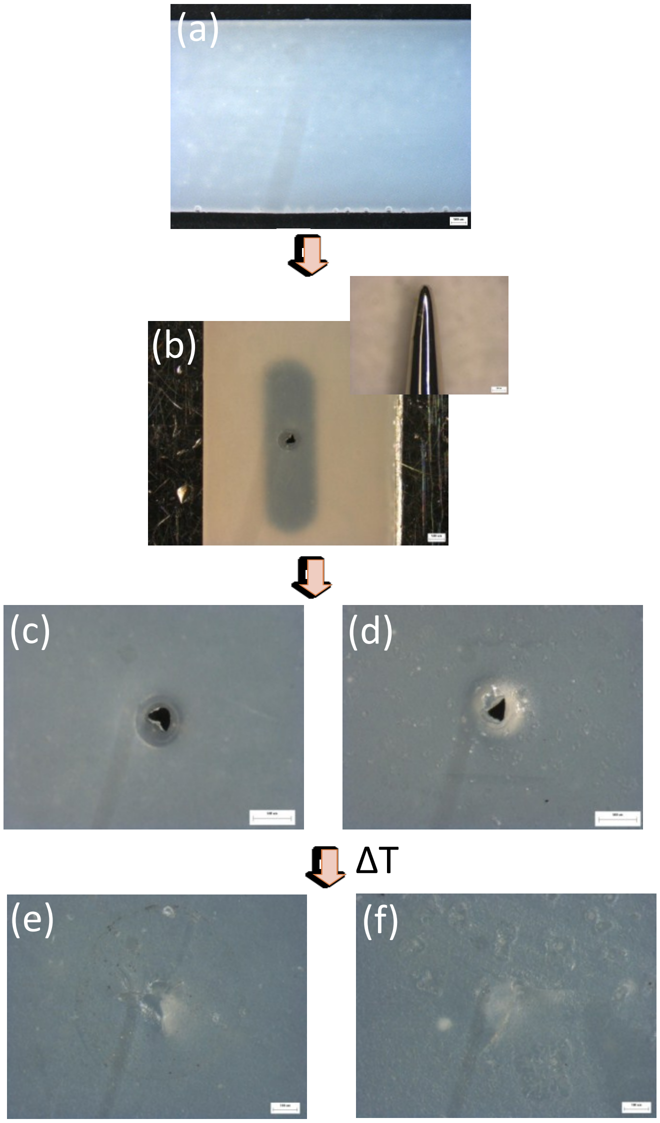

Figure A1.3.4. l-PCL(65k)$_{10}$n-PCL(3k)$_{90}$ puncture test showing stereomicrograhs of (a) virgin sample at RT, (b) punctured sample while clamped in the Linkam at RT using a 0.62 mm diameter needle tip, (c) close up topography of damaged area (top of sample), (d) close up topography of damaged area (bottom of sample), (e) sample thermally treated by hanging it in an isothermal oven at 80°C for 10 min, cooled at RT for 10 min (top of sample), and (f) bottom of sample after thermal treatment (Scale bar: 100 and 500 μm).

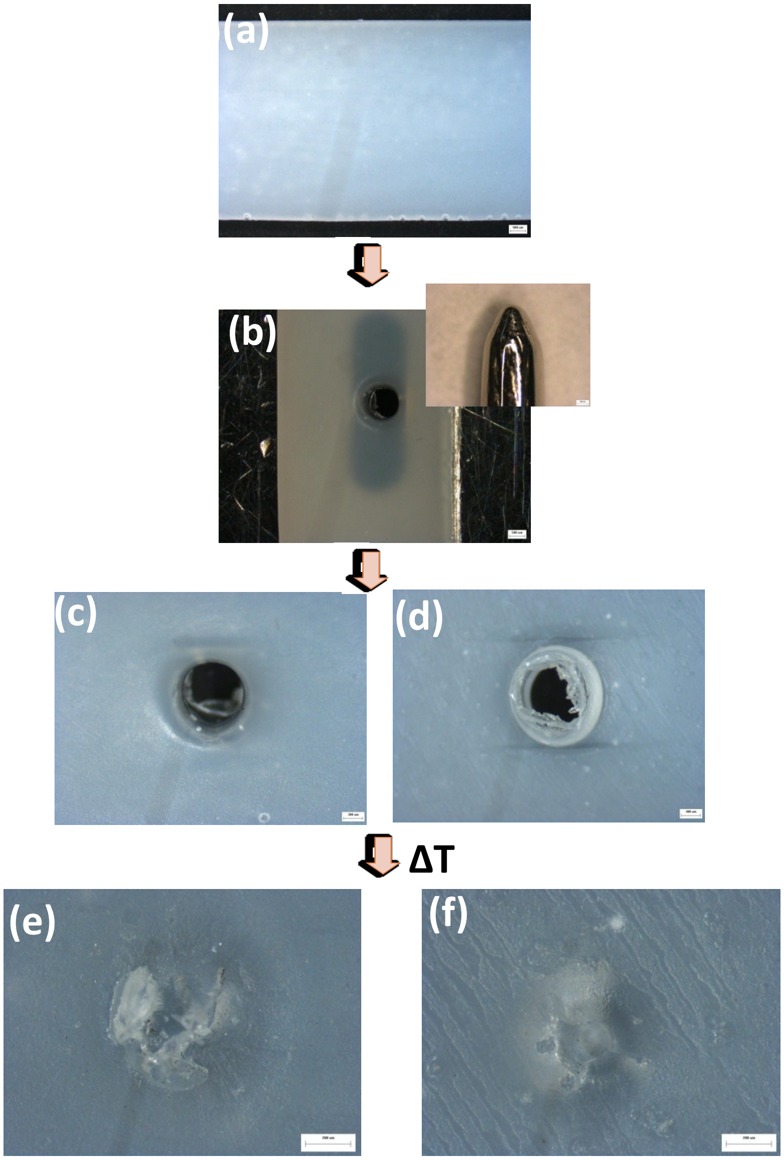

Figure A1.3.5. l-PCL(65k)$_{10}$n-PCL(3k)$_{90}$ puncture test showing stereomicrograhs of (a) virgin sample at RT, (b) punctured sample while clamped in the Linkam at RT using a 1.23 mm diameter needle tip, (c) close up topography of damaged area (top of sample), (d) close up topography of damaged area (bottom of sample), (e) sample thermally treated by hanging it in an isothermal oven at 80°C for 10 min, cooled at RT for 10 min (top of sample), and (f) bottom of sample after thermal treatment (Scale bar: 200, 300, 500 µm).

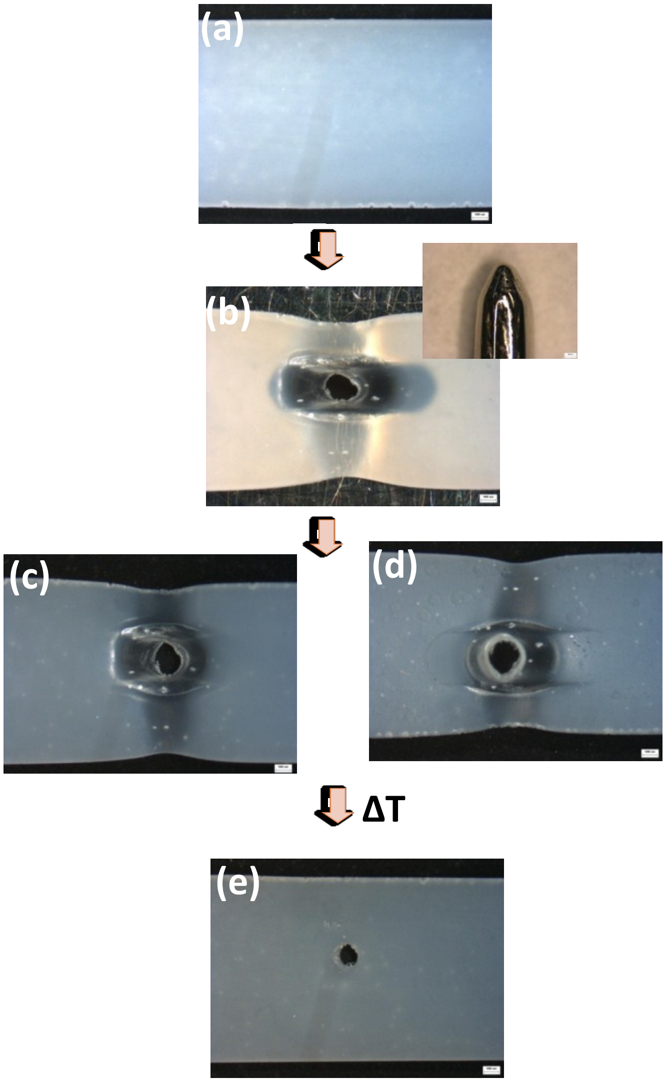

Figure A1.3.6. l-PCL(65k)$_{10}$n-PCL(3k)$_{90}$ puncture test showing stereomicrographs of (a) virgin sample at RT, (b) punctured sample while clamped in the Linkam at RT using a 1.23 mm diameter needle tip, (c) close up topography of damaged area (top of sample), (d) close up topography of damaged area (bottom of sample), (e) sample thermally treated by hanging it in an isothermal oven at 80°C for 10 min, cooled at RT for 10 min (top of sample), and (f) bottom of sample after thermal treatment where evidence of material removal was observed. (Scale bar: 500 μm).

APPENDIX 1.4

REVERSIBLE ADHESIVE STUDIES

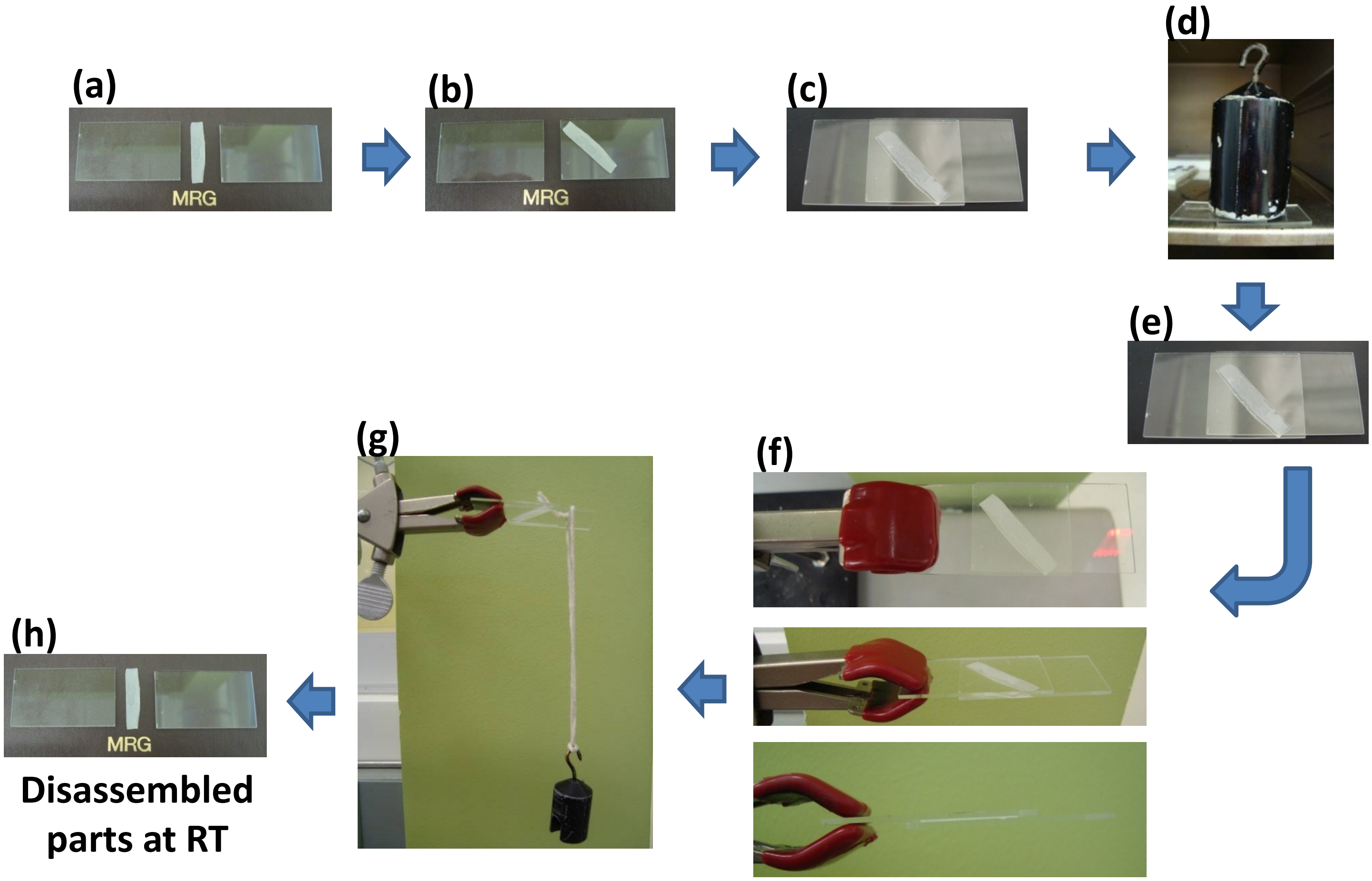

Figure A1.4.1. (a) Two-1mm thick glass slides with a ~0.6mm l-PCL$_{(65k)}$80wt-%:n-PCL$_{(3k)}$20wt-% thick SMASH adhesive, (b) placed adhesive on one glass slide at RT, (c) sandwiched adhesive between two glass slides at RT, (d) heat for 30 min at 150 °C using a 500 g weight, (e) cool at RT for 10 min, (f) clamped one end to see if SMASH adhesive can uphold the weight of system at RT, (g) hung 50 g weight with a string on system for about a 1 min at RT, and (h) disassembled parts at RT.

APPENDIX 1.5

SURFACE REVERSIBLE PLASTICITY STUDIES

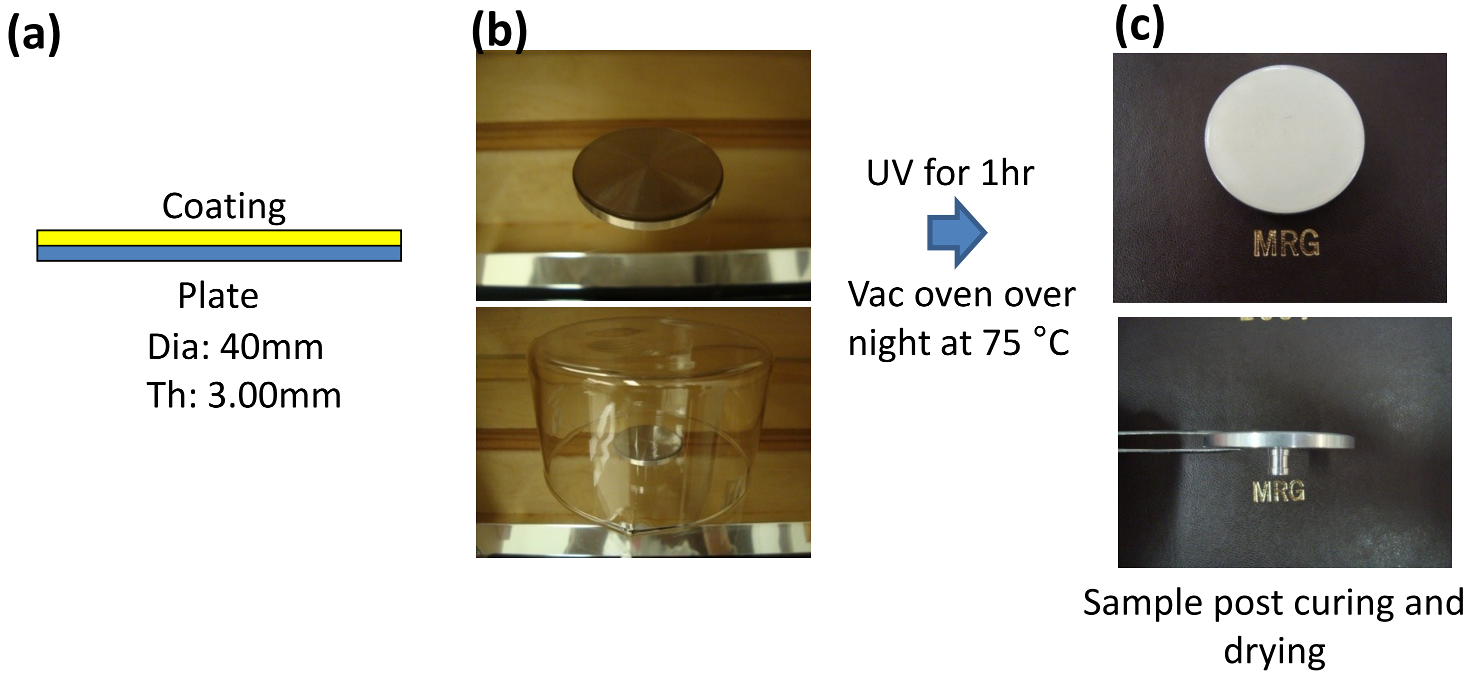

Figure A1.5.1. (a) schematic of system, (b) prepared a l-PCL(65k)$_{50wt-\%}$:n-PCL(3k)$_{50wt-\%}$ sample and UV cured on a rheometer plate. Chemistry bowl on top of sample during UV curing to control the chloroform evaporation. Sample cured for 1 h and dried in vacuum oven over night at 75 °C, and (c) images showing system post cure.

Table A1.5.1. Thickness measurements at location 1, 2, 3, 4 to study thickness variability post curing of the film.

Plate Location	Plate Thickness (mm)	Coating and Plate Thickness (mm)	Coating Thickness (mm)
1	3.00	3.45	0.45
2	3.00	3.43	0.43
3	3.00	3.41	0.41
4	3.00	3.50	0.50
			0.45
			AVERAGE

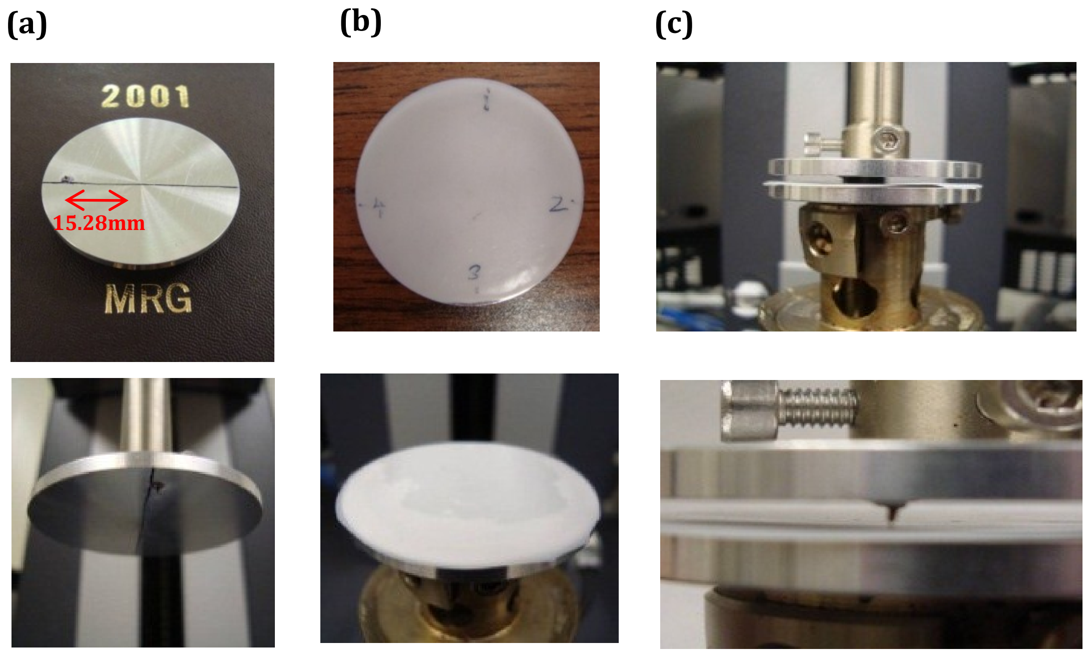

Figure A1.5.2. (a) top image shows the top plate with the indenter (diamond tip) and positioned 15.28 mm from the center. Lower image shows the top plate fastened in the rheometer, (b) top image shows the l-PCL(65k)$_{50wt\text{-}\%}$:n-PCL(3k)$_{50wt\text{-}\%}$ cured film where the lower image shows the plate fastened in the rheometer, and (c) top and lower image shows the side view of the top plate making contact with the lower plate to scratch the cured film.

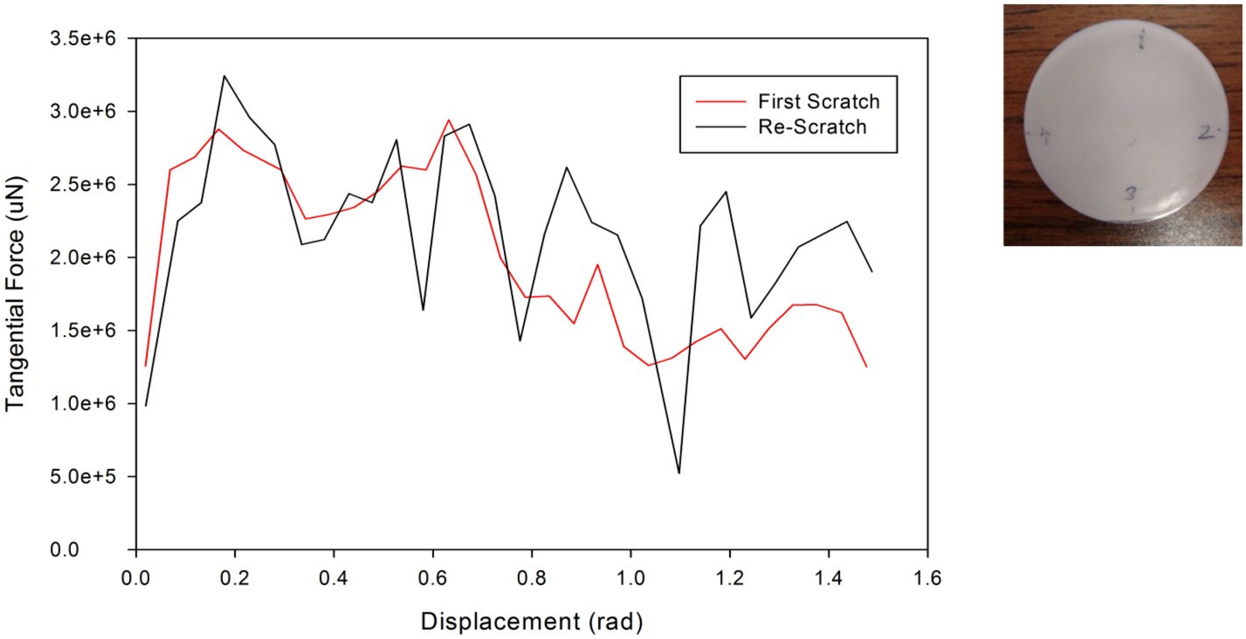

Figure A1.5.3. Graph showing tangential force (µN) vs displacement (rad) when a scratch was performed on the cured film from position from 1 to 2 (1.5 rad) (see inset image). To perform the scratch, the film was first indented by the indenter to penetrate the film and then scratched. These two steps were done using two methods: indentation testing and scratch testing. Indentation Testing: Squeeze/Pull off Compression Test to indent the coating at 3N, gap speed: 1 µm/sec, sampling time: 1 sec, Temp: 25 ^{0}C, normal force: experiment stopped when 3N was recorded. Scratch Test: Peak Hold Step to scratch the coating surface, hold angular velocity (rad/sec) at 0.05, temp: 25 ^{0}C, displacement (rad): when the displacement reached 1.5 rad the experiment stopped. Curves shows that the film did not have a smooth topography but instead peaks and valleys. This could be due to different thermal coefficients. The tangential force was calculated by dividing the torque values by the distance from the center of the plate to the indenter. Red curve is indicative of scratching the film the first time. The black curve is indicative of re-scratching the film in the same area.

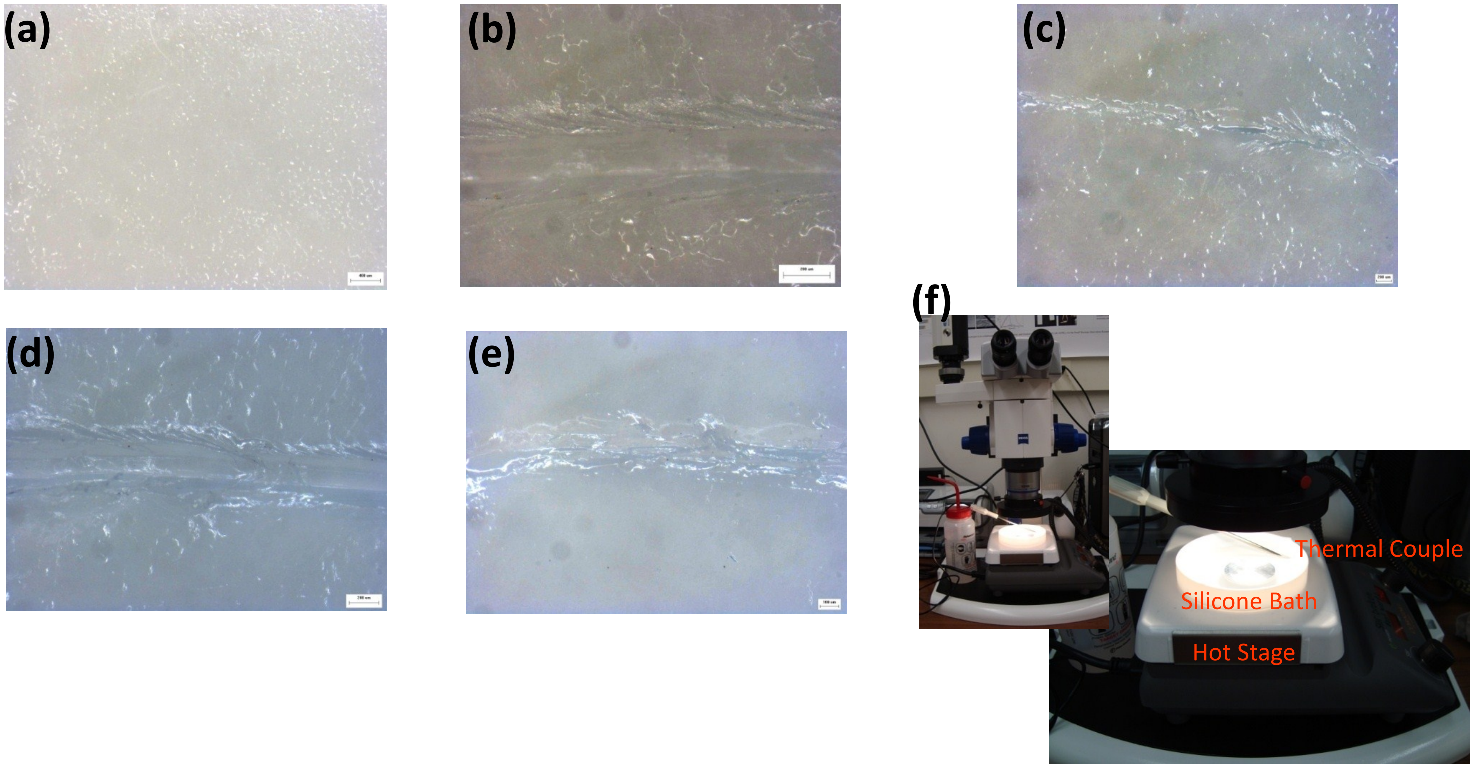

Figure A1.5.4. Stereo micrographs of (a) film surface pre-scratch, (b) film surface post-scratch (contrast enhancement tool on QCapture Pro software was used), (c) film surface post 1st healing treatment (contrast enhancement tool on QCapture Pro software was used), (d) film surface re-scratched, (e) film surface post 2nd healing treatment (contrast enhancement tool on QCapture Pro software was used), and (f) images showing the thermal treatment process. Placed the film-rheometer plate in a pre-heated silicone bath that was on the hot stage at 80 ^{0}C. The entire assembly was under a stereo microscope to visually record the healing process. A video was made of the healing process.

APPENDIX 1.6

SMALL ANGLE LIGHT SCATTERING (SALS) STUDIES

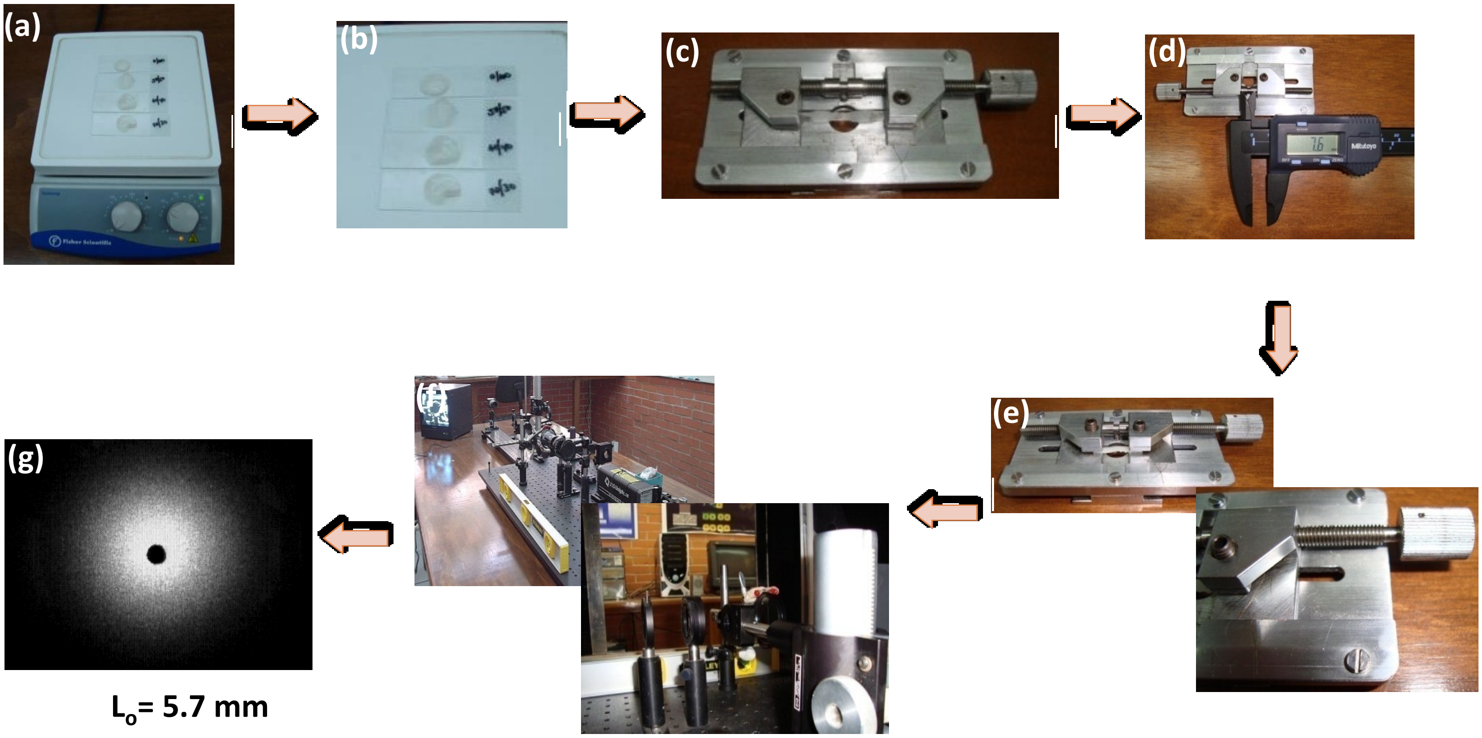

Figure A1.6.1. Schematic showing cold drawing experiment using Small Angle Light Scattering (SALS) for a l-PCL(65k)$_{70wt\text{-}\%}$:n-PCL(3k)$_{30wt\text{-}\%}$ sample. (a) Thermal removal conducted on hot stage for all compositions at 80 ^{0}C for 10 min, (b) cooled at RT for 10 min, (c) clamped sample in tensile device, (d) measure initial length pre-deformation, (e) deform sample by rotating knob 180°, (f) place tensile device in front of red laser in SALS equipment, and (g) obtained SALS image.

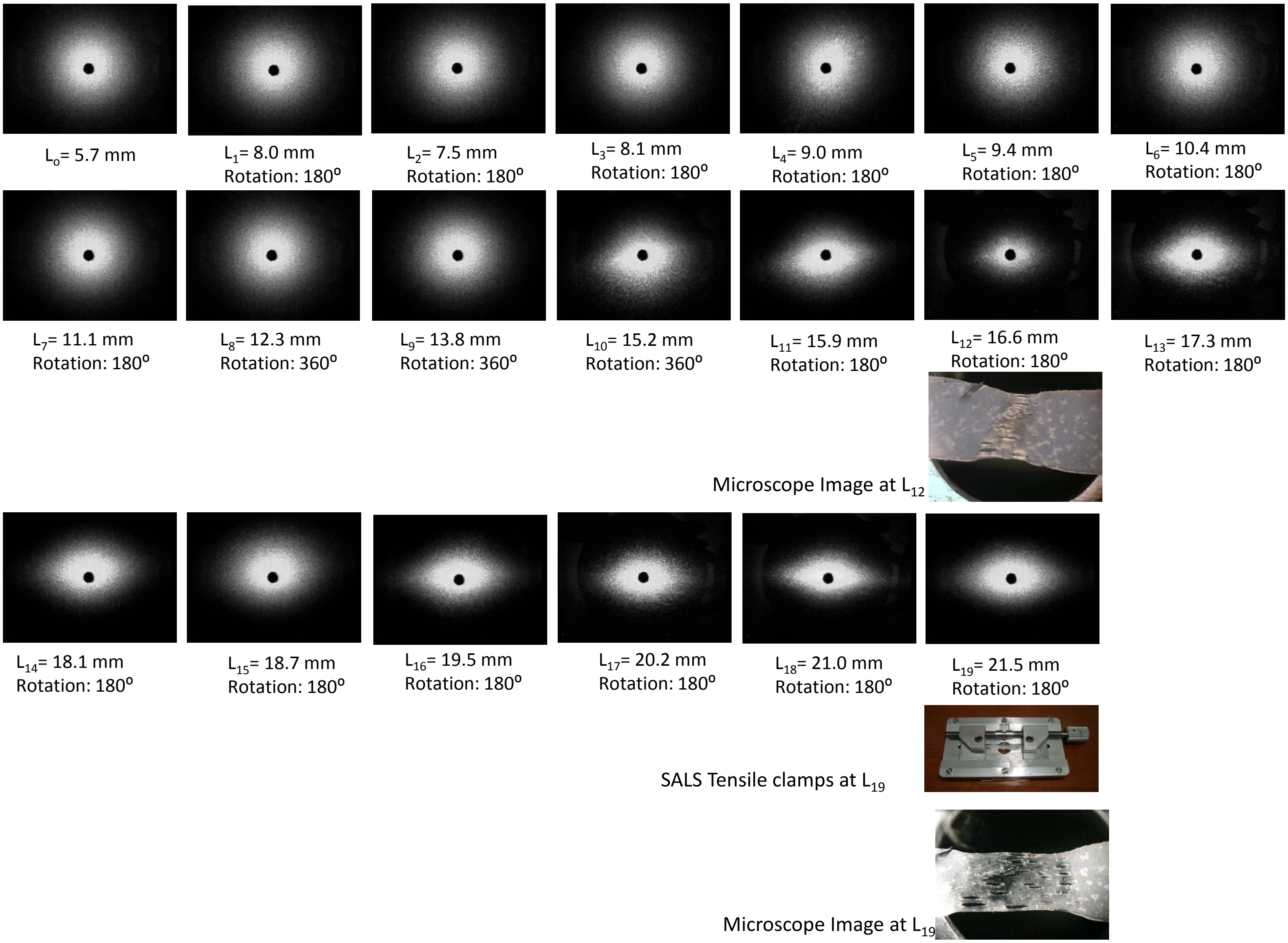

L_o= 5.7 mm

L_1= 8.0 mm
Rotation: 180°

L_2= 7.5 mm
Rotation: 180°

L_3= 8.1 mm
Rotation: 180°

L_4= 9.0 mm
Rotation: 180°

L_5= 9.4 mm
Rotation: 180°

L_6= 10.4 mm
Rotation: 180°

L_7= 11.1 mm
Rotation: 180°

L_8= 12.3 mm
Rotation: 360°

L_9= 13.8 mm
Rotation: 360°

L_{10}= 15.2 mm
Rotation: 360°

L_{11}= 15.9 mm
Rotation: 180°

L_{12}= 16.6 mm
Rotation: 180°

L_{13}= 17.3 mm
Rotation: 180°

Microscope Image at L_{12}

L_{14}= 18.1 mm
Rotation: 180°

L_{15}= 18.7 mm
Rotation: 180°

L_{16}= 19.5 mm
Rotation: 180°

L_{17}= 20.2 mm
Rotation: 180°

L_{18}= 21.0 mm
Rotation: 180°

L_{19}= 21.5 mm
Rotation: 180°

SALS Tensile clamps at L_{19}

Microscope Image at L_{19}

Figure A1.6.2. SALS images from a cold drawing experiment using a l-PCL(65k)$_{70wt\text{-}\%}$:n-PCL(3k)$_{30wt\text{-}\%}$ sample. Pre-deformation sample dimensions: 22.9 x 3.6 x 0.2 mm. Post-deformation sample dimensions: 35.3 x 2.6 x 0.1 mm. At length L_{10} an elliptical halo started to form where the sample started to become clear at the center.

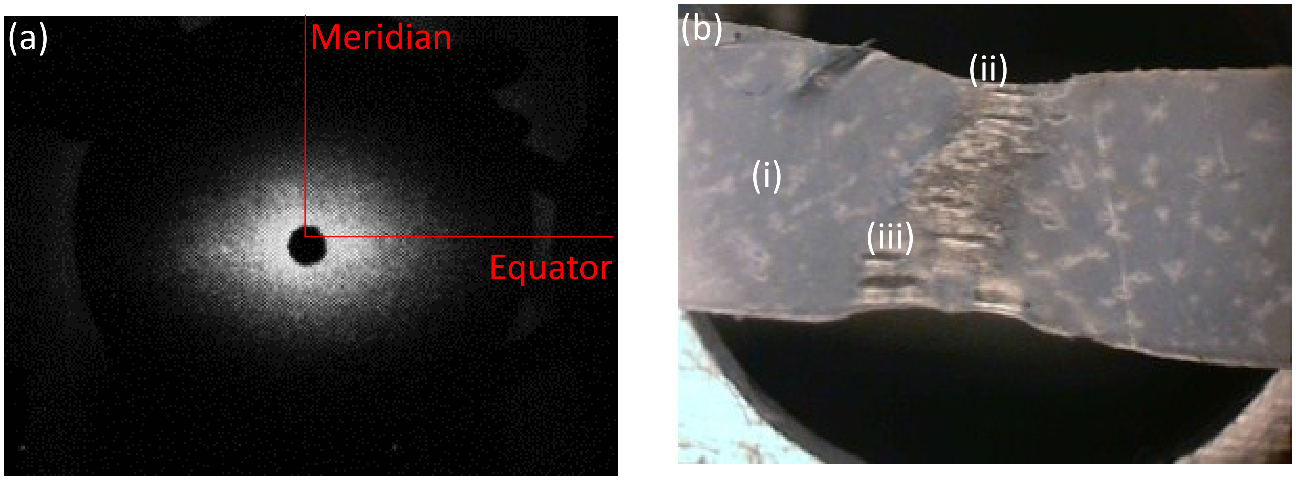

Figure A1.6.3. (a) SALS image at length L_{12}= 16.6 mm. The elliptical halo at the equator suggests that there is polymer chain orientation in the meridian, (b) microscope image at L12 (b) (i) sample is opaque, (b) (ii) sample is clear in center, (b) (iii) darker regions in the center is evidence of sample ripping during deformation.

Table A1.6.1. Table showing strain values of cold drawing SALS experiment using l-PCL(65k)$_{70wt\text{-}\%}$:n-PCL(3k)$_{30wt\text{-}\%}$ where the following equation was used to calculate the strain in percentage: Strain (%) = $(L_f\text{-}L_o)/(L_o)$ x 100.

Length Name	ΔL(mm)	Rotation (°)	%Strain
L0	5.7	180	0.0
L1	8	180	40.4
L2	7.5	180	31.6
L3	8.1	180	42.1
L4	9	180	57.9
L5	9.4	180	64.9
L6	10.4	180	82.5
L7	11.1	180	94.7
L8	12.3	360	115.8
L9	13.8	360	142.1
L10	15.2	360	166.7
L11	15.9	180	178.9
L12	16.6	180	191.2
L13	17.3	180	203.5
L14	18.1	180	217.5
L15	18.7	180	228.1
L16	19.5	180	242.1
L17	20.2	180	254.4
L18	21	180	268.4
L19	21.5	180	277.2

APPENDIX 1.7

TACK STUDIES

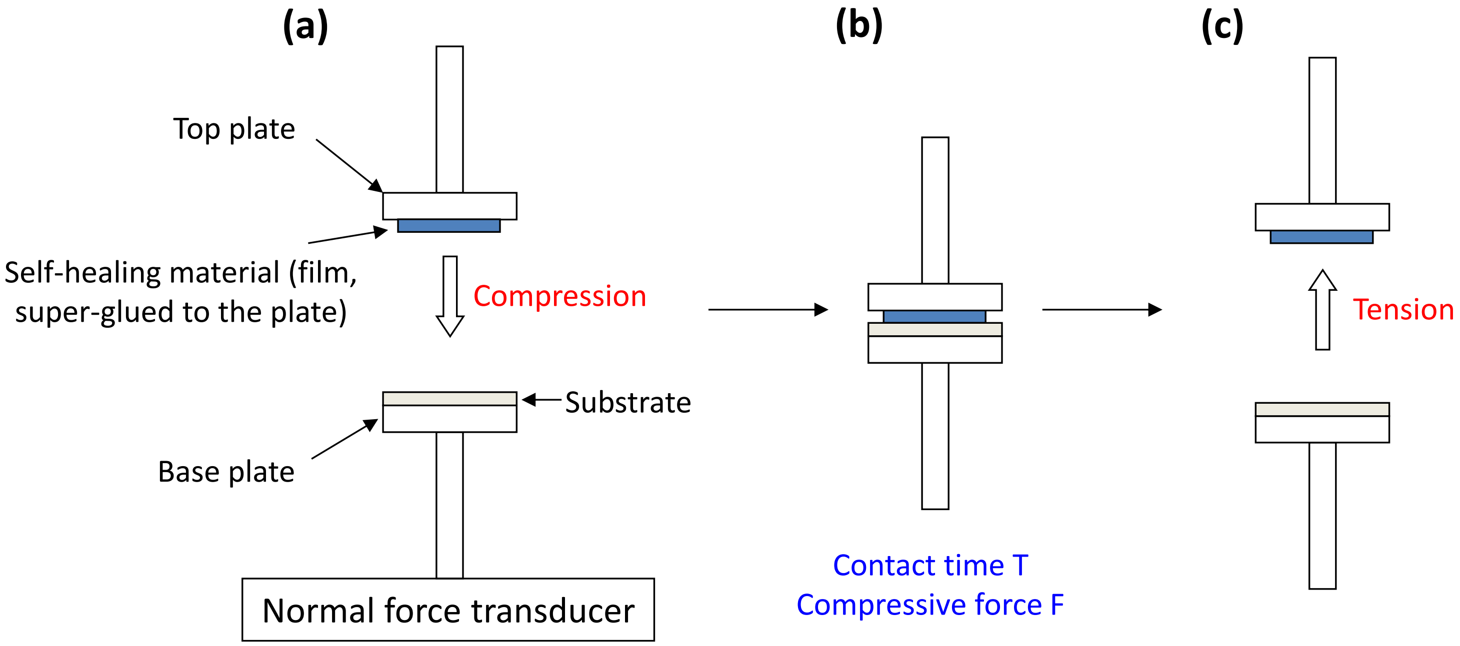

Scheme A1.7.1. (a) Performed a tack experiment with the TA AR-G2 rheometer utilizing the normal force transducer of the instrument. A l-PCL(65k)$_{50wt\text{-}\%}$:n-PCL(3k)$_{50wt\text{-}\%}$ film was super-glued to the top plate and the glass substrate was attached to the bottom plate. (b) A compression force was applied to allow complete film-substrate contact. (c) The tensile force was then conducted to separate the substrate from the film. This was in collaboration with Dr. Xiaofan Luo.

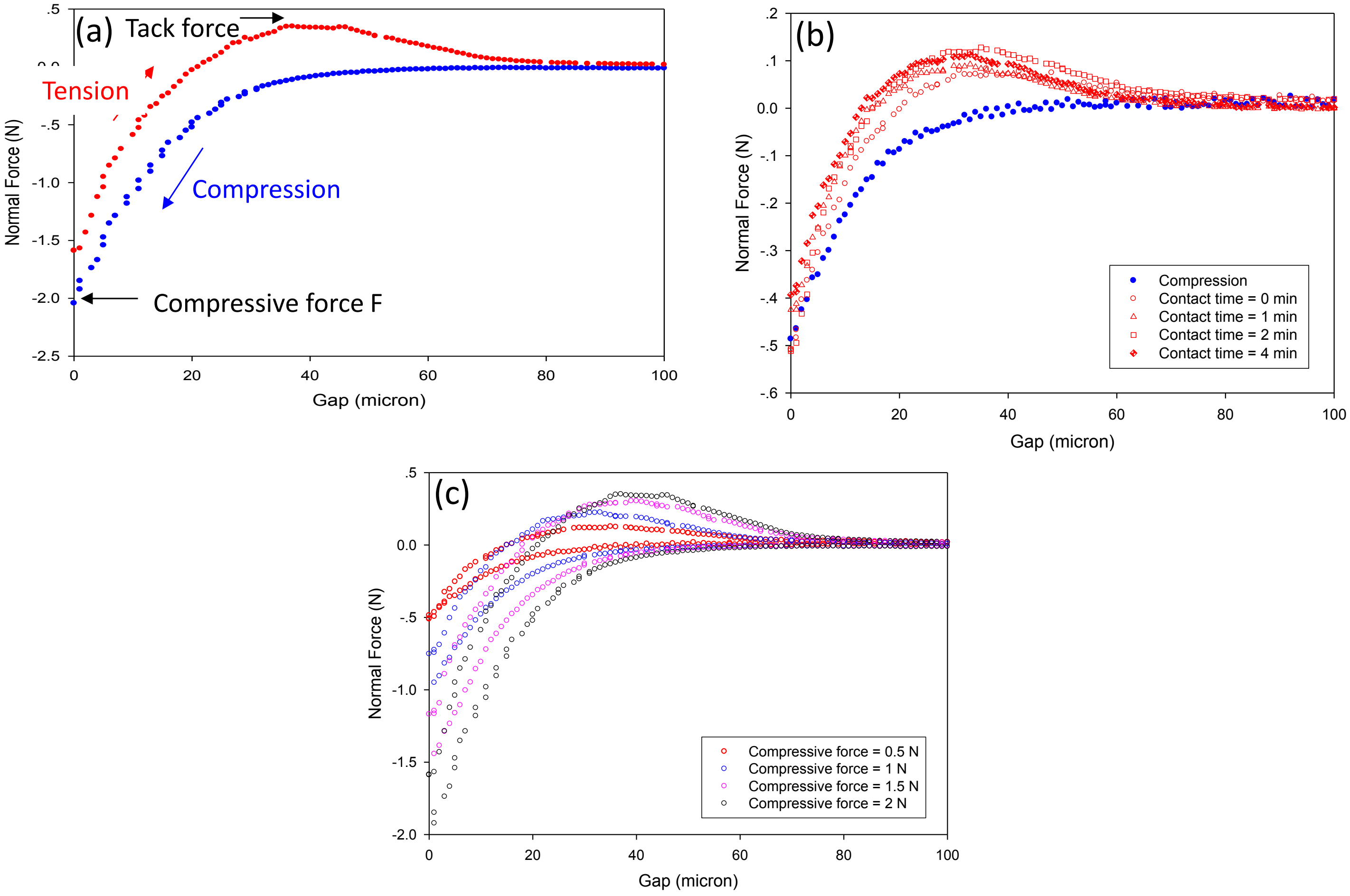

Figure A1.7.2. A typical compression-tension cycle using a l-PCL(65k)$_{50wt-\%}$:n-PCL(3k)$_{50wt-\%}$ film (0.9cm x 0.9cm) against a glass substrate where a TA AR-G2 Rheometer was used. (a) Representative graph of compression-tension cycle, (b) effect of contact time where the compressive force = 0.5 N and gap speed = 1 μm/s, and (c) effect of compressive force where contact time was 2 min, and gap speed was 1 μm/s.

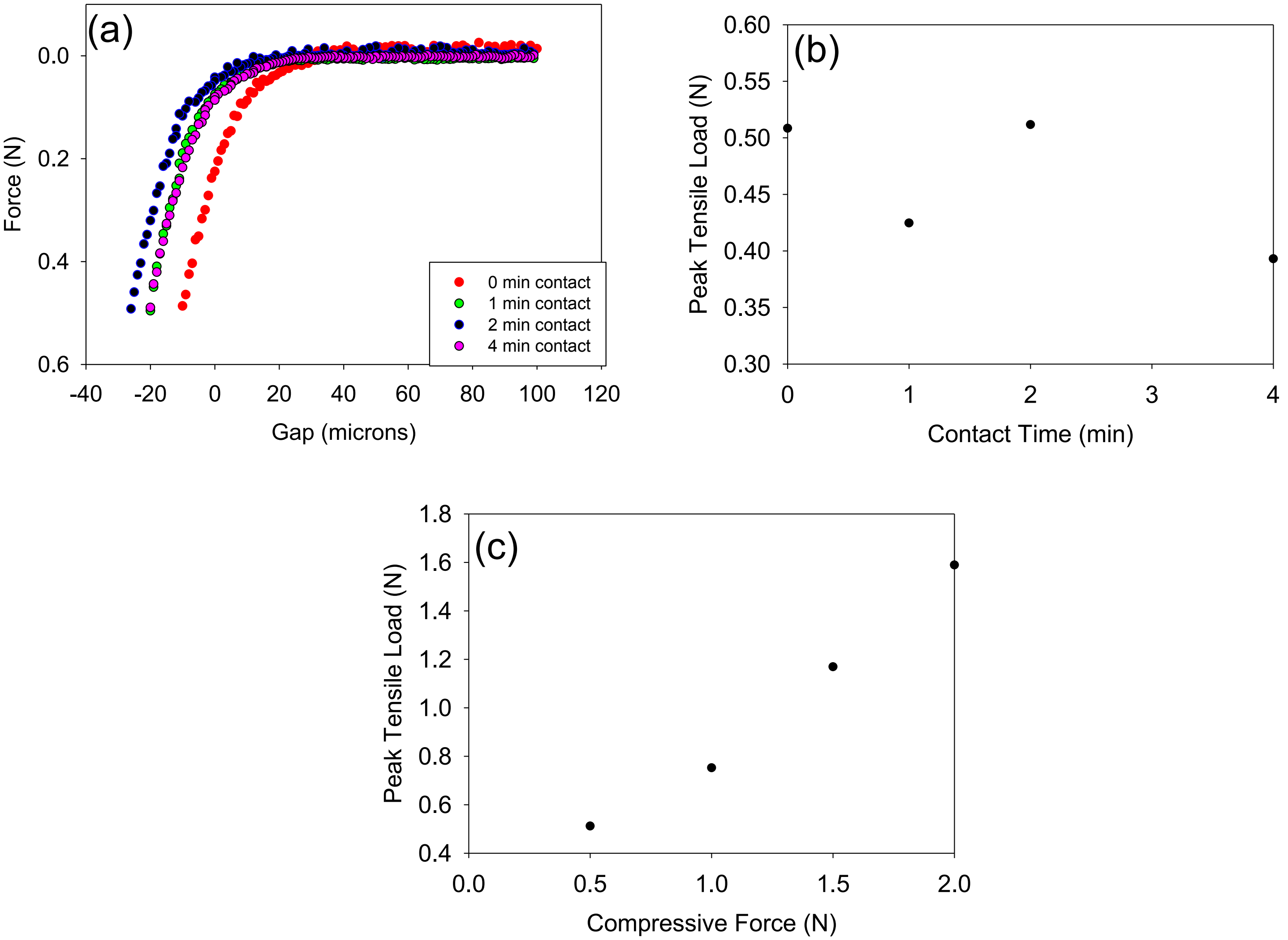

Figure A1.7.2. A l-PCL$_{50wt-\%}$:n-PCL$_{50wt-\%}$ sample was used where graphs shows (a) force vs gap distance showing tack measurements using a compressive force of 0.5 N., (b) tensile peak load vs contact time, and (c) tensile peak load vs compressive force.

APPENDIX 1.8

T-PEEL STUDIES

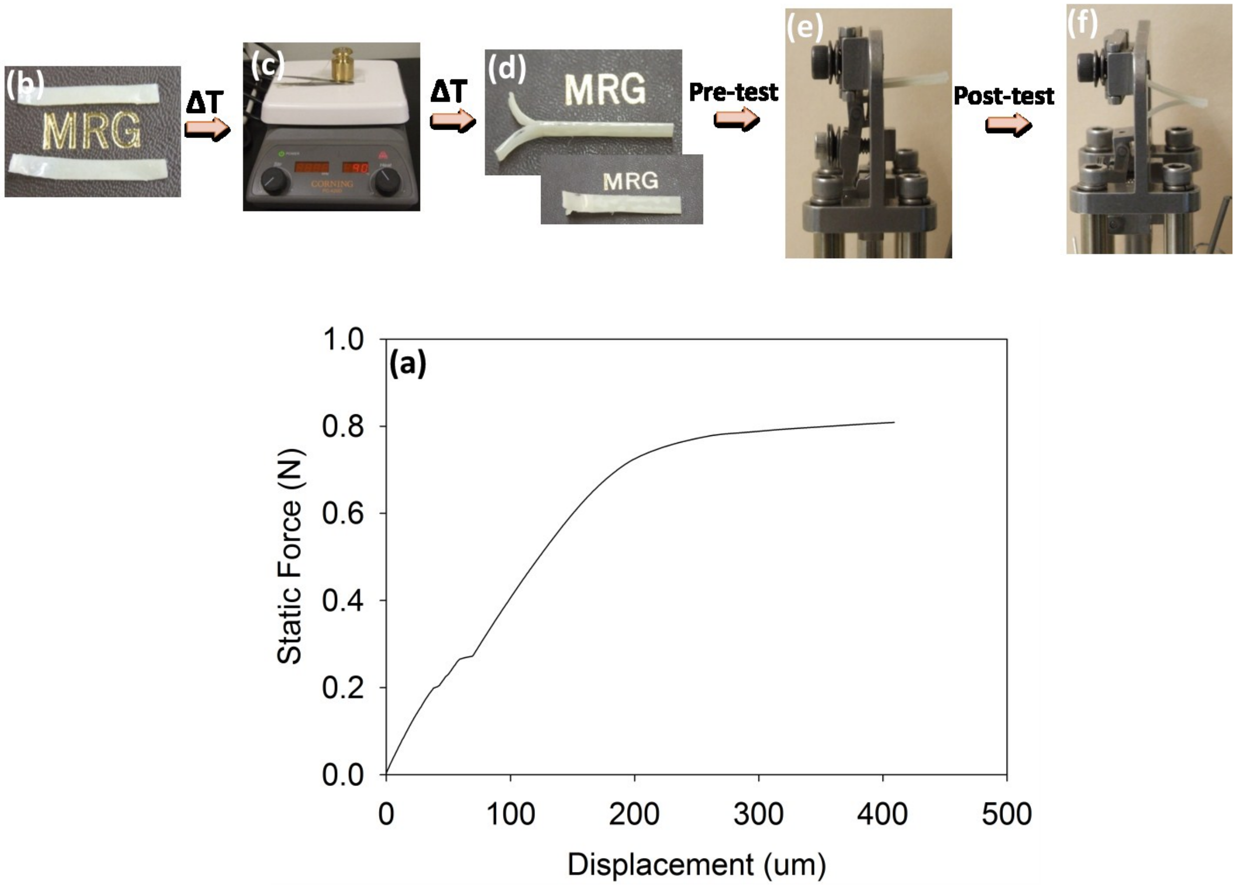

Figure A1.8.1. T-peel test showing (a) force vs displacement graph of a 6.50 (l) x 0.79 (th) mm l-PCL$_{50wt\text{-}\%}$:n-PCL$_{50wt\text{-}\%}$ sample, (b) two film strips were, (c) heated to 90 °C for 10 min and compressed to each other using a 200 g weight, (d) cooled for 10 min. at RT (e) clamped in the DMA pre-test, and (f) post-test. The following DMA procedure was conducted: equilibrated at RT, isothermal for 1.00 min., and ramped force at 0.10 N/min to 18 N.

APPENDIX 1.9

LAP SHEAR STUDIES

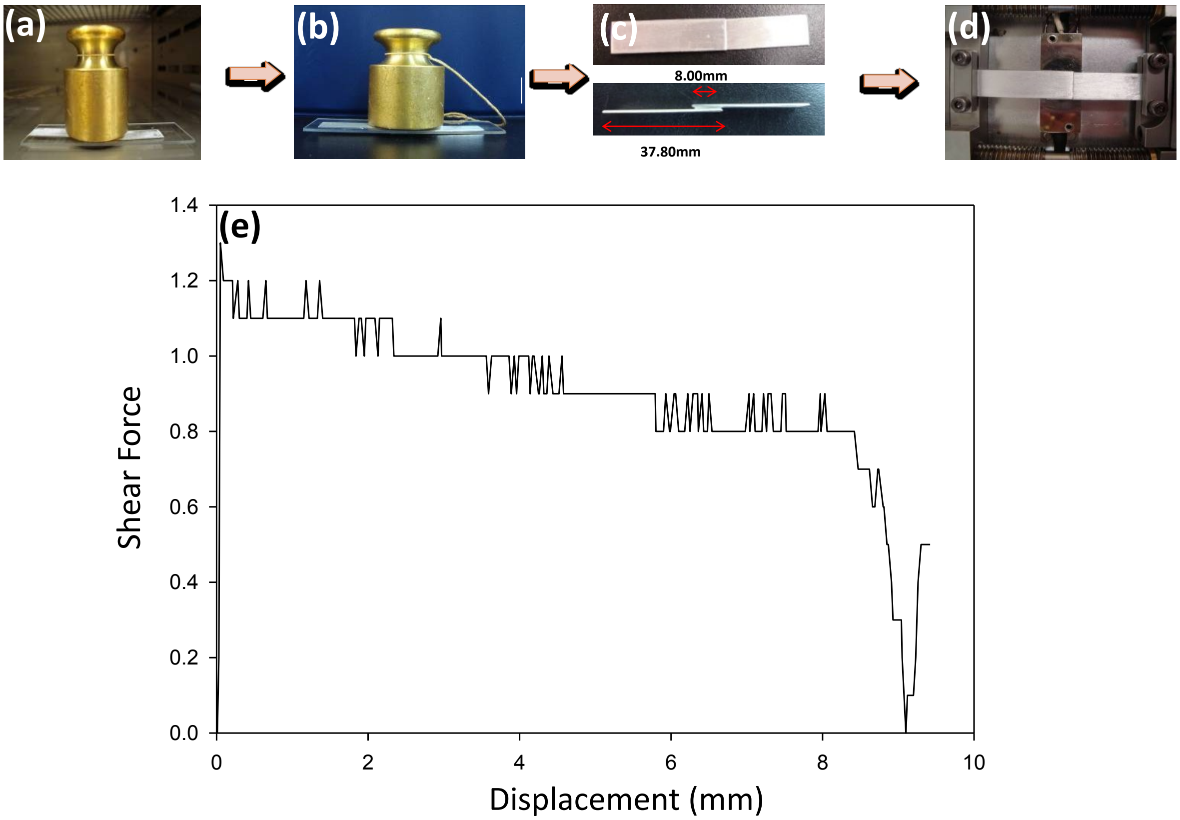

Figure A1.9.1. Lap shear experiment using l-PCL$_{60wt\text{-}\%}$:n-PCL$_{40wt\text{-}\%}$ sample to quantify adhesion of a sample-metal interface. (a) 0.67 mm thick sample was compressed between two 0.80 mm thick metallic strips using a 200 g weight and then placed in oven at 80 °C for 10 min. Metallic and polymer film surface were roughened using a 320 grit sandpaper before compression was applied to system, (b) system was cooled at RT for 10 min, (c) top and side views of system, (d) system clamped in the Linkam tensile stage using a deformation velocity of 100 µm/sec, 200 N load cell and a deformation temperature of RT, and (e) shear force vs displacement curve.

APPENDIX 1.10

TWO WAY SHAPE MEMORY (2WSM)

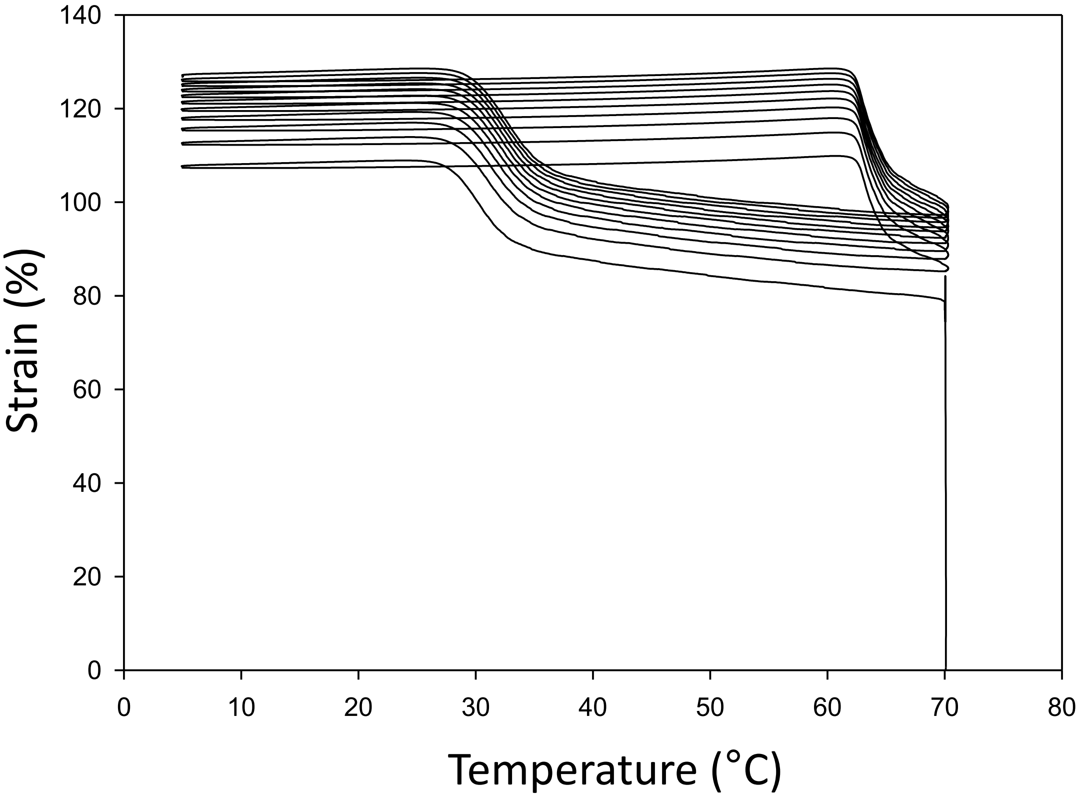

Figure A1.10.1. Experiment conducted to study the two way shape memory (2WSM) effect. l-PCL$_{50wt\text{-}\%}$:n-PCL$_{50wt\text{-}\%}$ sample was used where the temperature was equilibrate to 70.00 °C, isothermal for 1.00 min, force ramped at 0.10 N/min to 0.9 N, isothermal for 3.00 min, ramped at 2.00 °C/min to 5.00 °C, isothermal for 10.00 min, and ramped 2.00 °C/min to 70.00 °C. The cooling and healing step was conducted ten times to study the reproducibility of the 2WSM effect.

APPENDIX 1.11

POLY(Ɛ-CAPROLACTONE) (PCL) THERMOPLASTIC SM STUDIES

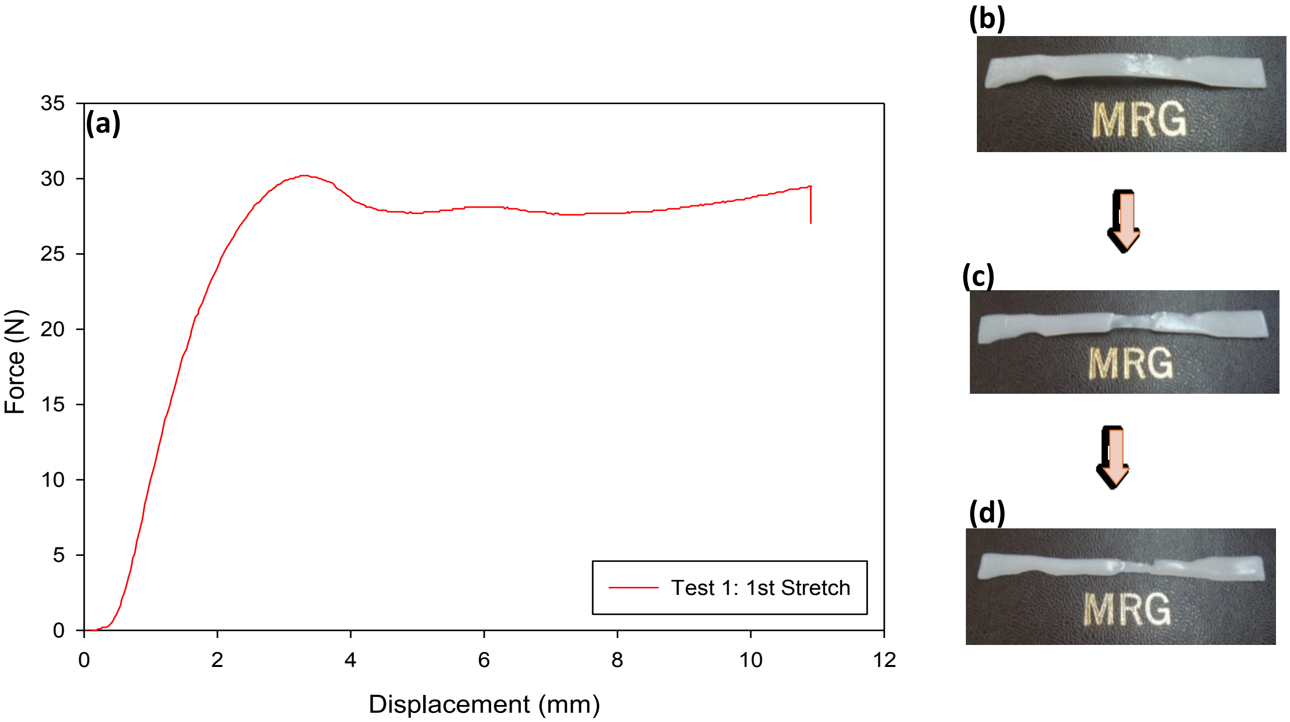

Figure A1.11.1. SM experiment on a l-PCL$_{100wt\text{-}\%}$ film so study the degree of shape recovery. (a) Force vs displacement graph of a 0.87 mm (average) thick l-PCL$_{100wt\text{-}\%}$ film. Images show samples at the (b) virgin, (c) post-deformation state, and (d) after thermally treated at 80 °C for 10 min and cooled at RT for 10 min. Tensile testing was conducted on the Linkam tensile stage using a 200 N load cell with a deformation velocity of 100 μm/sec and a deformation temperature of RT. The initial length of the sample was 54.98 mm, 62.56 mm post-deformation, and 60.14 mm after thermal treatment. Therefore, the %$_{deformation}$ was 14% with a %$_{recovery}$ of 32%. It is postulated that the %$_{recovery}$ is owed to the elastic recovery only where the plastic deformation was unrecoverable after thermal treatment due to the lack of crosslinks in the sample.

APPENDIX 2.0

AMORPHOUS SMASH SYSTEM

A.2 SUMMARY

Please refer to Chapter 6 for an explanation of experiments presented in this appendix.

APPENDIX 2.1

POLY(TERT-BUTYL ACRYLATE) (poly(tBA)):POLY(BUTYL ACRYLATE) (poly(BA)) COPOLYMER SMASH COATING STUDIES

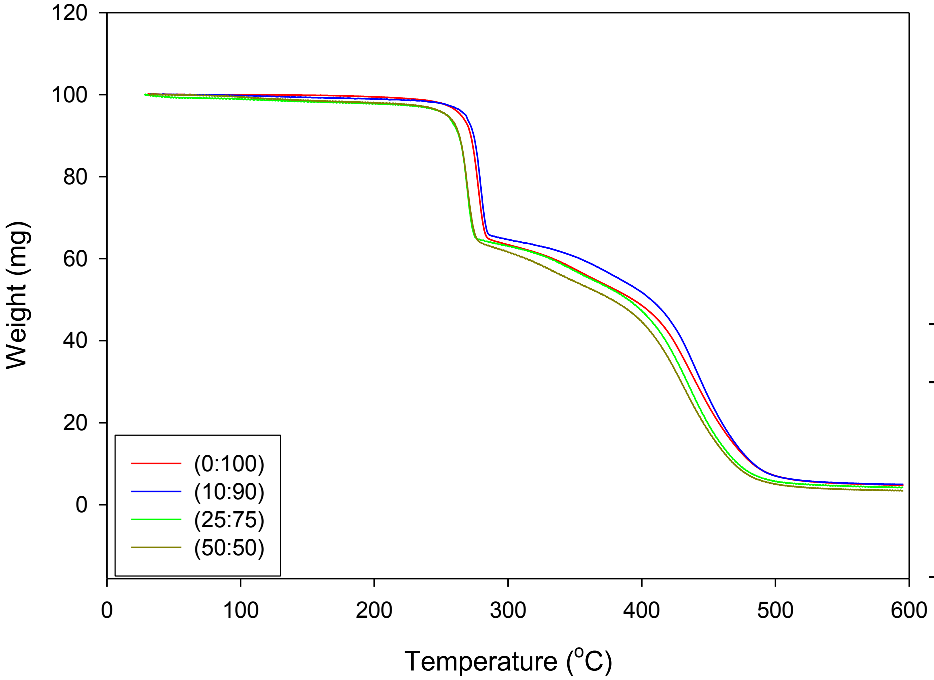

Sample	Onset Degradation (°C)
(0:100)	270.5
(10:90)	273.1
(25:75)	262.9
(50:50)	262.7

Figure A2.1.1. Thermogravimetric analysis (TGA) of the a l:n-tBA$_{82\%}$:BA$_{18\%}$ SMASH 1 mm thick films where the average onset degradation temperatures was approximately 267.31 °C (shown in table) among all compositions tested. The TGA method was 10 °C/min at 600 ° C .

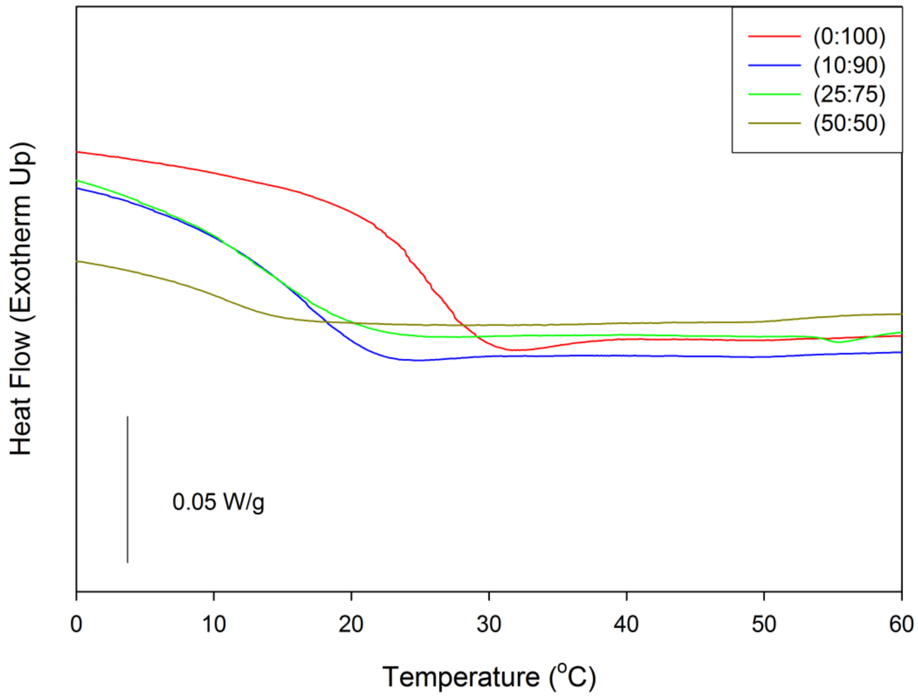

Sample	T_g (°C)
(0:100)	25.5
(10:90)	16.5
(25:75)	13.4
(50:50)	10.7

Figure A2.1.2. Differential Scanning Calorimetry (DSC) of the l:n-tBA$_{82\%}$:BA$_{18\%}$ SMASH 1 mm films where the Tg ranged from 10.72 °C to 25.51 °C (shown in table) among all compositions tested.

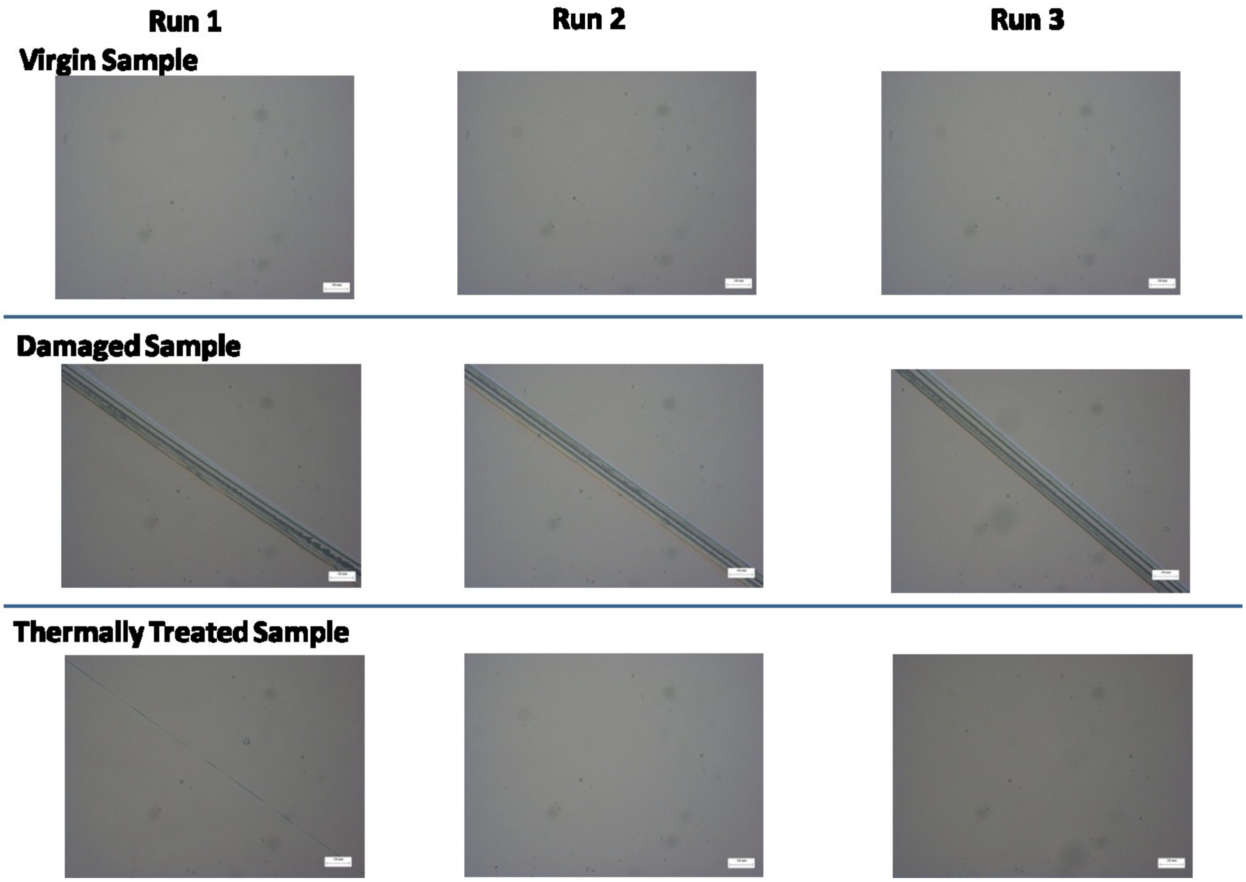

Figure A2.1.3. Optical micrographs (OM) of a l:n-tBA$_{82\%}$:BA$_{18\%}$ SMASH (50:50) coatings in its virgin, damaged and thermal treated states. Thermal removal was first conducted at 120 °C for 20 min and cooled at RT for 20 min prior to damage. The coating was then damaged at RT using the custom made scratch machine. The sample was then thermally treated for 1 h at 120 °C and cooled at RT for 20 min. No visible scar was evident after thermal treatment.

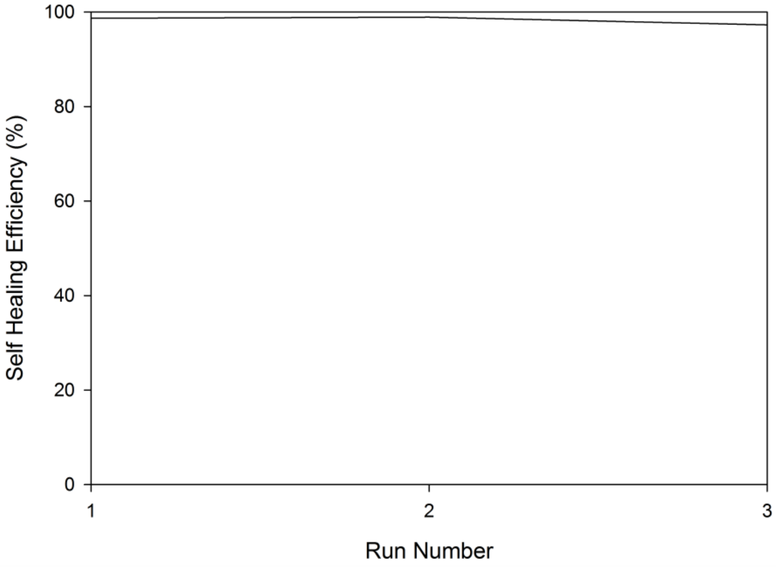

Sample	SS	TTS	SH (%)
Run 1	1.30E+05	1.73E+03	98.7
Run 2	1.49E+05	1.64E+03	98.9
Run 3	1.51E+05	4.11E+03	97.3
		AVERAGE	98.3
		STDEV	0.9

Figure A2.1.4. Graph showing self healing (SH) efficiency vs run number for the 1:n-$tBA_{82\%}$:$BA_{18\%}$ (50:50) SMASH coatings tested. The SH % was approximately 98% among all three runs (shown in table).

APPENDIX 2.2

CRAZING STUDIES USING l:n-tBA SMASH FILMS

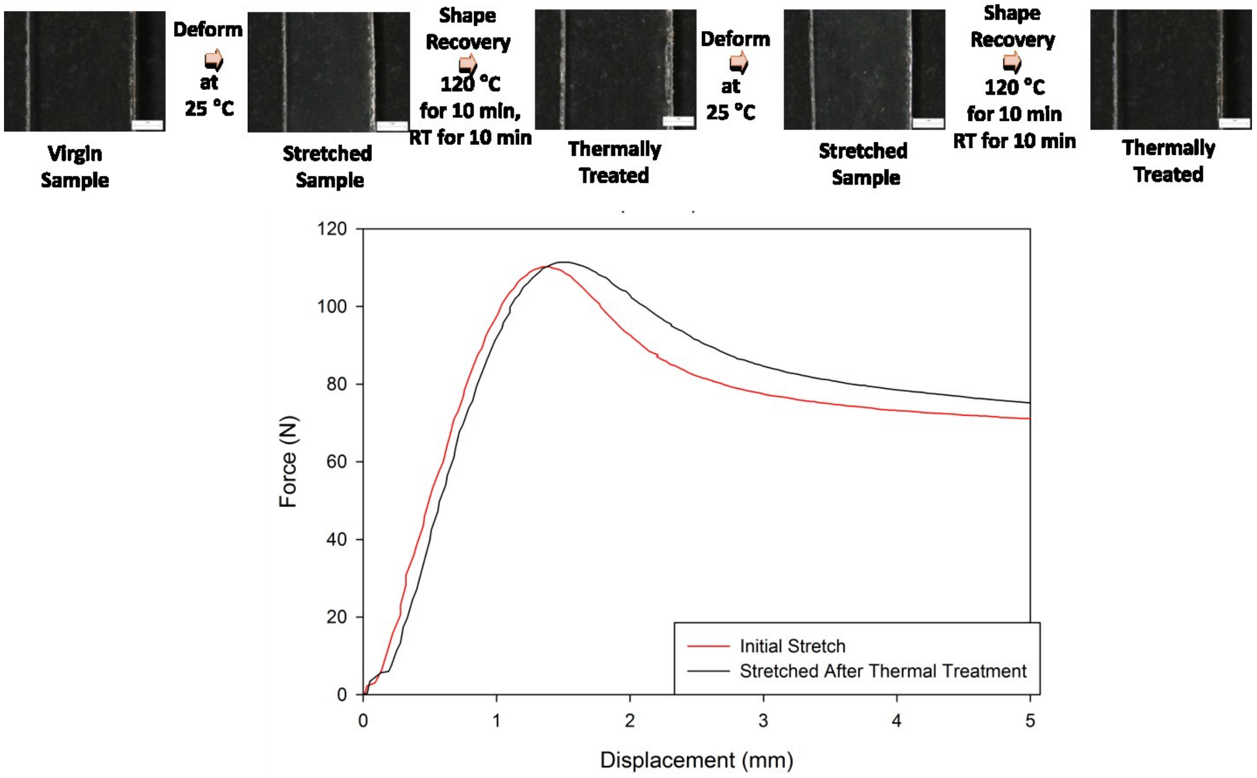

Figure A2.2.1. Tensile testing was performed to measure the degree of crazing formed as a function of deformation. Tensile testing of a l:n-tBA (0:100) 0.95 (average) mm thick film was conducted where crazing was evident during deformation. Linkam tensile stage was used to preform the tensile testing where the following parameters were used: $\text{Temp}_{\text{deformation}}$: RT, stretch rate: 100 μm/sec, and a load cell: 200 N. Thermal history removal was conducted prior to tensile testing where the film was heated at 120 °C for 10 min and cooled 10 min at RT. Force vs displacement curves were generated from the initial stretch and after thermal treatment steps where the sample was deformed to a displacement of 5 mm each time. The elastic, yield point and cold drawing region is evident on each curves. Optical micrographs (OM) are shown at each step of the process. Reversible crazing was evident after thermal treatment where the sample showed similar mechanical properties after thermal treatment.

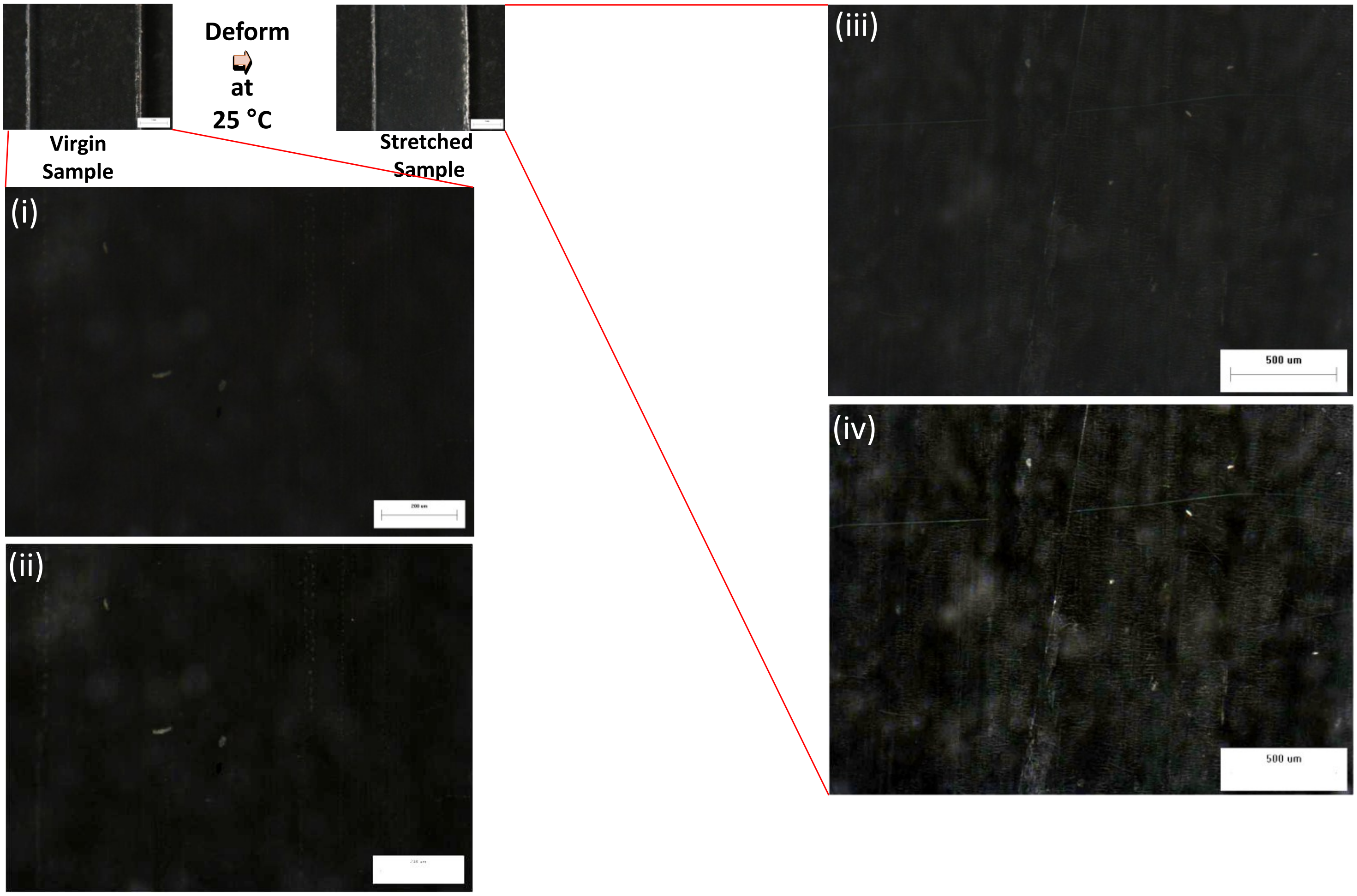

Figure A2.2.2. Optical micrographs (OM) are shown in the virgin and stretched state of the l:n-tBA (0:100) film tested and shown in Figure A2.2.1. The virgin sample showed no indication of crazing. Image (i) shows the OM of the sample in the virgin state and image (ii) shows the enhanced image of the virgin sample using Image J software to see the topography of the sample’s surface. The deformed sample showed crazes formed perpendicular to the loading direction. Image (iii) shows the OM of the stretched sample where (iv) shows the enhanced image of the stretched sample using ImageJ software to show the crazes.

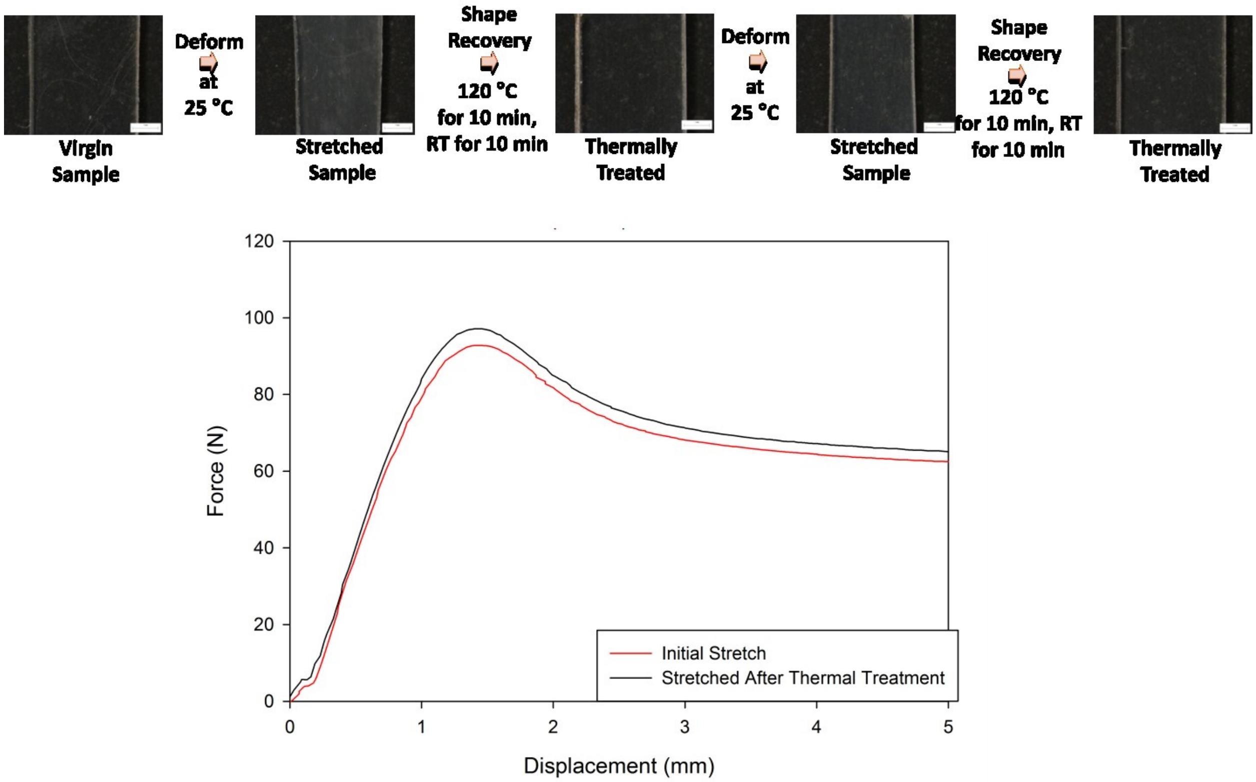

Figure A2.2.3. Tensile testing was performed to measure the degree of crazing formed as a function of deformation. Tensile testing of a l:n-tBA (10:90) 0.78 (average) mm thick film was conducted where crazing was evident during deformation. Linkam tensile stage was used to preform the tensile testing where the following parameters were used: $\text{Temp}_{\text{deformation}}$: RT, stretch rate: 100 µm/sec, and a load cell: 200 N. Thermal history removal was conducted prior to tensile testing where the film was heated at 120 °C for 10 min and cooled 10 min at RT. Force vs displacement curves were generated from the initial stretch and after thermal treatment steps where the sample was deformed to a displacement of 5 mm. The elastic, yield point and cold drawing region is evident on each curves. Optical micrographs (OM) are shown at each step of the process. Reversible crazing was evident after thermal treatment where the sample showed similar mechanical properties after thermal treatment.

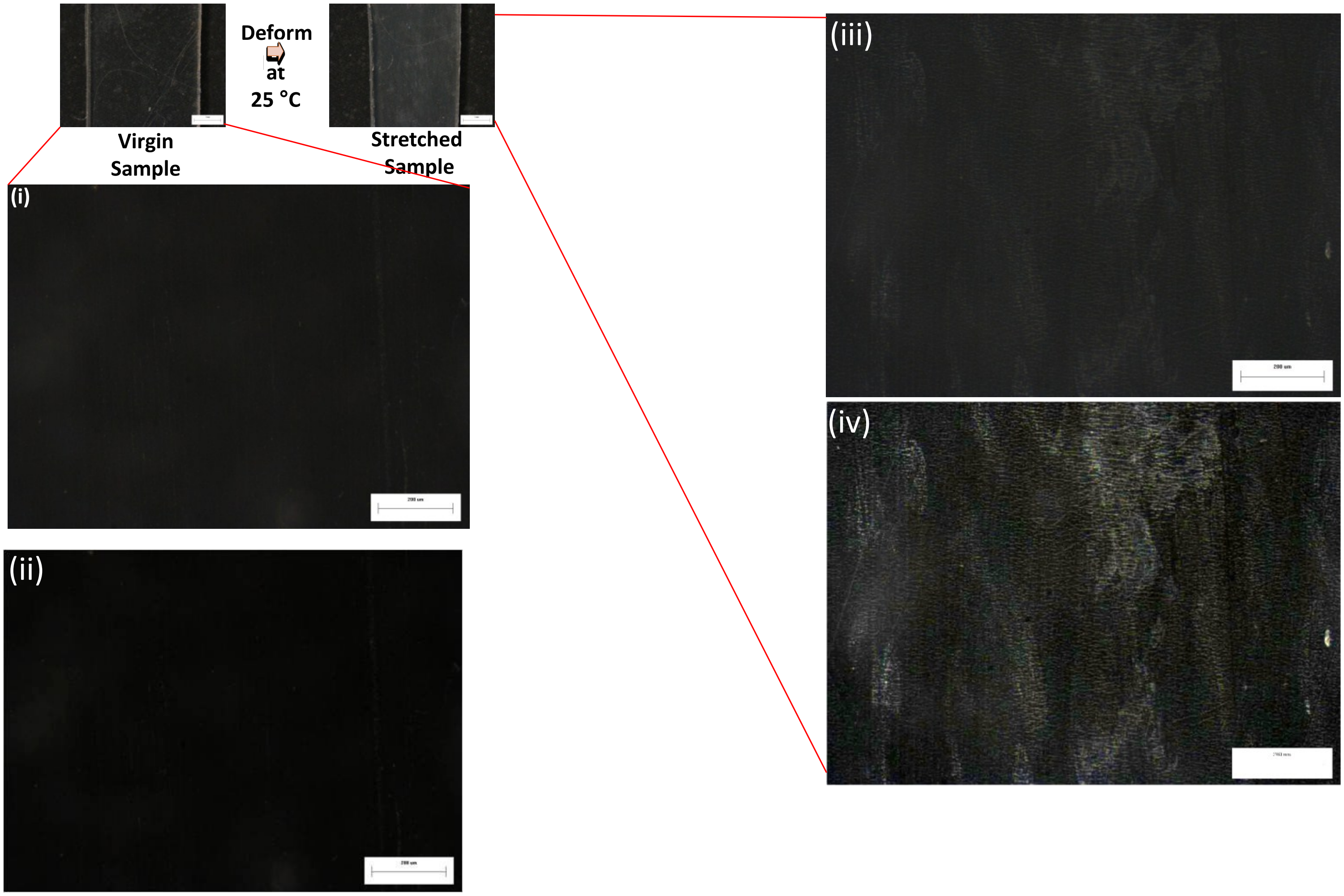

Figure A2.2.4. Optical micrographs (OM) are shown in the virgin and stretched state of the l:n-tBA (10:90) film tested and shown in Figure A2.2.3. The virgin sample showed no indication of crazing. Image (i) shows the OM of the sample in the virgin state and image (ii) shows the enhanced image of the virgin sample using Image J software to see the topography of the sample's surface. The deformed sample showed crazes formed perpendicular to the loading direction. Image (iii) shows the OM of the stretched sample where (iv) shows the enhanced image of the stretched sample using ImageJ software to show the crazes.

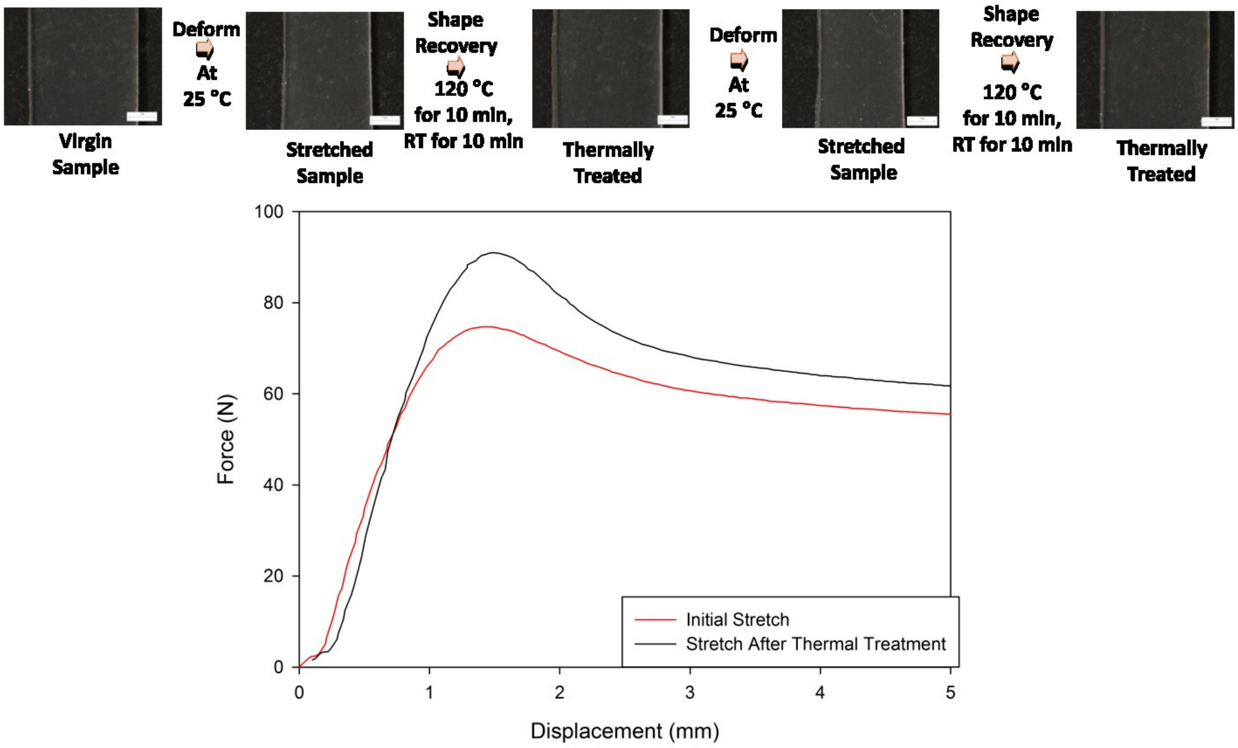

Figure A2.2.5. Tensile testing was performed to measure the degree of crazing formed as a function of deformation. Tensile testing of a l:n-tBA (25:75) 0.79 (average) mm thick film was conducted where crazing was evident during deformation. Linkam tensile stage was used to preform the tensile testing where the following parameters were used: Temp$_{\text{deformation}}$: RT, stretch rate: 100 μm/sec, and a load cell: 200 N. Thermal history removal was conducted prior to tensile testing where the film was heated at 120 °C for 10 min and cooled 10 min at RT. Force vs displacement curves were generated from the initial stretch and after thermal treatment steps where the sample was deformed to a displacement of 5 mm. The elastic, yield point and cold drawing region is evident on each curves. Optical micrographs (OM) are shown at each step of the process. Reversible crazing was evident after thermal treatment where the sample showed similar mechanical properties after thermal treatment.

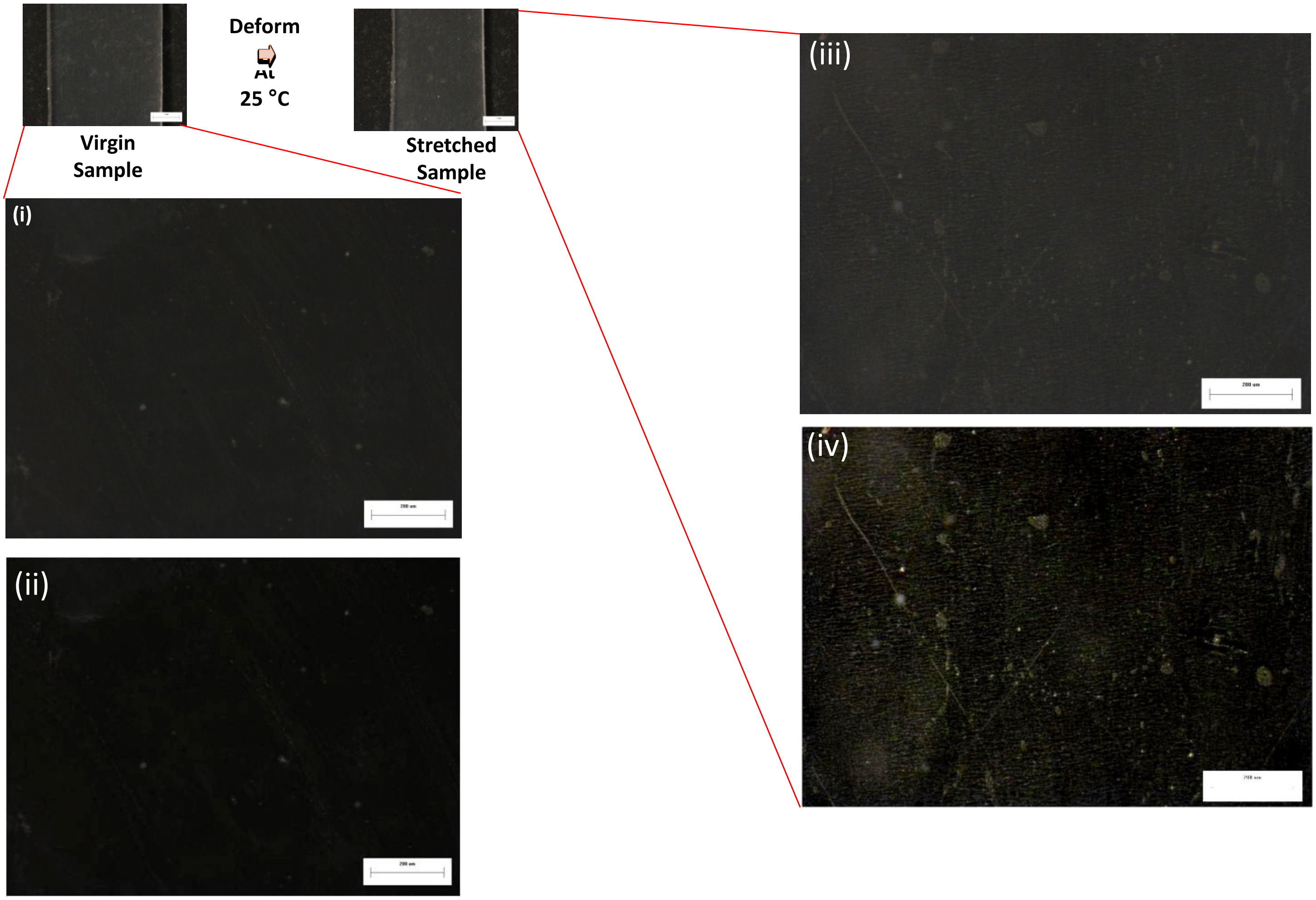

Figure A2.2.6. Optical micrographs (OM) are shown in the virgin and stretched state of the l:n-tBA (25:75) film tested and shown in Figure A2.2.3. The virgin sample showed no indication of crazing. Image (i) shows the OM of the sample in the virgin state and image (ii) shows the enhanced image of the virgin sample using Image J software to see the topography of the sample's surface. The deformed sample showed crazes formed perpendicular to the loading direction. Image (iii) shows the OM of the stretched sample where (iv) shows the enhanced image of the stretched sample using ImageJ software to show the crazes.

APPENDIX 2.3

SELF HEALING (SH) STUDIES USING l:n-tBA SMASH FILMS

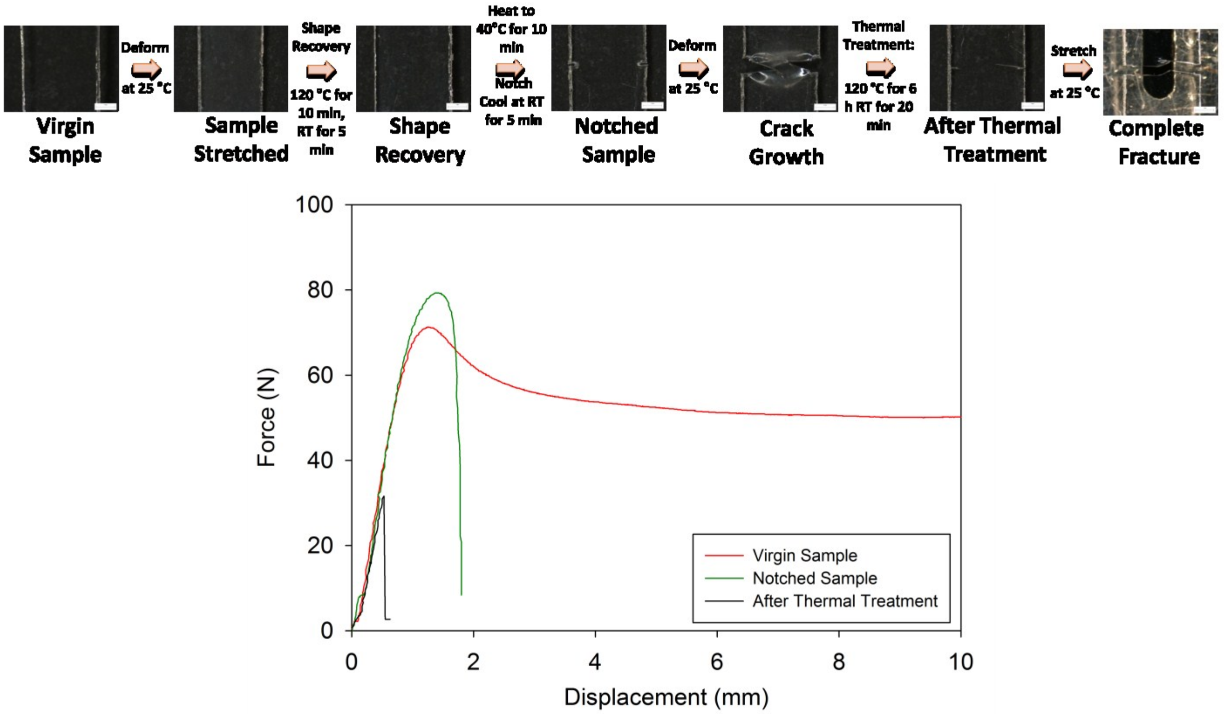

Figure A2.3.1. Force vs displacement graph used to evaluate the degree of healing for a n:l-tBA (0:100) 0.76 mm (average) thick film. A thermal removal was conducted prior to deformation where the film was heated at 120 °C for 10 min and cooled at 10 min at RT. The Linkam tensile stage was used to perform the uniaxial deformation where the following parameters were used: stretch temperature: RT, stretch rate: 27.8 µm/sec, load cell: 200 N. The red curve shows the deformation of the sample in its virgin state. The green curve shows the deformation in the sample's notched state and the black curve in the sample's thermally treated state. The optical micrographs (OM) shows the sample at the respective states of the SH experiment. Crack closure was evident however healing was not complete as cracks reopened after thermal treatment followed by complete sample fracture.

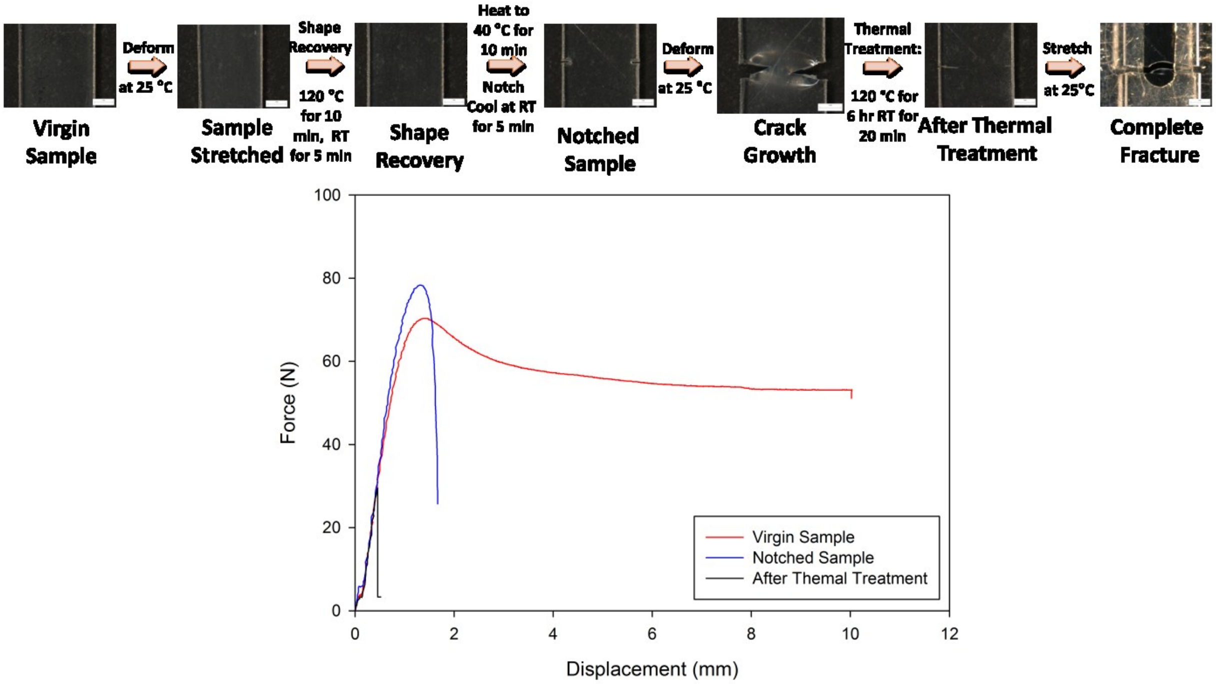

Figure A2.3.2. Force vs displacement graph used to evaluate the degree of healing for a n:l-tBA (10:90) 0.78 mm (average) thick film. A thermal removal was conducted prior to deformation where the film was heated at 120 °C for 10 min and cooled at 10 min at RT. The Linkam tensile stage was used to perform the uniaxial deformation where the following parameters were used: stretch temperature: RT, stretch rate: 27.8 µm/sec, load cell: 200 N. The red curve shows the deformation of the sample in its virgin state. The green curve shows the deformation in the sample's notched state and the black curve in the sample's thermally treated state. The optical micrographs (OM) shows the sample at the respective states of the SH experiment. Crack closure was evident however healing was not complete as cracks reopened after thermal treatment followed by complete sample fracture.

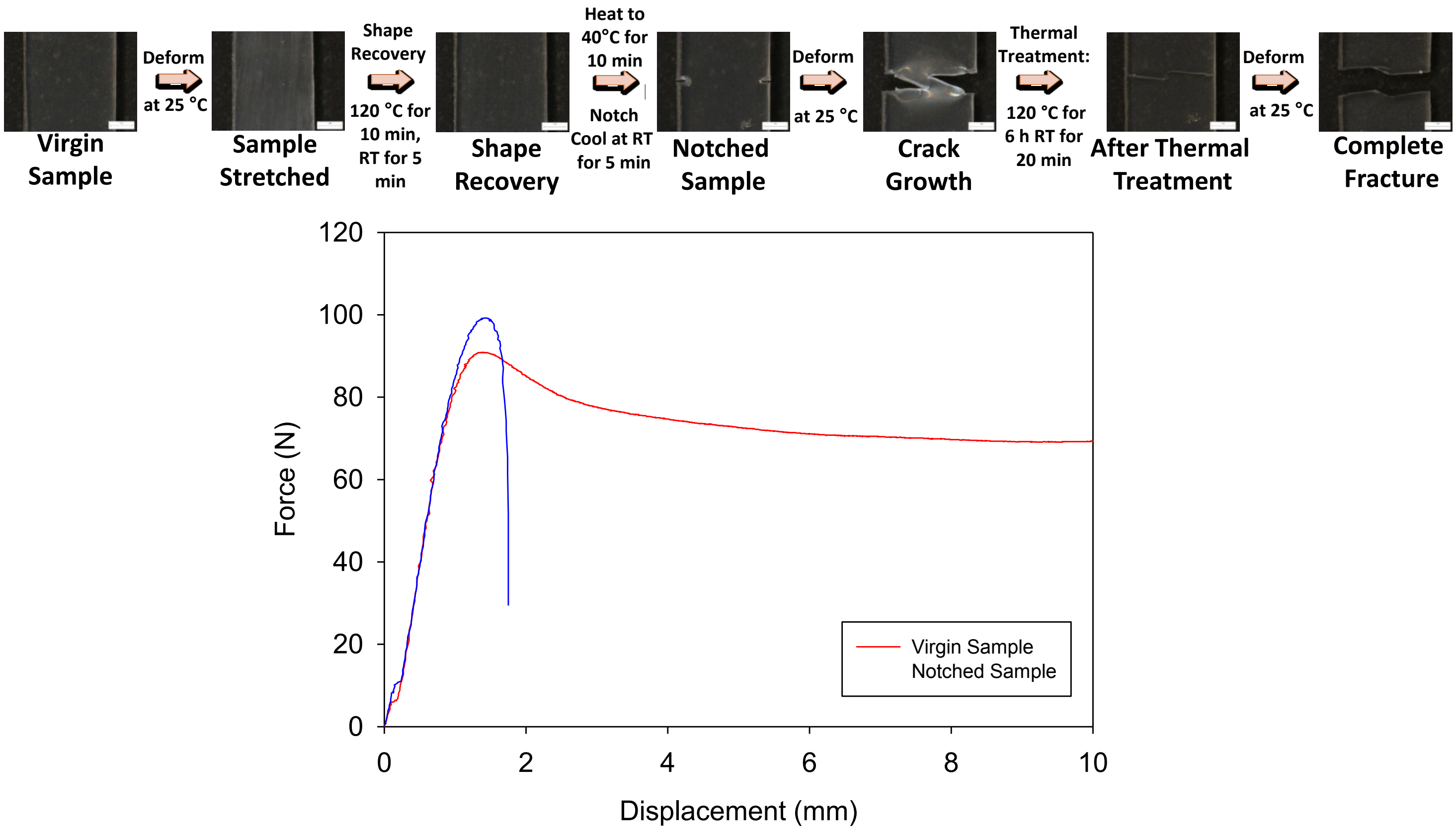

Figure A2.3.3. Force vs displacement graph used to evaluate the degree of healing for a n:l-tBA (25:75) 0.78 mm (average) thick film. A thermal removal was conducted prior to deformation where the film was heated at 120 °C for 10 min and cooled at 10 min at RT. The Linkam tensile stage was used to perform the uniaxial deformation where the following parameters were used: stretch temperature: RT, stretch rate: 27.8 µm/sec, load cell: 200 N. The red curve shows the deformation of the sample in its virgin state. The green curve shows the deformation in the sample's notched state. The optical micrographs (OM) shows the sample at the respective states of the SH experiment. Crack closure was evident however healing was not complete as cracks reopened after thermal treatment followed by complete sample fracture.

APPENDIX 3.0

ANISOTROPIC SHAPE MEMORY COMPOSITES (A-SMEC) SYSTEMS

(PVAc/SYLGARD 184)

A.3 SUMMARY

Please refer to Chapter 6 for an explanation of experiments presented in this appendix.

APPENDIX 3.1

ANISOTROPIC SHAPE MEMORY COMPOSITES (A-SMEC) SYSTEMS

PVAC/SYLGARD 184

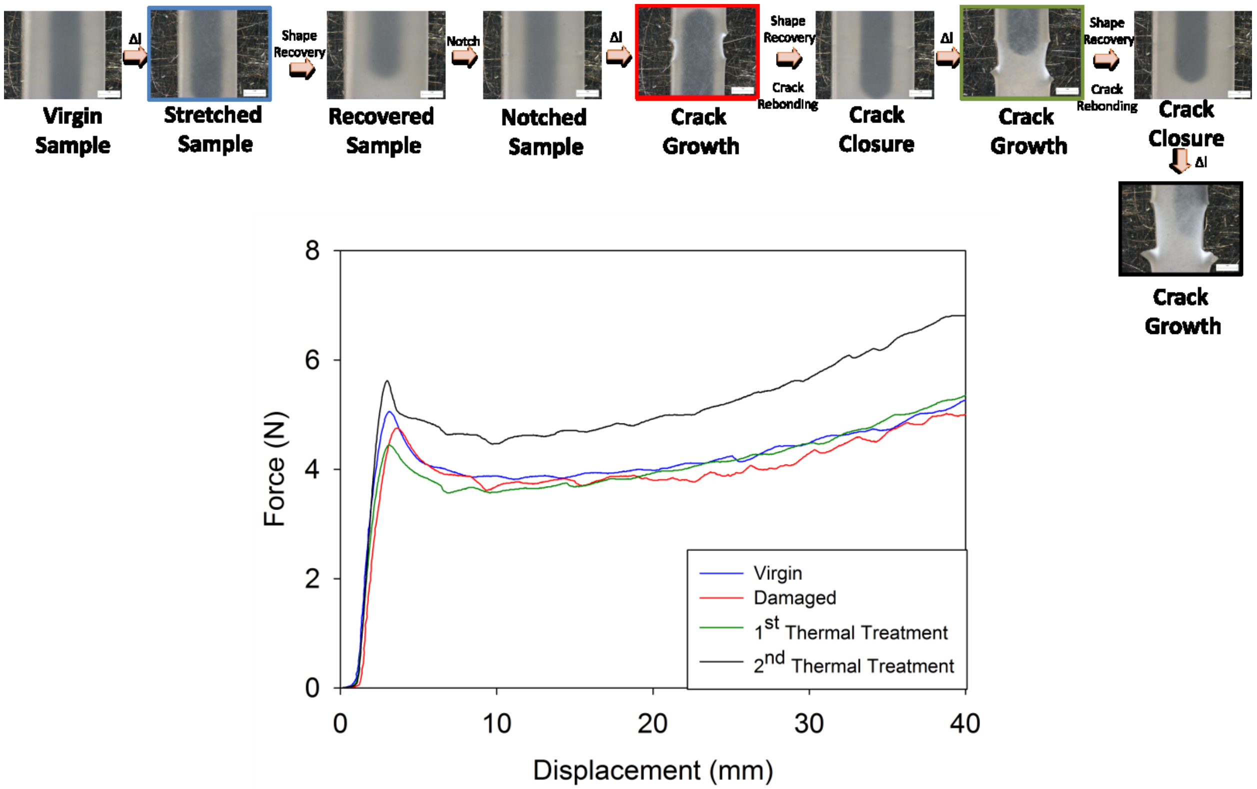

Figure A3.1.1. Force vs displacement graph used to evaluate the degree of healing for a PVAc A-SMEC where the PVAc fibers (M_w~249k g/mol) were aligned in the axial (0°) direction. The average thickness of the specimen was 0.36 mm. For the SH experiment, the sample was deformed in its virgin, notched and thermally treated state. The Linkam tensile stage was used to perform the tensile testing where the following parameters were used: load cell: 20 N, stretch temp: 25 °C, and displacement speed: 100 μm/sec. The first thermal treatment was 100 °C for 10 min, RT for 10 min and the 2nd thermal treatment was 100 °C for 1 h, RT for 1h. The optical micrographs (OM) shows the sample at the respective states of the SH experiment. Crack closure was evident however healing was not complete as the cracks reopened after thermal treatments.

Although the mechanical properties are higher after thermal treatment, the crack reopened and could lead to catastrophic damage during use over time.

APPENDIX 3.2

AERODYNAMIC STUDIES

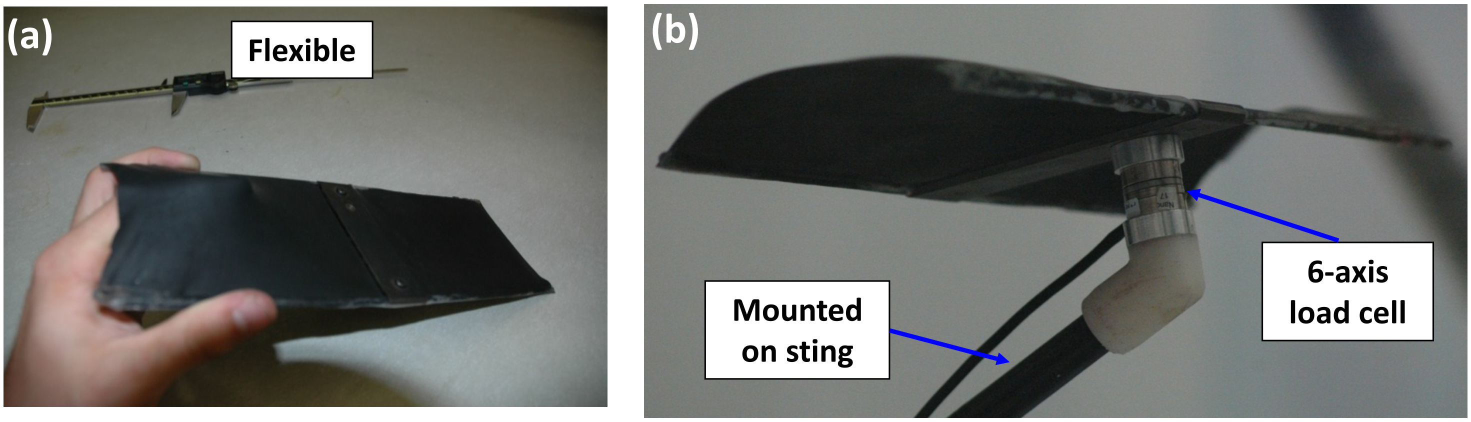

Figure A3.2.1. Images showing (a) the Brown University's prototype made from a commercially named, Dragon Skin, with a high performance platinum cure silicone rubber. (b) Showing the prototype mounted in the wind tunnel fixture. (Courtesy of Rye Waldman, Brown University)

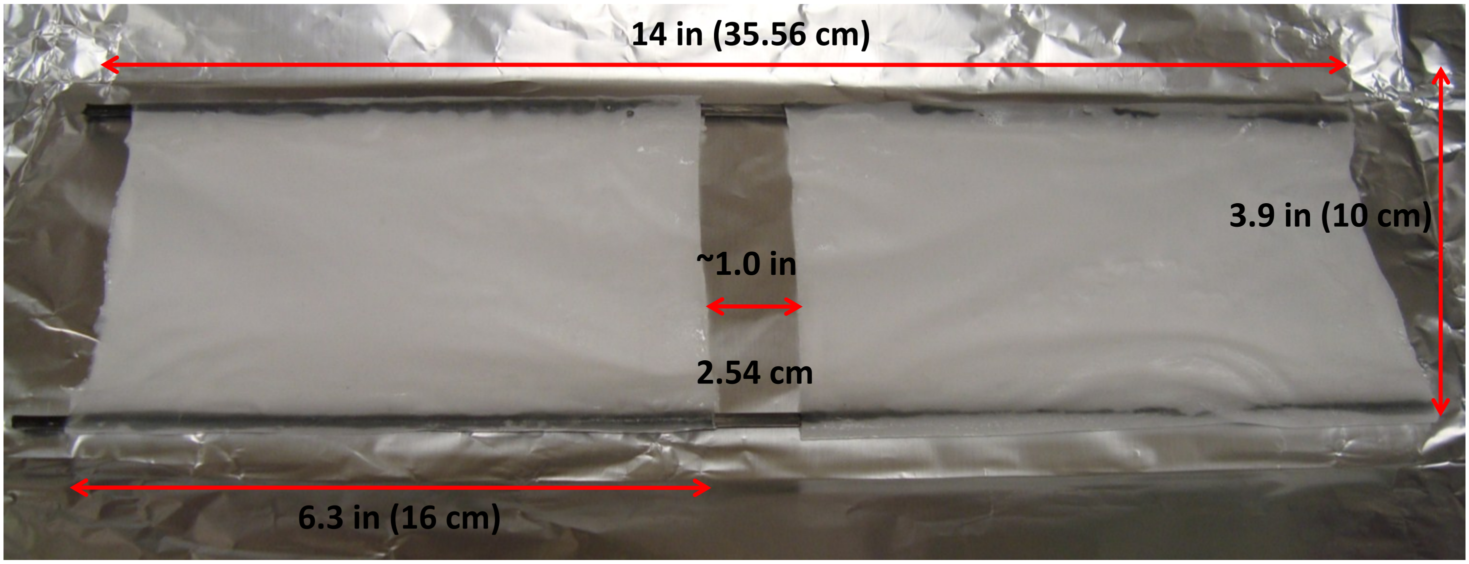

	Thickness (μm)	Weight (g)
Fiber Mat	389	0.90
Composite	569	4.80

	Thickness (μm)	Weight (g)
Fiber Mat	279	0.88
Composite	563	4.80

Figure A3.2.2. Image of Syracuse University's prototype using two 6.3 (l) x 3.9 (w) in A-SMEC skins where the leading and trailing edges were cured around 0.125 in diameter carbon rods by Sylgard184. The distance between the skins was approximately 1.0 in where the entire prototype weighed 24.8 g. The tables correspond to each sheet where the average thicknesses and weights of the fiber mat and composite are shown.

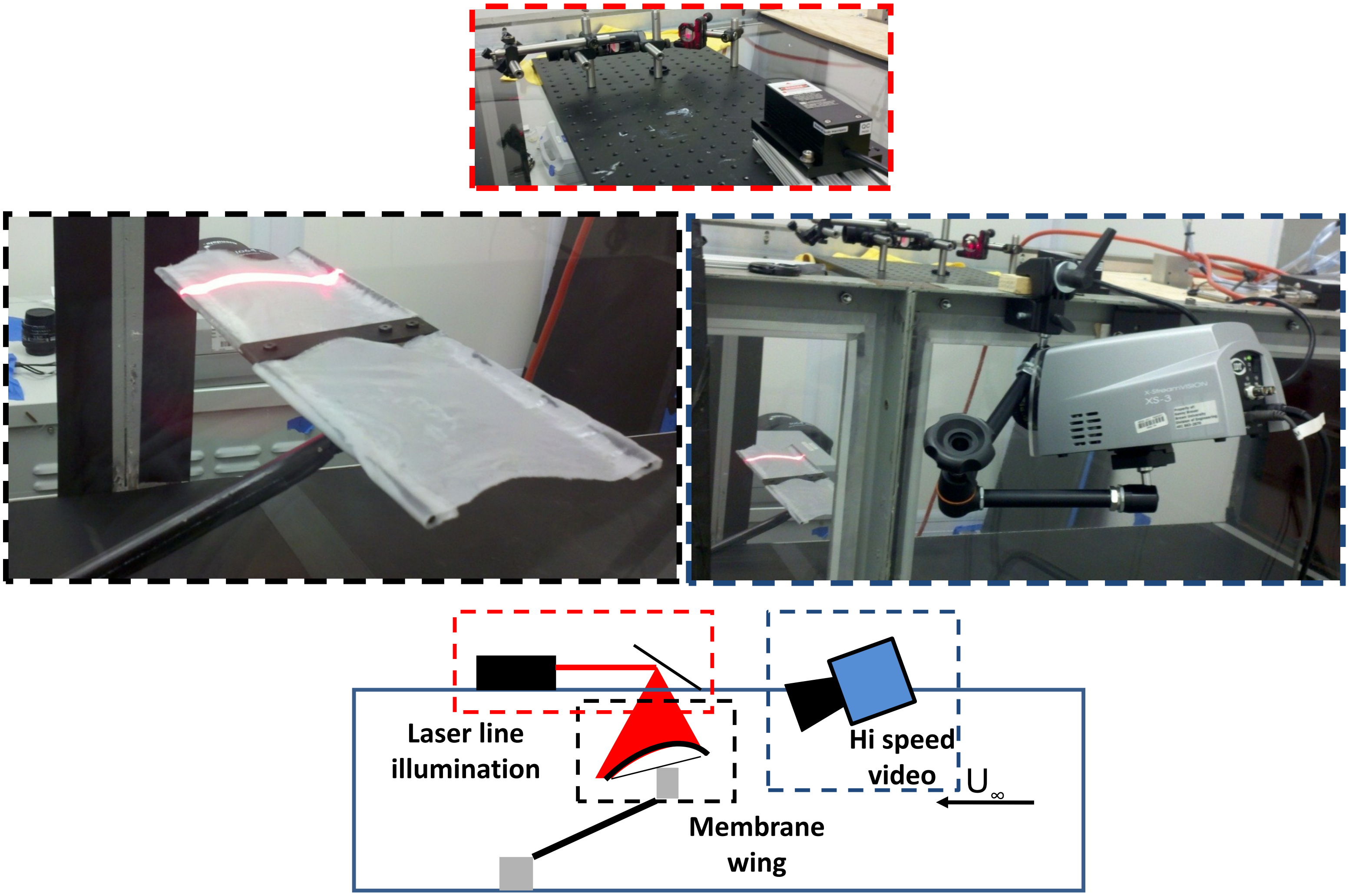

Figure A3.2.2. Schematic and images showing the wind tunnel set up at Brown University. The red dashed box shows the laser line illumination set up. The blue dashed box shows the hi speed video camera for movie capturing. The black dashed box shows Syracuse University's prototype mounted in the wind tunnel. (Courtesy of Rye Waldman, Brown University)

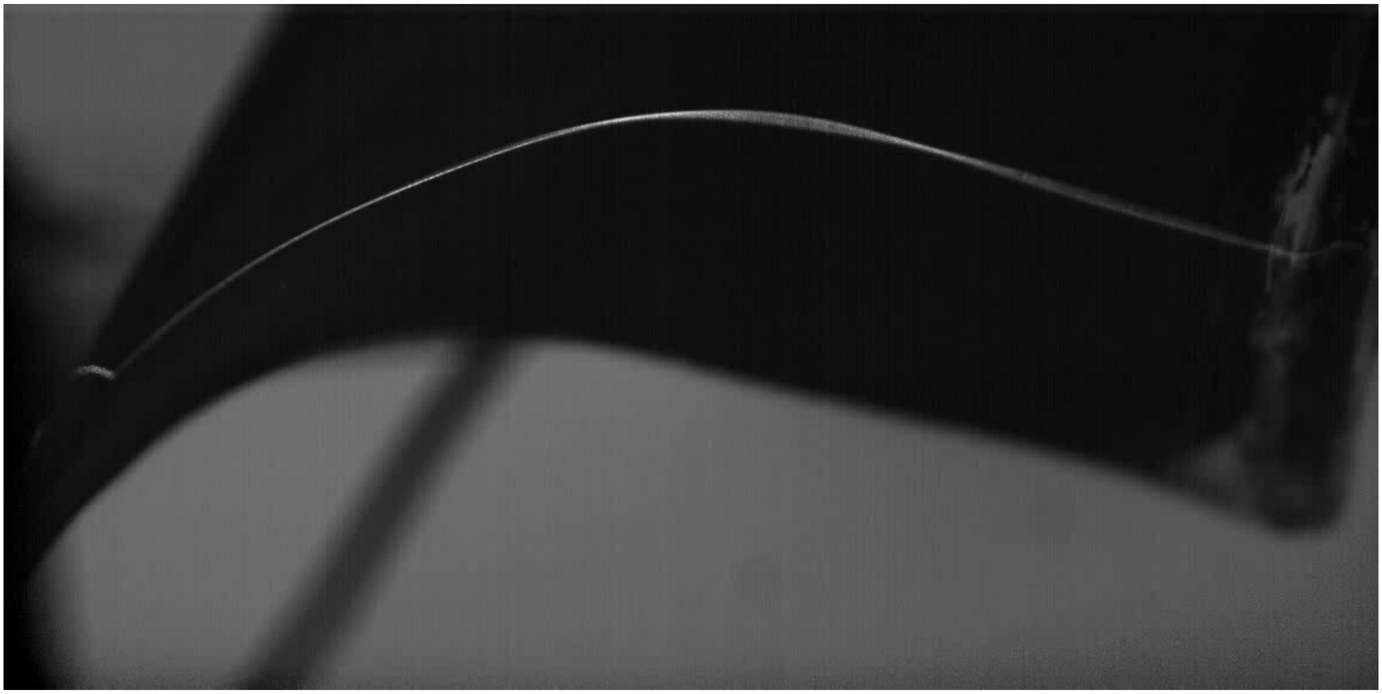

Figure A3.2.3. Syracuse University's prototype in the wind tunnel where the laser beam traces the airfoil along the width of the A-SMEC skin. (Courtesy of Rye Waldman, Brown University).

APPENDIX 4.0

ANISOTROPIC SHAPE MEMORY COMPOSITES (A-SMEC) LAMINATED COMPOSITES:

POLY(VINYL ACETATE) (PVAc)/SYLGARD184

A.4 SUMMARY

Please refer to Chapter 6 for an explanation of experiments presented in this appendix.

APPENDIX 4.1

ANISOTROPIC SHAPE MEMORY COMPOSITES (A-SMEC) LAMINATED COMPOSITES:

POLY(VINYL ACETATE) (PVAc)/SYLGARD184

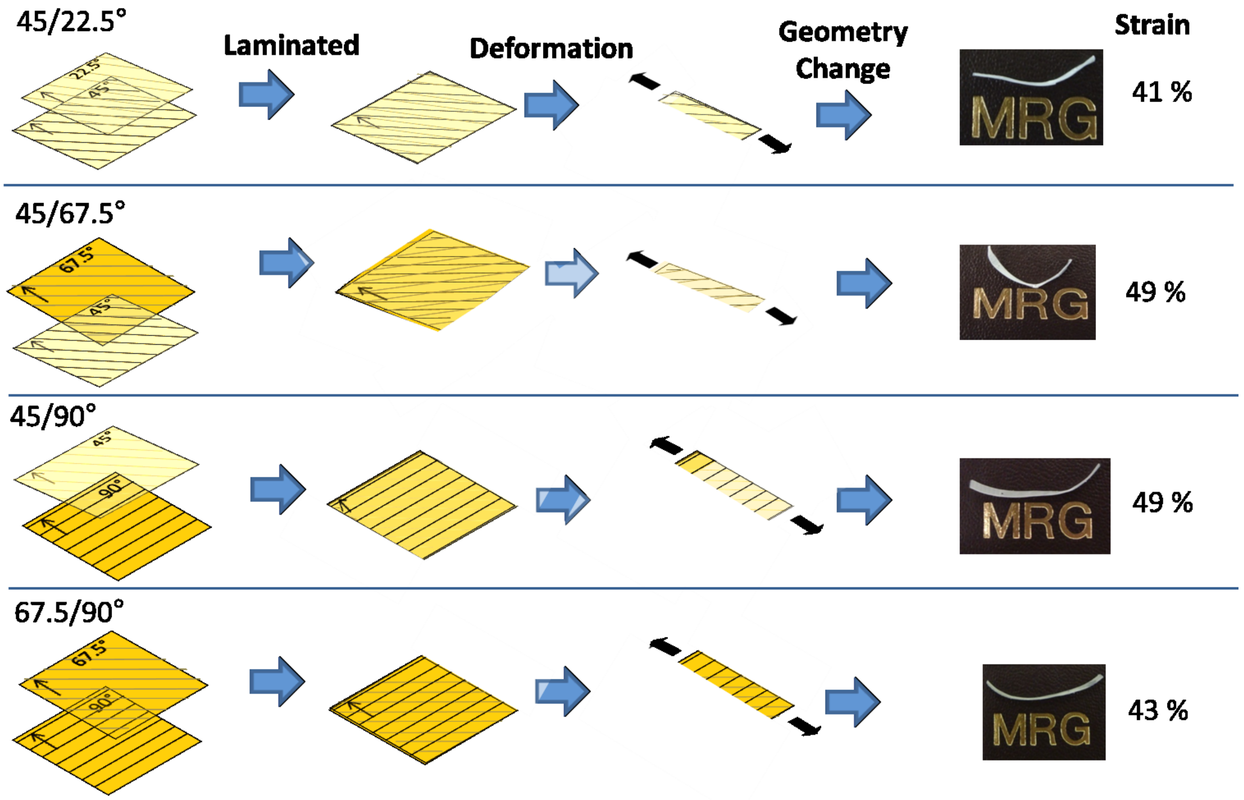

Figure A4.1.1. Schematic and images showing the laminated composites for the following systems: 45/22.5°, 45/67.5°, 45/90°, and 67.5/90°. The stereomicrographs show the specimens post deformation where the strain values are shown for the respective systems. Each strip was cut from the side of each system.

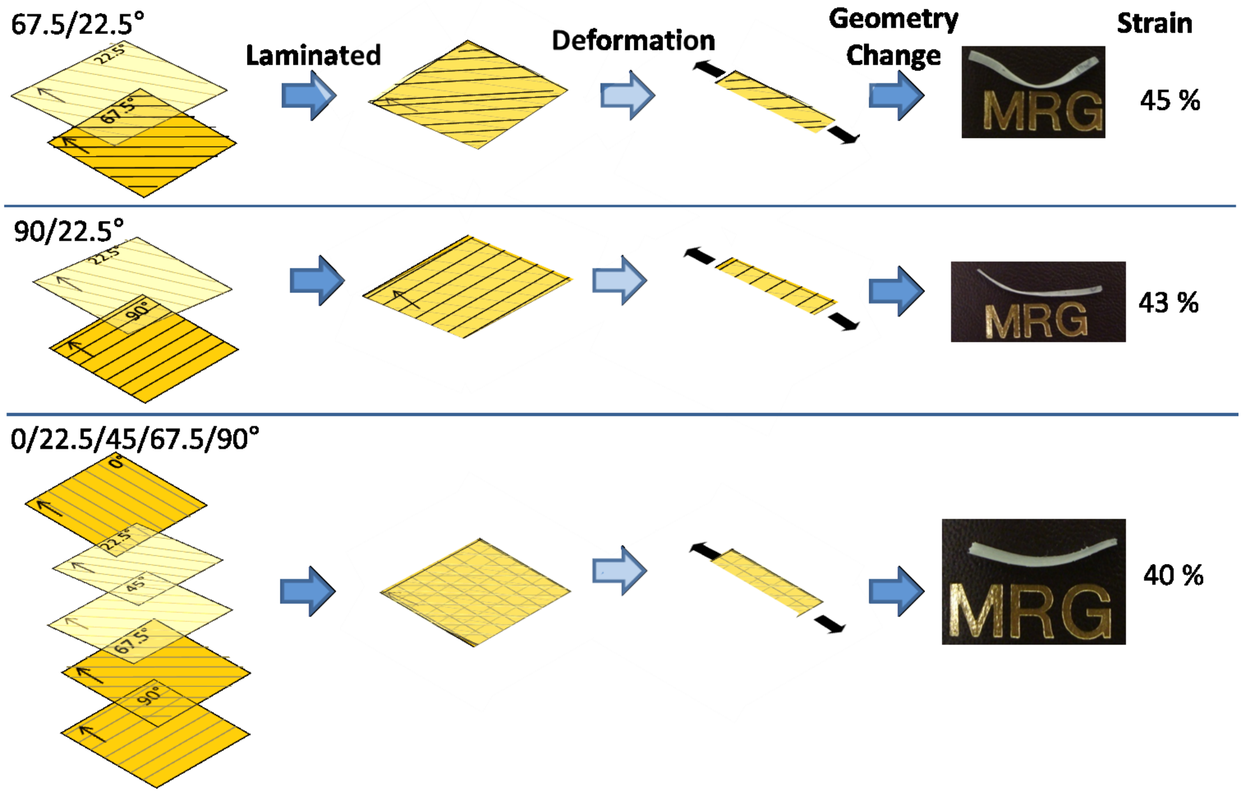

Figure A4.1.2. Schematic and images showing the laminated composites for the following systems: 67.5/22.5°, 90/22.5°, and 0/22.5/45/67.5/90°. The stereomicrographs show the specimens post deformation where the strain values are shown for the respective systems. Each strip was cut from the side of each system.

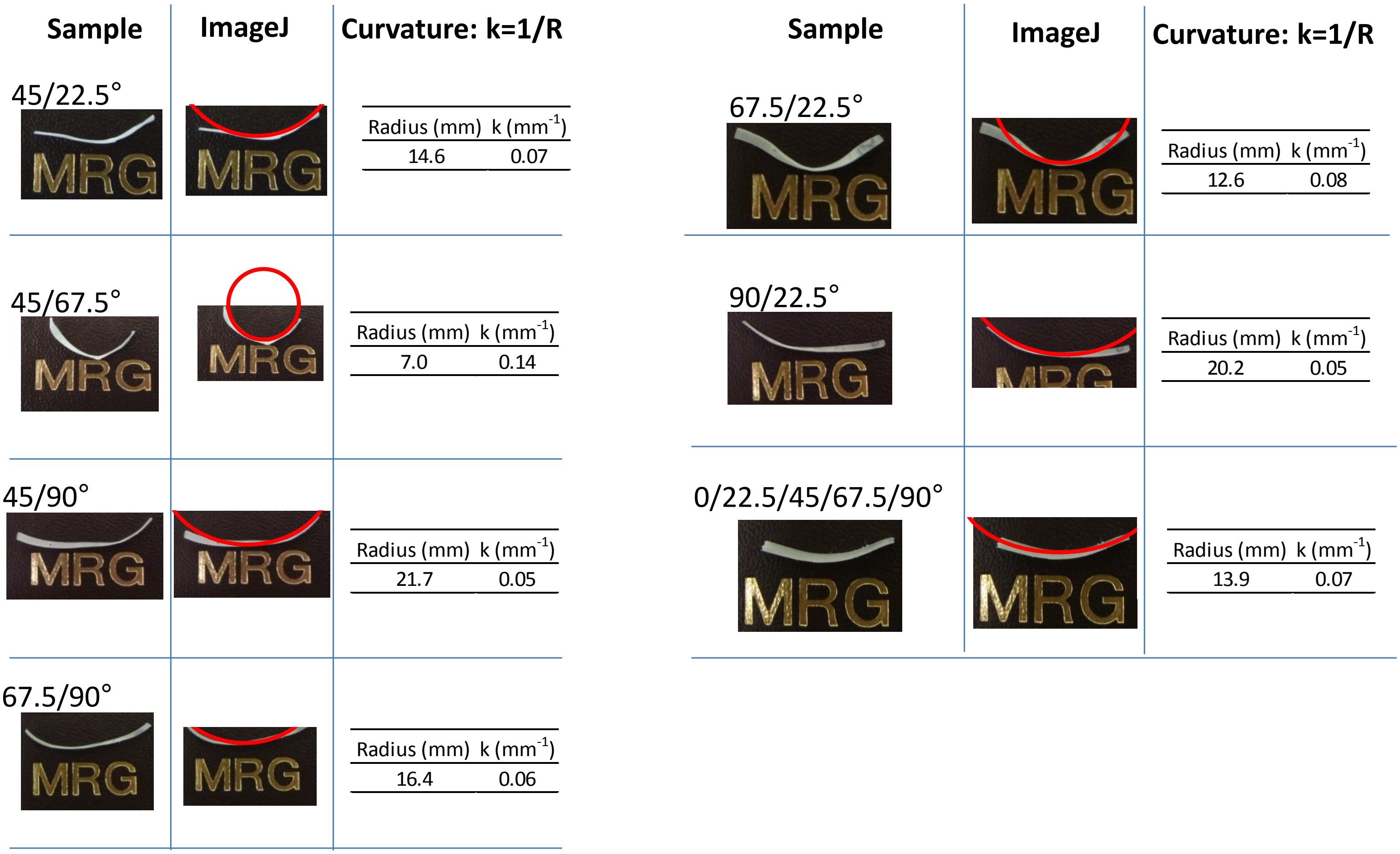

Sample	Radius (mm)	k (mm^{-1})
45/22.5°	14.6	0.07
45/67.5°	7.0	0.14
45/90°	21.7	0.05
67.5/90°	16.4	0.06
67.5/22.5°	12.6	0.08
90/22.5°	20.2	0.05
0/22.5/45/67.5/90°	13.9	0.07

Figure A4.1.3. Images showing the laminated composites for the following systems: 45/22.5°, 45/67.5°, 45/90°, and 67.5/90°, 67.5/22.5°, 90/22.5°, and 0/22.5/45/67.5/90°. The curvature values are presented where the values were calculated by analyzing each image using ImageJ software.

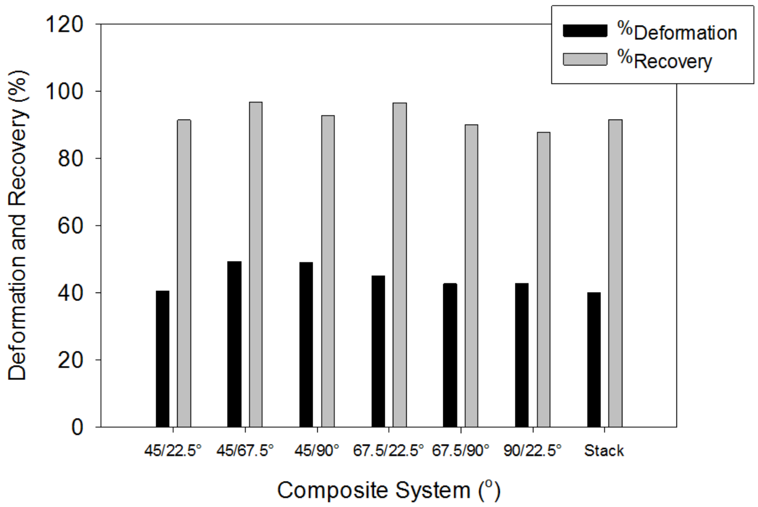

$$\%\text{deformed} = \frac{(L_{\text{deform}} - L_{\text{orig}})}{L_{\text{orig}}} * 100$$

$$\%\text{recovery} = \frac{(L_{\text{deform}} - L_{\text{recov}})}{(L_{\text{deform}} - L_{\text{orig}})} * 100$$

System	$\%_{deformation}$	$\%_{recovery}$
45/22.5°	41	91
45/67.5°	49	97
45/90°	49	93
67.5/22.5°	45	96
67.5/90°	43	90
90/22.5°	43	88
0/22.5/45/67.5/90°	40	92

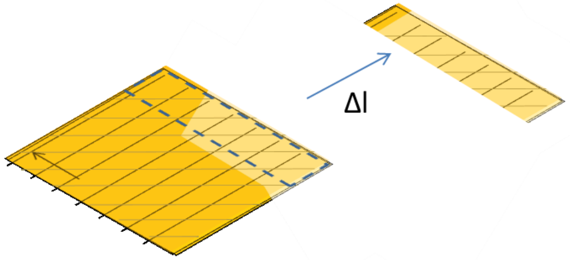

Figure A4.1.4. Graph showing the $\%_{\text{deformation}}$ and $\%_{\text{recovery}}$ as a function of laminated composites tested. The chart shows the numeric values of the $\%_{\text{deformation}}$ and $\%_{\text{recovery}}$ where the equations for each are shown.

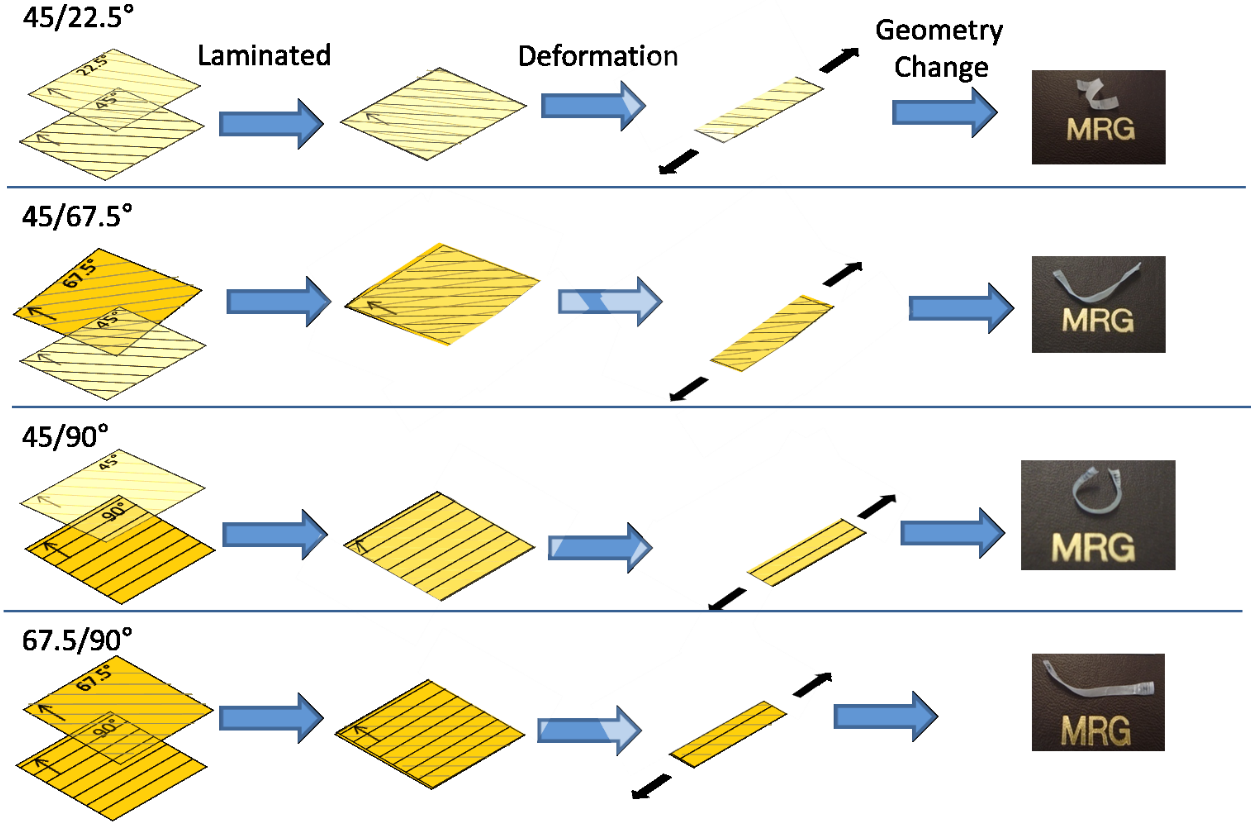

Figure A4.1.5. Schematic and images showing the laminated composites for the following systems: 45/22.5°, 45/67.5°, 45/90°, and 67.5/90°. The stereomicrographs show the specimens post deformation. Each strip was cut from the bottom of each system.

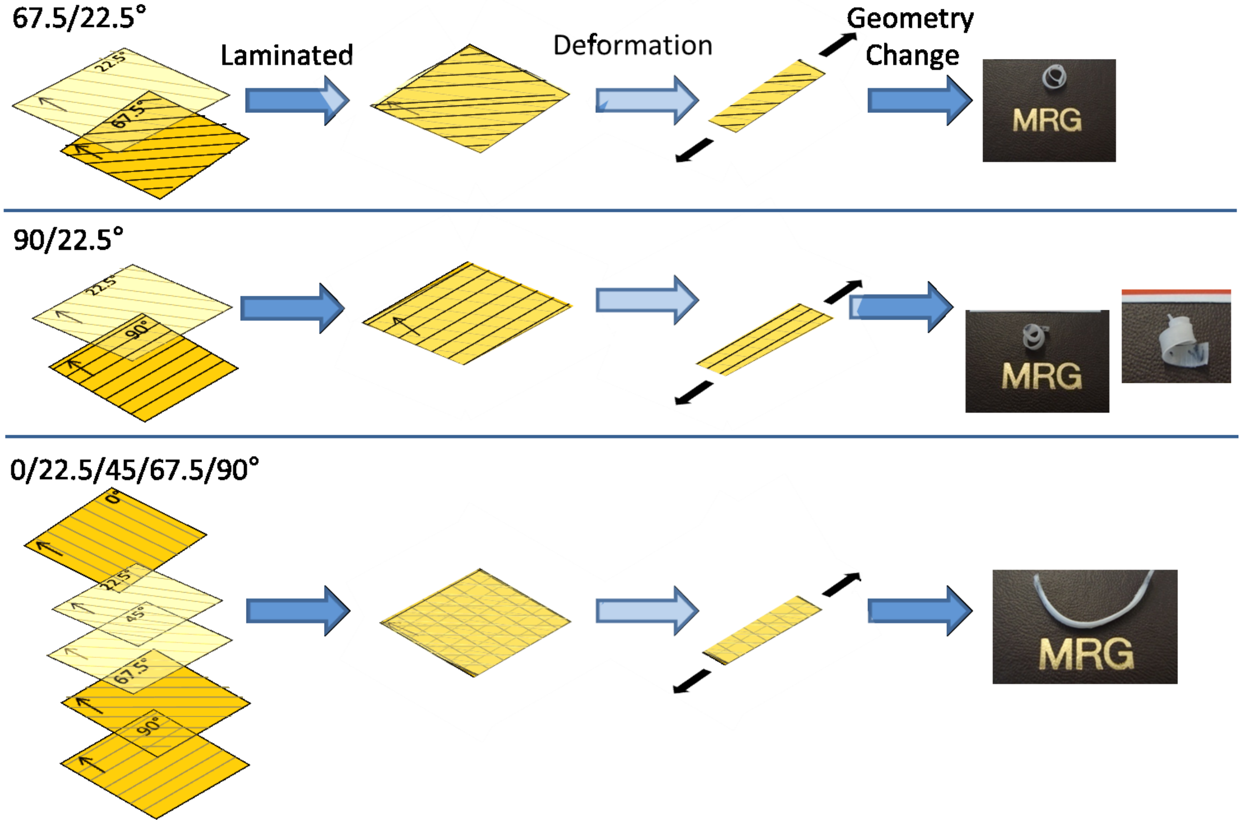

Figure A4.1.6. Schematic and images showing the laminated composites for the following systems: 45/22.5°, 45/67.5°, 45/90°, and 67.5/90°. The stereomicrographs show the specimens post deformation. Each strip was cut from the bottom of each system.

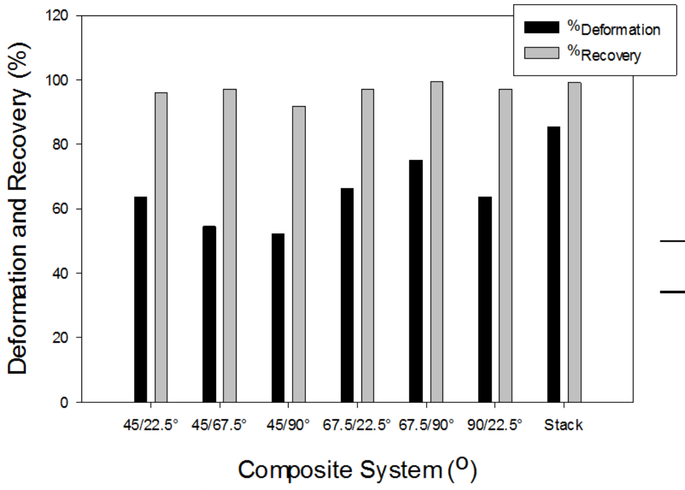

$$\%\text{deformed} = \frac{(L_{deform} - L_{orig})}{L_{orig}} * 100$$

$$\%\text{recovery} = \frac{(L_{deform} - L_{recov})}{(L_{deform} - L_{orig})} * 100$$

System	$\%_{deformation}$	$\%_{recovery}$
45/22.5°	63.6	95.9
45/67.5°	54.5	97.2
45/90°	52.2	91.8
67.5/22.5°	66.3	97.1
67.5/90°	75.1	99.4
90/22.5°	63.7	97.1
0/22.5/45/67.5/90°	85.3	99.1

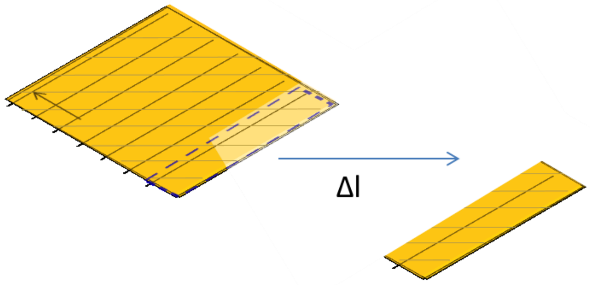

Figure A4.1.7. Graph showing the $\%_{deformation}$ and $\%_{recovery}$ as a function of laminated composite tested. The chart shows the numeric values of the $\%_{deformation}$ and $\%_{recovery}$ where the equations for each are shown.

Table A4.1.1. Table showing the weights and thicknesses of each ply and composite fabricated and tested.

Individual Plies				Laminated Composites		Syglard 184 Layer	
Laminated Composite	Square Angle (°)	Weight (mg)	Average Thickness (mm)	Weight (mg)	Average Thickness (mm)	Sylgard 184 weight (mg)	Sylgard 184 thickness (mm)
45/22.5°	45	115.3	0.18	264.4	0.4	35.7	0.02
	22.5	113.4	0.18				
45/67.5°	45	113.5	0.18	237.9	0.4	28.0	0.02
	67.5	96.4	0.16				
45/90°	45	103.8	0.17	241.9	0.3	30.3	0.01
	90	107.8	0.16				
67.5/22.5°	67.5	97.5	0.17	255.4	0.4	40.3	0.03
	22.5	117.6	0.19				
67.5/90°	67.5	112.0	0.19	252.1	0.4	43.9	0.04
	90	96.2	0.16				
90/22.5°	90	94.0	0.16	263.0	0.4	41.3	0.02
	22.5	127.7	0.21				
0/22.5/45/67.5/90°	0	108.6	0.17	**648.00**	**0.89**	**100.60**	**0.01**
	22.5	109.9	0.18				
	45	109.5	0.17				
	67.5	108.9	0.18				
	90	110.5	0.18				

APPENDIX 5.0

POLY (Ɛ-CAPROLACTONE) (PCL)/EPOXY COMPOSITE SH STUDIES

A.5 SUMMARY

Please refer to Chapter 6 for an explanation of experiments presented in this appendix.

APPENDIX 5.1

POLY(Ɛ-CAPROLACTONE) (PCL)/EPOXY COMPOSITE SELF HEALING (SH) STUDIES

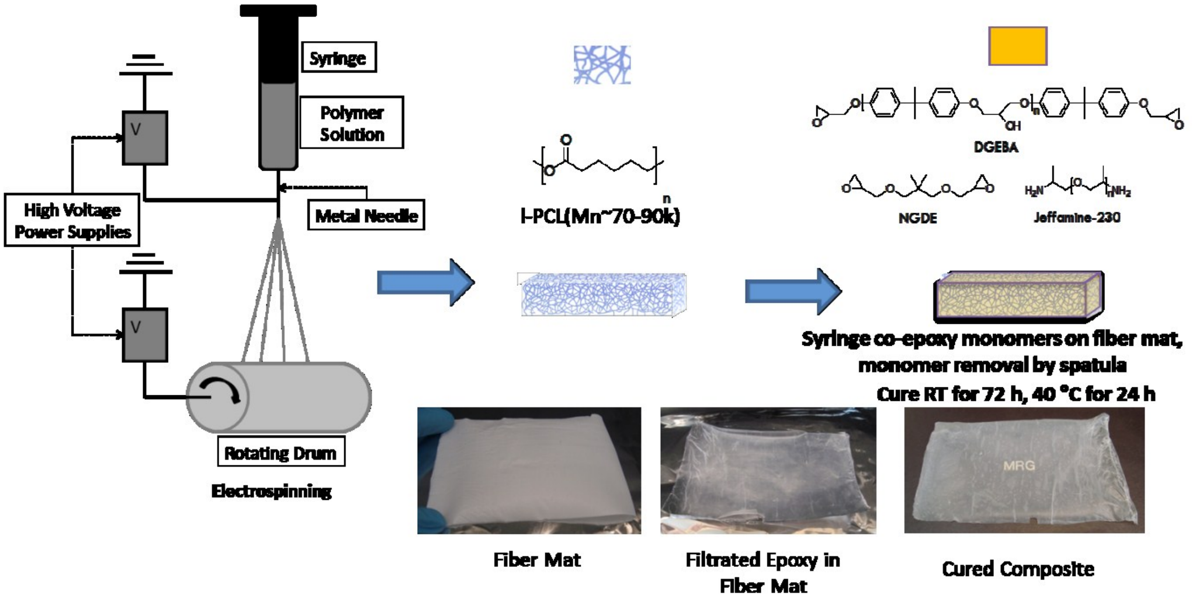

	Weight (g)	Thickness(mm)
Fiber Mat	0.38	0.17
Composite	2.15	0.31

Figure A5.1.1. Schematic showing the two step fabrication process of a PCL (M_w~70 - 90k)/Epoxy composite. The e-spinning parameters used were as follows: flow rate: 1.0 mL/h, needle tip to drum: 7 cm, voltage: 15 kV, translation on, rotation: 1500 RPM, e-spinning time: ~16 h, and drum voltage: 0 V. Images show the system in the fiber, infiltrated and cured state. The table shows the weight and average thicknesses of the fiber mat and cured composite. (Scheme adopted from Dr. Xiaofan Luo's Dissertation: Thermally Responsive Polymer Systems for Self-Healing, Reversible Adhesion and Shape Memory Applications)

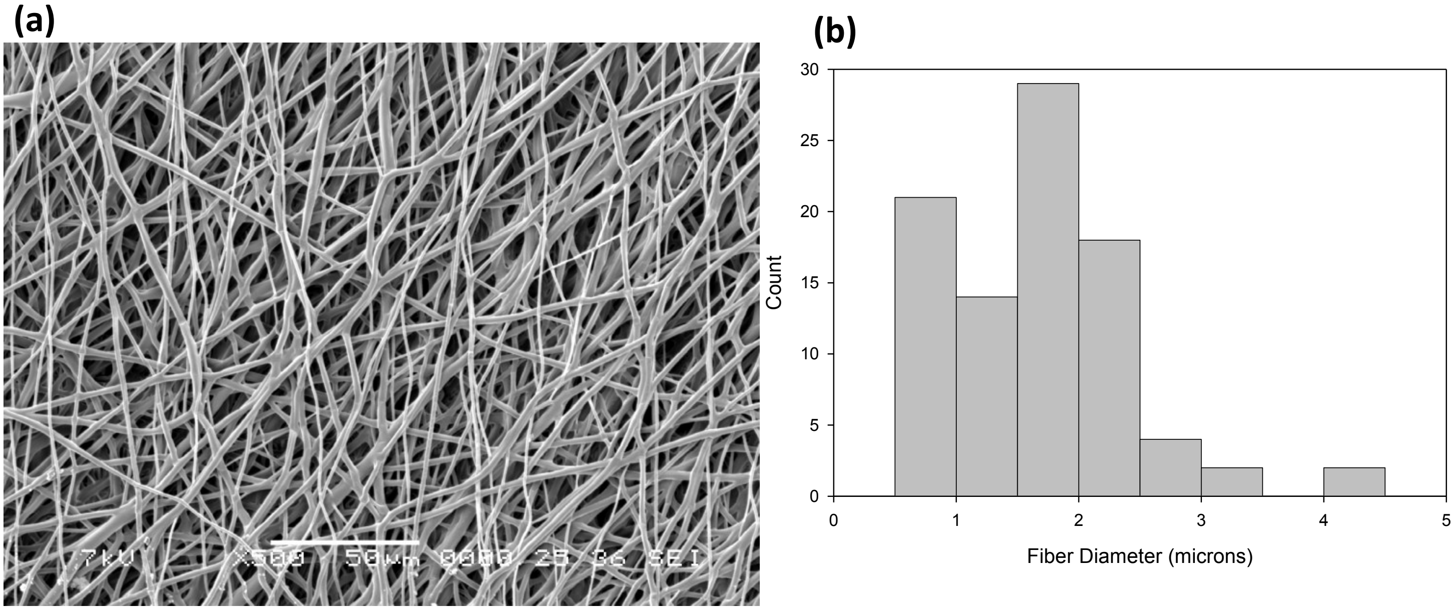

Figure A5.1.2. (a) Scanning electron microscopy (SEM) image showing a representative topography of the PCL (M_w~70 - 90k) fiber mat. The SEM was used to obtain the average fiber diameter of 1.66 ± 0.69 µm. (b) Graph showing histogram of the number of fibers measured vs fiber diameter values.

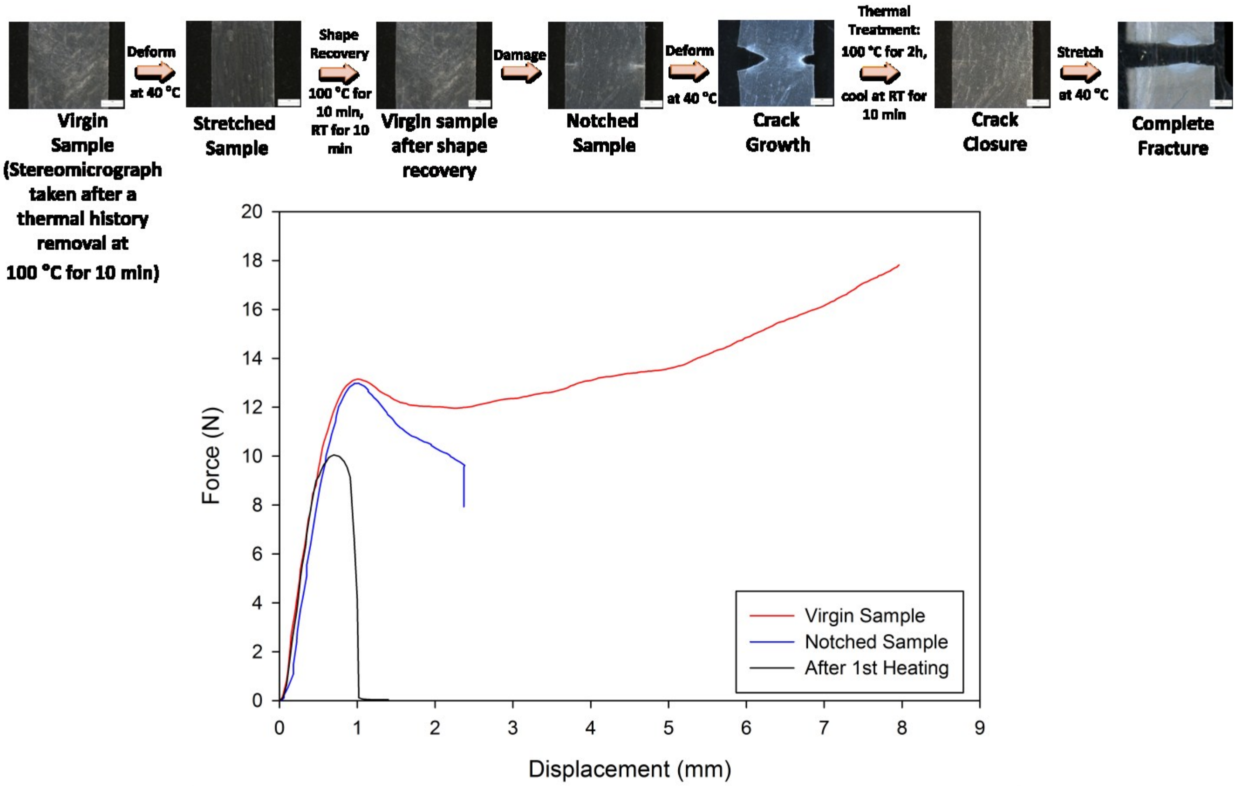

Figure A5.1.3. Force vs displacement graph used to evaluate the degree of healing for PCL (M_w~70 - 90k)/Epoxy composite. The Linkam tensile stage was used to preform the tensile testing where the following parameters were used: load cell: 20 N, stretch speed: 100 µm/sec and deformation temperature: RT. A dogbone was punched from the composite sheet where the average thickness of the specimen was 0.34 mm. Red curve shows the deformation of the sample in its virgin state. Blue curve shows the deformation in the samples notched state and black curve in the sample's thermally treated state. The elastic, yield point and cold drawing region was evident on the red and blue curves. The Optical micrographs (OM) showing the sample at the respective states of the SH experiment. The specimen showed no evidence of SH as the crack reopened and completely fractured after thermal treatment.

Fiber Mat

Filtrated Epoxy in Fiber Mat

Cured Composite

Sheet	Weight (g)	AVE Thickness (mm)
PCL Fiber Mat	0.91	0.36
Composite	7.15	0.78

Figure A5.1.4. Images showing the system in the fiber, infiltrated and cured state where the M_w of the PCL was approximately 65k. The table shows the weight and average thicknesses of the fiber mat and cured composite. The e-spinning parameters used were as follows: PCL/Chloroform + DMF: 2g / 8 mL + 2 mL, flow rate: 0.35 mL/h, needle tip to drum: 7cm, voltage: 12 kV, translation off, rotation: 3000 RPM, time: ~14h, drum voltage: 0 V.

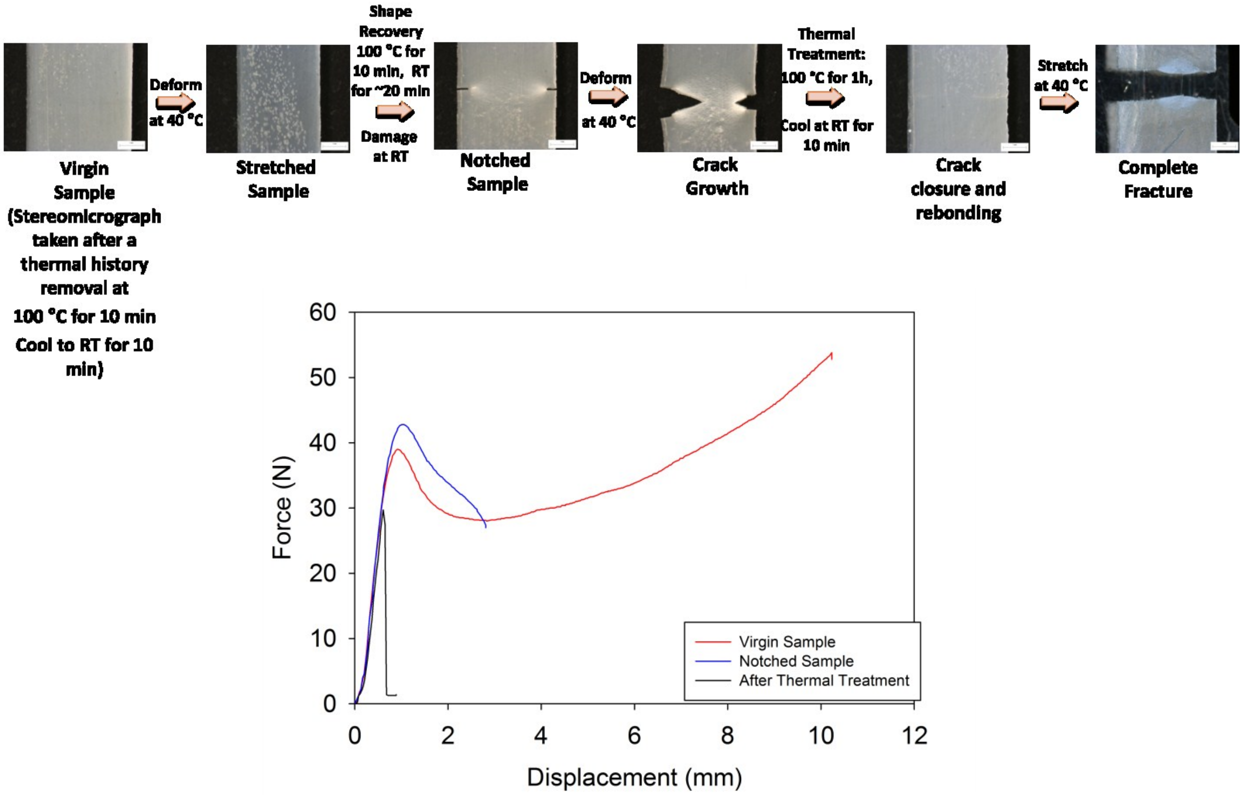

Figure A5.1.5. Force vs displacement graph used to evaluate the degree of healing for PCL (M_W~65k)/Epoxy composite. The Linkam tensile stage was used to perform the tensile testing where the following parameters were used: load cell: 200 N, stretch speed: 100 μm/sec and deformation temperature: 40 °C. A dogbone was punch from the composite sheet where the average thickness of the specimen was 0.79 mm. Red curve shows the deformation of the sample in its virgin state. Blue curve shows the deformation in the samples notched state and black curve in the sample's thermally treated state. Optical micrographs (OM) showing the sample at the respective states of the SH experiment. An important observation to point out is the higher yield point of the sample in it's damaged state when compared to its virgin state. This is owed to a longer cooling time which allowed the PCL chains to crystallize for a longer period of time. Although the sample was allowed to recrystallize there was no evidence of healing at the damaged site. An important observation to point out is the higher yield point of the sample in it's damaged state when compared to its virgin state. This is owed to a longer cooling time which allowed the PCL chains to crystallize for a longer period of time. Although the sample was allowed to recrystallize there was no evidence of healing at the damaged site.

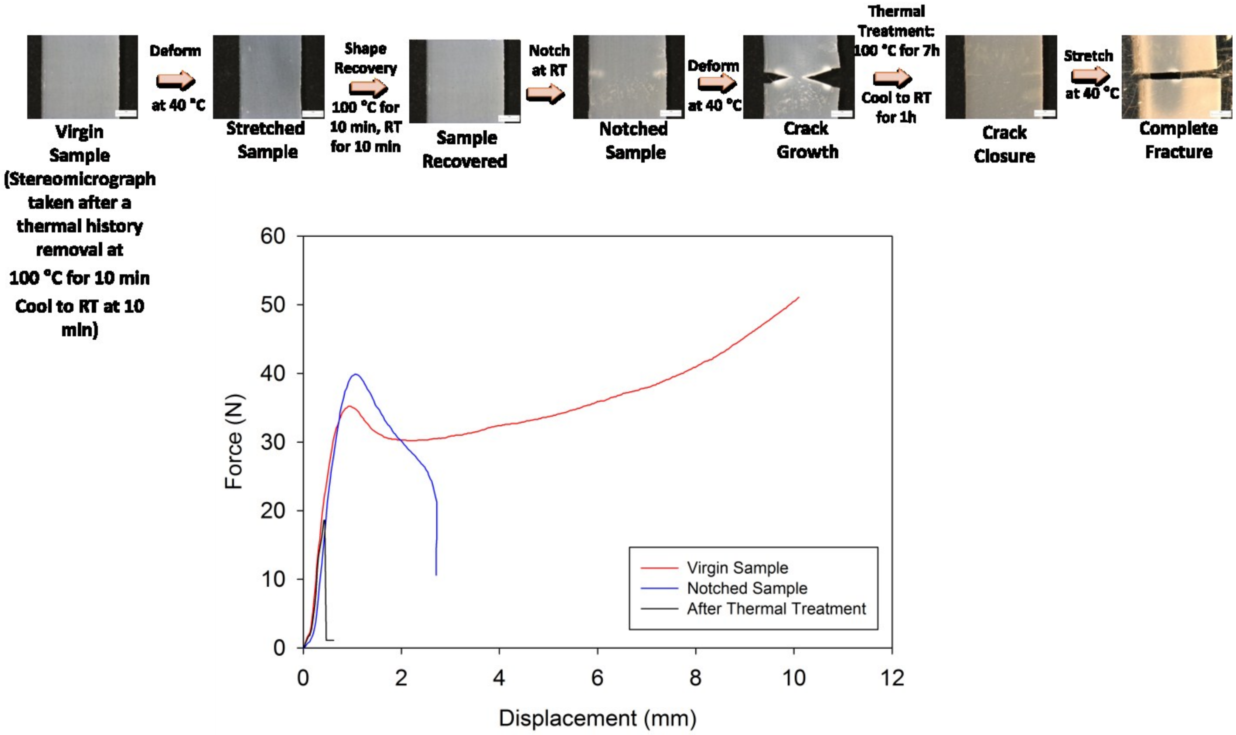

Figure A5.1.6. Force vs displacement graph used to evaluate the degree of healing for PCL (M_w~65k)/Epoxy composite. The Linkam tensile stage was used to perform the tensile testing where the following parameters were used: load cell: 200 N, stretch speed: 100 µm/sec and deformation temperature: 40 °C. A dogbone was punch from the composite sheet where the average thickness of the specimen was 0.66 mm. Red curve shows the deformation of the sample in its virgin state. Blue curve shows the deformation in the samples notched state and black curve in the sample's thermally treated state. Optical micrographs (OM) showing the sample at the respective states of the SH experiment.

APPENDIX 6.0

POLY(BUTYL METHACRYLATE) (PBMA):POLY(METHYL METHACRYLATE) (PMMA) SMASH T_g BASED COATING

A6.1 INTRODUCTION

Until now there has not been a shape memory (SM) and self healing (SH) coating that is a polymeric system that can recover elastic and plastic deformation while rebonding cracks. Specifications required to achieve such demand is a system that is transparent, has low viscosity, does not crystallize, is curable, has surface SM, and has a healing agent incorporated in the system. Some potential crosslinking monomers are styrene, tert (butyl acrylate), butyl acrylate, and methyl acrylate. We chose a co-polymer network system where tuning the T_g was achievable by varying the two monomer components. Additionally, we also included a healing agent that was a copolymer of the same T_g and also made from the two monomers as the SM network, but linear in the polymer chain architecture.

The glass transition (T_g) based SMASH system incorporates the use of amorphous polymers that exhibit the SMASH effect for transparent scratch repair coatings for industrial applications. This system is a class I polymeric system that is a covalently crosslinked glass thermoset[1]. These shape memory polymer (SMP) networks are known to be the simplest SMP type that exhibit a very sharp T_g and have great SM effects[1]. The SM effect is owed to the covalent crosslinks that prevent molecular slippage between chains due to strong chemical crosslinks. This system includes the use of an amorphous linear and crosslinked poly(butyl methacrylate) and poly(*methyl methacrylate)* (l-PBMA/PMMA:n-PBMA/PMMA) copolymer semi interpenetrating polymer network (SIPN) system. Here a l-PBMA/PMMA (60wt-%/40wt-%) co-thermoplastic was free radically polymerized by thermal initiation with a target molecular weight (M_w) of 40k g/mol and 53k g/mol to serve as the SH agent. As a starting point, we wanted to achieve a T_g of 50 °C. To attain this, the Flory Fox equation (Scheme A6.1.1) was used to calculate the required wt-% from each of the mononers used to fabricate the system. This equation used the T_g's of the individual monomers to acquire the desired wt-% of each. Since the T_g of BMA is 20 °C and the T_g of MMA is 105 °C, 60wt-% of BMA and 40wt-% of MMA were used to achieve a target T_g of 50 °C. A PBMA/PMMA SM network (n-PBMA/PMMA) was polymerized in the presence of l-PBMA/PMMA SH co-thermoplastic. Thermal, thermomechanical, and shape memory characterization were conducted on SMASH films to measure the SM effect of the systems. Scratch testing was then conducted on SMASH coatings to analyze and study the self healing efficiency. The weight content of the SH agent and the SM network was varied to optimize the SMASH effect.

A6.1.2 SAMPLE PREPARATION AND CHARACTERIZATION

l-PBMA/PMMA:n-PBMA/PMMA copolymer SMASH systems were made by photopolymerizing butyl methacrylate (BMA) and *methyl methacrylate* (MMA) monomers using tetraethyleneglycol dimethacrylate (TEGDMA) and 2,2-dimethoxy-2-phenylacetophenone (DMPA) as the crosslinker and photoinitiator, respectively, to form the SM amorphous network. The PBMA/PMMA co-thermoplastic (l-PBMA/PMMA) was mixed in the solution prior to photopolymerization. It is important to note that l-PBMA/PMMA was interpenetrating, not covalently bonded in the network to allow SH chains to diffuse to the site of damage. The l-PBMA/PMMA was made by thermal-initiated free radical polymerization where NMR analysis showed the feed weight and actual weight percentage of each monomer used were comparable

(Figure A6.1.2). Scheme A6.1.1 and Scheme A6.1.2 shows the chemical structures and sample preparation of the monomers and polymers used to make the SMASH system. The weight percentages (wt-%) of the SH agent and the SM network were varied to optimize the SM and SH effect. The following samples were prepared (l-PBMA/PMMA$_{wt\text{-}\%}$:n-PBMA/PMMA$_{wt\text{-}\%}$): l-PBMA/PMMA$_{0}$:n-PBMA/PMMA$_{100}$, l-PBMA/PMMA$_{10}$:n-PBMA/PMMA$_{90}$, and l-PBMA/PMMA$_{20}$:n-PBMA/PMMA$_{80}$. Gel Permeation Chromatography (GPC) was conducted in order to obtain the average molecular weight (M_w), number average molecular weight (M_n), dn/dc values, and the polydispersity index (PDI) values of the two co-thermoplastics synthesized. Figure A6.1.1 shows the corresponding curves and charts where one thermoplastic yielded a M_w of 40k g/mol and the other 53k g/mol. These two thermoplastics were used to make the SMASH systems for comparison of properties. Gel fractions (G) were then conducted and calculated to measure the weight percentage of the network formation after photopolymerization. Figure A6.1.3 shows a linear relationship where G decreases as the l-PBMA/PMMA co-thermoplastic wt-% increases for both the 40k g/mol and 53k g/mol thermoplastics used.

A6.1.3. THERMAL CHARACTERIZATION

Thermogravimetric analysis (TGA) was conducted in order to measure the onset degradation temperature. Figure A6.1.4 shows the corresponding graphs and charts. Differential scanning calorimetry (DSC) was used to measure the glass transition (T_g), which is the onset of long range coordinated chain molecular motion, of all samples tested. The samples were heated at 10 °C/min to 150.00 °C. The endothermic peak of all samples tested, shown in Figure A6.1.5, ranged from 40 to 60 °C range showing the l-PBMA/PMMA co-thermoplastic as a reference.

The T_g will assist in observing at which point the system will transition from a glass to a rubber state.

A6.1.4. THERMOMECHANICAL CHARACTERIZATION

DMA analysis was conducted on all samples to observe how the tensile storage modulus (E') changed as a function temperature. The samples were equilibrated at -50 °C, held at this temperature for 5 min, and then ramped to a temperature of 200 °C at to 3 °C/min. It is evident in Figure A6.1.6 that the onset of the T_g starts at ~50 °C where E' is ~1000 MPa. This is followed by the rubbery plateau where the polymeric chains in the system are in a rubber elasticity state where E' was ~1 MPa. Again, it is important to observe that the rubbery plateau is indicative of the crosslinks that construct the SM network and prevent polymer flow. This is evident among all compositions tested.

A6.1.5. SCRATCH TESTING

Once the thermomechanical properties were obtained, scratch testing was conducted to see if scratches induced on the SMASH coating could heal under a thermal stimulus (Scheme A6.1.3). First, an 80 μm coating was photopolymerized on a glass substrate for 1 h. Damage was induced by scratching the surface of the coating with a razor blade using a square set to assist in a linear damage. Locally, it is hypothesized that the polymer chains align in the direction of the scratch. Once damaged, the sample was placed in an isothermal oven at 150 °C for 10 min. At this temperature two effects occurred. The SM effect was initiated by allowing the crack surfaces to make complete contact with each other. This effect owes to the crosslinks in the SM network, which memorizes its permanent (undamaged state) and wants to return to its highly entropic state after damaged. Without material removal during damage, the SM n-PBMA/PMMA should allow crack closure where the crack surfaces meet and the l-PBMA/PMMA SH thermoplastic chains are free to molecularly diffuse to the damage site for crack healing.

Quantification of SH was done by analyzing optical microscopy (OP) images using ImageJ and Vision Assistant software (Scheme A6.1.4 and Scheme A6.1.5). Figure A6.1.7 to Figure A6.1.12 shows OP images of damaged and thermally treated samples for all compositions tested. Each OM image was converted to an 8-bit image and then imported into Vision Assistant where the damaged and healed areas in pixels were isolated and used to study the degree of healing. The following equation was used to quantify the SH efficiency:

$$SH_{Efficiency}(\%) = \frac{A_{ss} - A_{TTS}}{A_{ss}} x100\% \qquad \text{(A6-1)}$$

where A_{SS} is the scratched area (pixels) and A_{TTS} is the thermally treated area (pixels). SH efficiency was then plotted as a function of SH agent for all compositions tested. Figure A6.1.13 to Figure A6.1.14 shows the SH efficiency ranged from 30 - 70 % among all the samples. This SH range is quite low and leads to the conclusion that there may have been some material removal during the deformation and scratching process.

SEM images were then taken for all the samples in the scratched and thermally treated state. It is clear in Figure A6.1.15 to Figure A6.1.20 that complete crack closure and complete healing was not achieved. This further supports the notion that material may have been removed during the scratching process. The SEM images also reveal that the normal force applied to form the scratch was variable as the degree of damage was not uniform between samples. Another observation revealed in the SEM images is the smoothness of the coating surface after thermal treatment, suggesting that the treatment assisted in removing any blemishing on the coating surface.

A6.1.6. CONCLUSIONS

An amorphous l-PBMA/PMMA:n-PBMA/PMMA transparent copolymer SMASH system was fabricated where the thermal, thermomechanical, and SH characterization was quantified using two thermoplastics with two different M_w's of 40k g/mol and 53 g/mol. DSC reveals that the T_g was approximately in the 50 °C range while the DMA data showed a decrease in E' (from 10^2 to 1MPa) as the temperature increased. SH tests showed that only partial crack closure and healing was achieved. Material removal during damage may explain the low values of SH efficiency.

A6.1.7. REFERENCES

1. Liu, C.; Qin, H.; Mather, P. T. *Journal of Materials Chemistry* **2007,** 17, (16), 1543-1558.

A6.1.8 FIGURES

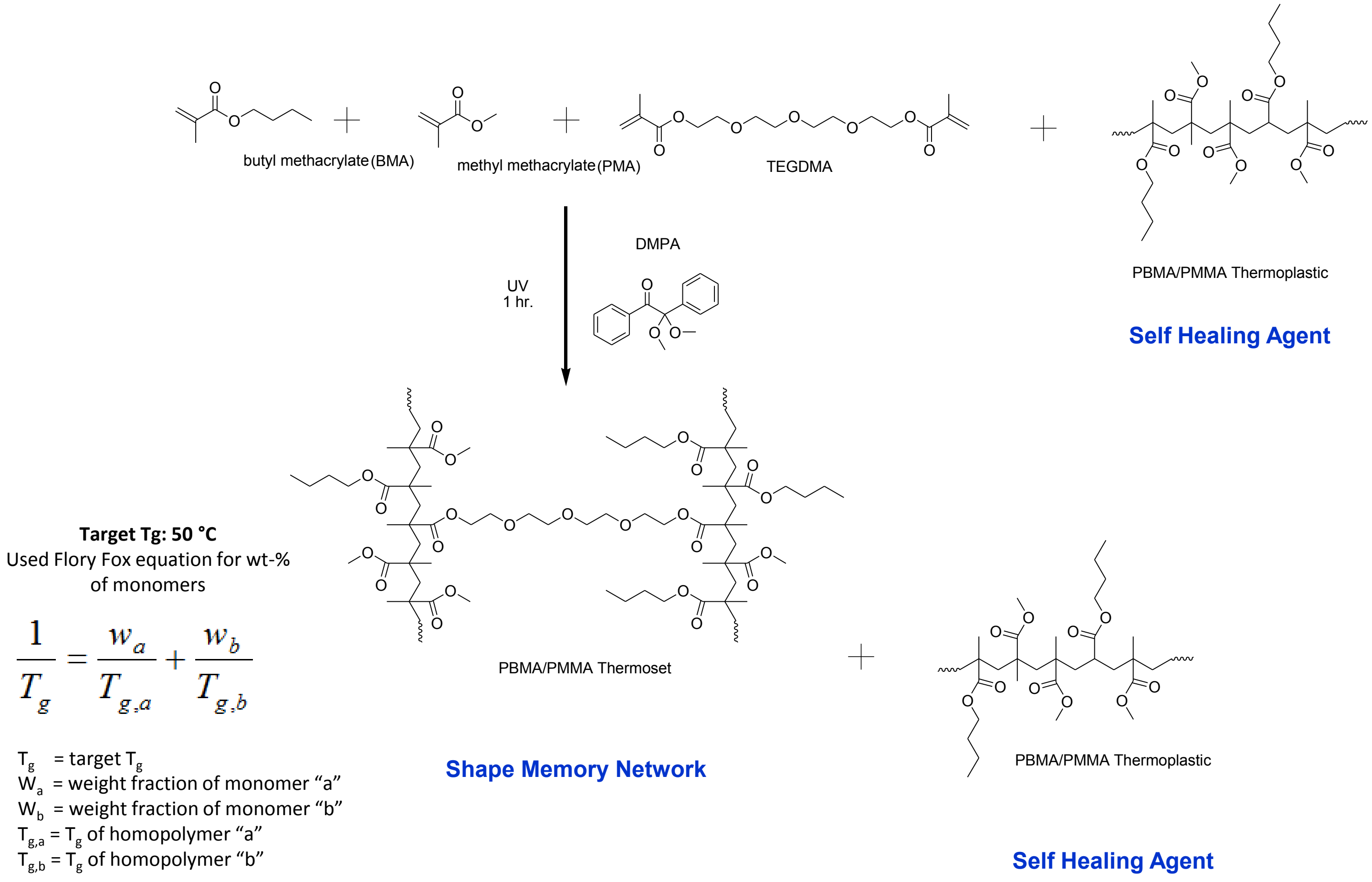

Target Tg: 50 °C
Used Flory Fox equation for wt-% of monomers

$$\frac{1}{T_g} = \frac{w_a}{T_{g,a}} + \frac{w_b}{T_{g,b}}$$

T_g = target T_g
W_a = weight fraction of monomer “a”
W_b = weight fraction of monomer “b”
$T_{g,a}$ = T_g of homopolymer “a”
$T_{g,b}$ = T_g of homopolymer “b”

Scheme A6.1.1. Schematic showing the chemical structures used to form the T_g based SMASH systems.

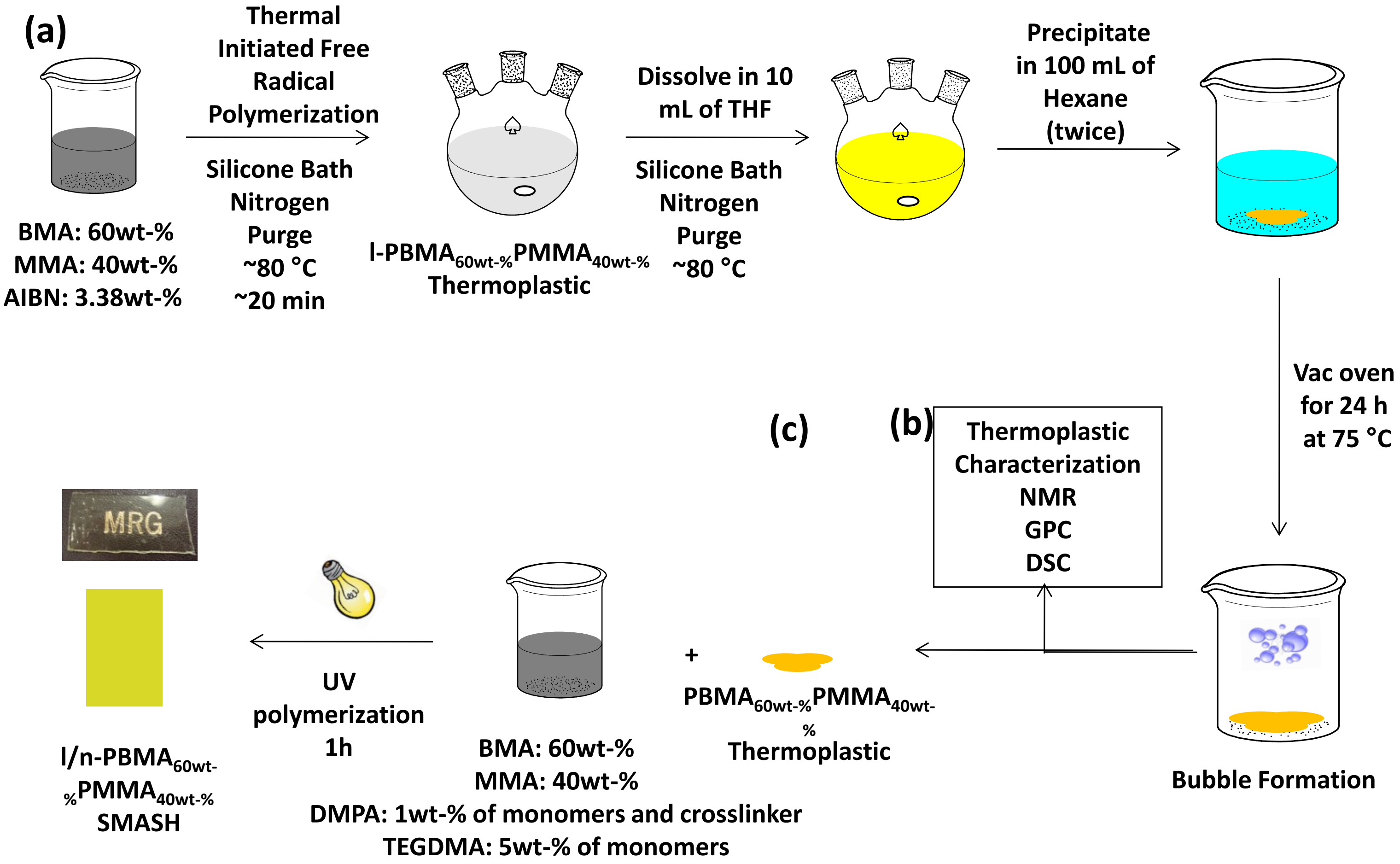

Scheme A6.1.2. Sample preparation of (a) poly(butyl methacrylate) (PBMA):poly(methyl methacrylate) (PMMA) thermoplastic (l-PBMA:PMMA) free radical polymerization process, (b) thermoplastic characterization process, (c) and polymerization of l:n-PBMA:PMMA SMASH films.

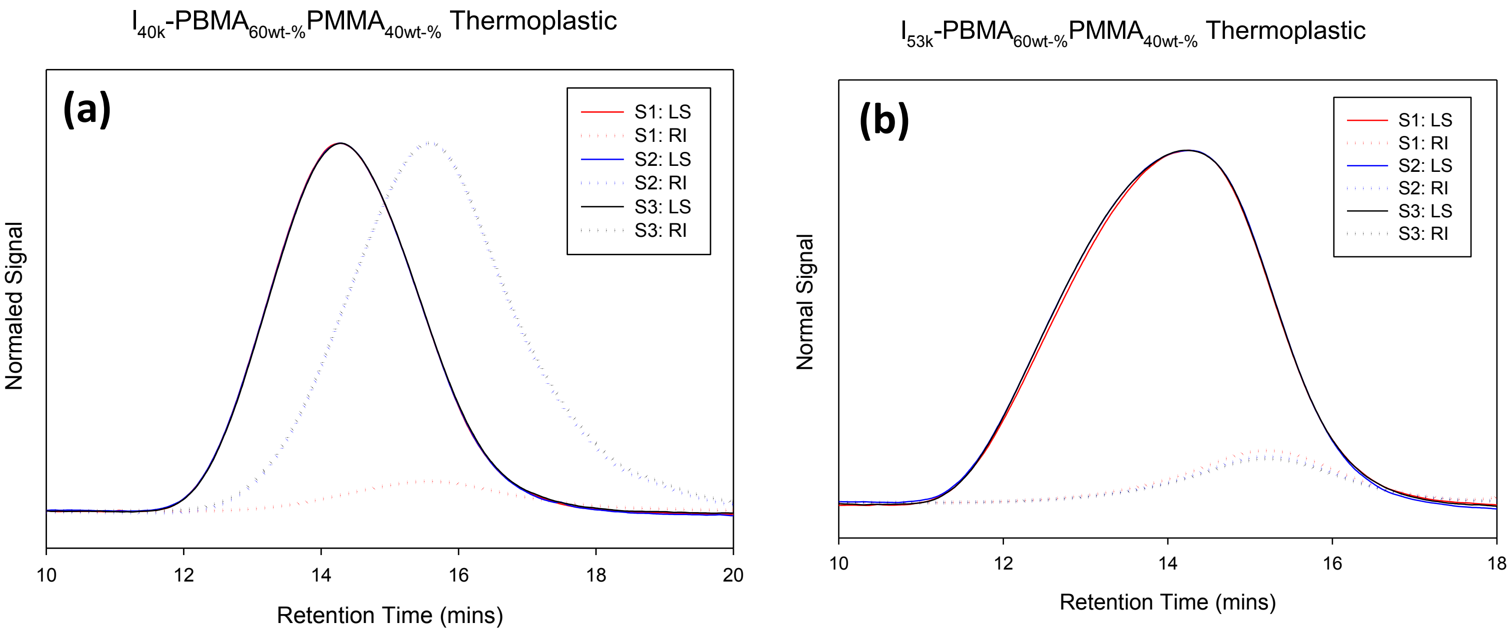

Sample	M_n	M_w	dn/dc	PDI
1	1.26E+04	4.13E+04	0.069	3.28
2	1.41E+04	3.94E+04	0.075	2.80
3	1.54E+04	3.88E+04	0.077	2.51
Average	1.40E+04	3.98E+04	0.074	2.86

Sample	M_n	M_w	dn/dc	PDI
1	2.32E+04	4.58E+04	0.072	1.98
2	2.69E+04	5.56E+04	0.060	2.07
3	2.51E+04	5.75E+04	0.056	2.29
Average	2.51E+04	5.30E+04	0.063	2.11

Figure A6.1.1. Gel Permeation Chromatography (GPC) of the poly(butyl methacrylate) (PBMA):poly(methyl methacrylate) (PMMA) thermoplastic (l-PBMA:PMMA) with an average molecular weight (M_w) of 40k and 53k g/mol made from two polymerization batches. Three solutions of 5 mg/ 1 mL THF were prepared to obtain the average molecular weight (M_w), number average molecular weight (M_n), dn/dc values, and the polydispersity index (PDI) values.

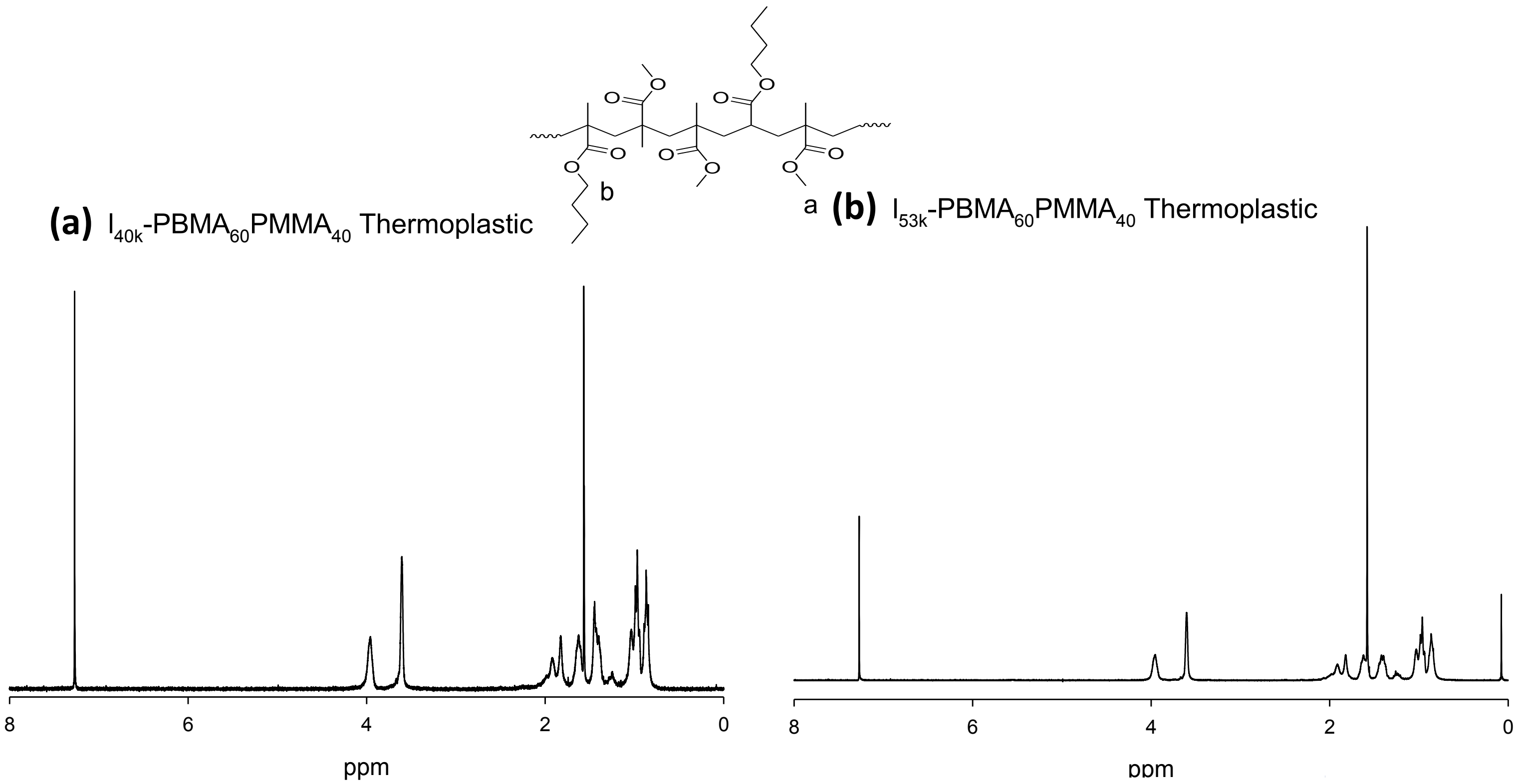

l_{40k}-PBMA$_{60}$PMMA$_{40}$ Thermoplastic

Ratio	BMA	MMA
Feed Weight (%)	60	40
Actual Mol	52.1	47.9
Actual Weight (%)	60.7	39.3

l_{53k}-PBMA$_{60}$PMMA$_{40}$ Thermoplastic

Ratio	BMA	MMA
Feed Weight (%)	60	40
Actual Mol	51.7	48.3
Actual Weight (%)	60.3	39.7

Figure A6.1.2. Nuclear magnetic resonance (NMR) spectrum of poly(butyl methacrylate) (PBMA):poly(methyl methacrylate) (PMMA) thermoplastic (l-PBMA:PMMA). Corresponding charts show the feed weight (%), actual mol, and actual weight (%) values of the experimental to actual values. Chemical structure of l-PBMA:PMMA is also shown identifying the proton resonances. Data collected with the assistance of Dr. Kazuki Ishida. (Reference: Guodong Liu et al., Studies on Binary Copolymerization and Glass Transition Temperatures of Methyl Methacrylate with Ethyl Methacrylate and n-Butyl Methacrylate, Journal of Applied Polymer Science, 2009, 114, 3939–3944.)

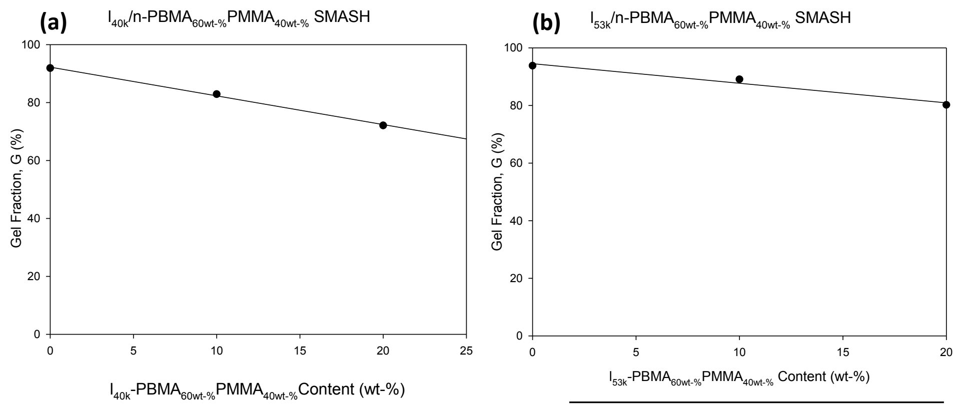

Composition	W_i (mg)	W_d (mg)	GF %
(0:100)	13.6	12.5	91.9
(10:90)	26.9	22.3	82.9
(20:80)	19.0	13.7	72.1

Composition	W_i (mg)	W_d (mg)	GF %
(0:100)	14.5	13.6	93.8
(10:90)	11.9	10.6	89.1
(20:80)	10.1	8.1	80.2

Figure A6.1.3. Degree of shape memory network formation was determined by gel fraction experiments where a specimen from each SMASH film mentioned above were cut and weighted before and after extraction and dried in the vacuum oven over night. (a) Shows a graph of gel fraction as a function of poly(butyl methacrylate) (PBMA):poly(methyl methacrylate) (PMMA) thermoplastic (l-PBMA:PMMA) with a M_w of 40k g/mol. The gel fraction process included submerging a specimen in 10 mL of THF. Solution was then placed in a shaker for 24 hr at 37 °C an then dried in a vac oven at 55 °C over night for THF solvent removal. (b) Shows a graph of gel fraction as a function of poly(butyl methacrylate) (PBMA):poly(methyl methacrylate) (PMMA) thermoplastic (l-PBMA:PMMA) with a M_w of 53k g/mol. The gel fraction process included submerging a specimen in 10 mL of THF and placed solution in a shaker for 48 hr at 37 °C. The solution was then placed in a vac oven at 55 °C over night for THF solvent removal. Line in graph represents the linear regression of the data where the gel fraction decreases with increasing l-PBMA:PMMA wt-% content. The charts correspond to the gel fractions calculated for each thermoplastic used as a function of composition tested.

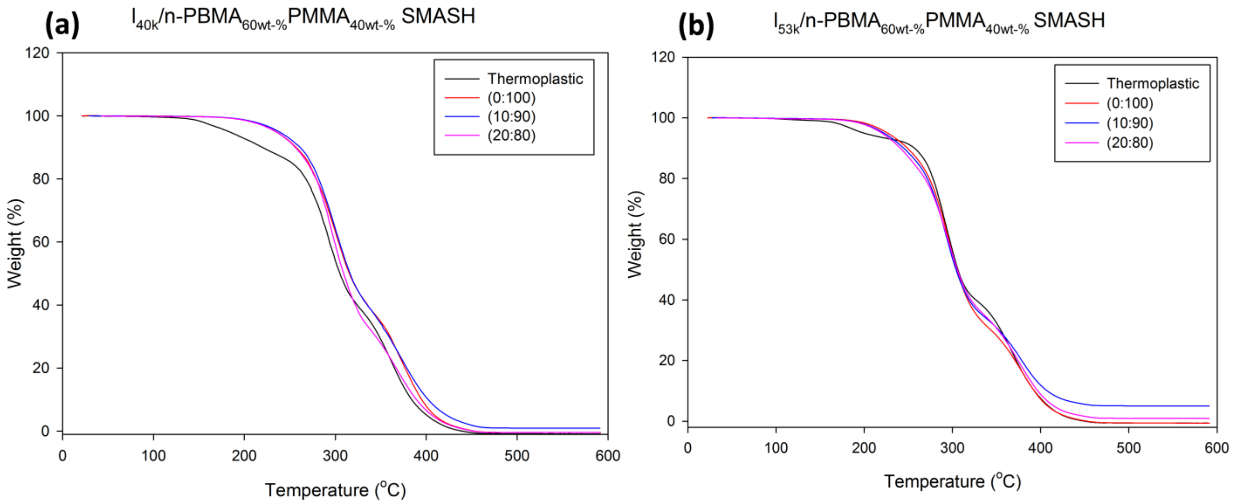

Sample	Onset Temperature (°C)
Thermoplastic	251
(0:100)	261
(10:90)	262
(20:80)	265

Sample	Onset Temperature (°C)
Thermoplastic	264
(0:100)	261
(10:90)	257
(20:80)	251

Figure A6.1.4. To measure the onset degradation temperature of all the SMASH films, thermogravimetric analysis (TGA) was conducted. (a) Shows a graph of weight % loss as a function of temperature for films that contained l-PBMA:PMMA with a M_w of 40k g/mol. (b) Shows data for SMASH films using l-PBMA:PMMA with a M_w of 53k g/mol. All onset degradations temperature were approximately 260 °C. The l-PBMA:PMMA was also tested for comparison among the SMASH films. TGA method was 600 ° C at 10 ° C/min. The charts correspond to the onset degradation temperatures as a function of composition tested.

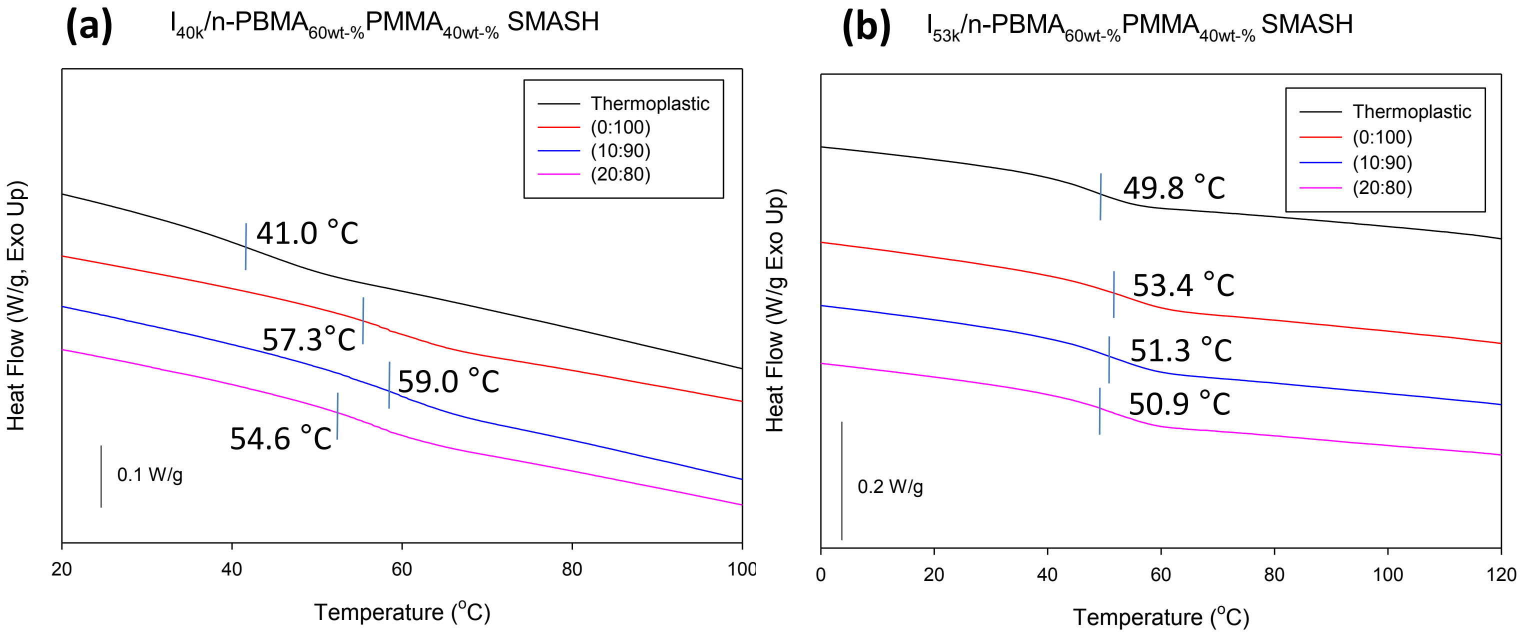

Figure A6.1.5. To measure the glass transition temperature (T_g) of all the SMASH films, differential scanning calorimetry (DSC) was used. (a) Shows a graph of heat flow vs temperature for SMASH films using l-PBMA:PMMA with a M_w of 40k g/mol. (b) Shows the heat flow vs temperature for SMASH films using l-PBMA:PMMA with a M_w of 53k g/mol. The l-PBMA:PMMA was also tested for comparison among the SMASH films. The T_g values ranged from 40 °C to 60 °C among all specimens tested. DSC method was 10 °C/min to 150 °C for second heating trace.

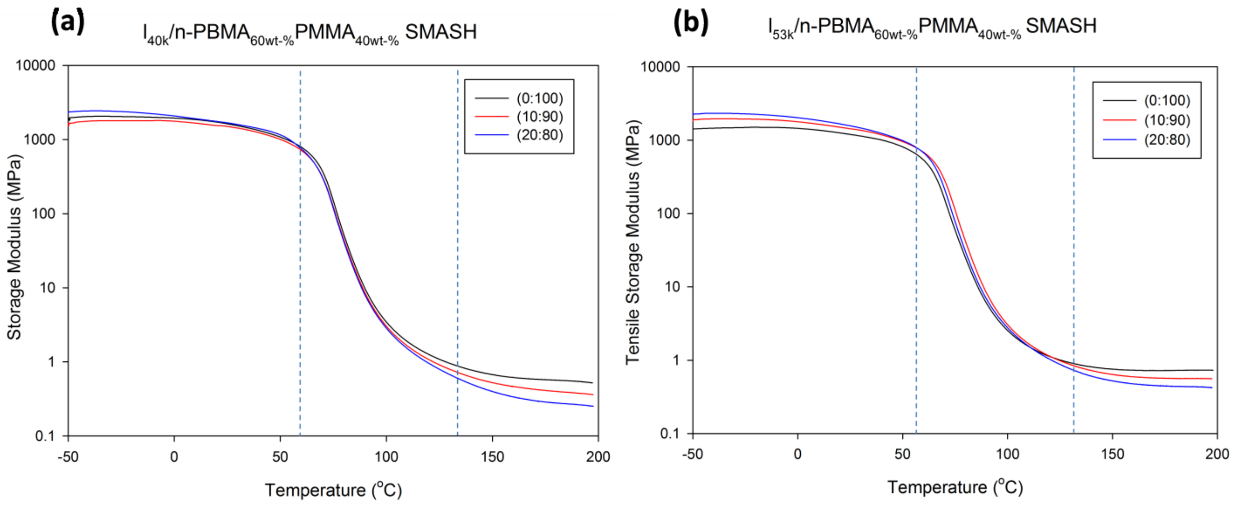

Figure A6.1.6. To measure and study the viscoelastic properties of the SMASH films, dynamic mechanical analysis (DMA) was used. (a) Shows a graph tensile storage modulus (E') vs temperature for SMASH films using l-PBMA:PMMA with a M_w of 40k g/mol. (b) Shows tensile storage modulus (E') vs temperature for SMASH films using l-PBMA:PMMA with a M_w of 53k g/mol. The T_g values ranged from 50 °C to 60 °C among all specimens tested. DMA method included equilibrating at -50 °C, isothermal for 5 min, ramp 3 °C/min to 200 °C. All curves exhibited a glass transition region followed by the rubber modulus plateau. The rubber plateau is inductive of the crosslinked density of the shape memory network in the rubber entropic state that is still prominent at a high temperature.

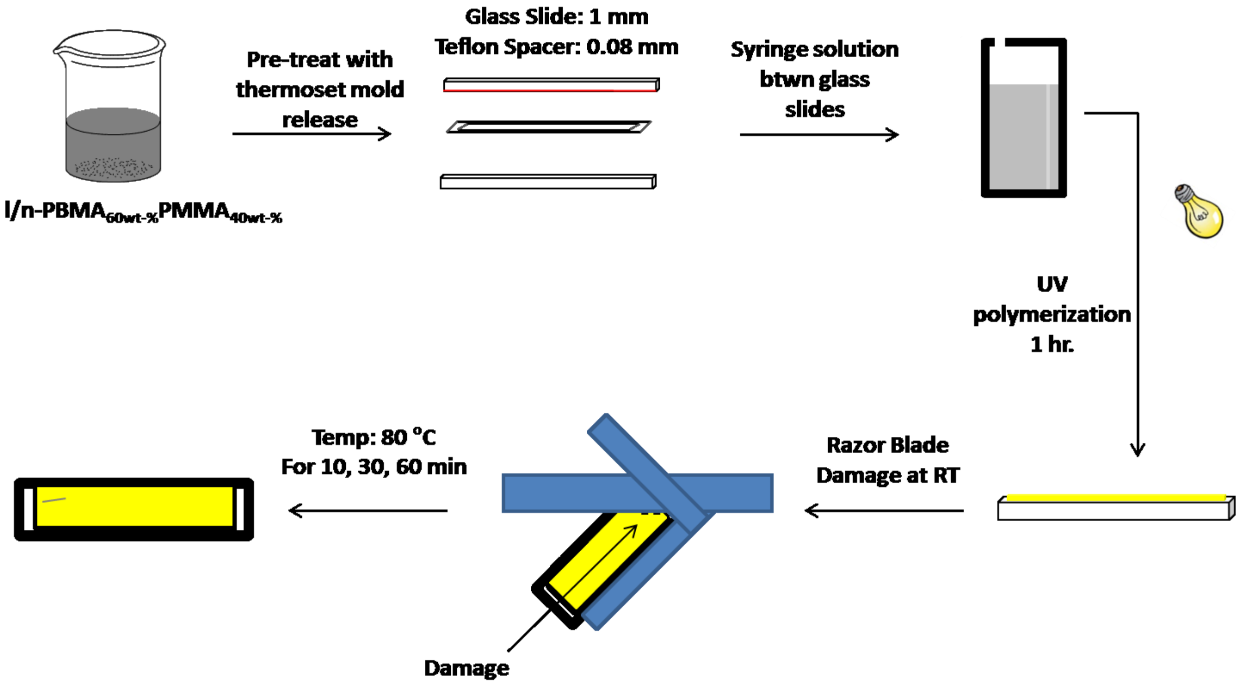

Scheme A6.1.3. Sample preparation and scratch testing of T_g based SMASH coating.

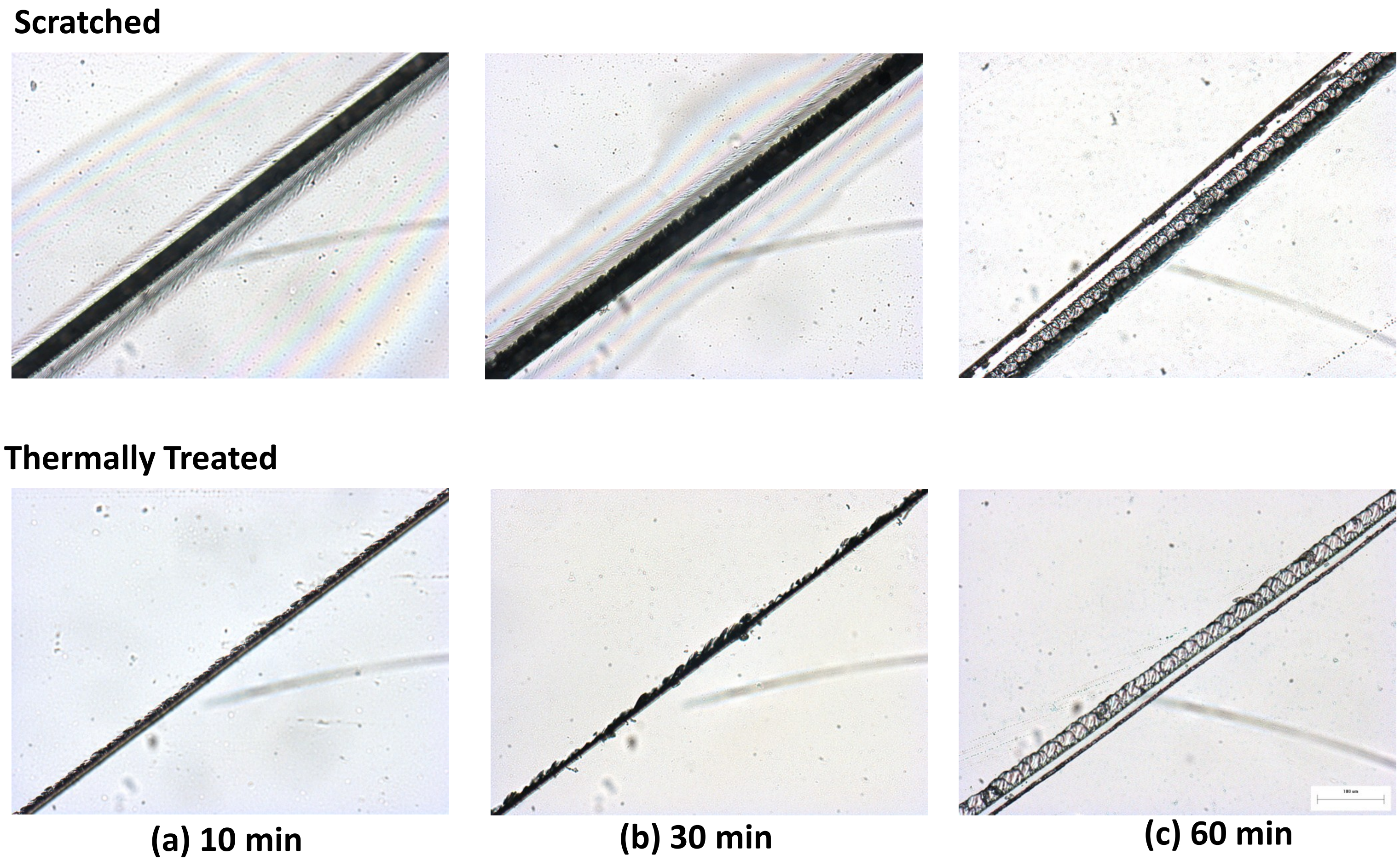

Figure A6.1.7. To measure the self healing (SH) efficiency of the SMASH coatings, optical microscopy (OM) micrographs of the coating in its scratched and thermally treated state were obtained. Three different thermal treatments were conducted to study the healing kinetics of the scratch. The healing times used were as follows: (a) 10 min, (b) 30 min, and (c) 60 min at 80 °C. A l_{40k}:n-$PBMA_{60wt\text{-}\%}PMMA_{40wt\text{-}\%}$ (0:100) SMASH coating was used for this study. Crack closure was evident among the thermally treated micrographs. This system was used as a control as the thermoplastic SH agent was not included in this system. (Scale bar: 100 μm)

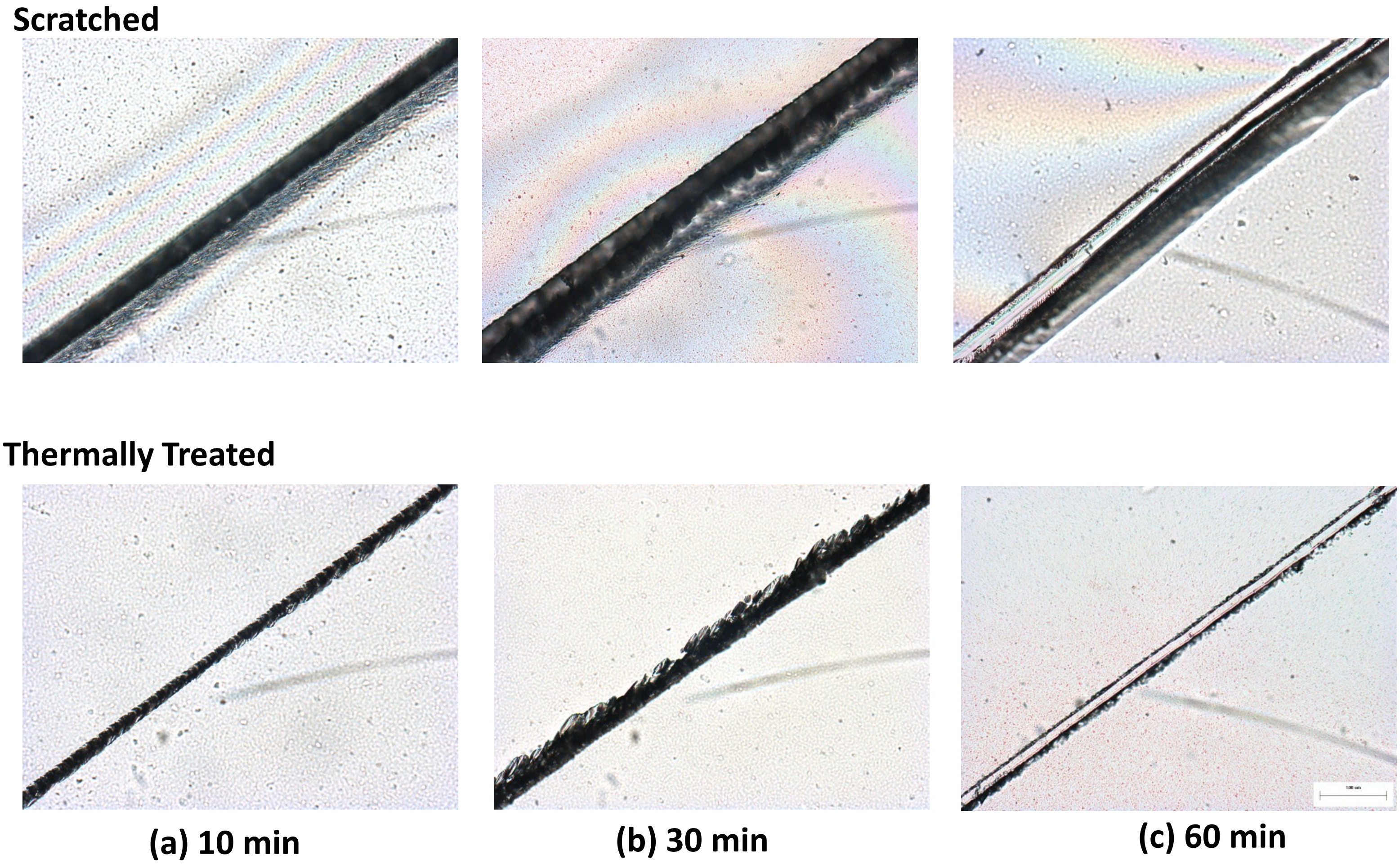

Figure A6.1.8. To measure the self healing (SH) efficiency of the SMASH coatings, optical microscopy (OM) micrographs of the coating in its scratched and thermally treated state were obtained. Three different thermal treatments were conducted to study the healing kinetics of the scratch. The healing times used were as follows: (a) 10 min, (b) 30 min, and (c) 60 min at 80 °C. A l_{40k}:n-PBMA$_{60wt\text{-}\%}$PMMA$_{40wt\text{-}\%}$ (10:90) SMASH coating was used for this study. Crack closure was evident among the thermally treated micrographs, but healing was not optimized as a scar was still visible. (Scale bar: 100 μm)

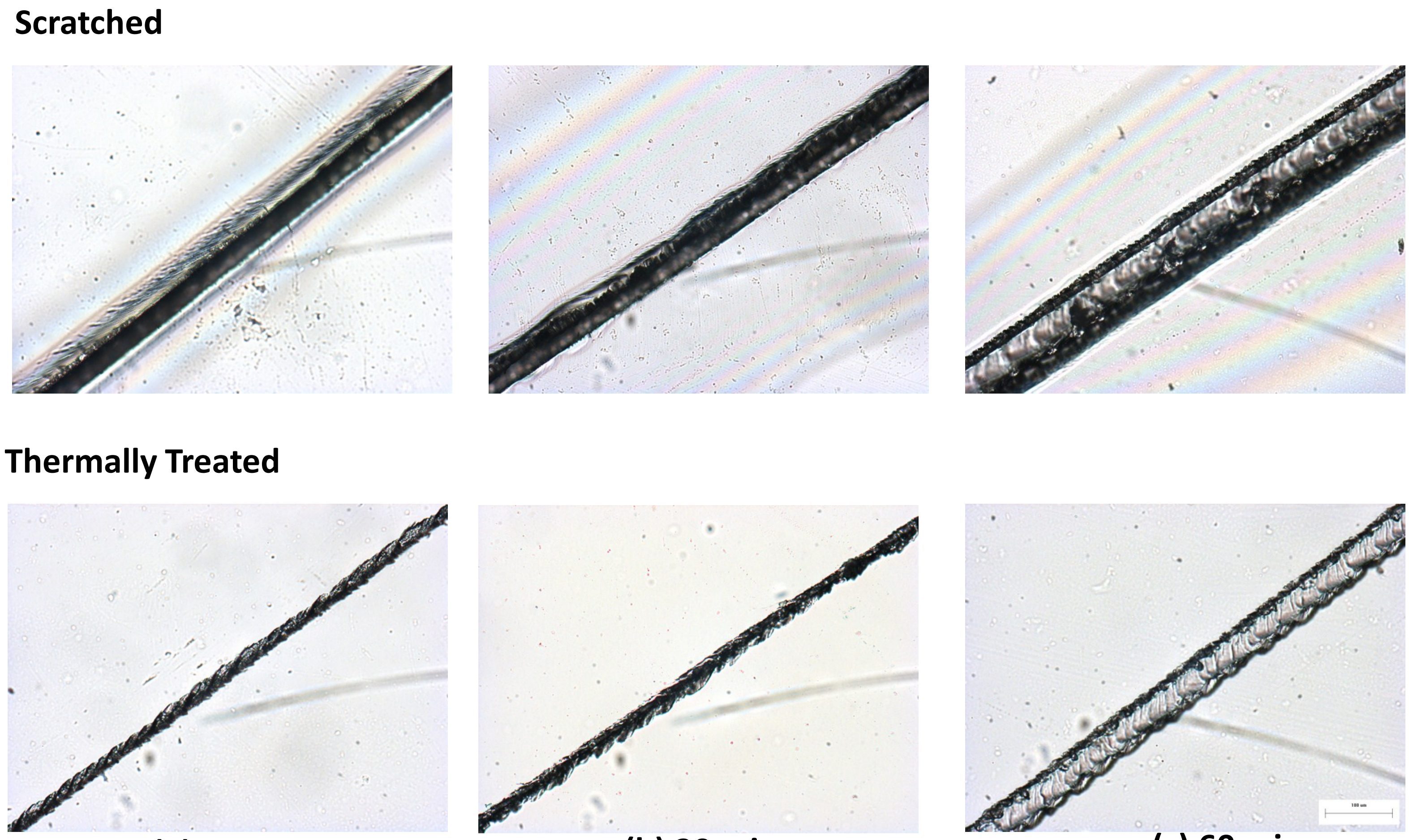

(a) 10 min (b) 30 min (c) 60 min

Figure A6.1.9. To measure the self healing (SH) efficiency of the SMASH coatings, optical microscopy (OM) micrographs of the coating in its scratched and thermally treated state were obtained. Three different thermal treatments were conducted to study the healing kinetics of the scratch. The healing times used were as followed: (a) 10 min, (b) 30 min, and (c) 60 min at 80 °C. A l_{40k}:n-$PBMA_{60wt\text{-}\%}PMMA_{40wt\text{-}\%}$ (20:80) SMASH coating was used for this study. Crack closure was evident among the thermally treated micrographs, but healing was not optimized as a scar was still visible. (Scale bar: 100 μm)

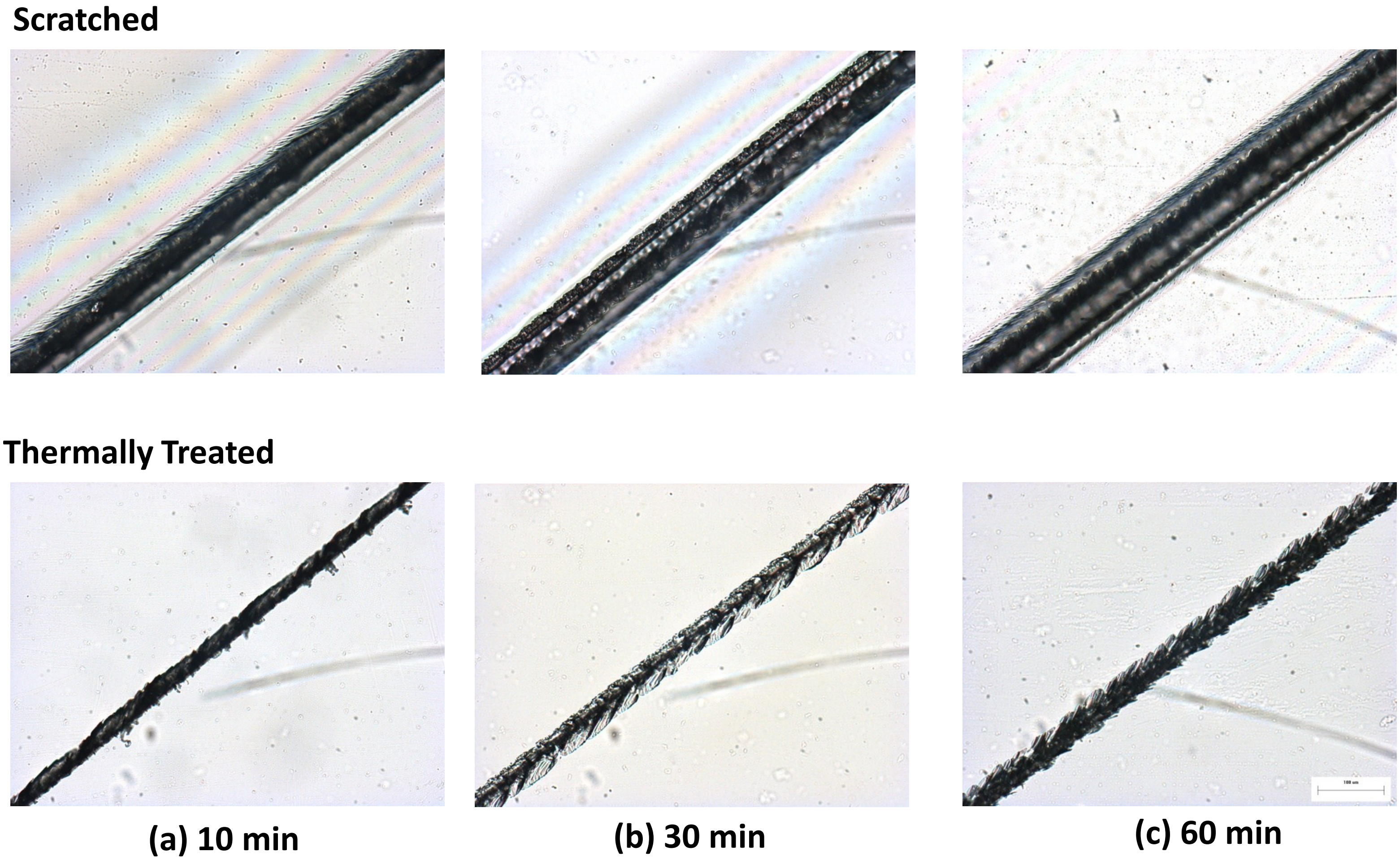

Figure A6.1.10. To measure the self healing (SH) efficiency of the SMASH coatings, optical microscopy (OM) micrographs of the coating in its scratched and thermally treated state were obtained. Three different thermal treatments were conducted to study the healing kinetics of the scratch. The healing times used were as followed: (a) 10 min, (b) 30 min, and (c) 60 min at 80 °C. A l_{53k}:n-$PBMA_{60wt\text{-}\%}PMMA_{40wt\text{-}\%}$ (0:100) SMASH coating was used for this study. Crack closure was evident among the thermally treated micrographs. This system was used as a control as the thermoplastic SH agent was not included in this system. (Scale bar: 100 µm)

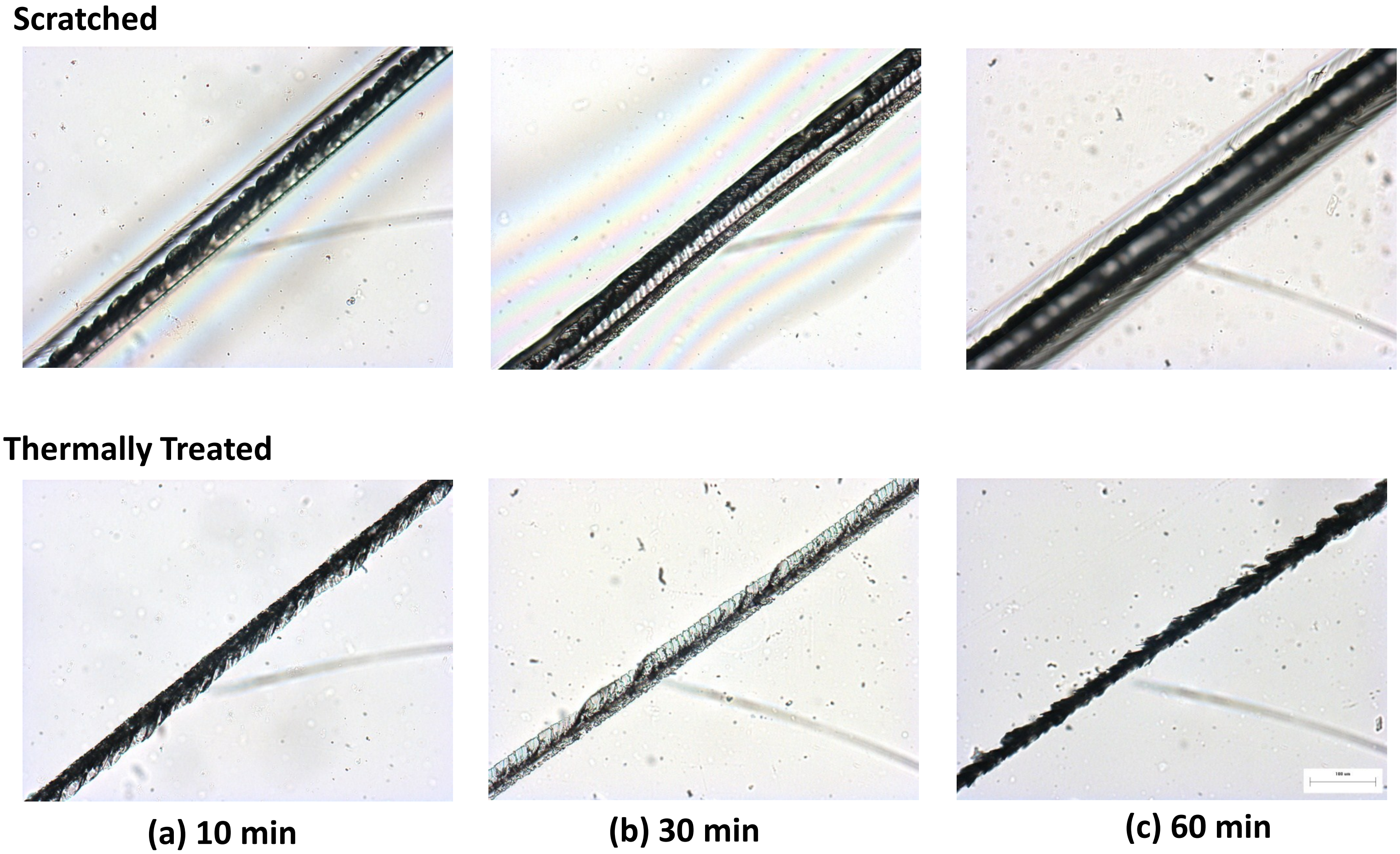

Figure A6.1.11. To measure the self healing (SH) efficiency of the SMASH coatings, optical microscopy (OM) micrographs of the coating in its scratched and thermally treated state were obtained. Three different thermal treatments were conducted to study the healing kinetics of the scratch. The healing times used were as followed: (a) 10 min, (b) 30 min, and (c) 60 min at 80 °C. A l_{53k}:n-PBMA$_{60wt\text{-}\%}$PMMA$_{40wt\text{-}\%}$ (10:90) SMASH coating was used for this study. Crack closure was evident among the thermally treated micrographs, but healing was not optimized as a scar was still visible. (Scale bar: 100 μm)

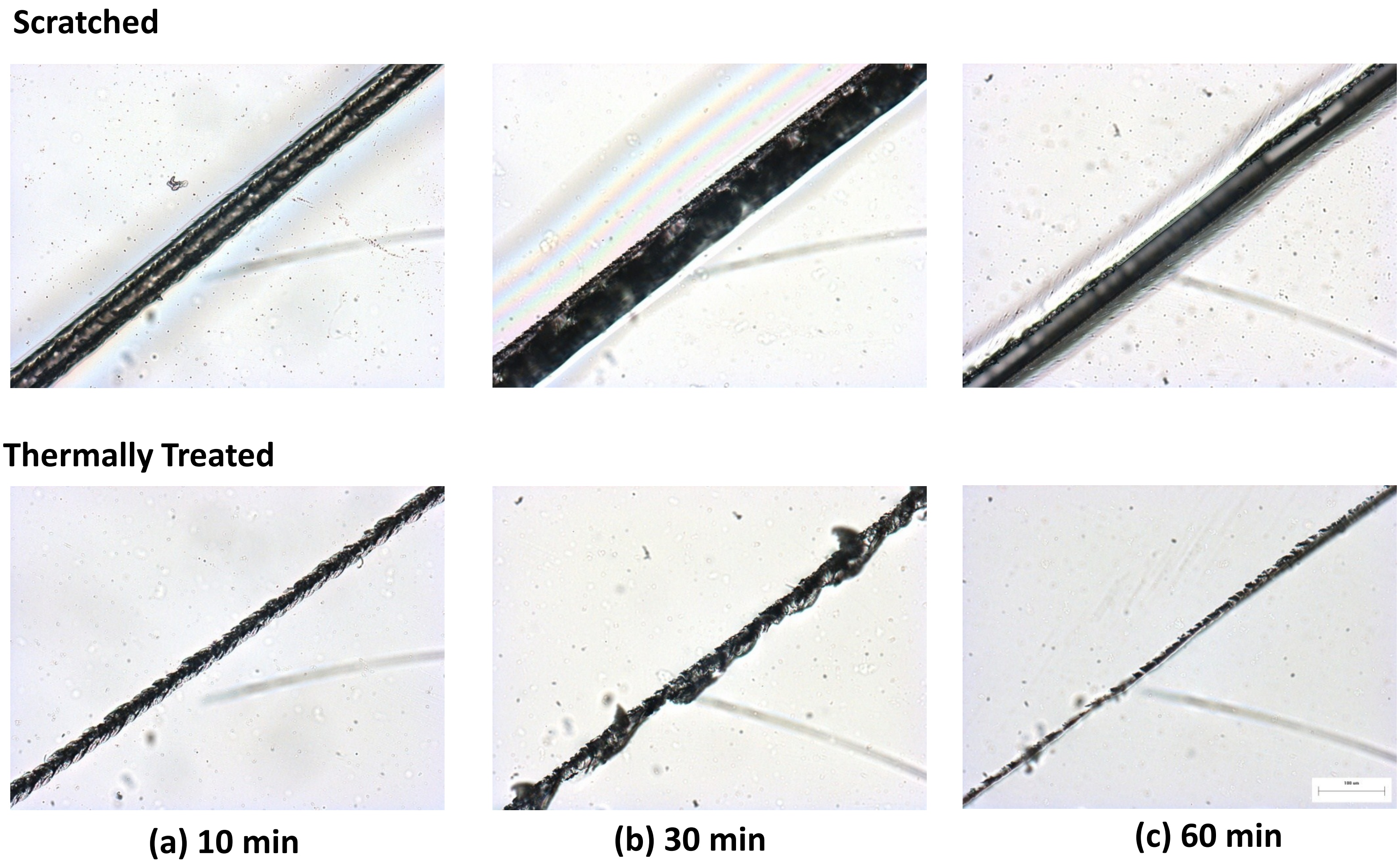

Figure A6.1.12. To measure the self healing (SH) efficiency of the SMASH coatings, optical microscopy (OM) micrographs of the coating in its scratched and thermally treated state were obtained. Three different thermal treatments were conducted to study the healing kinetics of the scratch. The healing times used were as followed: (a) 10 min, (b) 30 min, and (c) 60 min at 80 °C. A l_{53k}:n-PBMA$_{60wt\text{-}\%}$PMMA$_{40wt\text{-}\%}$ (20:80) SMASH coating was used for this study. Crack closure was evident among the thermally treated micrographs, but healing was not optimized as a scar was still visible. (Scale bar: 100 µm)

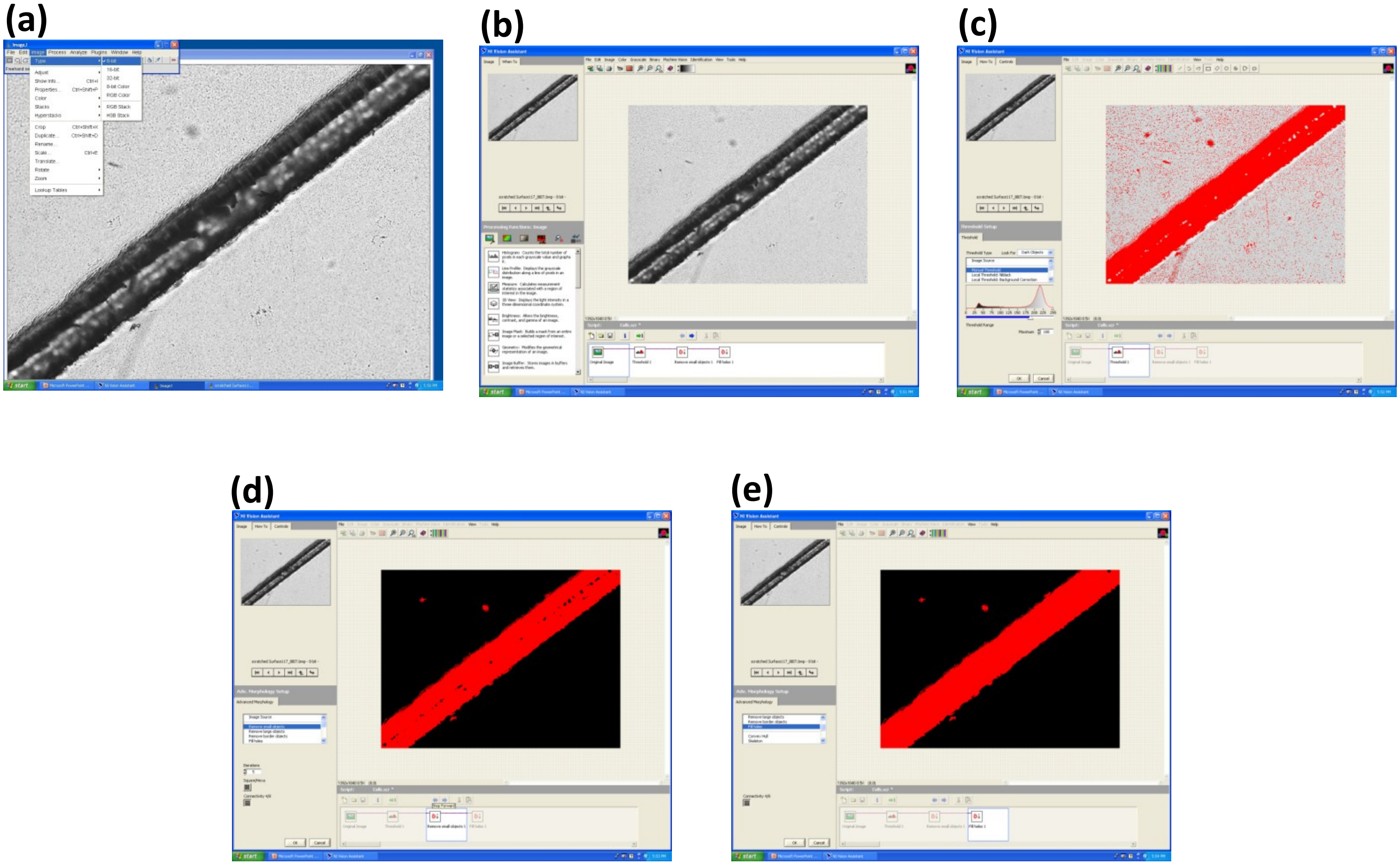

Scheme A6.1.4. Process of image analysis used for SH efficiency calculations. Image (a) of a damaged coating in ImageJ software to convert image to an 8-bit, (b) imported into Vision Assistant for image analysis, (c) performed a manual threshold (d) removed small objects, (e) filled in areas of the scratch in red.

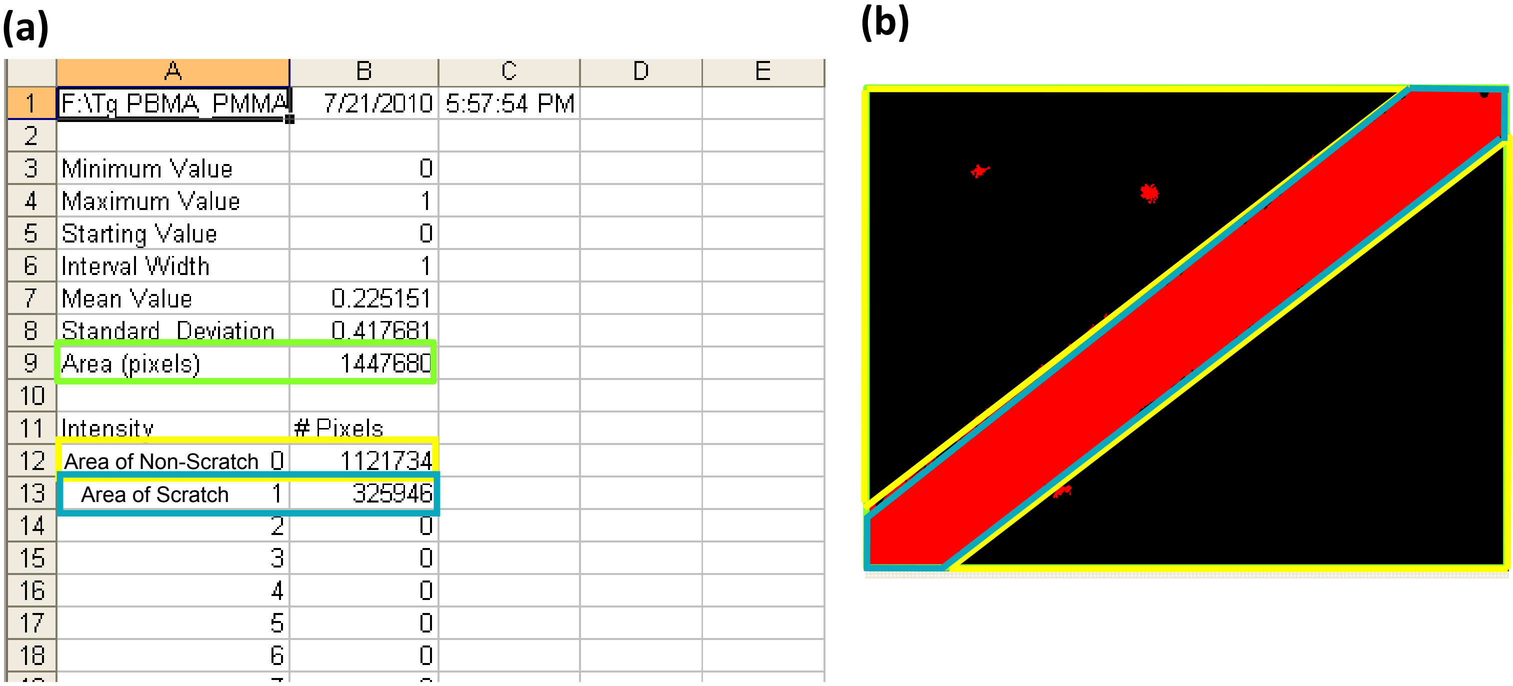

	A	B	C	D	E
1	F:\Tg PBMA_PMMA	7/21/2010	5:57:54 PM		
2					
3	Minimum Value	0			
4	Maximum Value	1			
5	Starting Value	0			
6	Interval Width	1			
7	Mean Value	0.225151			
8	Standard Deviation	0.417681			
9	Area (pixels)	1447680			
10					
11	Intensity	# Pixels			
12	Area of Non-Scratch 0	1121734			
13	Area of Scratch 1	325946			
14	2	0			
15	3	0			
16	4	0			
17	5	0			
18	6	0			

Scheme A6.1.5. Scratch test analysis output where (a) an excel file was generated showing the area in pixels of the non-scratch and scratch area of the image. The colored boxes are associated with the areas of the (b) scratched image.

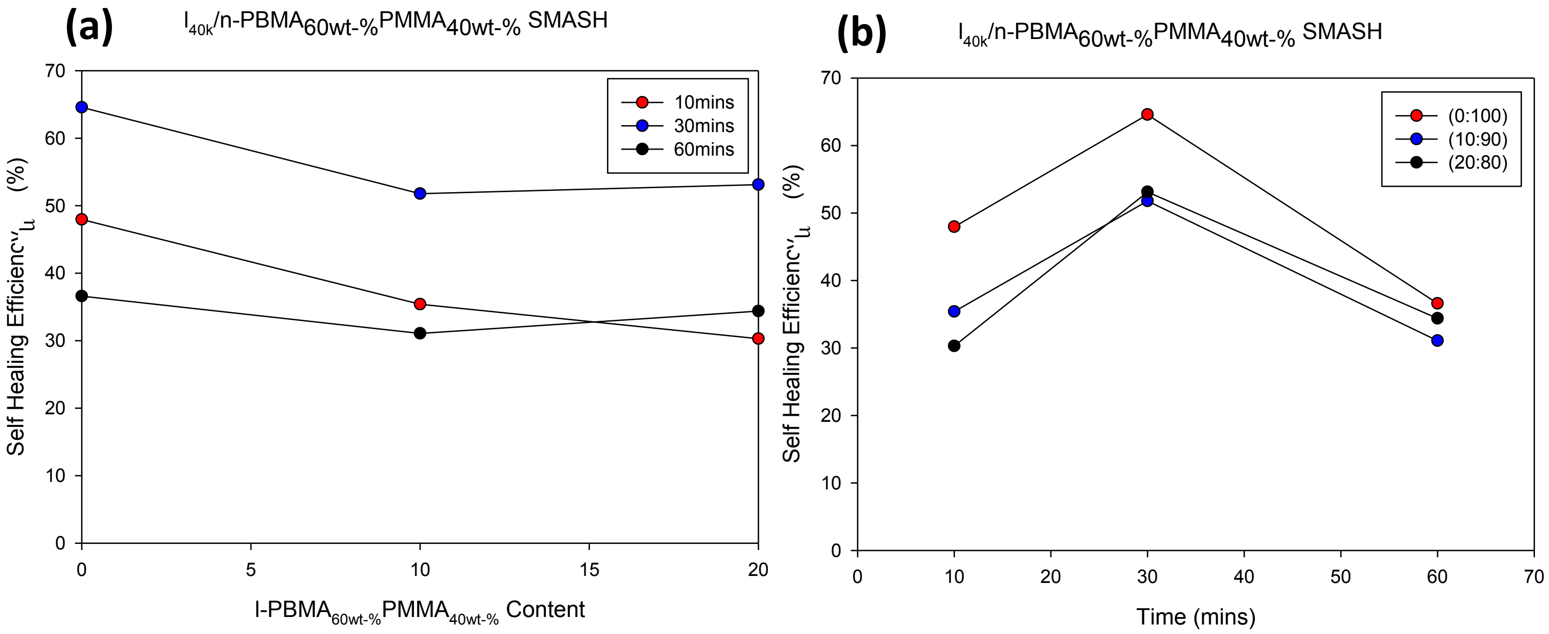

$$SH_{Efficiency}(\%) = \frac{SS - TTS}{SS} \bullet 100\%$$

where

SS = Scratched Surface

TTS = Thermally Treated Surface

Composition	Time (mins)	SS (Pixels)	TTS (Pixels)	Self Healing (%)
(0:100)	10	106408	55379	48.0
	30	140527	49785	64.6
	60	92667	58758	36.6
(10:90)	10	124488	80442	35.4
	30	309939	149492	51.8
	60	134929	93018	31.1
(20:80)	10	117746	82074	30.3
	30	193529	90747	53.1
	60	323175	212083	34.4

Figure A6.1.13. Graphs showing the self healing (SH) efficiency analysis for the SMASH coatings using l-PBMA:PMMA with a M_w of 40k g/mol where (a) shows the different thermal treatment times: 10 min, 30 min, and 60 min, and (b) the SMASH composition coatings tested: (0:100), (10:90) and (20:80). The figure also shows the SH efficiency equation used to calculate the SH values shown in chart.

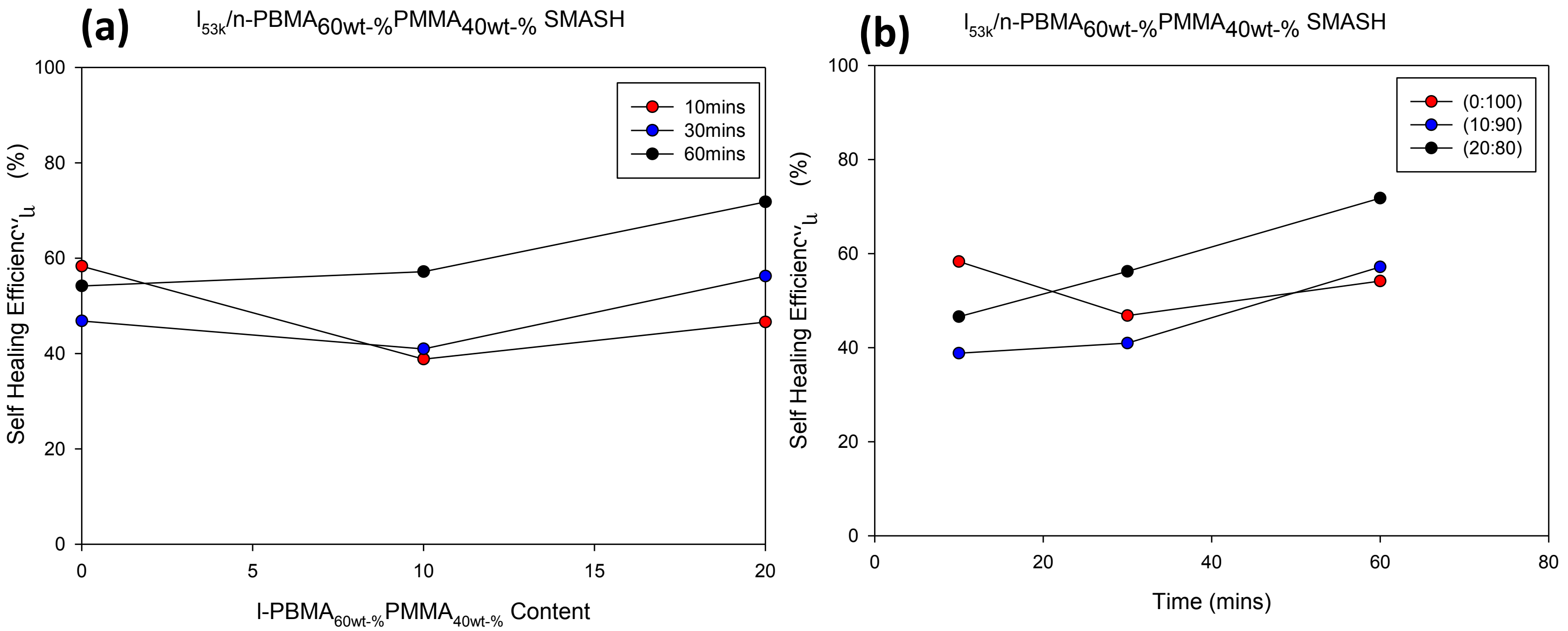

$$SH_{Efficiency}(\%) = \frac{SS - TTS}{SS} \bullet 100\%$$

where

SS = Scratched Surface

TTS = Thermally Treated Surface

Composition	Time (mins)	SS (Pixels)	TTS (Pixels)	Self Healing (%)
(0:100)	10	240550	100340	58.3
	30	291460	155001	46.8
	60	336135	154097	54.2
(10:90)	10	211094	129163	38.8
	30	230214	135944	40.9
	60	228990	98132	57.1
(20:80)	10	184475	98537	46.6
	30	257400	112668	56.2
	60	152796	43128	71.8

Figure A6.1.14. Graphs showing the self healing (SH) efficiency analysis for the SMASH coatings using l-PBMA:PMMA with a M_w of 53k g/mol where (a) shows the different thermal treatment times: 10 min, 30 min, and 60 min, and (b) the SMASH composition coatings tested: (0:100), (10:90) and (20:80). The figure also shows the SH efficiency equation used to calculate the SH values shown in chart.

Scratched

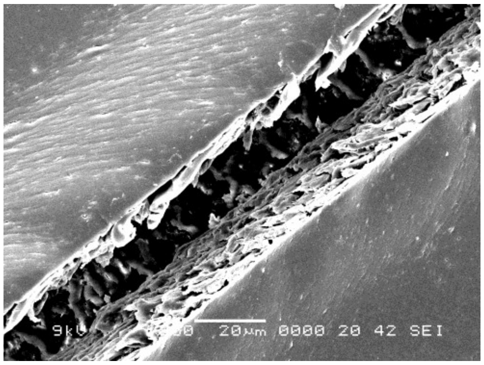

Thermally Treated

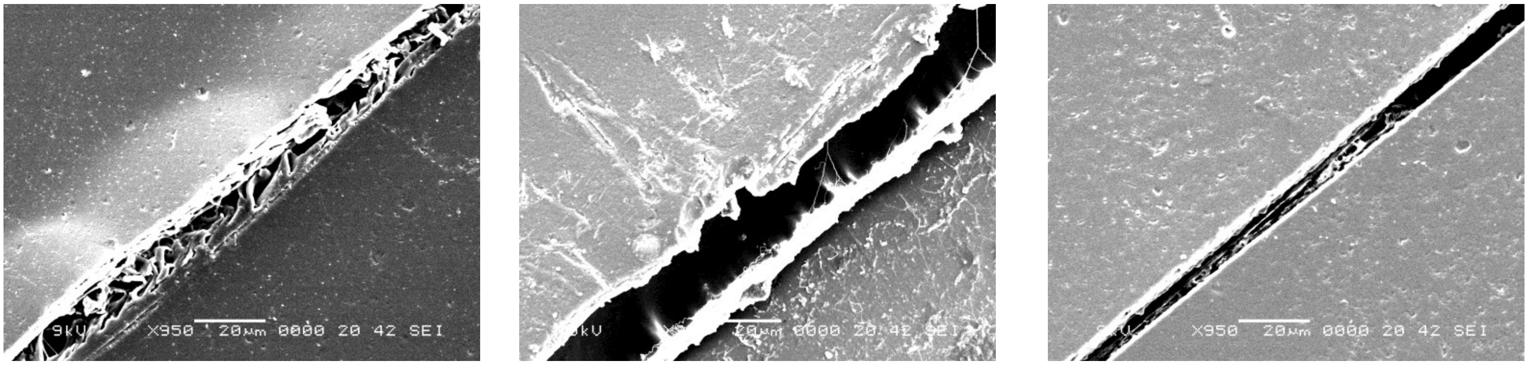

10 min **30 min** **60 min**

Figure A6.1.15. Scanning electron microscopy (SEM) micrographs of the SMASH l_{40k}:n-$PBMA_{60wt\text{-}\%}PMMA_{40wt\text{-}\%}$ (0:100) coating. The coating was in its scratched and thermally treated state at three different temperatures of 10 min, 30 min, and 60 min at 80 °C. SEM's reveal only partial crack closure was evident among the different thermal treatments. It is hypothesized that complete crack closure was not achieved due to material removal. Other factors may include a longer healing time at a higher temperature for complete closure of crack.

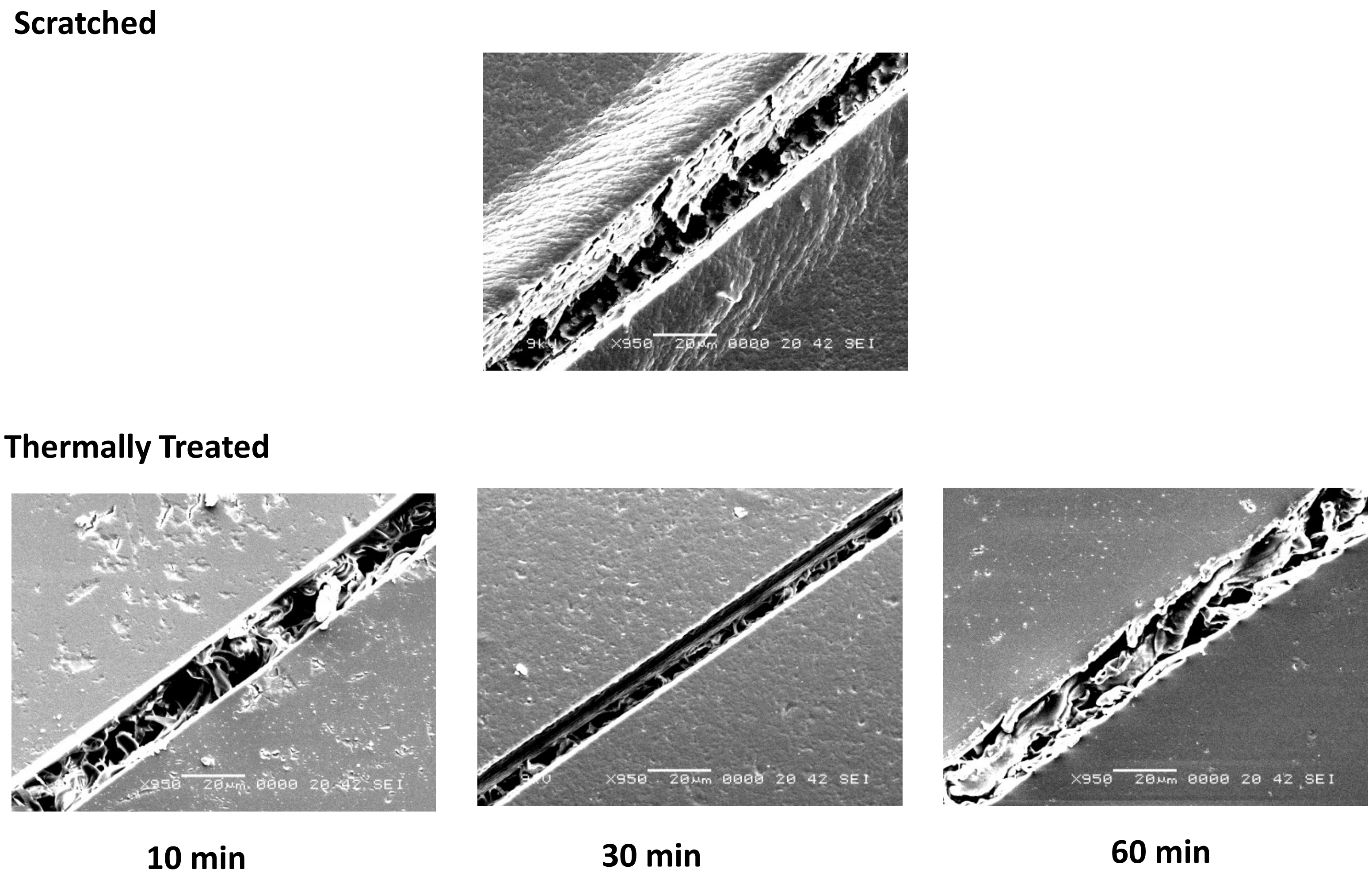

Figure A6.1.16. Scanning electron microscopy (SEM) micrographs of the SMASH l_{40k}:n-PBMA$_{60wt\text{-}\%}$PMMA$_{40wt\text{-}\%}$ (10:90) coating. The coating was in its scratched and thermally treated state at three different temperature of 10 min, 30 min, and 60 min at 80 °C. SEM's reveal only partial crack closure was evident among the different thermal treatments. It is hypothesized that complete crack closure was not achieved due to material removal. Other factors may include a longer healing time at a higher temperature for complete closure of crack.

Scratched

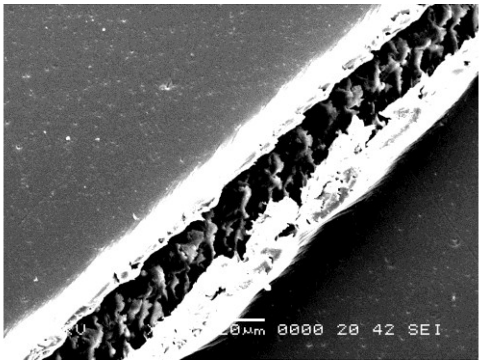

Thermally Treated

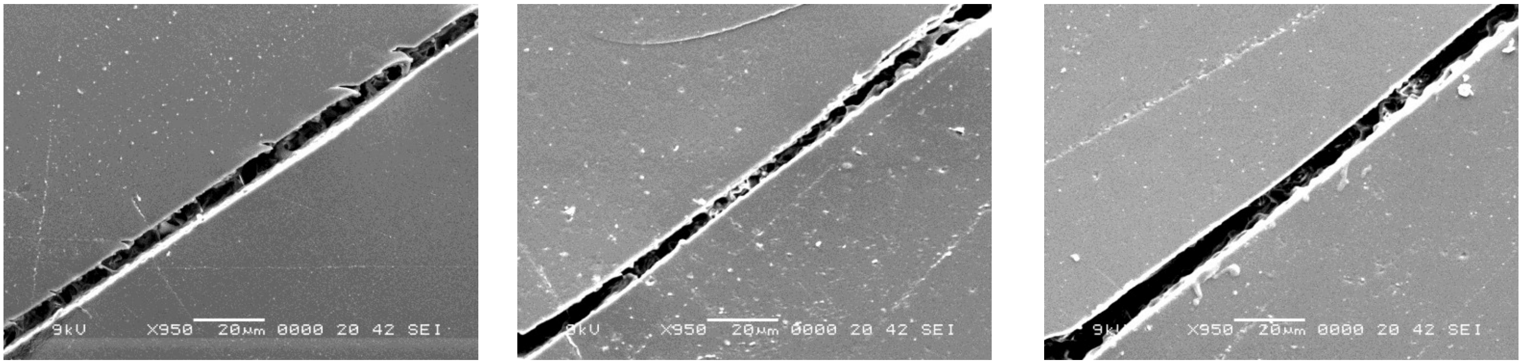

10 min **30 min** **60 min**

Figure A6.1.17. Scanning electron microscopy (SEM) micrographs of the SMASH l_{40k}:n-$PBMA_{60wt-\%}PMMA_{40wt-\%}$ (20:80) coating. The coating was in its scratched and thermally treated state at three different temperature of 10 min, 30 min, and 60 min at 80 °C. SEM's reveal only partial crack closure was evident among the different thermal treatments. It is hypothesized that complete crack closure was not achieved due to material removal. Other factors may include a longer healing time at a higher temperature for complete closure of crack.

Scratched

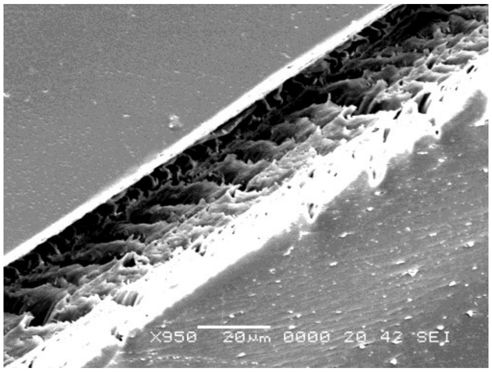

Thermally Treated

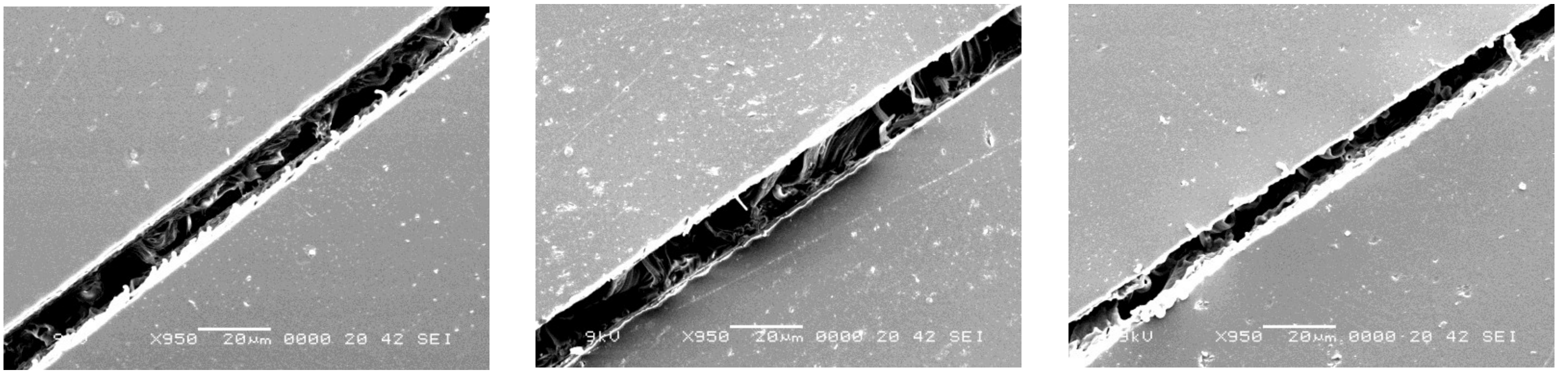

10 min **30 min** **60 min**

Figure A6.1.18. Scanning electron microscopy (SEM) micrographs of the SMASH l_{53k}:n-PBMA$_{60wt\text{-}\%}$PMMA$_{40wt\text{-}\%}$ (0:100) coating. The coating was in its scratched and thermally treated state at three different temperature of 10 min, 30 min, and 60 min at 80 °C. SEM's reveal only partial crack closure was evident among the different thermal treatments. It is hypothesized that complete crack closure was not achieved due to material removal. Other factors may include a longer healing time at a higher temperature for complete closure of crack.

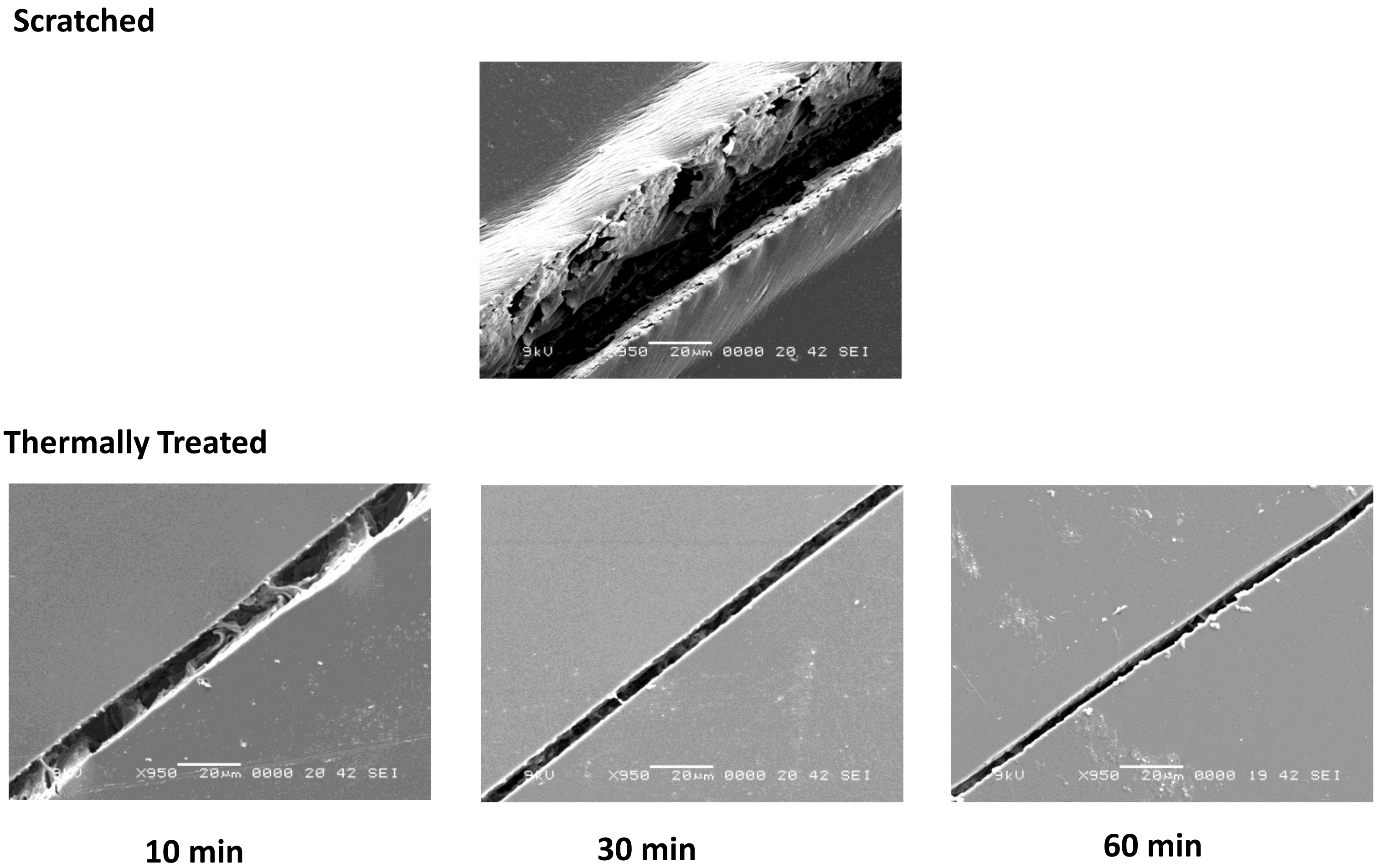

Figure A6.1.19. Scanning electron microscopy (SEM) micrographs of the SMASH l_{53k}:n-$PBMA_{60wt\text{-}\%}PMMA_{40wt\text{-}\%}$ (10:90) coating. The coating was in its scratched and thermally treated state at three different temperature of 10 min, 30 min, and 60 min. SEM's reveal only partial crack closure was evident among the different thermal treatments. It is hypothesized that complete crack closure was not achieved due to material removal. Other factors may include a longer healing time at a higher temperature for complete closure of crack.

Scratched

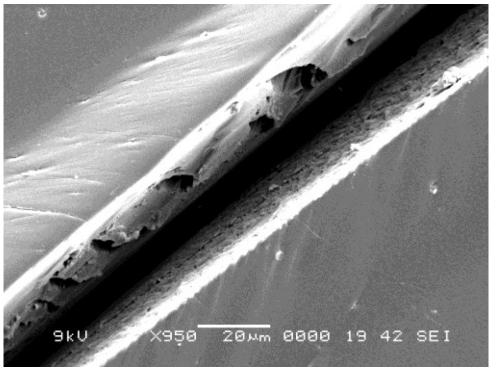

Thermally Treated

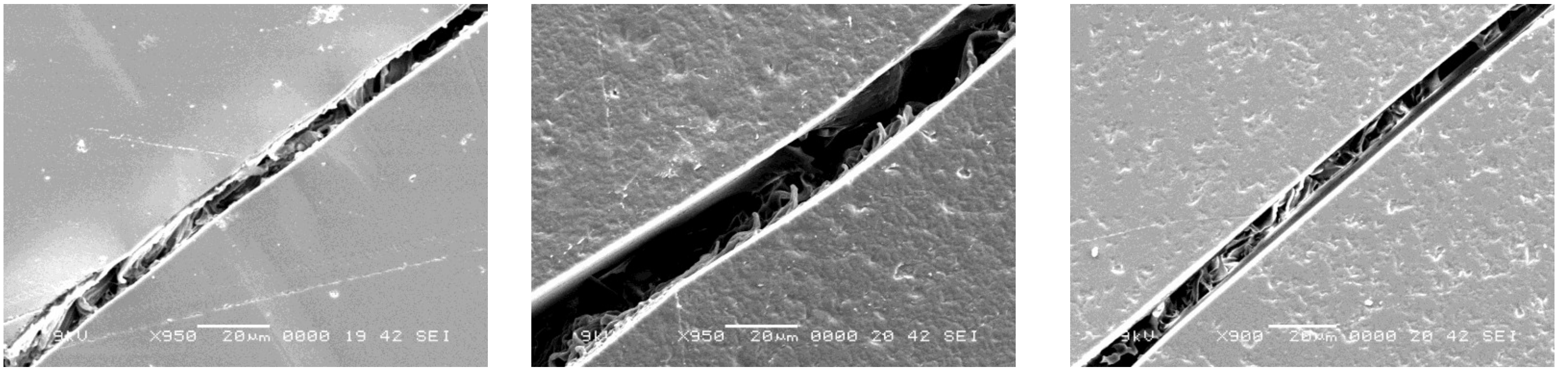

10 min **30 min** **60 min**

Figure A6.1.20. Scanning electron microscopy (SEM) micrographs of the SMASH l$_{53k}$:n-PBMA$_{60wt\text{-}\%}$PMMA$_{40wt\text{-}\%}$ (20:80) coating. The coating was in its scratched and thermally treated state at three different temperature of 10 min, 30 min, and 60 min. SEM's reveal only partial crack closure was evident among the different thermal treatments. It is hypothesized that complete crack closure was not achieved due to material removal. Other factors may include a longer healing time at a higher temperature for complete closure of crack.

APPENDIX 7.0

ANISOTROPIC SHAPE MEMORY ELASTOMERIC COMPOSITE (A-SMEC) POLY(Ɛ-CAPROLACTONE) (PCL)/SYLGARD184

A7.0 SUMMARY

This appendix focuses on the fabrication of anisotropic shape memory elastomeric composite (A-SMEC) composites using poly(ε caprolactone) (PCL), a semi-crystalline polymer, as the fiber reinforcements embedded in the Sylgard184 matrix. As shown in chapter 4, A-SMEC composites where fabricated using poly(vinyl acetate) (PVAc), an amorphous polymer, as fiber reinforcements. PCL A-SMEC were fabricated in order to prove the versatility of the shape memory assisted self healing (SMASH) and reversible plasticity shape memory (RPSM) among fiber reinforced composites. Fiber diameter analysis, thermal, thermomechanical, mechanical and self healing experiments are shown. Anisotropic shape memory elastomeric composites (A-SMEC) (aligned fibers) and shape memory elastomeric composites (SMEC) (randomly aligned fibers) were compared for mechanical properties.

APPENDIX 7.1

ANISOTROPIC SHAPE MEMORY ELASTOMERIC COMPOSITE (A-SMEC)

PCL(M_W~48k)/SYLGARD184

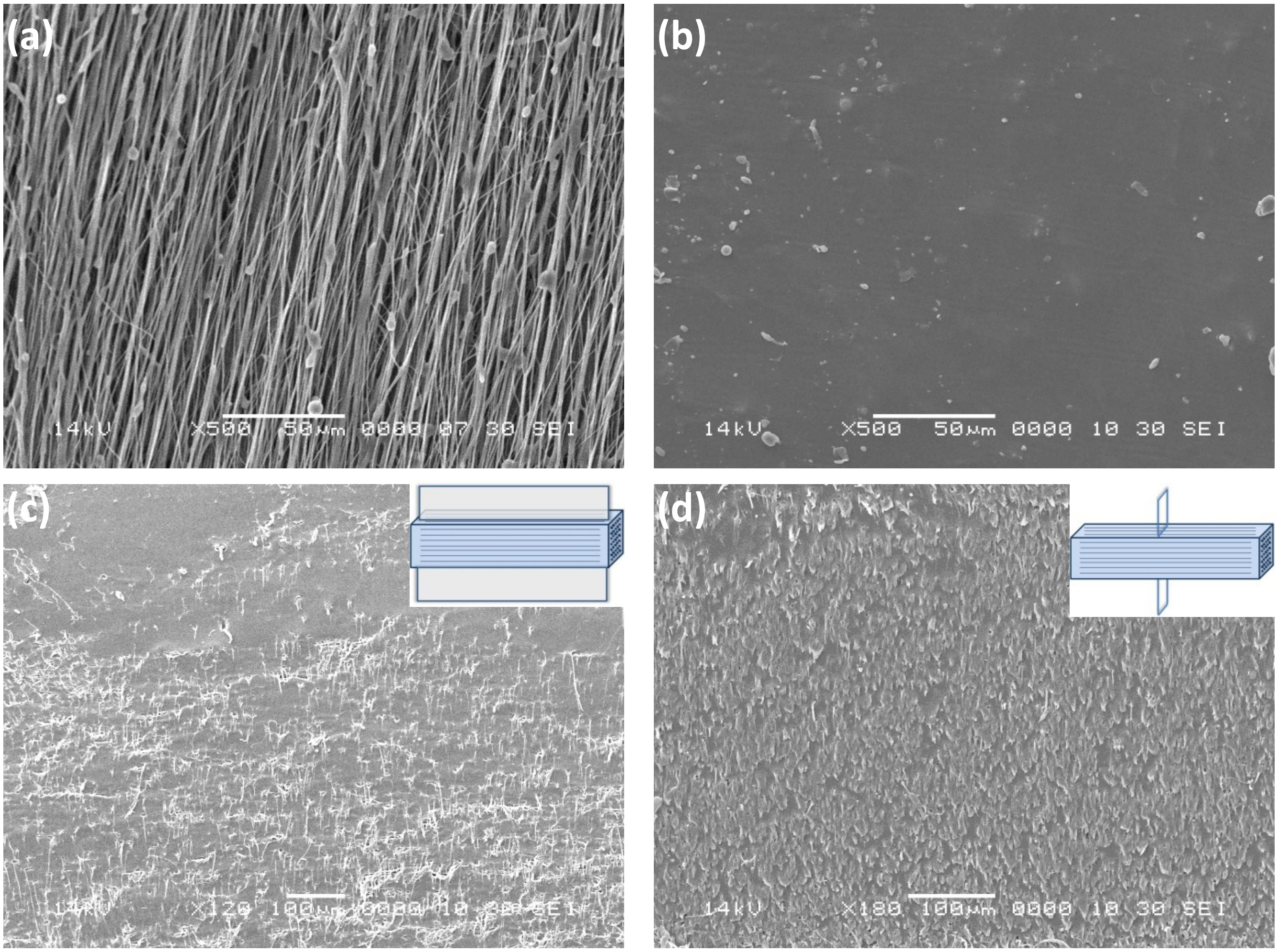

Figure A7.1.1. Scanning electron microscopy (SEM) micrographs showing (a) aligned fibers with an average fiber diameter of 1.04 ± 0.38 µm, (b) topography, (c) cross section in the axial direction (0°), (d) cross section in the transverse direction (90°) of the composite.

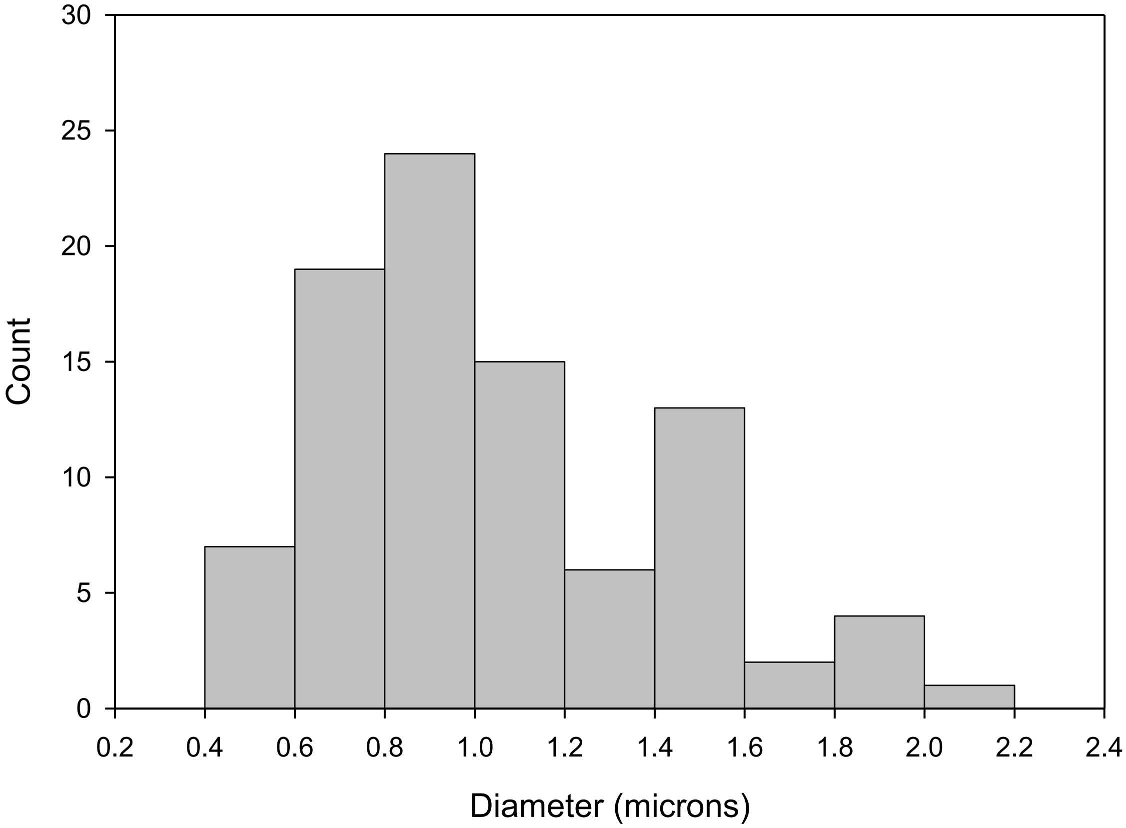

Figure A7.1.2. Histogram showing the distribution of the PCL (M_w= 48k) fiber diameter (average fiber diameter is 1.04 ± 0.38 µm).

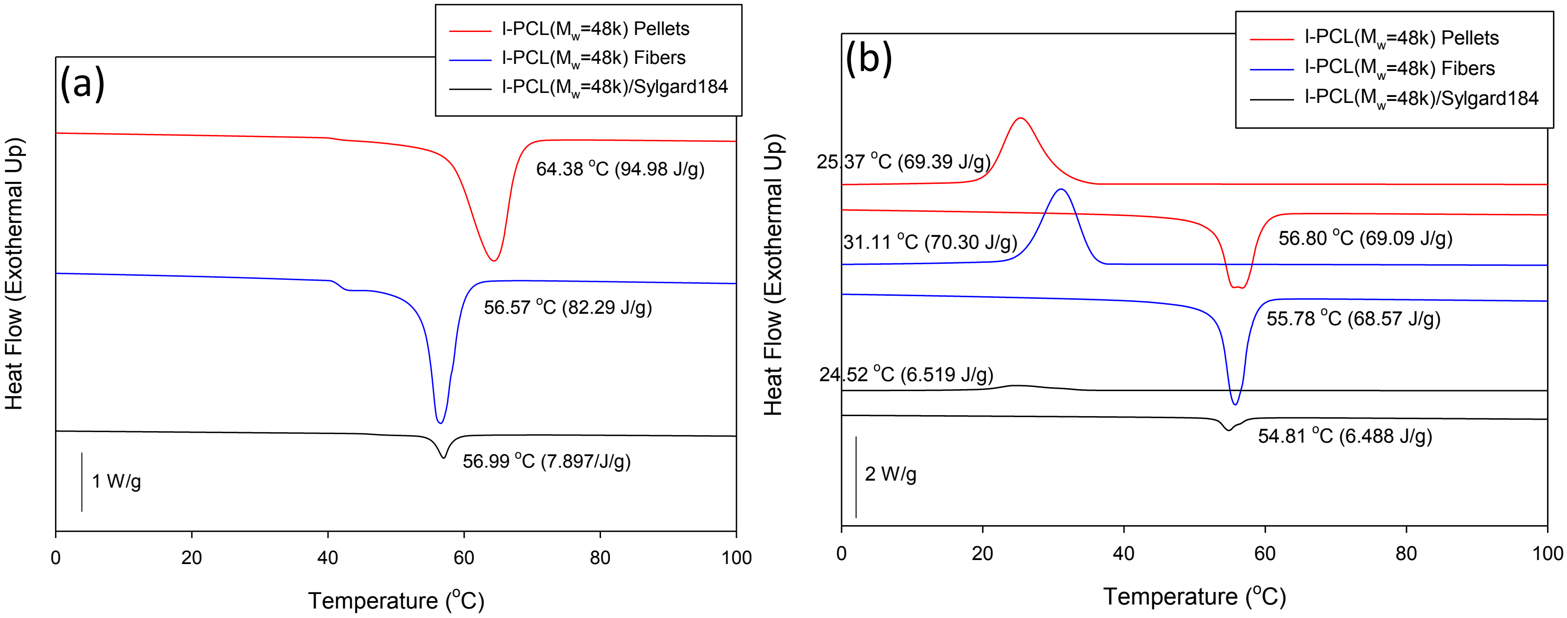

Figure A7.1.3. To study the crystalline (T_c) and melting (T_m) temperatures of systems, differential scanning calorimetry (DSC) traces showing (a) the first heating (b) the second heating for the PCL pellets (as purchased), PCL e-spun fibers and the composite state. The DSC method used was equilibrated -90.00 °C, ramped 10.00 °C/min to 120.00 °C, isothermal for 1.00 min, ramped 10.00 °C/min to -90.00 °C, isothermal for 1.00 min, and ramped 10.00 °C/min to 120.00 °C.

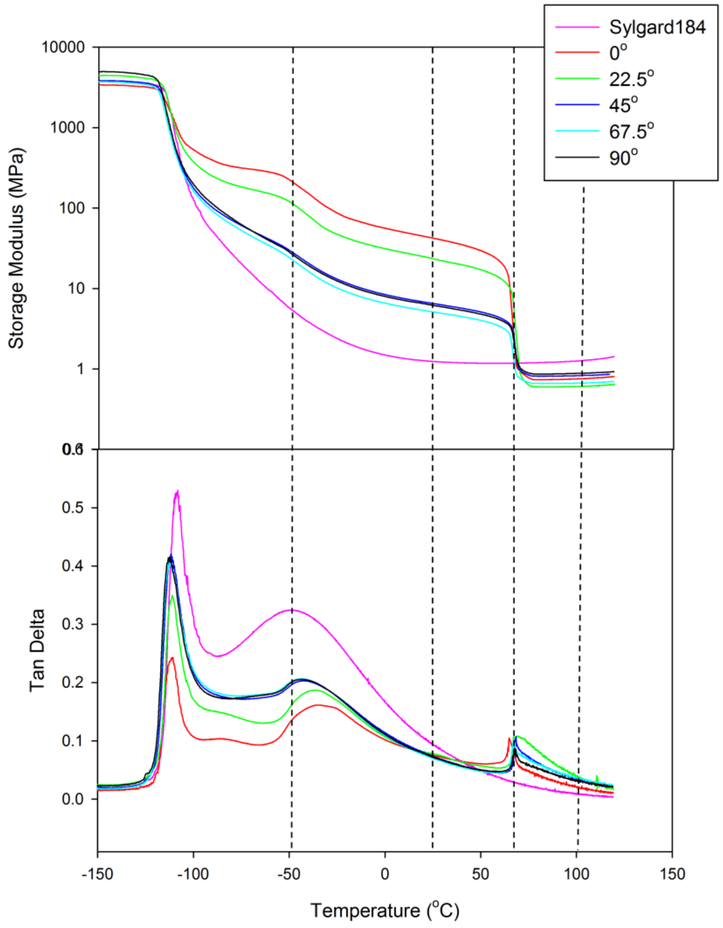

Figure A7.1.4. To study the viscoelastic polymeric properties of the systems, dynamic mechanical analysis (DMA) was conducted. Graph showing the tensile storage modulus (E') as a function of temperature where the tan delta is shown on the lower graph for all the composites at the various angles tested. The DMA method included equilibrating at -150.00 °C, isothermal for 5.00 min, and ramped 3.00 °C/min to 120.00 °C.

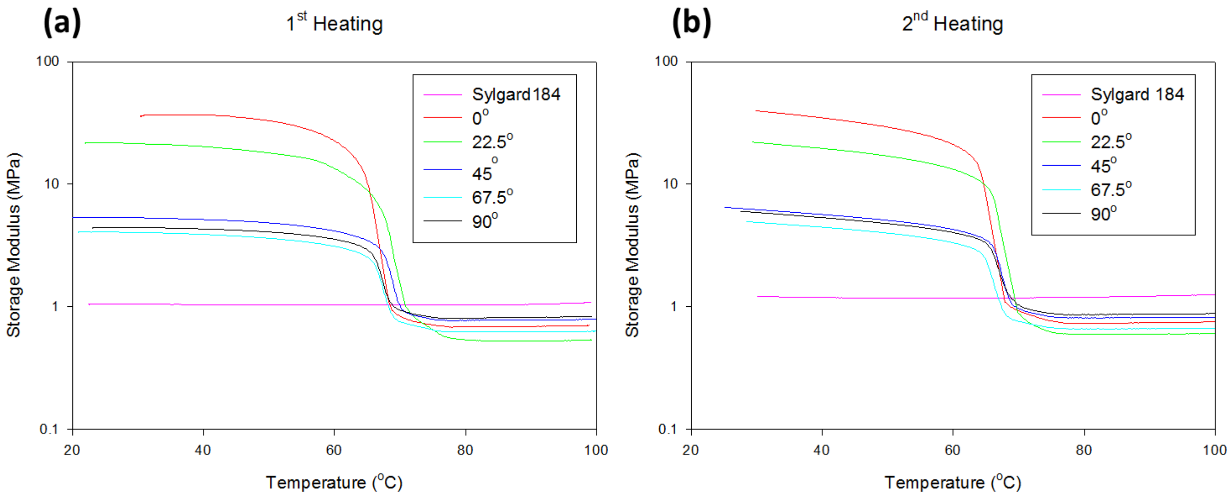

1st Heating

Angle (°)	$E'_{30°C}$ (MPa)	$E'_{100°C}$ (MPa)
Sylgard184	1.17	1.09
0	36.1	0.7
22.5	21.4	0.5
45	5.3	0.8
67.5	4.0	0.6
90	4.4	0.8

2nd Heating

Angle (°)	$E'_{30°C}$ (MPa)	$E'_{100°C}$ (MPa)
Sylgard184	5.6	1.3
0	39.7	0.8
22.5	21.9	0.6
45	6.2	0.8
67.5	4.9	0.7
90	5.9	0.9

Figure A7.1.5. Graph showing the tensile storage modulus (E') as a function of temperature for all single composites tested where (a) shows the 1st heating and (b) shows the 2nd heating. The charts correspond to each graph where the E' was recorded at 30 °C and 100 ° C. The method used to obtain this data included ramping the temperature at 3.00 °C/min to 100.00 °C.

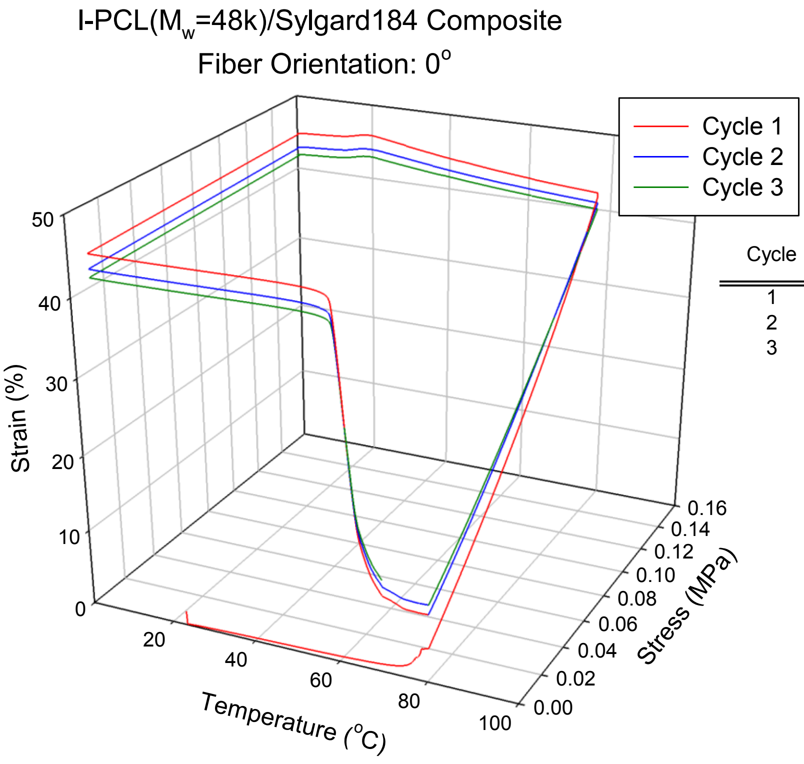

0 Degrees

Cycle	ε_m (%)	ε_u (%)	ε_p (%)	ε_p(N-1)(%)	R_f (%)	R_r (%)
1	47.5	45.9	8.9	1.9	96.6	83.9
2	45.6	44.0	10.2	8.9	96.5	96.4
3	44.6	43.0	12.1	10.2	96.3	94.4

Fixing Ratio

$$R_f(N) = \frac{\varepsilon_u(N)}{\varepsilon_m(N)} \times 100\%$$

Recovery Ratio

$$R_r(N) = \frac{\varepsilon_u(N) - \varepsilon_p(N)}{\varepsilon_u(N) - \varepsilon_p(N-1)} \times 100\%$$

ε_m = maximum strain achieved by deformation
ε_u = fixed strain after unloading
ε_p = permanent strain after recovery
N = cycle number

Figure A7.1.6. 3D plot showing a three cycle conventional one way shape memory (1WSM) for a specimen with fibers in the axial (0°) orientation. The equations displaced were used to calculate the fixing (R_f) and recovery (R_r) ratios where the chart shows the numerical values of R_f and R_r. The 1WSM method involved equilibrating the temperature to 80.00 °C, isothermal for 1.00 min, ramped force at 0.0500 N/min to 0.35 N, isothermal for 2.00 min, ramped to 2.00 °C/min to 5.00 °C, isothermal for 10.00 min, ramped to force 0.2000 N/min to 0.0010 N, isothermal for 3.00 min, ramped at 2.00 °C/min to 70.00 °C, isothermal for 1.00 min, and equilibrated at 80.00 °C to complete the cycle.

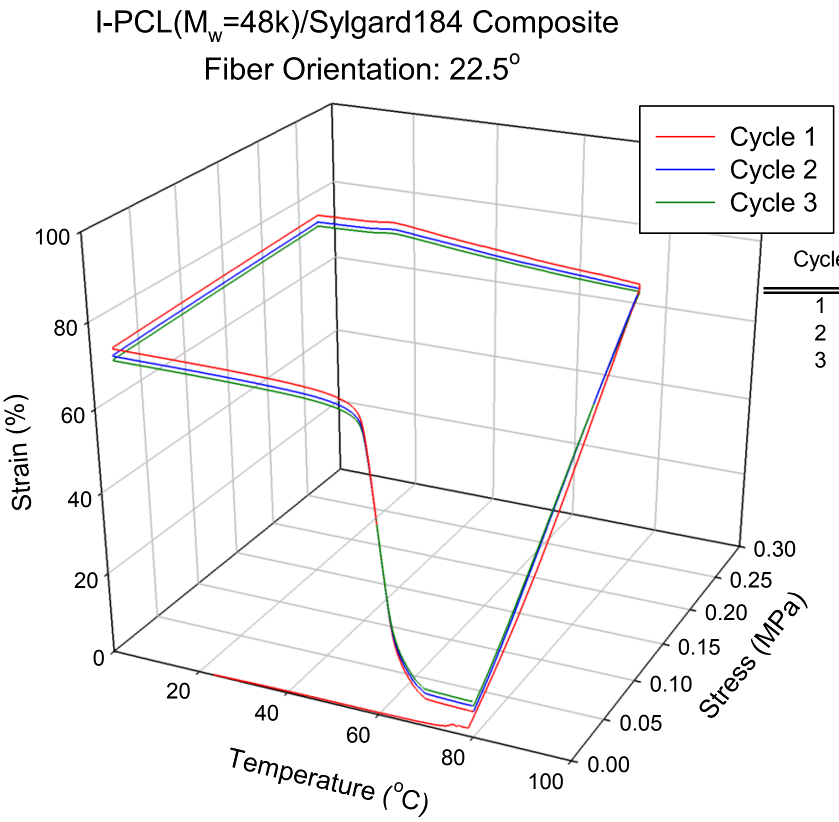

22.5 Degrees

Cycle	ε_m (%)	ε_u (%)	ε_p (%)	ε_p(N-1)(%)	R_f (%)	R_r (%)
1	78.5	75.2	6.4	0.0	95.8	91.6
2	76.8	73.5	7.8	6.4	95.8	97.9
3	75.8	72.5	8.8	7.8	95.7	98.4

Fixing Ratio

$$R_f(N) = \frac{\varepsilon_u(N)}{\varepsilon_m(N)} \times 100\%$$

Recovery Ratio

$$R_r(N) = \frac{\varepsilon_u(N) - \varepsilon_p(N)}{\varepsilon_u(N) - \varepsilon_p(N-1)} \times 100\%$$

ε_m = maximum strain achieved by deformation
ε_u = fixed strain after unloading
ε_p = permanent strain after recovery
N = cycle number

Figure A7.1.7. 3D plot showing a three cycle conventional one way shape memory (1WSM) for a specimen with fibers in the 22.5° orientation. The equations displaced were used to calculate the fixing (R_f) and recovery (R_r) ratios where the chart shows the numerical values of R_f and R_r.. The 1WSM method involved equilibrating the temperature to 80.00 °C, isothermal for 1.00 min, ramped force at 0.0500 N/min to 0.35 N, isothermal for 2.00 min, ramped to 2.00 °C/min to 5.00 °C, isothermal for 10.00 min, ramped to force 0.2000 N/min to 0.0010 N, isothermal for 3.00 min, ramped at 2.00 °C/min to 70.00 °C, isothermal for 1.00 min, and equilibrated at 80.00 °C to complete the cycle.

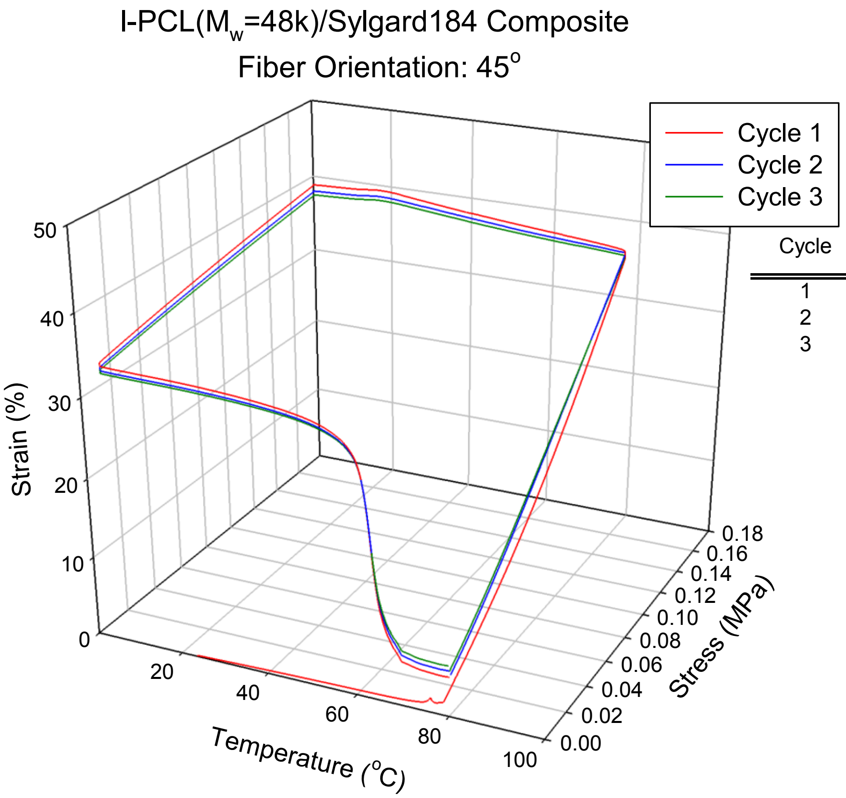

45 Degrees

Cycle	ε_m (%)	ε_u (%)	ε_p (%)	ε_p(N-1)(%)	R_f (%)	R_r (%)
1	41.2	35.1	5.0	0.1	85.3	85.8
2	40.4	34.5	5.8	5.1	85.5	97.8
3	39.9	34.2	6.4	5.8	85.9	97.9

Fixing Ratio

$$R_f(N) = \frac{\varepsilon_u(N)}{\varepsilon_m(N)} \times 100\%$$

Recovery Ratio

$$R_r(N) = \frac{\varepsilon_u(N) - \varepsilon_p(N)}{\varepsilon_u(N) - \varepsilon_p(N-1)} \times 100\%$$

ε_m = maximum strain achieved by deformation
ε_u = fixed strain after unloading
ε_p = permanent strain after recovery
N = cycle number

Figure A7.1.8. 3D plot showing a three cycle conventional one way shape memory (1WSM) for a specimen with fibers in the 45° orientation. The equations displaced were used to calculate the fixing (R_f) and recovery (R_r) ratios where the chart shows the numerical values of R_f and R_r. The 1WSM method involved equilibrating the temperature to 80.00 °C, isothermal for 1.00 min, ramped force at 0.0500 N/min to 0.35 N, isothermal for 2.00 min, ramped to 2.00 °C/min to 5.00 °C, isothermal for 10.00 min, ramped to force 0.2000 N/min to 0.0010 N, isothermal for 3.00 min, ramped at 2.00 °C/min to 70.00 °C, isothermal for 1.00 min, and equilibrated at 80.00 °C to complete the cycle.

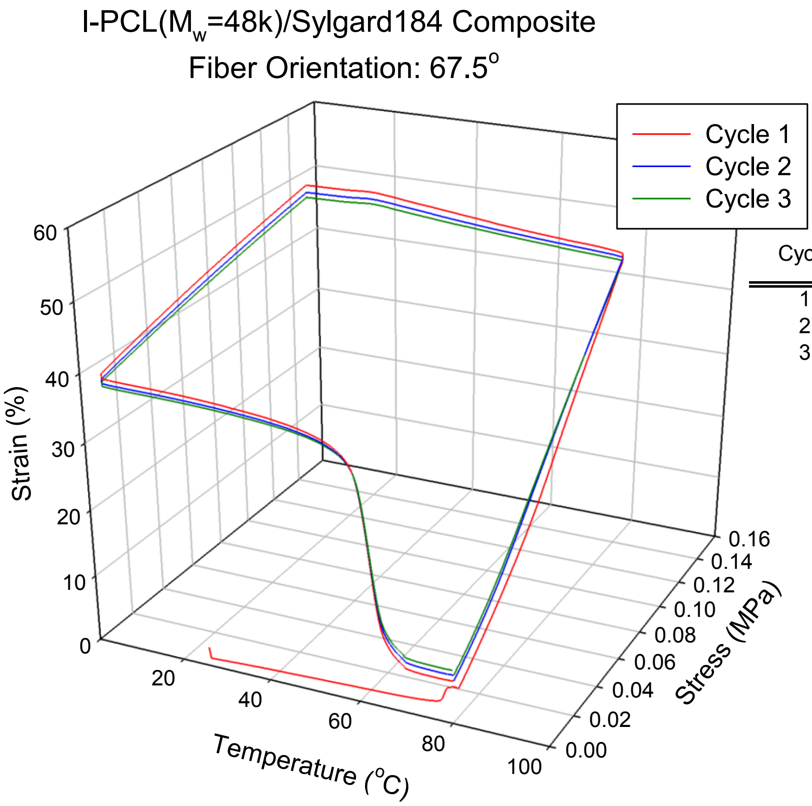

67.5 Degrees

Cycle	ε_m (%)	ε_u (%)	ε_p (%)	ε_p(N-1)(%)	R_f (%)	R_r (%)
1	50.4	41.2	6.4	1.9	81.9	88.6
2	49.3	40.6	7.3	6.4	82.4	97.4
3	48.6	40.1	8.0	7.3	82.6	97.9

Fixing Ratio

$$R_f(N) = \frac{\varepsilon_u(N)}{\varepsilon_m(N)} \times 100\%$$

Recovery Ratio

$$R_r(N) = \frac{\varepsilon_u(N) - \varepsilon_p(N)}{\varepsilon_u(N) - \varepsilon_p(N-1)} \times 100\%$$

ε_m = maximum strain achieved by deformation
ε_u = fixed strain after unloading
ε_p = permanent strain after recovery
N = cycle number

Figure A7.1.9. 3D plot showing a three cycle conventional one way shape memory (1WSM) for a specimen with fibers in the 67.5° orientation. The equations displaced were used to calculate the fixing (R_f) and recovery (R_r) ratios where the chart shows the numerical values of R_f and R_r.. The 1WSM method involved equilibrating the temperature to 80.00 °C, isothermal for 1.00 min, ramped force at 0.0500 N/min to 0.35 N, isothermal for 2.00 min, ramped to 2.00 °C/min to 5.00 °C, isothermal for 10.00 min, ramped to force 0.2000 N/min to 0.0010 N, isothermal for 3.00 min, ramped at 2.00 °C/min to 70.00 °C, isothermal for 1.00 min, and equilibrated at 80.00 °C to complete the cycle.

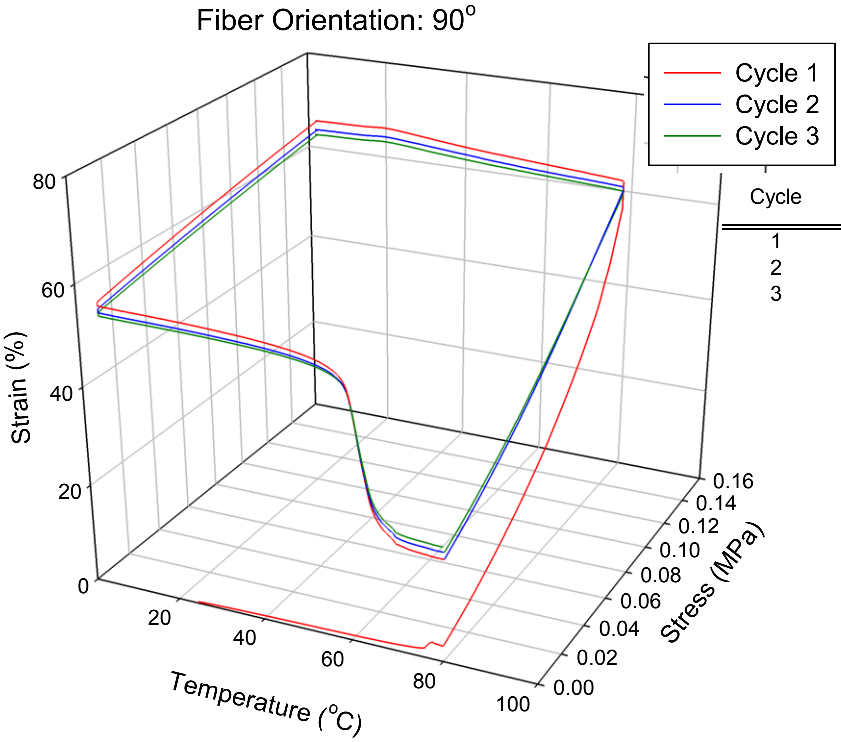

90 Degrees

Cycle	ε_m (%)	ε_u (%)	ε_p (%)	ε_p(N-1)(%)	R_f (%)	R_r (%)
1	67.9	58.0	20.7	0.2	85.4	64.5
2	66.1	56.7	22.1	20.7	85.8	96.1
3	65.0	56.1	23.1	22.1	86.2	97.0

Fixing Ratio

$$R_f(N) = \frac{\varepsilon_u(N)}{\varepsilon_m(N)} \times 100\%$$

Recovery Ratio

$$R_r(N) = \frac{\varepsilon_u(N) - \varepsilon_p(N)}{\varepsilon_u(N) - \varepsilon_p(N-1)} \times 100\%$$

ε_m = maximum strain achieved by deformation
ε_u = fixed strain after unloading
ε_p = permanent strain after recovery
N = cycle number

Figure A7.1.10. 3D plot showing a three cycle conventional one way shape memory (1WSM) for a specimen with fibers in the 90° orientation. The equations displaced were used to calculate the fixing (R_f) and recovery (R_r) ratios where the chart shows the numerical values of R_f and R_r. The 1WSM method involved equilibrating the temperature to 80.00 °C, isothermal for 1.00 min, ramped force at 0.05 N/min to 0.35 N, isothermal for 2.00 min, ramped to 2.00 °C/min to 5.00 °C, isothermal for 10.00 min, ramped to force 0.2000 N/min to 0.0010 N, isothermal for 3.00 min, ramped at 2.00 °C/min to 70.00 °C, isothermal for 1.00 min, and equilibrated at 80.00 °C to complete the cycle.

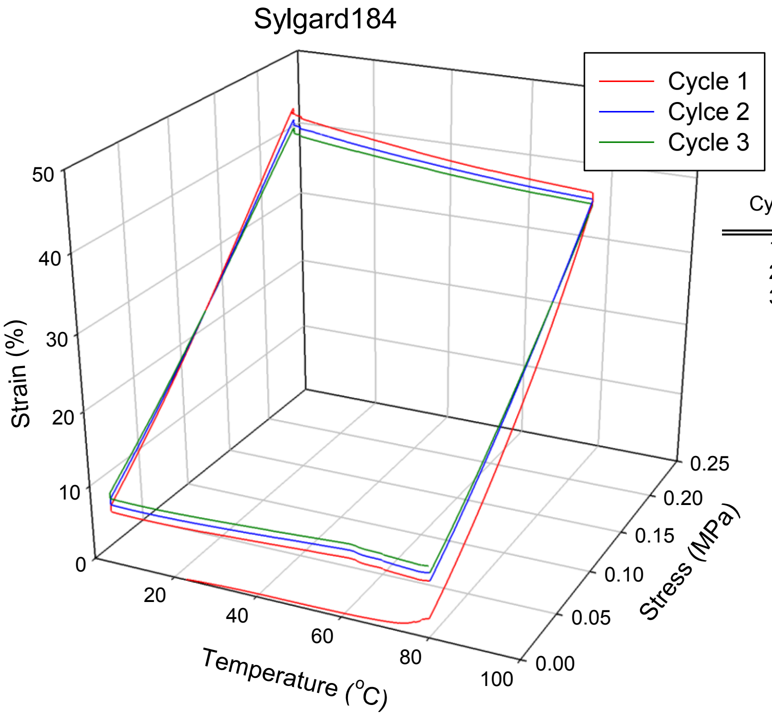

Sylgard184

Cycle	ε_m (%)	ε_u (%)	ε_p (%)	ε_p(N-1)(%)	R_f (%)	R_r (%)
1	44.3	8.9	7.6	0.1	20.2	15.2
2	42.7	9.7	8.6	7.6	22.8	50.8
3	41.6	10.7	9.5	8.6	25.8	59.1

Fixing Ratio

$$R_f(N) = \frac{\varepsilon_u(N)}{\varepsilon_m(N)} \times 100\%$$

Recovery Ratio

$$R_r(N) = \frac{\varepsilon_u(N) - \varepsilon_p(N)}{\varepsilon_u(N) - \varepsilon_p(N-1)} \times 100\%$$

ε_m = maximum strain achieved by deformation
ε_u = fixed strain after unloading
ε_p = permanent strain after recovery
N = cycle number

Figure A7.1.11. 3D plot showing a three cycle conventional one way shape memory (1WSM) for Sylgard184 specimen. The equations displaced were used to calculate the fixing (R_f) and recovery (R_r) ratios where the chart shows the numerical values of R_f and R_r. The 1WSM method involved equilibrating the temperature to 80.00 °C, isothermal for 1.00 min, ramped force at 0.0500 N/min to 0.3500 N, isothermal for 2.00 min, ramped to 2.00 °C/min to 5.00 °C, isothermal for 10.00 min, ramped to force 0.2000 N/min to 0.0010 N, isothermal for 3.00 min, ramped at 2.00 °C/min to 70.00 °C, isothermal for 1.00 min, and equilibrated at 80.00 °C to complete the cycle.

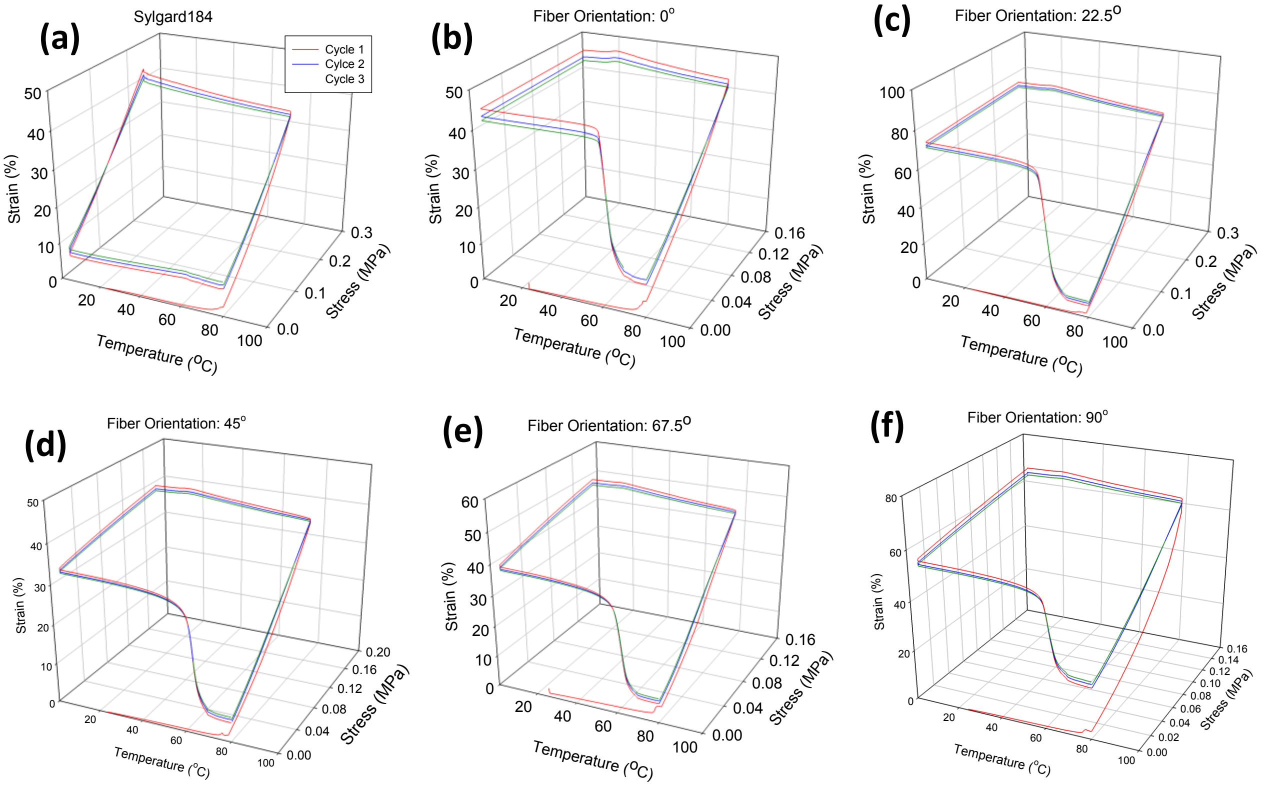

Figure A7.1.12. Conventional one way shape memory (1WSM) curves for all samples tested as a function of fiber orientation where (a) Neat Sylgard, (b) 0° (c) 22.5° (d) 45° (e) 67.5 ° and (f) 90°. This figure was added to allow for comparison among all specimens tested.

Table A7.1.1. Table showing the tensile storage modulus (E') at the following temperature for all composites studied: -150 °C , -50 °C, 25 °C, 60 °C, and 100 °C where neat Sylgard184 is shown as a reference.

Angle (°)	**$E'_{-150°C}$ (MPa)**	**$E'_{-50°C}$ (MPa)**	**$E'_{25°C}$ (MPa)**	**$E'_{60°C}$ (MPa)**	**$E'_{100°C}$ (MPa)**
Sylgard184	3577	5.6	1.2	1.2	1.3
0	3271	220.3	42.1	21.1	0.8
22.5	4438	118.4	23.3	13.2	0.6
45	3431	29.4	6.5	4.3	0.8
67.5	3478	23.8	5.1	3.3	0.7
90	4560	27.8	6.2	4.0	0.9

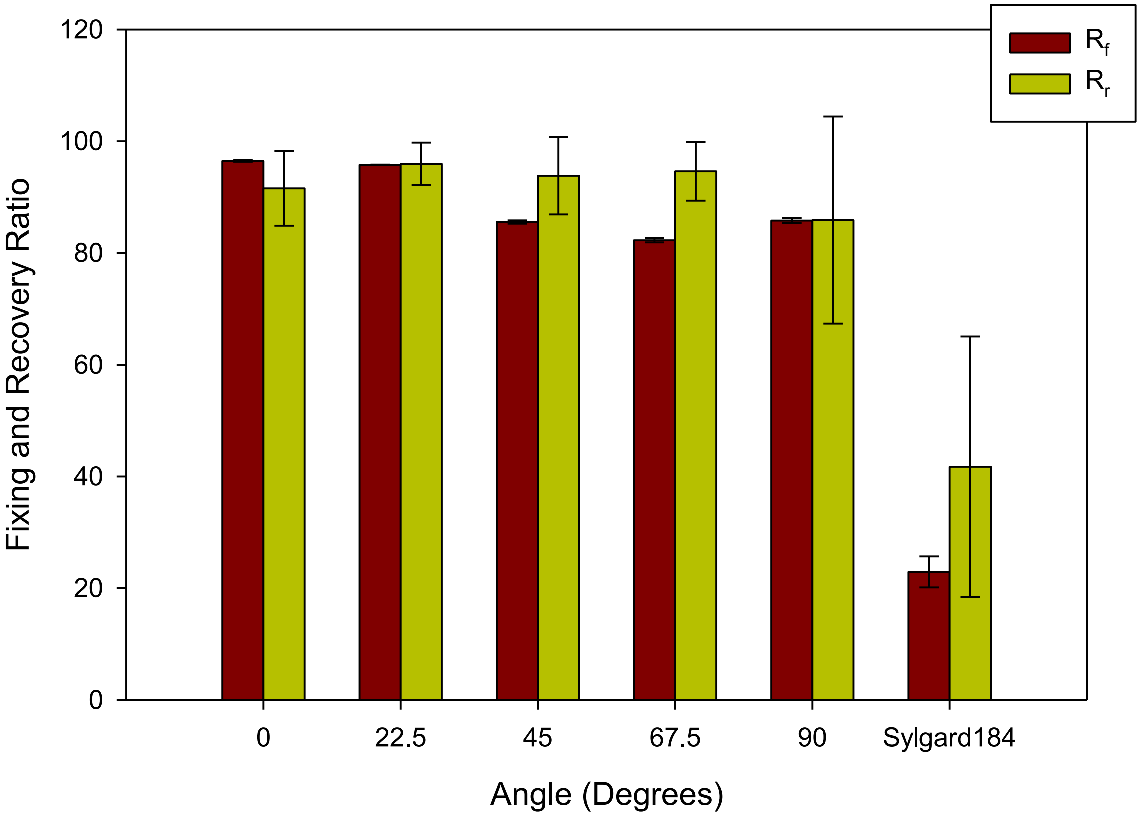

Figure A7.1.13. Fixing (R_f) and recovery (R_r) ratios for all the composites tested as a function of fiber orientation.

Table A7.1.2. Table showing the fixing (R_f) and recovery (R_r) ratios for all composites tested with Sylgard as a reference.

Angle (°)	R_f (%)	STDEV	R_r (%)	STDEV
0	96.5	0.1	91.6	6.7
22.5	95.8	0.1	96.0	3.8
45	85.6	0.3	93.8	6.9
67.5	82.3	0.4	94.6	5.2
90	85.8	0.4	85.9	18.5
Sylgard184	22.9	2.8	41.7	23.3

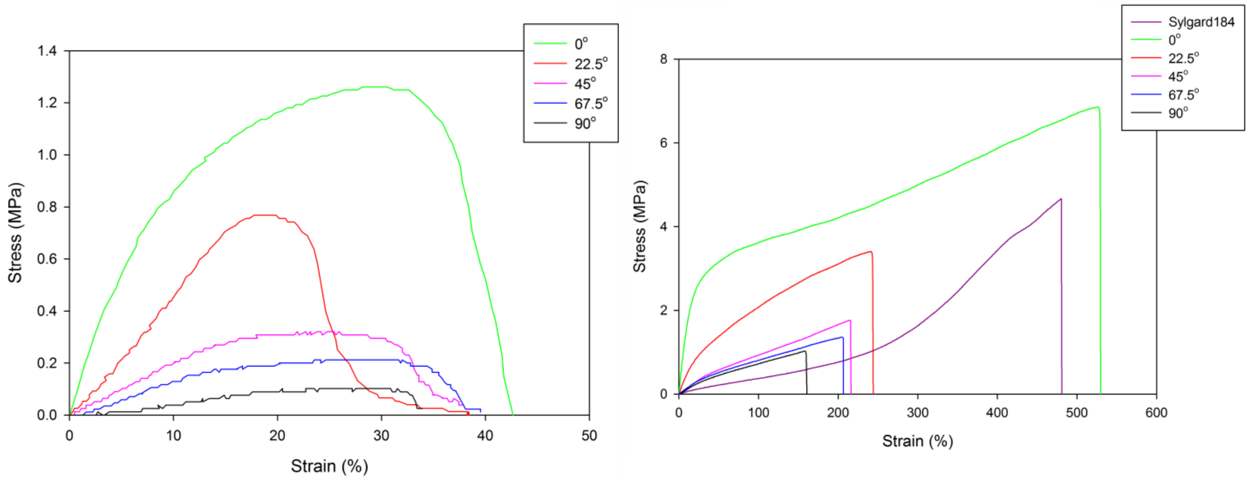

I-PCL Fiber Dogbone

Angle (°)	0	22.5	45	67.5	90
AVE Thickness	0.6	0.5	0.5	0.6	0.5
STDEV	0.01	0.01	0.00	0.04	0.03

ASMEC Dogbone

Angle (°)	0	22.5	45	67.5	90	Sylgard184
AVE Thickness	0.6	0.6	0.9	0.8	0.8	0.8
STDEV	0.02	0.04	0.06	0.07	0.10	0.05

Figure A7.1.14. Representative stress-strain curves of (a) fiber and (b) composite dogbone samples as a function of fiber orientation. Charts show the average thicknesses of four specimens used for mechanical testing. The dogbone geometry was ASTM Standard D638-03 Type IV, scaled down by a factor of 4. The mechanical testing parameters conducted on the Linkam tensile stage included using a 20 N load cell, stretch velocity: 100 µm/sec, $\text{Temp}_{\text{deformation}}$: 25 °C.

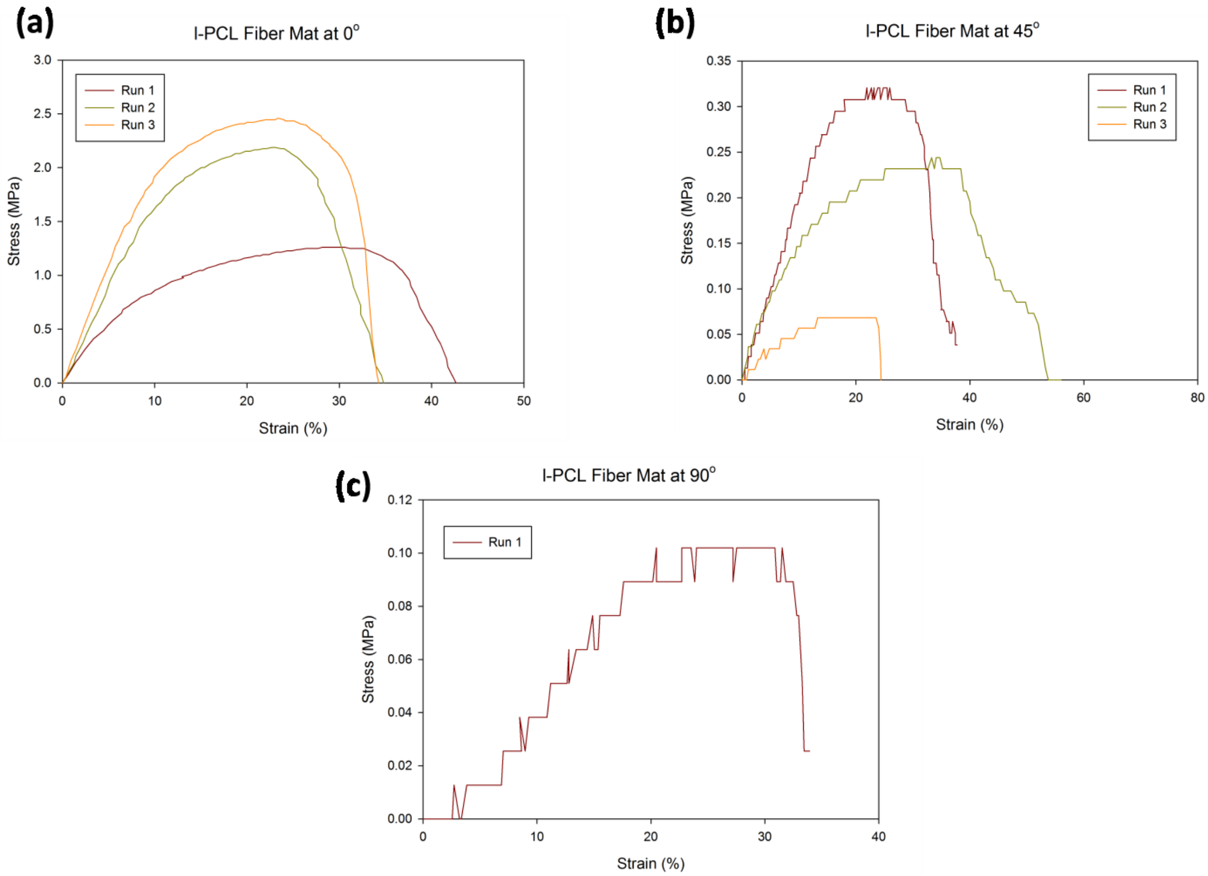

Figure A7.1.15. Stress-strain curves of fiber dogbone specimens showing (a) 0°, (b) 45°, and (c) 90° fiber orientation for three samples tested.

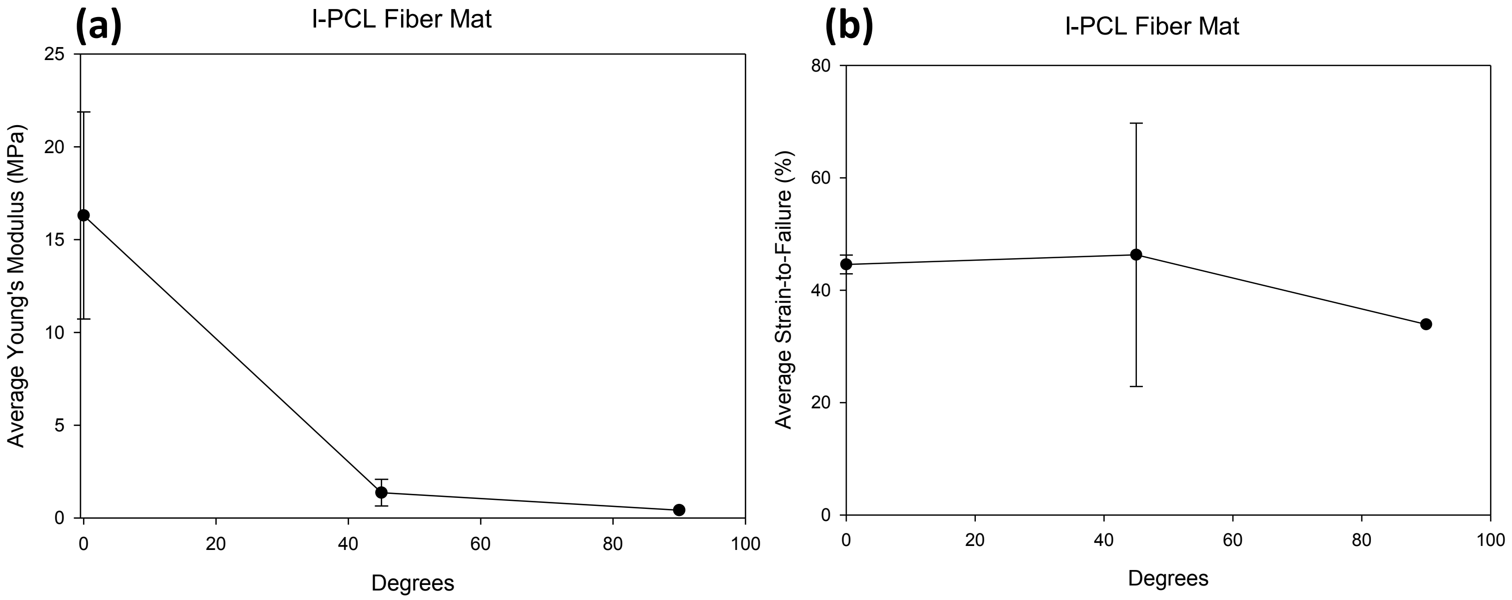

A7.1.16. Graphs showing the (a) average tensile storage modulus (E') and (b) the average strain-to-failure data for the fiber dogbone specimens.

Table A7.1.3. Tables showing the (a) average Young's modulus and (b) the average strain-to-failure for the fiber dogbone specimens tested for three samples.

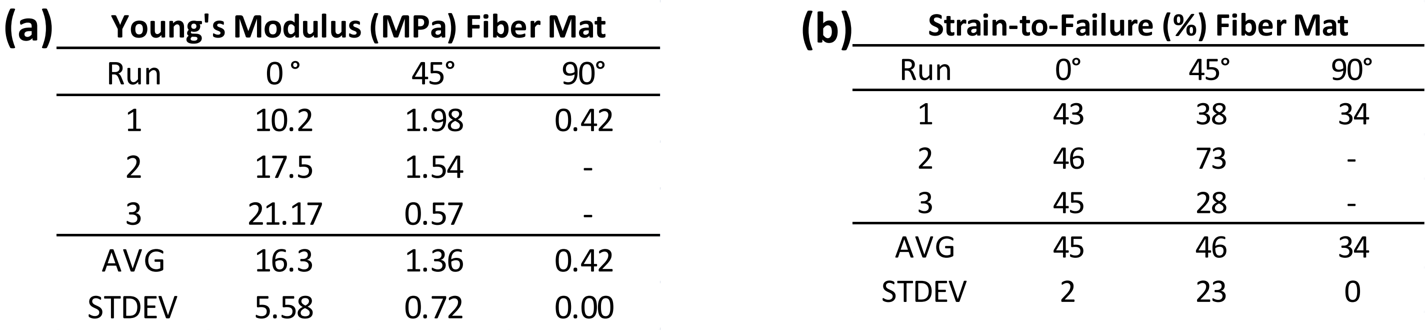

(a) Young's Modulus (MPa) Fiber Mat

Run	0 °	45°	90°
1	10.2	1.98	0.42
2	17.5	1.54	-
3	21.17	0.57	-
AVG	16.3	1.36	0.42
STDEV	5.58	0.72	0.00

(b) Strain-to-Failure (%) Fiber Mat

Run	0°	45°	90°
1	43	38	34
2	46	73	-
3	45	28	-
AVG	45	46	34
STDEV	2	23	0

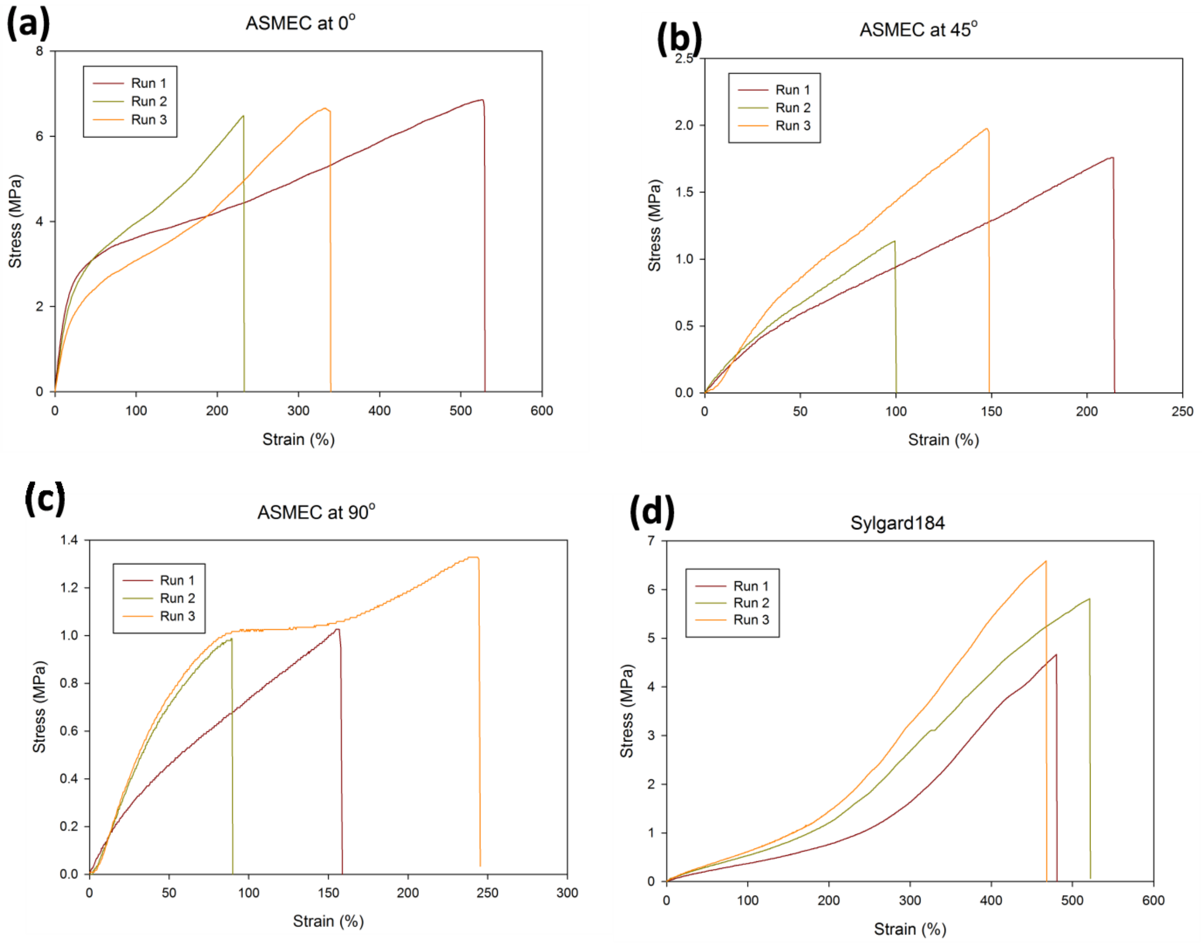

A7.1.17. Stress-strain curves of the composite samples showing (a) 0°, (b) 45°, and (c) 90° fiber orientation where (d) shows neat Sylgard184 as a reference. The mechanical testing was done on three different samples for each fiber orientation.

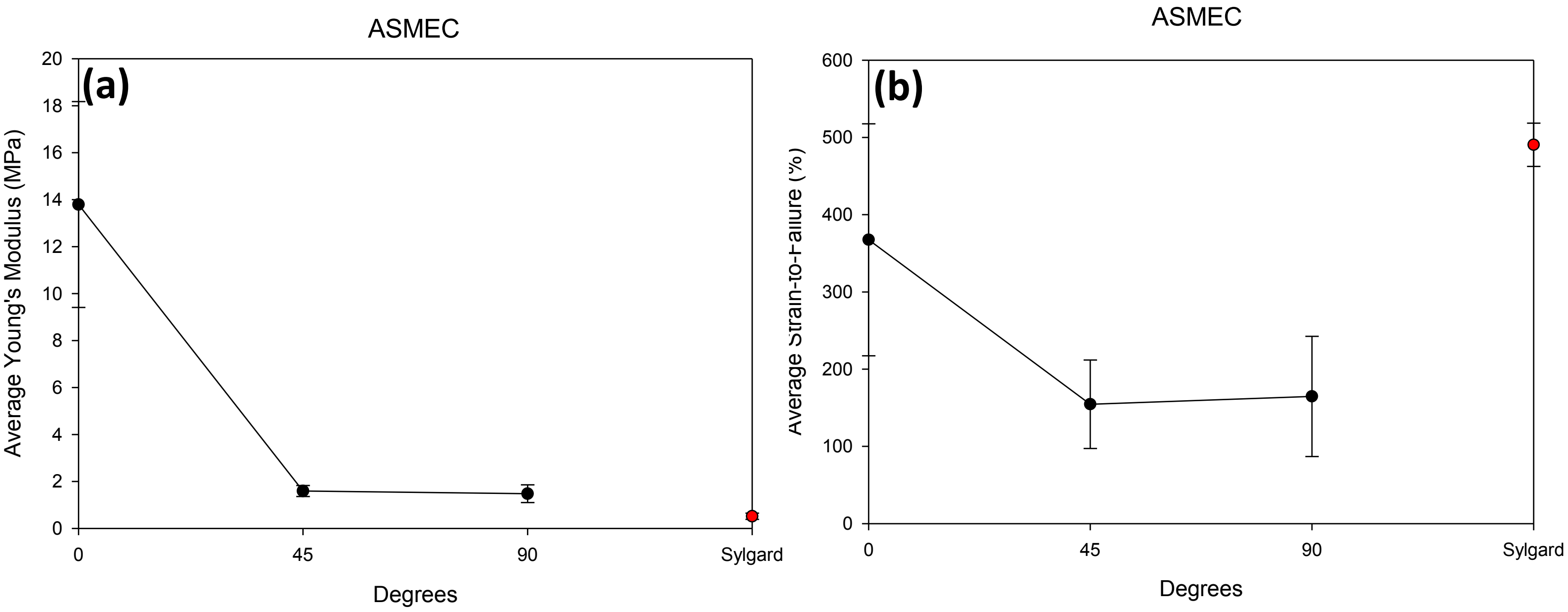

A7.1.18. Graphs showing the (a) average tensile storage modulus (E') and (b) the average strain-to-failure for the composite specimens as a function of fiber angle.

Table A7.1.4. Tables showing the (a) average young’s modulus (E’) and (b) the average strain-to- failure for the composite samples tested on three samples.

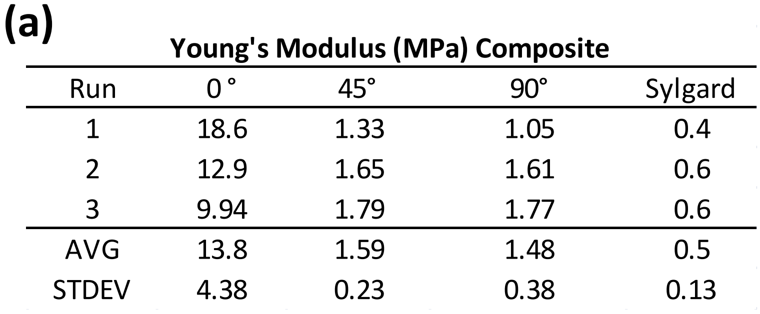

(a)

Young's Modulus (MPa) Composite

Run	0 °	45°	90°	Sylgard
1	18.6	1.33	1.05	0.4
2	12.9	1.65	1.61	0.6
3	9.94	1.79	1.77	0.6
AVG	13.8	1.59	1.48	0.5
STDEV	4.38	0.23	0.38	0.13

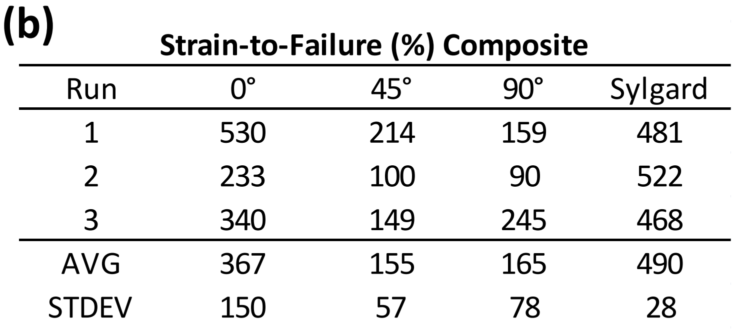

(b)

Strain-to-Failure (%) Composite

Run	0°	45°	90°	Sylgard
1	530	214	159	481
2	233	100	90	522
3	340	149	245	468
AVG	367	155	165	490
STDEV	150	57	78	28

APPENDIX 7.2

ANISOTROPIC SHAPE MEMORY ELASTOMERIC COMPOSITE (A-SMEC)

PCL(M_W~48K)/SYLGARD184 A-SMEC VS SMEC DATA COMPARISON

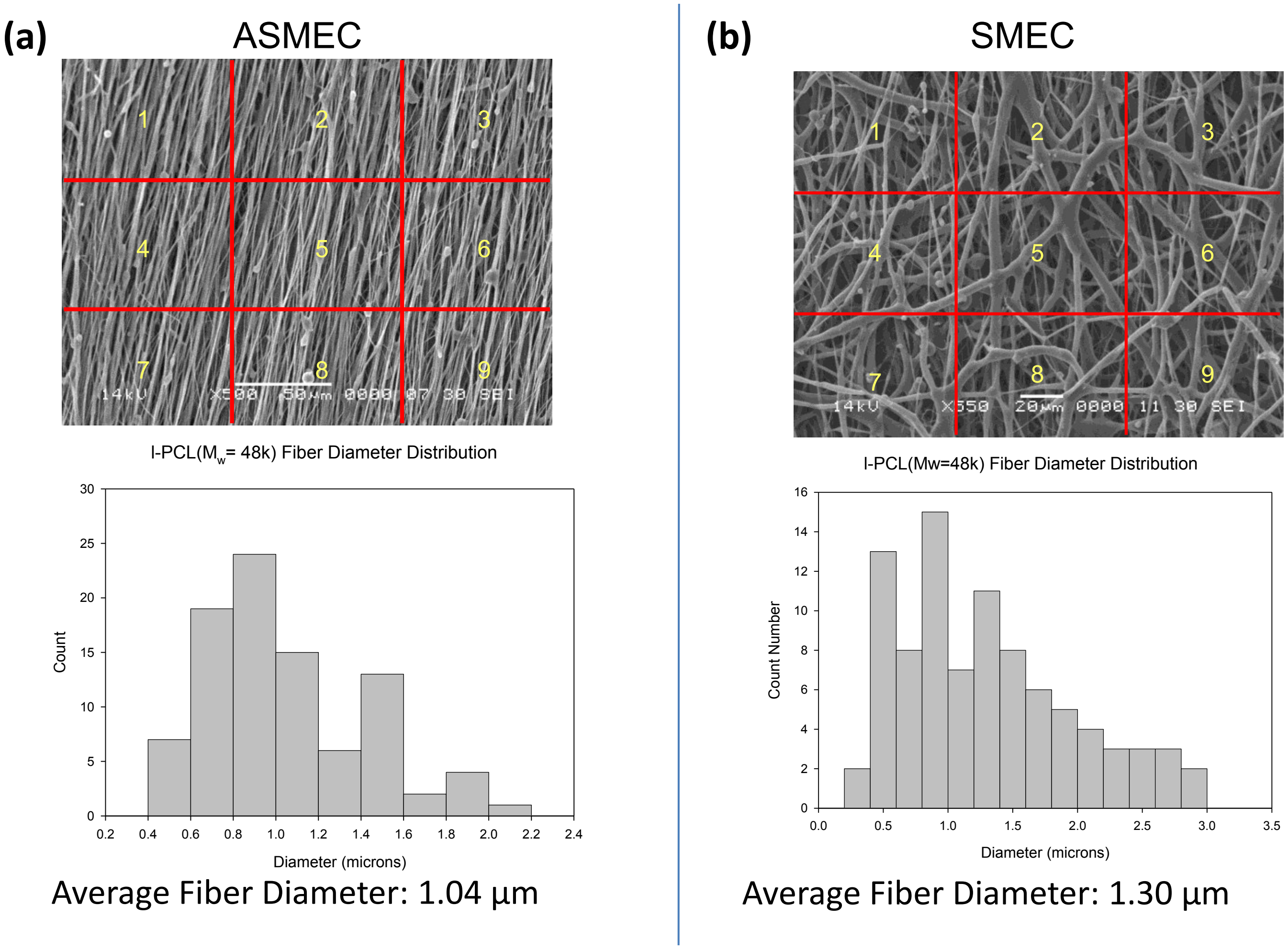

Average Fiber Diameter: 1.04 µm

Average Fiber Diameter: 1.30 µm

Figure A7.2.1. Figure showing the scanning electron microscopy (SEM) micrographs of the anisotropic and randomly aligned fiber mats used for fiber diameter comparisons. Histogram showing the distribution of the PCL fibers where the average fiber diameter is shown.

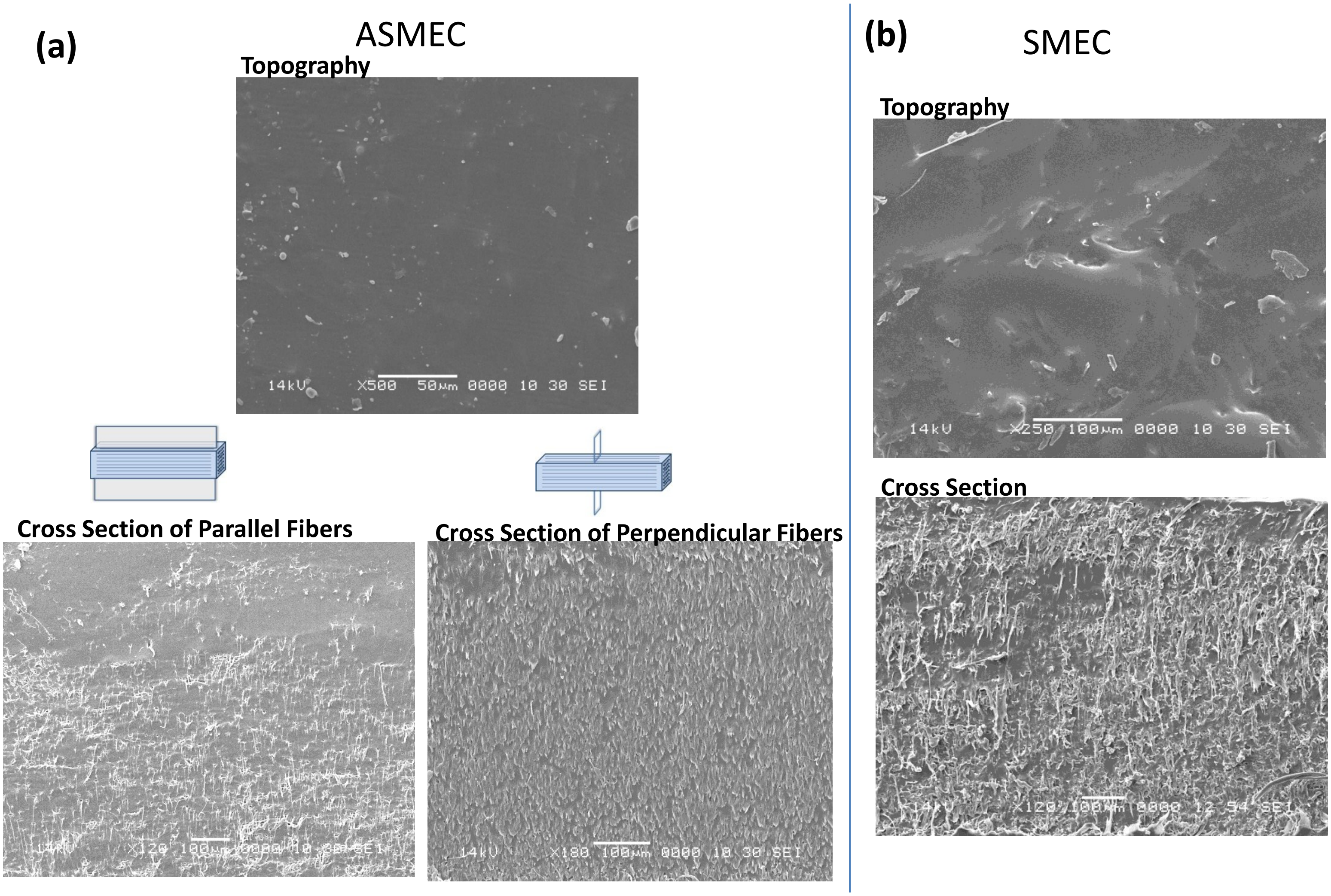

Figure A7.2.2. Scanning electron microscopy (SEM) micrographs showing the topography and morphology of the cross sections of the composite for the (a) A-SMEC and (b) SMEC systems.

Table A7.2.1. Tables showing the (a) weight of the fiber mat used to fabricate the A-SMEC and SMEC and the weight of the composite where the PCL wt-% was calculated by the difference in weights. (b) Shows the average thicknesses of the fiber mat and composites for the A-SMEC and SMEC systems.

(a)

System	Fiber Mat (g)	Composite (g)	PCL wt-%
ASMEC	0.53	2.55	20.57
SMEC	0.61	3.26	18.80

(b)

System	Sheets	Average Thickness (mm)
ASMEC	Fiber Mat	0.66
	Composite	0.86
SMEC	Fiber Mat	0.86
	Composite	1.04

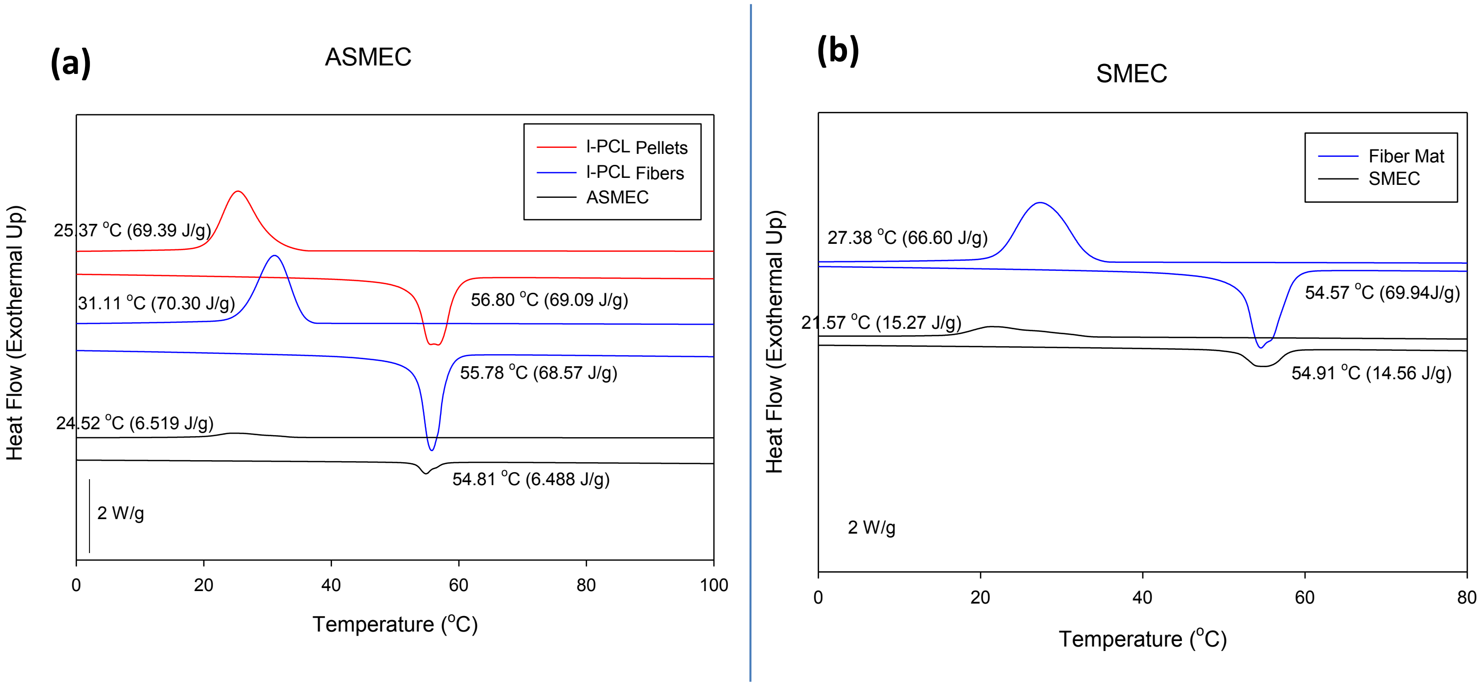

Figure A7.2.3. To study the crystalline (T_c) and melting (T_m) temperatures of systems, differential scanning calorimetry (DSC) experiments were performed. DSC traces showing (a) the 2nd heating for the A-SMEC and (b) SMEC where PCL pellets (as purchased), PCL e-spun fibers and the composite states were tested. The DSC method included equilibrating to -90.00 °C, ramped 10.00 °C/min to 120.00 °C, isothermal for 1.00 min, ramped 10.00 °C/min to -90.00 °C, isothermal for 1.00 min, and ramped 10.00 °C/min to 120.00 °C.

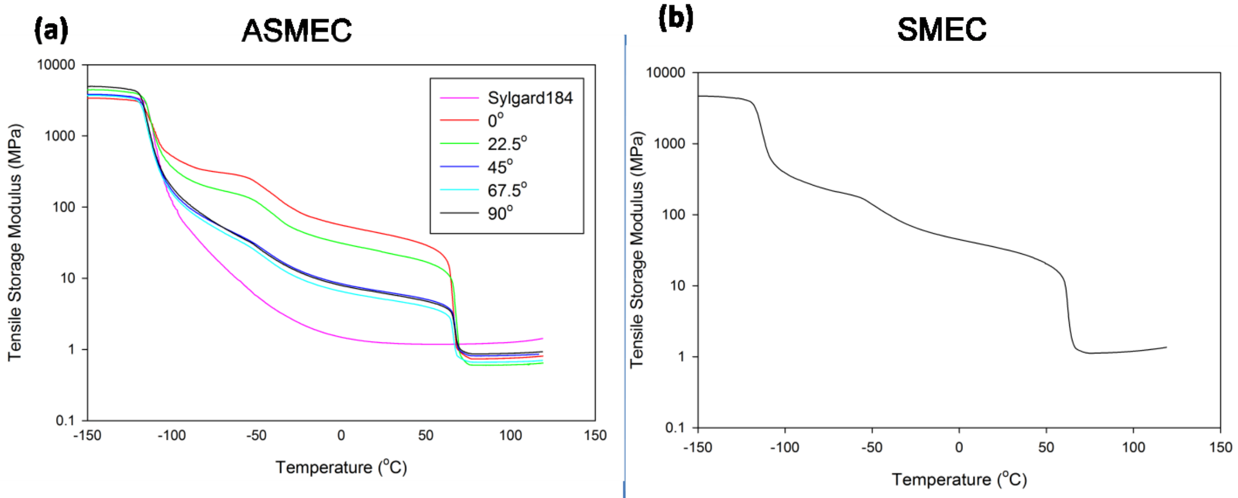

Angle (°)	$E'_{-150°C}$ (MPa)	$E'_{-50°C}$ (MPa)	$E'_{25°C}$ (MPa)	$E'_{60°C}$ (MPa)	$E'_{100°C}$ (MPa)
Sylgard184	3577	5.6	1.2	1.2	1.3
0	3271	220.3	42.1	21.1	0.8
22.5	4438	118.4	23.3	13.2	0.6
45	3431	29.4	6.5	4.3	0.8
67.5	3478	23.8	5.1	3.3	0.7
90	4560	27.8	6.2	4.0	0.9

	$E'_{-150°C}$ (MPa)	$E'_{-50°C}$ (MPa)	$E'_{25°C}$ (MPa)	$E'_{60°C}$ (MPa)	$E'_{100°C}$ (MPa)
SMEC	4463	139.5	32.87	12.07	1.192

Figure A7.2.4. To study the viscoelastic polymeric properties of the systems, dynamic mechanical analysis (DMA) was conducted. Graph showing the tensile storage modulus (E') as a function of temperature for (a) all the composites at various angles (A-SMEC) and (b) for the SMEC tested. The DMA method included equilibrating the temperature at -150.00 °C, isothermal for 5.00 min, ramping 3.00 °C/min to 120.00 °C. The charts correspond to each graph where the E' was recorded at -150 ° C, -60 ° C, 25 ° C, 60 ° C and 100 ° C.

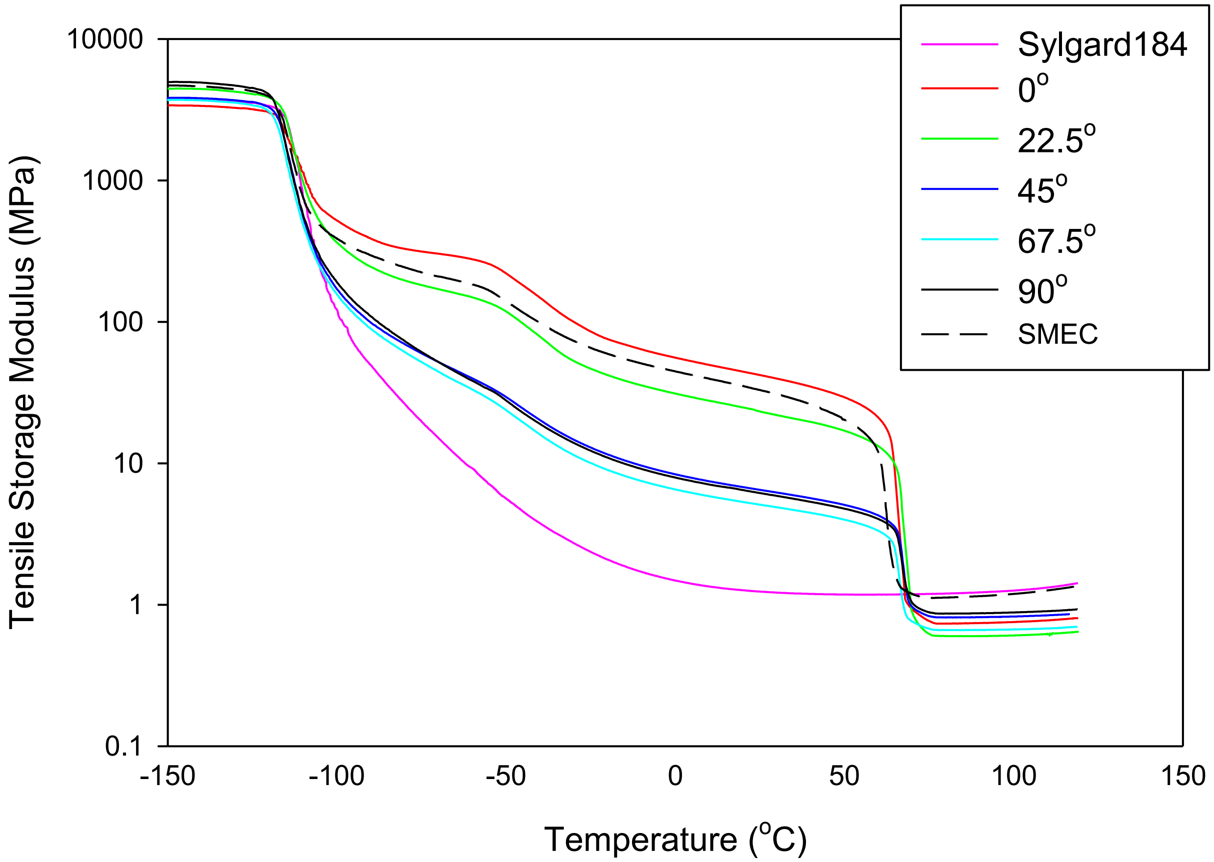

Figure A7.2.5. Graph showing the tensile storage modulus (E') as a function of temperature where the SMEC data was overlaid with the A-SMEC data for comparisons.

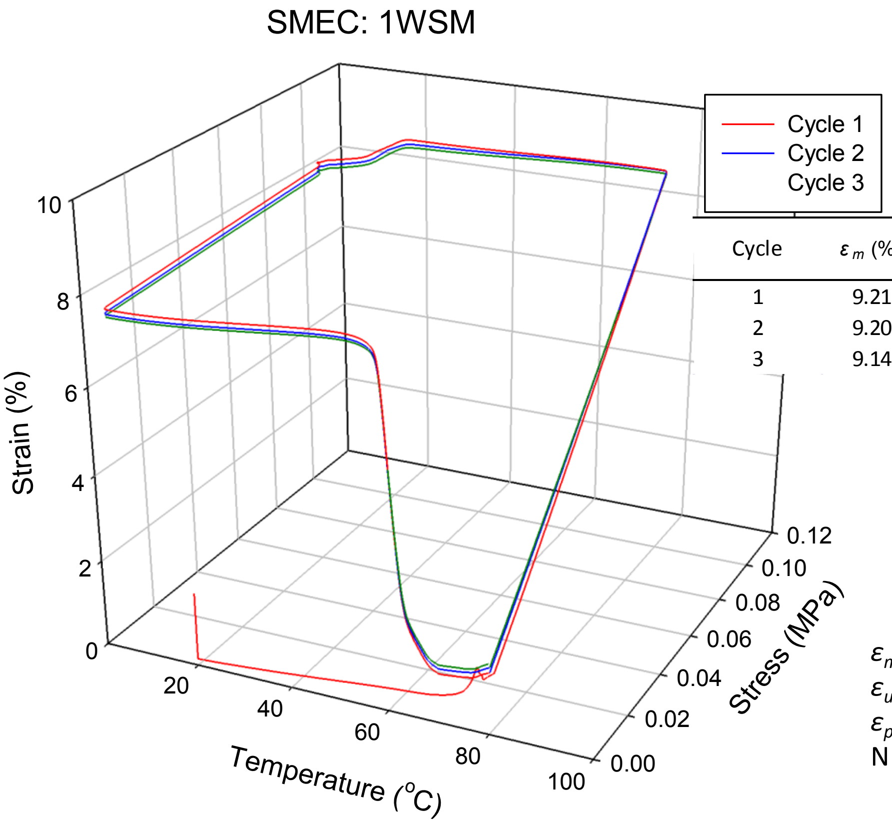

Cycle	ε_m (%)	ε_u (%)	ε_p (%)	ε_p (N-1) (%)	R_f (%)	R_r (%)
1	9.21	7.87	1.45	1.57	85.4	102.0
2	9.20	7.76	1.56	1.45	84.3	98.1
3	9.14	7.69	1.64	1.57	84.2	98.8

Fixing Ratio

$$R_f(N) = \frac{\varepsilon_u(N)}{\varepsilon_m(N)} \times 100\%$$

Recovery Ratio

$$R_r(N) = \frac{\varepsilon_u(N) - \varepsilon_p(N)}{\varepsilon_u(N) - \varepsilon_p(N-1)} \times 100\%$$

ε_m = maximum strain achieved by deformation
ε_u = fixed strain after unloading
ε_p = permanent strain after recovery
N = cycle number

Figure A7.2.6. 3D plot showing a three cycle conventional one way shape memory (1WSM) for a SMEC specimen. The equations displaced were used to calculate the fixing (R_f) and recovery (R_r) ratios where the chart shows the numerical values of R_f and R_r. The 1WSM method involved equilibrating the temperature to 80.00 °C, isothermal for 1.00 min, ramped force at 0.0500 N/min to 0.35 N, isothermal for 2.00 min, ramped to 2.00 °C/min to 5.00 °C, isothermal for 10.00 min, ramped to force 0.2000 N/min to 0.0010 N, isothermal for 3.00 min, ramped at 2.00 °C/min to 70.00 °C, isothermal for 1.00 min, and equilibrated at 80.00 °C to complete the cycle.

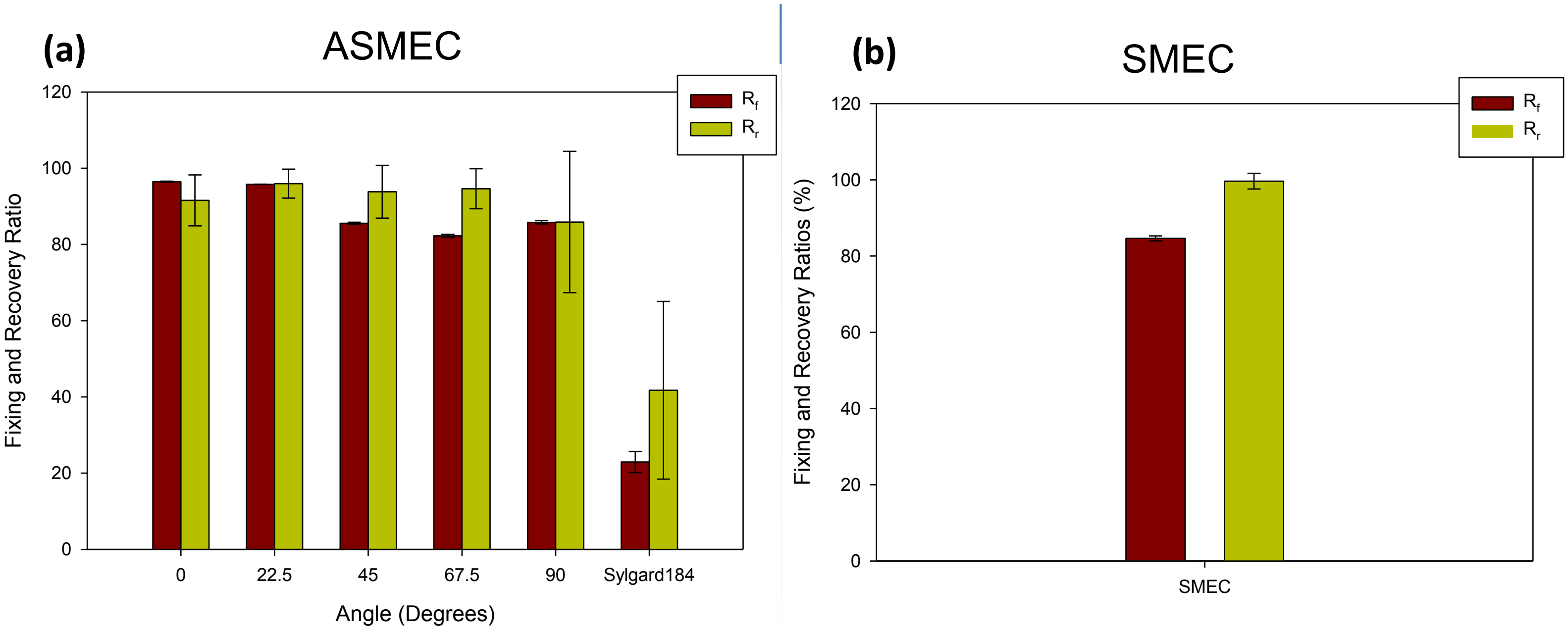

	Average F_f Ratio		Average R_r Ratio	
Angle (°)	R_f	STDEV	R_r	STDEV
0	96.5	0.1	91.6	6.7
22.5	95.8	0.1	96.0	3.8
45	85.6	0.3	93.8	6.9
67.5	82.3	0.4	94.6	5.2
90	85.8	0.4	85.9	18.5
Sylgard184	22.92	2.78	41.74	23.31

Average R_f Ratios		Average R_r Ratios	
R_f	STDEV	R_r	STDEV
84.6	0.7	99.6	2.1

Figure A7.2.7. Fixing (R_f) and recovery (R_r) ratios for the (a) A-SMEC and (b) SMEC systems. Charts correspond to the R_f and R_r for each system.

APPENDIX 7.3

ANISOTROPIC SHAPE MEMORY ELASTOMERIC COMPOSITE (A-SMEC)

PCL(M_w~65k)/SYLGARD184

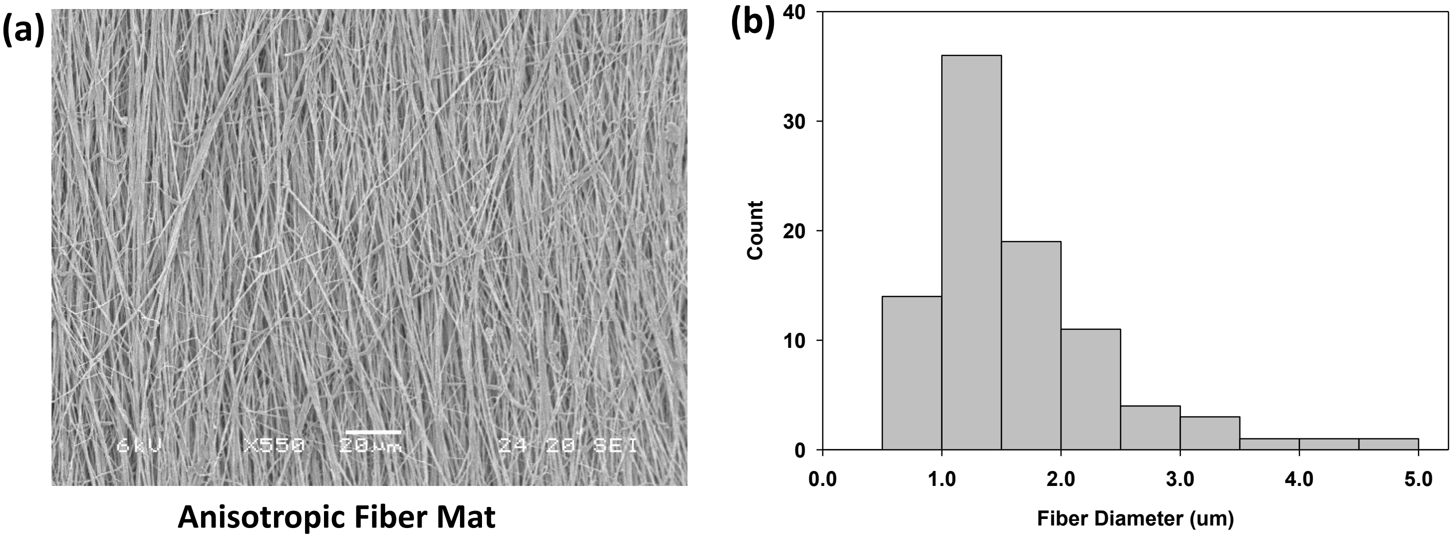

Anisotropic Fiber Mat

Average Diameter = 1.65 µm

Figure A7.3.1. (a) Scanning electron microscopy (SEM) micrographs showing the fiber topography of the fiber mat electrospun. (b) Histogram showing the distribution of the PCL fibers where the average fiber diameter is shown.

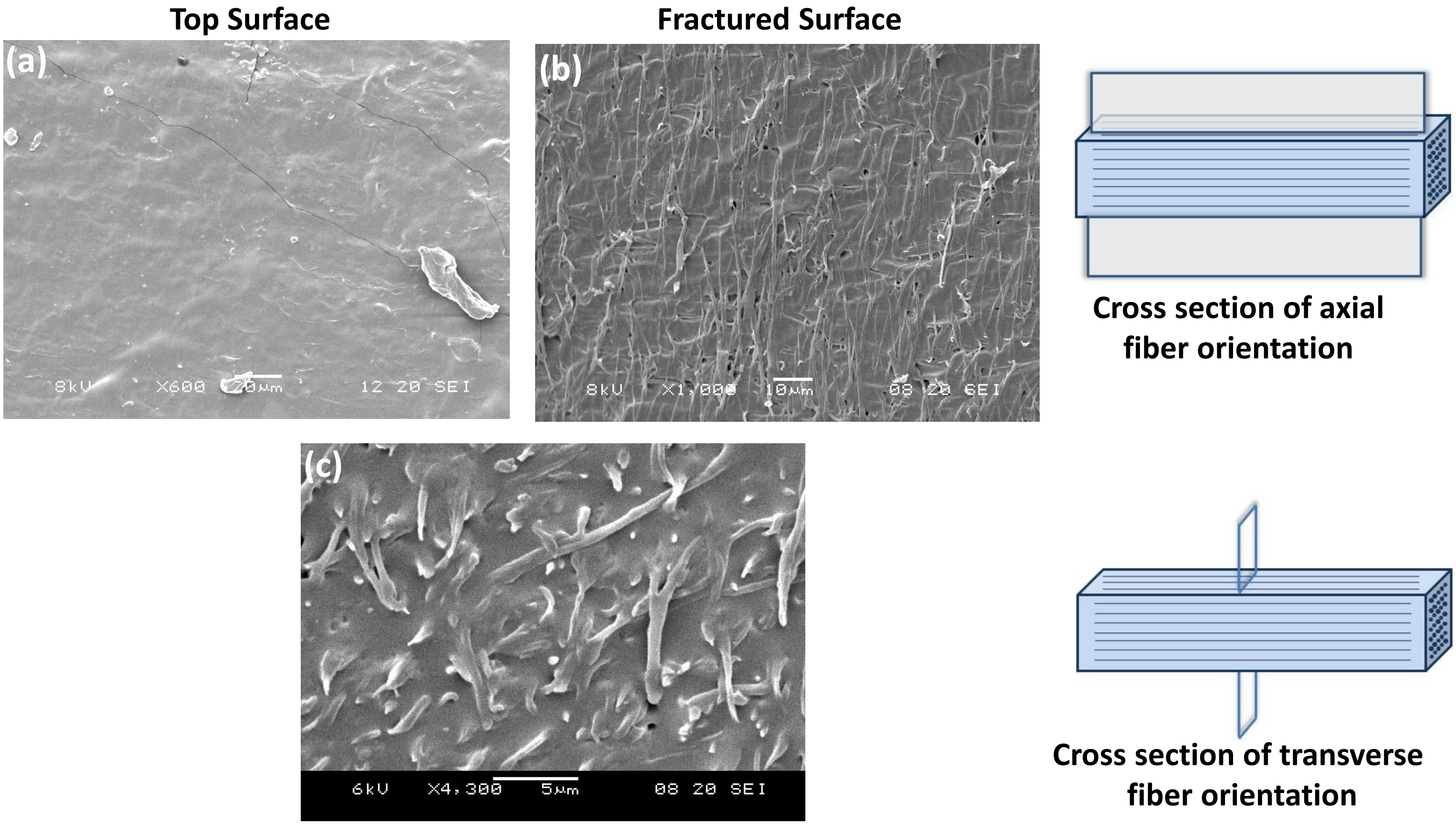

Figure A7.3.2. Scanning electron microscopy (SEM) micrographs showing (a) topography, (b) cross section in the axial direction (0°), (c) cross section in the transverse direction (90°) of the composite. The side images show a schematic of the cross section in relation to fiber orientation.

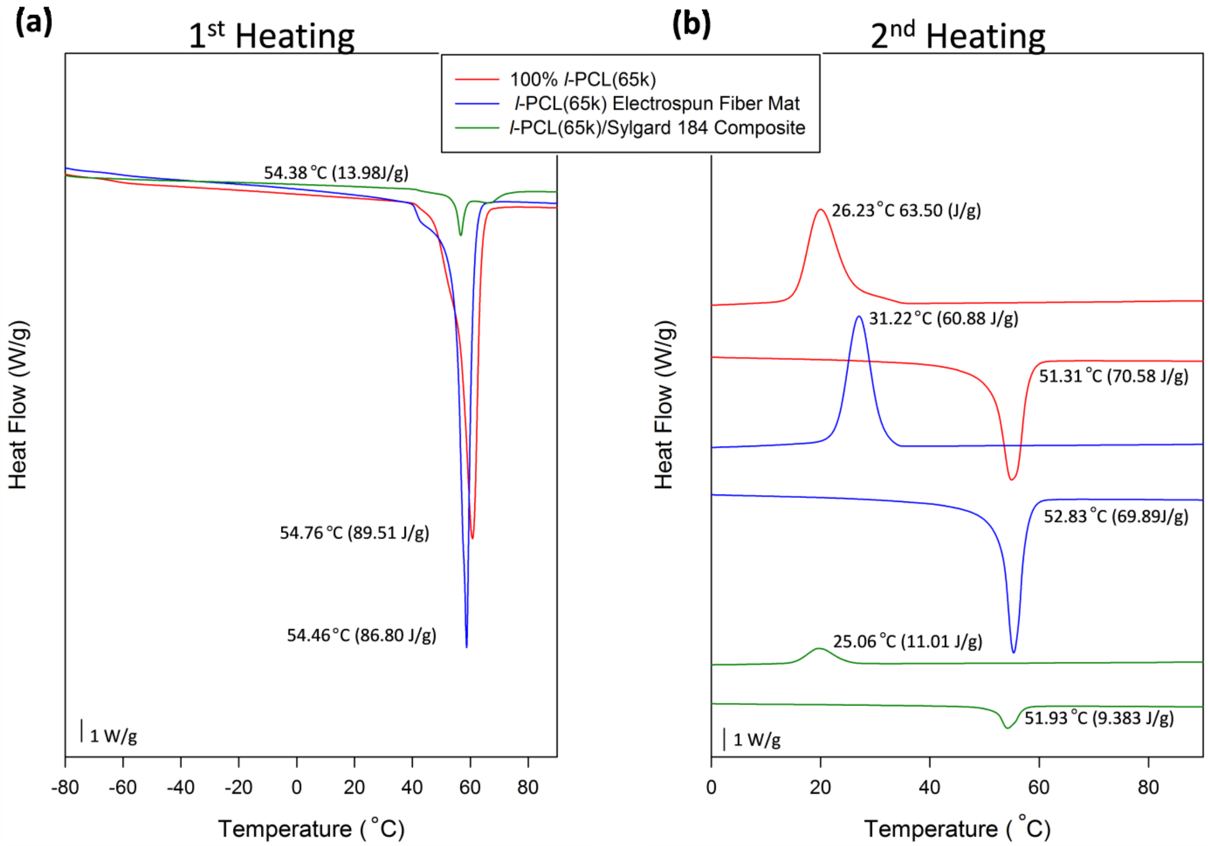

Figure A7.3.3. DSC traces showing (a) the 1st and (b) 2nd heatling for the A-SMEC system where PCL pellets (as purchased), PCL e-spun fibers and the composite states were tested. The DSC method included ramping to 10.00 °C/min to 100.00 °C, isothermal for 1.00 min, ramp at 10.00 °C/min to -10.00 °C, isothermal for 1.00 min, and ramp at 10.00 °C/min to 100.00 °C.

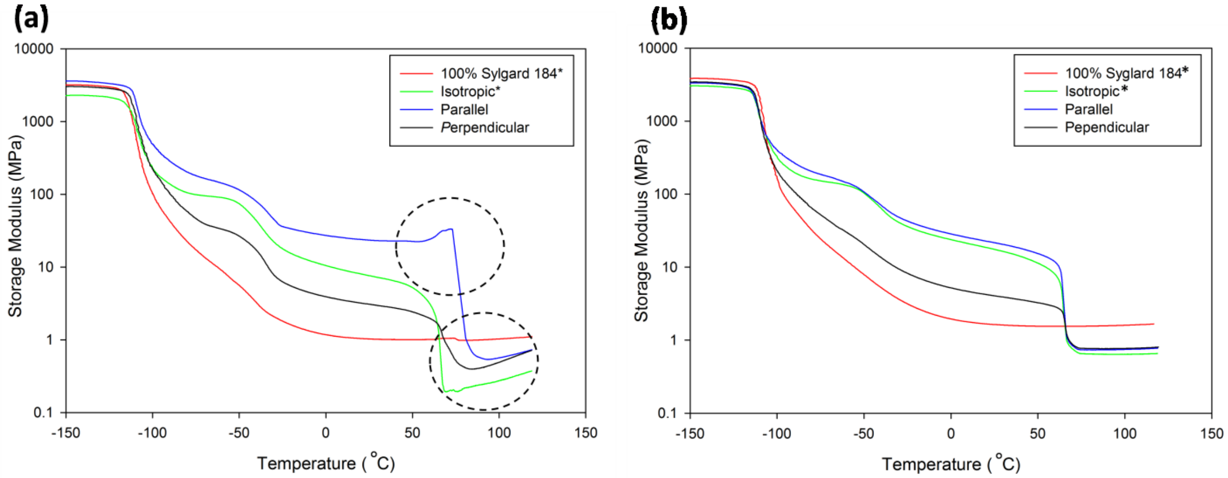

Tested As Made
Storage Modulus (MPa)

Samples	-150 °C	25 °C	80 °C	100 °C
Sylgard 184	3189.00	1.03	0.98	1.02
Composite (Isotropic)	2255.00	7.60	0.22	0.27
Composite (Parallel Fibers)	3591.00	23.36	1.44	0.56
Composite (Perpendicular Fibers)	3020.00	3.08	0.42	0.49

Thermally Conditioned
Storage Modulus (MPa)

-150 °C	25 °C	80 °C	100 °C
3809.00	1.64	1.57	1.60
3033.00	17.53	0.65	0.64
3318.00	21.62	1.73	0.74
3425.00	4.05	0.84	0.77

Figure A7.3.4. Graph showing the tensile storage modulus (E′) as a function of temperature for (a) the "as cured" composites with fibers in the axial and transverse direction where the DMA method included equilibrating at -150.00 °C, isothermal for 5.00 min, and ramped at 3.00 °C/min to 120.00 °C. (b) Shows specimens after being thermally conditioned where the DMA method included ramping at 3 °C/min to 100 °C, isothermal for 1 min, 3 °C/min to 0 °C, isothermal for 1 min, equilibrate at -150.00 °C, isothermal for 5.00 min, and ramp at 3.00 °C/min to 120.00 °C. Thermal condition was conducted as the peak in the blue curve in graph (a) was hypothesized that the specimen was completing the curing process. The charts correspond to E′ at the following temperature for the "as cured" and thermally treated specimens tested: -150 °C, 25 °C, 80 °C and 100 °C.

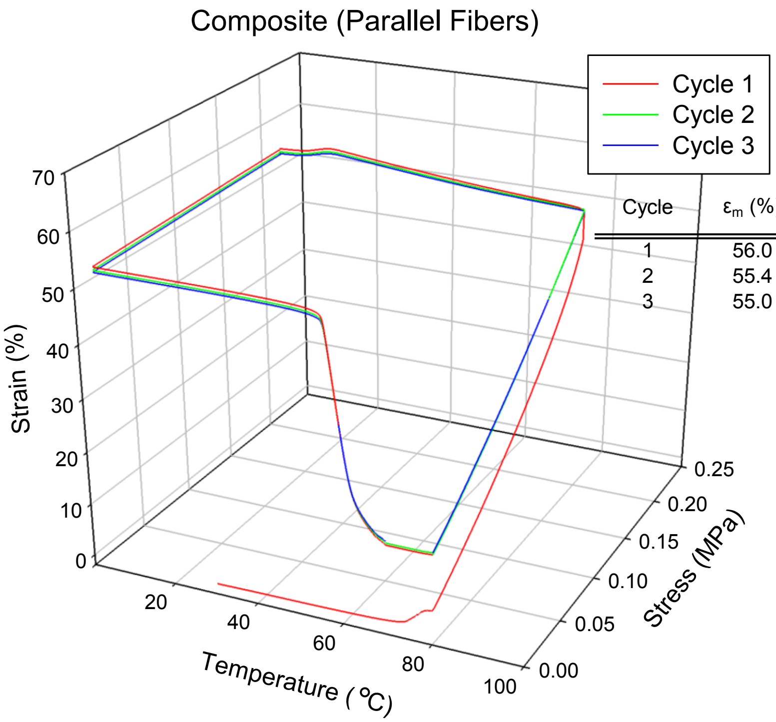

Parallel Fibers

Cycle	ε_m (%)	ε_u (%)	ε_p (%)	ε_p(N-1)(%)	R_f (%)	R_r (%)	Elastic Modulus (MPa)
1	56.0	54.7	15.0	4.5	97.7	79.2	0.38
2	55.4	54.1	15.4	15.0	97.7	99.0	0.51
3	55.0	53.8	15.6	15.4	97.7	99.5	0.51

Fixing Ratio

$$R_f(N) = \frac{\varepsilon_u(N)}{\varepsilon_m(N)} \times 100\%$$

Recovery Ratio

$$R_r(N) = \frac{\varepsilon_u(N) - \varepsilon_p(N)}{\varepsilon_u(N) - \varepsilon_p(N-1)} \times 100\%$$

ε_m = maximum strain achieved by deformation
ε_u = fixed strain after unloading
ε_p = permanent strain after recovery
N = cycle number

Figure A7.3.5. 3D plot showing a three cycle conventional one way shape memory (1WSM) for a specimen with fibers in the axial (0°) orientation. The equations displaced were used to calculate the fixing (R_f) and recovery (R_r) ratios where the chart shows the numerical values of R_f and R_r. The 1WSM method involved equilibrating the temperature to 80.00 °C, isothermal for 1.00 min, ramped force at 0.05 N/min to 0.59 N, isothermal for 2.00 min, ramped to 2.00 °C/min to 5.00 °C, isothermal for 10.00 min, ramped to force 0.2000 N/min to 0.0010 N, isothermal for 3.00 min, ramped at 2.00 °C/min to 70.00 °C, and isothermal for 1.00 min to complete the cycle.

Composite (Perpendicular Fibers)

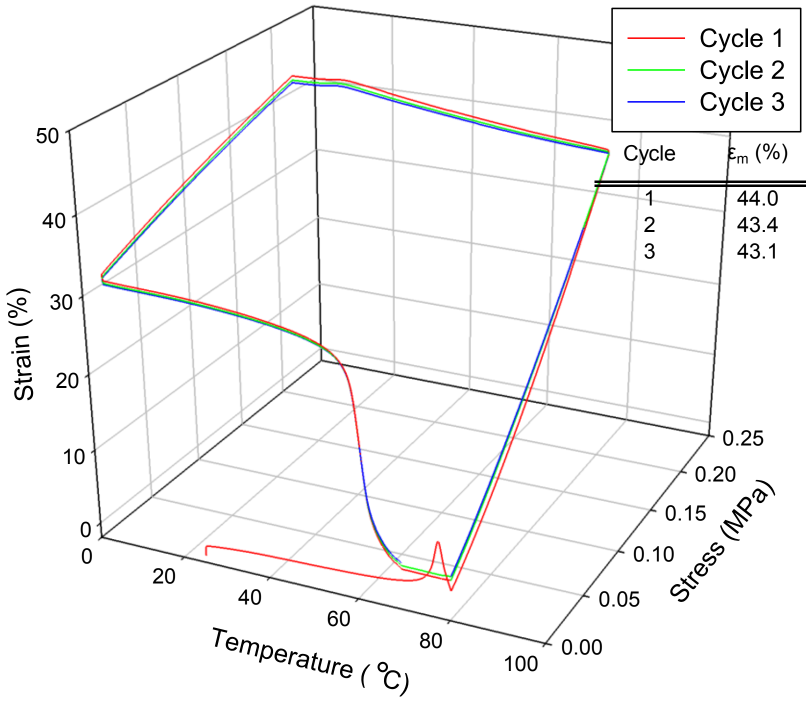

Perpendicular Fibers

Cycle	ε_m (%)	ε_u (%)	ε_p (%)	ε_p(N-1)(%)	R_f (%)	R_r (%)	Elastic Modulus (MPa)
1	44.0	33.9	3.4	2.2	77.1	96.3	0.38
2	43.4	33.5	3.9	3.4	77.3	98.3	0.51
3	43.1	33.4	4.1	3.9	77.5	99.1	0.51

Fixing Ratio

$$R_f(N) = \frac{\varepsilon_u(N)}{\varepsilon_m(N)} \times 100\%$$

Recovery Ratio

$$R_r(N) = \frac{\varepsilon_u(N) - \varepsilon_p(N)}{\varepsilon_u(N) - \varepsilon_p(N-1)} \times 100\%$$

ε_m = maximum strain achieved by deformation
ε_u = fixed strain after unloading
ε_p = permanent strain after recovery
N = cycle number

Figure A7.3.6. 3D plot showing a three cycle conventional one way shape memory (1WSM) for a specimen with fibers in the transverse (90°) orientation. The equations displaced were used to calculate the fixing (R_f) and recovery (R_r) ratios where the chart shows the numerical values of R_f and R_r. The 1WSM method involved equilibrating the temperature to 80.00 °C, isothermal for 1.00 min, ramped force at 0.0500 N/min to 0.45 N, isothermal for 2.00 min, ramped to 2.00 °C/min to 5.00 °C, isothermal for 10.00 min, ramped to force 0.2000 N/min to 0.0010 N, isothermal for 3.00 min, ramped at 2.00 °C/min to 70.00 °C, and isothermal for 1.00 min to complete the cycle.

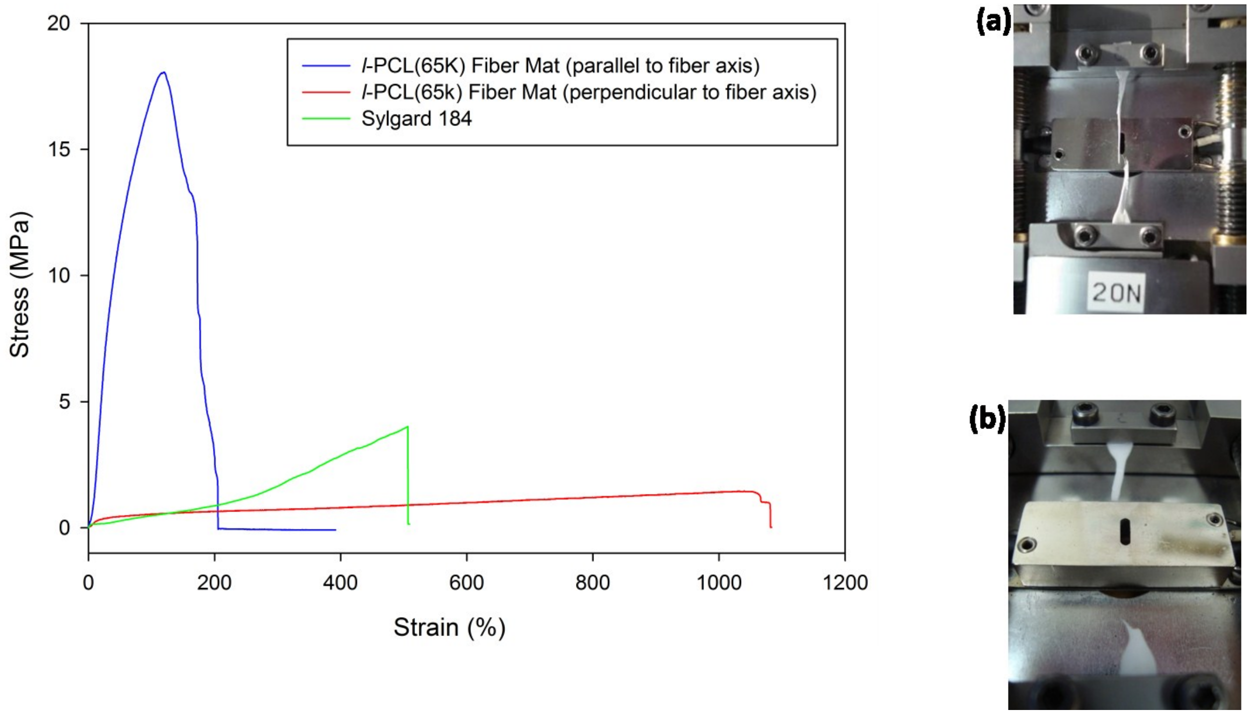

Figure A7.3.7. Stress-strain curves showing data for A-SMEC dogbone specimen with fibers in the axial and transverse direction where Sylgard184 is plotted as a reference. The dogbone geometry followed the ASTM standard D638-03 Type IV, scaled down by a factor of 4. The data was collected on the Linkam tensile stage where the following parameters were used: load cell: 20 N, stretch temperature: 25 °C, and deformation velocity: 50 µm/sec. (a) Image of specimen with fibers in the axial direction, and (b) specimen with fibers in the transverse direction deformed in Linkam tensile stage.

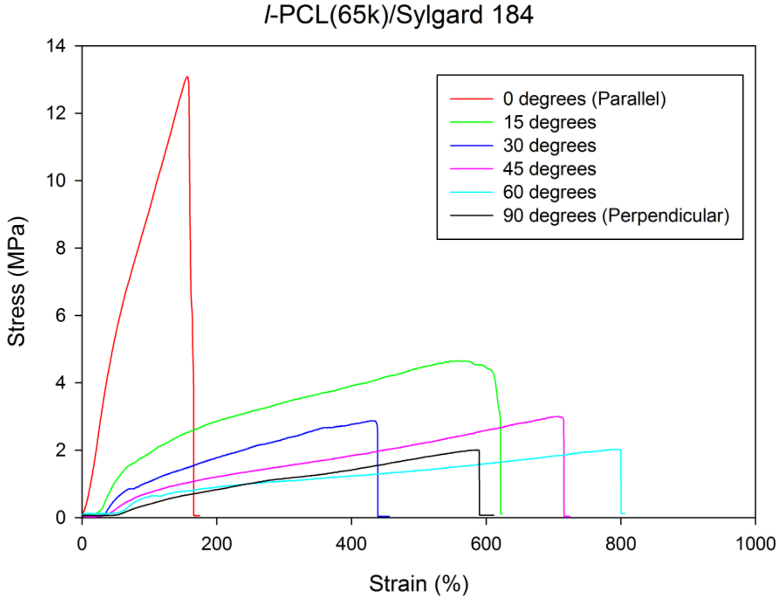

FIBER MAT: Dogbone			COMPOSITE: Dogbone			
Angle	**Weight (mg)**	**Average Thickness (mm)**	**Angle**	**Weight (mg)**	**Average Thickness (mm)**	**PCL wt-%**
0 (Parallel)	16.39	0.71	0 (Parallel)	87.9	0.89	18.65
15	15.45	0.46	15	68.66	0.70	22.50
30	12.06	0.37	30	51.79	0.52	23.29
45	12.75	0.37	45	53.57	0.53	23.80
60	12.62	0.42	60	59.93	0.60	21.06
90 (Perependicular)	14.86	0.44	90 (Perependicular)	87.92	0.95	16.90

Figure A7.3.8. Stress-strain curves showing data for A-SMEC dogbone specimens with fibers in the following fiber orientations: 0°, 15°, 30°, 45°, 60°, and 90°. The dogbone geometry followed the ASTM standard D638-03 Type IV, scaled down by a factor of 4. The data was collected on the Linkam tensile stage where the following parameters were used: load cell: 20 N, stretch temperature: 25 °C, and deformation velocity: 50 µm/sec. Charts show the weights and thicknesses of the fiber and composite dogbone specimens where the PCL wt-% was calculated from the difference in weights for all specimens tested. Images are the angle templates used to cut out the dogbones at the respective angles.

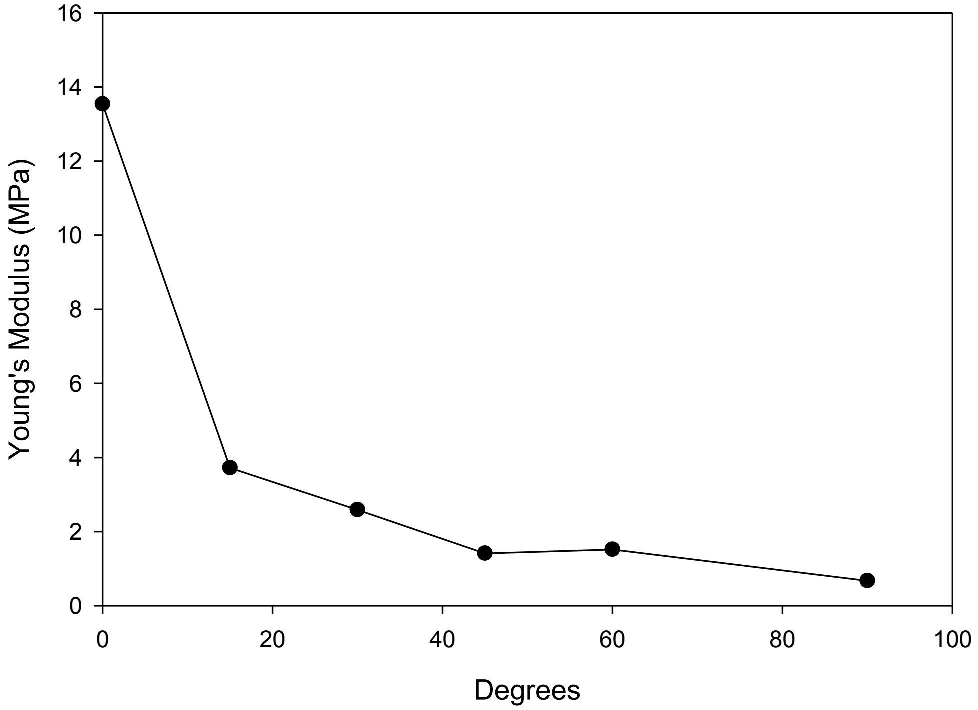

Angle	Youngs Modulus (MPa)
0 (Parallel)	13.54
15	3.72
30	2.58
45	1.41
60	1.51
90 (Perependicular)	0.67

Figure A7.3.9. Graph of Young modulus vs fiber orientation for all composites tested. The chart shows the Young's modulus numerical values in relation to fiber orientation in the composite.

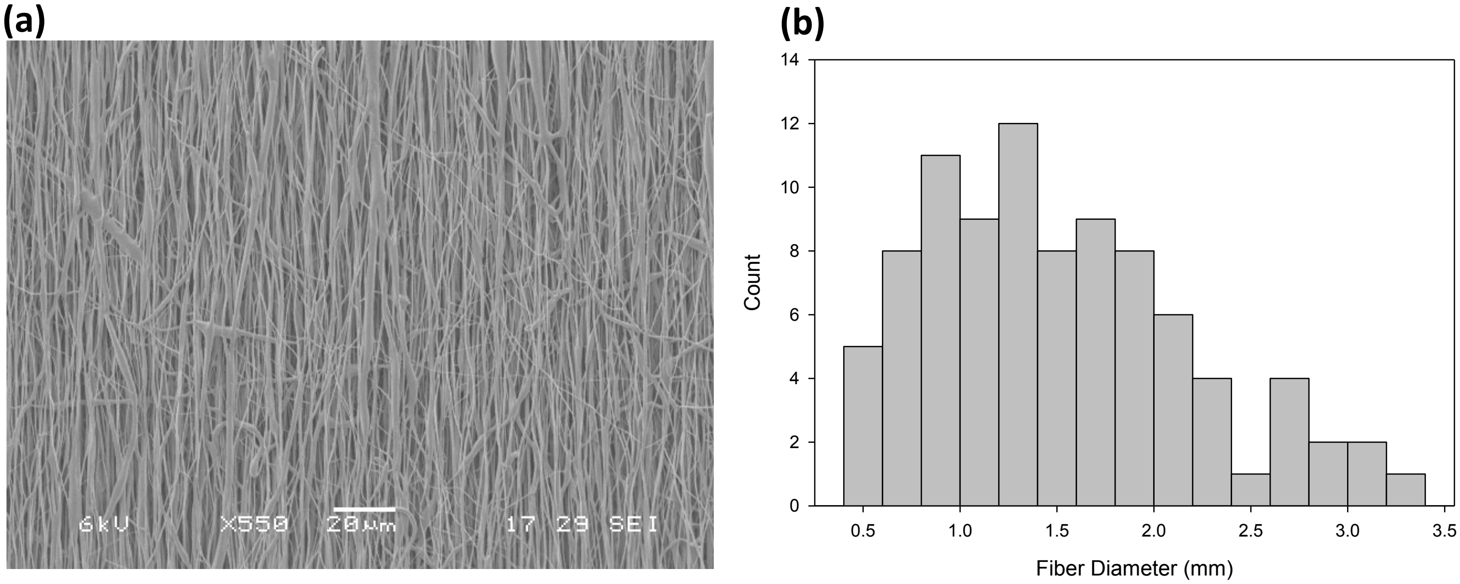

Average Diameter = 1.50 µm

Figure A7.3.10. (a) Scanning electron microscopy (SEM) micrographs showing the fiber topography of the fiber mat electrospun. (b) Histogram showing the distribution of the PCL fibers where the average fiber diameter is shown. This fiber mat was used to fabricate PCL A-SMEC laminated composite.

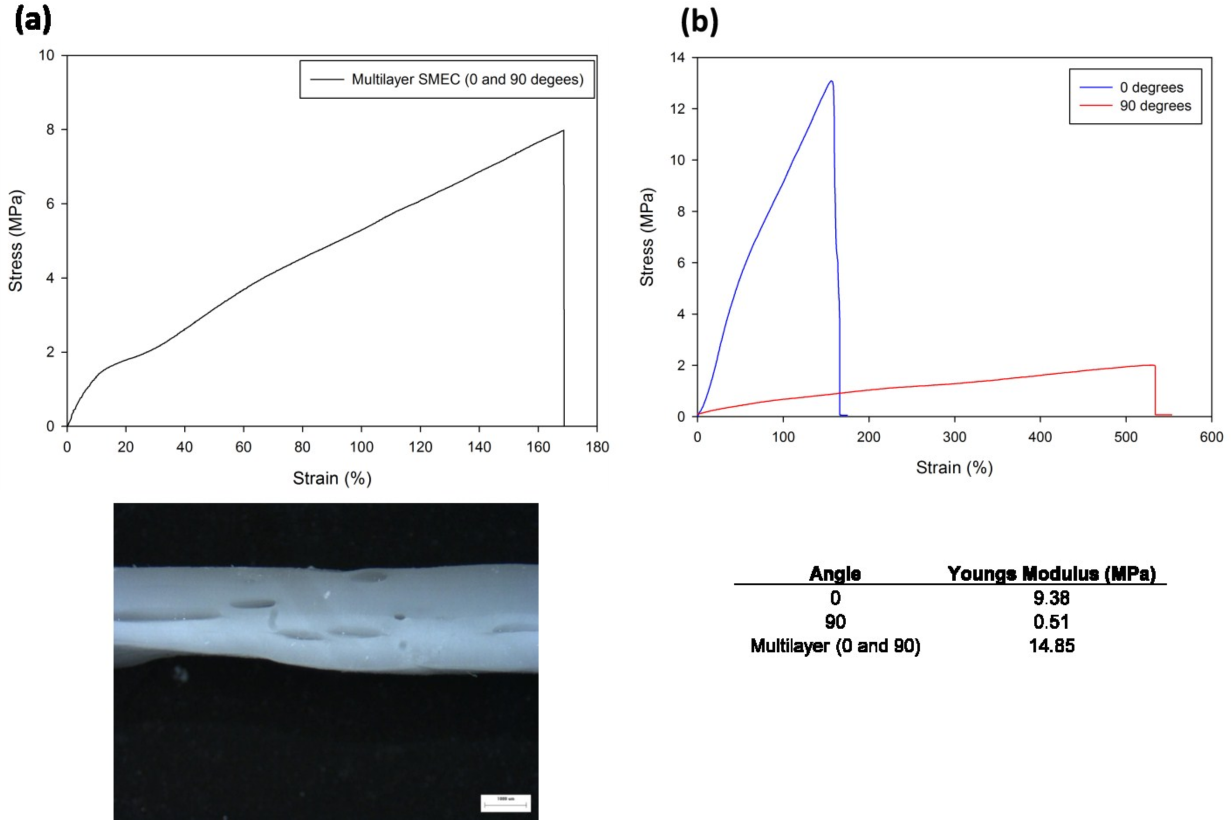

Angle	Youngs Modulus (MPa)
0	9.38
90	0.51
Multilayer (0 and 90)	14.85

Figure A7.3.11. (a) Stress-strain curve for a laminated composite where ply 1 had fibers in the axial direction and ply 2 had fibers in the transverse direction. The steromicrograph shows the cross section of the laminated composite. (b) Stress-strain curve for a single ply composite where the chart shows the corresponding Young's modulus of each system tested.

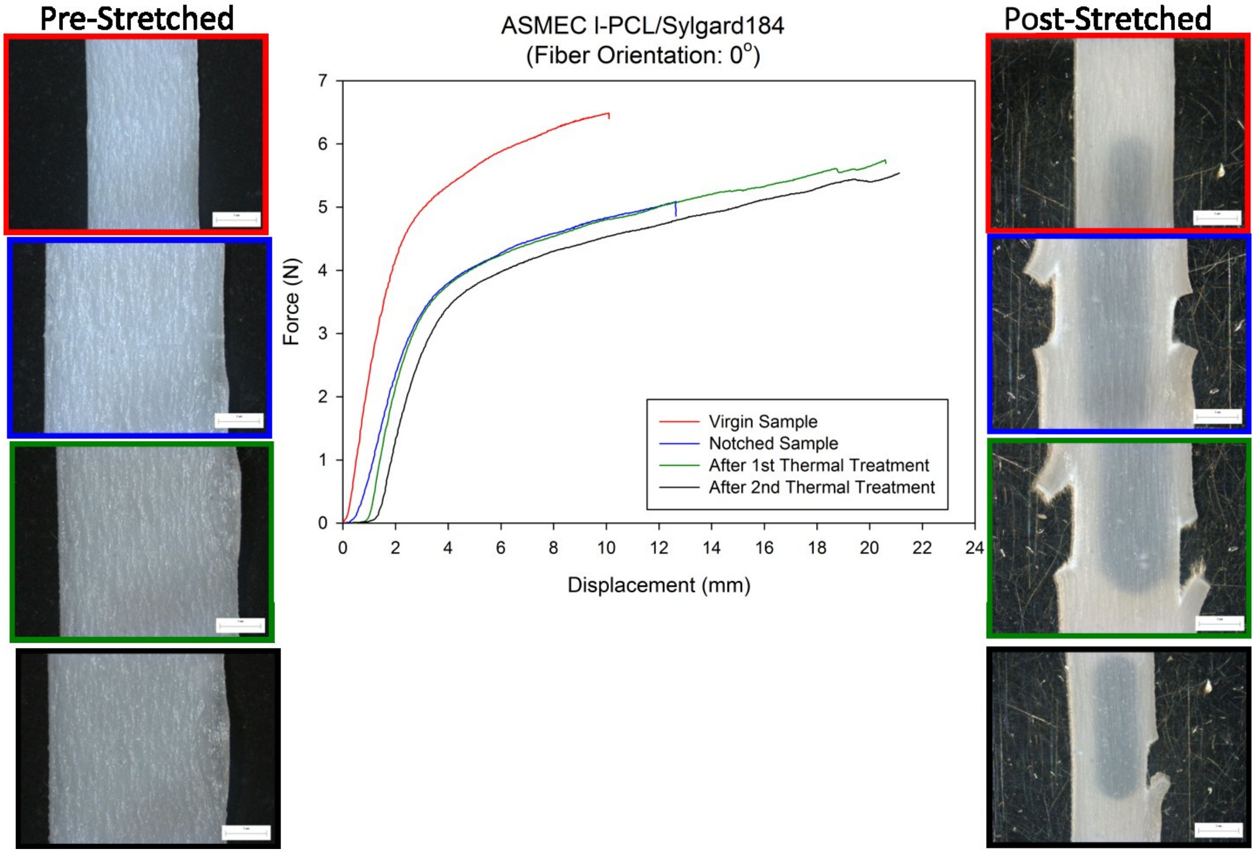

Figure A7.3.12. Stress-strain graph for a PCL A-SMEC system with fibers in the axial (0°) direction. Mechanical testing was performed on a specimen in its virgin, damaged (notched), and after the 1^{st} and 2^{nd} thermally treated states. The stereomicrographs show the specimen in its respective states. The mechanical testing was conducted on the Linkam tensile stage where the following parameters were used: load cell: 20 N, stretch temp: RT, and stretch speed: 100 μm/sec. The 1^{st} thermal treatment was 80 °C for 10 min and the 2^{nd} thermal treatment was 80 °C for 1h. The average thickness of this specimen was 0.34 mm. The data shows that the cracks do not propagate in a linear fashion along the width of the sample, but instead propagate parallel to the fiber orientation. The fibers that are parallel to the loading direction serve as reinforcements to prevent crack opening and propagation. It can be hypothesized that the reason for the crack growing parallel to the load is due to the elastomer matrix’s low modulus between the fiber bundles where the cracks are guided by taking the least resistant path.

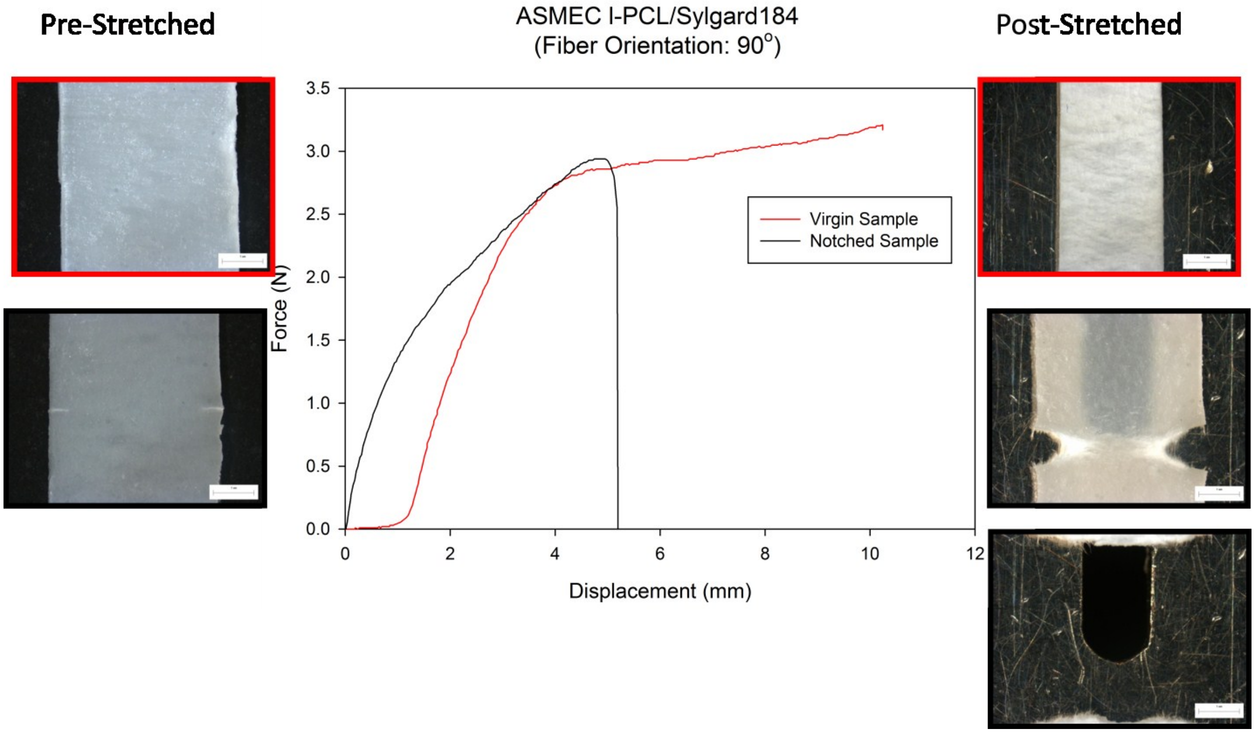

Figure A7.3.13. Stress-strain graph for a PCL A-SMEC system with fibers in the transverse direction. Mechanical testing was performed on a specimen in its virgin and damaged (notched) state. The stereomicrographs show the specimen in its respective states. The mechanical testing was conducted on the Linkam tensile stage where the following parameters were used: load cell: 20 N, stretch temp: RT, and stretch speed: 100 µm/sec. The 1st thermal treatment was 80 °C for 10 min. The average thickness of this specimen was 0.40 mm. Complete fracture was evident. The fibers that are perpendicular to the loading direction have less resistance to crack growth. The fibers in the transverse direction are no longer acting as reinforcements, but instead guiding the crack to propagate in a linear path across the width of the specimen.

APPENDIX 8.0

PCL:PEG WATER TRIGGERED SMASH SYSTEMS

A8.0 SUMMARY

This appendix focuses on further proving the versatility of the shape memory assisted self healing (SMASH) concept by fabricating a water triggered SMASH system. This was done by using ploy(ε-caprolactone) (PCL) with a molecular weight (M_w) of 3k g/mol and polyethylene glycol (PEG) with a M_w of 4k g/mol. Both semi-crystalline polymers were used to cure a PCL(3k)$_{60wt\text{-}\%}$:PEG(4k)$_{40wt\text{-}\%}$ co-network shape memory network (co-SMN) where 60 wt-% of PCL and 40 wt-% of PEG was used. A thermoplastic of PCL and PEG, both with a M_w of 10k and with the same wt-% used as the co-SMN was fabricated to make a l-PCL(10k)$_{60wt\text{-}\%}$:PEG(10k)$_{40wt\text{-}\%}$ co-polymer thermoplastic healing agent. The co-SMN and thermoplastic yielded a l-PCL(10k)$_{60wt\text{-}\%}$:PEG(10k)$_{40wt\text{-}\%}$:n-PCL(3k)$_{60wt\text{-}\%}$:PEG(4k)$_{40wt\text{-}\%}$ SMASH system. PEG provides hydrophilicity while the PCL provides good mechanical properties for the overall system. co-SMN was used for crack closure and the thermoplastic was used for crack rebonding. More specifically, hot water can activate the healing due to a combination of heat-activated shape memory and water-activated PEG plasticization. Polymer characterization, thermal, thermomechanical, mechanical and shape memory and self healing experiments are shown.

APPENDIX 8.1

PCL:PEG WATER TRIGGERED SMASH SYSTEMS

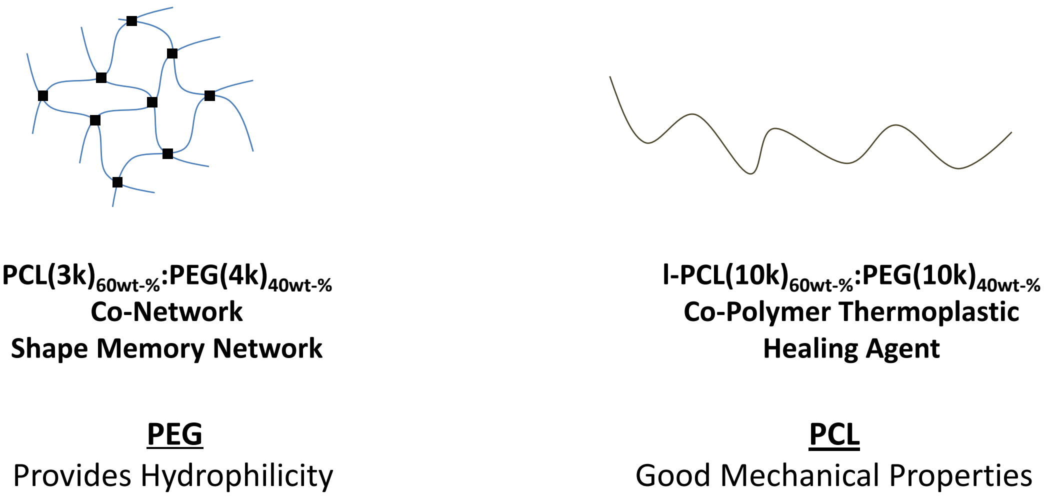

Scheme A8.1.1. Schematic of SMASH concept where hot water can activate the healing due to a combination of heat-activated shape memory and water-activated PEG plasticization.

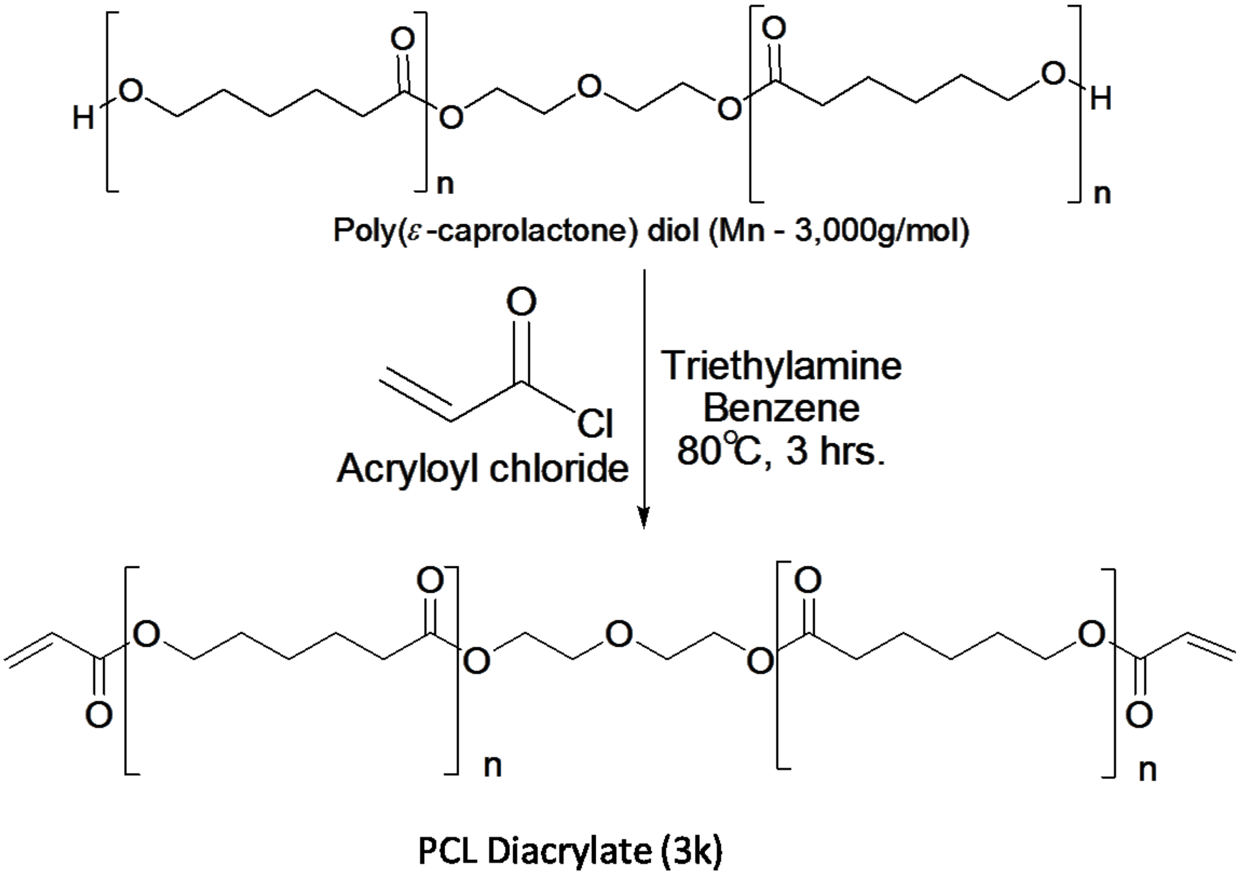

Scheme A8.1.2. Synthesis process of PCL diol to diacrylate.

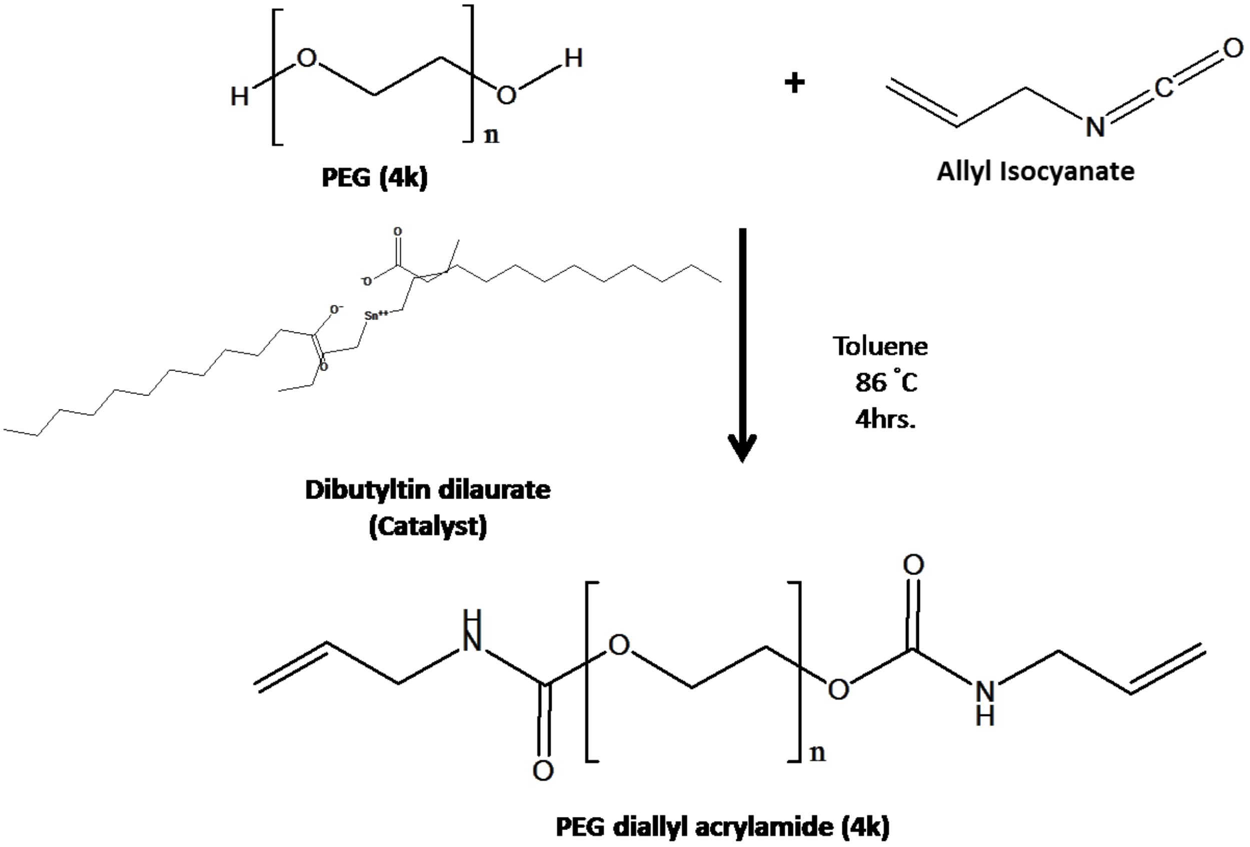

Scheme A8.1.3. Synthesis process of PEG to PEG diallyl acrylamide. (Synthesized by graduate student, Pine Yang)

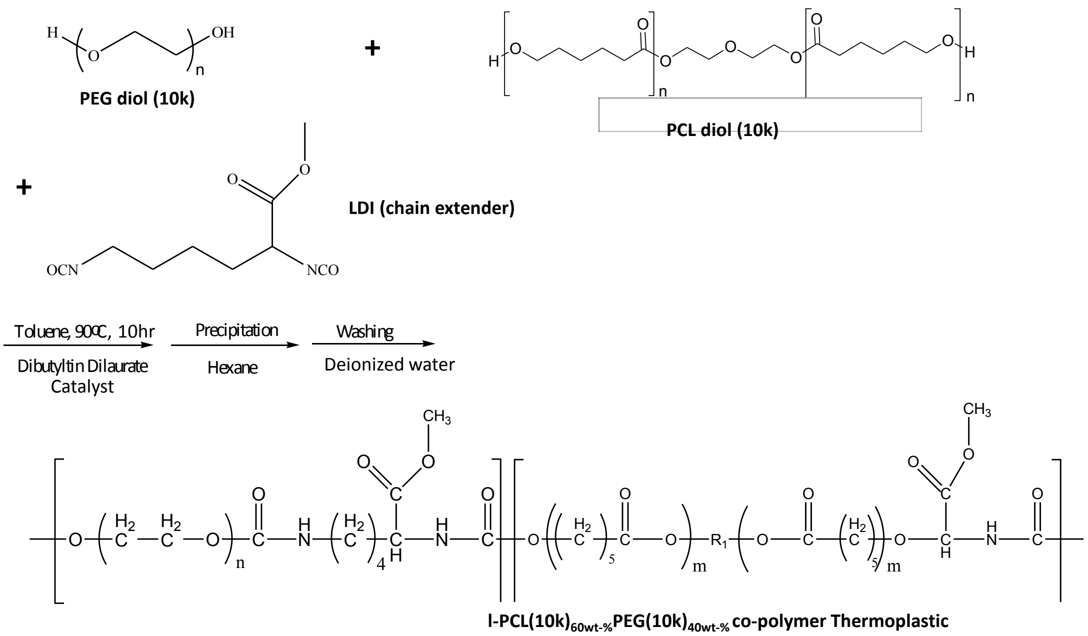

Scheme A8.1.4. Synthesis process of PCL:PEG thermoplastic (Synthesized by graduate student, Xinzhu Gu)

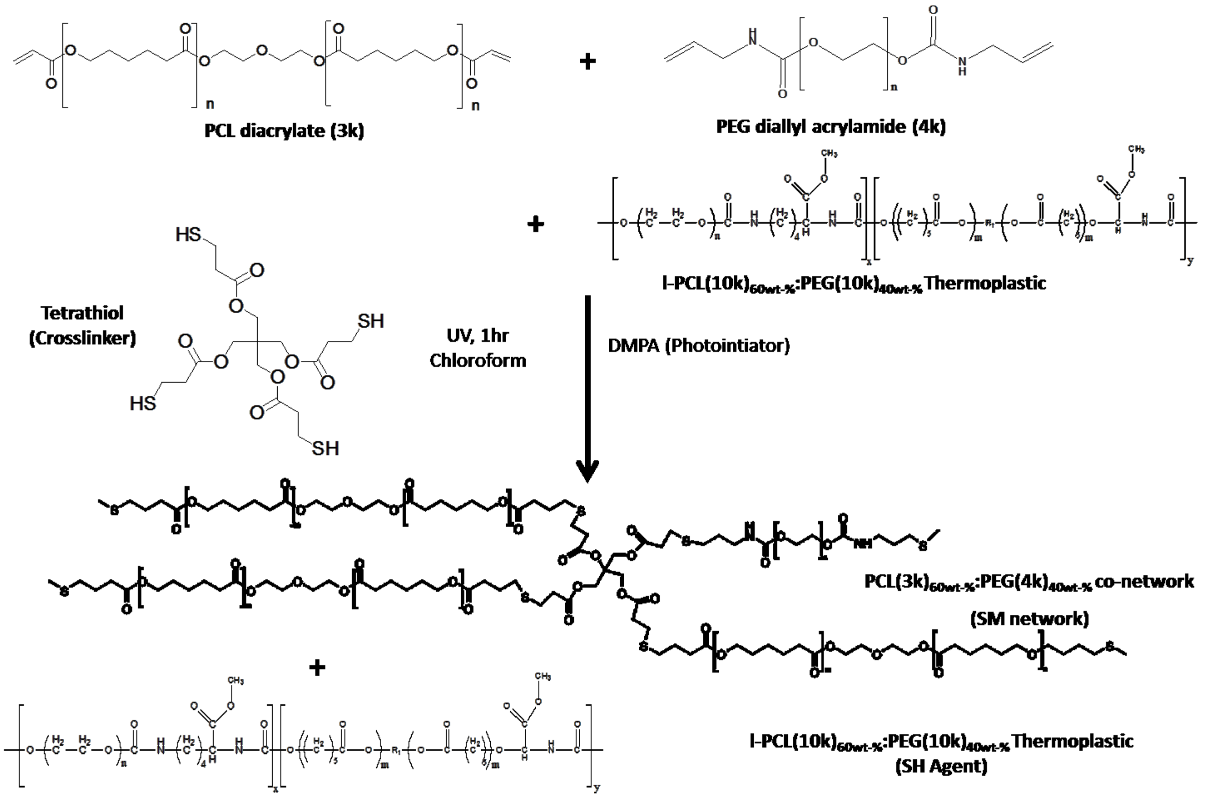

Scheme A8.1.5. Polymerization process of the PCL(3k)$_{60\text{wt-\%}}$:PEG(4k)$_{40\text{wt-\%}}$ SMASH films.

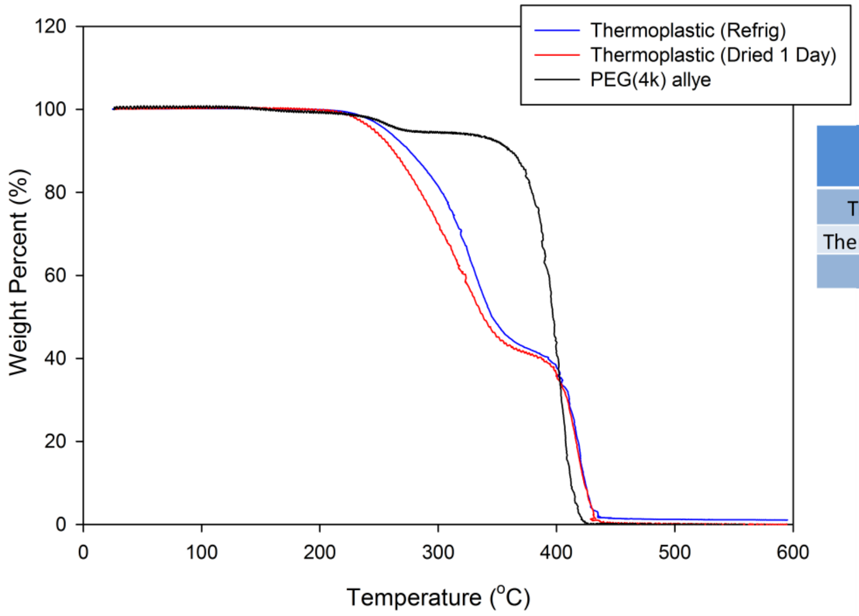

Composition	Temp at 99.5% Weight (°C)
Thermoplastic (Refrig)	220
Thermoplastic (Dried 1 day)	209
PEG (4k)	167

Figure A.8.1.1. To measure the onset degradation temperatures of the films, thermogravimetric analysis (TGA) experiments were conducted on the l-PCL(10k)$_{60wt\text{-}\%}$PEG(10k)$_{40wt\text{-}\%}$ co-polymer thermoplastic (refrigerated) and after on day of drying in the vac oven in order to ensure complete moisture removal. TGA was also conducted on the PEG(4k) allye. The graph shows the weight percent of decomposition as a function of temperature. The chart shows the temperature at 99.5% weight percent lost. The TGA method was 10 °C/min to 600 °C.

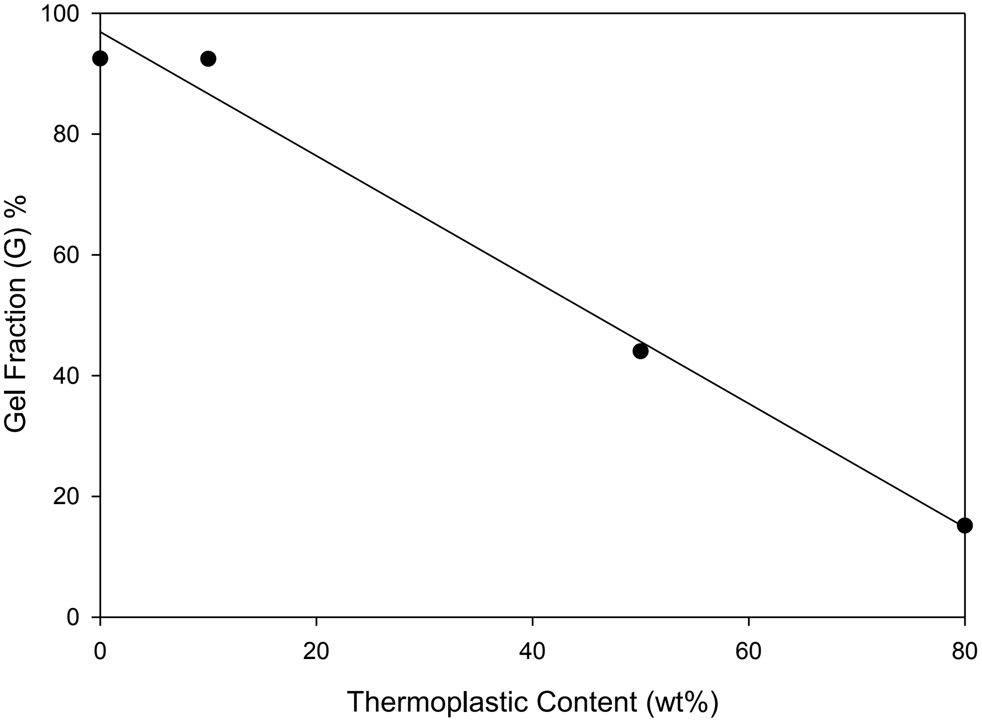

$$G(\%) = \frac{W_f}{W_i} \times 100$$

Composition	G(%)
(0:100)	92
(10:90)	92
(50:50)	44
(80:20)	15

Figure A.8.1.2. Degree of shape memory network formation was determined by gel fraction experiments where a specimen from each SMASH film were cut and weighted before and after extraction and dried in the vacuum oven over night. The graph shows the gel fraction percentage as a function of co-thermoplastic wt-% content. The equation was used to calculate the gel fractions where W_f is the weight after extraction and W_i is the weight before extraction. The chart shows the corresponding gel fractions as a function of SMASH films tested. All gel fractions were expected as the gel fractions values correspond to the wt-% of the network formed in the system. Line in graph represents the linear regression of the data where the gel fraction decreases with increasing thermoplastic content.

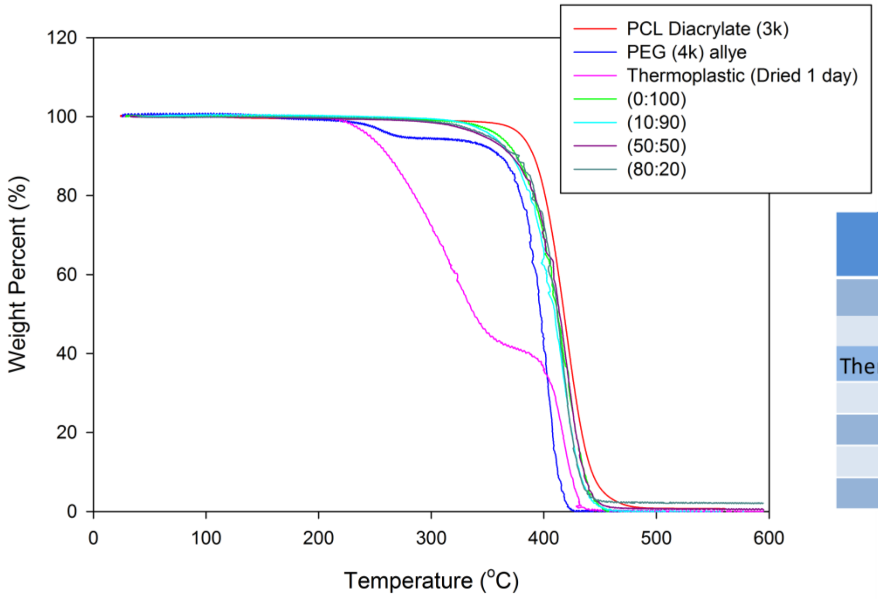

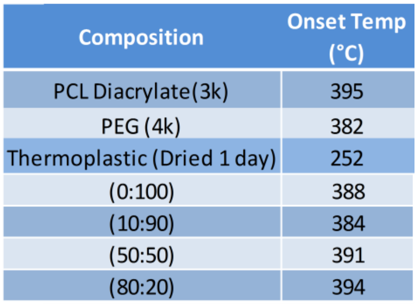

Composition	Onset Temp (°C)
PCL Diacrylate(3k)	395
PEG (4k)	382
Thermoplastic (Dried 1 day)	252
(0:100)	388
(10:90)	384
(50:50)	391
(80:20)	394

Figure A.8.1.3. To measure the onset degradation temperatures of the films, thermogravimetric analysis (TGA) experiments on all the SMASH compositions, PCL diacrylate, PEG, and PCL/PEG thermoplastic. The graph shows the weight percent of decomposition as a function of temperature. The chart shows the onset degradation temperature which ranged from 252 °C to 395 °C where the TGA method was 10 °C/min to 600 °C.

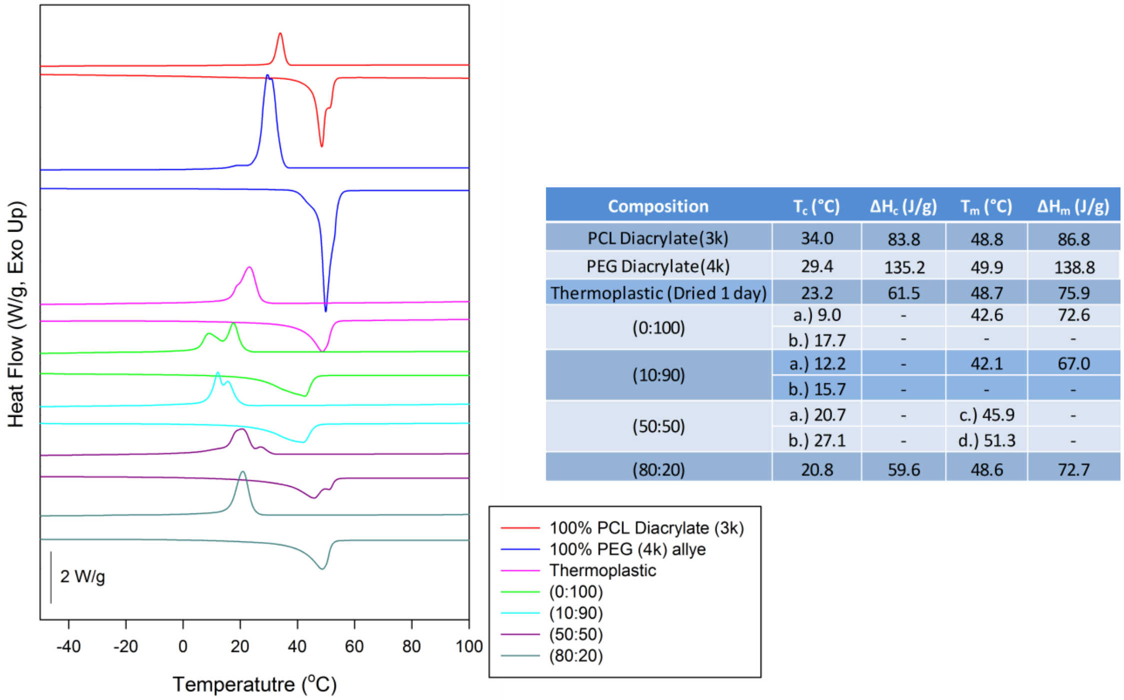

Composition	T_c (°C)	ΔH_c (J/g)	T_m (°C)	ΔH_m (J/g)
PCL Diacrylate(3k)	34.0	83.8	48.8	86.8
PEG Diacrylate(4k)	29.4	135.2	49.9	138.8
Thermoplastic (Dried 1 day)	23.2	61.5	48.7	75.9
(0:100)	a.) 9.0	-	42.6	72.6
	b.) 17.7	-	-	-
(10:90)	a.) 12.2	-	42.1	67.0
	b.) 15.7	-	-	-
(50:50)	a.) 20.7	-	c.) 45.9	-
	b.) 27.1	-	d.) 51.3	-
(80:20)	20.8	59.6	48.6	72.7

Figure A8.1.4. To measure the crystalline (T_c) and melting temperature (T_m) of all the SMASH films, differential scanning calorimetry (DSC) was used. The graph shows the heat flow as a function of temperature. The chart shows the T_m, T_c, heat of melting (ΔH_m) and heat of crystallization (ΔH_c) for all samples tested including the individual PCL and PEG diacrylate and PCL/PEG thermoplastic. a.) and b.) shown in the chart are indicative of the two small peaks in the crystalline peak. The DSC method included using a cooling rate at 10.00 °C/min to -85.00 °C and heating rate at 10.00 °C/min to 120.00 °C for all samples. The DSC method of PCL(3k) diacrylate for cooling was 3 °C/min to -85 ° C, and heating of 10 °C/min to 120 ° C.

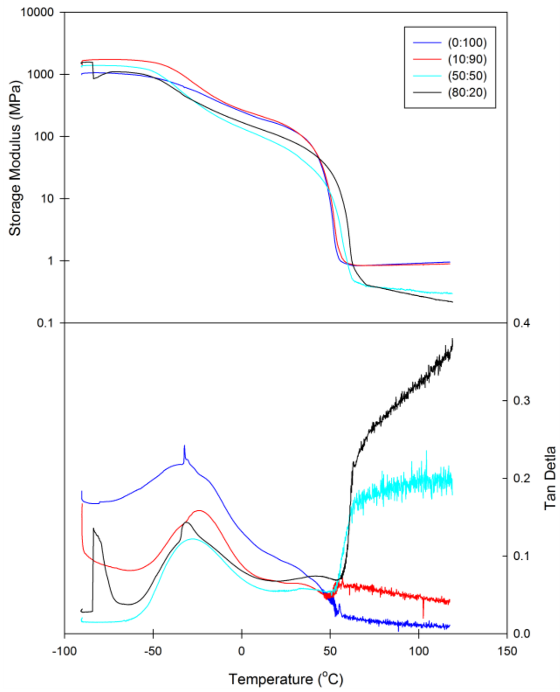

Composition	E' $_{-90\,°C}$ (MPa)	E' $_{25°C}$ (MPa)	E' $_{40°C}$ (MPa)	E' $_{80°C}$ (MPa)
(0:100)	1458	142.2	68.4	0.9
(10:90)	1641	150.3	67.8	0.9
(50:50)	1383	64.6	30.4	0.4
(80:20)	1556	92.2	54.0	0.4

Figure A8.1.5. To measure and study the viscoelastic properties, dynamic mechanical analysis (DMA) was used on all SMASH films fabricated. The top graph shows the tensile storage modulus (E’) as a function of temperature. The lower graph also shows the tan delta (ratio of storage to loss modulus) as a function of temperature. The chart corresponds to the E’ for all SMASH films tested at the following temperatures: -90 °C, 25 °C, 40 °C, and 80 °C. These temperatures were chosen to identify the thermomechanical properties during the following states: glass at -90 °C, semi-crystalline at 25 °C, and melting temperature at 40 °C and rubber state at 100 °C. The DMA method included ramping at 3.00 °C/min to 90.00 °C, isothermal for 20.00 min, ramp at 3.00 °C/min to -90.00 °C, isothermal for 5.00 min, and ramping at 3.00 °C/min to 120.00 °C.

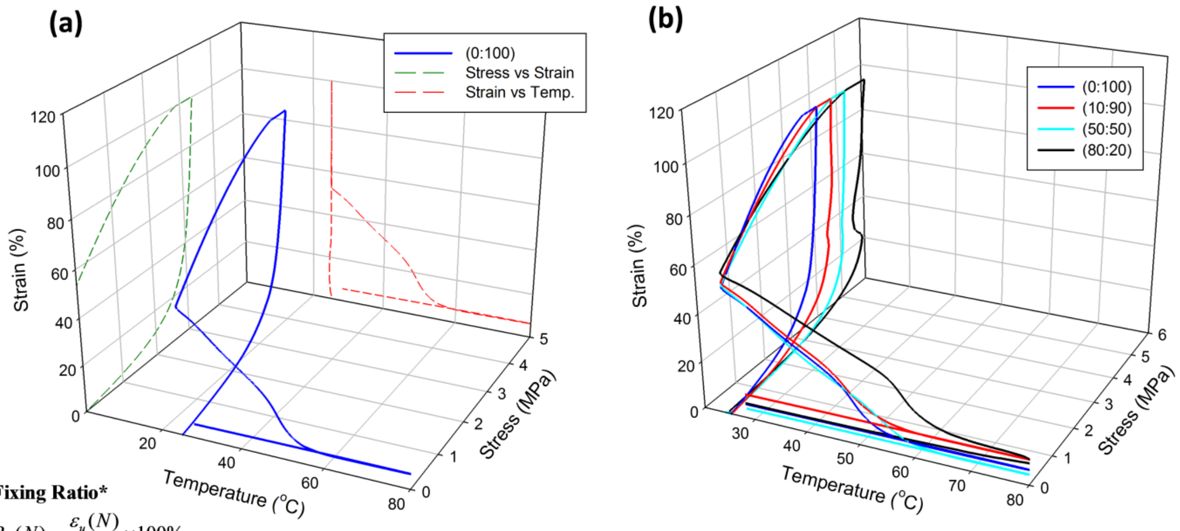

Fixing Ratio*

$$R_f(N) = \frac{\varepsilon_u(N)}{\varepsilon_m(N)} \times 100\%$$

Recovery Ratio*

$$R_r(N) = \frac{\varepsilon_u(N) - \varepsilon_p(N)}{\varepsilon_u(N) - \varepsilon_p(N-1)} \times 100\%$$

ε_m = maximum strain achieved by deformation
ε_u = fixed strain after unloading
ε_p = permanent strain after recovery
N = cycle number

Composition	ε_m (%)	ε_u (%)	ε_p (%)	ε_p (N-1) (%)	R_f (%)	R_r (%)
(0:100)	100	53.5	5.8	0.0034	53.5	89.1
(10:90)	100	55.7	10.0	0.0243	55.7	82.1
(50:50)	100	54.5	3.9	0.0104	54.5	92.8
(80:20)	100	59.5	6.2	0.0009	59.5	89.5

Figure A8.1.6. To measure reversibly plasticity shape memory (RPSM), dynamic mechanical analysis (DMA) was conducted for all SMASH films tested. Graph (a) shows RPSM for a (0:100) composition were the back face shows the strain vs temperature curve and the side face shows the stress-strain curve. Graph (b) shows all compositions over laid with each other for comparison. The method included equilibrating at 25.00 °C, isothermal for 1.00 min, ramp strain at 5.0000 %/min to 100.00 %, isothermal for 10.00 min, abort next seg if Static Force (N)< 0.01, ramp strain at 5.0000 %/min to 0.00 %, bring force to 0.001N, ramp at 3.00 °C/min to 80.00 °C, isothermal for 5.00 min, and ramp at 3.00 °C/min to 25.00 °C. Thermal removal treatment was conducted all sample prior to testing which included heating in isothermal oven at 80 °C for 10 min and cool to RT for 10 min. The equations shown are the fixing (R_f) and recovery (R_r) ratios where the chart shows their numeral values for each SMASH film tested.

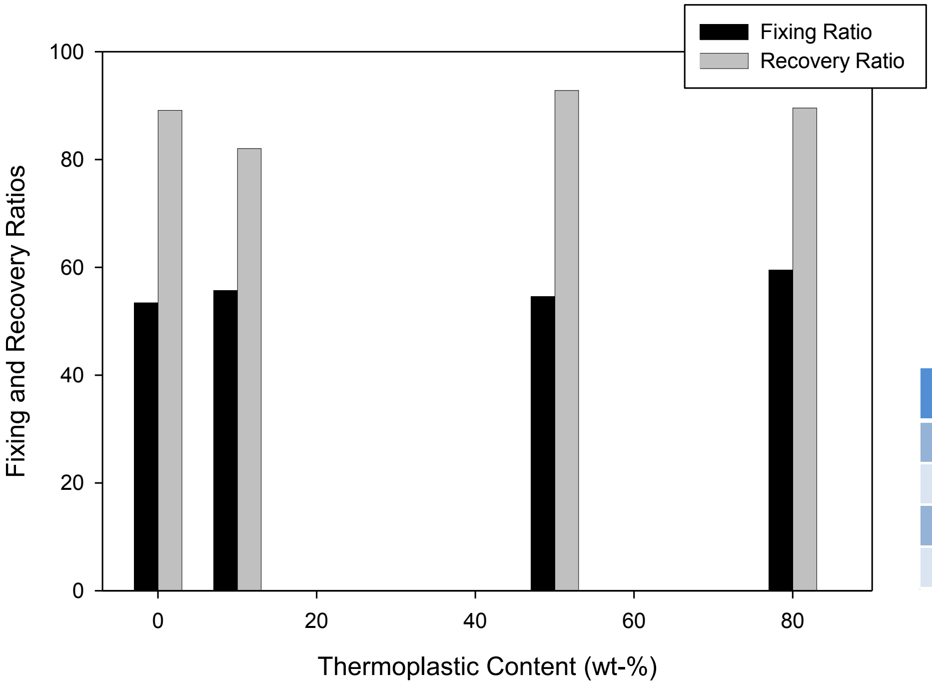

Composition	R_f (%)	R_r (%)
(0:100)	53.5	89.1
(10:90)	55.7	82.1
(50:50)	54.5	92.8
(80:20)	59.5	89.5

Figure A8.1.7. Bar graph showing the fixing (R_f) and recovery (R_r) ratios as a function of PCL:PEG thermoplastic content for all SMASH films tested. The chart shows the calculated R_f and R_r.

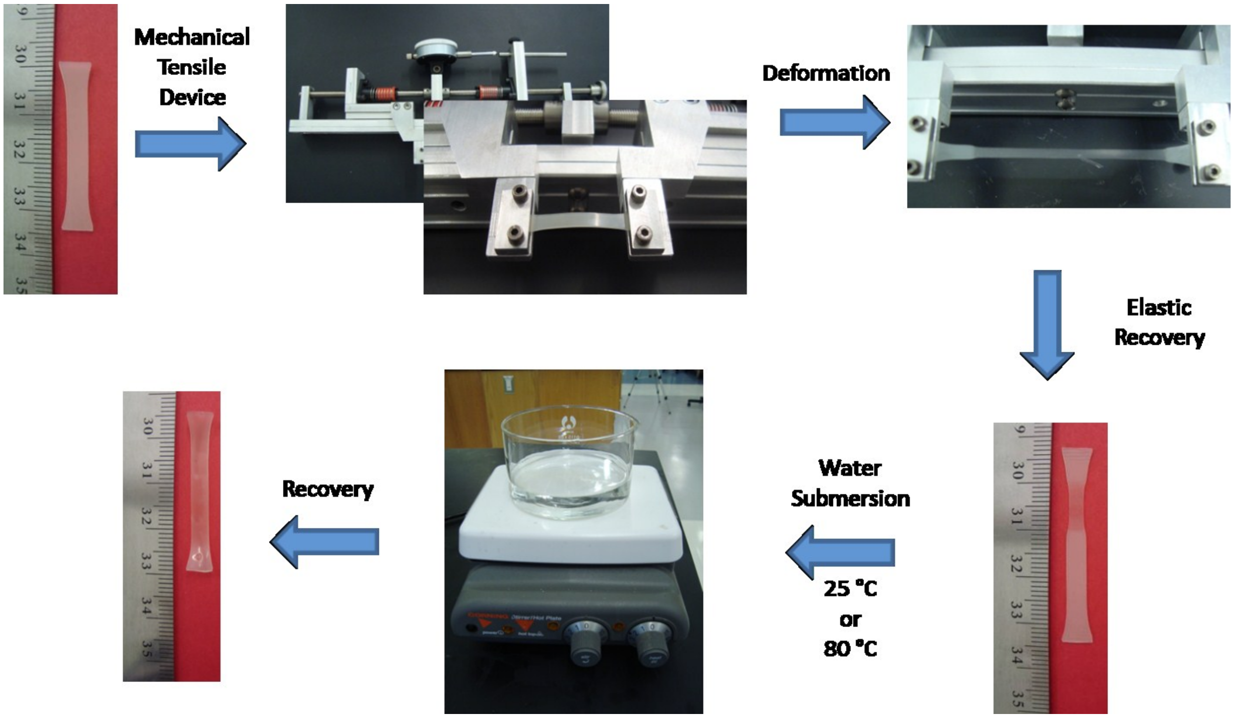

Scheme A8.1.6. Schematic of water triggered shape memory process where the temperature of the water bath is either at 25 °C or 80 °C.

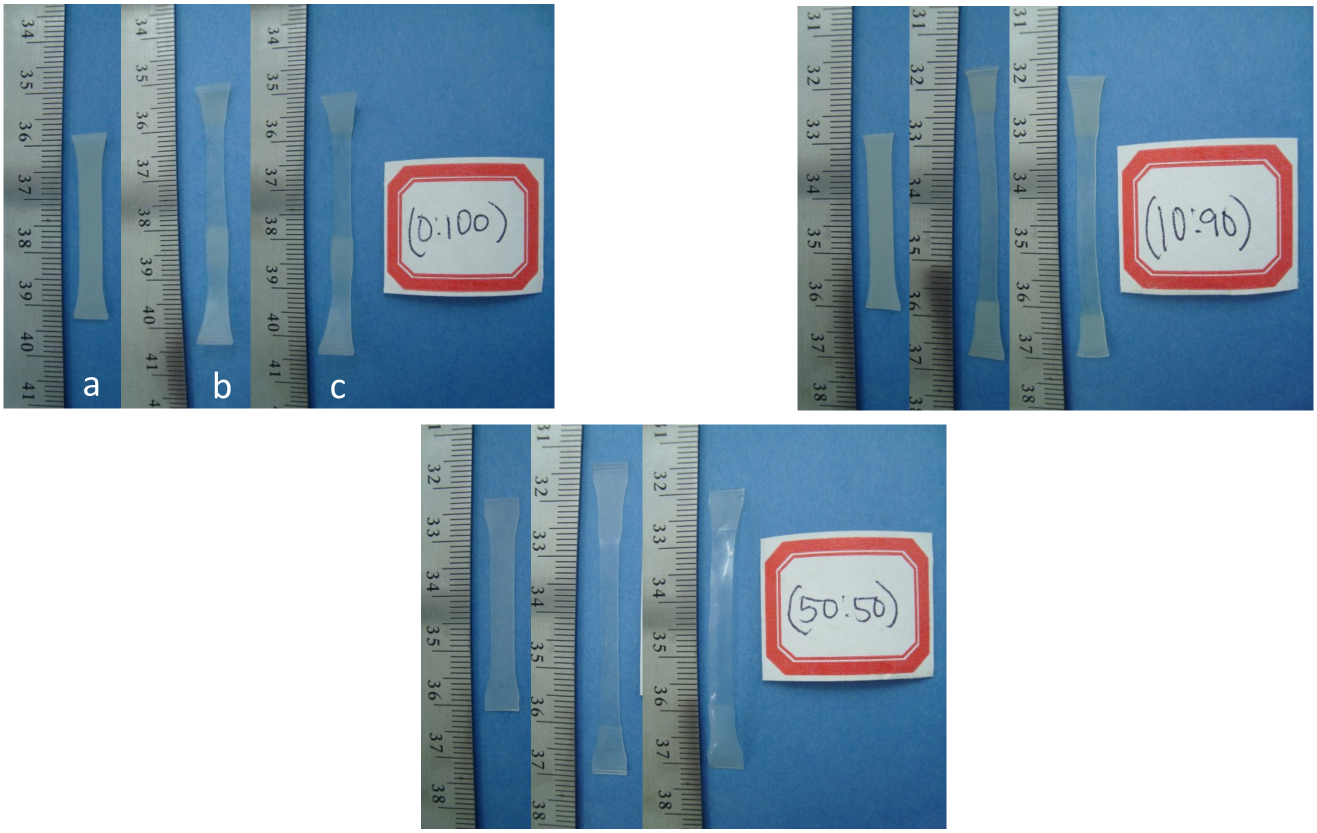

Figure A8.1.8. Images showing the a.) initial length, b.) stretched length, and c.) recovered length for the water triggered shape memory experiment where the each specimen from each composition was deformed and then recovered in a 25 °C water bath.

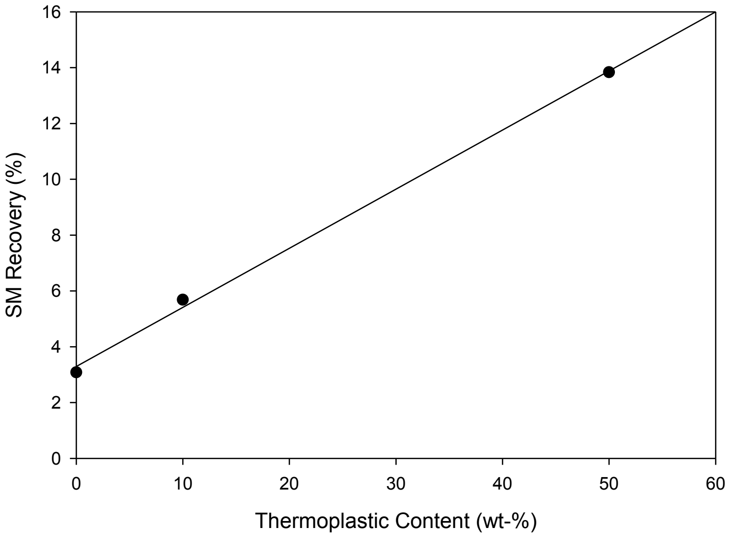

$$\%\text{deformed} = \frac{(L_{deform} - L_{orig})}{L_{orig}} * 100$$

$$\%\text{recovery} = \frac{(L_{deform} - L_{recov})}{(L_{deform} - L_{orig})} * 100$$

Composition	$\%_{deformation}$	$\%_{recov}$
(0:100)	49.5	3.1
(10:90)	62.4	5.7
(50:50)	45.4	13.8

Figure A8.1.9. Graph showing the shape memory recovery for specimens recovered in a 25 °C water bath as a function of PCL:PEG thermoplastic content for the samples tested. The equations were used to calculate the $\%_{deformation}$ and $\%_{recovery}$ for specimens tested.

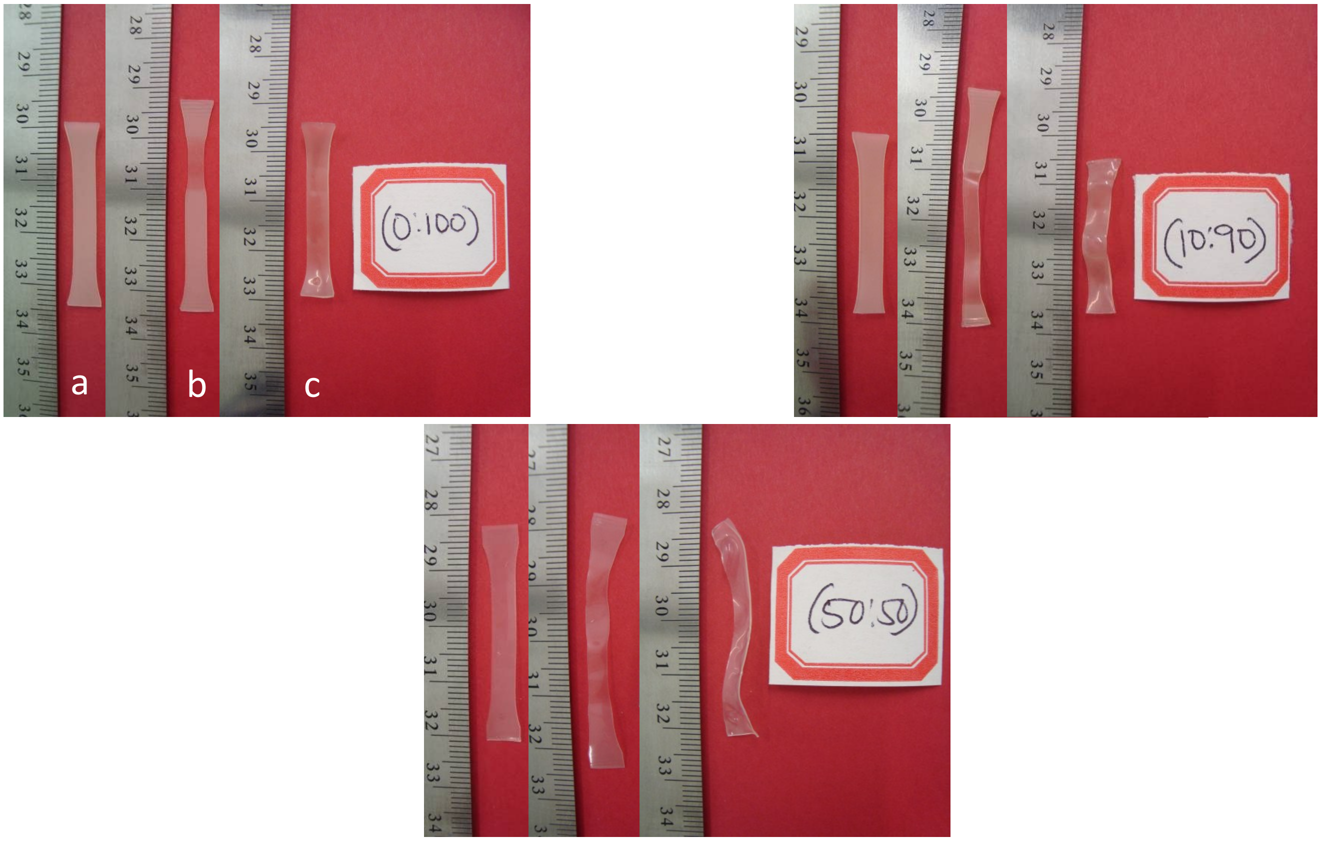

Figure A8.1.10. Images showing the a.) initial length, b.) stretched length, and c.) recovered length for the water triggered shape memory experiment where the each specimen from each composition was deformed and then recovered in a 80 °C water bath.

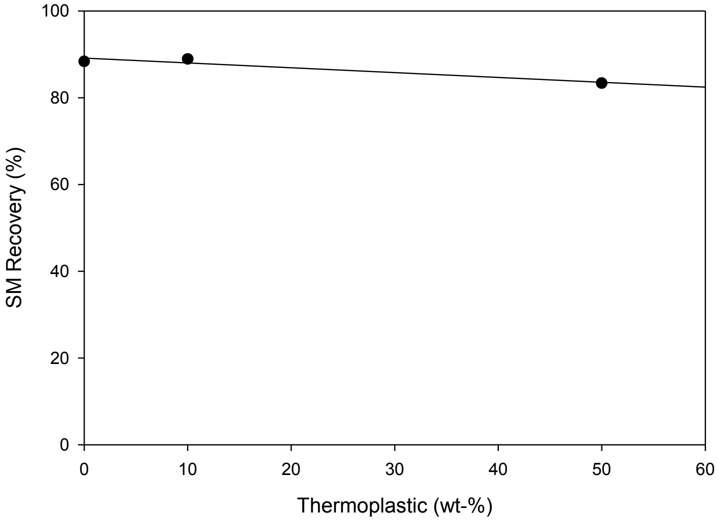

$$\%\text{deformed} = \frac{(L_{\text{deform}} - L_{\text{orig}})}{L_{\text{orig}}} * 100$$

$$\%\text{recovery} = \frac{(L_{\text{deform}} - L_{\text{recov}})}{(L_{\text{deform}} - L_{\text{orig}})} * 100$$

Composition	$\%_{\text{deformation}}$	$\%_{\text{recov}}$
(0:100)	20.9	88.4
(10:90)	45.5	88.9
(50:50)	22.4	83.4

Figure A8.1.11. Graph showing the shape memory recovery for specimens recovered in a 80 °C water bath as a function of co-thermoplastic content for the samples tested. The equations were used to calculate the $\%_{\text{deformation}}$ and $\%_{\text{recovery}}$ for specimens tested.

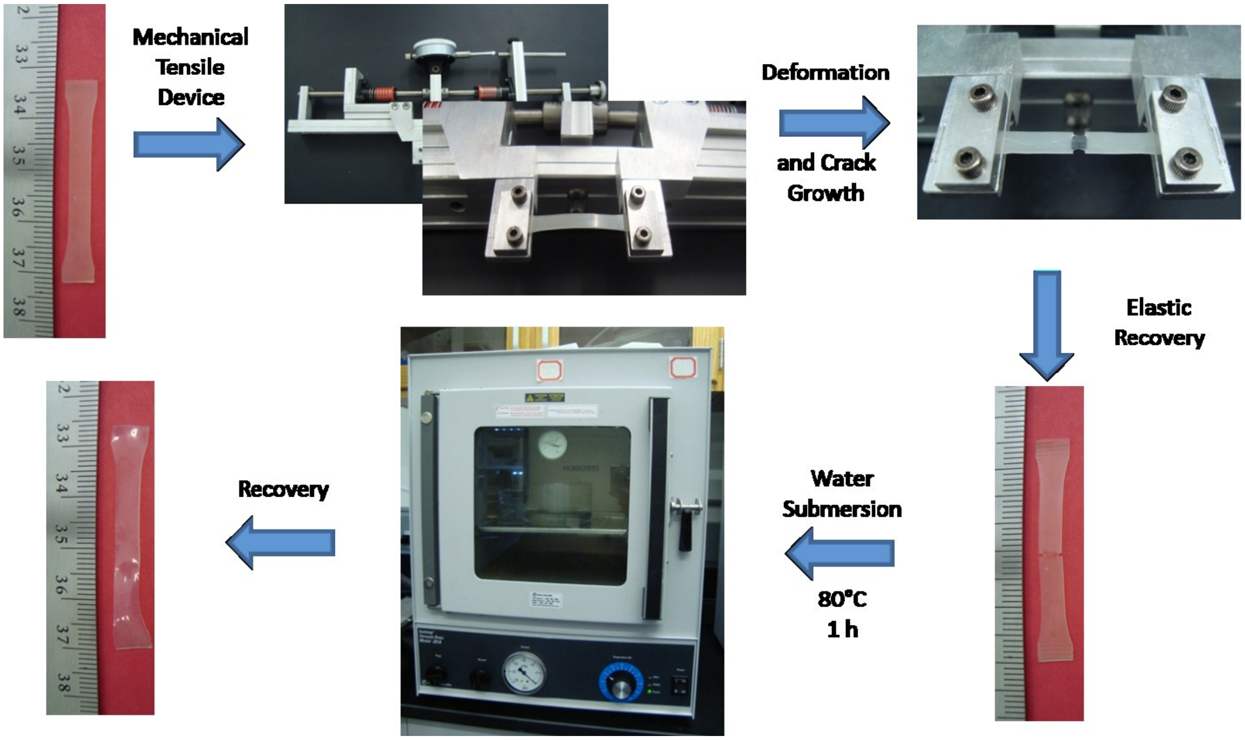

Scheme A8.1.7. Schematic showing the water triggered SMASH process.

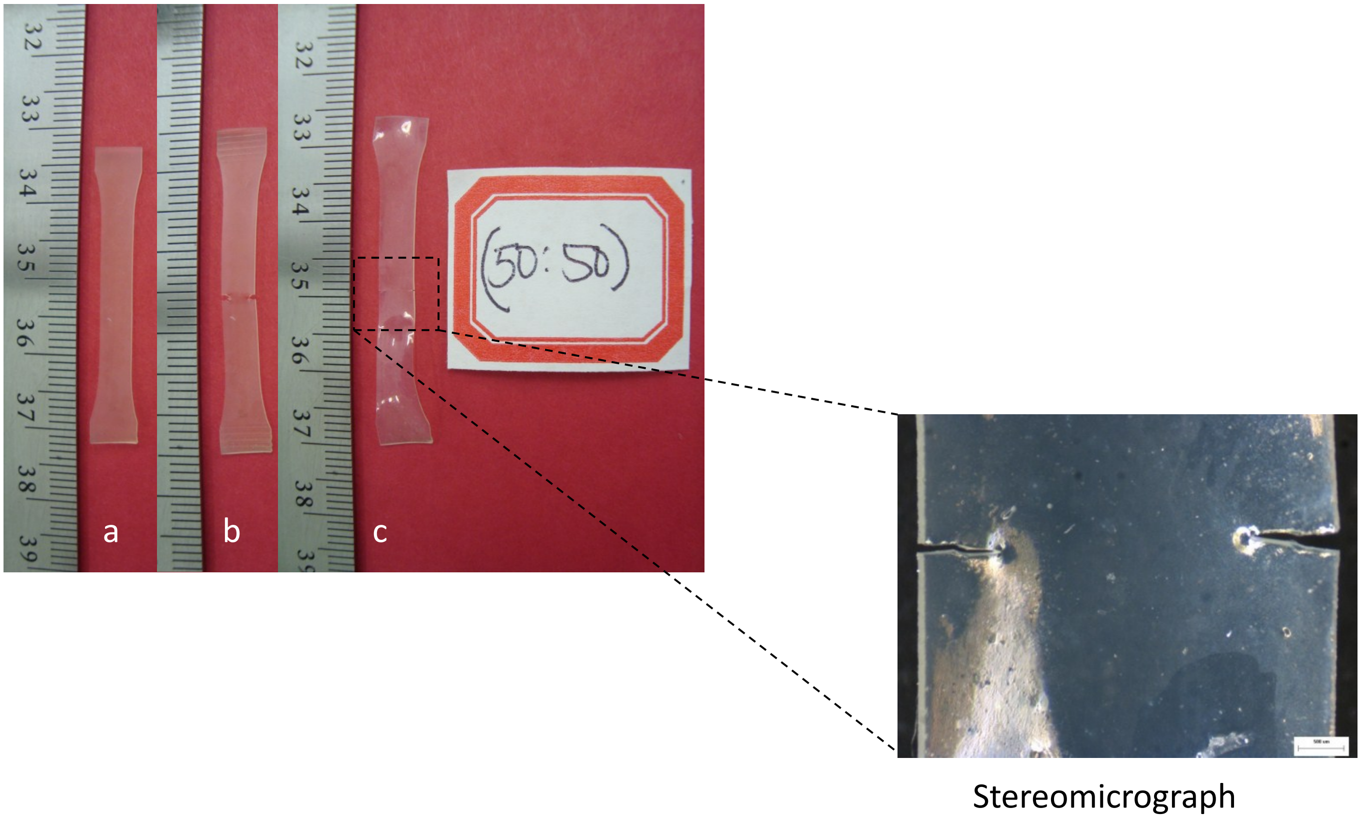

Figure A8.1.12. Images showing the a.) initial length, b.) stretched length, and c.) recovered length for the water triggered shape memory experiment, where a (50:50) specimen was damaged, deformed and then recovered in a 80 °C water bath. Stereomicrograph shows partial crack closure was evident, but crack rebonding was not achieved.

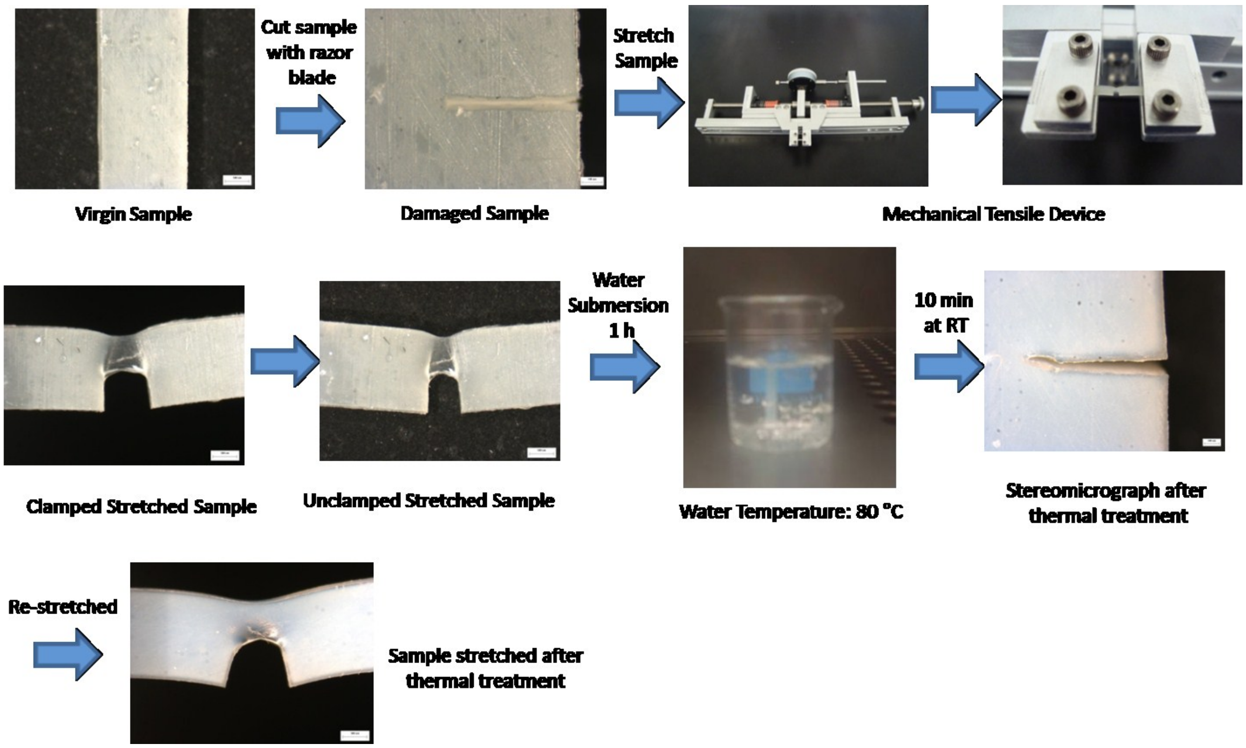

Scheme A8.1.8. Schematic showing the water triggered shape memory experiment, where a specimen was damaged, deformed and then recovered in a 80 °C water bath. Stereomicrographs are shown at each step of the experimental process. Images show partial crack closure was evident, but crack rebonding was not achieved.

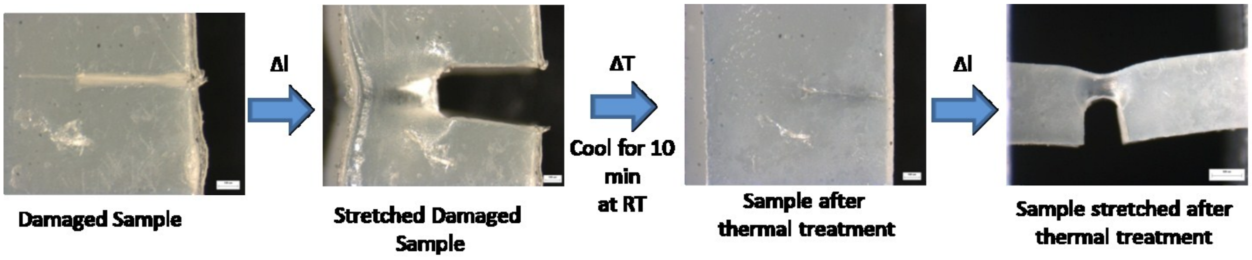

Scheme A8.1.9. Schematic showing heat triggered shape memory experiment where a specimen was damaged, deformed and then recovered at 80 °C in an isothermal oven. Stereomicrographs are shown at each step of the experimental process. Images show complete crack closure was evident, but crack rebonding was not achieved.

APPENDIX 9.0

l-PEO:n-PEG SMASH SYSTEM

A.9.0 SUMMARY

This appendix focuses on further proving the versatility of the shape memory assisted self healing (SMASH) concept by fabricating a fully hydrophilic SMASH polymeric system. Here, polyethylene oxide (PEO) with a molecular weight (M_w) of 100k g/mol and polyethylene glycol (PEG) with a M_w of 2 k g/mol was used. Initial studies of thermogravimetric analysis (*TGA*) and differential scanning calorimetry (DSC) was performed.

APPENDIX 9.1

l-PEO(100k):n-PEG(2k) SMASH SYSTEM

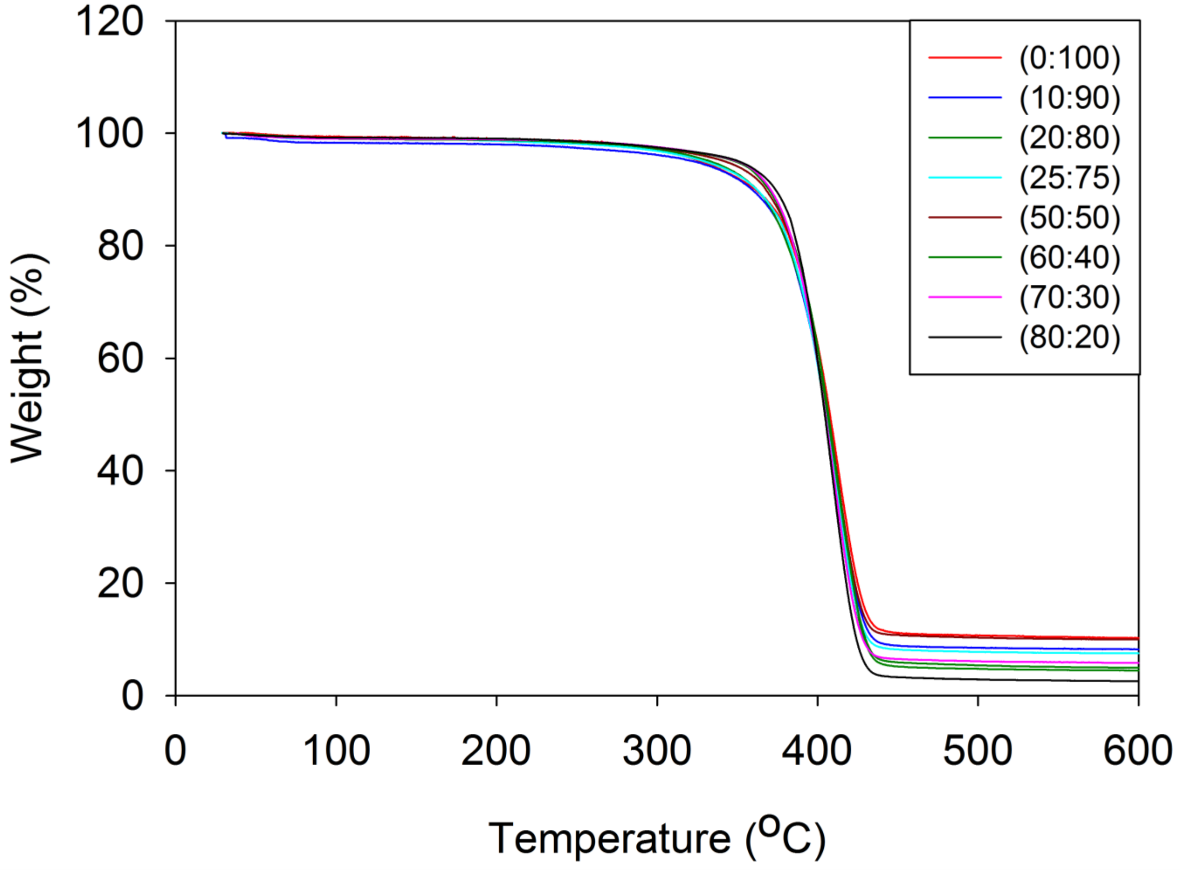

Figure A9.1.1. To measure the onset degradation temperature of all the SMASH films, thermogravimetric analysis (TGA) was conducted on all SMASH compositions shown. The TGA method included ramping the temperature to 600 °C at 10 °C/min. The onset degradation temperature was approximately 400 °C among all compositions.

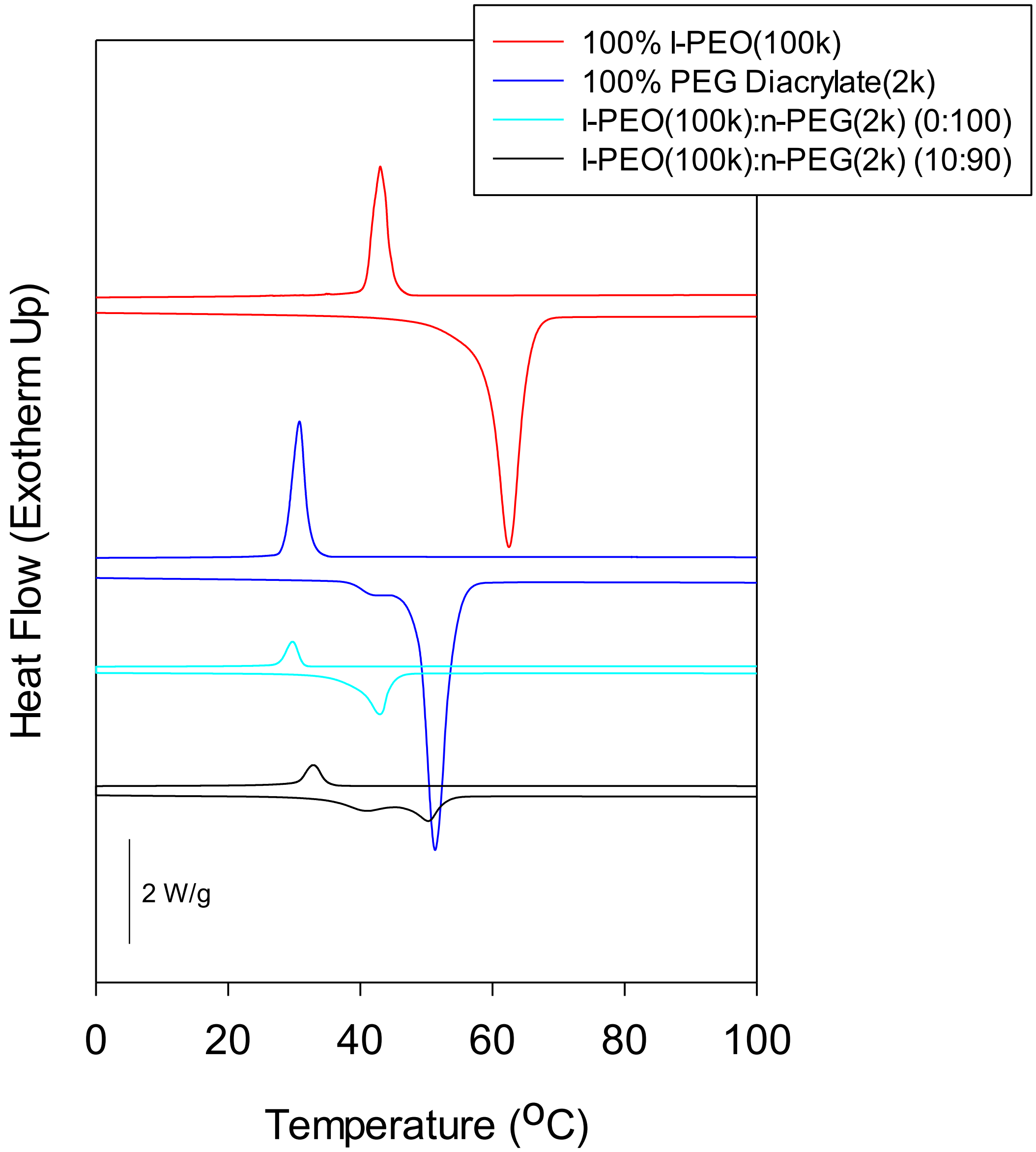

Figure A9.1.2. To measure the crystalline (T_c) and melting temperature (T_m) of all the SMASH films, differential scanning calorimetry (DSC) was used. The graph shows the heat flow as a function of temperature for all samples tested.

APPENDIX 10.0

SYLGARD184 CURING KINETICS

A10.0 SUMMARY

Chapter 4 and 5 focused on fabricating composites that involved using a silicone poly(dimethylsiloxane) (PDMS), commercial known as Sylgard184, as the elastomeric matrix. This appendix focuses on the curing kinetics of Sylgard184 at different temperatures. The experiments were conducted on a TA AR-G2 rheometer in order to study the rheological properties during cure. More specifically, time, temperature, shear storage (G') and shear loss modulus (G'') were studied. The experimental data was modeled using Sigmoidal, 4 Parameter to fit the data. In addition, the Arrhenius plot was used to calculate a theoretical activation energy (E_a) which is the the energy needed to start a chemical reaction. The theoretical activation energy (E_a) was then compared to the experimental data obtained. Theoretical gelation time ($t_{gel)}$ and the time at 99% cure ($t_{99\% \text{ cure}}$) of Sylgard was also calculated and also compared to the experimental data.

APPENDIX 10.1

SYLGARD184 CURING KINETICS

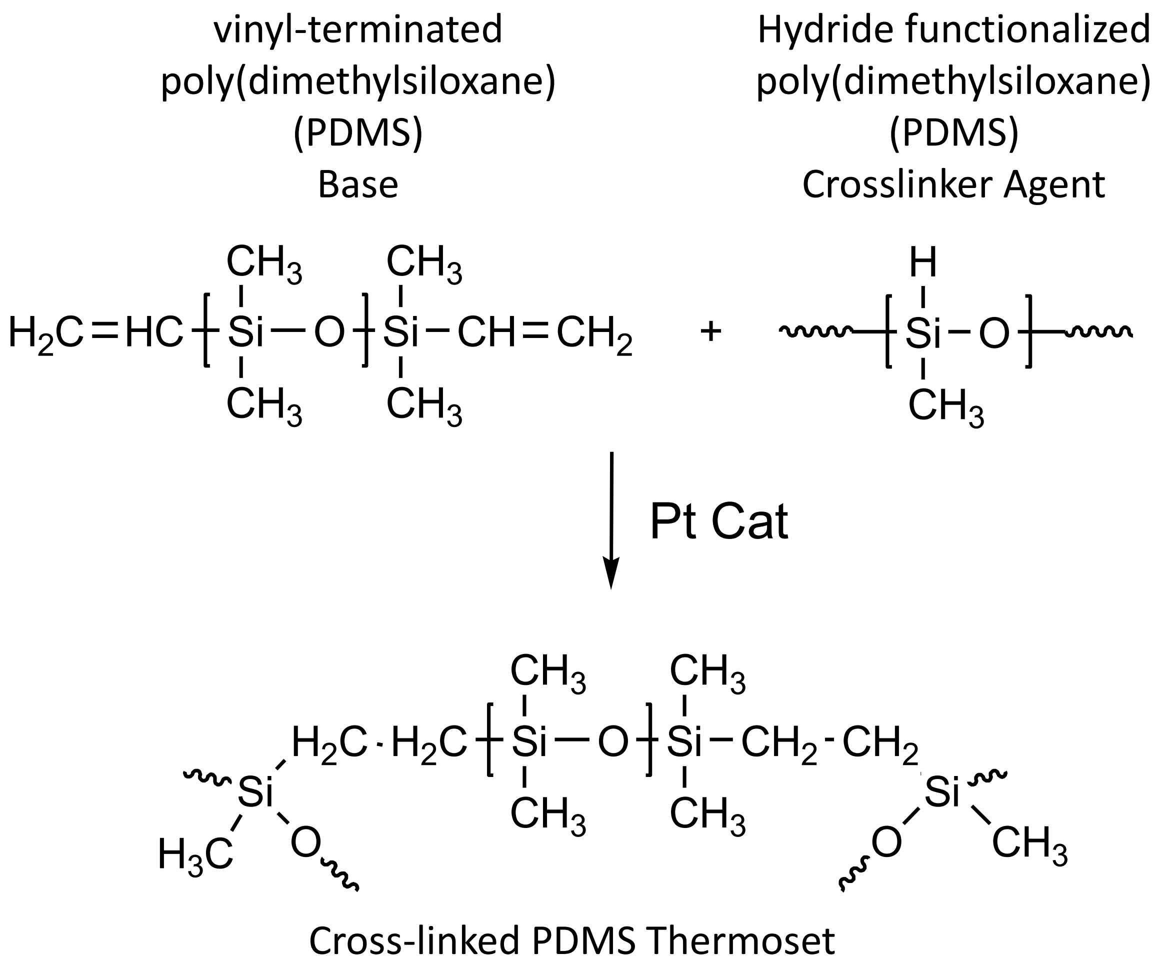

Scheme A10.1.1. Chemical process of curing poly(dimethylsiloxane) (PDMS) (commerical known as Sylgard184) through a hydrosilylation reaction that consists of an alkene reacting with the silicon hydride (present in the crosslinking agent) under the influence of a platinum (Pt) catalyst.

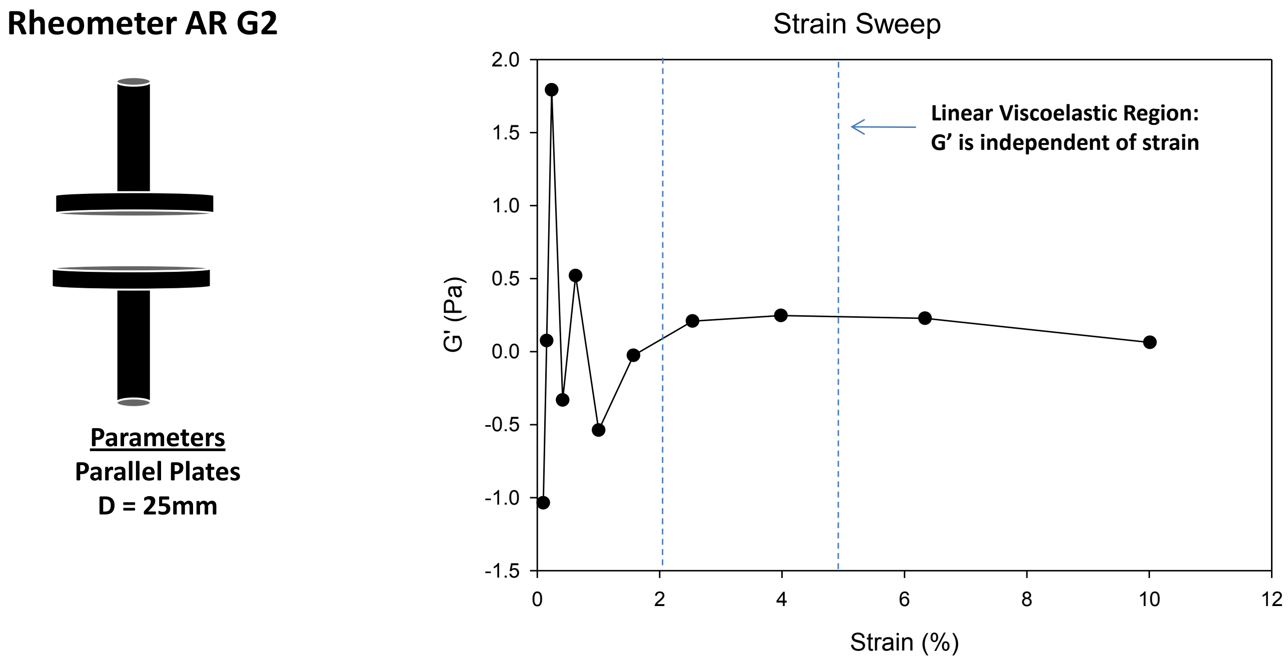

Figure A10.1.1. Schematic showing the rheological experiments setup used to study the curing kinetics of Sylgard184 where the graph shows the shear storage modulus (G’) vs strain %. The graph was used to obtain the region where G’ was independent of strain.

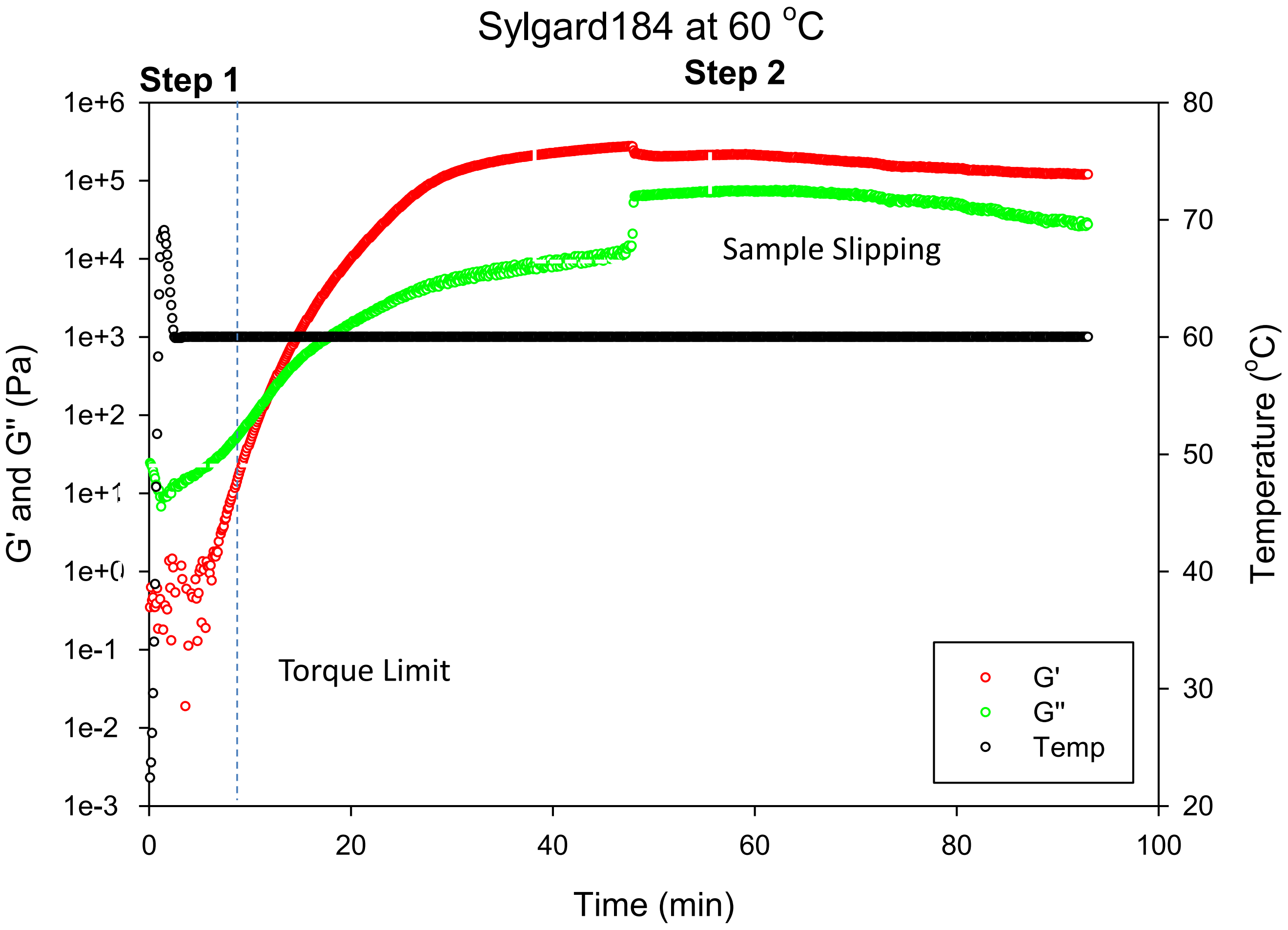

Figure A10.1.2. Graph showing the shear storage (G') and shear loss modulus (G") as a function of time to observe the onset of complete cure at 60 °C. Method 1 included a two step process. Step 1 was performed by conducting a temperature ramp step where the temperature ranged from 25 - 60 °C, equilibration time: 1 min, ramp rate at 60 °C/min, delay time: 1 sec, strain: 2%, at a frequency: 1 Hz. Step 2 included a time sweep step where the duration: 5 h, delay time: 1 sec, temperature: 60 °C, equilibration time: 1 min, Strain: 2% at a frequency: 1 Hz. The graph shows evidence of the torque limit of the instrument which is indicative to the noise in the data at the initial time of the experiment. Sample slipping was also evident at complete cure when G' and G'' plateaued in magnitude.

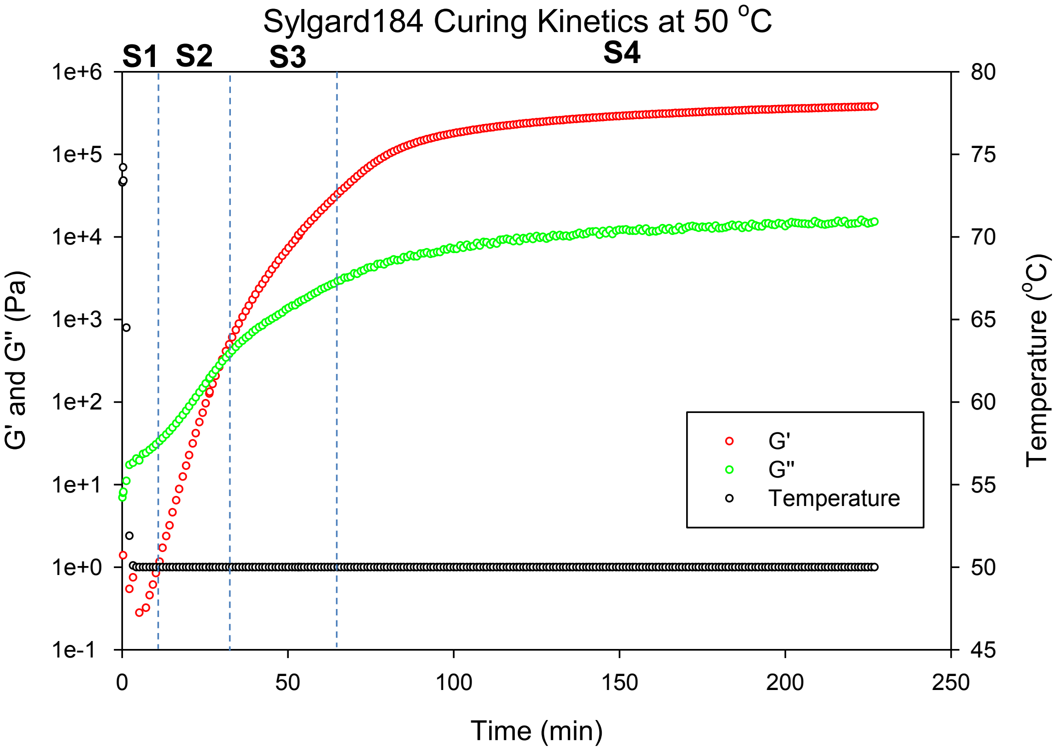

Figure A10.1.3. Graph showing the shear storage (G’) and shear loss modulus (G”) as a function of time to observe the onset of complete cure at 50 °C. Method 2 included a four step process. Step 1 was performed by conducting a temperature ramp step where the temperature ranged from 25 - 50 °C, equilibration time: 1 min, ramp rate at 60 °C/min, delay time: 25 sec, strain: 2%, at a frequency: 1 Hz. Step 2 included a time sweep where the duration: 5 h, delay time: 1 min, temperature: 50 °C, equilibration time: 1 min, strain: 5% at a frequency: 1Hz, step termination: G’(Pa) greater than 100Pa. Step 3 included a second time sweep step where the duration: 5 h, delay time: 1 min, temperature: 50 °C, equilibration time: 1 min, strain: 2%, frequency: 1 Hz, step termination: G’(Pa) greater than 10,000Pa. Step 4 included a third time sweep step where the duration: 5 h, delay time: 1 min, temperature: 50 °C, equilibration time: 1 min, strain: 1% at a frequency: 1 Hz. This entire process was conducted at the following temperatures: 50 °C, 60 °C, 70 °C, 80 °C, 90 °C, and 100 °C.

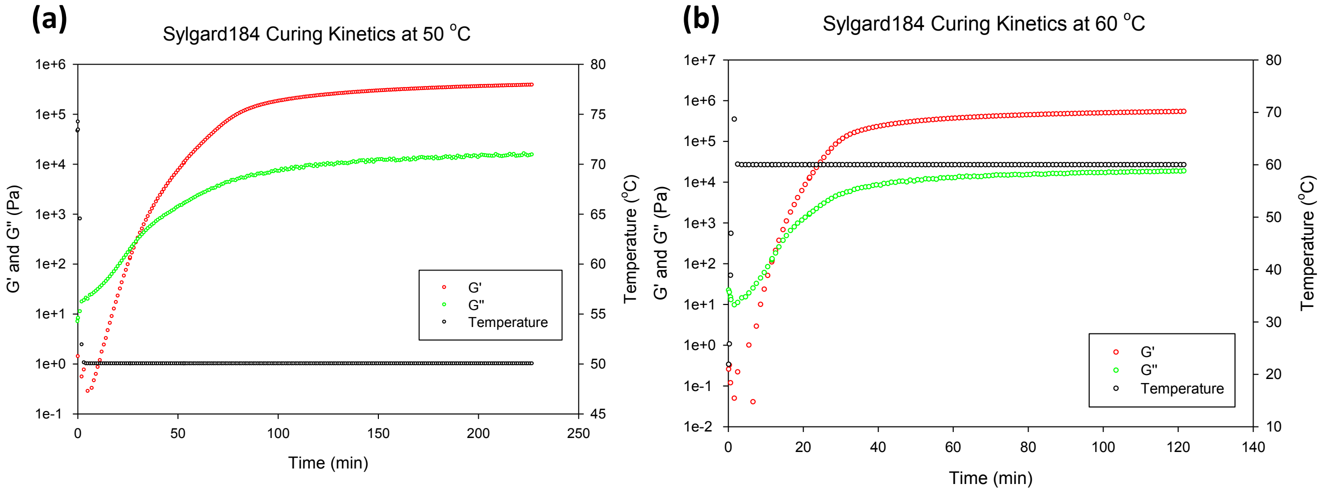

Figure A10.1.4. Graphs showing the shear storage (G'), shear loss modulus (G") and temperature as a function of time to observe complete Sylgard184 cure at (a) 50 °C and (b) 60 °C.

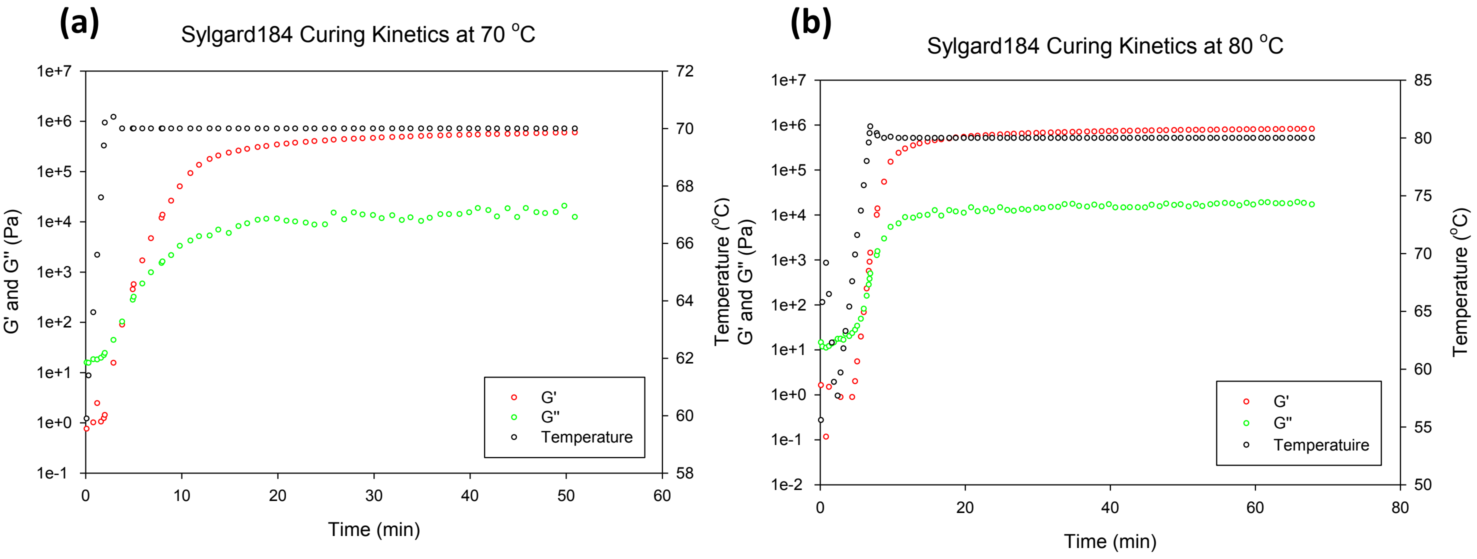

Figure A10.1.5. Graphs showing the shear storage (G’), shear loss modulus (G”) and temperature as a function of time to observe complete Sylgard184 cure at (a) 70 °C and (b) 80 °C.

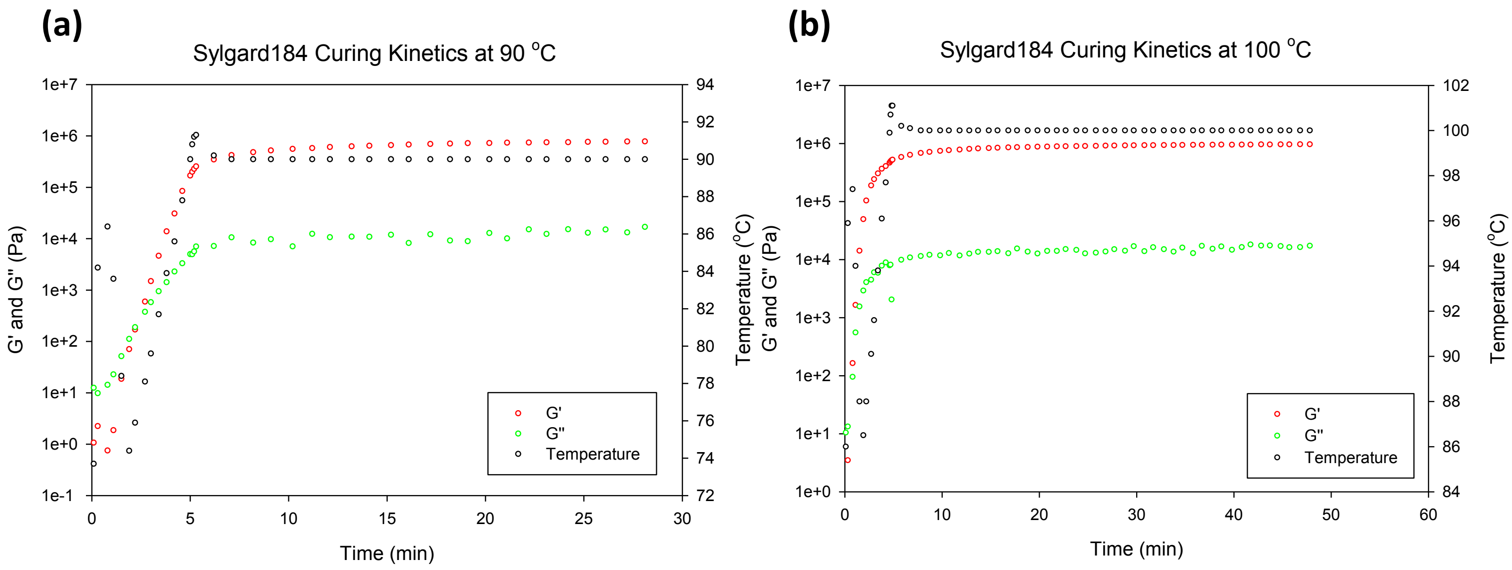

Figure A10.1.6. Graphs showing the shear storage (G'), shear loss modulus (G'') and temperature as a function of time to observe complete Sylgard184 cure at (a) 90 °C and (b) 100 °C.

Table A10.1.1. Table showing the gelation time (t_{gel}), shear storage (G') and loss storage (G'') modulus, complex viscosity (η*) at the gel point for Sylgard184 with respect to the temperatures tested.

Temperature (°C)	t_{gel} (min)	G'_{gel} (Pa)	G''_{gel} (Pa)	η^*_{gel} (Pas)
50	30.2	327.7	309.1	1.9
60	12.6	210.7	181.8	1.6
70	3.8	89.6	103.2	1.3
80	6.0	69.0	82.3	1.2
90	2.2	170.5	189.2	1.6
100	0.8	164.3	95.3	1.5

Sigmoidal, 4 Parameter

$$y = y_o + \frac{a}{1+e^{\left(\frac{-(x-x_o)}{b}\right)}}$$

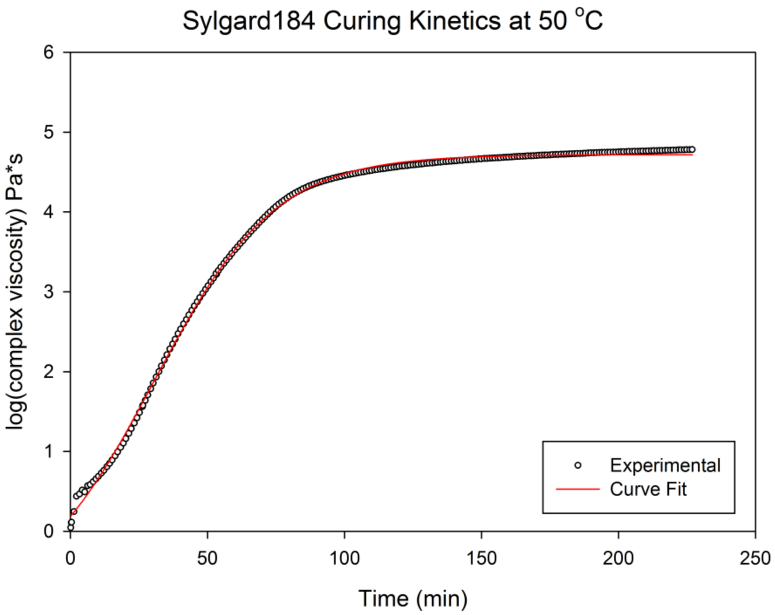

Figure A10.1.7. Equation showing how the experimental log(complex viscosity) vs time data can be fitted to a theoretical sigmoidal, 4 parameter model where y = log(ɳ*), y_o= log(ɳ*$_o$), a = log(ɳ*$_f$) - log(ɳ*$_o$), x = time, x_0 = t_{gel} , and b = constant.

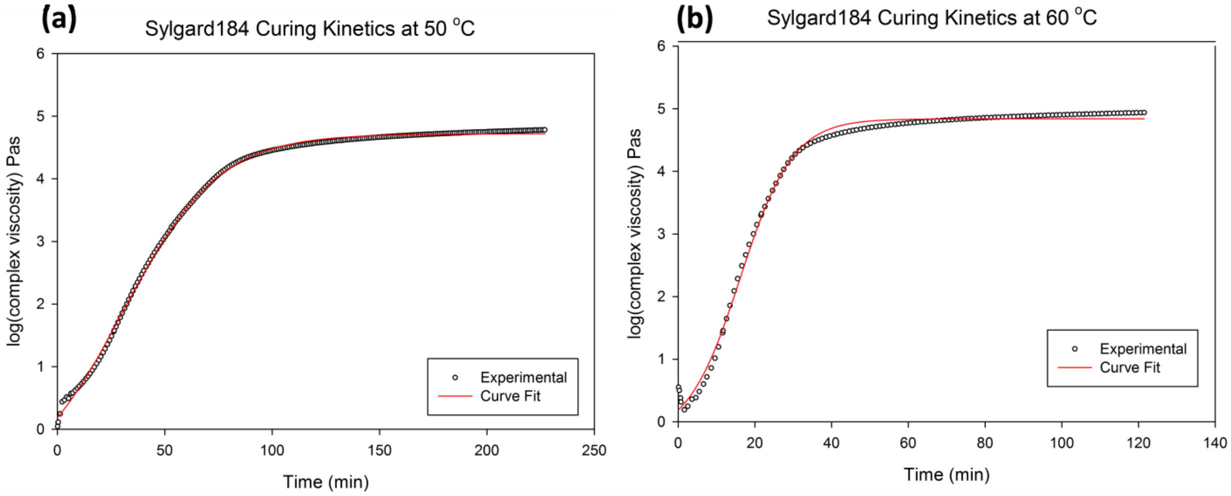

Figure A10.1.8. Graph showing the log(complex viscosity) vs time for experimental data fitted with the theoretical sigmoidal, 4 parameter model at (a) 50 °C and (b) 60 ° C.

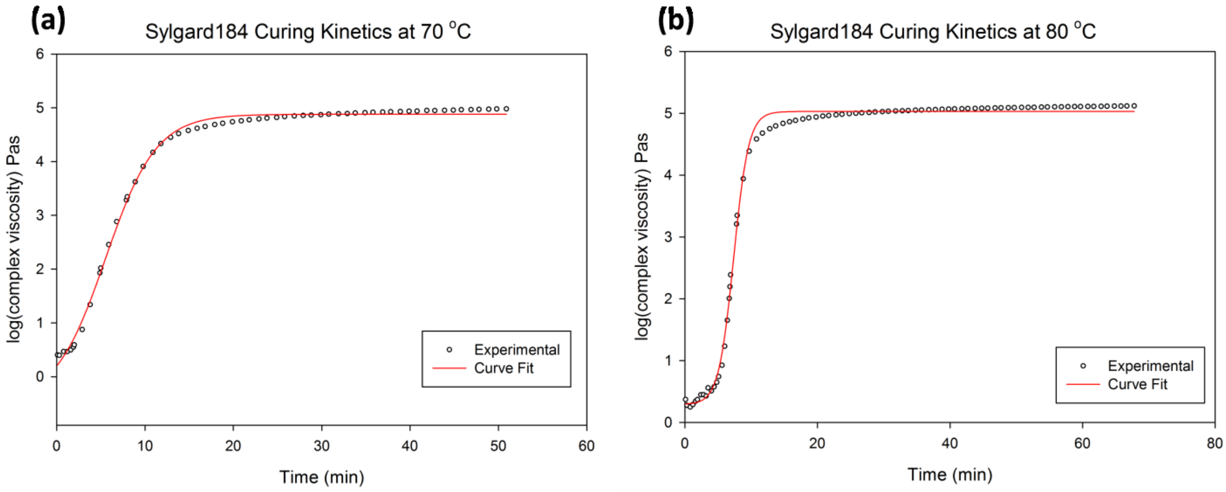

Figure A10.1.9. Graph showing the log(complex viscosity) vs time for experimental data fitted with the theoretical sigmoidal, 4 parameter model at (a) 70 °C and (b) 80 ° C.

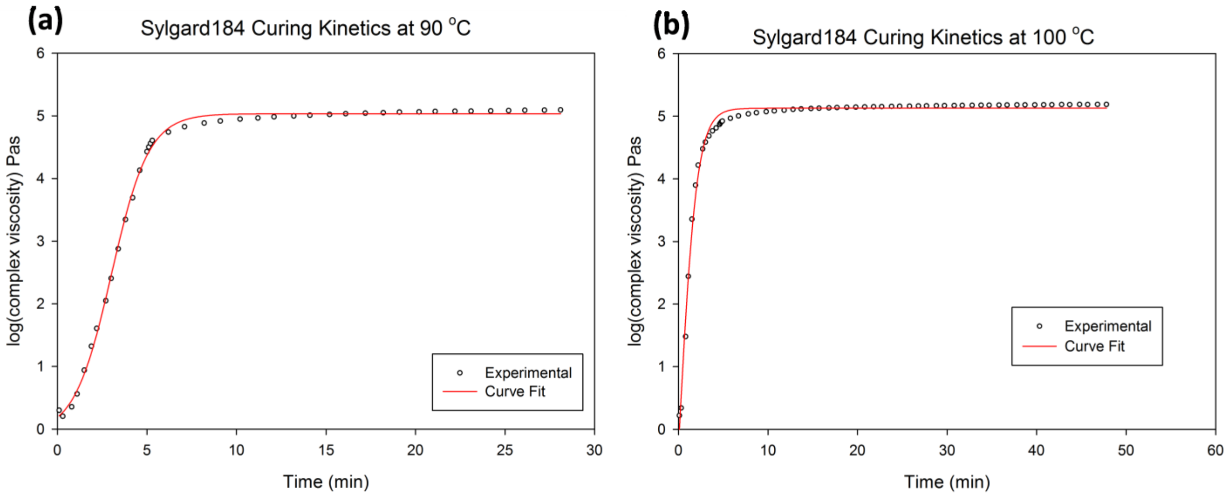

Figure A10.1.10. Graph showing the log(complex viscosity) vs time for experimental data fitted with the theoretical sigmoidal, 4 parameter model at (a) 90 °C and (b) 100 ° C.

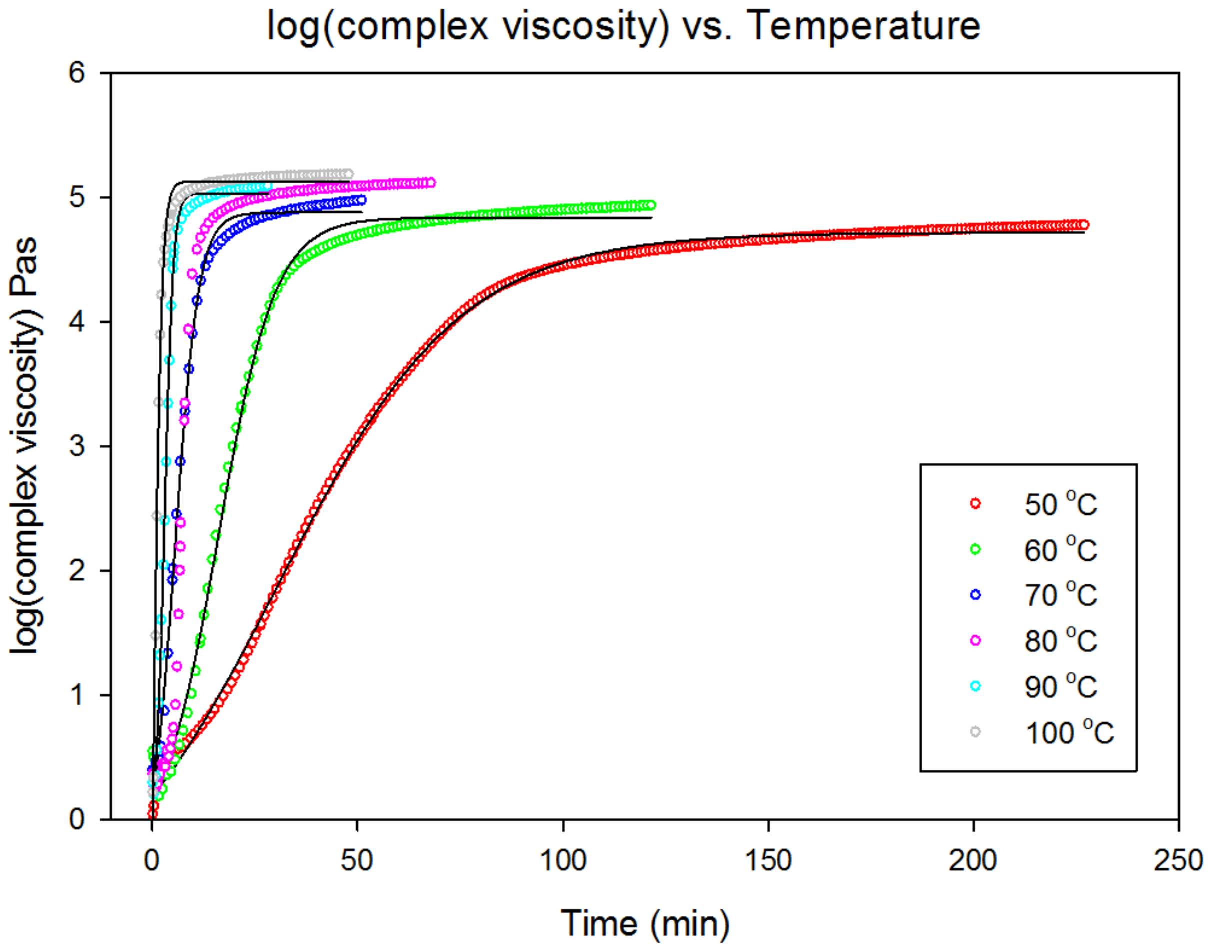

Figure A10.1.11. Graph showing the log(complex viscosity) vs time as a function of temperatures tested to cure Sylgard184. Temperature dependency on curing is evident where cure time decreases with an increase in temperature. Complete cure is evident when the log(complex viscosity) plateaus at a longer time frame.

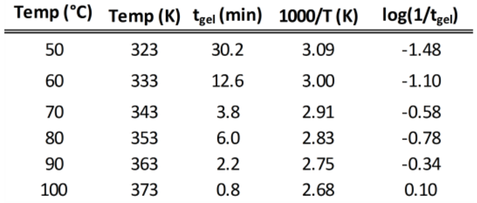

Temp (°C)	Temp (K)	t_{gel} (min)	1000/T (K)	log(1/t_{gel})
50	323	30.2	3.09	-1.48
60	333	12.6	3.00	-1.10
70	343	3.8	2.91	-0.58
80	353	6.0	2.83	-0.78
90	363	2.2	2.75	-0.34
100	373	0.8	2.68	0.10

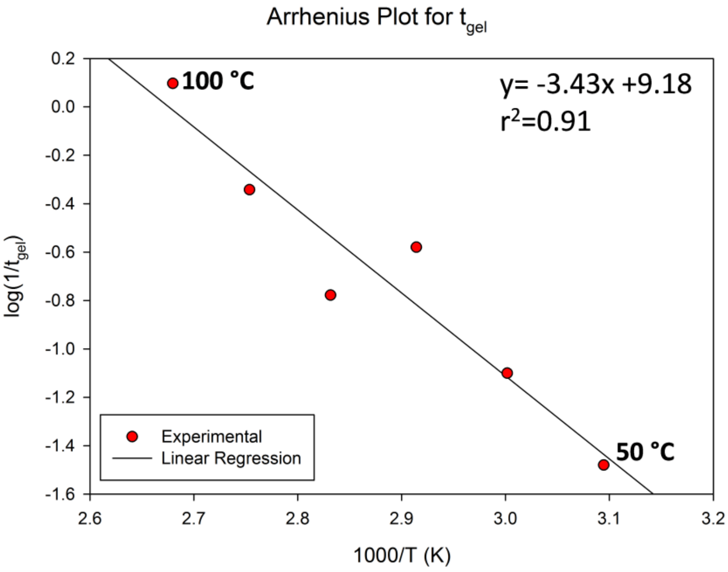

Figure A10.1.12. Arrhenius plot is used to understand the relationship between temperature and chemical reaction rates. This can be found by plotting log(1/t_{gel}) vs. 1000/T (K). Chart shows the temperature, gelation time (t_{gel}), 1000/T function, and log(1/t_{gel}) function. A linear regression line was fitted to the experimental data where the slope was used to find the activation energy (E_a) (the energy needed to start a chemical reaction) where the constants in the line equation was used to predict t_{gel} at any temperature.

Temp (°C)	Temp (K)	x=1000/T (K)	y=log(1/t_{gel}) y=mx+b	t_{gel} (min)
25	298	3.35	-2.33	211.8
30	303	3.30	-2.14	136.8
37	310	3.22	-1.88	76.0
40	313	3.19	-1.77	59.5
50	323	3.09	-1.44	27.3
60	333	3.00	-1.12	13.1
70	343	2.91	-0.82	6.6
80	353	2.83	-0.53	3.4
90	363	2.75	-0.27	1.8
100	373	2.68	-0.01	1.0

Temp (°C)	Experimental t_{gel} (min)	Theroetical t_{gel} (min)
50	30.2	27.3
60	12.6	13.1
70	3.8	6.6
80	6.0	3.4
90	2.2	1.8
100	0.8	1.0

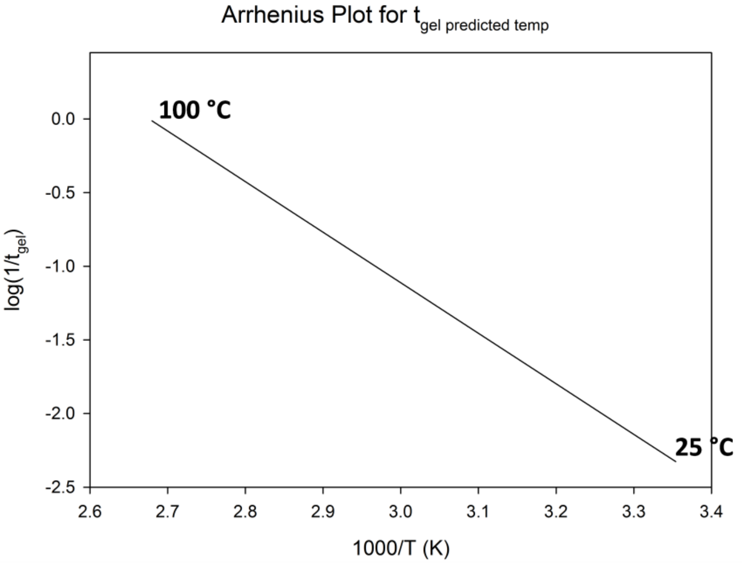

Figure A10.1.13. Arrhenius analysis used to predict the gelation times for a predicted temperature ($t_{gel\ predicted\ temp}$). Top table shows the 1000/T function, log(1/t_{gel}) function, and gelation time (t_{gel}) for predicted temperature. Bottom table compares the theoretical to experimental gelation times. Graph showing 1000/T vs log(1/t_{gel}) among all temperatures tested.

Solve for x ($t_{99\%\ cure}$)

$$x = -b\ln\left(\frac{a}{y-y_o}-1\right)+x_o$$

Temp (°C)	Temp (K)	$t_{99\%\ cure}$ (min)	1000/T (K)	log(1/$t_{99\%\ cure}$)
50	323	132.7	3.09	-2.12
60	333	47.7	3.00	-1.68
70	343	18.7	2.91	-1.27
80	353	12.5	2.83	-1.10
90	363	7.8	2.75	-0.89
100	373	4.6	2.68	-0.66

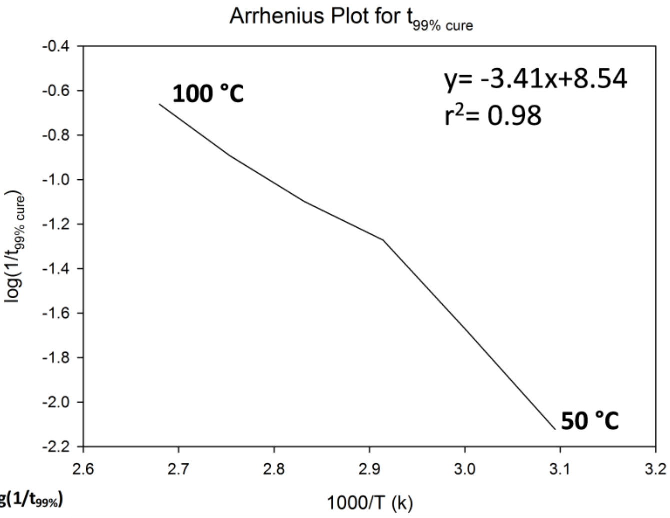

					y=log(1/$t_{99\%}$)
Temp (°C)	Temp (K)	$t_{99\%}$ (min)	$t_{99\%}$ (hrs)	x=1000/T (K)	y=mx+b
25	298	807.7	13.5	3.35	-2.91
30	303	523.0	8.7	3.30	-2.72
37	310	291.4	4.9	3.22	-2.46
40	313	228.6	3.8	3.19	-2.36

Figure A10.1.14. Arrhenius analysis used to predict the time of 99% cure ($t_{99\%\ predicted\ cure}$) where the equation shown was used to calculate this value. Top table shows the time for 99% cure ($t_{99\%\ cure}$), 1000/T, and log(1/$t_{gel\ cure}$). The bottom table shows the hours needed for 99% cure as a function of cure temperatures tested.

Table A10.1.2. Table showing the variables from the equations shown to solve for the theoretical time for 99% cure.

Sigmoidal, 4 Parameter

$$y = y_o + \frac{a}{1 + e^{\left(\frac{-(x-x_o)}{b}\right)}}$$

Solve for x ($t_{99\%\ cure}$)

$$x = -b \ln\left(\frac{a}{y - y_o} - 1\right) + x_o$$

Temp (°C)	a (Δlogη*)	b	x_0 (t_{gel})	y_0 (logη$^*_0$)	r^2	$y=y_0+(a*0.99)$ (logη$^*_{99\%}$)	$t_{99\%\ cure}$ (min)
50	5.69	22.26	30.38	-0.97	0.9991	4.66	132.7
60	5.09	6.86	16.15	-0.25	0.9963	4.79	47.7
70	5.36	2.86	5.54	-0.48	0.9974	4.83	18.7
80	4.74	1.13	7.35	0.29	0.9974	4.98	12.5
90	5.12	1.04	3.02	-0.08	0.9985	4.98	7.8
100	10.40	0.98	0.07	-5.27	0.9923	5.02	4.6

	Experimental			Theoretical		
Temp (°C)	$\log\eta^*_o$	$\log\eta^*_f$	$\log\eta^*_{99\%\,cure}$	$\log\eta^*_o$	$\log\eta^*_f$	$\log\eta^*_{99\%\,cure}$
50	0.05	4.78	4.73	-0.97	4.72	4.66
60	0.55	4.94	4.89	-0.25	4.84	4.79
70	0.40	4.98	4.93	-0.48	4.88	4.83
80	0.37	5.12	5.07	0.29	5.03	4.98
90	0.30	5.09	5.05	-0.08	5.03	4.98
100	0.22	5.19	5.14	-5.27	5.13	5.02

Experimental	Theoretical
$t_{99\%\,cure}$ (min)	$t_{99\%\,cure}$ (min)
184.9	132.69
94.5	47.67
39.9	18.70
41.8	12.55
18.2	7.81
19.8	4.59

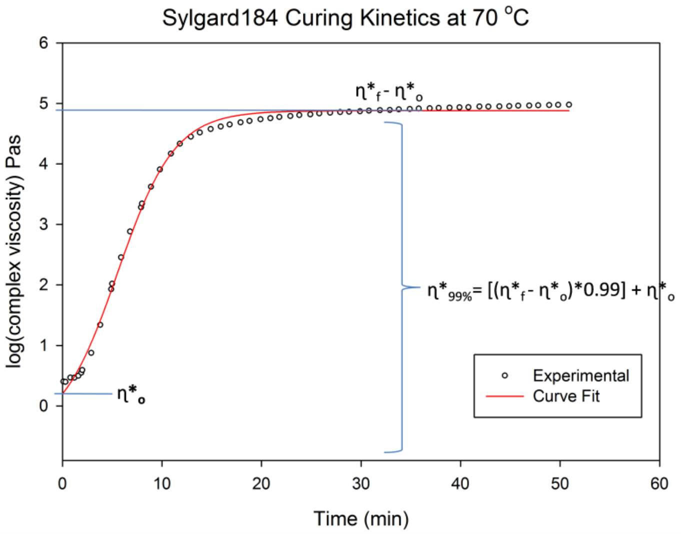

Figure A10.1.15. Graph showing the log(complex viscosity) vs time where it was used to calculate the theoretical log(complex viscosity) for any given temperature (top table). This was then used to calculate the theoretical time for 99% cure and compared to the experimental 99% cure (bottom table).

Table A10.1.3. Table showing shear storage (G') and shear loss modulus (G") for the initial and 99% cure, the complex viscosity (η*) at 99% cure and the time need to obtain 99% cure for Sylgard184 at the tested temperatures.

				99% of Final point				
Temperature (°C)	G'_o(Pa)	G''_o (Pa)	G'_f (Pa)	G''_f (Pa)	$G'_{99\%}$ (Pa)	$G''_{99\%}$ (Pa)	$\eta^*_{99\%}$ (Pas)	$t_{99\%\ cure}$ (min)
50	-0.58	6.951	3.8E+05	1.5E+04	3.7E+05	1.5E+04	4.7	184.9
60	0.26	22.38	5.4E+05	1.9E+04	5.4E+05	1.9E+04	4.9	94.5
70	0.76	15.85	6.0E+05	1.2E+04	5.9E+05	1.2E+04	4.9	39.9
80	1.64	14.65	8.2E+05	1.7E+04	8.2E+05	1.7E+04	5.1	41.8
90	1.07	12.52	7.8E+05	1.7E+04	7.7E+05	1.7E+04	5.0	18.2
100	-0.19	10.43	9.7E+05	1.7E+04	9.6E+05	1.7E+04	5.1	19.8

APPENDIX 11.0

SHAPE MEMORY ELASTOMERIC COMPOSITE (SMEC) TO ANISOTROPIC SHAPE MEMORY ELASTOMERIC COMPOSITE (A-SMEC)

A11.0 SUMMARY

This appendix focuses on the mechanical testing of stretching a randomly aligned poly(vinyl acetate) (PVAc) fibrous web to an anisotropic fibrous web in order to construct an anisotropic shape memory elastomeric composite (A-SMEC) system using an Intron machine. This was conducted in order to prove that fiber anisotropy can be achieved by a simple uniaxial loading. Preliminary studies included Instron testing with accompany scanning electron microscopy (SEM) micrographs to prove the anisotropy concept.

APPENDIX 11.1

SHAPE MEMORY ELASTOMERIC COMPOSITE (SMEC) TO ANISOTROPIC SHAPE MEMORY ELASTOMERIC COMPOSITE (A-SMEC)

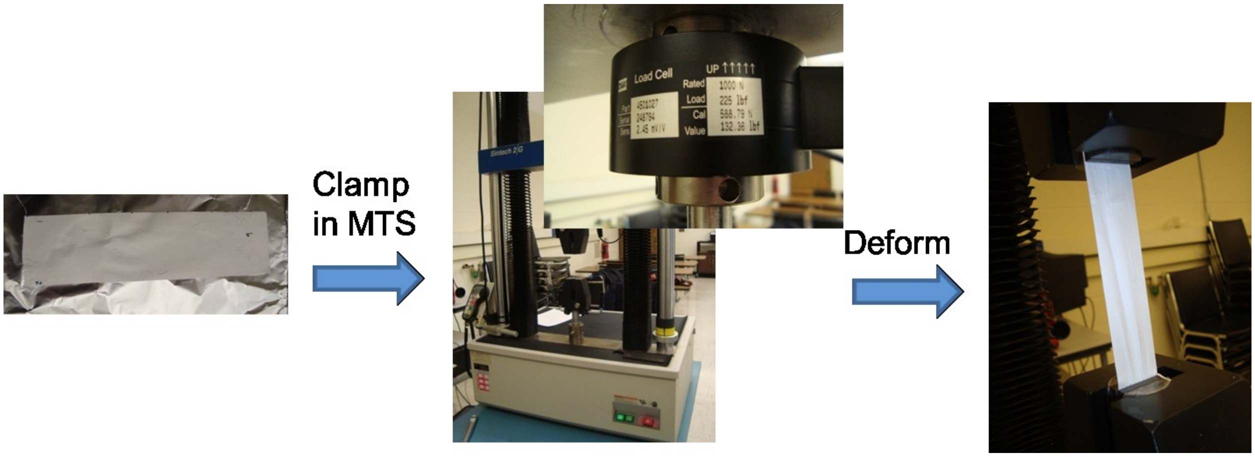

Scheme A11.1.1. Stretched a fiber mat strip on the MTS Instron in order to mechanically stretch a randomly aligned fiber mat to an aligned fiber mat by uniaxially deforming the specimen.

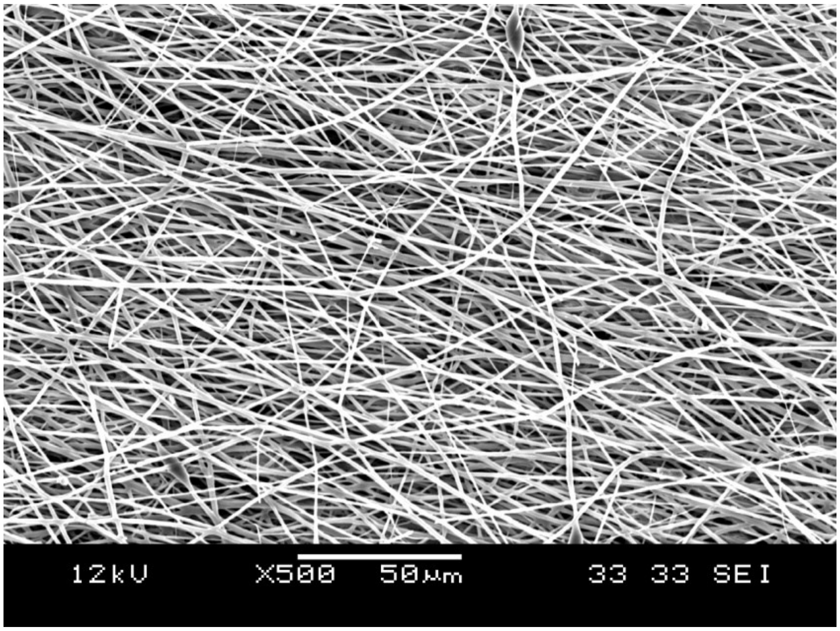

Pre-Stretching

Figure A11.1.1. Scanning electron microscopy (SEM) micrograph showing randomly aligned fibers prior to uniaxial stretching. Assisted by undergraduate student, Derek C. Weed.

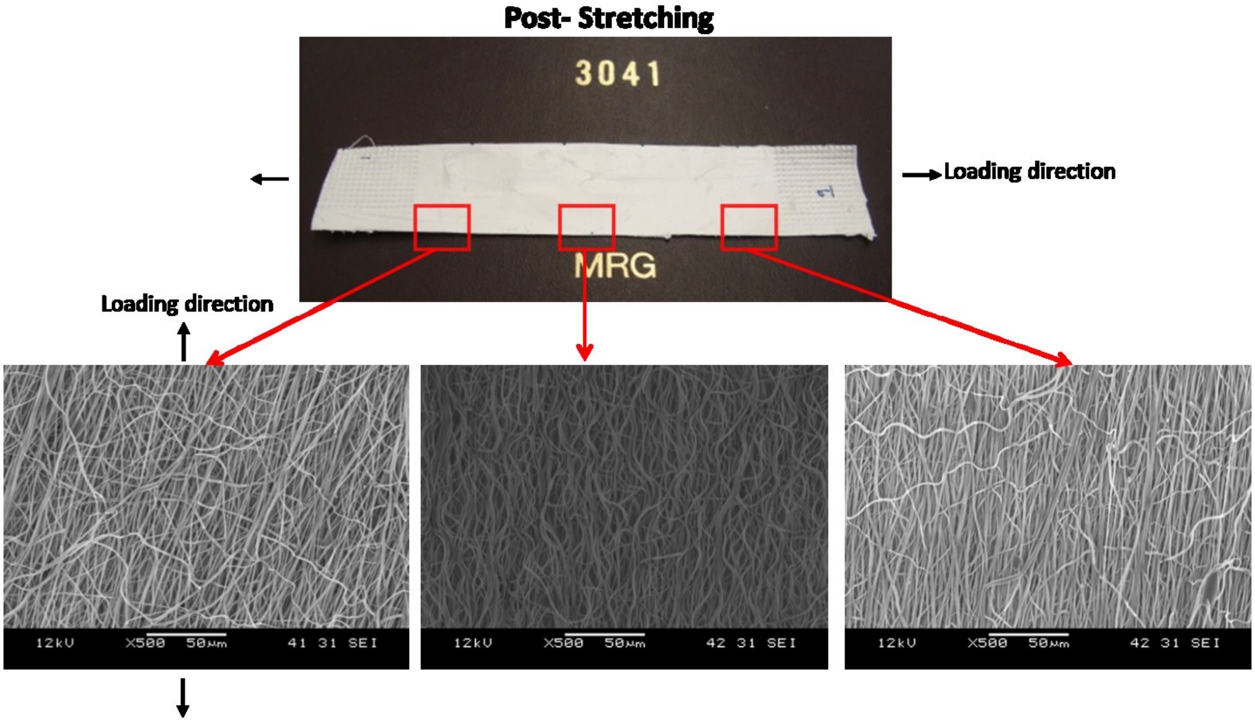

Figure A11.1.2. Scanning electron microscopy (SEM) micrograph of the stretched fiber mat strip where three regions of interest were analyzed to study fiber alignment as a function of uniaxial stretching. The regions closet the MTS clamps showed anisotropic fiber alignment where the fibers located in the center were not as aligned when compared to the outer regions. Arrows shown indicate loading direction. Assisted by undergraduate student, Derek C. Weed.

APPENDIX 12.0

DERIVATION OF LAMINATED COMPOSITE STRIP CURVATURE

In order to correlate curvature with strain and apply it to the curvature seen in the A-SMEC laminated composites explained in Chapter 5, the neutral axis (y_n), the flexural stiffness (EI) and bending moment (M) must be solved. This appendix shows detailed steps for solving this relationship. In Chapter 5, the curvature equation derived in this appendix was used for comparing the theoretical and experimental curvature for the laminate A-SMEC strips.

<u>First solve for the curvature (k) equation:</u>

Starting with Hooke's Law[1]:

$$\sigma = E\varepsilon$$

or

$$\varepsilon = \frac{\sigma}{E}$$

where $\sigma = \frac{My}{I}$, therefore,

$$\varepsilon = \frac{My}{EI}$$

where

•M = bending moment[1]

•EI =flexural stiffness[1]

The curvature (k) equation can be derived by the following relationship[1]:

$k = \frac{\epsilon}{y}$, therefore

$$\frac{\varepsilon}{y} = \frac{M}{EI}$$

Therefore, k can be expressed as[1, 2]

$$k = \frac{M}{EI}$$

This is the equation used to calculate the curvature in relation to the applied deformation on the dual laminate A-SMEC composite strips.

Solve for the neutral axis (y_n) equation:

Neutral axis (y_n) needs to be solved first in order to solve for the flexural stiffness and bending moment.

One can start with the uniaxial stress equation

$$\sigma = \frac{F}{A}$$

Solve for F

$$F = \sigma A$$

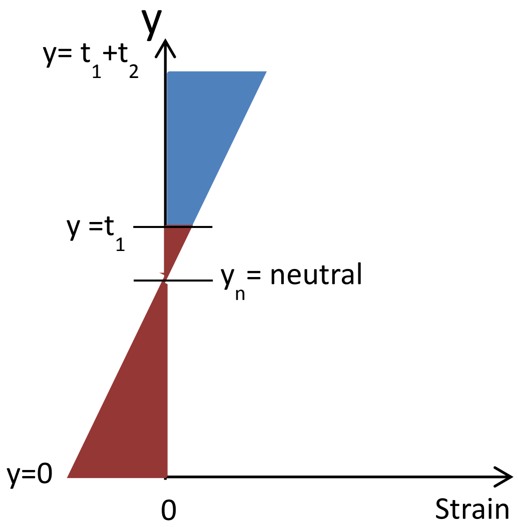

Scheme 1. Schematic of strain profile along the thickness of laminate.

F needs to be integrated along the thickness (y axis) and width (z axis) of the laminated composite. Therefore,

$$F = \int_{area} \sigma dA$$

where •$Area = dA = dydz$

•$\sigma = E\varepsilon$

$$F = \int_{z=0}^{b} \int_{y=0}^{t} E\varepsilon dydz$$

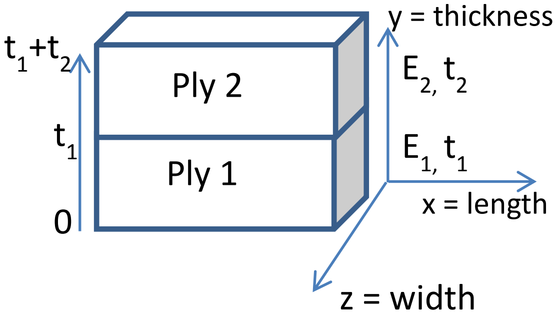

Scheme 2. Schematic of coordinate system related to dual laminated composite.

Since the net stress = 0 in order to apply static equilibrium, than net force = 0, therefore

$$0 = \int_{z=0}^{b} \int_{y=0}^{t} E\varepsilon dydz$$

where •$\varepsilon = ky$ [1]

- $y = y - y_n$ (y is the distance away from the neutral axis (y_n))

Therefore,

$$0 = \int_{z=0}^{b} \int_{y=0}^{t} Ek(y - y_n)dydz$$

where $c = \int_{y=0}^{t} Ek(y - y_n)dy$

$$0 = \int_{z=0}^{b} c\,dz = cz|_{z=o}^{b} = c(b - 0) = cb$$

Plug back in $c = \int_{y=0}^{t} Ek(y - y_n)dy$

$$0 = b\int_{y=0}^{t} Ek(y - y_n)dy$$

Integrate over the y axis along the thickness of the laminated composite system

$$0 = b\int_{y=0}^{t_1} E_1k(y - y_n)dy + b\int_{y=t_1}^{t_1+t_2} E_2k(y - y_n)dy$$

$$0 = bE_1k\frac{(y - y_n)^2}{2}|_{y=0}^{t_1} + bE_2k\frac{(y - y_n)^2}{2}|_{y=t_1}^{t_1+t_2}$$

$$0 = bE_1k\left[\frac{(t_1 - y_n)^2}{2} - \frac{(0 - y_n)^2}{2}\right] + bE_2k\left[\frac{(t_1 + t_2 - y_n)^2}{2} - \frac{(t_1 - y_n)^2}{2}\right]$$

$$0 = bE_1k\left[\frac{(t_1 - y_n)^2}{2} - \frac{(y_n)^2}{2}\right] + bE_2k\left[\frac{(t_1 + t_2 - y_n)^2}{2} - \frac{(t_1 - y_n)^2}{2}\right]$$

$$0 = \frac{bE_1k}{2}[\underset{\substack{\downarrow \\ \text{Expand (i)}}}{(t_1 - y_n)^2} - (y_n)^2] + \frac{bE_2k}{2}[\underset{\substack{\downarrow \\ \text{Expand (ii)}}}{(t_1 + t_2 - y_n)^2} - \underset{\substack{\downarrow \\ \text{Expand (iii)}}}{(t_1 - y_n)^2}]$$

Expand (i) and (iii) by using binominal theorem of $(x - y)^2 = x^2 - 2xy + y^2$, therefore

$$(t_1 - y_n)^2 = {t_1}^2 - 2t_1y_n + {y_n}^2$$

Expand (ii) by using the multinomial theorem of $(a + b - c)^2 = a^2 + b^2 + c^2 + 2ab - 2bc - 2ac$, therefore

$$(t_1 + t_2 - y_n)^2 = {t_1}^2 + {t_2}^2 + {y_n}^2 + 2t_1t_2 - 2t_2y_n - 2t_1y_n$$

Therefore,

$$\begin{aligned}0 = \frac{bE_1k}{2}&[{t_1}^2 - 2t_1y_n + {y_n}^2 - (y_n)^2]\\ &+ \frac{bE_2k}{2}[{t_1}^2 + {t_2}^2 + {y_n}^2 + 2t_1t_2 - 2t_2y_n - 2t_1y_n - ({t_1}^2 - 2t_1y_n + {y_n}^2)]\end{aligned}$$

Distribute the negative sign in (iii)

$$\begin{aligned}0 = \frac{bE_1k}{2}&[{t_1}^2 - 2t_1y_n + {y_n}^2 - (y_n)^2]\\ &+ \frac{bE_2k}{2}[{t_1}^2 + {t_2}^2 + {y_n}^2 + 2t_1t_2 - 2t_2y_n - 2t_1y_n - {t_1}^2 + 2t_1y_n - {y_n}^2]\end{aligned}$$

Remove the $({y_n}^2 - {y_n}^2)$, and $({t_1}^2 - {t_1}^2)$, and $(2t_1y_n - 2t_1y_n)$ terms

$$0 = \frac{bE_1k{t_1}^2}{2} - \frac{2bE_1kt_1y_n}{2} + \frac{bE_2k{t_2}^2}{2} + \frac{2bE_2kt_1t_2}{2} - \frac{2bE_2kt_2y_n}{2}$$

$$0 = \frac{bE_1k{t_1}^2}{2} - bE_1kt_1y_n + \frac{bE_2k{t_2}^2}{2} + bE_2kt_1t_2 - bE_2kt_2y_n$$

Factor out bk

$$0 = bk\left[\frac{E_1{t_1}^2}{2} - E_1t_1y_n + \frac{E_2{t_2}^2}{2} + E_2t_1t_2 - E_2t_2y_n\right]$$

Bring bk onto the left side of the equation

$$0 = \frac{E_1{t_1}^2}{2} - E_1t_1y_n + \frac{E_2{t_2}^2}{2} + E_2t_1t_2 - E_2t_2y_n$$

Factor out y_n

$$0 = \frac{E_1{t_1}^2}{2} + y_n(-E_1t_1 - E_2t_2) + \frac{E_2{t_2}^2}{2} + E_2t_1t_2$$

$$0 = \frac{E_1{t_1}^2}{2} - y_n(E_1t_1 + E_2t_2) + \frac{E_2{t_2}^2}{2} + E_2t_1t_2$$

$$y_n(E_1t_1 + E_2t_2) = \frac{E_1{t_1}^2}{2} + \frac{E_2{t_2}^2}{2} + E_2t_1t_2$$

Solve for y_n

$$\boxed{netural\ axis = y_n = \frac{\frac{1}{2}E_1{t_1}^2 + \frac{1}{2}E_2{t_2}^2 + E_2t_1t_2}{(E_1t_1 + E_2t_2)}}$$

The neutral axis will be used to solve for the flexural stiffness and bending moment.

Solve for the flexural stiffness (EI)

Start with the second moment of area for a beam:

$I = \int_{area} y^2 \, dA1$

and where

•$Area = dA = dydz$

•$y = (y - y_n)$ (y is the distance away from the neutral axis)

Therefore,

$I = \int_{z=o}^{b} \int_{y=o}^{t} (y - y_n)^2 \, dydz$

where •z = b = width
• y = t = thickness

Therefore,

$$EI = \int_{z=o}^{b} \int_{y=o}^{t} (y - y_n)^2 \, dydz$$

where

$c = \int_0^t (y - y_n)^2 \, dy$, therefore,

$$EI = E \int_{z=o}^{b} c \, dz$$

$$EI = Ecz|_{z=o}^{b} = Ec(b - o)$$

$$EI = Ecb$$

Now plug in $c = \int_{y=0}^{t} (y - y_n)^2 \, dy$, therefore

$$EI = bE\int_{y=0}^{t}(y-y_n)^2\,dy$$

Integrate over the y axis along the thickness of the laminated composite system

$$EI = bE_1\int_{y=0}^{t_1}(y-y_n)^2\,dy + bE_2\int_{y=t_1}^{t_1+t_2}(y-y_n)^2\,dy$$

Evaluate the integral

$$EI = bE_1\frac{(y-y_n)^3}{3}\Big|_{y=o}^{t_1} + bE_1\frac{(y-y_n)^3}{3}\Big|_{y=t_1}^{t_1+t_2}$$

$$EI = \left(bE_1\frac{(t_1-y_n)^3}{3} - bE_1\frac{(0-y_n)^3}{3}\right) + \left(bE_2\frac{(t_1+t_2-y_n)^3}{3} - bE_2\frac{(t_1-y_n)^3}{3}\right)$$

$$EI = \left(bE_1\frac{(t_1-y_n)^3}{3} - bE_1\frac{(-y_n)^3}{3}\right) + \left(bE_2\frac{(t_1+t_2-y_n)^3}{3} - bE_2\frac{(t_1-y_n)^3}{3}\right)$$

$$EI = bE_1\left(\frac{(t_1-y_n)^3}{3} - \frac{(-y_n)^3}{3}\right) + bE_2\left(\frac{(t_1+h_2-y_n)^3}{3} - \frac{(t_1-y_n)^3}{3}\right)$$

$$EI = \frac{bE_1}{3}(t_1-y_n)^3 - (-y_n)^3 + \frac{bE_2}{3}(t_1+t_2-y_n)^3 - (t_1-y_n)^3$$

$$EI = \frac{bE_1}{3}[(t_1-y_n)^3 + (y_n)^3] + \frac{bE_2}{3}[(t_1+t_2-y_n)^3 - (t_1-y_n)^3]$$

↓ ↓ ↓

Expand (i) Expand (ii) Expand (iii)

Expand (i) and (iii) by using the binominal theorem of $(x-y)^3 = x^3 - 3x^2y + 3xy^2 - y^3$, I can solve

$(t_1-y_n)^3 = t_1^3 - 3{t_1}^2y_n + 3t_1{y_n}^2 - {y_n}^3$

Expand (ii) by using the multinomial theorem of

$(a+b-c)^3 = a^3 + b^3 - c^3 + 3a^2b - 3a^2c + 3b^2a - 3b^2c + 3c^2a + 3c^2b - 6abc$, I can solve

$(t_1+t_2-y_n)^3 = {t_1}^3 + {t_2}^3 - {y_n}^3 + 3{t_1}^2t_2 - 3{t_1}^2y_n + 3{t_2}^2t_1 - 3{t_2}^2y_n + 3{y_n}^2t_1 + 3{y_n}^2t_2 - 6t_1t_2y_n$

Therefore,

$$\begin{aligned} EI = {} & \frac{bE_1}{3}[t_1{}^3 - 3t_1{}^2 y_n + 3t_1 y_n{}^2 - y_n{}^3 + (y_n)^3] \\ & + \frac{bE_2}{3}[t_1{}^3 + t_2{}^3 - y_n{}^3 + 3t_1{}^2 t_2 - 3t_1{}^2 y_n + 3t_2{}^2 t_1 - 3t_2{}^2 y_n + 3y_n{}^2 t_1 + 3y_n{}^2 t_2 - 6t_1 t_2 y_n \\ & - (t_1{}^3 - 3t_1{}^2 y_n + 3t_1 y_n{}^2 - y_n{}^3)] \end{aligned}$$

Simplify by factoring out a t_1 and removing $-y_n{}^3 + (y_n)^3$terms from (i) and distributing the negative sign in (iii)

$$\begin{aligned} EI = {} & \frac{bE_1 t_1}{3}[t_1{}^2 - 3t_1 y_n + 3y_n{}^2] \\ & + \frac{bE_2}{3}[t_1{}^3 + t_2{}^3 - y_n{}^3 + 3t_1{}^2 t_2 - 3t_1{}^2 y_n + 3t_2{}^2 t_1 - 3t_2{}^2 y_n + 3y_n{}^2 t_1 \\ & + 3y_n{}^2 t_2 - 6t_1 t_2 y_n - t_1{}^3 + 3t_1{}^2 y_n - 3t_1 y_n{}^2 + y_n{}^3] \end{aligned}$$

Simplify by removing $t_1{}^3 - t_1{}^3$, $y_n{}^3 - y_n{}^3$, $3t_1{}^2 y_n - 3t_1{}^2 y_n$ and $3y_n{}^2 t_1 - 3y_n{}^2 t_1$ terms

$$EI = \frac{bE_1 t_1}{3}[t_1{}^2 - 3t_1 y_n + 3y_n{}^2] + \frac{bE_2}{3}[t_2{}^3 + 3t_1{}^2 t_2 + 3t_2{}^2 t_1 - 3t_2{}^2 y_n + 3y_n{}^2 t_2 - 6t_1 t_2 y_n]$$

Factor out an t_2 from second term

$$EI = \frac{bE_1 t_1}{3}[t_1{}^2 - 3t_1 y_n + 3y_n{}^2] + \frac{bE_2 t_2}{3}[t_2{}^2 + 3t_1{}^2 + 3t_2 t_1 - 3t_2 y_n + 3y_n{}^2 - 6t_1 y_n]$$

Combine the blue terms in the second term to simplify

$$EI = \frac{bE_1 t_1}{3}[t_1{}^2 - 3t_1 y_n + 3y_n{}^2] + \frac{bE_2 t_2}{3}[t_2{}^2 + 3t_2 t_1 - 3t_2 y_n + 3(t_1{}^2 + y_n{}^2 - 2t_1 y_n)]$$

Simply the red terms further

$$EI = \frac{bE_1 t_1}{3}[t_1{}^2 - 3t_1 y_n + 3y_n{}^2] + \frac{bE_2 t_2}{3}[t_2{}^2 + 3t_2(t_1 - y_n) + 3(t_1 - y_n)^2]$$

Distribute $\frac{1}{3}$ in both terms

$$EI = bE_1 t_1 \left[\frac{t_1{}^2}{3} - \frac{3t_1 y_n}{3} + \frac{3y_n{}^2}{3}\right] + bE_2 t_2 \left[\frac{t_2{}^2}{3} + \frac{3t_2}{3}(t_1 - y_n) + \frac{3}{3}(t_1 - y_n)^2\right]$$

Simplify,

$$EI = bE_1 t_1 \left[\frac{t_1{}^2}{3} - t_1 y_n + y_n{}^2\right] + bE_2 t_2 \left[\frac{t_2{}^2}{3} + t_2(t_1 - y_n) + (t_1 - y_n)^2\right]$$

$$\downarrow \qquad\qquad\qquad\qquad \downarrow$$

The green terms can be written in the form: $(a-b)^2 = a^2 + b^2 - 2ab$

Therefore,

$$EI = bE_1 t_1 \left[\left(\frac{t_1}{2} - y_n\right)^2\right] + bE_2\, t_2 \left[\left(\frac{t_2}{2} + (t_1 - y_n)\ \right)^2\right]$$

However, $\frac{{t_1}^2}{12}$ needs to be added to the first term and $\frac{{t_2}^2}{12}$ needs to be added to the second term in order to obtain the original function

$$EI = bE_1 t_1 \left[\frac{{t_1}^2}{12} + \left(\frac{t_1}{2} - y_n\right)^2\right] + bE_2\, t_2 \left[\frac{{t_2}^2}{12} + \left(\frac{t_2}{2} + (t_1 - y_n)\right)^2\right]$$

where

$$netural\ axis: y_n = \frac{\frac{1}{2}E_1{t_1}^2 + \frac{1}{2}E_2{t_2}^2 + E_2 t_1 t_2}{(E_1 t_1 + E_2 t_2)}$$

Therefore EI equation reduces to:

$$\boxed{EI = E_1 \frac{b{t_1}^3}{12} + E_2 \frac{b{t_2}^3}{12} + \frac{bE_1 E_2 t_1 t_2 (t_1 + t_2)^2}{4(E_1 t_1 + E_2 t_2)}}$$

The equation above is the flexural stiffness for a laminated composite.

Solve for the bending moment (M)

Bending stress can be expressed as the following[1]:

$$\sigma = \frac{My}{I}$$

Solve for M

$$M = \frac{\sigma I}{y}$$

where

$\mathrm{I} = \int \mathrm{y}^2 \mathrm{dA}$ (Second moment of area for a beam)

Therefore,

$$M = \int \frac{\sigma y^2}{y} dA$$

This reduces to

$$M = \int \sigma y \, dA$$

M needs to be evaluated with respect to the thickness (y axis) and width (z axis). This therefore, requires two integrals:

$$M = \int_{z=o}^{b} \int_{y=o}^{t_1+t_2} \sigma(y,z)(y-y_n) \, dydz$$

Let $c = \int_{y=o}^{t_1+t_2} \sigma(y,z)(y-y_n) \, dy$, therefore

$$M = \int_{z=o}^{b} c \, dz$$

$$M = cz|_{z=0}^{b} = c(b-0) = cb$$

Now plug in $c = \int_{y=o}^{t_1+t_2} \sigma(y,z)(y-y_n) \, dy$

$$M = b \int_{y=o}^{t_1+t_2} \sigma(y,z)(y-y_n) \, dy$$

where $\sigma = E\varepsilon$

$$M = b\int_{y=o}^{t_1} E_1\varepsilon_1(y-y_n)\,dy + b\int_{y=t_1}^{t_1+t_2} E_2\varepsilon_2(y-y_n)\,dy$$

$$M = bE_1\varepsilon_1\frac{(y-y_n)^2}{2}\Big|_{y=0}^{t_1} + bE_2\varepsilon_2\frac{(y-y_n)^2}{2}\Big|_{y=t_1}^{t_1+t_2}$$

$$M = bE_1\varepsilon_1\left(\frac{(t_1-y_n)^2}{2} - \frac{(0-y_n)^2}{2}\right) + bE_2\varepsilon_2\left[\frac{(t_1+t_2-y_n)^2}{2} - \frac{(t_1-y_n)^2}{2}\right]$$

$$M = bE_1\varepsilon_1\left[\frac{(t_1-y_n)^2}{2} - \frac{{y_n}^2}{2}\right] + bE_2\varepsilon_2\left[\frac{(t_1+t_2-y_n)^2}{2} - \frac{(t_1-y_n)^2}{2}\right]$$

$$M = \tfrac{bE_1\varepsilon_1}{2}[\underbrace{(t_1-y_n)^2}_{\downarrow} - {y_n}^2] + \tfrac{bE_2\varepsilon_2}{2}[\underbrace{(t_1+t_2-y_n)^2}_{\downarrow} - \underbrace{(t_1-y_n)^2}_{\downarrow}]$$

Expand (i) Expand (ii) Expand (iii)

Expand (i) and (iii) by using binominal theorem of $(x-y)^2 = x^2 - 2xy + y^2$, therefore

$$(t_1-y_n)^2 = {t_1}^2 - 2t_1y_n + {y_n}^2$$

Expand (ii) by using the multinomial theorem of $(a+b-c)^2 = a^2 + b^2 + c^2 + 2ab - 2bc - 2ac$, therefore

$$(t_1+t_2-y_n)^2 = {t_1}^2 + {t_2}^2 + {y_n}^2 + 2t_1t_2 - 2t_2y_n - 2t_1y_n$$

Therefore,

$$M = \frac{bE_1\varepsilon_1}{2}[{t_1}^2 - 2t_1y_n + {y_n}^2 - {y_n}^2] + \frac{bE_2\varepsilon_2}{2}[({t_1}^2 + {t_2}^2 + {y_n}^2 + 2t_1t_2 - 2t_2y_n - 2t_1y_n) - ({t_1}^2 - 2t_1y_n + {y_n}^2)]$$

Distribute the negative sign in (iii)

$$M = \frac{bE_1\varepsilon_1}{2}[{t_1}^2 - 2t_1y_n + {y_n}^2 - {y_n}^2] + \frac{bE_2\varepsilon_2}{2}[{t_1}^2 + {t_2}^2 + {y_n}^2 + 2t_1t_2 - 2t_2y_n - 2t_1y_n - {t_1}^2 + 2t_1y_n - {y_n}^2]$$

Simply by removing ${t_1}^2 - {t_1}^2$, ${y_n}^2 - {y_n}^2$, and $2t_1y_n - 2t_1y_n$, therefore

$$M = \frac{bE_1\varepsilon_1}{2}[t_1{}^2 - 2t_1y_n] + \frac{bE_2\varepsilon_2}{2}[t_2{}^2 + 2t_1t_2 - 2t_2y_n]$$

Distribute$E_1\varepsilon_1\ and\ E_2\varepsilon_2$

$$M = \frac{b}{2}[E_1\varepsilon_1t_1{}^2 - 2E_1\varepsilon_1t_1y_n] + \frac{b}{2}\left[E_2\varepsilon_2t_2{}^2 + 2E_2\varepsilon_2t_1t_2 - 2E_2\varepsilon_2t_2y_n\right]$$

Combine (i) with (ii) and (iii)

$$M = \frac{b}{2}\left[E_1\varepsilon_1t_1{}^2 - 2E_1\varepsilon_1t_1y_n + E_2\varepsilon_2t_2{}^2 + 2E_2\varepsilon_2t_1t_2 - 2E_2\varepsilon_2t_2y_n\right]$$

Combine the y_n terms

$$M = \frac{b}{2}\left[E_1\varepsilon_1t_1{}^2 + E_2\varepsilon_2t_2{}^2 + 2E_2\varepsilon_2t_1t_2 - 2(\,E_1\varepsilon_1t_1 + E_2\varepsilon_2t_2)y_n\right]$$

where $y_n = \frac{\frac{E_1t_1{}^2}{2} + \frac{E_2t_2{}^2}{2} + E_2t_1t_2}{(E_1t_1 + E_2t_2)}$,

Therefore, M reduces to

$$\boxed{M = \frac{bE_1E_2\left(\varepsilon_{f1} - \varepsilon_{f2}\right)t_1t_2(t_1 + t_2)}{2(E_1t_1 + E_2t_2)}}$$

This is the bending moment for the laminated composite

When combining the EI (flexural stiffness) and M (bending moment) terms I obtain the following k (curvature) value[2, 3]:

$$\boxed{k = \frac{1}{R} = \frac{M}{EI} = \frac{6E_1E_2t_1t_2(t_1 + t_2)\left(\varepsilon_{f1} - \varepsilon_{f2}\right)}{(E_1t_1{}^2)^2 + (E_2t_2{}^2)^2 + 2E_1E_2t_1t_2(2t_1{}^2 + 3t_1t_2 + 2t_2{}^2)}}$$

Let

$\varepsilon_{f1} = R_{fixing_1} * \varepsilon_{deformation}$

$\varepsilon_{f2} = R_{fixing_2} * \varepsilon_{deformation}$

where

$R_{fixing_1} = fixing\ ratio\ from\ RPSM = \frac{\varepsilon_u}{\varepsilon_m}$ (see Section 5.2.4 and Table 5-1)

$\varepsilon_{deformation} = total\ deformation\ induced\ on\ system$

12.1 REFERENCES

1. Budynas, R. G., *Advanced Strength and Applied Stress Analysis*. WCB McGraw-Hill: 1999; Vol. 2.

2. Clyne, T. W., Residual stresses in surface coatings and their effects on interfacial debonding. *Interfacial Effects in Particulate, Fibrous and Layered Composite Materials* 1996, 116-, 307-330.

3. Darling, R. B., Introduction to Microelectromechanical Systems: Thermal Sensors and Actuators. 2011.

VITA

NAME OF AUTHOR: Erika D. Rodriguez

PLACE OF BIRTH: Fresno, CA, USA

DATE OF BIRTH: June 16, 1984

EDUCATION:

B.S. in Engineering Science, Smith College (2006)

M.S. Mechanical and Aerospace Engineering, Syracuse University (2008)

Ph.D. Mechanical and Aerospace Engineering, Syracuse University (2012)

PUBLICATIONS:

Erika D. Rodriguez, Patrick T. Mather. "Laminated Anisotropic Shape Memory Elastomeric Composites (A-SMEC): Fabrication and Mechanically Activated Shape Change (MASC)," Macromolecular Chemistry and Physics. (In Preparation)

Erika D. Rodriguez, Derek D. Weed, Patrick T. Mather. "Fabrication and Mechanical Testing of Anisotropic Shape Memory Elastomeric Composites (A-SMEC)," Macromolecular Chemistry and Physics. (In Preparation)

Erika D. Rodriguez, Sabrina M. Kowalski, Patrick T. Mather. "Transparent Self Healing Coatings via Shape Memory Assisted Self Healing (SMASH)," ACS Macro Letters. (In Preparation)

Erika D. Rodriguez and Patrick T. Mather. "Material Techniques and Polymeric Systems in Art Restoration," Accounts of Chemical Research (In Preparation)

Q. Ge, X. Luo, E.D. Rodriguez, X. Zhang, P.T. Mather, M.L. Dunn, and H. Qi, "Thermomechanical Behavior of Shape Memory Elastomeric Composites," J. Mech. Phys. Solids, **60**, 67-83 (2011).

Erika D. Rodriguez, X. Luo, and P.T. Mather, "Linear and Crosslinked Poly (ε-Caprolactone) Polymers for Shape Memory Assisted Self-Healing (SMASH)," *ACS Applied Materials and Interfaces* ASAP (2011).

Steven H. Collicott and E. Rodriguez, "Mass Center Anomalies from Asymmetric Propellant Positions in Spacecraft," 44th AIAA Aerospace Sciences Meeting and Exhibit, Reno, NV, January 2006.